

https://dspace.org/

The structure of the crust, the uppermost mantle, and the mantle transition zone beneath Madagascar

Andriampenomanana Ny Ony, Elamahalala Fenitra Sy Tanjona

2017

https://hdl.handle.net/10539/24986

Andriampenomanana Ny Ony, Elamahalala Fenitra Sy Tanjona (2017) The structure of the crust, the uppermost mantle, and the mantle transition zone beneath Madagascar, University of the Witwatersrand, Johannesburg, <http://hdl.handle.net/10539/24986>

Downloaded from a DSpace repository. https://dspace.org/

The structure of the crust, the uppermost mantle, and the mantle transition zone beneath Madagascar

by

E.F.S.T. Andriampenomanana Ny Ony

A thesis submitted to the Faculty of Science, University of the Witwatersrand, Johannesburg, in fulfillment of the requirements for the degree of Doctor of Philosophy.

October 2017

Declaration

I declare that this thesis is my own, unaided work. It is being submitted in fulfillment of the requirements for the Degree of Doctor of Philosophy in the University of the Witwatersrand, Johannesburg. It has not been submitted before for any degree or examination in any other University.

_____

E. F. S. T. Andriampenomanana Ny Ony

This 25th day of October 2017

Abstract

Since the arc assembly and continental collision of the East African Orogen some 640 million years ago, Madagascar has gone through several geodynamic and tectonic episodes that have formed and subsequently modified its lithosphere. This thesis aims to investigate the structure of the crust, the uppermost mantle, and the mantle transition zone beneath Madagascar to gain insights into the relationship between present-day lithosphere structure and tectonic evolution, and to evaluate candidate models for the origin of the Cenozoic intraplate volcanism. To address these issues, local, regional, and teleseismic events recorded by several temporary seismic networks; the MAdagascar-COmoros-MOzambique (MACOMO), the SEismological signatures in the Lithosphere/Asthenosphere system of SOuthern MAdagascar (SELASOMA), and the Réunion Hotspot and Upper Mantle – Réunions Unterer Mantel (RHUM-RUM) were used to complement the seismic events recorded by the permanent seismic stations in Madagascar. The different methods used and the primary results of this study are explained in each section of this thesis.

In the first part of this thesis, crustal and uppermost mantle structure beneath Madagascar was studied by analyzing receiver functions using an *H*-κ stacking technique and a joint inversion with Rayleigh-wave phase-velocity measurements. Results reflect the eastward and northward progressive development of the western sedimentary basins of Madagascar. The thickness of the Malagasy crust ranges between 18 km and 46 km. The thinnest crust (18-36 km thick) is located beneath the western basins and it is due to the Mesozoic rifting of Madagascar from eastern Africa. The slight thinning of the crust (31-36 km thick) along the east coast may have been caused by crustal uplift and erosion when Madagascar moved over the Marion hotspot and India broke away from it. The parameters describing the crustal structure of Archean and Proterozoic terranes, including thickness, Poisson's ratio, average shear-wave velocity, thickness of mafic lower crust, show little evidence of secular variation. Slow shear-wave velocity of the uppermost mantle (4.2-4.3 km/s) are observed beneath the northern tip, central part and southwestern region of the island, which encompass major Cenozoic volcanic provinces in Madagascar.

The second part of the thesis describes a seismic tomography study that determines the lateral variation of *Pn*-wave velocity and anisotropy within the uppermost mantle beneath Madagascar. Results show an average uppermost mantle *Pn*-velocity of 8.1 km/s. However, zones of relatively low-*Pn*-velocity (~7.9 km/s) are found beneath the Cenozoic volcanic provinces in the northern, central, and southwestern region of the island. These low-*Pn*-velocity zones are attributed to thermal anomalies that are associated with upwelling of hot mantle materials that gave rise to the Cenozoic volcanism. The direction of *Pn* anisotropy shows a dominant NW-SE direction of fast-polarization in the northern region and around the Ranostara shear zone, in the south-central Madagascar. The anisotropy in the uppermost mantle beneath these regions aligns with the existing geological framework, *e.g.* volcanic complex and shear zones, and can be attributed to a fossil anisotropy. The *Pn* anisotropy in the southwestern region, around the Morondava basin, is E-W to NE-SW-oriented. It can be attributed either to the mantle flow from plate motion, the African superplume, or the Mesozoic rifting from Africa. Results from this study do not show any substantial evidence of the formation of a diffuse boundary of the Lwandle plate, cutting through the central region of Madagascar. Station static delays reflect the significant variation in the Moho depth beneath the island.

In the third part of the thesis, the thickness of the mantle transition zone beneath Madagascar, which is sensitive to the surrounding temperature variation, has been estimated by stacking receiver functions. Single-station and common-conversion-point stacking procedures show no detectable thinning of the mantle transition zone and thus no evidence for a thermal anomaly in the mantle under Madagascar that extends as deep as the mantle transition zone. Therefore, this study supports an upper mantle origin for the Cenozoic volcanism. However, the resolution of the study is not sufficient to rule out the presence of a narrow thermal anomaly as might arise from a plume tail.

Overall, the findings in this research are broadly consistent with the crustal and upper mantle structure of Madagascar determined by previous studies, but provides significantly greater detail with regard to the crustal and uppermost mantle structure as more seismic stations were used.

Dedication

In memory of my brother,

Mahery Samisoa Lala Andriampenomanana,

1977 – 2016.

Acknowledgements

First and foremost I would like to give my highest thanks to God.

Financial assistance for this PhD program was provided by the AfricaArray program and the National Science Foundation (NSF) in the USA through grants EAR-0838426 and 0838387. I am indebted to these organizations for having provided me with the financial support. Without this support this research would have been impossible.

To my supervisors, Prof. Raymond Durrheim and Prof. Andrew Nyblade, I would like to express my deepest gratitude and appreciation for their invaluable guidance. I would also like to thank Prof. Michael Wysession for providing valuable comments in this research, and Prof. Gérard Rambolamanana and the Institut et Observatoire de Géophysique d'Antananarivo (IOGA) - Université d'Antananarivo (Madagascar) for giving me the opportunity to pursue my Doctoral studies.

I am very grateful to the field team who assisted with the installation, servicing, and demobilization of seismic stations for the MAdagascar-COmoros-MOzambique (MACOMO) project, including Dr Patrick Shore, Dr Ghassan Aleqabi, Dr Martin Pratt, Ms Tsiriandrimanana Rakotondraibe and Mr Rina Ramarolahy. I am also thankful for the help and constructive comments of Dr Elisa Rindraharisaona, Dr Andriamiranto Raveloson, Dr Erica Emry, Dr Ahmed Hosny Ali and Dr John Paul O'Donnell.

Special thanks to Prof. Charles Ammon, Prof Jordi Julià, Prof. Thomas Hearn, and Prof. Thomas Owens for their codes which I made extensive use in this research. Most of figures in this thesis have been produced thanks to the Generic Mapping Tools (GMT; Wessel and Smith, 1998).

My sincere thanks to the staff in the School of Geosciences of the University of the Witwatersrand (South Africa), especially the Head of School Prof. Roger Gibson and the administrative assistants Mrs Sharon Ellis, Mrs Rayline Karim and

Mrs Lenah Mtiyane, for having provided assistance and resources for the time I spent in South Africa as a PhD student. Also, I would like to take this opportunity to express my appreciation to my friends in the AfricaArray group of this School for making my stay in South Africa better. I am also grateful to the staff of the Department of Geosciences at Pennsylvania State University (USA), especially the administrative assistants, Mrs Antonia Mooney and Mrs Barbara Peragine, for having provided assistance for the time I spent in the USA as a visiting scholar. I would also like to thank the team of Deike 444 at the Department of Geosciences at Penn State University, with whom I shared knowledge and problems concerning our research during our weekly group meeting. I would also like to express my gratitude to Mrs Michele Chernega for hosting me during my stay in State College (Pennsylvania, USA), and my friends Dr Atefeh Mohammadpour, Dr Carol Destro, Jocely Souza, Laiz Fiorilli for making it memorable.

I would like to thank Prof. Frederik Tilmann, Prof. Karin Sigloch and Prof. Guilhem Barruol for giving me the access to use seismic data from the SEismological signatures in the Lithosphere/Asthenosphere system of SOuthern MAdagascar (SELASOMA) and the Réunion Hotspot and Upper Mantle – Réunions Unterer Mantel (RHUM-RUM) seismic networks. Also, IRIS (FDSN code: II, Scripps Institution of Oceanography, 1986), AFRICAARRAY (FDSN code: AF, Penn State University, 2004), GEOFON (FDSN code: GE, GEOFON Data Centre, 1993) and GEOSCOPE (FDSN code: G, Institut de Physique du Globe de Paris (IPGP) & Ecole et Observatoire des Sciences de la Terre de Strasbourg (EOST), 1982) for additional seismic data.

Finally, I would like to thank my family and friends for their constant support and patience with my studies.

Contents

Declaration ... **iii**
Abstract ... **v**
Dedication ... **vii**
Acknowledgements ... **ix**
Contents ... **xi**
List of Figures ... **xv**
List of Tables ... **xviii**
List of Acronyms ... **xix**
Chapter 1 ... **1**
General introduction ... **1**
1.1 Introduction ... 1
1.2 Motivation and Objectives ... 3
1.3 Literature review: Geology of Madagascar ... 4
1.3.1 Madagascar within Gondwana ... 5
1.3.2 Rifting from Africa ... 6
1.3.3 Rifting from India ... 7
1.3.4 Sedimentary basins ... 10
1.3.5 Precambrian basement ... 13
1.3.6 Volcanism ... 15
1.3.7 Shear zones of Madagascar ... 17
1.3.8 Evidence of Neogene uplift ... 19
1.4 Literature review: Previous geophysical studies ... 20
1.4.1 Seismicity and seismotectonics of Madagascar ... 20
1.4.2 Crustal thickness from previous studies ... 21
1.4.3 Mantle structure from previous studies ... 23
Chapter 2 ... **25**
Data and Methodology ... **25**
2.1 Introduction ... 25
2.2 Data acquisition ... 29
2.2.1 Permanent broadband seismic stations ... 30
2.2.2 Temporary broadband seismic stations: MACOMO project ... 30
2.2.3 Temporary broadband seismic stations: SELASOMA project ... 36
2.2.4 Temporary broadband seismic stations: RHUM-RUM project ... 36
2.2.5 Summary ... 37
2.3 Isolation of receiver functions ... 39
2.3.1 Overview of receiver function ... 39
2.3.2 Theory ... 41
2.3.3 Data preparation ... 42
2.3.4 Deconvolution of receiver functions ... 50
2.3.5 Application and data selection ... 53
2.4 Crustal thickness and *Vp/Vs* ratio from the *H-κ* stacking method ... 56
2.4.1 The *H-κ* stacking procedure of Zhu and Kanamori (2000) ... 56
2.4.2 Estimation of uncertainty from the bootstrapping technique ... 58

2.4.3 Error ellipse estimation 60
2.4.4 Poisson's ratio and *Vp/Vs* ratio 61
2.4.5 Application 62
2.5 Crustal structure from the joint inversion of receiver functions and the dispersion of Rayleigh-wave phase velocities 66
2.5.1 Independent inversion of receiver function and surface wave dispersion measurements 66
2.5.2 Criteria for the joint inversion of receiver function and surface wave dispersion measurements 69
2.5.3 Linearized inversion procedure 70
2.5.4 Application 72
2.5.5 Uncertainties estimation 79
2.6 Locating local earthquakes 81
2.6.1 Picking arrivals 81
2.6.2 Locating earthquakes with the *HYPOELLIPSE* program 82
2.6.3 Application 84
2.7 *Pn* tomographic imaging of the uppermost mantle 88
2.7.1 *Pn* waves 88
2.7.2 Seismic anisotropy 89
2.7.3 *Pn* tomography 90
2.7.4 Application 95
2.7.5 Regularization of the velocity-anisotropy trade-off 99
2.7.6 Error estimation 101
2.7.7 Resolution analysis 103
2.8 Receiver function imaging of the mantle transition zone 106
2.8.1 The Clapeyron slope 107
2.8.2 Transition zone discontinuities 107
2.8.3 Topography on the transition zone discontinuities 109
2.8.4 Isolation of receiver functions 110
2.8.5 Depth migration of receiver functions and moveout correction 111
2.8.6 Stacking procedure 112
2.8.7 Application: Single-station stacking 113
2.8.8 Application: Common-conversion point stacking 114
2.8.9 Error estimation 116
Chapter 3 119
The structure of the crust and uppermost mantle beneath Madagascar from receiver function analysis 119
3.1 Introduction 119
3.2 Results 121
3.2.1 *H-κ* stacking method 121
3.2.2 Join inversion method 122
3.2.3 Summary of estimates from *H-κ* stacking and joint-inversion 126
3.2.4 Comparison of crustal thickness estimates from *H-κ* stacking and the joint-inversion method 130
3.2.5 Structure of the sedimentary basin 131
3.2.6 Structure of the Paleoarchean to Mesoarchean terrane 134
3.2.7 Structure of the Neoarchean terrane 134
3.2.8 Structure of the Paleoproterozoic terrane 135

3.2.9 Structure of the Mesoproterozoic terrane....136
3.2.10 Structure of the Neoproterozoic terrane....136
3.3 Discussion....137
3.3.1 The western sedimentary basin: opening and seismic velocity....138
3.3.2 Crustal stretching and thinning beneath the western sedimentary basin of Madagascar....139
3.3.3 Crustal thinning in the eastern coast of Madagascar....140
3.3.4 Evidence of little secular variation of the Precambrian crust....140
3.3.5 Crustal lithologies of Madagascar....142
3.3.6 Airy model of isostatic equilibrium....143
3.3.7 Evidence of thermal anomalies in the uppermost mantle....144
3.4 Conclusion....145
Chapter 4....147
Uppermost mantle velocity and anisotropy beneath Madagascar from *Pn* tomography....147
4.1 Introduction....147
4.2 Results....149
4.2.1 *2D*-isotropic inversion....149
4.2.2 *2D*-anisotropic inversion....151
4.2.3 Low-*Pn*-velocity regions in the uppermost mantle....154
4.2.4 *Pn* anisotropy fast-polarization directions....155
4.2.5 Station static delays....156
4.3 Discussion....159
4.3.1 Low-*Pn*-velocity zones: focus of upwelling of hot mantle material and Cenozoic intraplate volcanism....159
4.3.2 Seismic anisotropy signatures and tectonic framework....161
4.3.3 Implication to the formation of the Lwandle plate....166
4.3.4 Low-*Pn*-velocity in the Antongil craton....167
4.3.5 Crustal structure from static delays....167
4.4 Conclusion....168
Chapter 5....171
Receiver function imaging of the mantle transition zone beneath Madagascar....171
5.1 Introduction....171
5.2 Results....172
5.2.1 Single-station stacking....173
5.2.2 Common-conversion point stacking....176
5.3 Discussion....183
5.3.1 The mantle transition zone thickness....183
5.3.2 Implication to the thermal anomaly beneath Madagascar....184
5.4 Conclusion....185
Chapter 6....187
General discussion and conclusion....187
6.1 Introduction....187
6.2 General discussion....188
6.2.1 Thickness of the crust beneath Madagascar....188
6.2.2 Crustal lithologies of Madagascar....190
6.2.3 Evidence of little secular variation from seismic properties....191

6.2.4 Structure of the western sedimentary basin of Madagascar.....192
6.2.5 Thermal anomalies and origin of the Cenozoic intraplate volcanism.193
6.2.6 Seismic anisotropy in the uppermost mantle beneath Madagascar.....195
6.2.7 Island uplift: evidence of thermal buoyancy.....198
6.3 General conclusion.....198
6.3.1 Crustal structure beneath Madagascar 199
6.3.2 *Pn* velocity and anisotropy: origin of the Cenozoic volcanism and tectonic framework.....201
6.4 Recommendations for future studies.....202
References 203
Appendices.....217
Appendix A 218
Appendix B 239
Appendix C 244
Appendix D 255
Appendix E 276
Appendix F.....290

List of Figures

Figure 1.1: Reconstruction of Gondwana at the end of Neoproterozoic.....6

Figure 1.2: Map showing the current location of Madagascar, the Davie Ridge, and the Somali and Mozambique basins.....7

Figure 1.3: Separation of Madagascar from surrounding subcontinents 8

Figure 1.4: A simplified geologic map of Madagascar.....9

Figure 1.5: Formation of the sedimentary basin of Madagascar.....11

Figure 1.6: An example of lavakas (erosional gullies) 20

Figure 2.1: Propagation of seismic waves.....26

Figure 2.2: Three-component seismograms.....27

Figure 2.3: Response curves of different types of seismometers.....28

Figure 2.4: Installation of the seismic station ZOBE in Ankazobe.....32

Figure 2.5: A sketch showing an operational MACOMO station.....32

Figure 2.6: Myself and Tsiriandrimanana Rakotondraibe servicing the seismic station AMPY in Ampanihy 33

Figure 2.7: Our truck getting stuck during the servicing trip in Mandabe.....34

Figure 2.8: Histogram showing the data collected for the MACOMO project.....35

Figure 2.9: Location of the permanent and temporary broadband stations.....37

Figure 2.10: Synthetic radial receiver function waveform. Corresponding seismic ray diagram of *P-to-S* converted phase 40

Figure 2.11: Predicted travel times of P-wave 44

Figure 2.12: Predicted travel times of different seismic phases.....44

Figure 2.13: *P*-arrival adjustment for the seismic event 45

Figure 2.14: Transformation of ZNE to ZRT coordinate system.....47

Figure 2.15: Preprocessed waveforms for the seismic event on 08th August 2007, 17:04:58 UTC in Java, Indonesia, with Magnitude 7.4 48

Figure 2.16: Ray diagram showing two adjacent impinging seismic rays.....49

Figure 2.17: The water-level deconvolution technique.....52

Figure 2.18: Distribution of 143 earthquakes 54

Figure 2.19: Receiver functions from a permanent (ABPO) and a temporary (LAHA) seismic station 55

Figure 2.20: *H*-κ stacking results for seismic station VINA 64

Figure 2.21: Dispersion curves of Rayleigh-wave phase-velocity for the station VINA.....73

Figure 2.22: Group of radial receiver functions computed with Gaussian 1.0 and 2.5 75

Figure 2.23: An example of joint inversion of radial receiver functions and Rayleigh-wave phase-velocity dispersion curve 77

Figure 2.24: Joint inversion of Rayleigh wave phase velocities and receiver functions for station VINA 78

Figure 2.25: Example of shear-wave velocity structure 80

Figure 2.26: A plot of the 81 shear-wave velocity models 81

Figure 2.27: An example of *P*-arrivals picking, using Antelope 86

Figure 2.28: Distribution of 647 regional earthquakes considered for the study 87

Figure 2.29: Schematic diagram of *Pn* propagation 88

Figure 2.30: Map showing the 47 seismic stations and 647 regional seismic events before the selection criteria 97

Figure 2.31: All *Pn* arrivals selected for the inversion 98

Figure 2.32: Trade-off between velocity-damping and data fitting coefficients 100

Figure 2.33: Plot of the velocity-to-anisotropy trade-off and the anisotropy-to-velocity trade-off curves 101

Figure 2.34: Standard errors of the velocity and anisotropy magnitude 102

Figure 2.35: Recovered checkerboard *Pn* velocities from the tomographic inversions 104

Figure 2.36: Recovered checkerboard *Pn* anisotropy values from the tomographic inversions 105

Figure 2.37: A sketch showing the effect of the Clapeyron slope to the topography of the 410 km and 660 km discontinuities around a hot or cold region 110

Figure 2.38: A stacked trace from a single-station stacking 113

Figure 2.39: Map showing the theoretical *Ps* conversion points at depths 410 km and 660 km 114

Figure 2.40: A stacked trace from a common-conversion point stacking 115

Figure 2.41: Stacked traces obtained from two different 1D reference models 116

Figure 2.42: An example of stacked trace with the 95% confidence bound 117

Figure 2.43: Example of vertical error measurement from the 95% confidence bounds for the station ANLA 118

Figure 3.1: Contour maps of the crustal thickness and Poisson's ratio 122

Figure 3.2: Maps showing the thickness and the average shear-wave velocity of the sedimentary basin 124

Figure 3.3: Contour maps showing the crustal thickness, the average crustal shear-wave velocity, and the average uppermost mantle shear-wave velocity 125

Figure 3.4: Crustal thickness values estimated from *H-κ* stacking versus the joint-inversion method 130

Figure 3.5: The crustal velocity profiles for seismic stations grouped by geological region.....132

Figure 3.6: Elevation of Madagascar along the profile A-B. Crustal thickness values for seismic stations along the same profile 144

Figure 4.1: Uppermost mantle isotropic *Pn*-velocity variations 150

Figure 4.2: Uppermost mantle *Pn*-velocity variations accounting for anisotropy152

Figure 4.3: *Pn*-velocity anisotropy of the uppermost mantle obtained from *Pn* travel-time tomography.....153

Figure 4.4: Elevation of Madagascar along the profile A-B. *Pn* velocity values along the same profile 155

Figure 4.5: Station static delay times obtained from the inversion.....158

Figure 4.6: Map showing the lateral variation of *Pn* velocity, *Pn* anisotropy, and *SKS* shear-wave splitting in the northern part of Madagascar 164

Figure 4.7: Map showing the lateral variation of *Pn* velocity, *Pn* anisotropy, and *SKS* shear-wave splitting in the south-central part of Madagascar 165

Figure 5.1: Single-station stacking of *P* receiver functions 175

Figure 5.2: Map of Madagascar showing the location of Cretaceous and Cenozoic volcanic provinces.....178

Figure 5.3: Results from common-conversion point stacking of *P* receiver function profiles along profiles A-A' and A1-A1' 179

Figure 5.4: Results from common-conversion point stacking of *P* receiver function profiles along profiles B-B' and B1-B1' 180

Figure 5.5: Results from common-conversion point stacking of *P* receiver function profiles along profiles C-C' and C1-C1' 181

Figure 5.6: Results from common-conversion point stacking of *P* receiver function profiles along profiles D-D' and D1-D1' 182

Figure A.1: Receiver functions for all stations 220

Box A.1. This appendix shows how the bootstrapping procedure works. 227

Figure A.2: H-κ stacking results from all the considered seismic stations 229

Figure A.3: Joint inversion results from all stations used in the study. 234

Figure C.1: Single station stacking of *P* receiver functions observed for all seismic station for Gaussian factor 0.5 and 1.0.....244

Figure C.2: Single station stacking of *P* receiver functions observed for a few nodes for Gaussian factor 0.5.....254

List of Tables

Table 2.1: Permanent and temporary broadband seismic stations 38

Table 2.2: *H-κ* stacking results from *Vp* of 6.3 km/s, 6.5 km/s, and 6.8 km/s and their average 65

Table 2.3: Quality of earthquake location in *HYPOELLIPSE* based on the values of SEH and SEZ. 84

Table 2.4: Velocity structure model used for locating local earthquakes in the program *HYPOELLIPSE*.....85

Table 3.1: Typical shear-wave velocity of sedimentary rocks.....123

Table 3.2: Summary of crustal structure for stations located in the Phanerozoic sedimentary basins 127

Table 3. 3: Summary of crustal structure for stations located within Precambrian terranes 128

Table 4.1: Static station, number of event recorded per station, delay times, and errors. 157

Table 5.1: Summary of mantle transition zone thicknesses for the single-station stacking of *P* receiver functions 174

Table 5.2: Summary of mantle transition zone thicknesses for the common-conversion point stacking of *P* receiver functions 177

Table A.1: List of teleseismic events used to compute receiver functions. 218

Table B.1: List of local and regional Earthquakes 239

List of Acronyms

CEA – Commissariat à l'Energie Atomique et aux Energies Alternatives.

CMAP – Central Madagascar Alkaline Province.

DASE – Département d'Analyse et Surveillance de l'environnement du CEA.

DMC – Data Management Center.

EAO – East African Orogen.

EAR – East African Rift.

FDSN – Federation of Digital Seismograph Networks.

IOGA – Institut et Observatoire de Géophysique d'Antananarivo.

IRIS – Incorporated Research Institutions for Seismology.

LPO - Lattice-Preferred Orientation.

LSQR – Least Squares QR.

LVZ – Low Velocity Zone.

MACOMO – Madagascar Comoros Mozambique.

NMAP – Northern Madagascar Alkaline Province.

OBS – Ocean-Bottom Seismometer.

PASSCAL – Portable Array Seismic Studies of the Continental Lithosphere.

RHUM-RUM – Réunion Hotspot and Upper Mantle – Réunions Unterer Mantel.

RMS – Root Mean Square.

SELASOMA – Seismological Signatures in the Lithosphere/Asthenosphere system of Southern Madagascar.

SMAP – Southern Madagascar Alkaline Province.

SNR – Signal-to-Noise Ratio.

SPO – Shape-Preferred Orientation.

s.p.s – samples per second.

WDC – Western Dharwar Craton.

Chapter 1

General introduction

1.1 Introduction

Madagascar displays 2.5 billion years of the Earth's history (Collins, 2000). The lithosphere of the island was first reworked during the Neoproterozoic arc assembly and continental collision of the East African Orogen (EAO) (Stern, 1994; Collins, 2000). This is followed by the Cambrian amalgamation of Gondwana in which the crust that form the present-day Madagascar was situated at the suture of East and West Gondwana (Collins, 2000; 2006). The process that led to the isolation of the island began with the Mesozoic rifting of the East Gondwana plate (Australia-Antarctica-Seychelle-India-Madagascar) from Africa, which was followed by a sequence of break-aways from Antarctica, Australia, Seychelles, and India (*e.g.* Torsvik et al., 1998; Piqué, 1999a; Raval and Veeraswamy, 2003). The succession of rifting events was believed to be the cause of massive eruptions of tholeiitic-basaltic lavas that occurred mostly along the coastal perimeter of the island (*e.g.* Schlich, 1975; Norton and Sclater, 1979; Mahoney et al., 1991). Madagascar became an island by the end of the Cretaceous (*ca.* 85 Ma) and has since remained tectonically stable. However, volcanic activities took place around the northern, central, and southern regions of the island during the Cenozoic, precisely from Neogene to Quaternary (<1 Ma), primarily erupting alkali basalt lavas.

Therefore, Madagascar offers opportunities to understand the structure and evolution of the continental lithosphere due to complex tectonic events such as the formation of basin margin, continental break-up and rifting, influence of plume to the lithosphere, and the mechanism resulting in the intraplate volcanism.

This thesis presents separate studies of the crustal structure, the uppermost mantle *Pn* velocity and anisotropy, and the mantle transition zone thickness beneath Madagascar by analyzing seismic waves generated by local, regional, and distant earthquakes. For the first project, structural responses beneath seismic stations, or "receiver functions", were extracted and jointly inverted with surface wave (Rayleigh waves) phase-velocity dispersion measurements to constrain crustal structure beneath the recording station. The second project uses the travel-time of *Pn* waves to tomographically image the lateral variations of seismic velocity and seismic anisotropy in the uppermost mantle. The last project carries out receiver function stacking procedures in order to estimate the thickness of the mantle transition zone.

This introductory chapter states the problems to be addressed and the main goals of this research. Also, I present a brief literature review of the geology of Madagascar and previous geophysical studies that have been conducted there. Since the three main projects of this thesis are separated into chapters but investigate the same tectonic region, the geologic background is given only in the first chapter and is not repeated. Chapter 2 discusses the seismic stations used in this research and the different methodologies applied for each project. Chapter 3, 4, and 5 present the achieved results, followed by discussions, interpretations, and subsequent conclusions of each of the three projects. Chapter 6 concludes the thesis with a general discussion and synthesis of findings, discussing their implications for the tectonic evolution and provides some recommendation for further studies.

1.2 Motivation and Objectives

The long and complex geological processes reshaped and brought permanent changes to the Malagasy lithosphere, which are recorded in the surface geology of the island. They resulted in an unusual geologic framework that raises perplexing questions. For example: the origin of the anomalously high surface-topography in the central region, the occurrence of lavakas (erosional gully) in numerous places, and the existence of Cenozoic intraplate volcanism in several regions of the island. Madagascar is therefore a suitable locality for studying the relationship between tectonic evolution and present-day lithosphere structure, and also, the origin of intraplate volcanism.

Madagascar is the fourth largest island in the world but very little is known about the deep structure. Only four permanent broadband seismic stations, in addition to the small seismic network of seven permanent short-period seismic stations, were operated in Madagascar. This lack of data restricted the seismological investigation of the Earth's interior beneath the region.

Early this decade, between 2011 and 2012, the MAdagascar-COmoros-MOzambique (MACOMO) project temporarily deployed broadband seismic stations all over Madagascar (details in Chapter 2). The MACOMO project aimed to investigate the source of the Madagascar intraplate volcanism. The stations yielded one to two years of seismic data at new 26 sampling points throughout the island. I was involved in the installation, the servicing, and the demobilization of these seismic stations. Besides, nearly at the same period, further temporary broadband stations were deployed in the southern area of Madagascar for two different projects (details in Chapter 2).

These arrays of temporary stations densified the seismic network of Madagascar and enabled a locale-scale investigation of the lithosphere.

The main goals of this study are:

(i) Infer the crustal and uppermost mantle structure beneath Madagascar beneath the new sampling points that correspond to station locations, *viz.* the thickness and velocity structure of the sedimentary basin; the thickness, the bulk Poisson's ratio, and the shear-wave velocity structure of the crust; and the shear-wave velocity structure of the uppermost mantle.

(ii) Deduce the geodynamic links between past tectonic events, the crustal composition and structure, the surface geology, and the current tectonic framework of Madagascar.

(iii) Locate any low-seismic-velocity zone in the upper mantle beneath Madagascar that may explain the presence of the Madagascar intraplate Cenozoic volcanism.

(iv) Identify any flow or strain produced by the low-seismic-velocity zone in order to evaluate candidate models for the origin of the Cenozoic volcanism.

(v) Estimate the mantle transition zone thickness beneath Madagascar in order to verify whether the low-seismic-velocity zone is a mantle plume source.

1.3 Literature review: Geology of Madagascar

This section begins with an overview of the geology of Madagascar, starting from its paleoposition far back in the Precambrian, the Mesozoic sequence of rifting, the Cenozoic tectonic activities, and the present surface geology and tectonic framework.

The paleoposition of Madagascar relative to Africa has been debated over the years. Some authors suggested that Madagascar was located further south, near Mozambique (*e.g.* Wegner, 1924; Tarling, 1971). Others postulated that the island was close to its current position (*e.g.* Darracott, 1974; Forster, 1975). Du Toit

(1937) has suggested that Madagascar was situated further to the north, adjacent to Tanzania and Kenya. The latter position was supported by physiographic, gravity, paleomagnetic, paleogeographic and salt structures observations by Smith and Hallam (1970), and has been adopted for the current study of Madagascar.

1.3.1 Madagascar within Gondwana

During the amalgamation of Gondwana, different pre-existing blocks participated in complex tectonic processes, such as collision and accretion, which deformed and metamorphosed the lithosphere and created new blocks (Powell et al., 1993). Azania block (an Archean and Paleoproterozoic crust constituted of Arabia-Ethiopia-Somalia-Madagascar) and the Congo-Tanzania-Bangweulu block at *ca.* 650-630 Ma formed the East African Orogeny (EAO) block (Collins and Pisarevsky, 2005). The amalgamation of Gondwana was concluded in the Late Neoproterozoic and Early Cambrian (*ca.* 570-510 Ma).

The reconstruction of Gondwana has located Madagascar between four cratons: the Antarctic, Dharwar, Arabo-Nubian and Nubian-Tanzanian (*e.g.* Agrawal et al., 1992; Kusky et al., 2003). Figure 1.1 shows a reconstruction of Gondwana at 544 Ma (Kusky et al., 2003).

The idea that Madagascar was positioned adjacent to Tanzania and Kenya was postulated by Du Toit (1937) from coastal outline observations. It was revised by Smith and Hallam (1970) from a least-square fit of the 500-fathom bathymetric contours and confirmed by the paleomagnetic study of McElhiny and Embleton (1976). In addition, E-W trending magnetic anomalies have been observed in the Mozambique Channel (Norton and Sclater, 1979) and in the Somali basin (*e.g.* Rabinowitz et al., 1983). These observations validate the northerly position of Madagascar within Gondwana, and will be adopted for further analysis and interpretation in this thesis.

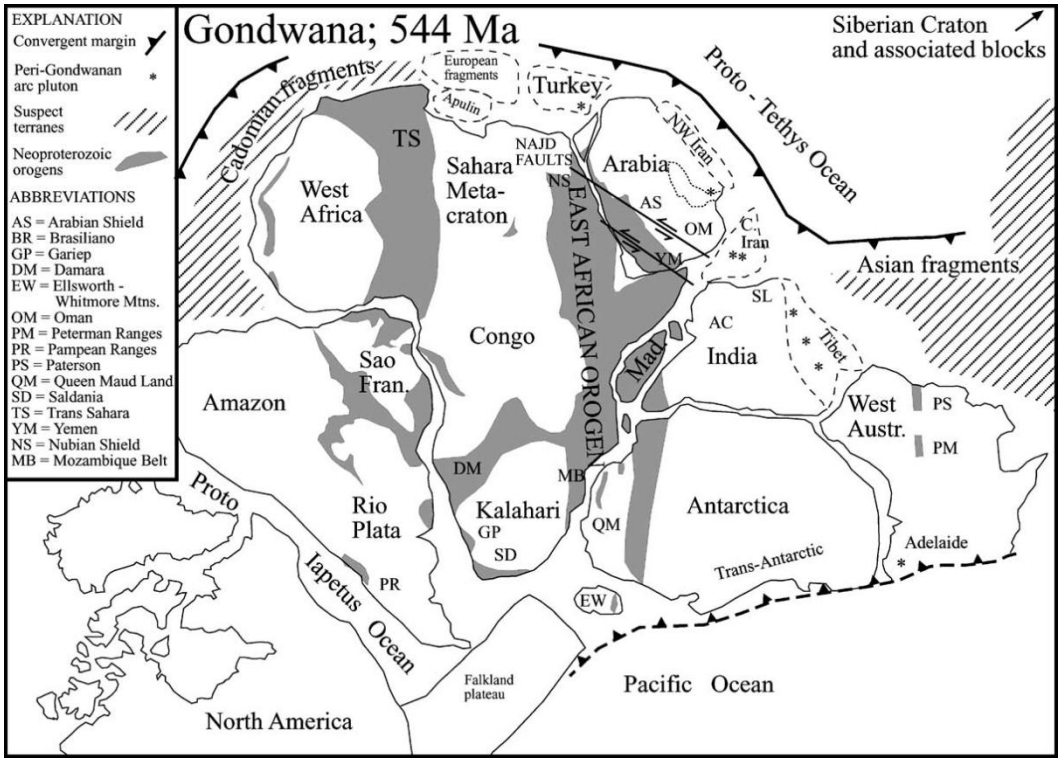

Figure 1.1: Reconstruction of Gondwana at the end of Neoproterozoic, ~544 Ma, and the emplacement of Madagascar (taken from Kusky et al., 2003).

1.3.2 Rifting from Africa

Gondwana began to split up in the Early Jurassic (*ca.* 200-180 Ma) into two landmasses: the West Gondwana, which is constituted by South America and Africa, and the East Gondwana, comprising Madagascar-Seychelles-Antarctica-Australia-India.

East Gondwana drifted south-southeasterly, relative to Africa, in the Late Jurassic (*ca*. 165-130 Ma). This continental-drift is believed to be guided by the transform fault (the Davie fracture zone) located in the middle of the Mozambique Channel which separates Africa and Madagascar (*e.g.* Kusky et al., 2007). This separation resulted in the opening of the Mozambique Channel and the formation of the Somali and the Mozambique oceanic basins separated by the Davie ridge (Figure 1.2) (Rabinowitz et al., 1983; Piqué, 1999a).

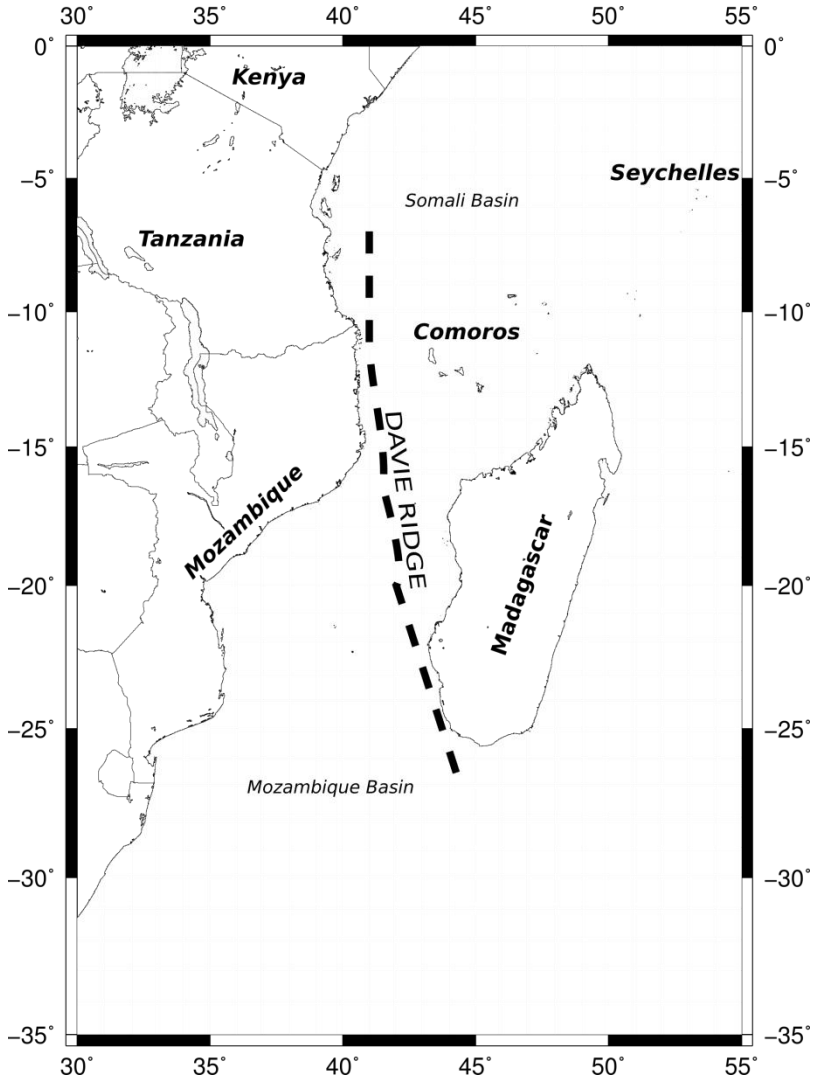

Figure 1.2: Map showing the current location of Madagascar, the Davie Ridge, and the Somali and Mozambique basins.

1.3.3 Rifting from India

East Gondwana broke apart in a series of separation events in the Late Mesozoic (*ca.* 133 Ma). This preceded the isolation of Madagascar. The India-Madagascar-Seychelles block was separated from the Australia-Antarctica block at *ca.* 130 Ma (*e.g.* Besse and Courtillot, 1988). Then, India and the Seychelles drifted away northwardly from Madagascar at *ca.* 90 Ma (*e.g.* Mahoney et al., 1991; Storey et al., 1995). Each separation was accompanied by important magmatic activities.

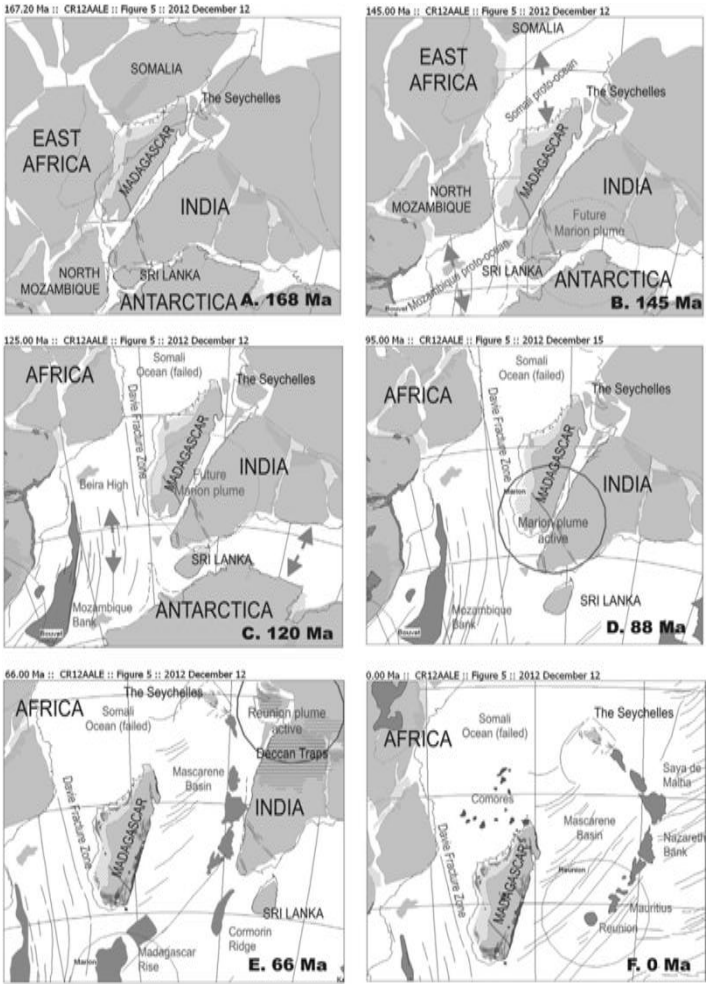

Figure 1.3: Separation of Madagascar from surrounding subcontinents in Gondwana between 168 Ma to present (taken from Reeves, 2014).

A hotspot reconstruction places the southeastern region of Madagascar above the Marion hotspot during the Late Cretaceous (*ca.* 95-85 Ma). The passage of the Madagascar/India block over the Marion hotspot likely weakened and fractured the overriding plate. This accordingly led to the separation of India from Madagascar (*e.g.* Storey et al., 1995; Torsvik et al., 1998; Raval and Veeraswamy, 2003). The cratonic lithosphere of the Western Dharwar Craton (WDC) was fractured during the breakup and left its fragments along the eastern regions of Madagascar (*e.g.* Raval and Veeraswamy, 2003). Figure 1.3 shows the stage of breaking-up of East Gondwana and the isolation of Madagascar (Reeves et al., 2014).

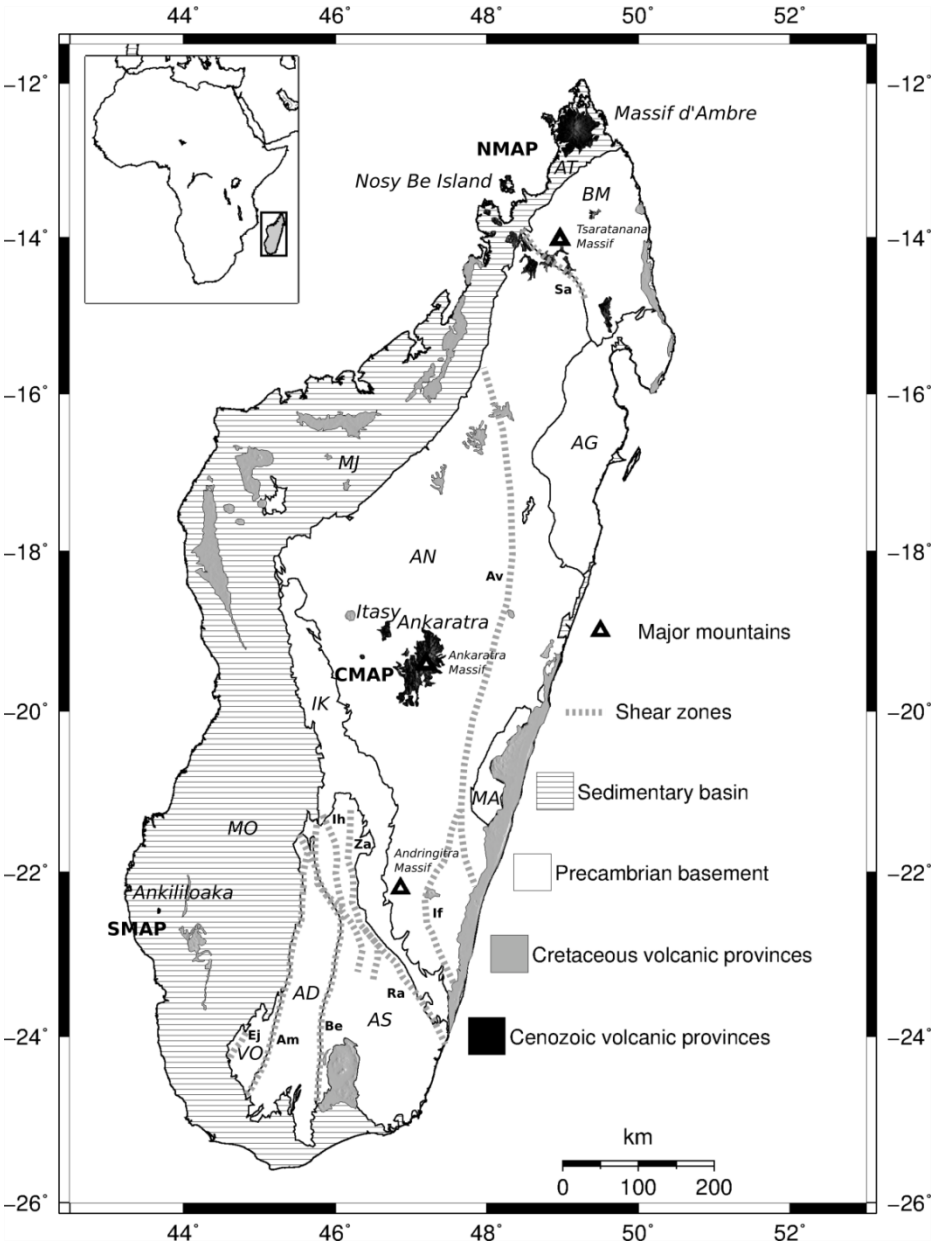

Figure 1.4: A simplified geologic map of Madagascar showing the different geological units, shear zones, volcanic provinces, major mountains, and place names referred to in the text (modified from Tucker et al. 2012). Initials are major: Sedimentary basin: MO – Morondava basin, MJ – Mahajanga basin, and AT – Antsiranana basin; Geological units: VO – Vohibory terrane, AS – Anosyen terrane, AD – Androyen terrane, IK – Ikalamavony terrane, AN – Antananarivo terrane, MA – Masora craton, AG – Antongil craton, and BM – Bemarivo terrane. The most prominent shear zones are shown in the map: Ej – Ejeda, Am – Ampanihy, Be – Beraketa, Ih – Ihosy, Za – Zazafotsy, Ra – Ranotsara, If – Ifanadiana, Av – Angavo, and Sa – Sandrakota shear zones.

New evidence from U-Pb zircons revealed the existence of old continental crust (*ca.* 3.0-2.5 Ga) beneath the young plume-related Mauritius island (<9 Ma) (Ashwal et al., 2017). The ancient crust, referred as "Mauritia", presents affinity with the central-east of Madagascar and is believed to be part of Madagascar and southern India, subsequent to the rifting.

Madagascar was completely separated from India by the end of the Cretaceous and remained tectonically stable since *ca.* 85 Ma.

The current surface geology of Madagascar may be generally divided into two main structural domains (Figure 1.4): the western third part of the island is covered by Late Carboniferous to present sedimentary basin (Fourno and Roussel, 1994) and the remaining eastern two-thirds consists predominantly of Precambrian and Early Paleozoic rocks which were reworked during the formation of the EAO block (Nicollet, 1990). In addition, several volcanic provinces are found throughout the island.

1.3.4 Sedimentary basins

The formation of the sedimentary basin along the western coast of Madagascar is strongly related to the fragmentation of East Gondwana from Africa. While within Gondwana, Karoo sedimentary deposits began to fill the deep grabens along the western side of Madagascar in the Permian-Triassic. These grabens are associated with the opening and rifting that subsequently broke up Gondwana. Their filling progressed from south to north and from west to east, which characterizes the northward and eastward progressive opening of the basin (Besairie, 1971; Piqué, 1999b).

Rajaomazava (1992) proposed that three major fracturing directions controlled the basin formation along the western region of Madagascar: directions N30E, N85E, and N170E. In his interpretation, the N85E and N170E fractures promoted the southward drift of Madagascar and guided the opening of the pull-apart basins of Antsiranana, Mahajanga, and Morondava (Figure 1.5).

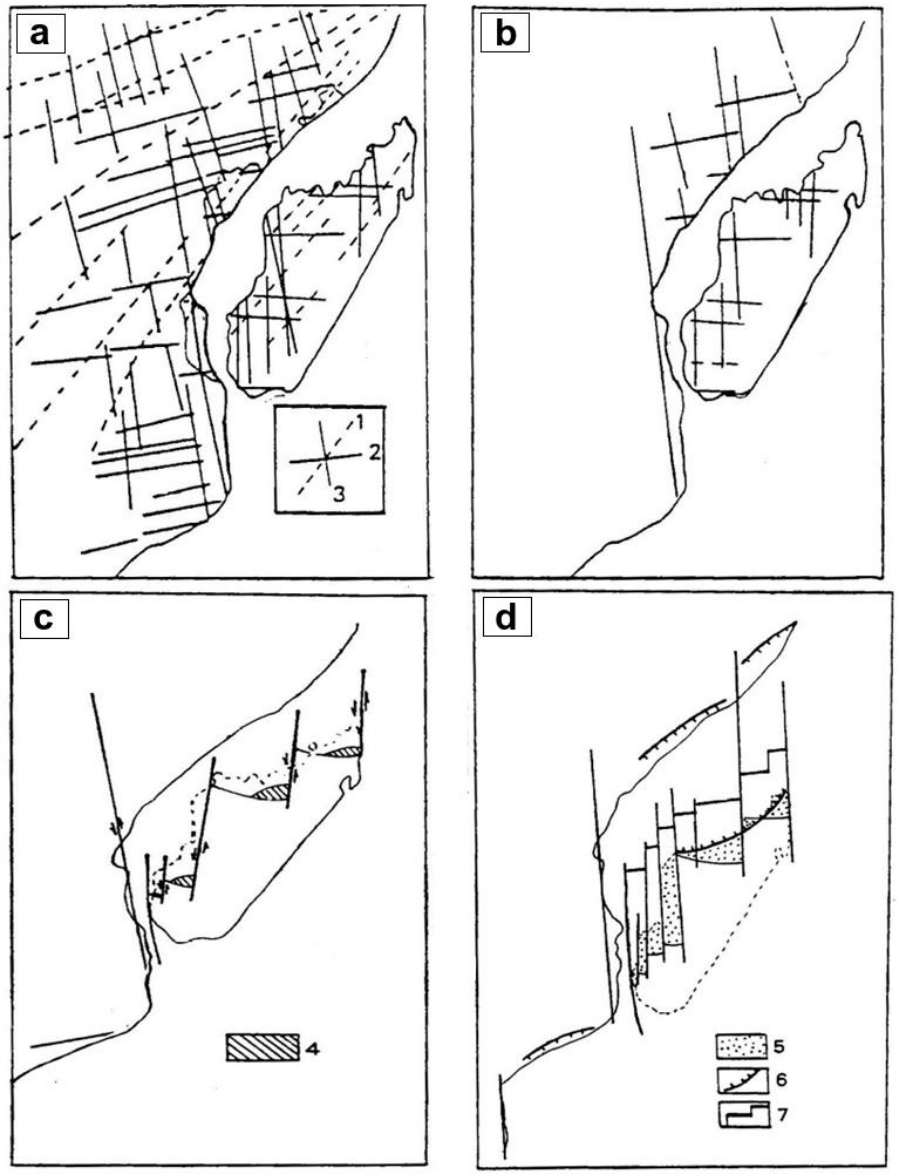

Figure 1.5: Formation of the sedimentary basin of Madagascar: a) The three major fracturing directions events ([1] - N30E; [2] - N85E; [3] - N170E); b) N85E and N170E groups promoted and guided the opening; c) Initial opening of the pull-apart basins of Diego, Mahajanga and Morondava ([4] - High sedimentation area); d) Flexures taking N30E direction ([5] - Sediments; [6] - Flexures; [7] - Magnetic anomalies) (taken from Rajaomazava, 1992).

The sedimentary basin of Madagascar is generally divided in three major basins: the Antsiranana, Mahajanga, and Morondava basins, which are in the northern, northwestern, and southern regions, respectively (Figure 1.4). The sedimentary rocks in these basins range in age from the Carboniferous to the present, with the

basal formations consisting of Karoo sediments. The basin lies over reworked Precambrian basement (*e.g.* Besairie, 1971, 1973).

Besairie (1967) estimated the thickness of the sedimentary basin to be around 10 km in its southern part and thinning out toward the north and east.

The Karoo Supergroup of Madagascar can be divided into three lithostratigraphic units (*e.g.* Besairie, 1967; Boast and Nairn, 1982). From the base to the top:

The Sakoa Group

The Sakoa Group is the oldest sedimentary deposit in Madagascar, from Late Carboniferous to Early Permian in age. It has been estimated to have a thickness of 2000 m in the south of the basin and thins out towards north. Besairie (1972) subdivided the Sakoa Group into four formations: (I) at the bottom, 50-450 m thick Late Carboniferous glacial beds with tillites, (II) 100-150 m thick Early Permian coals with Glossopteris and Gangamopteris, (III) red sandstones and siltstones with thickness of 1400 m according to Besairie (1972) - Razafimbelo (1987) and between 20-400 m according to Coffin and Rabinowitz (1988), and (IV) on top 20-30 m of Vohitola Permian marine limestones. The lower parts of this sequence are observed only in the southern region of Morondava basin.

The Sakamena Group

The Sakamena Group is estimated to be around 4000 m thick in the south and has a thickness of 20 m in the north (*e.g.* Coffin and Rabinowitz, 1988). Its age ranges from the Late Permian to Middle Triassic. Sakamena Group is characterized by three sequences. The Lower Sakamena has a thickness between 500-3000 m and is composed of conglomerate with components of limestone and crystalline succeeded on top by shales, sandstones and minor conglomerates. Late Permian reptiles are observed in this sequence (*e.g.* Coffin and Rabinowitz, 1988). The Middle Sakamena has 250- to 300-m-thick sequence of sandstones and shales

deposited in lakes or lagoons in the Early Triassic. The Upper Sakamena has a thickness of 500 m and characterized by Middle Triassic sandy and micro-conglomeratic sandstones.

The Isalo Group:

The Isalo Group has a thickness of 1700 m in the north and up to 6000 m in the southern region (*e.g.* Coffin and Rabinowitz, 1988). The group ranges in age from Middle Triassic to Early Jurassic. Isalo group is typically subdivided into three formations (Besairie, 1972): Isalo I constitutes of white or grey coarse grained arkosic conglomerates and sandstones; Isalo II consists generally of fluvial sandstones and conglomerates (Piqué et al., 1999b); and Isalo III is composed of shales, sandstones, and limestones.

1.3.5 Precambrian basement

The Precambrian basement of Madagascar can be divided into six terranes (Tucker et al., 2012). From north to south: the Bemarivo terrane, the Antongil-Masora craton, and the Antananarivo, Ikalamavony, Androyen-Anosyen, and Vohibory terranes (Figure 1.4).

Paleoarchean to Mesoarchean

The Antongil-Masora craton contains the oldest rocks in the island (*ca.* 3.3 Ga) which are principally Paleoarchean to Mesoarchean migmatite gneiss suites and Neoarchean metasedimentary and orthogneissic formations (Besairie, 1968, 1969; Tucker et al., 2011). The unit is located in the eastern coast in two areas: the Antongil craton in the north and the Masora craton. The Antongil-Masora is a fragment of WDC left behind during the dislocation of India from Madagascar.

Neoarchean

The Antananarivo terrane is composed generally of Neoarchean (*ca.* 2.5 Ga) orthogneisses and paragneisses that grade from greenschist to granulite facies (Tucker et al., 2011, 2012). It is located in the central high plateau and occupies the major portion of the Precambrian basement of Madagascar.

Paleoproterozoic

The Androyen-Anosyen terrane is composed mainly of Paleoproterozoic (*ca.* 2.0-1.8 Ga) rocks. It constitutes the southernmost part of the Precambrian shield of Madagascar (Tucker et al., 2012). Geochronological data (from detrital zircons) and common geological characteristics, such as a Paleoproterozoic gneissic basement and sequence of Neoarchean and Paleoproterozoic platform sediments, point to similarities between the Androyen and Anosyen sub-domains, leading to their consideration as a single terrane.

Mesoproterozoic

The Ikalamavony terrane is dominated by the Ikalamavony Group of *ca.* 1.08-0.98 Ga ages, which includes higher-grade Mesoproterozoic metasedimentary and meta-igneous rocks, as well as younger Neoproterozoic sedimentary rocks (Tucker et al., 2007). It is a NNW-SSE-trending unit that forms the western and south-central part of the Precambrian shield of Madagascar.

Neoproterozoic

Neoproterozoic terranes in Madagascar can be found in two areas, north, in the Bemarivo terrane, and south, in the Vohibory terrane.

The Bemarivo terrane is characterized by Neoproterozoic (*ca.* 758-708 Ma) intrusive granitic and volcanosedimentary rocks. U-Pb zircon geochronology indicates two different domains to the north and south, separated by shear zones. Older *ca.* 740-750 Ma old rocks occupy the southern domain and consist mainly of metasedimentary and plutonic calc-alkaline rocks. The northern domain is composed of *ca.* 715-720 Ma old rocks, including both extrusive and intrusive rocks (Tucker et al., 2012).

The Vohibory terrane is an oceanic terrane of early Neoproterozoic age (*ca.* 850 Ma). It is located west of the Androyen-Anosyen terrane and composed of intercalations of metabasalts, acidic volcanic rocks, and chemical metasedimentary rocks (Jöns and Schenk, 2008).

1.3.6 Volcanism

Volcanism in Madagascar can be grouped, by age and lava composition, into two groups: the Cretaceous manifestations, which are generally composed of tholeiitic basaltic lavas; and the Cenozoic manifestations, which are mainly alkali basalt eruptions (*e.g.* Besairie, 1973; Norton and Sclater, 1979).

Cretaceous volcanism

The Cretaceous volcanic activities in Madagascar (*ca.* 95-85 Ma) are principally associated with the Mesozoic rifting. The lithosphere of the Madagascar/India block was weakened and fractured when the plate overrode the Marion hotspot (*e.g.* Storey et al., 1995; Torsvik et al., 1998; Raval and Veeraswamy, 2003). This not only fragmented India from Madagascar, but caused intensive eruptions of crustal-derived dacite/alkali rhyolite and mantle-derived tholeiitic basalt magmas as well. These basalt floods likely once covered the entire surface of Madagascar (Storey et al., 1995).

Cretaceous volcanic provinces are principally observed all along the periphery of Madagascar: the eastern coast, the western sedimentary basin, and in the south - along the Volcan de l'Androy (Figure 1.4) (*e.g.* Mahoney et al., 1991; Rasamimanana, 1996).

Even though the presumed location of the Marion hotspot was close to Madagascar during the Cretaceous and it subsequently participated in the volcanic eruption, isotopic (Sr-Nd) and geochemical evidences have dismissed a mantle plume source as the cause of the Cretaceous activities (Bardintzeff et al., 2010). Bardintzeff et al. (2010) rather pointed out that the composition of magma samples suggests a lithospheric and asthenospheric source, possibly through the reactivation of old lithospheric-scale shear zone preceding the fragmentation of India and Madagascar.

Cenozoic volcanism

Madagascar was isolated and became an island about 85 Myr ago, and has remained tectonically quiet since then as it is situated remote from plate boundaries, *viz.* the East African Rift (EAR) and the Indian mid-oceanic ridges. Though Madagascar had not undergone to any major tectonic activities, volcanic activities anomalously began to erupt in some areas during the Cenozoic. The Cenozoic volcanic eruptions are not as voluminous as the Cretaceous manifestations and are mainly composed of alkali basalt magmas (*e.g.* Emerick and Duncan, 1982, 1983; Rasaminanana, 1996; Bardintzeff et al., 2010).

K-Ar isotopic data range the age of igneous rocks from the Cenozoic volcanic provinces between 28 Ma and 0.5 Ma (*e.g.* Emerick and Duncan, 1982, 1983; Bardintzeff et al., 2010), but rocks with 50 Ma age are observed in some areas. In the central part of Madagascar, around the Ankaratra area, igneous rocks age between 28 Ma and 3 Ma. The Ankililoaka province, in the southwestern coast of Madagascar, age is *ca.* 9 Ma. The youngest eruptions (*ca.* 2 Ma to 0.55 Ma) were in the northern region of Madagascar, in the Massif d'Ambre and the Nosy Be

Island. These three Cenozoic volcanic provinces are commonly referred to the Southern Madagascar Alkaline Province (SMAP), the Central Madagascar Alkaline Province (CMAP), and the Northern Madagascar Alkaline Province (NMAP) (Figure 1.4).

The origin of the Cenozoic volcanism in Madagascar had long been debated. Several hypotheses had been proposed to explain the origin of the anomalous Cenozoic eruptions in Madagascar. A few researches have linked the volcanic activities to the past tectonic history of Madagascar. For example, Nougier et al. (1986) hypothesized a reactivation of an ancient and lithosphere-scale fracture zone during the Tertiary. On the other hand, connections to the neighboring regional tectonic events have also been suggested. Emerick and Duncan (1982) linked the Cenozoic volcanic activities to the Comoros volcanic provinces. Some authors have proposed a hot asthenospheric mantle derived from the African Superplume (*e.g.* Ebinger and Sleep, 1998; Forte et al., 2010). Other authors have proposed that the EAR system continues to Comoros and Madagascar, giving rise to the volcanic activities (*e.g.* Calais et al., 2006; Stamps et al., 2014).

Bardintzeff et al. (2010), from the geochemical and isotopic evidences, suggested that CMAP and SMAP share the same mantle source, which is located in the lower part of the lithosphere. It is different to the Cretaceous emission source.

1.3.7 Shear zones of Madagascar

Madagascar is cut by several N-S or NW-SE trending crust-scale shear zones. Some of them are rooted in the mantle. These shear zones frequently mark the boundaries of the major geological domains (for example, Ampanihy, Ranotsara, Beraketa, and Sandrakota shear zones), or lie within them (for example, Ejeda, Ihosy, Zazafotsy, and Angavo-Ifanadiana shear zones) (Figure 1.4) (*e.g.* Martelat et al., 2000, 2014; Raharimahefa and Kusky, 2010). The major shear zones are described below:

- The Sandrakota shear zone is located in the northern region of Madagascar, separating the Antananarivo domain from the Bemarivo domain. It is a 100-km-long and 50-km-wide NW-SE-trending high-strain zone (Thomas et al., 2009).

- The Angavo-Ifanadiana shear-zone, a 800-km-long and a 20-to-60-km-wide and shear zone, located in the eastern side of the Antananarivo domain from north to south. It is a N-S trending highly-strained zone characterized by a major strike-slip shear zone (Nédélec et al., 2000). The Angavo-Ifanadiana shear zone is very similar to the Achankovil shear zone in India (Raharimahefa et al., 2013).

- The Ranotsara shear zone marks the boundary between the Anosyen sub-domain and the Ikalamavony domain. It is a 20-km-wide and 350-km-long strike-slip shear zone with a N-S to NW-SE trend. This shear zone is believed to have been active during the conclusion of the EAO (de Wit et al., 2001) and is usually used to estimate the actual position of Madagascar within Gondwana (*e.g.* Collins and Windley, 2002). Schreurs et al. (2010) proposed that the Ranotsara shear zone is characterized by a NW-SE trending brittle normal faults along its length and a ductile deflection zone in its central segment, with a NW-SE trending brittle normal faults along its length.

- Three major N-S trending (between N0 and N15) and 20-km-wide shear-zones are identified in the southwestern part of the Malagasy Precambrian shield. The Beraketa shear zone is mainly N-S trending and a 250-km-long strike-slip shear zone. It constitutes the contact between the Anosyen and Androyen domains (*e.g.* Martelat et al., 2000, 2014). The Ampanihy shear zone separates the Androy domain from the Vohibory domain and trends N-S parallel to the Beraketa shear zone. The Ejeda shear zone is located in the western part of the Vohibory domain. The lengths of the Ejeda and

Ampanihy shear zones are not well defined as they extend under sedimentary cover.

- The Ihosy and Zazafotsy shear zones are parallel N-S trending features. They are highly strained 5- to 15-km-wide and 350-km-long ductile shear zones, located within the northernmost portion of the Anosyen sub-domain (Martelat et al., 2000, 2014).

1.3.8 Evidence of Neogene uplift

The topography of the central part of Madagascar is anomalously high (>1 km) for a Precambrian crust. It even exceeds 2 km in the Tsaratanàna Massif and Ankaratra Massif, in the NMAP and CMAP, respectively. Observations confirm a broad active uplifting of Madagascar, which has produced a high concentration of lavakas (erosional gullies, an example in Figure 1.6) and seismic activities in certain region.

De Wit (2003) proposed an extensive uplift of northern and central Madagascar in the Neogene (*ca.* 10-15 Ma). This is characterized by juvenile canyons, such as lavakas or channels, which cut through Cenozoic rocks in the area. He suggested that there is a link between the Cenozoic volcanic activities and the presumed Neogene uplift, and also the occurrence of seismicity in the area. Cox et al. (2010) observed that the occurrence of lavakas, in the central highlands of Madagascar, surprisingly correlates with the seismicity. They observed that around 80% of seismic events happen inside lavakas-prone area. Roberts et al. (2012) came up with an estimation of uplift rates in Madagascar from the observation of the shape of river valleys. They proposed that Madagascar has been uplifted, at a rate of ~0.2-0.4 mm/yr, since the early Miocene (15 Myr).



Figure 1.6: An example of lavakas (erosional gullies) in the central highland of Madagascar (from http://voices.nationalgeographic.com/files/2013/10/getimage.jpg).

1.4 Literature review: Previous geophysical studies

Though geologic investigations of Madagascar date back to the beginning of the 20th century, very little is known about the deeper structure. Very few geophysical studies have been conducted to explore the lithospheric structure beneath the island.

In this section, I present an overview of previous crustal- and lithospheric-scale geophysical investigations that were conducted in Madagascar for different regions using a variety of approaches.

1.4.1 Seismicity and seismotectonics of Madagascar

Seismicity of Madagascar has been studied, up until now, by using data from a small network of short-period seismic stations, operated by the Institut et Observatoire de Géophysique d'Antananarivo (IOGA) of the Université

d'Antananarivo (Madagascar). Consequently, very few studies have been published focusing on the seismicity and seismotectonics of the island.

Previous studies of seismicity show that Madagascar is characterized by moderate seismicity (M<4). Seismic events are mostly observed in the Cenozoic volcanic provinces and occur generally in the lower crust with an average depth of 21 km (*e.g.* Bertil and Regnoult, 1998; Rindraharisaona et al., 2013). All findings agree that the origin of stresses is likely linked to pre-existing structure. A thermal bulge underlying the Cenozoic volcanic provinces has been proposed (*e.g.* Bertil and Regnoult, 1998; Rindraharisaona et al., 2013).

Earthquake focal-mechanism solutions generally show normal faults, with average dip of 55°, in the central highlands and reveal a E-W extensional stress regime. This likely suggests that the region is probably an extensional diffuse plate boundary (*e.g.* Grimison and Chen, 1988; Bertil and Regnoult, 1998; Rindraharisaona et al., 2013).

1.4.2 Crustal thickness from previous studies

A few studies have investigated, in a whole or partly, the crust of Madagascar using seismological or gravimetric methods.

Using the gravimetric method, Fourno and Roussel (1994) estimated the thickness of the crust beneath the central plateau of Madagascar using a linearized inversion procedure in the spectral domain to Bouguer anomalies. They produced with a contour map of the crustal thickness beneath the central part of the island that ranges between 25 km and 40 km. Rakotondraompiana et al. (1999) analyzed the transfer function between Bouguer anomalies, and relief together with a forward modeling of gravimetric profiles and ranged the thickness of the crust beneath the central part of Madagascar between 25 km and 35 km. Rajaomazava (1992), in his gravimetric study of the subsidence in the Morondava basin, presented a contour map of the Moho depth beneath the Morondava basin and the central region of Madagascar. Thicknesses of the crust were obtained from an isostatic calculation

and range between 32 km and 36 km beneath the Morondava basin and between 32 km and 38 km beneath the central highlands. Crustal thickness models for all of Africa, obtained from modeling satellite gravity data, show Moho depths in Madagascar ranging between 35 km and 42 km (Tedla *et al.* 2011; Tugume *et al.* 2013).

For the seismological studies, Rakotondrainibe (1977) estimated the thickness of the crust in the center of Madagascar to be around 36 km by analyzing the travel-time of body waves. For the same area, Rambolamanana et al. (1997) inferred a crustal thickness of 42 km using the simultaneous inversion for hypocentral parameters and velocity, while the receiver function studies of Rai et al. (2009) obtained 38 km. Rindraharisaona et al. (2013) used a joint inversion of receiver functions and surface wave dispersion measurements to estimate the thickness beneath the four existing permanent broadband seismic stations in Madagascar. From north to south, they found crustal thicknesses of 35 km beneath SBV, 42 km beneath (ABPO), 39 km beneath VOI, and 35 km beneath FOMA. The surface wave tomography of the lithosphere beneath Africa and Arabia of Pasyanos and Nyblade (2007) ranges the crustal thickness beneath Madagascar between 25 km and 35 km, while the global model CRUST2 (Bassin et al., 2000) gives 36 km to 45 km. A recent investigation of the crust in the southern part of Madagascar using joint inversion receiver functions and surface waves derived from ambient noise (Rindraharisaona et al., 2017), revealed a thinning of ~60% to 13 km of the crust beneath the sedimentary basin, thick and faster Archean crust compared to Proterozoic crust, and thin crust (~30 km) along the eastern coast.

These findings suggest generally thick crust beneath the central highlands with a decrease in thickness towards the coastal periphery, especially westwards. However, a contrasting observation was recently published by Paul and Eakin (2017) from a receiver function analysis. They found that the central part of Madagascar is thin (~39 km), while the east coast is characterized by a 44-km-thick crust.

1.4.3 Mantle structure from previous studies

The structure of the mantle beneath Madagascar has hardly been studied due to lack of seismic data.

Rakotondraompiana et al. (1999) estimated the thickness of the lithosphere beneath the central part of Madagascar between 62 km and 77 km. They pointed out that this lithospheric thinning suggests an extensive E-W extension of the island. The thinning of the lithosphere is also mentioned in Rindraharisaona et al. (2013) and coincides with slowest asthenosphere.

The recently deployed temporary broadband station in Madagascar (details in Chapter 2) allowed Pratt et al. (2017) to conduct a surface wave tomography of Madagascar. Upper mantle low-shear-wave-velocity zones were found underlying the Cenozoic alkaline volcanic provinces in the northern (NMAP) and central (CMAP) regions of Madagascar, reaching a depth of 150 km. In addition, a low velocity zone was found at depths 50-150 km beneath the southwestern alkaline province (SMAP). These low velocity zones were interpreted to be asthenospheric upwellings that caused the Cenozoic volcanic activities. A delamination of mantle lithosphere was also proposed beneath the CMAP, which likely caused the uplift in the region.

Reiss et al. (2016) used shear-wave splitting and waveform modeling to investigate the seismic anisotropy of the lithosphere and the asthenosphere in the southern region of Madagascar. They observed a rotation of the fast-polarization directions from NE around the sedimentary basin, to NW around the central part, and NE in the east coast. They interpreted the variation of the anisotropy to be the result of an important crustal anisotropy, which could be caused by a ~150-km-wide ductile deformation zone.

Ramirez et al. (submitted), in their shear-wave splitting analysis, observed that the fast polarization direction of the seismic anisotropy in the northern part of Madagascar is characterized by ~E-W fast polarization directions, which can be attributed to NE-oriented mantle flow from the African superplume or plate

motion modified by SW-oriented mantle flow from the Comoros hot spot. They have observed a circular pattern of shear-wave splitting fast polarization directions in the central part of Madagascar, which can be attributed to upwelling asthenosphere caused by lithospheric delamination interacting with mantle flow from the superplume or plate motion. They have attributed the direction of SKS anisotropy in the southwestern region to a small-scale mantle flow, while to a fossil anisotropy in the lithosphere for the anisotropy in the southern part.

The following chapter presents and discusses the data, tools, and techniques used for the three main projects of this study.

Chapter 2

Data and Methodology

2.1 Introduction

The energy released by an earthquake, or any source of ground-motion (such as quarry blasts, nuclear explosions, etc), propagates away from the source as seismic waves. The wave properties depend largely on the physical properties of the medium that they cross. The study of these waves reveals valuable information concerning the deep interior of the Earth.

Seismic waves that travel through the interior of the Earth are called body waves (*P* and *S* waves), while those that are guided by the surface are called surface waves (Love and Rayleigh waves) (Figure 2.1). They differ from one another by their speed, the movement of particles when they pass by, the medium in which they can propagate, etc. For example:

(1) *P* waves (*P* stands for Primary) are compressional or longitudinal waves, with a typical velocity of 6 km/s in the upper crust (depth <15 km). They arrive first at seismic station.

(2) *S* waves (*S* is Secondary) are shear or transverse waves, which propagate with a typical velocity of 3.5 km/s in the upper crust. They do not travel through liquid.

(3) Love and Rayleigh waves travel along the surface of the Earth with a typical velocity of 3.5-4.5 km/s. These waves are the interference of horizontally-polarized *S*-waves and their multiples (Love waves) or the combination of *P*-waves and vertically-polarized *S*-waves (Rayleigh waves). They are usually observed after the *S*–waves.

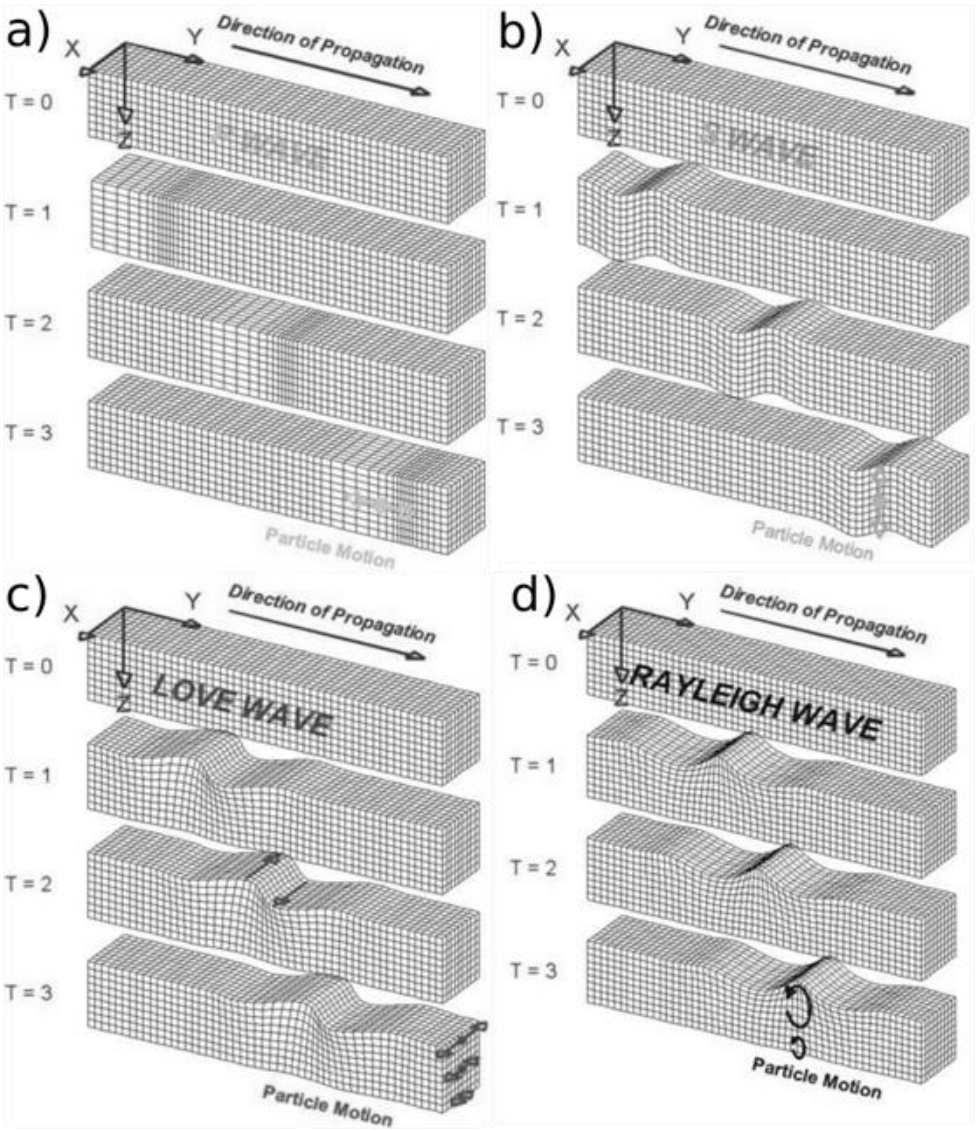

Figure 2.1: Propagation of seismic waves: body waves, (a) P waves and (b) S waves, and surface waves, (c) Love waves and (d) Rayleigh. Cubes represent particles that constitute the medium (from http://www.geo.mtu.edu/UPSeis/waves.html).

Seismometers (or seismographs) are instruments used to measure the movement of the ground. Triaxial seismometers are commonly employed to record the vertical (up-down direction) and horizontal (north-south and east-west directions) of the movement of the ground. Histories of the ground-motion are presented as waveforms, showing the displacement, velocity, or acceleration of the ground as a function of time. They are called seismograms. An example of seismograms recorded at the seismic station ABPO during the Magnitude 7.0 earthquake in Irian Jaya – Indonesia, on 27th July 2015, 21:41:21 UTC, is shown in Figure 2.2.

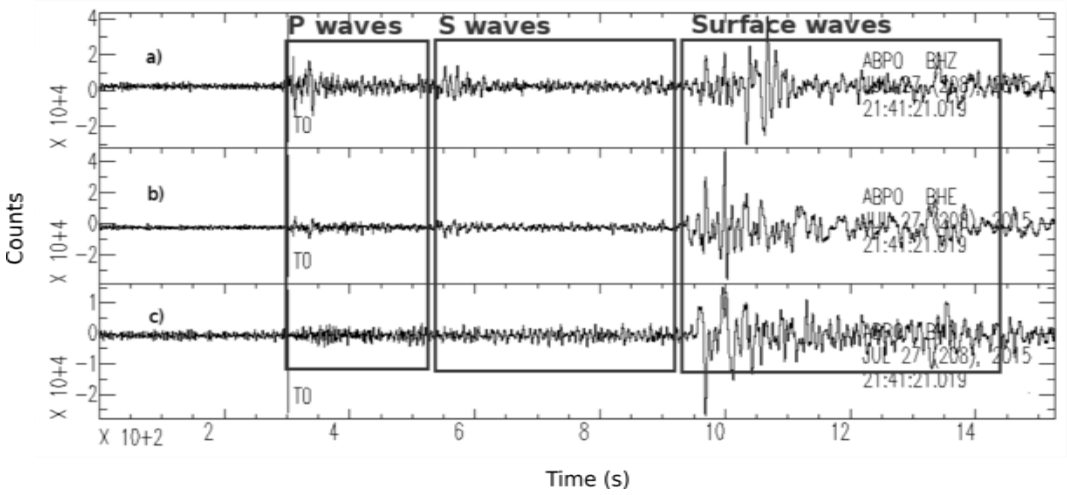

Figure 2.2: Three-component seismograms recorded at seismic station ABPO for the seismic event occurred in Irian Jaya, Indonesia on 27th July 2015, 21:41:21 UTC, depth of 39 km, with magnitude of 7.0. T0 marks the primary wave or *P* wave. (a) is the record at the vertical component, (b) is the east-west component, and (c) is the north-south component. The boxes show approximately *P*-wave and *S*-wave with their multiples and the surface waves.

Seismometers are classified by the range of frequency that they are sensitive to. They are characterized by the instrument response (the ground-motion amplification versus frequency or period), which define the range of frequency (or period) that the seismometer can detect. This corresponds to the large amplification in the seismometer response curve. Figure 2.3 shows typical response of several types of seismometers: Short Period, Long Period, and Broadband. As shown in the figure: Short Period seismometers are generally sensitive to vibration between 1 Hz to 10 Hz, Long Period seismometers can detect seismic signals with frequency that ranges from 0.01 Hz to 0.1 Hz, and

Broadband seismometers detect a wide range of frequencies – hence it is called "broad".

In modern seismology, seismic signals recorded by seismometers are converted into digital signals, which can be easily stored, exchanged, or processed.

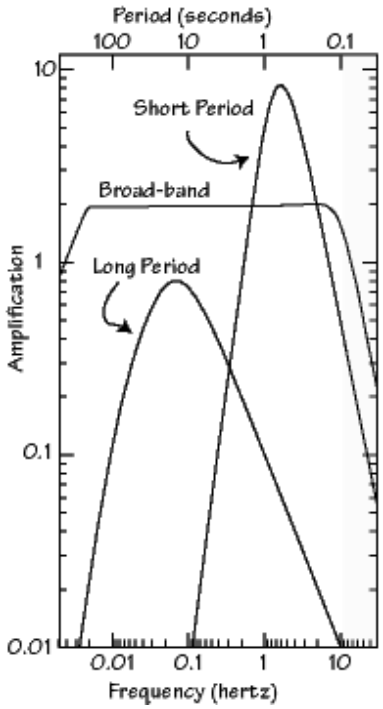

Figure 2.3: Response curves of different types of seismometers. *x*-axis shows the range of frequencies and *y*-axis is the amplification of the ground-motion (taken from http://eqseis.geosc.psu.edu/~cammon/HTML/Classes/IntroQuakes/Notes/seismometers.html).

Seismic data used in this thesis are records from temporary and permanent broadband seismic stations. Details about these stations are summarized in section 2.2.

The data analysis and interpretation was preceded by two years of field work, 2011-2013, in which I participated on the deployment, servicing, and the demobilization of seismic stations for the MAdagascar COmoros MOzambique (MACOMO) project. Field teams were from the Washington University in Saint Louis, Missouri, USA (including Michael Wysession, Patrick Shore, Ghassan Aleqabi, and Martin Pratt) and from the University of Antananarivo, Madagascar

(including myself, and Tsiriandrimanana Rakotondraibe). The field work is briefly summarized in Section 2.2.2.

2.2 Data acquisition

The first seismic station in Madagascar, a short period seismic station, was deployed in 1898 by Jesuit missionaries at the IOGA to study the seismicity of the island. A series of deployments and relocations of short period stations densified the network until 2001, when 11 short-period stations were deployed. Currently, seven short-period permanent stations are functional, which are mainly around the highland of the center part of Madagascar. They are operated by the IOGA and affiliated to the CEA/DASE Seismic Network (FDSN Code: RD, http://www-dase.cea.fr/public/dossiers_thematiques/alerte_aux_forts_seismes/description_en.html). As these short-period stations were not used in this work, no further detail of them will be presented in this thesis.

Recording seismic stations used in this study are generally the 26 broadband stations from the MACOMO project (FDSN Code: XV, Wysession et al., 2012, doi:10.7914/SN/XV_2011). However, existing five permanent broadband stations were also used: ABPO (GSN Network, FDSN Code: II, http://ida.ucsd.edu/?q=station/abpo), FOMA (GEOSCOPE Network, FDSN Code: G, http://geoscope.ipgp.fr), VOI and SBV (GEOFON Network, FDSN Code: GE, http://geofon.gfz-potsdam.de/), and SKRH (AFRICAARRAY Network, FDSN Code: AF, http://www.africaarray.psu.edu/). In addition, several temporary broadband stations from two other simultaneous experiments were used to fill the gap in station distribution in the southern part of Madagascar: seven broadband stations from the Seismological Signatures in the Lithosphere/Asthenosphere system of Southern Madagascar (SELASOMA) experiment (FDSN Code: ZE, Tilmann et al., 2012, doi: 10.14470/MR7567431421), and 10 broadband stations from the Réunion Hotspot and Upper Mantle – Réunions Unterer Mantel (RHUM-RUM) project (FDSN Code: YV Network: Sigloch and Barruol, 2012).

2.2.1 Permanent broadband seismic stations

The first broadband seismic station in Madagascar was deployed in Ambohipanompo (Station code: ABPO). It has been operational since 2007 and the data are available online. Different sensors have been installed in ABPO: Streckeisen STS-1 Seismometer with Metrozet E300, Streckeisen STS-2 Seismometer, Kinemetrics Episensor ES-T, Streckeisen STS-1V/VBB Seismometer, Streckeisen STS-1H/VBB Seismometer and Paroscientific microbarograph.

The second broadband seismic station is FOMA. It was deployed in 2008 in Fort-Dauphin, and data from this station are available online. Different sensors are available in the station FOMA: Streckeisen STS-2 Seismometer, EE08 Temperature + Humidity Sensor and Vaisala PTB110 Analog Barometer.

Two broadband seismic stations were deployed in Vohemar (SBV) and Vohitsaoka (VOI) in 2009. Both seismic stations have Streckeisen STS-2 Seismometer as sensor and the data are available online.

The last permanent seismic station is SKRH. This station was deployed in Sakaraha in 2014. The station has a Trillium Compact seismometer. The data are available online.

2.2.2 Temporary broadband seismic stations: MACOMO project

Seismic data used in this thesis are generally from the MACOMO project. MACOMO project was supplied with equipment by PASSCAL. Each seismic station was equipped: with a 24-bit data logger (Quanterra Q330) subsystem to control the station and convert analog to digital data, a broadband sensor (Guralp CMG-3T, StreckeisenSTS-2, or Nanometrics Trillium 120PA) to measure the ground-motion, a GPS clock for absolute timing (clock), and batteries and solar panels for power supply.

Installation of seismic station

Locations of seismic stations were preselected by considering the geography and geology of the region before the installation. Then, a scouting trip was done in May 2011 to verify the accessibility of the site. The selection criteria of the site generally depended on: the accessibility of the area, the possible seismic-noise sources in the region, the land ownership and future land use issues, and the safety and security of the site. Stations for the MACOMO project were generally deployed on private properties or government premises (*e.g.* National parks, Army bases…).

The abovementioned equipments were buried ~1 m deep inside two plastic barrels for each station. Only the GPS antenna and solar panels are seen at the surface. Figure 2.4 shows the installation of a seismic station ZOBE and Figure 2.5 is a sketch showing the configuration of an operational MACOMO station.

The installation of the MACOMO stations was divided in two parts:

(1) The first part of the installation: September 2011, 10 seismic stations were deployed mostly along the coast of Madagascar for two years: ANLA – ANTS – DGOS – LAHA – LONA – MAHA – MAJA – MARO – MMBE – VATO.

(2) The second part of the project: September 2012, another 16 seismic stations were deployed for one year to densify the array until the end of the project in September 2013: AMPY – CPSM – BAEL – BAND – BANJ – BARY – BATG – BERG – BITY – BKTA – MKVA – SOLA – TANS – VINA – ZAKA – ZOBE.



Figure 2.4: Installation of the seismic station ZOBE in Ankazobe. In foreground: Michael Wysession, Patrick Shore, Ghassan Aleqabi, myself (crouching in white T-shirt), Rina Randrianasolo (crouching in grey T-shirt), and Tsiriandriamanana Rakotondraibe.

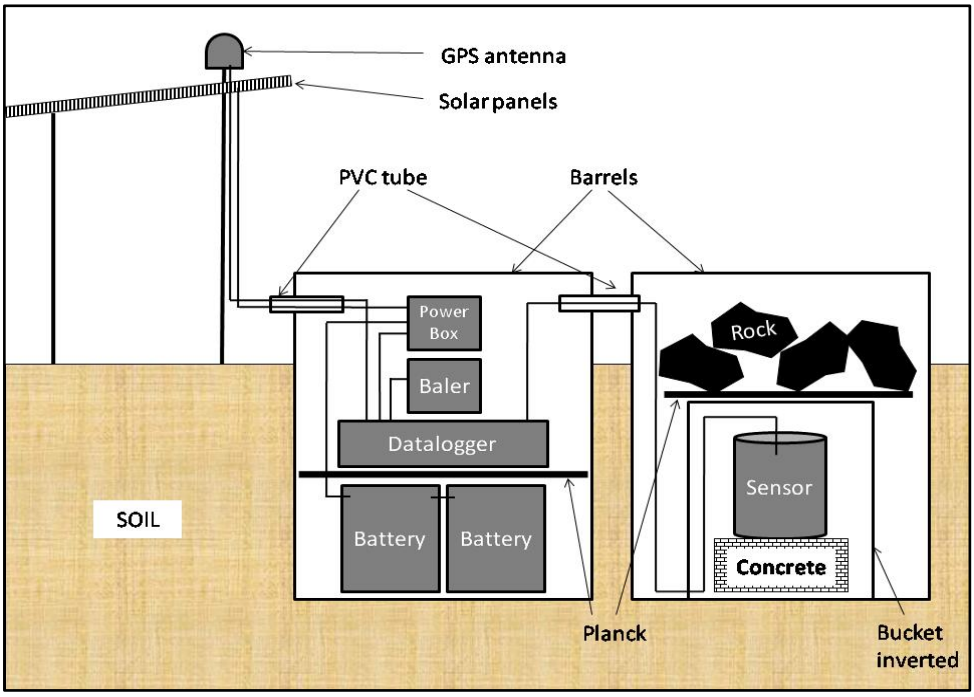

Figure 2.5: A sketch showing a cross section of an operational MACOMO station.

Servicing seismic stations

No telemetry system was used for the MACOMO project. Data were retrieved manually on site. We (I and Tsiriandrimanana Rakotondraibe) took a field trip in May 2012 and May 2013 to service seismic stations that accessible at this time of the year. The objectives of the trips were to retrieve seismic data and to check the stations' state of health.

Few stations were accessible during these trips because of the weather in Madagascar at this period. Figure 2.6 and Figure 2.7 show our team servicing the seismic station AMPY and stuck in the middle of a river when taking a trip to service the station MMBE, respectively.



Figure 2.6: Myself (standing) and Tsiriandrimanana Rakotondraibe (crouching) servicing the seismic station AMPY in Ampanihy.



Figure 2.7: Our truck getting stuck during the servicing trip in Mandabe.

Demobilizing seismic stations

At the end of project, in September 2013, all seismic stations were removed from the site, which gave us 28 new points of measurement because seismic stations MARO and VATO were relocated to KIRI and MAGY, respectively, due to security issues.

A total of 28 stations were deployed for the MACOMO project (Figure 2.8).

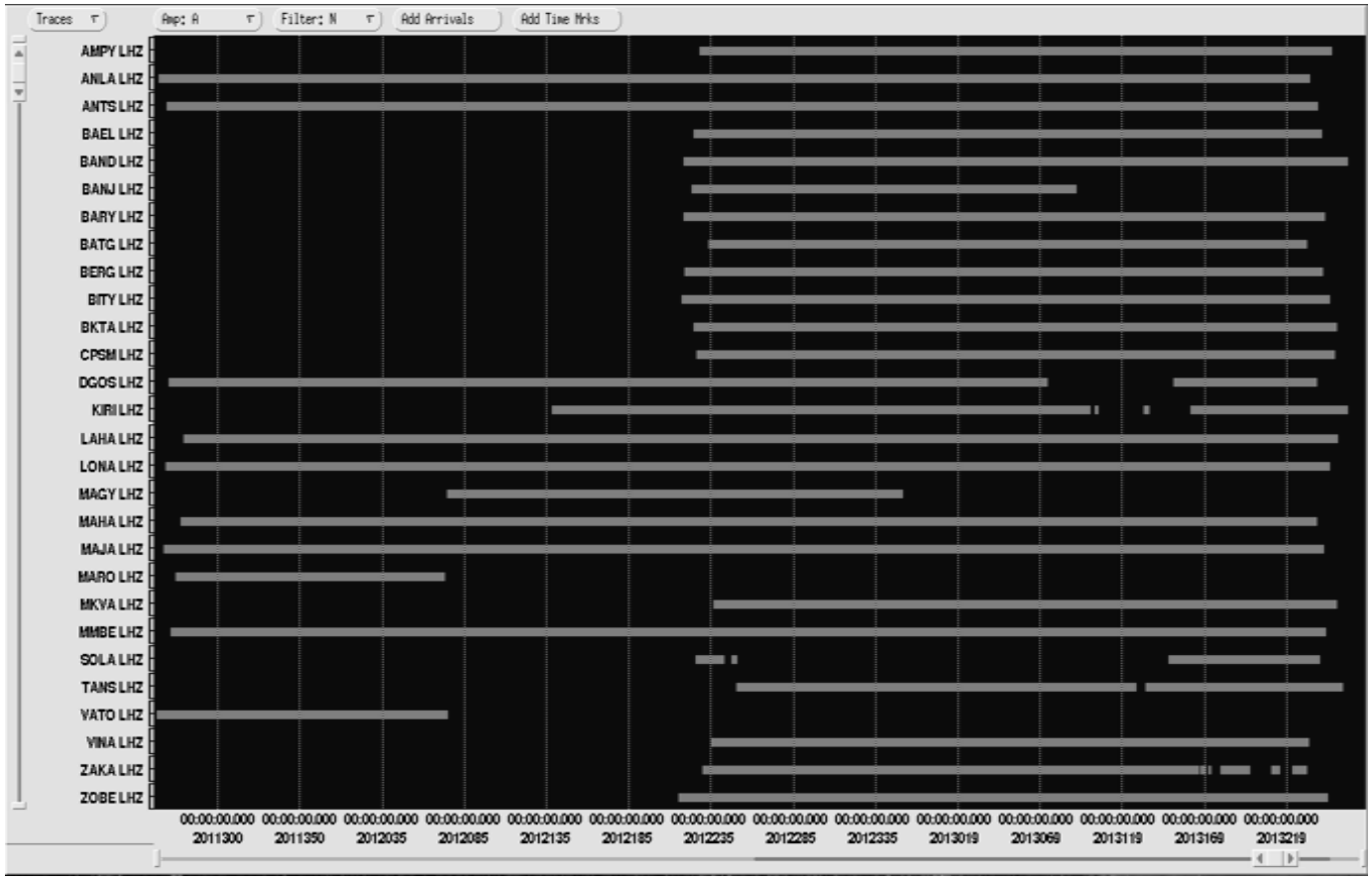

Figure 2.8: Histogram showing the data collected for the MACOMO project.

2.2.3 Temporary broadband seismic stations: SELASOMA project

Another project deployed simultaneously 51 temporary seismic stations in southern of Madagascar between 2012 and 2014: the SEismological signatures in the Lithosphere/Asthenosphere system of SOuthern MAdagascar (SELASOMA) project. The project aimed to study the lithosphere in southern Madagascar around the Ranotsara shear-zone. 25 seismic stations in this project were broadband stations and installed perpendicular to the main shearing direction of the Ranotsara shear zone to study the structure of the region.

I had access to seven of these 25 stations for this work which are: MS04, MS07, MS10, MS12, MS16, MS19 and MS23.

2.2.4 Temporary broadband seismic stations: RHUM-RUM project

In addition, broadband seismic stations were deployed as the land-station part of the the Réunion Hotspot and Upper Mantle – Réunions Unterer Mantel (RHUM-RUM) project, while the most part of the stations were ocean-bottom seismometers (OBS) deployed in the Indian Ocean around Reunion, Mauritius, and Rodriguez Islands. I was involved in the deployment and retrieving of these OBS stations. This project aimed to image the mantle plume under the Réunion hotspot.

I used 10 stations from RHUM-RUM project: five stations deployed along the southeastern coast of Madagsacar, RUM1 – RUM2 – RUM3 – RUM4 – RUM5, and five stations deployed on the Iles Eparses (islands around Madagascar), EURO – GLOR – JNOV – MAYO – TROM.

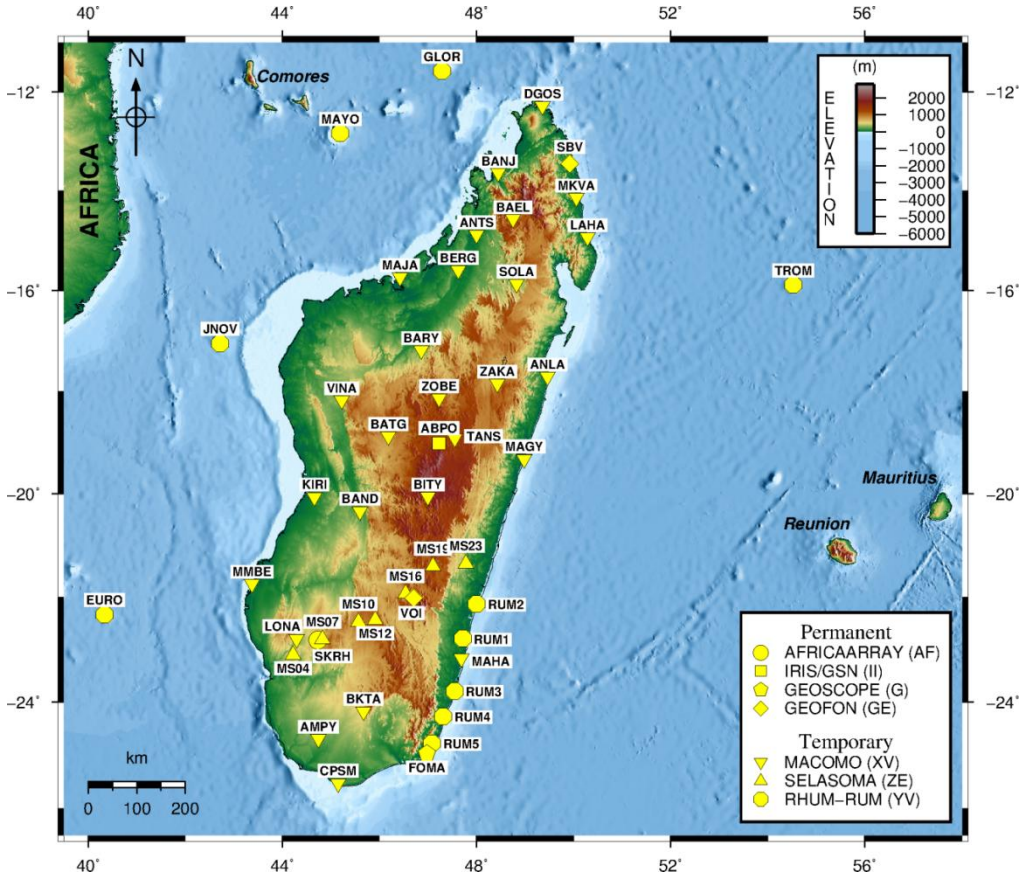

Figure 2.9: Location of the permanent and temporary broadband (yellow symbols) stations used in this study. Elevation is obtained from ETOPO1 (Amante and Eakins, 2009).

2.2.5 Summary

In summary, a total of 48 broadband seismic stations (Table 2.1 and Figure 2.9) from permanent and temporary deployment were used to achieve the objectives of this thesis. Briefly,

(1) 26 seismic stations are from the MACOMO project,
(2) 5 seismic stations are from the permanent stations,
(3) 7 seismic stations are from the SELASOMA project,
(4) and 10 stations are from the RHUM-RUM project.

I used 37 seismic stations for the receiver function analysis; RHUM-RUM stations were excluded due to policy on the use of the data. Besides, TANS from the MACOMO project was also excluded in the receiver function analysis due to insufficiency of data (only ~2 months of data). I used all 48 stations for the tomography part of the thesis.

Table 2.1: Permanent and temporary broadband seismic stations used in the study.

Code	Site	Latitude	Longitude	Altitude [m]	Start	End
		PERMANENT SEISMIC STATIONS				
		GSN				
ABPO	Ambohimpanompo, Madagascar	-19.018	47.229	1528	2007/04/04	-
		GEOSCOPE				
FOMA	Fort Dauphin, Madagascar	-24.97565	46.978877	28	2008/09/01	-
		GEOFON				
SBV	Sambava, Madagascar	-13.4584	49.9212	65	2009/11/19	-
VOI	Vohitsoka, Madagascar	-22.0260	46.7059	993	2009/11/26	-
		AFRICAARRAY				
SKRH	Sakaraha, Madagascar	-22.827	44.732	891	2012/08/16	-
		TEMPORARY SEISMIC STATIONS				
		MACOMO				
AMPY	Ampanihy, Madagascar	-24.7033	44.7436	252.4	2012/08/15	2013/12/31
ANLA	Analava, Madagascar	-17.7062	49.4599	33.3	2011/09/21	2013/12/31
ANTS	Antsohihy, Madagascar	-14.8843	47.9993	12.2	2011/09/26	2013/12/31
BAEL	Bealanana, Madagascar	-14.5397	48.7467	1147.8	2012/08/11	2013/12/31
BAND	Malaimbandy, Madagascar	-20.3428	45.5964	178.6	2012/08/05	2013/12/31
BANJ	Ambanja, Madagascar	-13.6426	48.4537	17.3	2012/08/10	2013/12/31
BARY	Antanimbary, Madagascar	-17.1845	46.8571	265.7	2012/08/05	2013/12/31
BATG	Tsiroanamandidy, Madagascar	-18.8786	46.1871	1552.2	2012/08/20	2013/12/31
BERG	Port Berge, Madagascar	-15.58	47.6277	67.8	2012/08/06	2013/12/31
BITY	Ibity, Madagascar	-20.0608	47.0001	1566	2012/08/04	2013/12/31
BKTA	Beraketa, Madagascar	-24.1822	45.673	576	2012/08/11	2013/12/31
CPSM	Cap Ste. Marie, Madagascar	-25.5358	45.15	172.8	2012/08/13	2013/12/31
DGOS	Deigo Suarez, Madagascar	-12.2825	49.3606	33.5	2011/09/27	2013/12/31
KIRI	Kirindy, Madagascar	-20.0676	44.6595	70.1	2012/05/04	2013/12/31
LAHA	Antalaha, Madagascar	-14.9344	50.2911	11.1	2011/10/06	2013/12/31
LONA	Analavelona, Madagascar	-22.8057	44.2959	416.6	2011/09/25	2013/12/31
MAGY	Vatomandry, Madagascar	-19.3179	48.9785	22.2	2012/03/14	2013/12/31
MAHA	Mahabo, Madagascar	-23.1714	47.6899	31	2011/10/04	2013/12/31
MAJA	Mahajanga, Madagascar	-15.7323	46.4263	35.7	2011/09/24	2013/12/31
MARO	Marofandilia, Madagascar	-20.1331	44.5515	32.9	2011/10/01	2013/12/31
MKVA	Makirovana, Madagascar	-14.1368	50.0608	19.6	2012/08/23	2013/12/31
MMBE	Morombe, Madagascar	-21.7501	43.3721	32	2011/09/28	2013/12/31
SOLA	Mandritsara, Madagascar	-15.8636	48.8263	316.8	2012/08/12	2013/12/31
TANS	Antananarivo, Madagascar	-18.9176	47.5511	1397.9	2012/09/06	2013/12/31
VATO	Vatomandry, Madagascar	-19.3314	48.9824	23	2011/09/20	2013/12/31
VINA	Beravina, Madagascar	-18.1769	45.2247	293.8	2012/08/22	2013/12/31
ZAKA	Ambatondrazaka, Madagascar	-17.8471	48.423	814.2	2012/08/17	2013/12/31
ZOBE	Ankazobe, Madagascar	-18.1369	47.2289	1614.2	2012/08/02	2013/12/31
		SELASOMA				
MS07	Madagascar	-22.8124	44.8289	663	2012/04/28	2014/12/31
MS10	Madagascar	-22.4735	45.5668	972	2012/05/04	2014/12/31
MS12	Madagascar	-22.4374	45.9150	1038	2012/05/03	2014/12/31
MS16	Madagascar	-21.9357	46.5430	772	2012/05/01	2014/12/31
MS19	Madagascar	-21.4093	47.1028	1140	2012/05/07	2014/12/31
MS23	Madagascar	-21.3542	47.7780	254	2012/04/27	2014/12/31
		RHUM-RUM				
EURO	Europa	-22.344	40.3401	10	2011/04/06	2013/12/09
GLOR	Grande Glorieuse	-11.5824	47.2895	4	2011/04/18	2013/12/11
JNOV	Juan De Nova	-17.0543	42.7125	8	2011/04/11	2013/12/00
MAYO	Mayotte	-12.8456	45.1868	41	2011/04/15	2014/01/14
RUM1	Vohimasy, Madagascar	-22.8022	47.7175	45	2012/09/25	2014/08/31
RUM2	Manakara, Madagascar	-22.1367	48.0022	11	2012/09/23	2014/08/31
RUM3	Manambondro, Madagascar	-23.7988	47.5459	8	2012/09/27	2014/08/30
RUM4	Manenterina, Madagascar	-24.2767	47.3157	15	2012/09/28	2014/08/29
RUM5	Mahatalaky, Madagascar	-24.7852	47.0851	21	2012/09/30	2014/08/27
TROM	Tromelin	-15.8885	54.5218	6	2011/04/23	2013/12/16

2.3 Isolation of receiver functions

Receiver functions were used for the crustal and uppermost mantle studies, in the first project, and mantle transition zone estimation, for the third project of this thesis. This section presents an overview of the receiver function method and the processing steps used to construct receiver functions beneath each seismic station.

2.3.1 Overview of receiver function

Determinations of crustal and mantle structure from seismic observations worldwide in both the oceans and continents provide baseline constraints on many fundamental Earth processes, for example, crustal genesis, tectonic plate motions, plateau uplift, magmatism, the formation of mineral deposits such as petroleum, and, in more general terms, understanding Earth's geologic history as a whole.

Mathematically, seismic signals recorded at a receiver (seismometer) are the convolution of the source-time function at the earthquake's focal point and the Earth's response along the propagation path. These waves sample the Earth interior and contain valuable information about the source mechanism and the structure of the propagating medium. Any signal incorporated in the seismic traces can be extracted by deconvolution processes, depending on the interests and objectives of the study. Langston (1997) first introduced the deconvolution of the Earth's response beneath seismic stations, called receiver functions, from seismic traces to study the structure of the crust and the upper mantle under Corvallis, Oregon.

Parts of the energy from incoming *P*-waves at the boundary between geologic layers with contrasting seismic velocities (*e.g.* basin-basement, crust-mantle, and lithosphere-asthenosphere…) are converted into *S*-waves. These phases are known as the *P-to-s* converted phases or *Ps* phases. A similar phenomenon happens for an incoming *S*-wave, yielding the *Sp* phases, but we only use *Ps* phase in this study.

Receiver functions are radial impulse responses that represent the vertical impedance structure of the Earth beneath the recording seismic station (Figure 2.10). They are time series showing the *Ps* phases and their crustal multiples (*PpPs* and *PsPs+PpSs*), and are obtained by applying a deconvolution technique to remove the earthquake source-time function and instrument response from the three-component seismograms recorded at a seismic station.

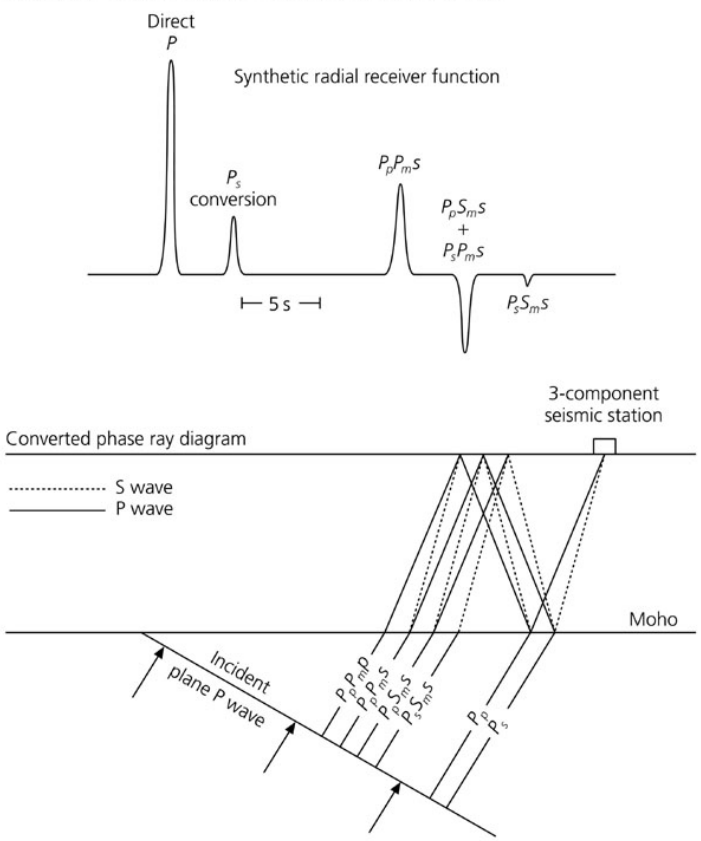

Figure 2.10: (Top) Synthetic radial receiver function waveform. (Bottom) Corresponding seismic ray diagram of *P-to-S* converted phase (*Ps* phase) and its multiples (*PpPs* and *PsPs+PpSs*) at the Mohorovicic discontinuity (Moho) for a single layer over a half space. (taken from Stein and Wysession, 2003; http://epsc.wustl.edu/seismology/book/chapter6/chap6_sr/6_3_07.jpg).

These seismic arrivals, *Ps* phases and their multiples (*PpPs* and *PsPs+PpSs*), are interpreted in order to estimate the crustal thickness and the depth of any other discontinuities, and to study the physical properties of the shallow to deep earth (Zandt and Ammon, 1995; Zhu and Kanamori, 2000).

Their amplitudes and arrival times are functions of the physical properties of the crust and mantle beneath the receiver (Langston, 1979; Owens et al. 1984; Ammon et al. 1990; Cassidy 1992). In fact, the amplitudes are controlled by the dimension of the velocity contrast (*i.e.* boundary or discontinuity) as well as the incidence angle of the incoming *P*-wave. The arrival times depend on the distance from the discontinuity to the surface, the seismic velocities (velocity of *P*- and *S*-waves) of the medium between the discontinuity and the surface, and the angle of incidence or ray parameter of the P-wave. Thus, the shape of pulses that represent the receiver function can be broad, sharp, low amplitude, or high amplitude.

The rule of thumb in receiver analyses is that the horizontal resolution (lateral extension) of the receiver function is approximately equal to the depth of the discontinuity of interest (Julià et al., 2000). To illustrate this, an incoming teleseismic *P*-wave, from the northern azimuth, converted at the Moho located at 30 km depth, samples laterally 30 km to the north of the station. However, the sample point may vary according to the azimuth of the impinging *P*-wave and distance of the source. This makes the receiver functions a powerful tool to study the azimuthal variation of discontinuities (*e.g.* dipping Moho). The vertical range/aperture depends simply, instead, on the length (in time) of the trace that is considered for the processing: the more the time window is extended, the deeper is the depth of investigation.

2.3.2 Theory

The displacement of the ground recorded at a seismic station for an incoming *P*-wave wave in a ZRT (Vertical, Radial, and Transverse) coordinate system is described as the following convolutions (Langston, 1979):

$$\begin{aligned} Z(t) &= I(t) * S(t) * H_Z(t) \\ R(t) &= I(t) * S(t) * H_R(t) \\ T(t) &= I(t) * S(t) * H_T(t) \end{aligned} \tag{2.1}$$

where *Z(t)*, *R(t)*, and *T(t)* are the vertical, radial, and tangential component of ground motion, *I(t)* is the instrument response, *S(t)* is the source time function,

and $H_Z(t)$, $H_R(t)$, and $H_T(t)$ are respectively the vertical, radial and tangential impulse responses (or receiver functions) of the structure beneath the station.

In his source equalization procedure, Langston (1979) assumed that $Z(t)$ behaves as a Dirac delta function, thus $S(t)$ can be approximated from:

$$I(t) * S(t) \simeq Z(t) \tag{2.2}$$

Consequently, by assuming that the instrument responses are similar for the three components and by bringing Equation (2.2) into Equation (2.1), $H_R(t)$ and $H_T(t)$ can be obtained from the deconvolution of $I(t)*S(t)$ from $R(t)$ and $T(t)$.

Since the convolution in time domain is equivalent to a simple multiplication in frequency domain, then we have:

$$\begin{aligned} H_R(\omega) &= \frac{R(\omega)}{I(\omega)S(\omega)} \simeq \frac{R(\omega)}{Z(\omega)} \\ H_T(\omega) &= \frac{T(\omega)}{I(\omega)S(\omega)} \simeq \frac{T(\omega)}{Z(\omega)} \end{aligned} \tag{2.3}$$

where $Z(\omega)$, $R(\omega)$, $T(\omega)$, $I(\omega)$, $S(\omega)$, $H_R(\omega)$, and $H_T(\omega)$ are the Fourier transform of $Z(t)$, $R(t)$, $T(t)$, $I(t)$, $S(t)$, $H_R(t)$, and $H_T(t)$, respectively.

Equation (2.3) is the equation defining the so-called receiver function. The obtained receiver functions in Equation (2.3) are subsequently translated into the time domain by applying the inverse Fourier transform.

2.3.3 Data preparation

Raw seismic data from all temporary seismic stations listed in Table 2.1 were extracted from a local database; while data from permanent stations were downloaded from the Data Management Center (DMC) of the Incorporated Research Institutions for Seismology (IRIS) as they are available online. Note that RHUM-RUM data were not used in the receiver function analysis. Several data

preparation processes must be applied to the raw seismograms before the deconvolution.

Selecting seismic events for the processing

The seismic events used in this thesis were selected from the seismic catalog provided by the Wilber 3 web application of the IRIS website (https://ds.iris.edu/wilber3/find_event). Earthquakes that occurred between September 2011 to September 2013 were considered for the temporary stations, and earthquakes between April 2007 and October 2015 for the permanent stations. A total of 1394 seismic events were obtained from the earthquake catalog and used for the event selection criteria. Two criteria were set for the selection:

(1) Only earthquakes that have magnitude Mw ≥ 5.5 were considered in order to have clear *P*-arrival thus high signal-to-noise ratio (SNR) in the seismograms.

(2) Earthquakes that occurred at epicentral distance between 30° and 95° away from each seismic station were selected. The sharp velocity contrasts between the upper and lower mantle at 410 km and 660 km depths produce two triplications (which are seismic phases that arrive nearly at the same time with the *P* wave) for events at distance between 13° and 28° (Figure 2.11). These arrivals interfere with the actual *P*-arrivals. Consequently, the minimum epicentral distance was set to 30° to avoid them. On the other hand, *P*-wave energies diffracted at the core-mantle boundary, called *Pdiff* phases, are generally observed at a recording station from events occurring at distances greater than 98°. Thus, these arrivals were avoided by using only events with epicentral distance less than 95°. Besides, from the predicted travel time curves, only *P*-waves are expected to arrive first at the seismic station for events with an epicentral distance between 30° to 95° (Figure 2.12).

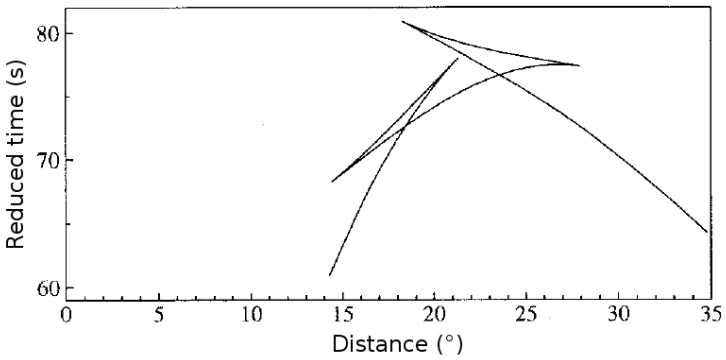

Figure 2.11: Predicted travel times of P-wave. Two triplications are observed for the range of distance between 13° and 28° (taken from Shearer (2000)).

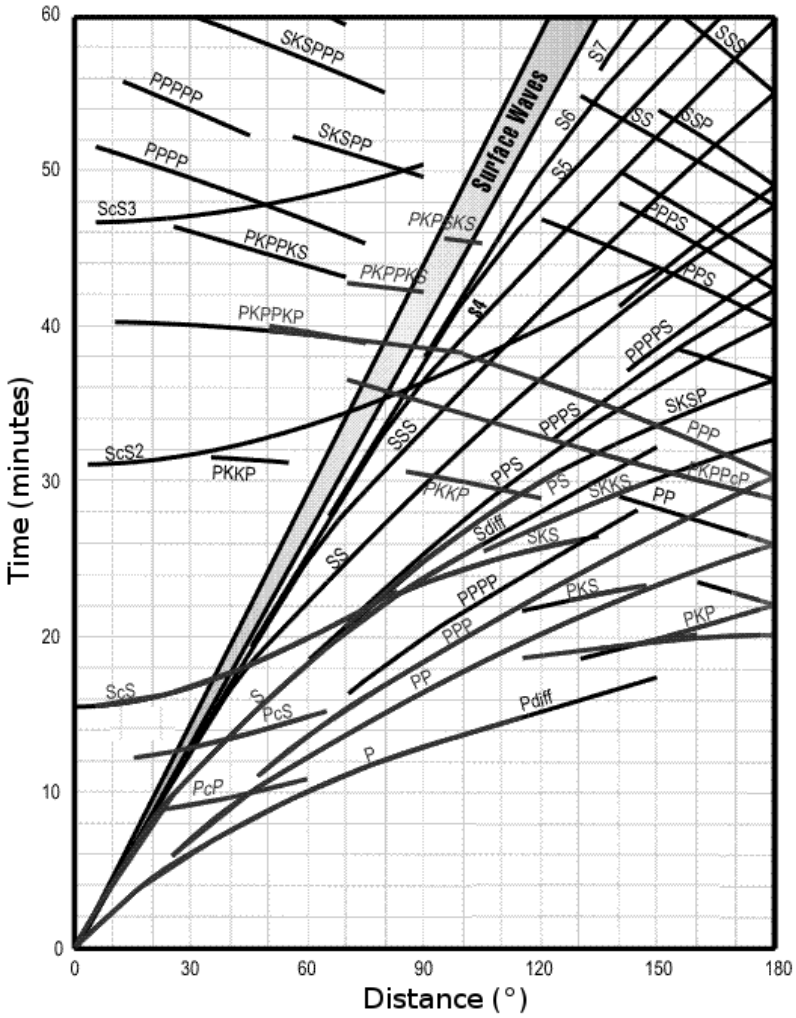

Figure 2.12: Predicted travel times of different seismic phases (http://Earthquake.usgs.gov).

Picking and windowing *P*-wave phases

The predicted arrival time of *P*-waves of these selected events were, initially, computed based on their longitude, latitude, origin time and depth of the seismic event and the longitude and latitude of the seismic station. In this procedure, the interior of the Earth is divided into isotropic layers, here the global *1D*-velocity model *ak135* (Kennett et al., 1995) was used. Then by considering the positions of the seismic event and station, the origin time of the event, the seismic velocity at each layer, and the law of refraction applied to seismic waves, the travel time of the *P*-wave thus the arrival time in the seismogram is estimated from ray-tracing. The predicted arrival time of *P*-wave helps to identify the actual arrival of the phase at the recording station.

Then, the obtained predicted *P*-arrival was visually inspected in the waveform and manually adjusted to the actual *P*-arrival if it does not match. For example, in Figure 2.13, the predicted arrival of *P*-wave (T0) occurs ~2 s earlier than the actual arrival (P).

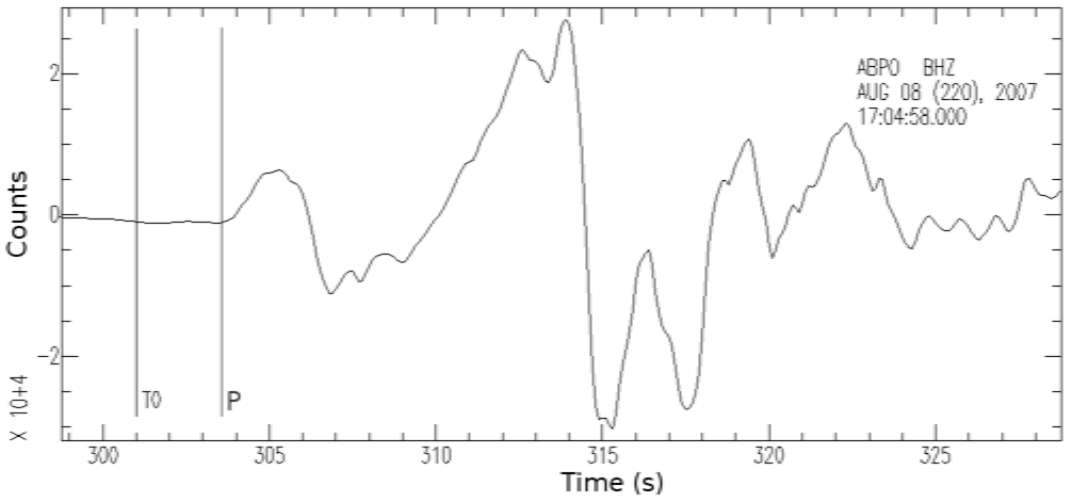

Figure 2.13: *P*-arrival adjustment for the seismic event on 08th August 2007, 17:04:58 UTC in Java, Indonesia, with Magnitude 7.4. The predicted arrival of *P*-wave (T0) occurs ~2 s earlier than the actual arrival (P).

Finally, when the exact time of the *P*-arrival is known and picked, the waveforms were cut 10 s before and 100 s after it. Each trace was windowed at 10 s earlier to

avoid any loss of the *P*-arrival and 100 s long because the resulting receiver functions will be subsequently used for the study of the mantle transition zone.

Detrending, tapering, filtering, and decimating seismograms

A systematic shift, typically linear, can be observed in the seismograms due, usually, to sensor drift (the mass-position). The linear trend may cause regular increases or decreases in the waveforms which could negatively affect any further processing. The procedure, called "detrending", forces their mean to zero and reduces overall variation.

After windowing the seismograms, the sudden change (or the edge effect) in the beginning and ending of the sample sequence is removed by tapering the waveform. In this procedure, the first and last point of the seismogram is forced to zero, and then increases smoothly to its original value towards the interior point relative to each end (the first and last point).

Different source of vibration (such as the Earth's background noise, instrumental noise, surrounding noise, etc) may affect the measurement of the ground-motion. A filter with a 0.05 Hz (in order to remove instrumental low-frequency noise) to 5 Hz pass band was applied.

Finally, as the original waveforms were sampled at 40 samples per second (s.p.s), the data samples were decimated to 10 s.p.s to speed up the subsequent inversion.

Rotating seismograms

P-waves are compressional waves, which squeeze and stretch the material by spreading back and forth parallel to the direction of propagation (Figure 2.1). As a longitudinal wave, the maximum energy of a *P*-wave is observable on a coordinate system that has a component parallel to its direction of propagation. Consequently, seismograms were rotated from ZNE coordinates system to ZRT

coordinate system (up-down, radial, and tangential components). The radial component R is the direction along the great circle connecting the epicenter and the seismometer, the tangential component T is the direction perpendicular to the propagation path, and Z component is the same for both systems (Figure 2.14).

The transformation from ZNE to ZRT coordinates is actually a 2D-rotation. It is expressed as:

$$\begin{bmatrix} R \\ T \\ Z \end{bmatrix} = \begin{bmatrix} cos\theta & sin\theta & 0 \\ -sin\theta & cos\theta & 0 \\ 0 & 0 & 1 \end{bmatrix} \begin{bmatrix} E \\ N \\ Z \end{bmatrix} \qquad with \qquad \theta = \frac{3\pi}{2} - \xi \tag{2.4}$$

ξ is the back azimuth. It is the angle of the vector pointing from the seismic station to the epicenter measured clockwise from north.

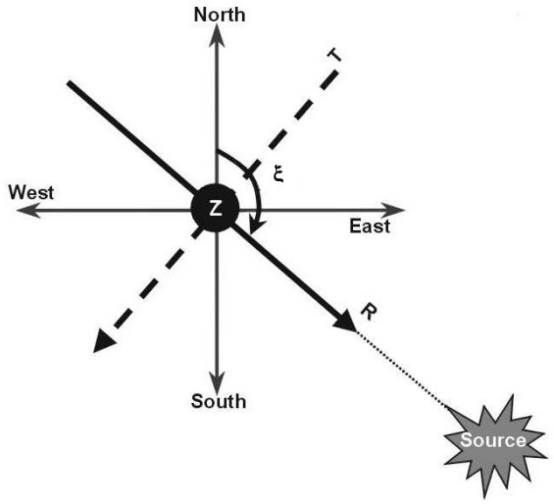

Figure 2.14: Transformation of ZNE coordinate system (up-down, north-south, and east-west components) to ZRT coordinate system (up-down, radial, and tangential components).

All of these steps were performed before the deconvolution of the receiver functions in each seismic station. An example of the preprocessed waveforms of the seismic events in Figure 2.13 is shown in Figure 2.15.

Note that the first arrival, *i.e. P* arrival, in Figure 2.15 corresponds to the first significant departure of the waveform from the background noise. The high amplitude following the *P*-arrival, at approximately 10 s, can be explained as source function, depending on the focal mechanism at the hypocenter.

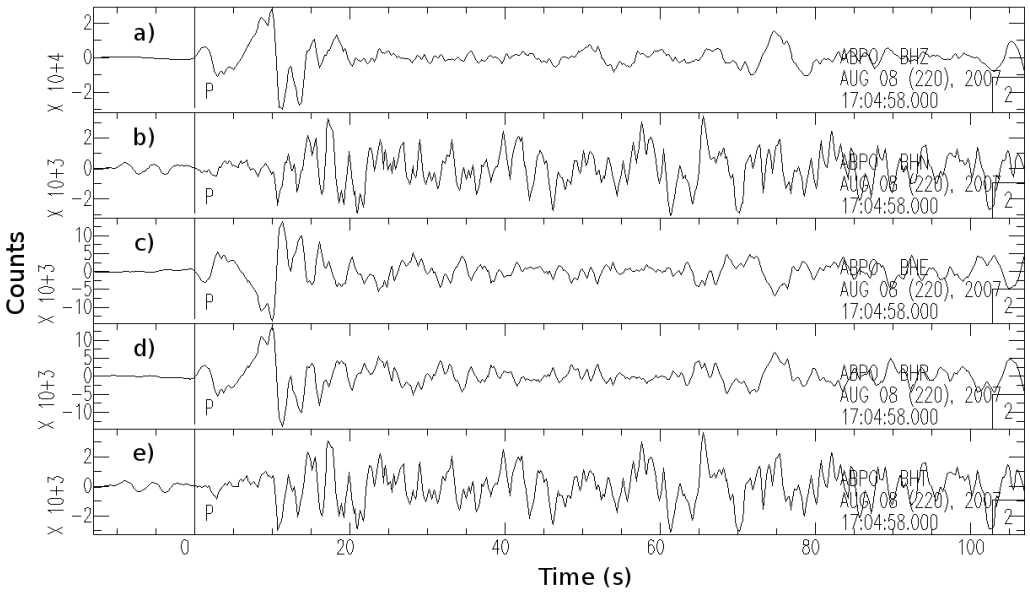

Figure 2.15: Preprocessed waveforms for the seismic event on 08th August 2007, 17:04:58 UTC in Java, Indonesia, with Magnitude 7.4. (a) Vertical component Z, (b) East-West component E, (c) North-South component N, (d) Radial component R, and (e) Tangential component.

Ray parameters

The ray parameter is a geometric property of a seismic ray. It remains constant for rays originating from the same incoming ray, even though after reflection, refraction, or conversion at a discontinuity. Assume that the seismic rays are plane waves that propagate through a layered spherical Earth. Applying Snell's law of refraction to the interface at every two successive layers, the ray parameter "*p*" is described by the relationship:

$$\frac{r_1 \sin\ i_1}{V_1} = \frac{r_2 \sin\ i_2}{V_2} = \cdots = \frac{r_n \sin\ i_n}{V_n} = p \qquad (2.5)$$

$V_1, V_2, \ldots, V_n$ are the seismic velocities at each layer; $r_1, r_2, \ldots, r_n$ are the distance between the center of the Earth to the interfaces; $i_1, i_2, \ldots, i_n$ are the incidence angles; and p is the ray parameter.

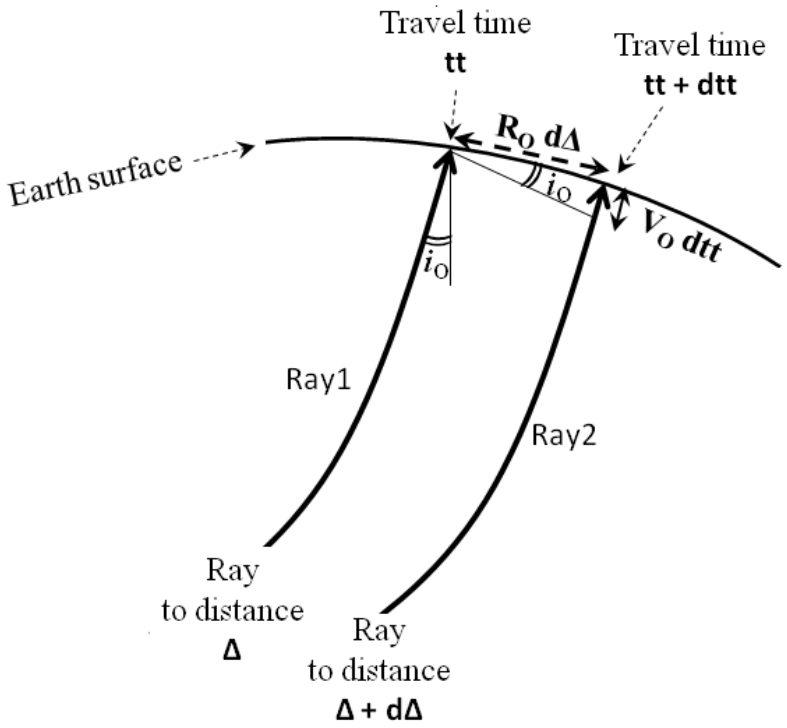

Figure 2.16: Ray diagram showing two adjacent impinging seismic rays (Ray1 and Ray2) from the same source.

The ray parameter for each seismic ray was estimated using an algorithm based on the travel-time and derivatives of rays for a given epicentral distance and source depth (Lowrie, 2007). This technique uses the derivative or slope of the travel time curve to calculate the ray parameter from a simple geometry. Two adjacent impinging rays coming from the same source are used in this approach, Ray1 and Ray2 in Figure 2.16. Ray2 impinges at the surface further (at a distance $\Delta+d\Delta$) and later (at time $tt+dtt$) than Ray1 (distance Δ and time tt). Note that Δ is the angular distance and tt is the travel time of the ray between the source and the impinging point at the surface. The angle of incidence of Ray1, i_O, is geometrically equal to the angle between the segment connecting the two ray perpendicularly, from the point of Ray1 to Ray2, and the surface. The distance between the points of Ray1 and Ray2 at the surface is $R_O.d\Delta$ (where R_O is the radius of the Earth and $d\Delta$ is the extra angular distance of Ray2). The extra distance crossed by Ray2 is equal to $V_0\ dtt$ (where V_0 is the near surface velocity and dtt is the extra traveling time of Ray2). Then the sine of the angle of

incidence, *sin* i_0, is obtained from the hypotenuse $R_0\, d\Delta$ and opposite side $V_0\, dtt$, expressed as:

$$\sin\ i_0 = \frac{V_0 dtt}{R_0 d\Delta} \tag{2.6}$$

Finally, the derivative or slope of the travel time is obtained by rearranging this equation:

$$\frac{dtt}{d\Delta} = \frac{R_0 \sin\ i_0}{V_0} \tag{2.7}$$

The right side of Equation (2.7) represents the expression of the ray parameter as shown in Equation (2.5). It shows that the ray parameter is the derivative or slope of the travel time.

2.3.4 Deconvolution of receiver functions

There are several methods to deconvolve the receiver functions from the initial waveform. In this section we present two different approaches, the water-level deconvolution of Langston (1979), which is in the frequency domain, and the iterative deconvolution of Ligorria and Ammon (1999), in time domain.

The water-level deconvolution

The deconvolution of receiver function was, previously, conducted by division in frequency domain.

In practice, the denominator of Equations (2.3) may be very small or even zero, which tends $H_R(\omega)$, and $H_T(\omega)$ to infinity. To avoid this, the source equalization is implemented by applying the water-level method in the frequency domain to stabilize the processing. In this method, the small or zero values are replaced by a fraction of the maximum value of the denominator. This fixes the minimum

allowable value of the amplitude spectrum of the receiver function and cancels out all frequencies that are lower than it. Consequently, the water-level method performs a simultaneous high-pass, low-pass, and band-stop filtering. Figure 2.17 illustrates the method.

Let us consider only the radial receiver function $H_R(\omega)$ for the following. For the tangential receiver function, $H_T(\omega)$, replace $R(\omega)$ with $T(\omega)$ in the expression. When the water-level method is applied, the deconvolution in Equation (2.3) is replaced by:

$$H(\omega) = \frac{R(\omega)\bar{Z}(\omega)}{\phi(\omega)} G(\omega) \tag{2.8}$$

with

$$\phi(\omega) = \max\{Z(\omega)\bar{Z}(\omega), c.\max[Z(\omega)\bar{Z}(\omega)]\}$$

were $\bar{Z}$ is the complex conjugate of Z, c is the water-level parameter which determines the accepted minimum amplitude of the denominator of Equation (2.3).

And the Gaussian filter $G(\omega)$ is

$$G(\omega) = \xi \ e^{-\left(\frac{\omega^2}{4a^2}\right)} \tag{2.9}$$

ξ is a constant that acts as a normalization parameter, and a is the width of the Gaussian filter.

The low-pass Gaussian filter is generally applied to attenuate the high-frequency in the receiver functions.

When using this technique, the water-level is obtained from trial and error, which makes it still unstable and complicated to implement automatically.

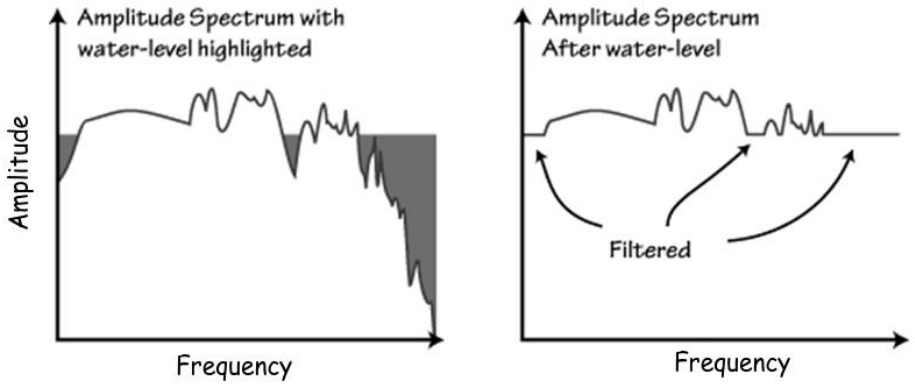

Figure 2.17: The water-level deconvolution technique. All frequencies smaller than the water-level parameter (gray shade) are attenuated (modified from Ammon, 1997).

The iterative deconvolution

The iterative deconvolution of Ligorria and Ammon (1999) is performed in the time domain.

From Equation (2.3), the receive function is obtained by deconvolving the vertical-component seismogram from the radial-component seismogram. In the opposite way, the resulting seismogram from the convolution of the vertical-component seismogram with the receiver function best matches the radial-component seismogram. The iterative deconvolution is principally based on this principle by assuming that the receiver function is a sum of delta-like functions.

After all the preprocessing steps in Section 2.3.3, the Gaussian filter in Equation (2.9) is, firstly, applied to the radial and vertical components of the preprocessed seismograms. Then, the process of receiver function "building" is done as follows:

(1) The arrival time of the first peak of the receiver function is estimated by cross-correlating the radial-component and vertical-component seismograms.

(2) Knowing the location of the first peak, the first pulse of the receiver function is built from it, and then convolved with the vertical component, which creates a predicted radial seismogram.

(3) The fit between the predicted and the observed radial seismograms is then evaluated from least-square minimization.

(4) The process is repeated for a predefined number of iterations in order to locate other peaks of the receiver function.

In summary, the receiver function is built by fitting, from a least-square minimization technique, the observed radial seismogram with the convolution of the observed vertical-component seismogram and a sequence of delta-function-like peaks. The sequence of peaks represents the radial receiver function and is updated during the iteration. A similar process is performed for the tangential receiver functions, with the difference of tangential seismograms used instead of radial seismograms.

The stability issue observed in the frequency domain technique does not exist in the time domain technique. This makes the iterative deconvolution much easier to implement in an automated fashion compared to the water-level deconvolution. The iterative time-domain deconvolution was used to estimate the receiver function in this study.

2.3.5 Application and data selection

In total, 143 seismic events were selected and subsequently used to estimate receiver functions. They are listed in Table A.1 of Appendix A and shown in Figure 2.18.

The Gaussian filter applied to the seismograms prior to the deconvolution controls the frequency of the receiver functions. In general, lower-frequency (~0.5 Hz) receiver functions best sample any deep discontinuity in the lower crust and the upper mantle, whereas the higher-frequency (~1.25 Hz) constrains discontinuities in the shallower parts of the crust (Owens and Zandt, 1995; Ligorria and Ammon,

1999). Consequently, receiver functions were calculated for two overlapping frequencies, which correspond to Gaussian filter widths of 1.0 and 2.5 (corner frequencies of 0.5 Hz and 1.25 Hz, respectively). The deconvolution was run for 200 iterations using the program *iterdecon* of Ammon (1997).

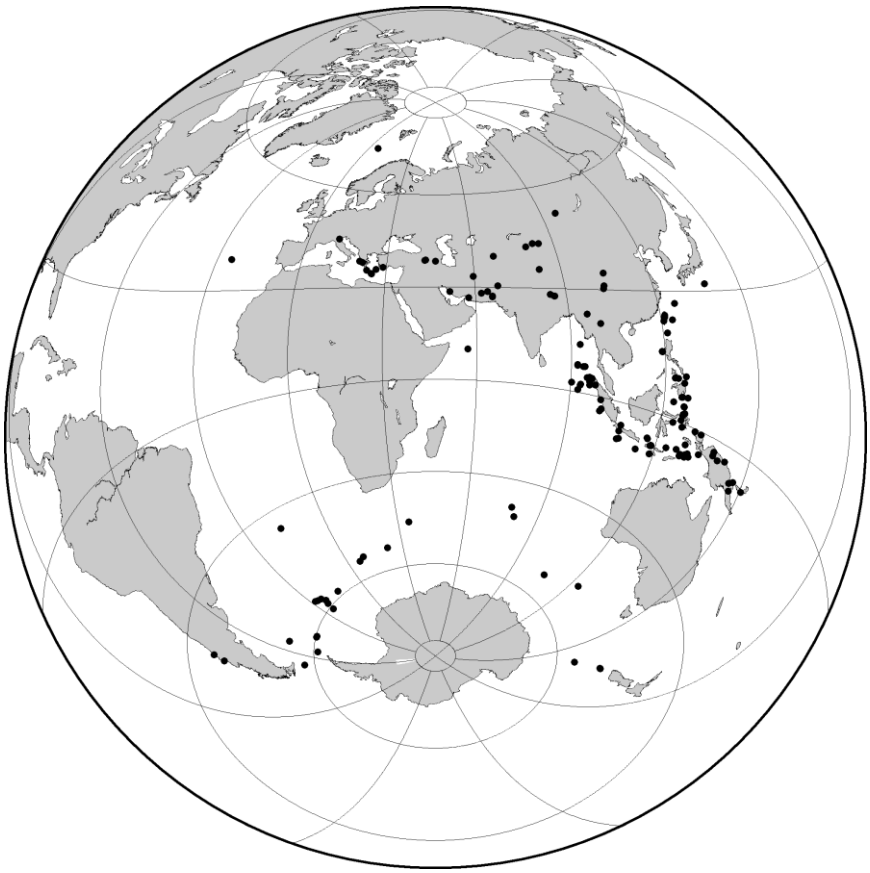

Figure 2.18: Distribution of 143 earthquakes (black dots) used to compute receiver functions.

The quality of the receiver functions was evaluated by convolving back each radial receiver function with its corresponding observed vertical-component seismogram in order to recover the radial-component seismogram. Only radial receiver functions that recovered at least 85% of the observed radial-component seismogram were utilized for further analysis (Ligorria and Ammon, 1999).

Tangential receiver functions are usually considered to study the degree of heterogeneity and isotropy of the propagating medium (Cassidy, 1992). Small amplitudes of tangential receiver functions indicate a predominantly homogenous and isotropic medium beneath the receiver. Consequently, radial receiver

functions that are associated with biased and uneven prominent-amplitude tangential receiver functions were also discarded.

A total of 653 radial receiver functions were obtained from all the stations. Examples of receiver functions computed from a permanent (ABPO) and temporary (LAHA) seismic station are shown in Figure 2.19. Receiver functions from all the stations are shown in Figure A.1 of Appendix A.

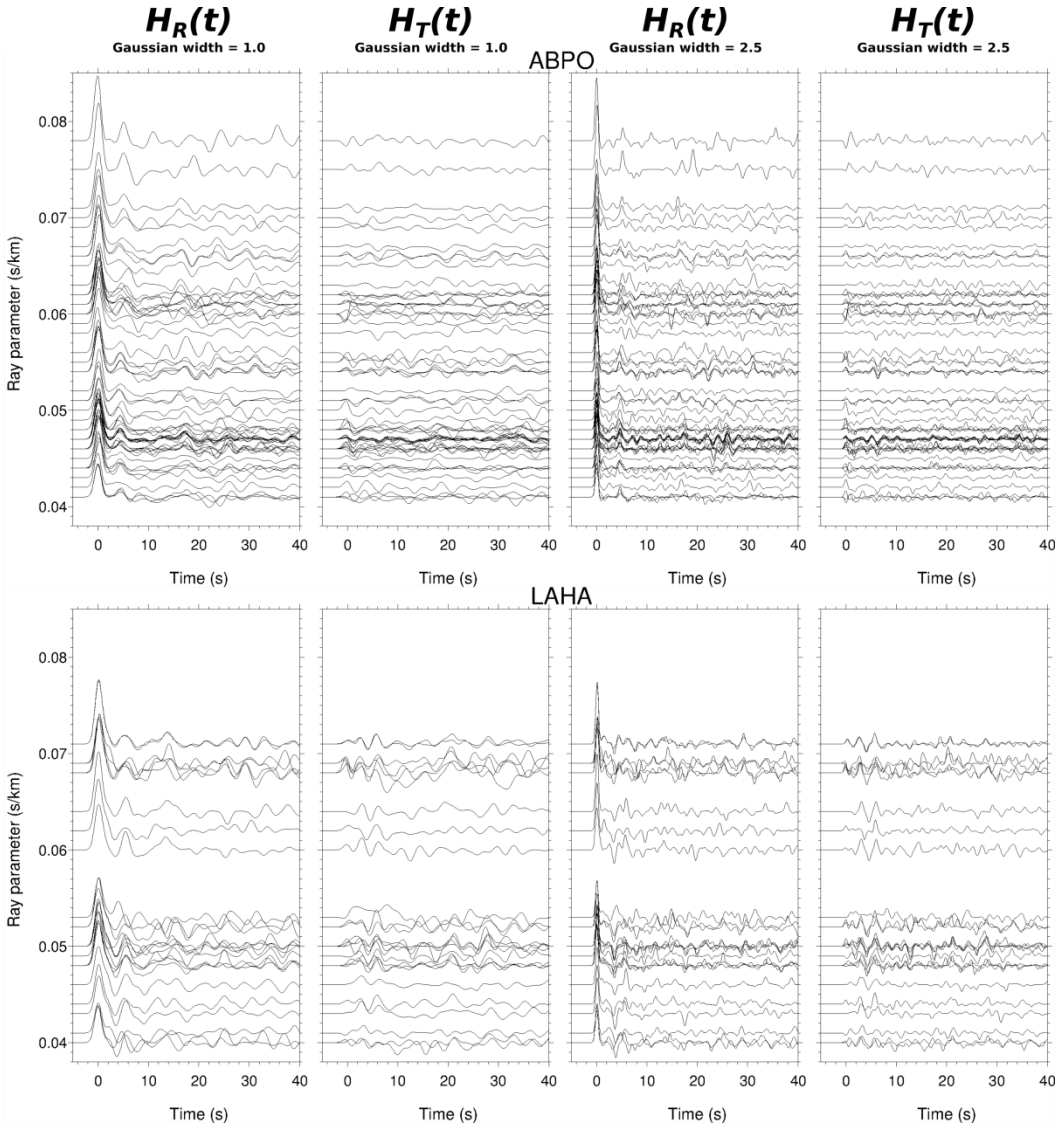

Figure 2.19: Receiver functions from a permanent (ABPO) and a temporary (LAHA) seismic station. From left to right for each station: radial receiver function $H_R(t)$ from Gaussian 1.0, tangential receiver function $H_T(t)$ from Gaussian 1.0, radial receiver function $H_R(t)$ from Gaussian 2.5, and radial receiver function $H_T(t)$ from Gaussian 2.5. Note the difference in the number and distribution of ray parameters the receiver functions for the two stations.

2.4 Crustal thickness and *Vp/Vs* ratio from the *H-κ* stacking method

The procedure of stacking seismograms in processing seismic data increases the SNR and enhances the overall data quality. The *H-κ* stacking method developed by Zhu and Kanamori (2000) was applied to the receiver function waveforms to estimate the crustal thickness (*H*) and *Vp/Vs* ratio (*κ*) beneath the seismic stations used in this thesis. This method is used for the first project of this study and results are shown in Chapter 3.

2.4.1 The *H-κ* stacking procedure of Zhu and Kanamori (2000)

By assuming that teleseismic waves are plane waves, Kind and Vinnik (1988) proposed that arrival time of the three phases, *Ps*, *PpPs*, and *PsPs+PpSs*, can be obtained from the following moveout expressions:

$$\left.\begin{aligned} t_{Ps} &= H\sqrt{\frac{\kappa^2}{V_P^2}-p^2}-\sqrt{\frac{1}{V_P^2}-p^2} \\ t_{PpPs} &= H\sqrt{\frac{\kappa^2}{V_P^2}-p^2}+\sqrt{\frac{1}{V_P^2}-p^2} \\ t_{PsPs+PpSs} &= 2H\sqrt{\frac{\kappa^2}{V_P^2}-p^2} \end{aligned}\right\} \quad (2.10)$$

where t_{Ps}, t_{PpPs} and $t_{PsPs+PpSs}$ are respectively the predicted arrival times of *Ps*, *PpPs* and *PsPs+PpSs*, *Vp* is the *P*-wave velocity, *H* is the crustal thickness, *κ* is the *Vp/Vs* ratio, and *p* is the ray parameter.

H or *κ* can be straightforwardly obtained from one of the relations in Equation (2.10) by fixing one of them. However, Zhu and Kanamori (2000) pointed out the trade-off between *H* and *κ* when using only the arrival time of *Ps* in the calculation, as it is the clearest phase in the receiver function. They mentioned that

a change of 0.1 in κ involves a change of 4 km for H. To reduce this uncertainty, the arrival time of the two reverberated phases of *Ps* (*i.e. PpPs* and *PsPs+PpSs*) were used to add supplementary control in the calculation.

The *H-κ* stacking method of Zhu and Kanamori (2000) applies a grid search of H and κ by transforming the receiver functions from the time-amplitude domain into thickness-*Vp/Vs* domain. The method works as follows:

(1) The predicted arrival times of the three phases, *Ps*, *PpPs*, and *PsPs+PpSs*, are calculated for a pair (H, κ), obtained from the grid search, and an assumed *P*-wave velocity (*Vp*) of the bulk crust, which depends on the geology of the area.

(2) Then, for each radial receiver-function waveform, the amplitude of the trace corresponding to the above predicted arrival times are taken and summed by calculating the objective function of $s(H,\kappa)$ for one couple (H,κ):

$$s(H,\kappa) = \sum_{j=1}^{N} w_1\, r_j\,(t_{Ps}) + w_2 r_j\left(t_{PpPs}\right) - w_3 r_j\left(t_{PsPs+PpSs}\right) \qquad (2.11)$$

where w_1, w_2, and w_3 are the weights assigned to the *Ps*, *PpPs*, and *PsPs+PpSs* phases, respectively, the sum of the weights being unity; r_j is the amplitude of the radial receiver function; t_{Ps}, t_{PpPs} and $t_{PsPs+PpSs}$ are the arrival times of the phases; H is the crustal thickness; κ is the *Vp/Vs* ratio; and N is the number of receiver functions used.

(3) And the procedure is repeated for different values of (H, κ) from the grid.

(4) Finally, the best estimation of the crustal thickness (H) and the *Vp/Vs* ratio (κ) corresponds to the maximum value of $s(H,\kappa)$ which, accordingly, best matches the arrival times of *Ps*, *PpPs* and *PsPs+PpSs* phases.

2.4.2 Estimation of uncertainty from the bootstrapping technique

Uncertainties in the estimation of H and κ may be introduced by the choice of the receiver-function traces used during the stacking procedure. Thus several estimations of H and κ were performed by resampling the original dataset and repeating the measurement. The distribution of the estimates can be studied to select the average and the uncertainty.

The approach of Julià and Mejía (2004) was applied to estimate the uncertainty on the results from the H-κ stacking technique. It applies a bootstrap resampling procedure (Efron and Tibshirani, 1991) in order to calculate one average and one-standard-deviation error around the best-estimated values of H and κ. The approach works as follows:

(1) First, a bootstrap sample is created from all the receiver functions obtained in a seismic station. It is a replication of the original data set by randomly selecting receiver-function samples from the original receiver functions. The selection may be repetitive but the original and bootstrap sample must have the same number of receiver function.

For example, assume that we originally have a data set X of N receiver functions:

$$X = \{x_1, x_2, x_3, \ldots, x_N\}$$

(N was typically 15 in this study.)

The first bootstrap sample, X^*_1 (the subscript 1 designates that this is the first bootstrap sample), is generated by randomly choosing N receiver functions from X. For example:

$$X^*_1 = \{x_7, x_1, x_1, x_3, \ldots, x_{N^*}\}$$

(N^* indicates the N-th receiver function in the bootstrap sample.)

(2) The *H-κ* stacking procedure, in the above section, is applied to the bootstrap sample X^*_1, which yields to the first estimation of the crustal thickness H_1 and the *Vp/Vs* ratio κ_1.

(3) The procedure is then repeated for different bootstrap sample depending on the number of replications, *B*, chosen. For example:

$X^*_2 = \{x_2, x_2, x_8, x_3, \ldots, x_{N^*}\}$	yields to	H_2 and κ_2.
$X^*_3 = \{x_7, x_3, x_{10}, x_4, \ldots, x_{N^*}\}$	yields to	H_3 and κ_3.
……	…….	……
$X^*_B = \{x_{11}, x_7, x_8, x_8, \ldots, x_{N^*}\}$	yields to	H_B and κ_B.

It gives *B* estimates of *H*, which are $\{H_1, H_2, \ldots, H_B\}$, and κ, which are $\{\kappa_1, \kappa_2, \ldots, \kappa_B\}$.

(4) Finally, one value of *H* and κ and their corresponding error of estimation are obtained by calculating their average, $\bar{H}$ and $\bar{\kappa}$, and sample standard deviation, σ_H and σ_κ, from:

$$\left.\begin{aligned} \bar{H} = \frac{1}{B}\sum_{i=1}^{B} H_i \qquad and \qquad \bar{\kappa} = \frac{1}{B}\sum_{i=1}^{B} \kappa_i \\ \sigma_H = \sqrt{\sum_{i=1}^{B} \frac{(H_i - \bar{H})^2}{(B-1)}} \qquad and \qquad \sigma_\kappa = \sqrt{\sum_{i=1}^{B} \frac{(\kappa_i - \bar{\kappa})^2}{(B-1)}} \end{aligned}\right\} \quad (2.12)$$

H_i and κ_i are estimates from different bootstrap samples ($i = 1$ *to* B).

Efron and Tibshirani (1991) empirically suggested that randomness in the standard error is insignificant if the *B* is higher than 200 replications.

2.4.3 Error ellipse estimation

The error ellipse, also known as confidence ellipse, is also estimated in the Julià and Mejía (2004) approach. In practice, it plots an isocontour of the percentage of estimates that fall within a band around the mean of the Gaussian-distributed estimates. The error ellipse is used in the approach of Julià and Mejía (2004) because the estimates here, *H* and *κ*, are *2D*-Gaussian distributed and co-vary.

Mathematically, the covariance of the *B* estimates of *H* and *κ* is obtained from:

$$cov(H,\kappa) = \frac{1}{(B-1)}\sum_{i=1}^{B}(H_i - \bar{H})(\kappa_i - \bar{\kappa}) \tag{2.13}$$

The covariance matrix, $\mathcal{R}$, is subsequently obtained and used to extract the parameters of the ellipse that defines the confidence region of the bivariate data. It is described by the following matrix:

$$\mathcal{R} = \begin{pmatrix} \sigma_H^2 & cov(H,\kappa) \\ cov(H,\kappa) & \sigma_\kappa^2 \end{pmatrix} \tag{2.14}$$

The square root of the eigenvalues of the covariance matrix gives the length of the ellipse axes.

It is common in statistical studies to show estimates that fall within one, two, or three standard deviations of the mean. The rule of thumb is that the confidence interval is:

(1) 68.27% of estimates fall within one-standard-deviation of the mean.
(2) 95.45% of estimates fall within two-standard-deviation of the mean.
(3) 99.73% of estimates fall within three-standard-deviation of the mean.

Also, the coefficient of correlation is obtained from:

$$r_{H\kappa} = \frac{cov(H,\kappa)}{\sigma_H \sigma_\kappa} \tag{2.15}$$

2.4.4 Poisson's ratio and *Vp/Vs* ratio

The Poisson's ratio is a mechanical property that controls the elastic deformation of a material when static or dynamic stresses are exerted. In our case, the material is a rock that constitutes the crust.

Poisson's ratio studies cover a wide variety of application in geosciences. It can be obtained from a straightforward laboratory-measurement to study the elastic property of rocks, for example, or from field measurement to evaluate the *in situ* stresses of the embedding rock masses beneath the area.

Assume that a cylindrical rock, with length l and diameter δ, is subjected to a tensional or compressional stress parallel to its axis. The deformation of the rock will be observed perpendicular to the axial direction. The Poisson's ratio, denoted ν, is the ratio of transverse strain to axial (or longitudinal) strain. It is expressed as:

$$\nu = -\frac{d\varepsilon_{transverse}}{d\varepsilon_{axial}} \tag{2.16}$$

where $d\varepsilon_{transverse}$ and $d\varepsilon_{axial}$ are respectively the transverse and axial strain.

For the above cylindrical rock, $\nu = -(\Delta\delta/\delta)/(\Delta l/l)$ where Δ presents the slight deformation in length and diameter.

Generally, for most common materials ν ranges between 0 and 0.5 for solids. A Poisson's ratio of 0 means no (or very little) lateral expansion when the material is compressed. Poisson's ratio of 0.25 is typical for crystalline crustal rocks, and 0.5 indicates a material that is incompressible.

The movement of the particles associated with the propagation of seismic waves generates stress and strain disturbance (Figure 2.1). The Poisson's ratio can be expressed in term of *P*-wave velocity (*Vp*) and *S*-wave velocity (*Vs*), or directly from the *Vp/Vs* ratio, for an isotropic medium:

$$\nu = \frac{1}{2}\left[1 - \frac{1}{\left[\frac{V_P}{V_S}\right]^2 - 1}\right] \tag{2.17}$$

In this study, the Poisson's ratio is estimated in order to typify the bulk crustal rock-formation in different regions.

2.4.5 Application

Receiver functions from a Gaussian width of 1.0 were generally *H-κ*-stacked for all stations. Receiver functions computed with a Gaussian width of 2.5 were only employed to verify the consistency of the estimation. However, *P*-to-*s* converted phases from Gaussian width 2.5 are easy to identify for some stations, *viz.* MAHA, MS07, MS10, MS16, and VOI, thus, higher-frequency receiver functions were stacked for these stations. The program *hkstack* of Julià and Mejía (2004) was used for the stacking.

Clear *Ps* phases from the velocity contrast in the sediment-basement interface can make the *Ps* and Moho reverberations difficult to identify as they are hidden or interfered by *Ps* arrivals and reverberations from the sediment-basement interface. Consequently, I did not use the *H-κ* stacking technique for seismic stations located in the sedimentary basins, where the *Ps*-arrivals from the Moho are completely covered by the Ps-arrival from the sediment-basement interface (*viz.* DGOS, BANJ, MAJA, KIRI, MMBE, SKRH, LONA and MS04).

When applying the *H-κ* stacking technique, weights for the *Ps*, *PpPs*, and *PsPs+PpSs* phases are usually chosen depending upon their clarity in the receiver-function waveforms. When all three phases were distinctly seen in the receiver-function waveforms, weighting factors of $w_1 = 0.4$, $w_2 = 0.3$ and $w_3 = 0.3$ were used. However, when the *PpPs* and *PsPs+PpSs* phases were less observable than the *Ps* phase, a higher weight of 0.6 was given to the *Ps* phase, and smaller but similar weights of 0.2 to the *PpPs* and *PsPs+PpSs* phases.

The stacking procedure requires an initial estimate of the average *P*-wave velocity (*Vp*) of the crust in the calculation. A *Vp* = 6.5 km/s was chosen for the stacking procedure, which is the global *Vp* for Precambrian rocks (*e.g.* Christensen and Mooney, 1995), as this method was applied only for seismic stations in the Precambrian basement of Madagascar. The *H* and κ intervals were kept as small as possible, 0.02 km and 0.001 respectively, when performing the grid search.

The uncertainty in the estimation was assessed by replicating the original dataset 200 times. Then the average and one-standard-deviation of the 200 estimates from the 200 bootstrap samples were obtained from Equation (2.12).

However, the choice of the initial average crustal *Vp* may influence the estimation of *H* and κ. The stacking procedure was repeated for *Vp* = 6.3 km/s and Vp = 6.8 km/s. Overall uncertainties in *H* and κ were obtained by combining the formal uncertainties from the bootstrap method with the range of *H* and κ values obtained when using different *Vp* values (Table 2.2). The overall uncertainties for each station are ±1-3 km for the Moho depth and ± 0.02 for κ.

An example of *H*-κ stacking for station VINA is shown in Figure 2.20. Estimates of the crustal thickness and bulk crustal *Vp/Vs* ratio and their standard deviation, obtained from Equation (2.12), the correlation coefficient obtained from Equation (2.15), and the 95%-confidence interval are shown in this figure.

A bootstrapping procedure for the station AMPY and *H*-κ stacking results from all stations are shown in Box A.1 and Figure A.2 of Appendix A, respectively.

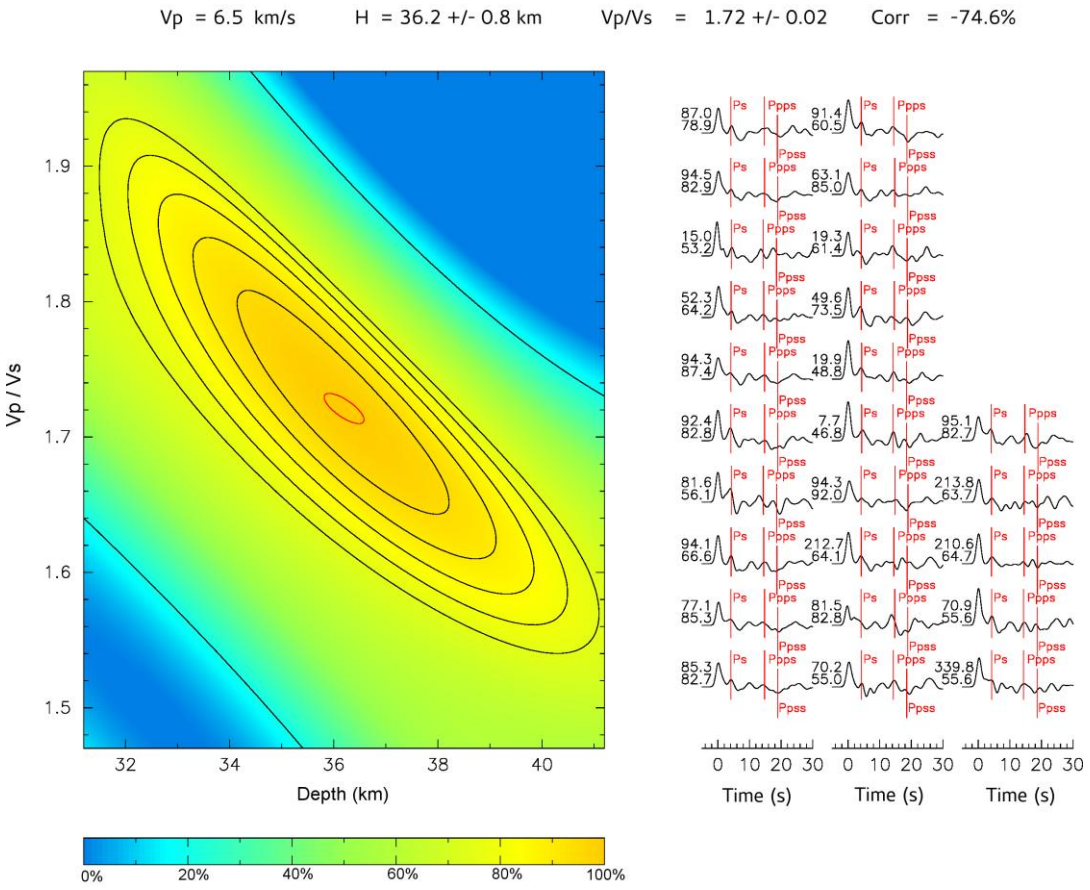

Figure 2.20: *H*-κ stacking results for seismic station VINA. (*Left*) *H*-κ parameter space with the optimal values for *H* and κ (center of red ellipse). The red contour is the 95% confidence bound (which corresponds to a band around the mean within two standard deviations) and the black contours map out the percentage values, in the color scale bar, of the normalized objective function given in Equation (1). (*Right*) Receiver functions labeled by the event back-azimuth (top number) and epicentral distance (bottom number), both in degrees. The optimal results for *H* and κ obtained are summarized along the top with their formal uncertainties and shown with the red contour on the left panel.

Table 2.2: *H-κ* stacking results from *Vp* of 6.3 km/s, 6.5 km/s, and 6.8 km/s and their average. *#Data* is the number of stacked receiver functions, *Vp* is the starting *P*-wave velocity, *H* and σ_H are respectively the crustal thickness and the uncertainty, κ and σ_κ are respectively the *Vp/Vs* ratio and the uncertainty, *H** and *κ** are the statistical average of the estimates, thickness and *Vp/Vs* respectively, from the three values of *Vp* with their standard deviation *Std_H** and *Std_κ**.

Station	#Data	Vp = 6.3 km/s				Vp = 6.5 km/s				Vp = 6.8 km/s				Average			
		H*(km)*	σ_H	κ	σ_κ	***H****(km)*	σ_H	κ	σ_κ	***H****(km)*	σ_H	κ	σ_κ	***H**** *(km)*	***Std_H****	***κ****	***Std_ κ****
ABPO	59	42.3	0.7	1.65	0.02	43.9	0.7	1.65	0.02	46.2	0.7	1.64	0.02	44.1	2.0	1.65	0.01
AMPY	8	24.6	3.0	1.87	0.12	25.5	2.4	1.86	0.10	26.8	3.2	1.85	0.11	25.6	1.1	1.86	0.01
ANLA	24	42.0	1.2	1.71	0.04	43.5	1.4	1.70	0.04	45.6	1.6	1.70	0.05	43.7	1.8	1.70	0.01
ANTS	22	27.6	0.9	1.85	0.06	28.6	0.9	1.84	0.06	30.2	0.9	1.83	0.06	28.8	1.3	1.84	0.01
BAEL	24	32.2	0.8	1.78	0.04	33.5	0.9	1.77	0.04	35.3	0.9	1.76	0.04	33.7	1.6	1.77	0.01
BAND	17	32.5	1.7	1.76	0.08	33.6	1.7	1.76	0.08	35.4	1.8	1.75	0.07	33.8	1.5	1.76	0.01
BARY	11	38.6	2.4	1.75	0.07	40.0	2.5	1.74	0.08	42.2	2.6	1.73	0.07	40.3	1.8	1.74	0.01
BATG	13	40.8	1.4	1.78	0.05	42.3	1.4	1.77	0.05	44.6	1.4	1.76	0.04	42.6	1.9	1.77	0.01
BERG	20	29.0	1.5	1.90	0.04	30.1	1.3	1.89	0.04	31.7	1.4	1.88	0.04	30.3	1.4	1.89	0.01
BITY	14	40.2	2.4	1.75	0.06	41.6	2.4	1.75	0.06	43.8	2.2	1.74	0.04	41.9	1.8	1.75	0.01
BKTA	12	38.1	1.1	1.66	0.04	39.5	1.1	1.65	0.04	41.6	1.2	1.64	0.04	39.7	1.8	1.65	0.01
CPSM	9	27.0	1.0	1.83	0.07	28.0	1.0	1.82	0.07	29.5	1.3	1.81	0.08	28.2	1.3	1.82	0.01
FOMA	24	35.3	1.4	1.73	0.05	36.5	1.6	1.73	0.06	38.5	1.7	1.72	0.06	36.8	1.6	1.73	0.01
LAHA	26	30.6	1.7	2.07	0.08	31.7	1.5	2.07	0.07	33.4	1.5	2.06	0.07	31.9	1.4	2.07	0.01
MAGY	17	27.9	1.8	1.81	0.12	28.9	1.9	1.80	0.12	30.6	2.2	1.79	0.13	29.1	1.4	1.80	0.01
MAHA	14	34.6	1.2	1.82	0.05	35.9	0.9	1.81	0.04	37.9	1.0	1.80	0.04	36.1	1.7	1.81	0.01
MKVA	12	30.2	1.0	2.00	0.06	31.3	1.2	1.99	0.06	32.9	1.3	1.98	0.06	31.5	1.4	1.99	0.01
MS07	13	26.0	2.3	1.90	0.15	26.9	2.4	1.89	0.15	28.4	2.8	1.88	0.16	27.1	1.2	1.89	0.01
MS10	12	34.9	1.1	1.79	0.06	36.2	1.1	1.79	0.05	38.1	1.2	1.78	0.05	36.4	1.6	1.79	0.01
MS12	9	39.4	1.7	1.65	0.05	40.9	1.6	1.64	0.04	43.1	1.8	1.63	0.05	41.1	1.9	1.64	0.01
MS16	17	40.2	0.7	1.69	0.02	41.6	0.8	1.68	0.02	43.8	0.9	1.68	0.02	41.9	1.8	1.68	0.01
MS19	15	39.4	1.3	1.79	0.04	40.8	1.3	1.79	0.04	43.0	1.5	1.78	0.04	41.1	1.8	1.79	0.01
MS23	20	40.3	3.3	1.75	0.07	41.6	2.9	1.75	0.06	43.8	2.9	1.74	0.06	41.9	1.8	1.75	0.01
SBV	7	28.5	1.7	1.81	0.09	29.6	1.9	1.81	0.09	31.1	2.0	1.80	0.09	29.7	1.3	1.81	0.01
SOLA	9	31.8	1.3	1.71	0.04	33.0	1.2	1.70	0.04	34.7	1.6	1.69	0.05	33.2	1.5	1.70	0.01
VINA	25	34.9	0.7	1.73	0.03	36.2	0.8	1.72	0.02	38.2	0.8	1.71	0.02	36.4	1.7	1.72	0.01
VOI	8	41.8	2.3	1.67	0.07	43.1	2.4	1.67	0.07	45.4	1.9	1.66	0.05	43.4	1.8	1.67	0.01
ZAKA	16	40.1	1.8	1.74	0.04	41.4	1.7	1.74	0.03	43.5	1.8	1.73	0.04	41.7	1.7	1.74	0.01
ZOBE	14	44.7	1.7	1.67	0.06	46.3	2.1	1.67	0.07	48.8	2.0	1.66	0.06	46.6	2.1	1.67	0.01

Note that *H**, *κ**, *Std_H**, and *Std_κ** are statistical averages and standard deviations obtained directly from basic statistic equation of average and standard deviation but not obtained from Equation (2.12).

2.5 Crustal structure from the joint inversion of receiver functions and the dispersion of Rayleigh-wave phase velocities

In geophysical studies, the physical properties of the ground observed or measured at the surface (*e.g.* magnetic field, gravity field, resistivity, seismic waves …) are usually inverted to infer the structure of Earth's interior. However, the use of only one type of observation may limit the resolution of the method. Sometimes, combining one observation with other complementary measurement of the same parameters in the inversion provides tighter constraints of the Earth structure than inverting them independently. This type of inversion is called a joint inversion. In order that a joint inversion can be performed, both data must sample the same area of the propagating medium so that they provide complementary information in the same region.

In this study, radial receiver function data and surface wave dispersion measurements were jointly inverted to constrain the Earth structure as they both are primarily sensitive to *S*-wave velocity.

This method is used for the first project of this study and results are shown in Chapter 3.

2.5.1 Independent inversion of receiver function and surface wave dispersion measurements

Inversion of receiver functions only

Teleseismic events are used in the analysis of receiver functions so that seismic waves can be assumed as plane waves and impinging *P*-waves arrive at the receiver with steep angle of incidence. Even though the receiver functions were extracted from *P*-waves, *Ps* phases influence the horizontal component in the seismogram (Ammon, 1991). This portrays their dependence on the shear velocity

beneath the station. Consequently, when inferring the structure of the Earth, receiver functions are usually inverted into *S*-wave velocity structure (Owens et al., 1984). Then, *P*-wave velocities are deduced from the relation between Poisson's ratio (σ), *P*-wave velocity (*Vp*), and S-wave velocity (*Vs*) by assuming a constant σ (*e.g.* Equation (2.17)). Also, the bulk density (ρ) is inferred from empirical relation between *Vp* and ρ (Berteussen, 1977):

$$\rho = 0.32\, V_P + 0.77 \tag{2.18}$$

Ammon et al. (1990) analyzed the resolution and the non-uniqueness of the inversion of receiver functions to one-dimensional velocity structures by using synthetic receiver functions, which were computed from velocity model ("the true model"). The synthetic receiver function, if inverted to produce a velocity model, should ideally recover the initial true model. However, they pointed out the non-uniqueness of the inversion. In fact, many acceptable solution models corresponded to the inversion of the synthetic receiver function. In addition, they affirmed that the primary sensitivity of the inversion is the sharp change in velocity and relative traveltime. The authors suggested combining different complementary information in the inversion to select the best one from the various models that fit the data.

Inversion of surface wave dispersions measurements only

Surface waves are seismic waves that travel along the surface of the Earth. They are grouped into two types: Rayleigh waves (a combination of *P*- and *S*-waves polarized in the vertical plane, denoted *P*-*SV*) and Love waves (*S*-waves polarized in the horizontal plane trapped in the vicinity of the Earth's surface, denoted *SH*). Rayleigh-waves can spread along the surface of homogeneous medium, compared to Love waves which need a variation of the velocity structure with depth of the underlying structure.

Surface waves are dispersive, which means that their velocities are a function of the frequency or period. In surface wave dispersion analysis, the propagation

velocity of the wavepacket (or group velocity) or the velocity of the phase of any frequency (or phase velocity) are usually studied to evaluate this variation of the velocity with the frequency of the wave. Surface waves with varying wavelength can be observed at some depths with decaying amplitude, as they are originally generated by body waves. They propagate at the velocity characteristic of these depths. Group or phase velocities can be then isolated for particular wavelength, hence frequency or period, which reveals the velocity at different depths. This variation of the surface wave velocity with frequency is called the surface wave dispersion and the plot is called the dispersion curve.

Julià et al. (2000) carefully analyzed the variation with depth of the sensitivity function of *S*-wave velocity, *P*-wave velocity, and density in the surface wave dispersion. They pointed out the dissimilarity of their contribution to dispersion data. *S*-wave velocity contributes more into the surface wave dispersion measurements all through the depth compared to *P*-wave velocity and density. Consequently, in the same way as the receiver-function inversion, surface wave dispersion curves are usually inverted into shear-wave velocity structure. Then, *P*-wave velocity and density structures are obtained from empirical relationship as described above.

Summary

In summary, receiver function inversion is very sensitive to the sharp gradient of the relative velocity variation, suggesting a good constraint of any discontinuities in the crust and mantle. However, it cannot resolve the absolute seismic velocity of the medium beneath the receiver. On the other hand, surface wave dispersion is a powerful tool to infer the absolute velocity of the medium as it is primarily sensitive to *S*-wave velocity as well as *P*-wave velocity and density.

2.5.2 Criteria for the joint inversion of receiver function and surface wave dispersion measurements

In order that two independent data can be jointly inverted, the consistency and complementarity of both observations must be taken into account (Julià et al., 2000).

If both observations describe the similar variation of physical gradients, there is no need to apply the joint inversion. The data used in this type of inversion must bring complementary information. As shown in the previous section, receiver functions are very sensitive to the abrupt change in velocity as a function of depth, thus, depicts accordingly the location of sub-horizontal discontinuities. But, their inversion yields only to the relative seismic velocity of the subsurface. The surface wave dispersion data, conversely, as it is extremely sensitive to the *S*-wave velocity, provides an absolute velocity measurement of the subsurface. Therefore, combining both types of information will locate any seismic discontinuity in the Earth's crust or upper mantle and will characterize the absolute seismic velocity of each layer.

For the consistency of the joint inversion, it is reasonable to consider the data from both observations at the same sampling point. Therefore, the data used in the joint inversion of receiver function and surface wave measurements must sample the same area in order to constrain the shear velocity beneath the station. As described in Section 2.3.1, receiver functions show the impedance structure of the Earth beneath the recording seismic station. Conversely, surface wave dispersion curves show the average velocity of the medium between the source and the recording station. The surface wave tomography uses this property to infer a three-dimensional variation of the surface wave in a region. Thus, the dispersion curve for a single point can be extracted from the 3D-model inferred from the seismic tomography at a particular point of the area, for example at the location of the seismic station.

2.5.3 Linearized inversion procedure

The linearized inversion procedure developed by Julià et al. (2000, 2003) was applied to jointly invert the radial receiver functions and Rayleigh-wave phase-velocity dispersion measurements.

This section is a summary of the linearized inversion procedure, which is well discussed in Julià et al. (2000, 2003). The approach uses a linearized inversion procedure in which a weighted combination of least squares norms for each data set (radial receiver functions and Rayleigh-wave phase-velocity dispersion curves) is minimized. Normalization is required and performed using the number of data points and variance of each data set.

The observed receiver functions or dispersion curves can be expressed mathematically as the relation:

$$d = F[m] \tag{2.19}$$

In which d is an N-dimensional vector representing the data points (receiver functions or dispersion curves), m is an M-dimensional vector expressing the model (subsurface structure). The observation, d, can be interpreted as the effect of a mathematical non-linear operator $F[]$ with the model m.

The linear iterative approach of Menke (1984) inverted the non-linear relation, in Equation (2.19), as:

$$\delta d = \nabla F|_{m_n} . \delta m_n \tag{2.20}$$

$$m_{n+1} = m_n + \delta m_n \tag{2.21}$$

In these relations, δd is the residual data vector obtained from $\delta d = d - F[m_n]$; δm is the model correction vector, in which $\delta m = m - m_n$; and n is a subscript designating the dimension N of the vector d.

Equation (2.20) is an overdetermined system of equations. In fact, the dimension N of the observation d is greater than the dimension M of the model m ($N>M$).

The generalized inversion theory of Menke (1984), using linear inverse operator, solved the Equation (2.21) as:

$$\delta m_n = \left(\nabla F|_{m_n}\right)^{-g}.\delta d \tag{2.22}$$

where the inverse operator, $\left(\nabla F|_{m_n}\right)^{-g}$, is obtained from the minimizing operation of the function χ for the inversion of dispersion curves, using a differential damped least-square scheme (Russell, 1987):

$$\chi = \left\|\delta d - \nabla F|_{m_n}.\delta m_n\right\|^2 + \theta^2\|D.\delta m_n\|^2$$

with

$$D = \begin{pmatrix} 1 & -1 & 0 & \cdots & 0 \\ 0 & 1 & -1 & \cdots & 0 \\ 0 & 0 & 1 & \cdots & 0 \\ \vdots & \vdots & \vdots & \ddots & \vdots \\ 0 & 0 & 0 & \cdots & 1 \end{pmatrix} \tag{2.23}$$

The element of the vector $D.\delta m_n$ are the first differences between shear velocity perturbations in adjacent layers. An influence of the norm θ^2, called "the smoothness parameter", is implemented to avoid the rapid change in velocity with depth during the inversion. A starting model m_o is required by the inversion procedure to start the inversion.

The inversion presented here is a simultaneous inversion of receiver functions and surface wave dispersion curves. Thus, a joint prediction error was defined to perform the joint inversion by using the differential damped least-square in Equation (2.23). The joint prediction error is given by the relation:

$$E_{(y|z)} = \frac{p}{N_y}\sum_{i=1}^{N_y}\left(\frac{y_i - \sum_{j=i}^{M} Y_{ij}\,x_j}{\sigma_{y_i}}\right)^2 + \frac{1-p}{N_z}\sum_{i=1}^{N_z}\left(\frac{z_i - \sum_{j=i}^{M} Z_{ij}\,x_j}{\sigma_{z_i}}\right)^2 \tag{2.24}$$

where y and z are, respectively, the residual dispersion curve and receiver function; while Y and Z are, respectively, the corresponding partial derivative matrix. N_y and N_z are the number of the data points for each data set, $\sigma_{y_i}^2$ and

$\sigma_{z_i}^2$ are the corresponding variances, and p is called "the influence factor or parameter".

As the procedure is a joint inversion of two different data sets (receiver function and surface wave dispersion curves) the solutions could be influenced by one set of the data. In this joint inversion procedure, this ambiguity is controlled by the influence factor (*i.e.* p). $p = 0$ corresponds to the use of only the z observations (which are the receiver functions), while $p = 1$ means the use of only the y data (which are the dispersion curves) in the inversion.

2.5.4 Application

Radial receiver functions computed from both Gaussian widths (1.0 and 2.5) were used in the joint inversion. Surface wave data were obtained from the surface wave tomography of Madagascar by Pratt et al. (2017) and consist of the dispersion curves of the phase-velocity of Rayleigh-waves. Small preparations of the data were conducted prior to the actual inversion: *viz.* smoothing the dispersion curves, creating a starting model, and grouping, stacking, and normalizing receiver functions. The program *jointsmth* of Julià et al. (2000, 2003) was used for the inversion.

Surface wave dispersion curves

Dispersions of the Rayleigh-waves phase velocities by Pratt et al. (2017) were used in the joint inversion as it is the only surface wave tomography hitherto conducted in Madagascar using local data. All of the seismic stations used in this seismic tomography are used in this project.

The original dispersion curves were noisy and present slight offsets due to the different techniques used by Pratt et al. (2017) to extract the phase-velocity of Rayleigh-waves for various frequencies. Consequently, a three-point moving

average was applied to smooth the dispersion curves out before the inversion (Figure 2.21). Dispersion velocities between 5 to 100 second period ranges were considered for the inversion.

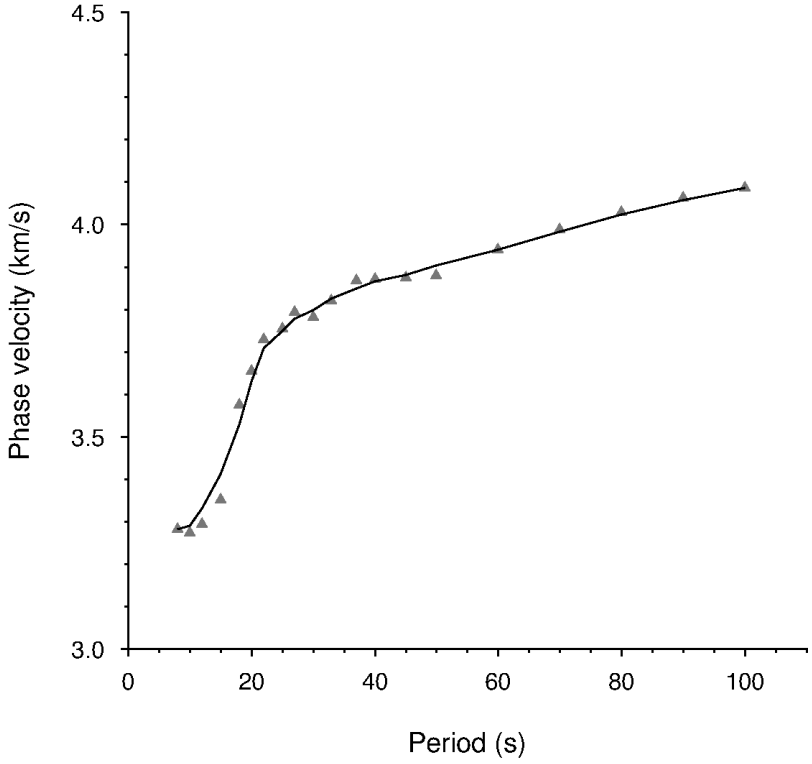

Figure 2.21: Dispersion curves of Rayleigh-wave phase-velocity for the station VINA. Gray triangles are points on dispersion curve from Pratt et al. (2017) and black line is the dispersion curve from 3-point moving average

Starting model

Any inversion technique requires a starting model to initiate the procedure. It consists of a variation of the *P*-wave velocity, *S*-wave velocity, and density with depth beneath the seismic station.

An isotropic medium of 38-km-thick crust and a linear shear-wave-velocity that increases across the crust from 3.4 to 4.0 km/s, overlying a flattened Preliminary Reference Earth Model (PREM) model for the mantle (Dziewonski and Anderson, 1981) was used as starting model in the joint inversion. Poisson's ratios from the *H-κ* stacking procedure, obtained from each station, were respectively used in the starting model for each corresponding station to calculate the value of *Vp*, from

Equation (2.17), and the density, from using the empirical relation in Equation (2.18). The Earth was divided into isotropic layers in which the thicknesses of the first and second layers were, respectively, 1 and 2 km, and the layer thickness increased to 2.5 km for depths between 3 and 60.5 km, 5 km for depths between 60.5 and 260.5 km, and 10 km below 260.5 km depth. The velocity structure from the inversion is fixed to the PREM model for depths below 200 km because surface wave dispersions show only a good vertical resolution until this depth (*e.g.* Julià et al., 2003, 2008).

The starting model for the stations located in sedimentary basins was slightly different. The top 10.5 km of the sedimentary basin was replaced by a linear shear-wave velocity structure increasing from 2.2 km/s to 3.6 km/s. Poisson's ratio was set to 0.35 for the top 3 km and then 0.29 for the remaining 7 km. The remaining layers are similar as the previous one.

Grouping, stacking, and normalizing receiver functions

Radial receiver functions that have sampled the zone beneath each station were used to check for laterally varying structures beneath the station. They were grouped and stacked by backazimuth and ray-parameter to account for the moveout from variations in incident angle (Julià et al., 2008). A minimum of three receiver functions were required for stacking. Stacking the traces increases the SNR and enhances the converted phases. One to nine groups of radial receiver functions for both lower and higher frequencies were obtained for each station. An example of a group of receiver functions is shown in Figure 2.22.

Ammon (1997) suggested that radial receiver functions computed from the iterative deconvolution and subsequently used for inversion must be normalized by the area of the averaging function. For the Gaussian width factor used in this study, 1.0 and 2.5, low- and high-frequency receiver functions are divided by 0.57 and 1.42, respectively. These values are obtained from (Ammon, 1997; http://eqseis.geosc.psu.edu/~cammon/HTML/RftnDocs/seq01.html).

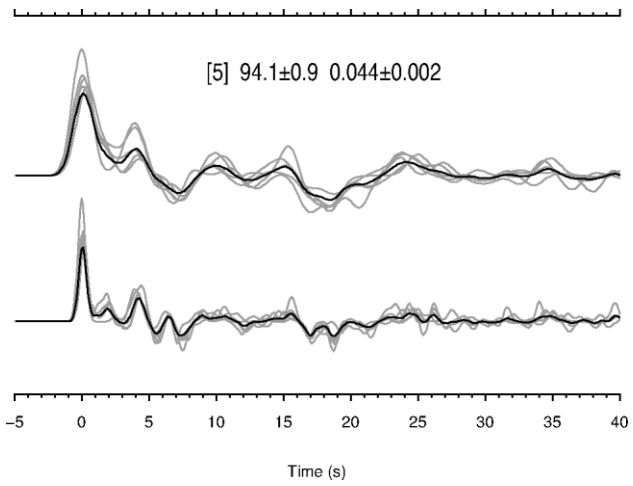

Figure 2.22: Group of radial receiver functions computed with Gaussian 1.0 (top) and 2.5 (bottom), with a range an average ± one standard deviation backazimuth of 94.1 ± 0.9° and ray parameter of 0.044 ± 0.002 s/km at station VINA. Gray and black lines are the observed and average receiver functions, respectively. Numbers on top of waveforms are the number of the stacked traces (in square bracket) and the average backazimuth and ray parameter ± one standard deviation, respectively.

Inversion parameters: smoothness and influence parameters

As described in the starting-model section, the Earth's interior is presented as comprising thin parallel homogenous layers with specific velocity. Unrealistically abrupt changes in velocity for adjacent layers are controlled by the smoothness parameters (Equation (2.23)). In this study, this parameter was kept as low as possible, equal to 0.1, during the inversion to avoid an oversmoothing of the velocity structure.

Two different sets of data (receiver functions and surface wave dispersion curves) were jointly inverted to infer one velocity structure in this study. As stated in Section 2.5.1, the shear-wave velocity structure of the Earth can be directly inferred from an independent inversion of receiver functions only or surface wave dispersion curves only, suggesting that it can be influenced by one of the input data. The influence parameter was implemented in the calculation to control the trade-off between fitting the receiver functions and the phase-velocity dispersion

curves during the inversion. The minimum value of this parameter, p = 0, corresponds to a pure receiver function inversion while the maximum value, p = 1, means an inversion of surface waves dispersion only. In this study, equal weight, p = 0.5, was given to the input data during the inversion.

Joint inversion of single groups

Every single-group of radial receiver functions (computed from Gaussian widths of 1.0 and 2.5) was jointly inverted with the corresponding Rayleigh-wave phase-velocity dispersion curve for the seismic station to reproduce a *S*-wave velocity structure.

Generally, the inversion was run for 6 iterations which by time the obtained model generally showed a good fit between the observed and predicted of receiver functions and surface wave dispersion. The output of the inversion is the variation of the shear-wave velocity with depth. Figure 2.23 shows an example of single-group inversion of four groups of receiver functions gathered at station VINA. Receiver functions computed from Gaussian widths of 1.0 and 2.5 are used in the inversion. Resulting velocity structures from the different groups show comparable shear-wave velocity for each layer (Figure 2.23).

Joint inversion of all the groups

The resulting velocity structures from the single-group inversion do not change significantly and present comparable shear-wave velocity for each layer (less than 0.1 km/s of variation), also show similar thickness of crust. The similarity of the shear-wave velocity structures suggests insignificant lateral variation of the structure beneath the stations. Consequently, all the groups of radial receiver functions were jointly inverted at once with the surface wave data to deduce the shear-wave velocity beneath each station.

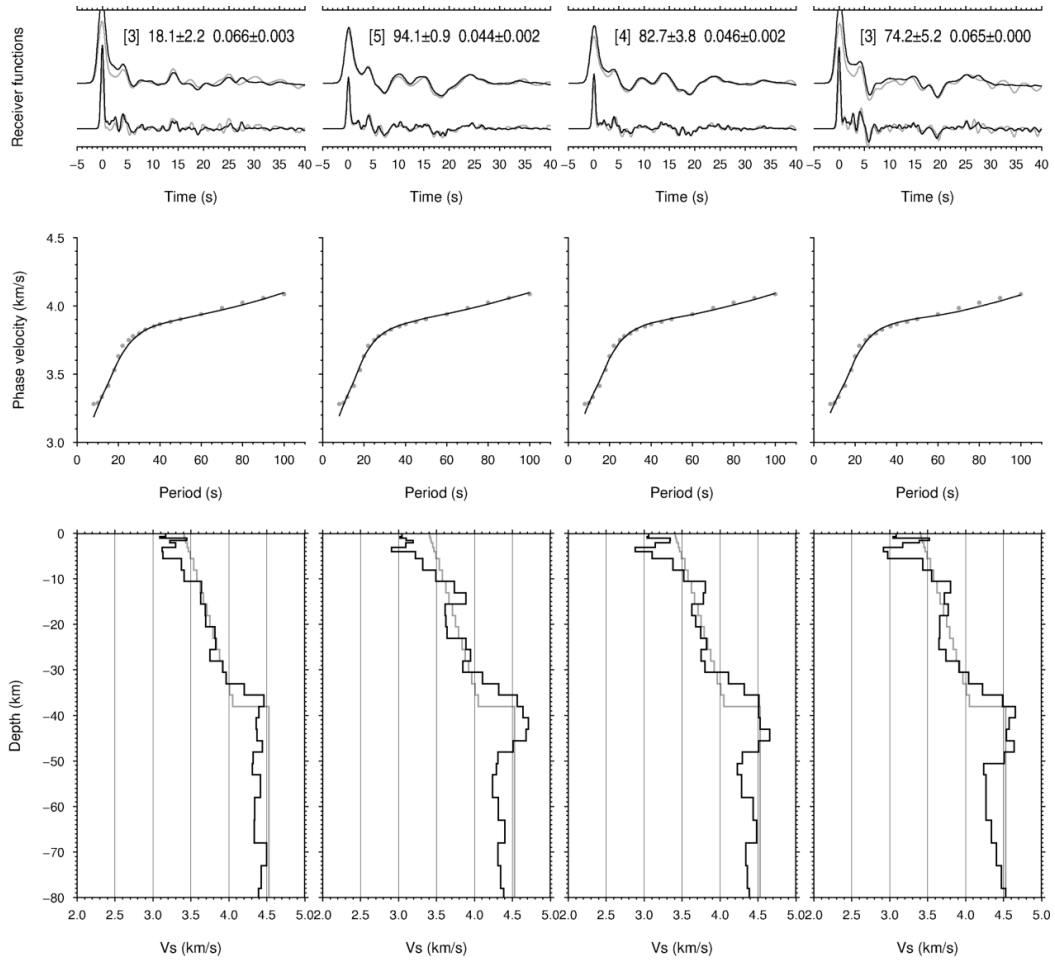

Figure 2.23: An example of joint inversion of radial receiver functions and Rayleigh-wave phase-velocity dispersion curve for different groups of receiver functions for station VINA. Top: gray and black lines are the observed and predicted radial receiver functions, respectively, for Gaussian width of 1.0 (top) and 2.5 (below). Middle: the observed and predicted Rayleigh-wave phase-velocity dispersion curves are shown in gray dots and black line, respectively. Bottom: gray line is the starting model; black line is the obtained shear-wave velocity structure.

The inversion was also run for 6 iterations which yield a good fit of the observed and predicted of both inputs. The outcome of the inversion does not present any significant changes in velocity compared to the single-group inversion (Figure 2.24). Thus, shear-wave velocity results from the inversion of all groups of receiver functions at each station were considered for further analyses and interpretations. Results from all stations are shown in Figure A.3 of Appendix A.

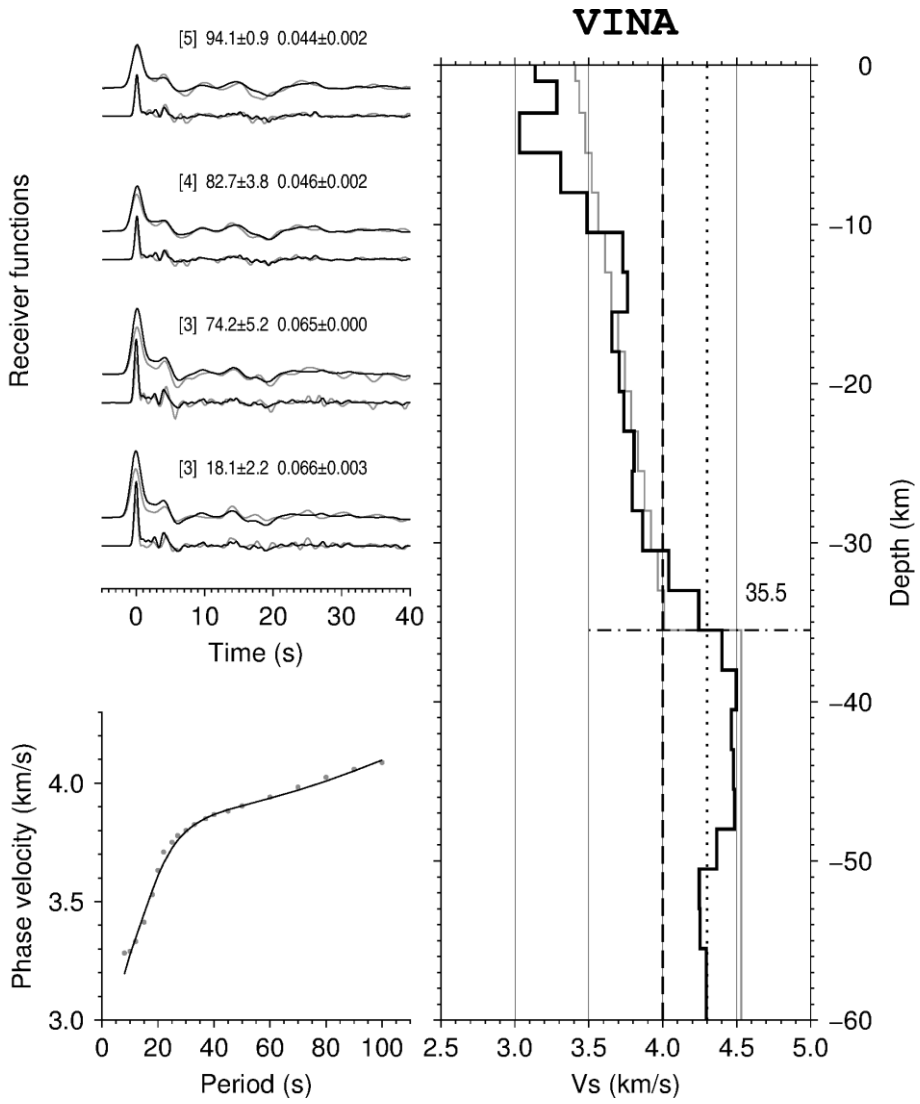

Figure 2.24: Joint inversion of Rayleigh wave phase velocities and receiver functions for station VINA. (*Top left*) Gray and black lines are the observed and predicted radial receiver functions, respectively, estimated for Gaussian filter widths of 1.0 (*top*) and 2.5 (*bottom*). The numbers on top of the waveforms are the number of receiver functions stacked (in square bracket) and the average backazimuth and ray parameter (± one standard deviation) for the stack, respectively. (*Bottom left*) The observed and predicted dispersion curves of the phase velocity, shown with gray dots and a black line, respectively. (*Right*) The starting velocity model (gray line) and predicted velocity structure (black line). The horizontal dash-dot line and number indicate the Moho depth (in km). The vertical dashed and dotted lines correspond to *Vs* values of 4.0 km/s and 4.3 km/s.

2.5.5 Uncertainties estimation

Following the approach of Julià et al. (2005), uncertainties in the estimation of the velocity structure can be assessed by repeating the inversion for a range of weighting parameters (smoothness and influence parameter) and different starting models (by changing the Poisson's ratios or using global model).

Nine different models were used as starting models in this assessment:

(1) 5 linearly varying velocity models, identical to the starting model in the previous section, but with different Poisson's ratios (0.22, 0.24, 0.26, 0.28, and 0.30),

(2) 3 global velocity models: *ak135* (Kennet et al., 1995), *prem* (Dziewonski and Anderson, 1981), and *iasp91* (Kennett and Engdahl, 1991),

(3) and, an homogenous 38-km-thick crust over a homogenous half-space.

Each starting model was used in turn in the joint inversion in which the smoothness parameter was changed from 0.3, 0.5 to 0.7, and the influence parameter changing from 0.1, 0.2 to 0.3. In total, 81 models were obtained and subsequently used to evaluate the uncertainty. Figure 2.25 shows example of inversion using different starting models.

The 81 resulting shear-wave velocity models, plotted together, show uncertainties in the crustal shear-wave velocity to be generally about ±0.1 km/s (Figure 2.26), and translate into uncertainties of no more than 2-3 km in Moho location, when a sharp change in velocity is observed between the crust and mantle, and less than 5 km, when a gradational Moho is observed (*i.e.* a smooth variation of shear-wave velocity).

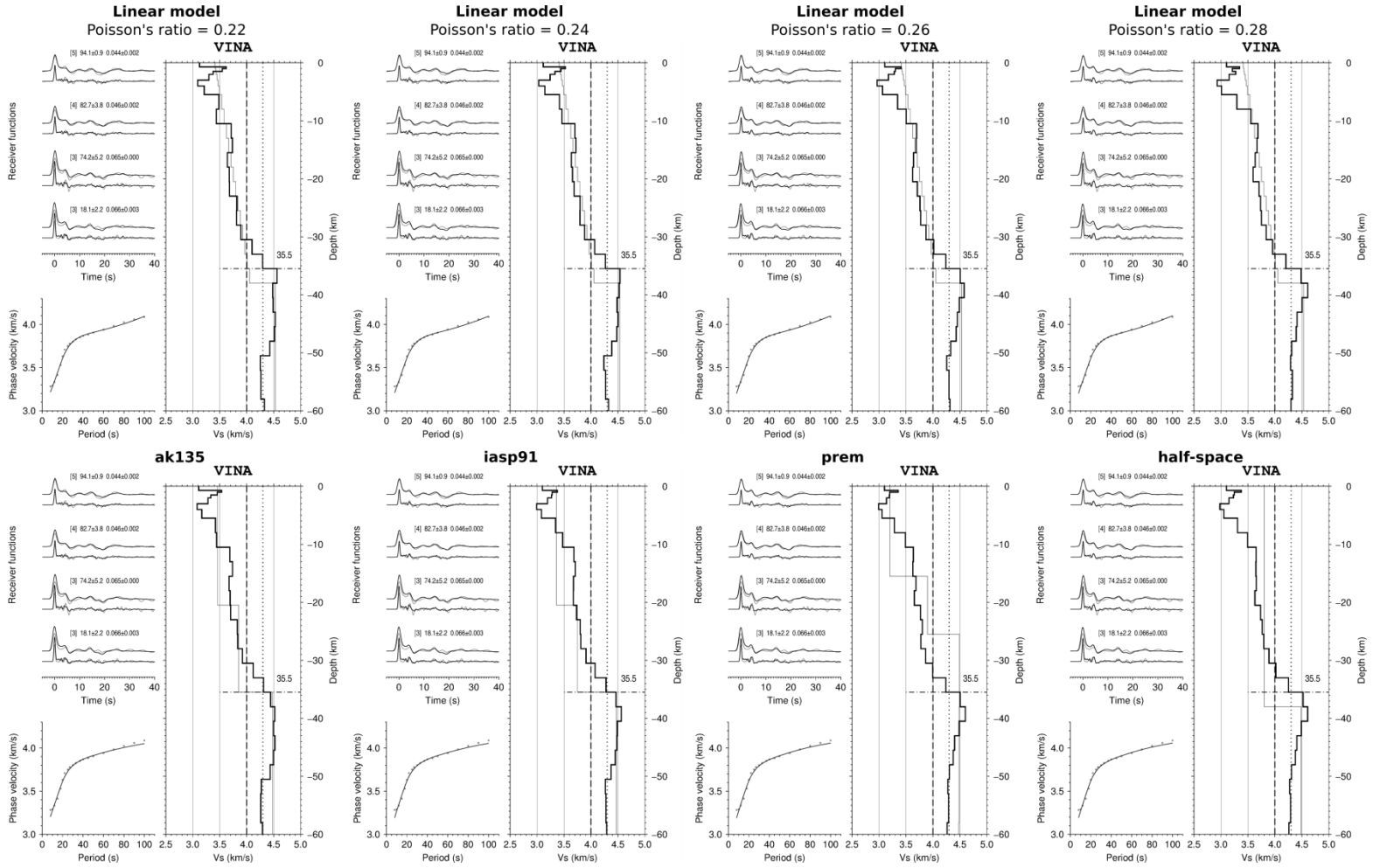

Figure 2.25: Example of shear-wave velocity structure for different starting model, computed with smoothness parameter 0.5 and influence parameter 0.1. Captions are similar as in Figure 2.24.

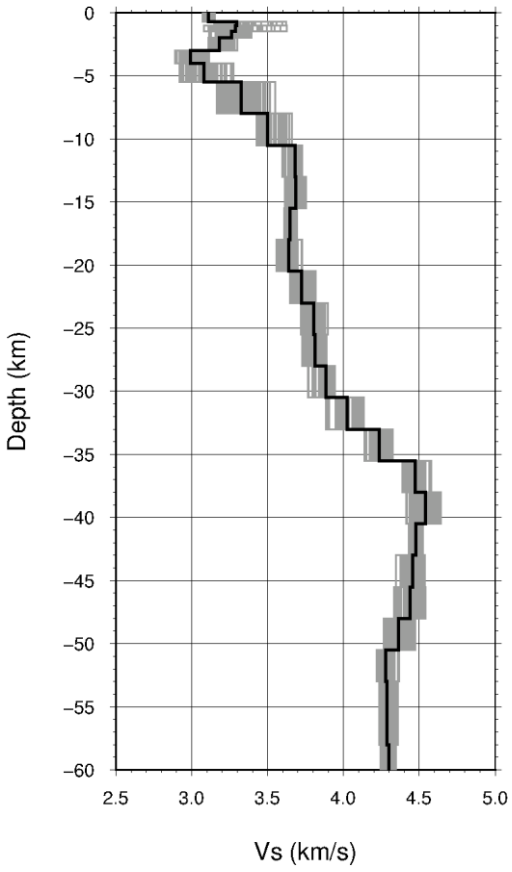

Figure 2.26: A plot of the 81 shear-wave velocity models by repeatedly inverting the data using different parameters and starting models for station VINA. Gray lines are the results from different starting model. Black line is the average shear-wave velocity model.

2.6 Locating local earthquakes

This section presents the method used for locating local and regional earthquakes which were used for the second project of this study, *i.e.* the tomography of the uppermost mantle beneath Madagascar.

2.6.1 Picking arrivals

The arrival times of *P*- and *S*-waves are used to locate earthquakes (longitude, latitude, depth, and origin time). The magnitude is obtained from the amplitude of

the seismogram and its corresponding period, the epicentral distance, and the depth.

The seismic tomography requires well-determined locations of seismic events. Generally, the more seismic stations that detect an event, the better the event is located. Consequently, seismograms from all permanent seismic stations in Table 2.1 were windowed at the time where earthquakes with the desired characteristics occurred.

Seismograms were bandpass filtered between 1 Hz and 15 Hz to give emphasis to the high frequency body wave arrivals and assort the picking of *P*- and *S*- arrivals.

2.6.2 Locating earthquakes with the *HYPOELLIPSE* program

HYPOELLIPSE event location program (Lahr, 1989) was used to locate seismic events. This program is based on the minimization of the root-mean-square (RMS) of the travel-time residuals (Geiger, 1912). Briefly, the workflow of the program *HYPOELLIPSE* when applying Geiger's method is as follows:

(1) A theoretical hypocenter and origin time are initially set, preferably in the vicinity of the actual location of the earthquake. They are defined by the trial longitude, the trial latitude, the trial depth, and the trial origin time (*Xo, Yo, Zo*, and *To*, respectively).

(2) A calculated travel-time, $Tcalc_i$ is computed from the theoretical location of the seismic event and the station *i*. Thus, it is a function of (*Xo, Yo, Zo).*

(3) The travel-time residual, Res_i, at station *i* is subsequently obtained from the difference of the observed arrival-time, $Tobs_i$, and the calculated travel-time, $Tcalc_i$, of the *P*- or *S*-arrival at the station.

(4) And, *Xo, Yo, Zo*, and *To*, are iteratively corrected until the sum of the squares of the travel-time residual is small by applying the iterative least-square technique of Geiger (1912).

The travel-time residual is expressed mathematically as:

$$Res_i = Tobs_i - (To + Tcalc_i + D_i) \tag{2.25}$$

where D_i is the time delay at the station *i* caused by the elevation or other sources.

The idea in this approach is to reduce Res_i at each station by correcting, or changing, the hypothetical hypocenter and origin time. Let *dXo, dYo, dZo,* and *dTo* be the change.

After this change has been applied, the new residual, R_i, at station *i* is written as

$$R_i = Res_i + \frac{\partial Res_i}{\partial Xo} dXo + \frac{\partial Res_i}{\partial Yo} dYo + \frac{\partial Res_i}{\partial Zo} dZo + \frac{\partial Res_i}{\partial To} dTo + higher\ order\ terms \tag{2.26}$$

Assuming that small changes *dXo, dYo, dZo,* and *dTo* have been made, higher order terms are negligible. Besides, $Tobs_i$, *To* and D_i are independent of *Xo*, *Yo*, and *Zo*. Consequently, by considering Equation (2.25), the Equation (2.26) can be expressed as:

$$R_i = Res_i - \frac{\partial Tcalc_i}{\partial Xo} dXo - \frac{\partial Tcalc_i}{\partial Yo} dYo - \frac{\partial Tcalc_i}{\partial Zo} dZo - \frac{\partial Tcalc_i}{\partial To} dTo \tag{2.27}$$

Equation (2.27) shows the equation of the predicted residual for one observed arrival (*P* or *S*) at a seismic station in terms of the unknown *dXo, dYo, dZo,* and *dTo*.

Equation (2.27) has four unknowns and thus can be solved mathematically if there are at least four equations (*i.e.* four observations). However, many observations (*P*- or *S*-arrival), accordingly many equations, will be generally obtained. This will lead to the overdetermination of the four unknowns. As a result, a least-square technique is applied by minimizing the root-mean-square:

$$RMS = \sqrt{\frac{\sum_{i=1}^{n} w_i R_i^2}{\sum_{i=1}^{n} w_i}} \tag{2.28}$$

The weight w_i is implemented in the minimization to account for the quality of the data, which can be function of distance, azimuth, etc…

Error ellipse estimation is implemented in the program to evaluate the standard error. This is well described in Lahr (1984). In brief, *HYPOELLIPSE* calculates a one-standard-deviation confidence ellipsoid (68% confidence limit) which is specified by the major semi-axis of the ellipsoid's horizontal projection (SEH) and the largest vertical deviation measured from the center of the ellipsoid (SEZ). SEH are uncertainties in epicentral locations while SEZ are uncertainties in source depth. *HYPOELLIPSE* qualifies the accuracy of the location depending on the horizontal and vertical errors (SEH and SEZ) (Table 2.3):

Table 2.3: Quality of earthquake location in *HYPOELLIPSE* based on the values of SEH and SEZ.

Quality	SEH and SEZ
A	≤ 1.34 km
B	≤ 2.67 km
C	≤ 5.35 km
D	> 5.35 km

2.6.3 Application

In summary, the time intervals of seismic data used from each seismic network for the tomography study are:

(1) MACOMO stations: September 2011 to September 2013.

(2) SELASOMA stations: May 2012 to September 2013.

(3) RHUM-RUM stations: April 2011 to December 2013.

(4) GSN station: September 2011 to November 2013.

(5) GEOSCOPE station: September 2011 to November 2013.

(6) GEOFON stations: October 2011 to September 2013.

Seismic data from these networks were stored in an *Antelope* database (http://www.brtt.com/software.html) where *P*- and *S*-arrivals were manually picked (Figure 2.27). 9321 picks (*P*- and *S*-arrivals) from 47 seismic stations were extracted from the Antelope database and used as input for the program *HYPOELLIPSE*.

Also, a velocity model is required in the travel-time calculation. The velocity structure used for locating earthquakes is the average and interpolated velocity models from 37 seismic stations obtained in the joint inversion of receiver functions and surface wave dispersion measurements in this thesis (Table 2.4).

The iteration to minimize the RMS in Equation (2.28) was run to a maximum of 100 iterations. However, *HYPOELLIPSE* stops the iteration when the new RMS is equal to the previous one.

Table 2.4: Velocity structure model used for locating local earthquakes in the program *HYPOELLIPSE*.

Depth (km)	Vp (km/s)	Vs (km/s)
0.0	5.4	3.0
1.0	5.6	3.1
2.0	5.7	3.2
3.0	5.9	3.3
4.0	5.8	3.3
5.5	5.8	3.3
8.0	6.0	3.4
10.5	6.1	3.5
13.0	6.4	3.6
15.5	6.6	3.7
20.5	6.7	3.8
25.5	6.7	3.8
30.5	7.0	4.0
35.5	7.3	4.1
38.0	7.4	4.2
40.5	7.7	4.3
43.0	7.8	4.3
45.5	7.9	4.4
50.5	7.9	4.4
58.0	8.0	4.4
63.0	8.1	4.5

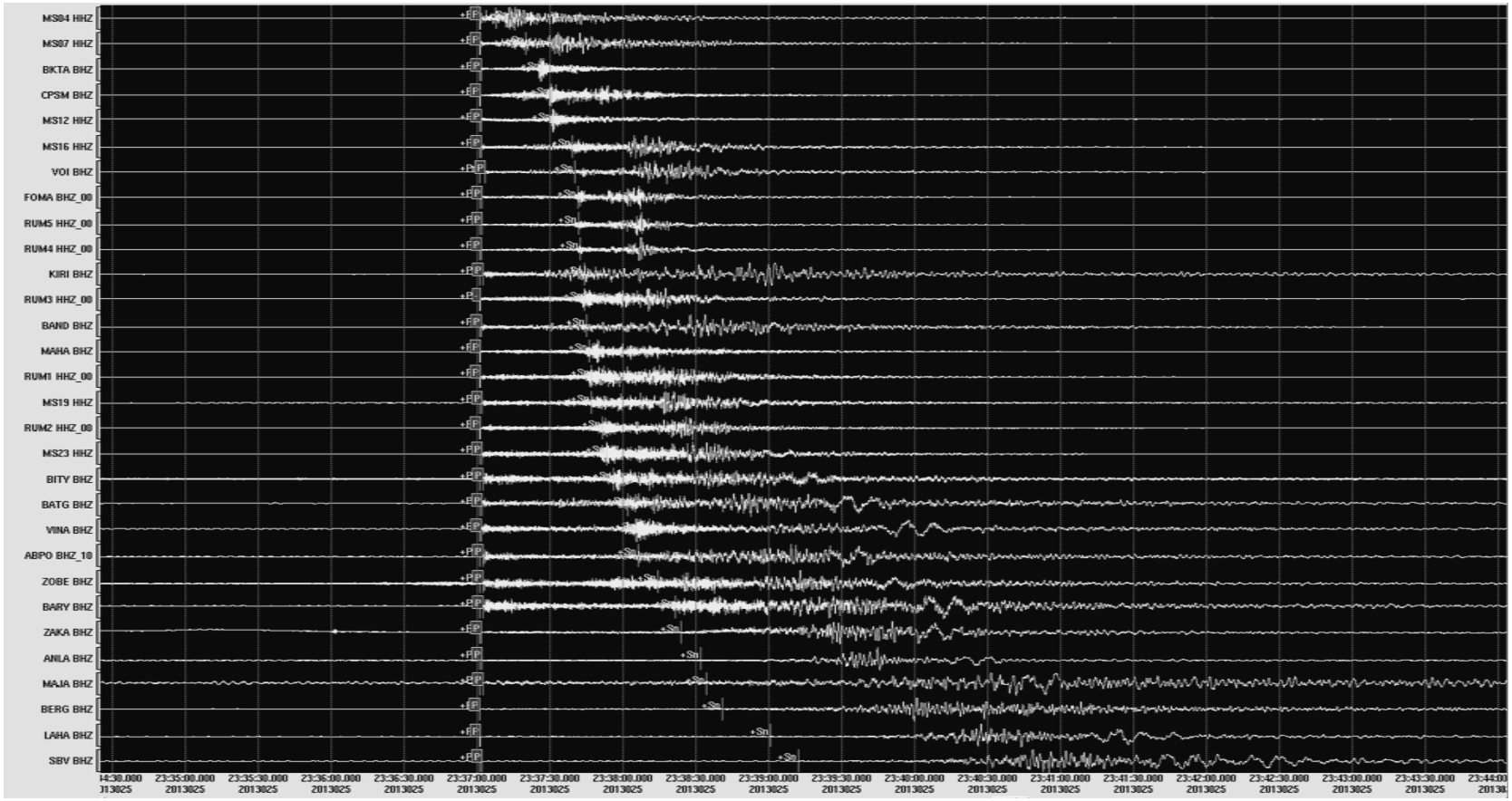

Figure 2.27: An example of *P*-arrivals picking, using Antelope, for the magnitude 5.3 earthquake occurred in the southwestern offshore of Madagascar on the 25th January 2013 23:37:01 UTC. Grey boxes, with a letter "P", are *P*-arrivals.

After the locating process, event locations with RMS higher than 1 s were not considered for further processing. Finally, a total of 647 local and regional earthquakes were located from *HYPOELLIPSE* in which:

(1) 59 % are quality A,

(2) 19 % are quality B,

(3) 9 % are quality C,

(4) 13 % are quality D.

A total of 8325 first arrivals were obtained from these seismic events which are recorded from 47 seismic stations. The distribution of these events is shown in Figure 2.28 and their hypocentral information is in Table B.1 of Appendix B.

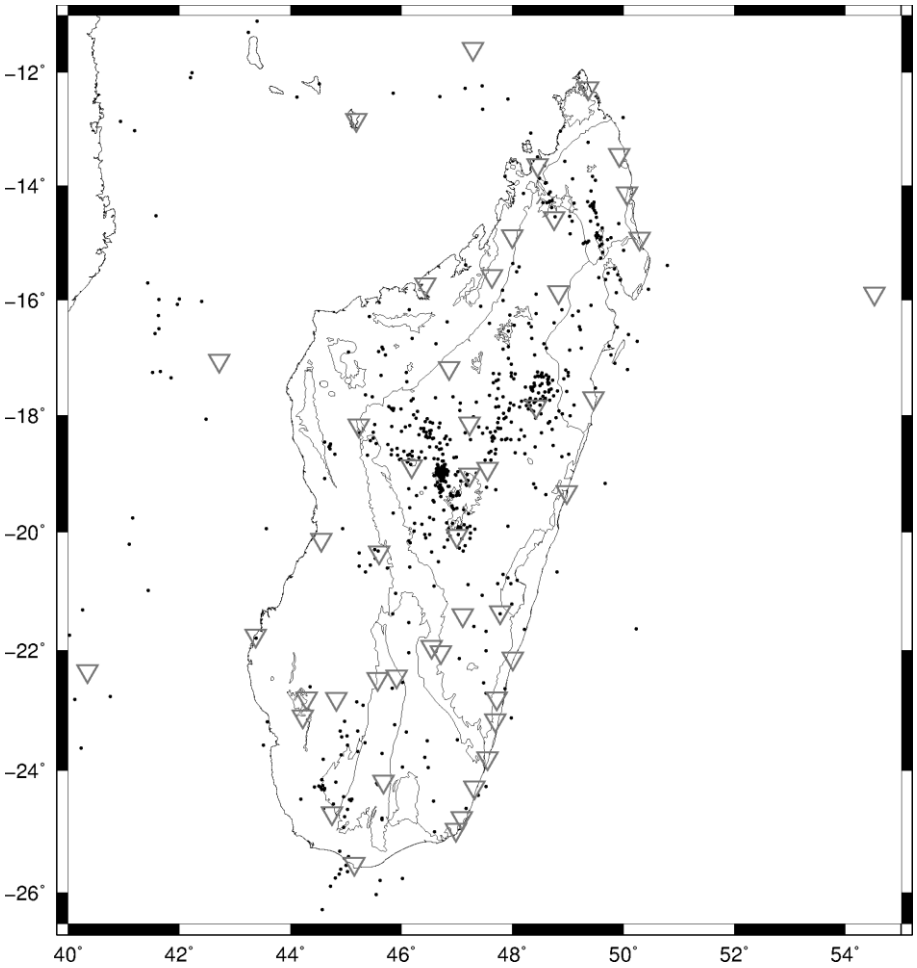

Figure 2.28: Distribution of 647 regional earthquakes (black dots) considered for the study, plotted on top of geological units (thin gray lines). A high density of seismic events is observed in the central part of the island, around Alaotra, Ankaratra, and Itasy. Inverted triangles are seismic stations used in the locating process.

2.7 *Pn* tomographic imaging of the uppermost mantle

This section presents the method used in the second project of this study for the tomographic imaging of the uppermost mantle, and results are shown in Chapter 4.

Knowing the location of earthquake, the travel time of seismic waves can be evaluated to quantify the velocity of the Earth's interior. This technique is called seismic tomography and consists of imaging the subsurface of the Earth based on travel times of seismic waves.

2.7.1 *Pn* waves

Mohorovičić first identified the *Pn* phase from seismic observations in 1909. *Pn* phases, also called head waves, are seismic *P*-waves that are refracted at the crust-mantle boundary (Figure 2.29). Their propagation has long been studied to investigate regional structure tectonics and also other thermally related phenomena.

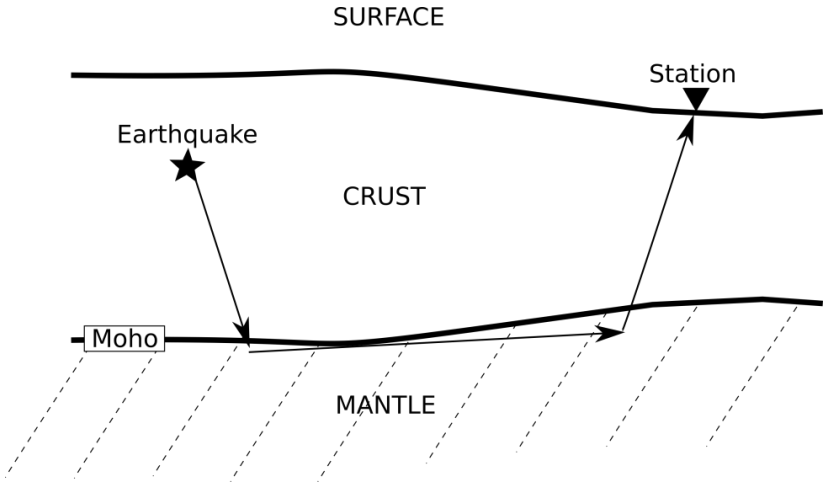

Figure 2.29: Schematic diagram of *Pn* propagation. The ray path is the combination of three segments related to the seismic source, the mantle, and the receiver.

Pn-wave phase travels faster compared to other crustal phases and arrives first at the receiver beyond certain epicentral distance, as it tunnels the higher-velocity medium, in the uppermost mantle. Thus, *Pn* waves sample the uppermost mantle and can be used to infer its velocity structure.

The amplitude of *Pn* wave decreases when it travels along the uppermost mantle. Several factors can influence its velocity along the path. Isotropic variations in the *Pn* arrival times and velocity are principally attributed to variations in crustal velocity, Moho depth, and also the pressure, temperature, and composition in the upper mantle (*e.g.* Black and Braile, 1982; Perry et al., 2006). Therefore, the study of *Pn* waves reveals valuable information, not only, for the crustal parameters, but also the mantle lid structure.

2.7.2 Seismic anisotropy

Anisotropy describes the variation of a material's physical or mechanical properties depending on the direction. The property of anisotropy can be observed in both single crystal and compounds. A very simple example is in wood splitting, which is much easier along the axis of its trunk than perpendicular to it.

The seismic anisotropy is usually explained as the result of two different mechanisms. It can be the result of the combination of stacked isotropic-materials, usually called heterogeneous materials. In this case, the anisotropy is called shape-preferred orientation (SPO). However, it can be observed in homogeneous materials as the result of crystal lattice. This type of anisotropy is called the lattice-preferred orientation (LPO) anisotropy (*e.g.* Long and Silver, 2009; Savage, 1999). For the case of the mantle, the seismic anisotropy is generally the result of LPO.

Olivine is known as the most important constituent of the upper mantle. Material flow within the upper mantle orients the olivine crystals of the rocks in this region.

In general, the seismic anisotropy is linked to the orientation of olivine strain ellipsoid axes. The fast axis of olivine has the same direction to the longest strain while the slow direction is parallel to the shortest strain. Consequently, the fast axes (*a* axes) are parallel to the direction of the maximum shearing strain under simple shear conditions, with the slow axes (*b* axes) perpendicular to it (*e.g.* Karato and Wu, 1993).

Therefore, the fast *Pn* directions are associated with the orientation of olivine crystals due to stress, strain, creep and flow, or the alignment of features such as dikes and melt-filled lenses within the upper mantle (*e.g.* Silver, 1996; Savage, 1999). Thus, seismic anisotropy reveals the strain associated with the mantle flow and records the strain history of a region. In most cases, it mirrors the latest tectonic activities that a region experienced.

2.7.3 *Pn* tomography

Overview

Scheidegger and Willmore (1957) studied the refracted phases of *P* waves from single-station time analysis. They described the theoretical refraction travel time as:

$$t_{ij} = a_i + b_j + \frac{\Delta_{ij}}{V_P} \tag{2.29}$$

where a_i is the time term of an event i, b_j is the time term of a receiver j, Δ_{ij} is the distance between the event i and the receiver j, and V_P the *P*-wave velocity of the refractor.

Vp in Equation (2.29) may be uniform, laterally varying, vertically varying, or vary with direction.

In the 1960s, due to the lack of seismic stations, most of the *Pn* studies were performed using data from exploration seismic refraction surveys. Hess (1964)

first observed that the velocity of *Pn* waves in the uppermost mantle depends strongly on the azimuth of the shots and receivers.

Backus (1965) introduced the anisotropy term by defining the *P* refractor velocity with a weak anisotropy as:

$$V_P^2 = c_P^2 + A + Csin(2\theta) + Dcos(2\theta) + Esin(4\theta) + Fcos(4\theta) \qquad (2.30)$$

where c_p is the assumed isotropic velocity, θ is the backazimuth, and *A, C, D, E,* and *F* are the anisotropic parameters derived from elastic constants.

The subsequent *Pn*-wave studies included the slowness term in their analysis to take into account the anisotropy effect in the theoretical refraction travel-time in Equation (2.29). For example, Bamford (1977) conducted a *Pn*-wave velocity and anisotropy study using exploration seismic refraction data and defined the travel-time of *Pn* phases as:

$$t_{ij} = a_i + b_j + \frac{\Delta_{ij}}{V_P} + \frac{1}{2(c_P^2 + A)^{3/2}}\left(R_i + R_j - \Delta_{ij}\right)[Csin(2\theta) + Dcos(2\theta) + Esin(4\theta) + Fcos(4\theta)] \qquad (2.31)$$

where R_i and R_j are respectively the horizontal distance between the refraction points to shot *i* and the receiver *j*, and the remaining variables are similar to the Equation (2.29) and (2.30).

Hearn's method (Hearn, 1996) was used in this thesis and is described below.

Hearn's method (1996)

Pn ray path is the combination of three segments (Figure 2.29): (1) the source-to-mantle path through the crust, (2) the passage through the uppermost mantle (the lid), and (3) the up-going mantle-to-receiver path back through the crust. In the approach of Hearn (1996), residuals in *Pn* travel-times are tomographically inverted to deduce the lateral velocity variation of the uppermost mantle and the

seismic anisotropy, which is described by the magnitude and direction of the fastest wave propagation.

Hearn (1996) divided the surface of the uppermost mantle into a set of two-dimensional cells, and then described the travel time residuals, t_{ij}, of the ray between station *i* and earthquake *j* as:

$$t_{ij} = a_i + b_j + \sum \Delta_{ijk} (s_k + A_k cos2\theta + B_k sin2\theta) \quad (2.32)$$

where a_i is the static delay for station *i*, b_j is the static delay for event *j*, θ is the back azimuth angle, Δ_{ijk} is the distance traveled by the ray *ij* in mantle cell *k* (it is 0 if the ray *ij* does not cross the cell k), and s_k is the slowness perturbation (inverse of velocity), and A_k and B_k are two anisotropic coefficients. The 4θ terms in Equation (2.30) were neglected in Hearn's approach as they are very small and will not influence the propagation.

A regularized least-squares method is used when solving the set of travel-time equations in Equation (2.32). These multiple travel-time equations are obtained from all the rays, between event-station pair, in which the unknowns are the station and event delays (a_i and b_j), the mantle-lid slowness (s_k), and the two anisotropic coefficients (A_k and B_k). The anisotropy parameters, the magnitudes and directions of the fastest wave propagation, within the cell *k* are estimated by $\sqrt{A_k^2 + B_k^2}$ and $(1/2)arctan(B_k/A_k)$, respectively.

The velocity and the anisotropy are independently regularized by implementing Laplacian damping in the inversion. Consequently, the solution is controlled by damping parameters. The smoothness of the velocity is controlled by damping the slowness s_k and the smoothness of the anisotropy is controlled by damping the two anisotropy coefficients, A_k and B_k. The damping coefficients control the trade-off between errors and resolution: typically, low values provide good resolution but large errors, and high damping gives poor resolution but small errors. The regularization of the velocity-anisotropy trade-off is discussed later.

Inversion theory

A preconditioned version of the least squares QR (LSQR) factorization algorithm of Paige and Saunders (1982a, 1982b) is used in the Hearn's method to solve the set of travel-time equations. The LSQR is a popular method for solving large linear systems in a least square problem as it has easy-to-implement numerical properties. It decomposes the matrix into a product of an orthogonal matrix (Q) and an upper triangular matrix (R).

The resulting equations from Equation (2.32) are first translated into matrix form as:

$$\boldsymbol{Gm} = \boldsymbol{d} \tag{2.33}$$

where $\boldsymbol{G}$ is a matrix including the parameter coefficients (delays, slowness, anisotropic coefficients), $\boldsymbol{m}$ is a vector containing all parameters that are going to be solved: the station and event delays (a_i and b_j, respectively), slowness perturbations (s_k), and anisotropy parameters (A_k, and B_k), and $\boldsymbol{d}$ is the observed travel times (t_{ij}).

The matrix $\boldsymbol{G}$ is also called the data kernel which relates the observed residual data with the model parameters. $\boldsymbol{G}$ is a large and sparse matrix containing mostly zero elements (from $\Delta_{ijk} = 0$ of Equation (2.32), when the ray ij does not pass through the cell k). As a result, it requires a LSQR method to invert the Equation (2.33)

Hearn (1996) introduced the preconditioning in the inversion when applying the LSQR method to iteratively find the least squares solution $\boldsymbol{z}$ and the final solution $\boldsymbol{m}$ from the following equation:

$$\boldsymbol{GP^{-1}z} = \boldsymbol{d} \tag{2.34}$$

where $\boldsymbol{z} = \boldsymbol{Pm}$, and $\boldsymbol{P}$ the preconditioning matrix.

The least squares solution is defined by:

$$\boldsymbol{z} = ((\boldsymbol{GP^{-1}})^{\boldsymbol{T}}(\boldsymbol{GP^{-1}}))^{-\mathbf{1}}(\boldsymbol{GP^{-1}})^{\boldsymbol{T}}\boldsymbol{d} \quad (2.35)$$

The preconditioning is implemented to speed up the numerical process, but will not affect the solution of the inversion (Paige and Saunders, 1982a, 1982b).

Station and event delays

Both station and event delays (a_i and b_j, respectively) mirror the structure of the subsurface underlying the region and can be used to extract information about the thickness of the crust and velocity of both crust and mantle. Station static delays are functions of the crustal thickness, the crustal seismic velocity, and the mantle seismic velocity. Event static delays are function of these parameters plus the accuracy in source parameters (*e.g.* event depth and origin time).

By assuming a uniform crustal velocity, the station or event static delays are given by the following expression:

$$delay = \int (s_{crust}^2 - s^2)^{1/2} dz \quad (2.36)$$

where s_{crust} is the crustal slowness as a function of depth and s the mean velocity of the uppermost mantle. This integral is calculated from the sea level to the Moho depth for the station static delay and from the hypocenter depth to the Moho depth for the event static delay.

Hearn and Ni (1994) calculated that for a crust with a 6.3 km/s average velocity, a relative change of 1 s in the delay time corresponded to a 10.4 km variation in the crustal thickness.

2.7.4 Application

Selection of first arrivals to be used in the inversion

Not all earthquake located by *HYPOELLIPSE* were used for the inversion, as some first arrivals were crustal phases (*Pg*) rather than *Pn*. As shown in Section 2.6.3, a total of 8325 first arrivals were obtained from 647 regional earthquakes recorded at 47 seismic stations.

In order to guarantee that only *Pn* phases were used in the inversion and to guarantee the consistency and quality of the solution, different criteria were iteratively applied to the above cited data:

(1) Only seismic events inside the seismic network were considered in the tomography study. That is to ensure the accurate location of the event.

(2) Each travel time was corrected for receiver topography to account for the time taken by the ray between the sea level and the elevation of the station. The crust above sea level was assumed to have a *P*-wave velocity of 5.5 km/s (Hearn et al., 1991).

(3) Only seismic events that occurred between the ranges of epicentral distance of 200 km and ~1500 km were considered in the study. The minimum distance corresponds to the *Pg*-*Pn* cross-over distance, X_C, for a 35-km-thick crust, and average crustal and mantle *P*-wave velocity of 6.4 km/s and 8.1 km/s, respectively (these values are averages from the joint inversion of radial receiver functions and Rayleigh-wave phase-velocity dispersions) from the equation:

$$X_C = 2H\sqrt{\frac{V_{mantle} + V_{crust}}{V_{mantle} - V_{crust}}} \tag{2.37}$$

where H is the crustal thickness, and V_{crust} and V_{mantle} are the average crustal and mantle velocity, respectively.

Pn phases can be observed for events with epicentral distance greater than X_C. The maximum distance corresponds to the largest distance obtained from *HYPOELLIPSE*.

(4) Each seismic event must be recorded by at least five seismic stations.

(5) Each seismic station must record at least five seismic events.

(6) The travel-time versus the epicentral distance was fitted to an iterative least-square straight line and travel-time that residuals larger than 6 s relative to the straight line were discarded.

The selection criteria left 424 seismic events and 44 seismic stations from which 4541 *Pn* travel times were obtained.

Figure 2.30 shows the ray paths between events and stations, the distribution of the selected seismic events and stations. As expected, the ray paths present a good coverage, especially over along the Precambrian basement of Madagascar. The extreme northern, western, and southern parts of the island are poorly covered.

Figure 2.31 is a plot of travel times versus epicentral distances. The mean *Pn* velocity, 8.10 km/s, was obtained from the inverse of the slope of the best-fit line, while the mean crustal delay, 6.2 s, was given by its intercept.

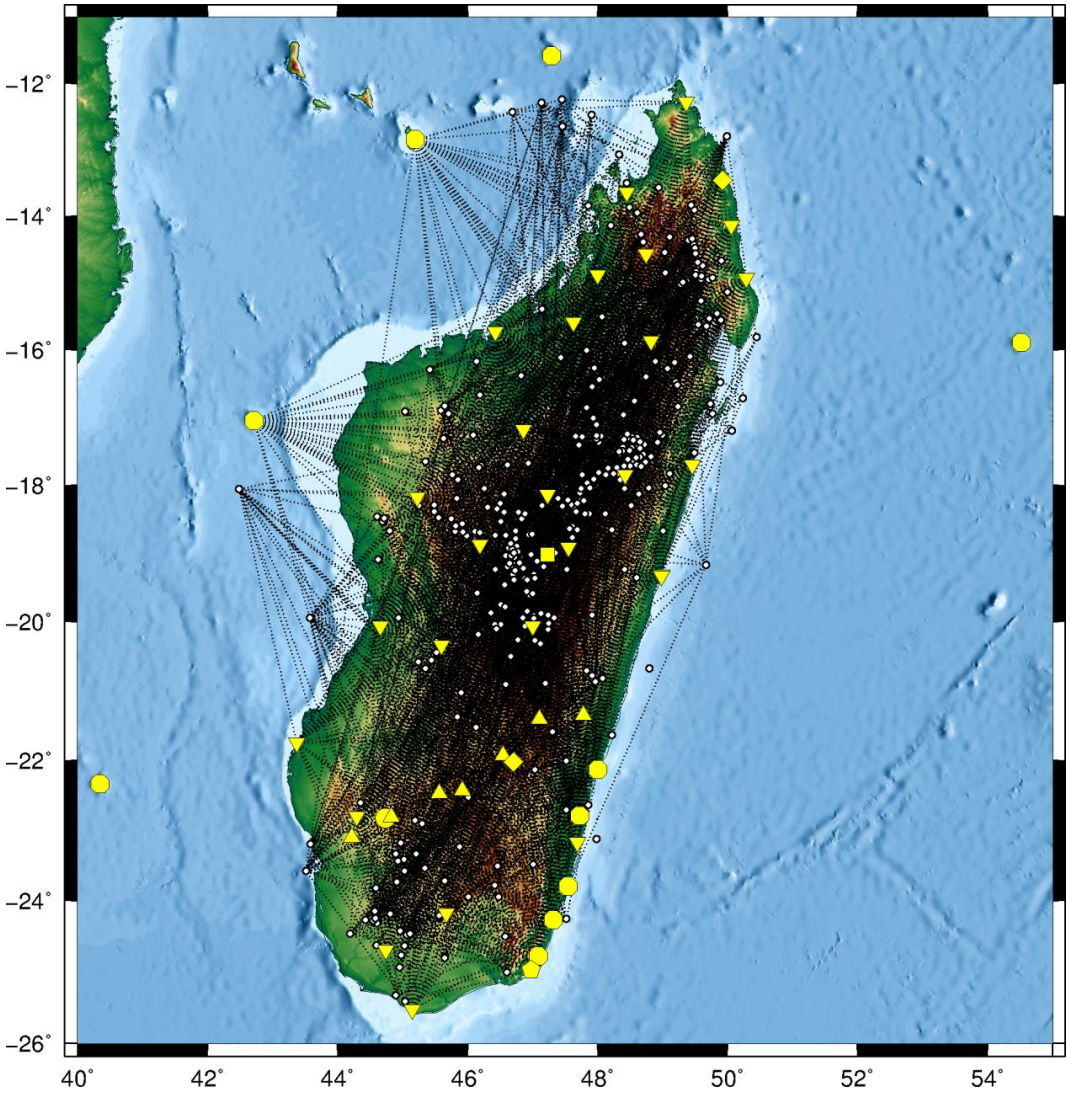

Figure 2.30: Map showing the 47 seismic stations (yellow symbols) and 647 regional seismic events (white dots) before the selection criteria. Black dashed lines show the 4541 *Pn* rays that connect the 44 seismic stations with the 424 seismic events after the data selection criteria were applied. Note that the eastern Precambrian area is well covered compared to the western sedimentary basins.

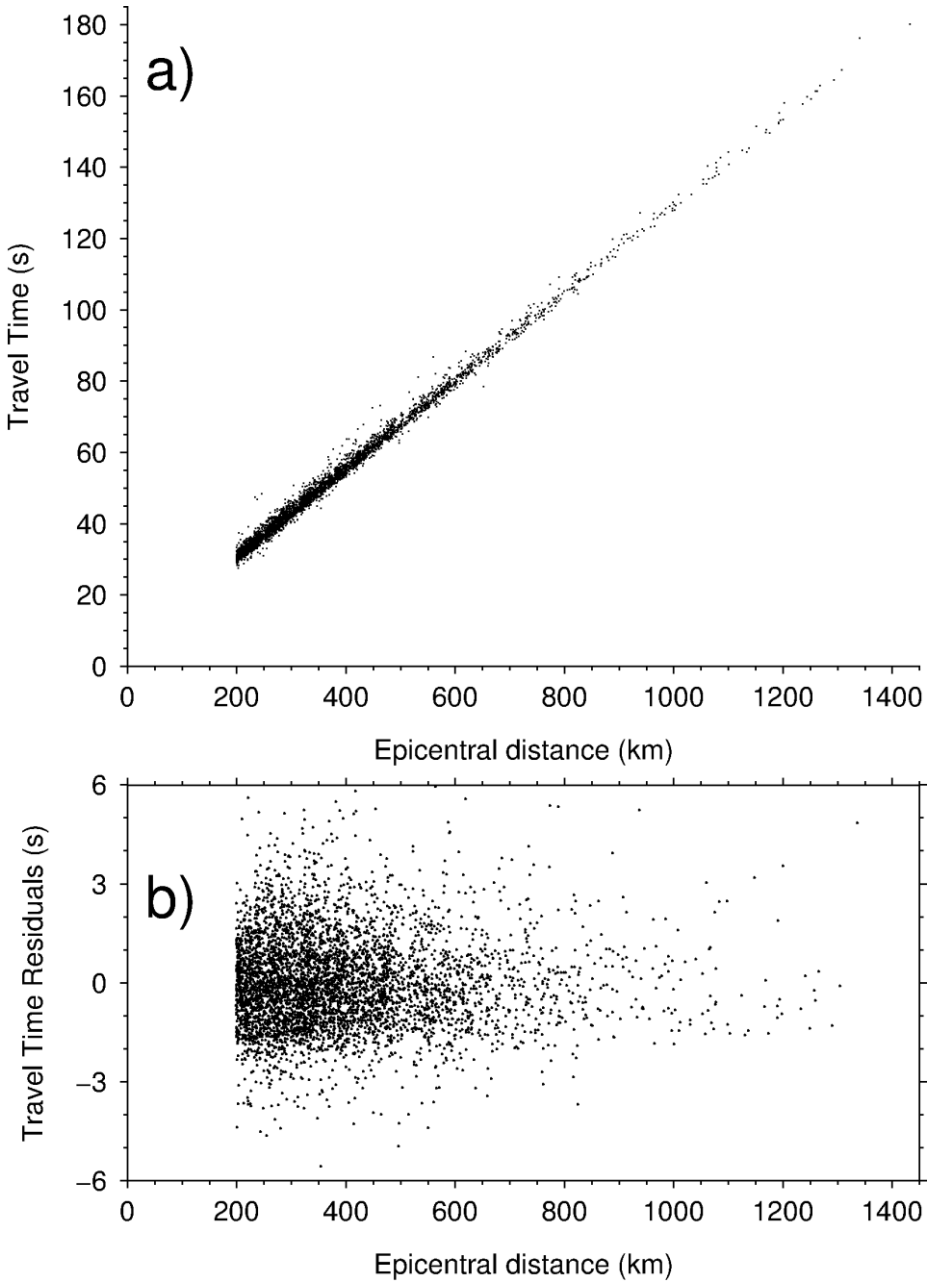

Figure 2.31: All *Pn* arrivals selected for the inversion. (a) Plot of travel times versus epicentral distances. A least-squares straight-line fit to the data shows an average Pn velocity of 8.10 km/s (from the inverse of the slope) and an average crustal mean delay of 6.2 s (from the intercept). (b) Plot of the travel-time residuals of each arrival relative to the best-fit line.

2.7.5 Regularization of the velocity-anisotropy trade-off

Selecting the best appropriate damping parameter is crucial in the regularized least-square inversion because it controls the trade-off between errors and resolution. The damping coefficient of the velocity was set first by omitting the anisotropic part in the inversion. It was chosen through trial and error according the resolution of the obtained structure, the error observation, and the consistency with the geology to avoid over- or under-damping. In this process, inversions of the observed data were run for 100 iterations to solve Equation (2.32). As Hearn's method evaluate the velocity and anisotropy cell by cell, the surface of the uppermost mantle was divided into 1/8-degree square cells (0.125° x 0.125°) grid.

After a number of trials, the structure obtained from a damping coefficient of 500 appeared to be geologically acceptable, which shows reasonable pattern of velocity anomalies, and reasonably low in error (Figure 2.32).

Once the damping value is obtained for the velocity, it was used to evaluate the damping value of the anisotropy. Following the approach of Hearn (1996), the relative trade-off between the velocity variations and the anisotropy variations was assessed in order to select the best damping coefficient for the anisotropy calculation. This involved building two sets of synthetic checkerboard models: the first model was characterized by laterally-varying sinusoidal perturbations of velocity with no anisotropy variations, and the second model is the inverse, a sinusoidal varying anisotropy parameters without velocity variations. The synthetic models were inverted using the travel times and ray paths that were used for the real data with a velocity damping coefficient fixed at 500, as previously found, while the damping coefficient for the anisotropy calculation was changed. The RMS of the anisotropy magnitude and the velocity perturbations were subsequently evaluated.

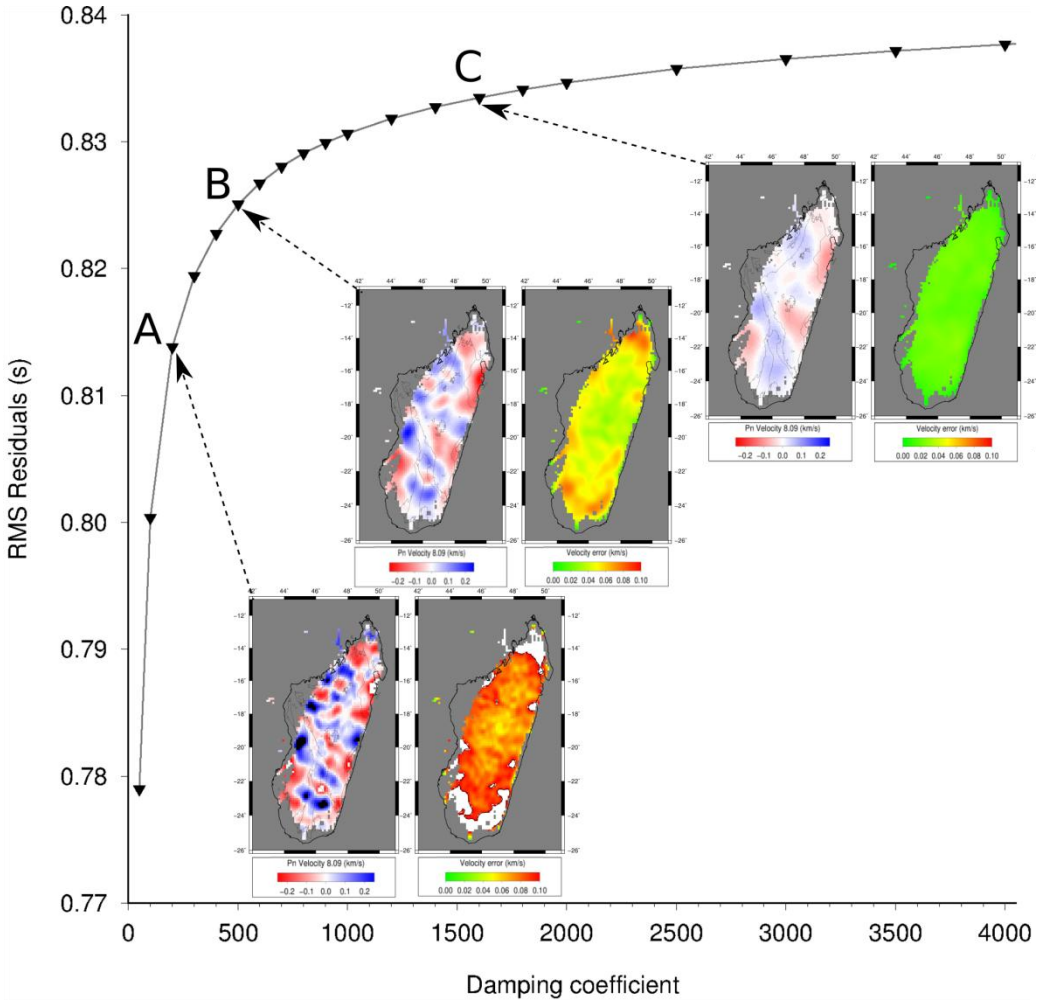

Figure 2.32: Trade-off between the velocity-damping and data fitting coefficients. The six maps represent the *Pn* velocity and error from the inversions calculated using three different damping values (A=200, B=500, C=1600). Note that over-damping (C) gives poor resolution but a low error, while under-damping (A) represents a higher resolution, but unrealistic features with a large error. The best damping value, which gives the acceptable model, is obtained at the "knee" of the curve (B=500). Therefore, a damping coefficient of 500 is used for further analysis.

Hearn (1996) stated that the best value of the anisotropy damping constant would match the velocity-to-anisotropy trade-off [*i.e.* the ratio RMS(anisotropy only)/RMS(velocity only)] with the anisotropy-to-velocity trade-off [*i.e.* the ratio RMS(velocity only)/RMS(anisotropy only)].

After a number of inversions, the two curves intersected at a value of ~600 for the anisotropy damping coefficient (Figure 2.33).

Therefore, damping coefficients of 500 and 600 were used for the velocity and anisotropy, respectively, for further computation and interpretation. In addition, only grid cells that were crossed by at least 10 ray paths were considered.

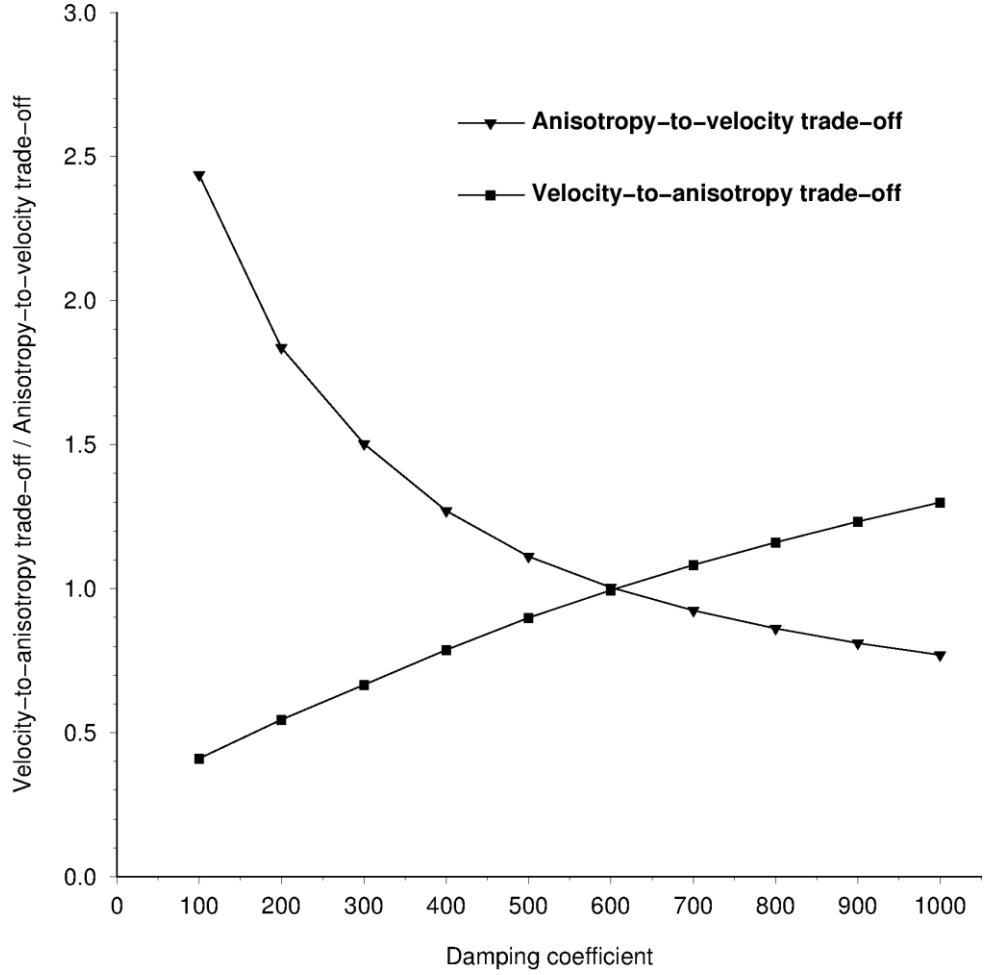

Figure 2.33: Plot of the velocity-to-anisotropy trade-off and the anisotropy-to-velocity trade-off curves. The damping that corresponds to the intersection of both curves is the best anisotropy damping coefficient for the inversion. In this case, it is 600.

2.7.6 Error estimation

A bootstrap resampling technique was applied to resample the observed data set in order to evaluate the standard error of the tomography inversion. Similar to the approach described in the Section 2.4.2, the bootstrapping technique randomly

selects travel times from the original data set and inverts them to infer the *Pn* velocity of the uppermost mantle. As Hearn and Ni (1994) suggested, the original data sets were resampled 100 times, then one-standard-deviation error was obtained from the resulting bootstrap samples.

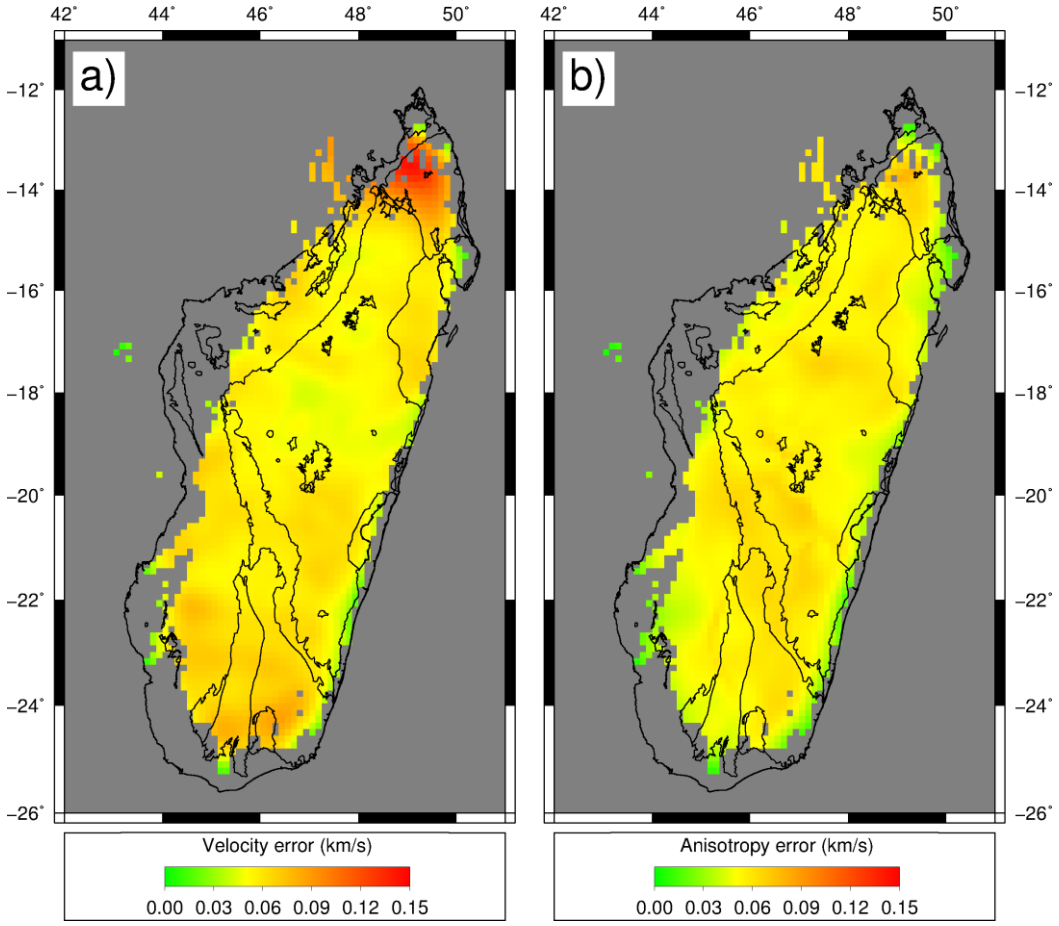

Figure 2.34: Standard errors of the velocity (a) and anisotropy magnitude (b) obtained from the bootstrap resampling technique. Errors are less than 0.09 km/s for the velocity and less than 0.06 km/s for the anisotropy. High errors are related to regions with a low density of ray paths, especially in the northernmost and southernmost parts of the island. Also plotted are the major geological unit boundaries in Figure 1.4.

The RMS error of the residuals is 0.7 s, which is probably related to systematic errors: for example, uncertainties in event locations. Standard errors of both velocity and anisotropy are less than 0.08 km/s and 0.06 km/s, respectively (Figure 2.34). The highest errors in velocity and anisotropy magnitude estimations are observed in regions where the ray-path density is the lowest, especially along

the edge of the sampled area and in the northernmost and southernmost parts of Madagascar. The error is lower than 0.05 km/s for both velocity and anisotropy across the areas that have a high density of ray paths.

2.7.7 Resolution analysis

The consistency of the resulting model was checked by inverting synthetic data sets. Sinusoidal checkerboards were built to assess the influence of ray coverage on the spatial resolution of the tomography. This involved creating a checkerboard sinusoidal test model with velocity varying between -0.30 km/s and +0.30 km/s relative to the average *Pn* velocity, 8.1 km/s, of both velocity and anisotropy amplitudes. The anisotropy direction was set to be a succession of N-S and E-W trends. *Pn* ray paths, seismic stations, and seismic events used for the tomographic inversion of the real data were utilized to compute synthetic *Pn* arrival times. Gaussian noises were added to the synthetic travel times with a standard deviation of 0.7 s, which is equivalent to the RMS error of the residuals obtained from the actual inversion.

The synthetic travel times were inverted by considering identical inversion parameters as the real data and different checkerboard sizes (1.00° x 1.00°, 1.25° x 1.25°, 1.50° x 1.50°, 1.75° x 1.75°, 2.0° x 2.0°, 2.25° x 2.25°, 2.50° x 2.50°, 2.75° x 2.75°, and 3.00° x 3.00°) to recover the checkerboard pattern. The tests indicate that *Pn* velocities with 1.25° x 1.25° cell sizes can be resolved for most of the regions (Figure 2.35), but the resolution can reach as small as 1.00° x 1.00° in the center part of the island, mostly around the Antananarivo domain, where the density of ray paths is highest. However, the resolution weakens around the edge of the sampled area. The *Pn* anisotropy also can be resolved for a grid size of 1.25° x 1.25° (Figure 2.36).

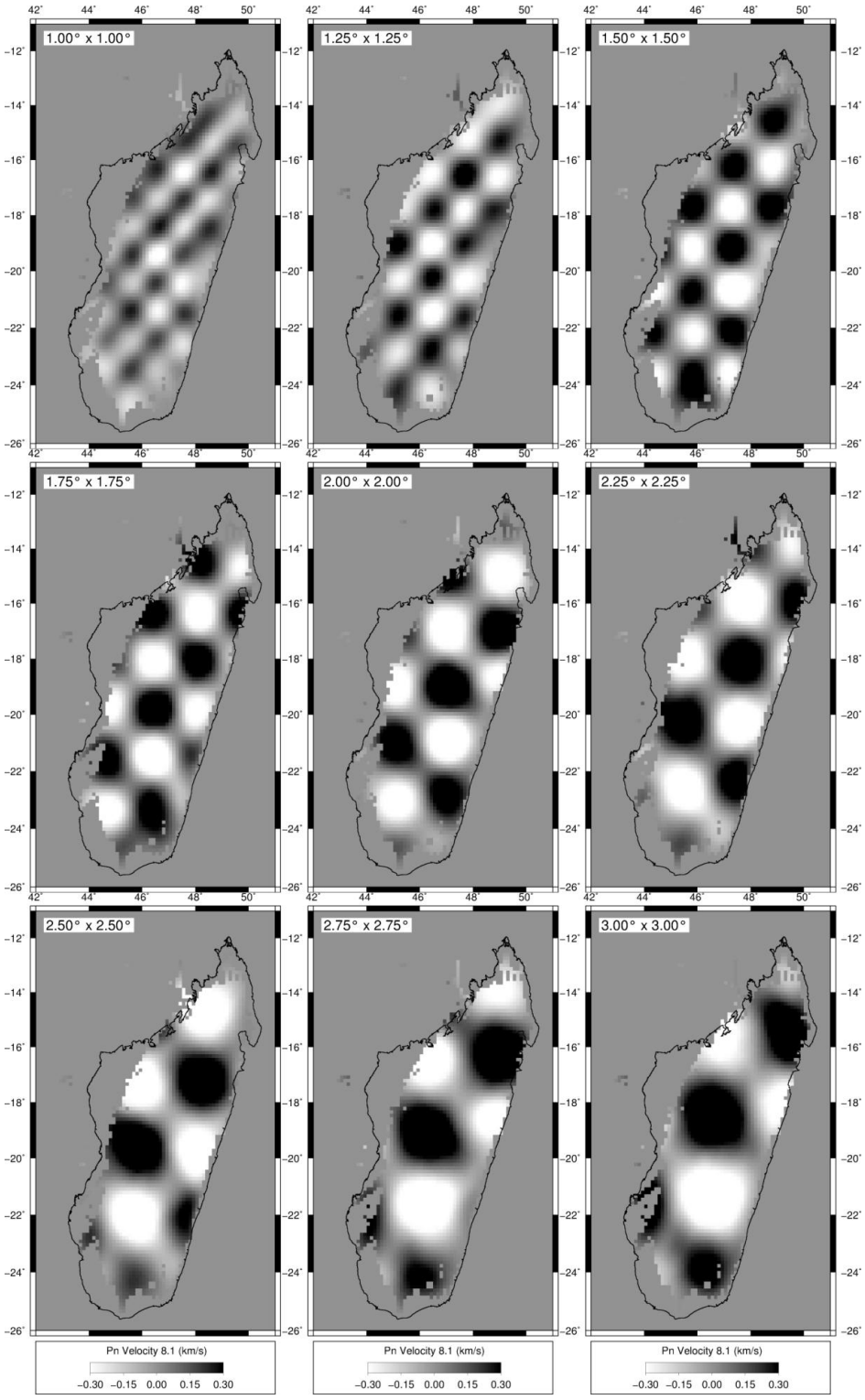

Figure 2.35: Recovered checkerboard *Pn* velocities from the tomographic inversions using different checkerboard sizes (1.00° x 1.00°, 1.25° x 1.25°, 1.50° x 1.50°, 1.75° x 1.75°, 2.0° x 2.0°, 2.25° x 2.25°, 2.50° x 2.50°, 2.75° x 2.75°, and 3.00° x 3.00°). The velocity perturbation is a sinusoidal variation between -0.3 km/s and +0.3 km/s.

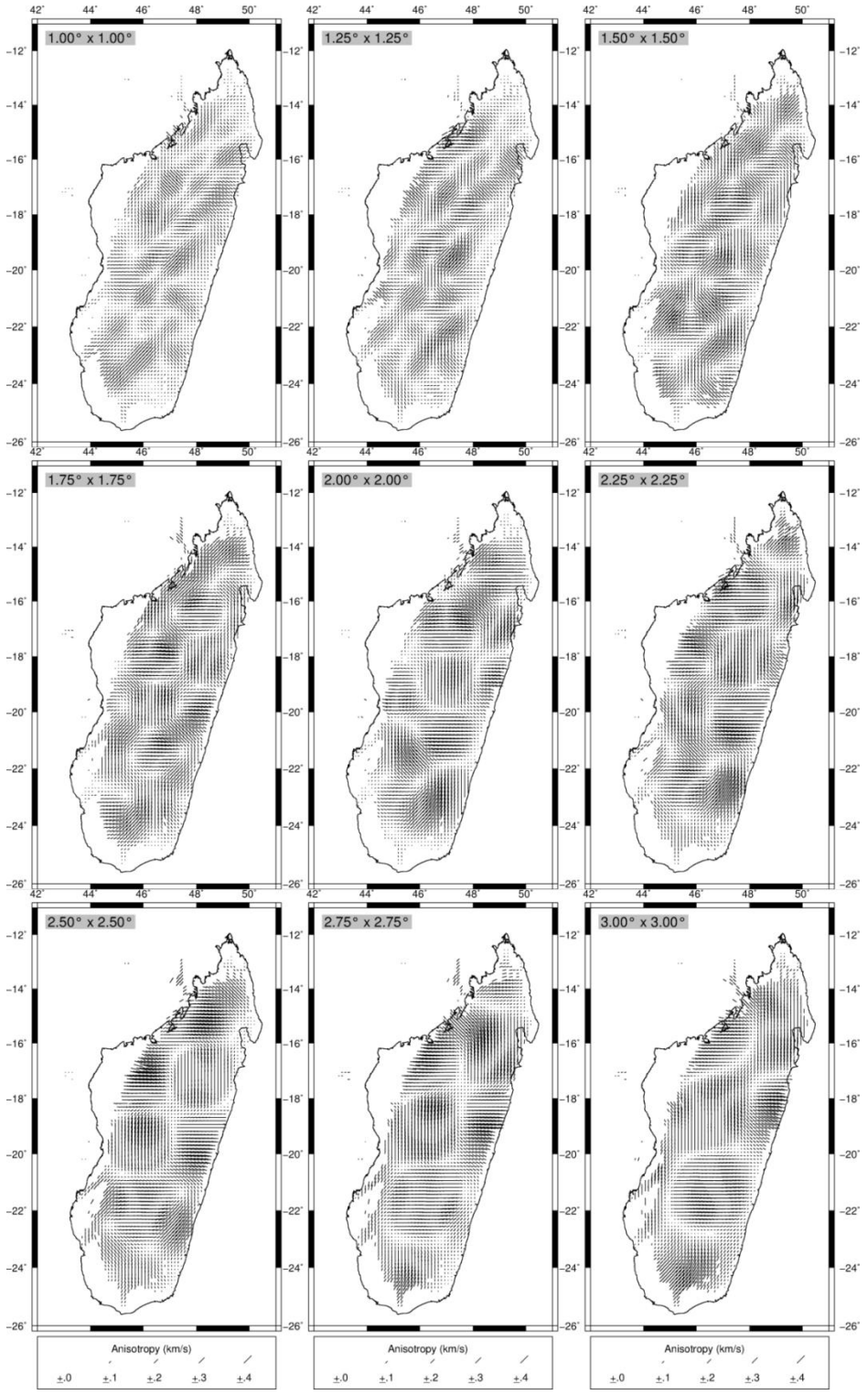

Figure 2.36: Recovered checkerboard *Pn* anisotropy values from the tomographic inversions using different checkerboard sizes (1.00° x 1.00°, 1.25° x 1.25°, 1.50° x 1.50°, 1.75° x 1.75°, 2.0° x 2.0°, 2.25° x 2.25°, 2.50° x 2.50°, 2.75° x 2.75°, and 3.00° x 3.00°).

2.8 Receiver function imaging of the mantle transition zone

This method is used for the third project of this study, and results are shown in Chapter 5.

The Earth's mantle is the thickest layer within the Earth's interior, between the crust and the outer core, and is divided into the upper mantle and the lower mantle by the transition zone. It is predominantly solid and composed by silicate rocks. However, the mantle behaves as an extremely viscous fluid in some region of the Earth, for example around tectonic plate boundaries or mantle plumes. Previous studies also suggested, by analyzing the water content of ultradeep diamonds, that a huge reservoir of water is trapped in the mantle transition zone, especially in the vicinity of subduction zones (Pearson et al., 2014).

The mantle transition zone is bounded by two discontinuities at depths approximately 410 km and 660 km, commonly called the 410 km and 660 km discontinuities (they are referred to the *410* and *660* in this manuscript). They are generally interpreted to be the result of mineral phase rearrangements and transformations in olivines (Bina and Helffrich, 1994).

Seismology provides powerful tools to observe the *410* and *660*. For example, in reflection seismology, they can directly be observed as triplications in the travel times of both *P* and *S* waves (see Figure 2.11). Davis et al. (1989) used the underside reflections of *PKPPKP* phases (also called *P'P'*, which are *P* waves that traverse the Earth's core, are reflected at the Earth's surface and re-traverse the Earth's core again) and found the sharp discontinuities at the *410* and *660* to be less than 5 km. Shearer (1991) used the reflection and conversion of long-period *P, S, SS*, and *PP* phases (*PP* and *SS* phases are *P* and *S* phases reflected twice at the Earth's surface, respectively) to identify these discontinuities. Revenaugh and Jordan (1991) analyzed *ScS* reverberations (which are *S* waves that reflected at the core-mantle boundary) to image several discontinuities within the upper mantle including the *410* and *660*.

In addition, *P*-to-*s* converted phases have also been used in the study of the transition zone (*e.g.* Vinnik et al., 1977). The mineral transformation associated with each discontinuity results in minerals that characterized by different elastic properties. This gives in return significant impedance contrasts at the discontinuities that favor the conversion of impinging *P* waves into *S* waves. Consequently, *Ps* converted phases from the mantle transition zone can be straightforwardly observed in the receiver-function waveforms in the same way as in crustal study. Receiver functions were used in this part of the thesis to study the topography of the *410* and *660*.

2.8.1 The Clapeyron slope

The Clapeyron slope is mentioned in this section because of the presence of olivine phase transformations in the discontinuities. It is a key point in phase transitions and is obtained from the Clausius-Clapeyron relation in thermodynamics:

$$\frac{dP}{dT} = \frac{\Delta H}{T\Delta V} \tag{2.38}$$

where dP/dT is the slope characterizing the variation in pressure P as a function of the variation in temperature T, ΔH is the change in the enthalpy, and ΔV is the specific volume change of the phase transformation.

The Clapeyron slope describes the slope of the boundary between two phases on a pressure-temperature diagram. A phase transition is called exothermic if the Clapeyron slope is positive ($dP/dT>0$), while it is called endothermic if $dP/dT<0$.

2.8.2 Transition zone discontinuities

A series of reorganization of atoms in olivine marks the beginning of the transition zone at the *410* and its interior boundary at the *660*. In addition, mid-

transition zone discontinuity can also be sometimes observed at depths around 520 km, also known as the 520 km discontinuity. This thesis does not focus on this mid-transition discontinuity.

The sudden increase in seismic velocities at the *410* and *660* occurs generally over interval of depth of 5 km or even less (*e.g.* Davis et al., 1989; Shearer, 2000).

The 410 km discontinuity

The discontinuity in seismic velocity at the *410* is attributed to the first order transition of the olivine, α-phase, into its high-pressure polymorphs wadsleyite, β-phase (*e.g.* Bina and Helffrich, 1994). Laboratory experiments show that the transition α-β occurs at temperatures of ~1673 K and pressures of ~13 GPa (*e.g.* Akaogi et al., 1989).

The phase transition at the *410* is characterized by a positive Clapeyron slope. The approach of Bina and Helffrich (1994) predicted the Clapeyron slope of the α-β transformation to be +2.9 MPa/K at the temperature of ~1673 K.

The discontinuity at the *410* is portrayed by an increase of the *P*-wave velocity by ~6%, the *S*-wave velocity by ~4%, and the density to ~5% (Kennet and Engdahl, 1991; Melbourne and Helmberger, 1998).

The 660 km discontinuity

The *660* bounds the interior part of the transition zone. It is believed to be the result of the transition of ringwoodite (γ-phase) into perovskite + magnesiowüstite. Such transformation of olivine phase is observed at temperatures of ~1900 K and pressures of ~24 GPa.

The transition at this discontinuity is endothermic (*i.e.* negative Clapeyron slope). Bina and Helffrich (1994) found that the phase boundary has a slope of -1.9 MPa/K at temperature of ~1673 K.

The discontinuity is marked by increasing of *P*-wave velocity to 2%, S-wave velocity to 4.8%, and density to 5.2% (Shearer and Flanagan, 1999).

2.8.3 Topography on the transition zone discontinuities

As described in the above section, the phase transition at the *410* is characterized by a positive Clapeyron slope. It suggests that a rise in temperature corresponds to a rise in pressure, hence an increase in depth. Conversely, this corresponds to a decrease in pressure (or depth) for the *660*, as the Clapeyron slope is negative for this discontinuity. On the other hand, a decrease in temperature reduces the pressure, hence decreases the depth of the *410*, while increases the pressure (depth) of the *660*. Figure 2.37 is a summary of the aforesaid mechanisms.

All of these suggest that the topography of the transition zone discontinuities depends on the temperature of the surrounding region. The *410* is depressed in the vicinity of hot region, while the *660* is elevated. Consequently, the transition zone is thinner. Around a cold region, the *410* is elevated while the *660* is depressed. In this case, the transition zone is thicker (Bina and Helffrich, 1994) (Figure 2.37).

In summary, the topography of the transition zone discontinuities can be used as "mantle thermometer" (Owens, 2000) to identify any hot or cold regime in the mantle. In terms of geodynamics, the hot region could be mantle plumes while the cold region could be a slab.

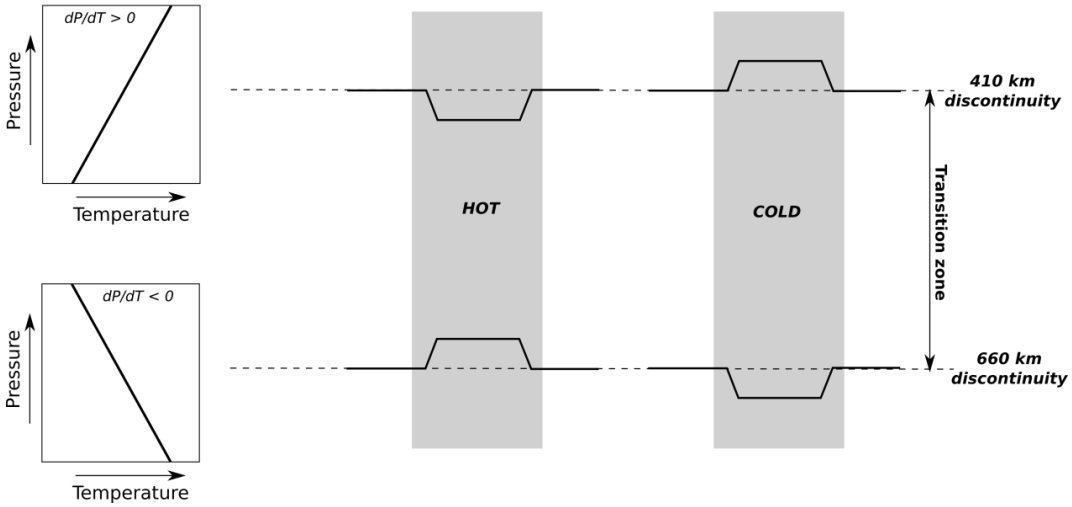

Figure 2.37: A sketch showing the effect of the Clapeyron slope to the topography of the 410 km and 660 km discontinuities around a hot or cold region. Black lines in the left-hand panels represent the slope *dP/dT*.

The global average thickness of the transition zone has been found to be between 240 km and 260 km from receiver functions and *SS*-precursors data (Shearer, 1991; Lawrence and Shearer, 2006). In this part of the thesis, the transition zone thickness was estimated from the analysis receiver function by applying a stacking procedure.

2.8.4 Isolation of receiver functions

Receiver functions used in this part of the thesis are obtained from the crustal analysis in the first part of the thesis. All the processes for the isolation of receiver functions are the same as those detailed in Section 2.3, with the exception that a Gaussian width of 0.5 and 1.0 (equivalent to corner frequencies of 0.24 Hz and 0.5 Hz) were used in this section, as we are interested only in the wide variation of the transition zone thickness (Owens, 2000).

2.8.5 Depth migration of receiver functions and moveout correction

The receiver function time series were converted into depth using the approach of Owens (2000). In this approach, the subsurface is assumed to be a stack of horizontal and homogenous layers, with predefined thickness, in which the *Vp* and *Vs* of the different layers were obtained from a given 1D reference velocity model. Each layer is separated by a theoretical discontinuity at a depth *d* in which a single ray is assumed to be converted from *P* to *S* wave.

Gurrola et al. (1994) showed that the theoretical arrival time of *Ps* phases, T_{Ps}, relative to the *P*-wave arrival at a depth *d* can be expressed mathematically as:

$$T_{Ps}(p) = \int_{-d}^{0} \left(\sqrt{\frac{1}{(Vs(z))^2} - p^2} - \sqrt{\frac{1}{(Vp(z))^2} - p^2} \right) dz \qquad (2.39)$$

where *Vp(z)* and *Vs(z)* are the *P*- and *S*-wave velocities at the depth *z*, respectively, and *p* is the ray parameter.

The receiver functions were obtained from different sources with 360° azimuthal-distribution and epicentral distance between 30-95°. Such divergence in source-receiver offsets generates systematic variations in the arrival times of the *P*-to-*s* converted phases, known as the moveout. Consequently, a move-out correction is brought into the calculation to remove such effect using *a priori P*- and *S*-wave velocities of the subsurface. For a vertically incident *P* wave (*i.e.* the incidence angle is $i = 0$), the ray parameter, as defined in Equation (2.5), is equal to 0. Thus, its travel time is obtained from Equation (2.39) as:

$$T_{Ps}(0) = \int_{-d}^{0} \left(\frac{1}{Vs(z)} - \frac{1}{Vp(z)} \right) dz \qquad (2.40)$$

Therefore, the predicted moveout of the *Ps* phase is expressed as:

$$\Delta T_{Ps} = T_{Ps}(p) - T_{Ps}(0) \quad (2.41)$$

The theoretical *Ps* arrival time at a discontinuity of depth *d* computed in Equation (2.39) is then corrected for moveout and subsequently associated with the individual receiver function time series to obtain the amplitude of the receiver function at a particular depth *d*.

2.8.6 Stacking procedure

Once the radial receiver functions are migrated into depth, the amplitudes of individual receiver functions that sample a predefined area are summed in order to obtain stacked amplitudes at every depth.

The amplitude of the receiver function at every depth could have been obtained from a single trace, but in seismic-signal processing, the procedure of stacking seismic traces improves the SNR which enhances the *Ps* phases. Mathematically, the stacked amplitude at a depth *d* is given by the relation:

$$A(d) = \frac{1}{N}\sum_{i=1}^{N} A_i(T_{Ps}^i) \quad (2.42)$$

where *A(d)* is the stacked amplitude at a depth *d*, *N* is the number of receiver functions to be stacked, and $A_i(T^i_{Ps})$ the amplitude of the receiver function *i* at the time T^i_{Ps}.

The stacking procedure can be applied for all the traces (radial receiver functions) obtained by a seismic station to image the discontinuity beneath it, called single-station stacking, or by binning all traces from different seismic stations that sample a predefined area (*e.g.* circular bin, rectangular bin…) at a particular depth, or the common-conversion point stacking.

2.8.7 Application: Single-station stacking

For the depth migration, theoretical arrival times of the *Ps* phases at different depths, with depth intervals of 5 km from the surface to a depth of 800 km, were calculated using the *TauP* package (Crotwell et al., 1999). This package computes Equation (2.39) and applies automatically the moveout correction. The *1D* reference velocity model was the global Earth velocity model *ak135* (Kennet et al., 1995), with the crustal part replaced by the velocity model beneath each seismic station obtained from the joint inversion of receiver functions and surface wave data (first part of this thesis) to reduce the error from using a global velocity model.

In the single-station stacking, all migrated receiver functions obtained on a seismic station were stacked to obtain one single trace per station. An example of a stacked trace from the station ANLA is shown in Figure 2.38.

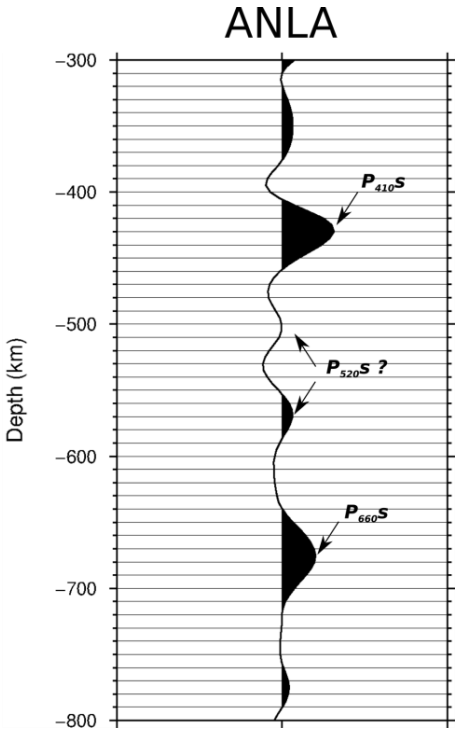

Figure 2.38: A stacked trace from a single-station stacking obtained at the seismic station ANLA. P-to-S converted phases at the 410 km and 660 km discontinuities are clearly observed. Besides, mid-transition zone *Ps* phases are present.

2.8.8 Application: Common-conversion point stacking

Similarly as in the single-station stacking, individual receiver functions were migrated into depth using the *ak135* velocity model (Kennet et al., 1995) with the crustal part replaced by the average velocity model obtained from all the seismic stations in the first part of this thesis, because all the traces were migrated at once. Also, the Earth's interior was divided into 5-km-thick layers from the surface to depth of 800 km. This part was also performed using *TauP* package (Crotwell et al., 1999).

The theoretical conversion points (or piercing points) of *Ps* phases at each theoretical discontinuity were also obtained from the *TauP* package during the ray tracing. Figure 2.39a shows the theoretical conversion points at depths of 410 km and 660 km.

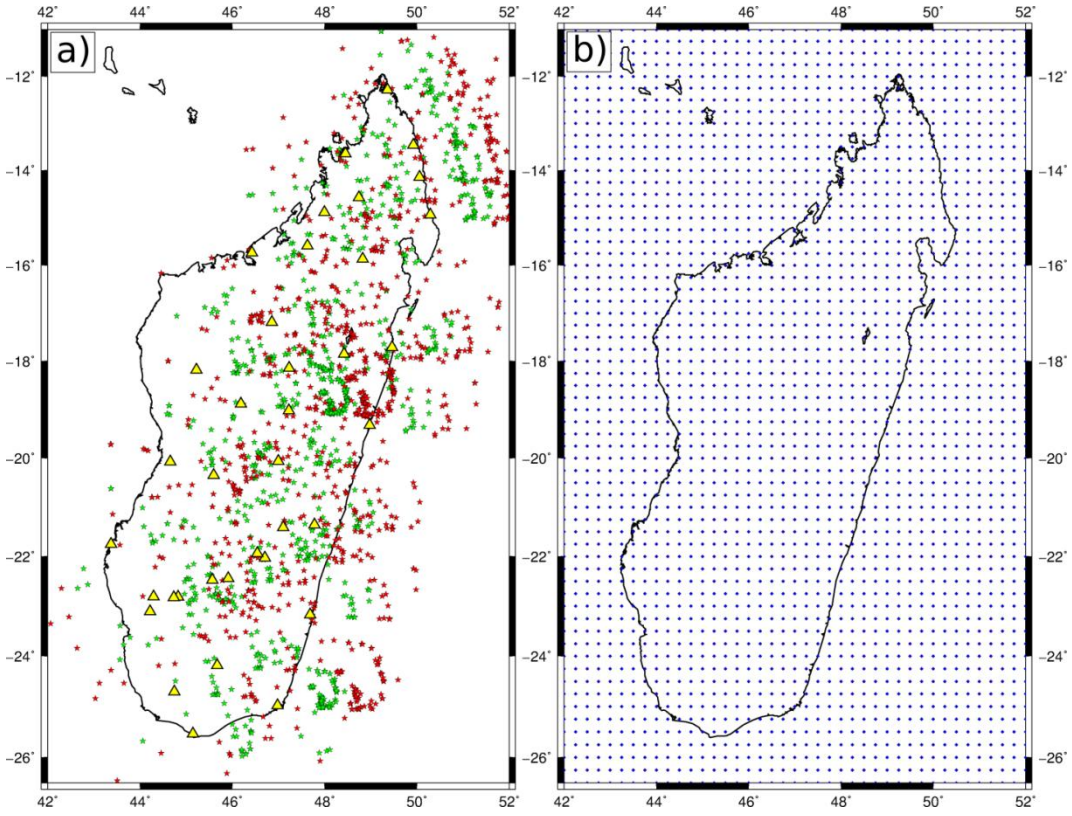

Figure 2.39: (a) Map showing the theoretical *Ps* conversion points at depths 410 km (green stars) and 660 km (red stars). Yellow triangles are seismic stations used for the study. (b) Nodes used for the common-conversion point stacking (blue points).

The common-conversion point stacking procedure of Owens et al. (2000) were used to stack the migrated receiver functions from multiple stations but sample the same region. In this approach, a preset 0.25° grid of nodal points was predefined in the study area (Figure 2.39b). Then, conversion points at every depth that fall within circular bins with variable-radius were binned. The circular bins were centered at the predefined nodes with an initial radius of 0.50°. Its radius is incremented at 0.25°-step if one of these conditions were not met: (1) a minimum of 30 conversion points (hence traces) and (2) data from at least three stations were found in each bin, and the maximum bin radius was limited at 1° (Owens, 2000). Finally, amplitudes of receiver functions corresponding to the conversion points at each bin were stacked to yield one single trace per bin.

An example of a stacked trace from the common-conversion point stacking obtained at the node centered at the latitude -20.00° and longitude 47.00°, with radius between 0.75° and 1°, number of traces between 30 and 50, and number of seismic stations between 4 and 12 at every depth is shown in Figure 2.40.

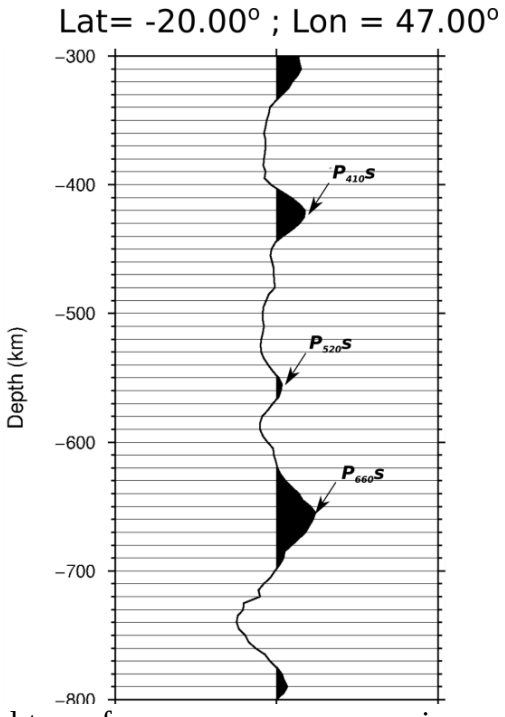

Figure 2.40: A stacked trace from a common-conversion point stacking obtained at the node centered at the latitude -20.00° and longitude 47.00°. *P*-to-*S* converted phases at the 410 km and 660 km discontinuities are clearly observed. Besides, mid-transition zone *Ps* phase is present.

2.8.9 Error estimation

The choice of the *1D* reference velocity in the depth migration affects the estimation of the depth of discontinuities in the stacking. The error related to the reference model was assessed by using different velocity models (*ak135* and *iasp91*) and different depth intervals (2 km, 5 km, and 10 km) in the depth migration procedure before the stacking procedure. The difference in discontinuity depths for the range of reference models is less than 10 km (Figure 2.41). Thus, I estimated the uncertainty attributed by the reference model in the estimation of discontinuity depths to be ± 10 km.

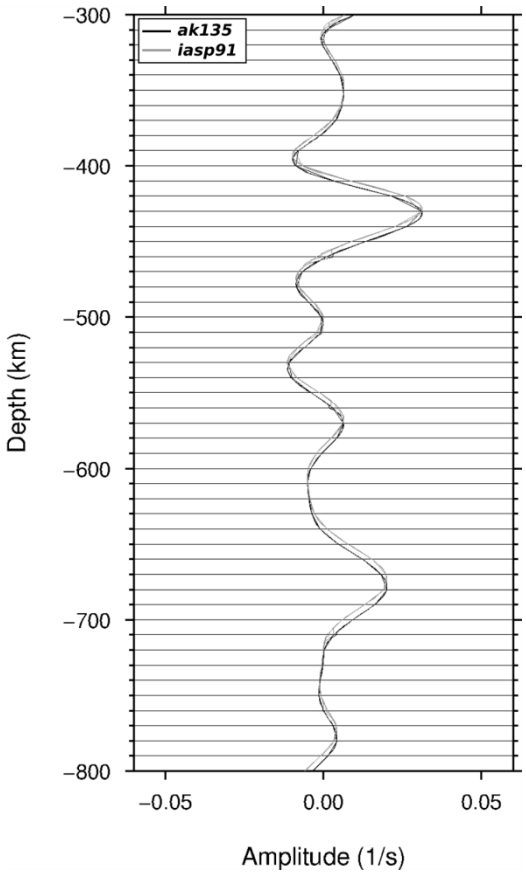

Figure 2.41: Stacked traces obtained from two different 1D reference models (ak135 and iasp91) with three depth different intervals (2 km, 5 km, and 10 km) in the depth migration.

In addition, the bootstrapping technique of Efron and Tibshirani (1991) described in section 2.4.2 was, once more, used to estimate uncertainties in the amplitudes of the *Ps* conversions. 200 replication samples of the original dataset were used to estimate the 95% confidence bounds (correspond to the grey area in Figure 2.42) at each station, for the single-station stacking, and at a selected node, for the common-conversion point stacking. Examples of stacked traces with the 95% confidence bounds from a single-station and a common-conversion point stacking are presented in Figure 2.42.

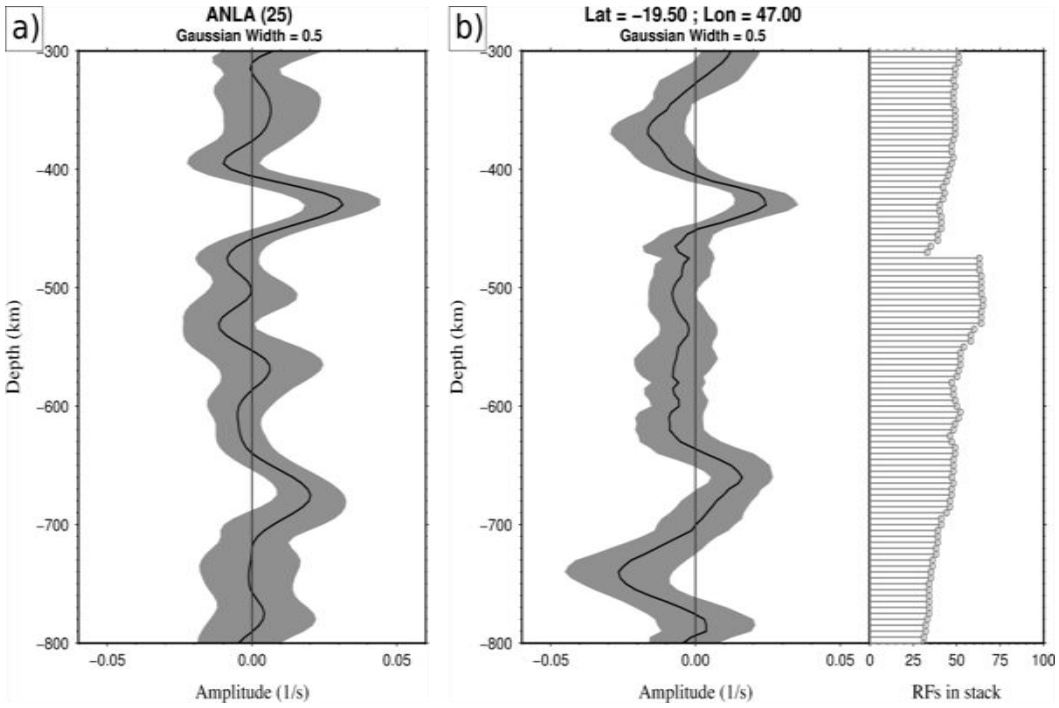

Figure 2.42: (a) An example of stacked trace with the 95% confidence bound for the station ANLA. The number in brackets next to the station name is the number of stacked traces. (b) An example of stacked trace with the 95% confidence bound for the node (lat = -19.50°, lon = 47.00°). Histograms in the right hand panel represent the number of traces stacked at each depth interval.

A confidence bound not well above the "zero" amplitude, for *Ps410* and *Ps660* at a seismic station or node, corresponds to a high uncertainty that could actually mean a close to or zero amplitude for the phase. Consequently, the result in this station or node is not acceptable for interpretation. Stacked trace for all stations and a few selected nodal with the 95% confidence are shown, respectively, in Figure C.1 and Figure C.2 of Appendix C.

The vertical errors at the discontinuities were measured directly from the 95% confidence bounds and the stacked trace as shown in Figure 2.43.

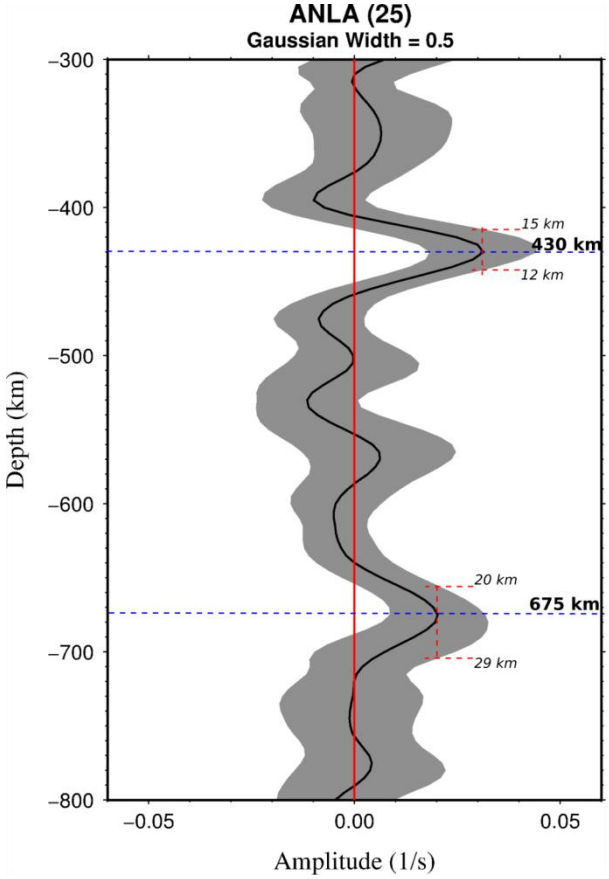

Figure 2.43: Example of vertical error measurement from the 95% confidence bounds for the station ANLA. Dashed blue lines correspond to the estimated depths of the 410 km and 660 km discontinuities. Vertical errors (dashed red lines) are obtained from the distance between the full stack peaks and the corresponding upper and lower confidence bounds for the same amplitude (Emry et al., 2015).

Chapter 3

The structure of the crust and uppermost mantle beneath Madagascar from receiver function analysis

3.1 Introduction

Different tectonic events have formed and reshaped the Precambrian lithosphere of Madagascar: the Late Neoproterozoic and Early Cambrian (*ca.* 570-510 Ma) continental collision and arc assembly of the East African Orogeny (EAO) (Stern, 1994; Collins, 2000), the Mid Mesozoic (*ca.* 200-180 Ma) rifting that was associated with the break-up of West- and East-Gondwana (*e.g.* Kusky et al., 2007), the sudden Late Mesozoic (*ca.* 90 Ma) separation of India from Madagascar (*e.g.* Mahoney et al., 1991; Storey et al., 1995), and the Cenozoic (*ca.* 28-0.55Ma) volcanism (*e.g.* Emerick and Duncan, 1982, 1983; Nougier et al., 1986; Rasaminanana, 1996).

Thus, Madagascar offers an interesting geological framework that can be used to understand the tectonic evolution of the crust. However, due to lack of data, very little was previously known about the deep structure of the lithosphere of the

island. The few previous studies of the crust and lithosphere beneath Madagascar using gravity and seismic data found that the crust is thickest (~42 km) in the central part of Madagascar becomes thinner (~30-35 km) towards the coast.

The main contribution of this study is the investigation of the crustal and uppermost mantle structure beneath Madagascar at a local scale. This was enabled by the recent deployments of temporary broadband seismic stations across the island, yielding 37 new point estimates of crustal thickness, shear-wave velocity structure, and Poisson's ratio, along with estimates of uppermost mantle shear-wave velocity. Findings from this study shed new light on the opening of the western sedimentary basin and the related thinning of the crust in the area; crustal composition; secular variation in Archean and Proterozoic crustal genesis; the origin of high elevations; and geodynamic links between regions of low mantle velocities and crustal structure.

As described in the previous chapter, this part of thesis is based on the analysis of receiver functions. The thickness and bulk Poisson's ratio of the crust were estimated from a receiver function stacking procedure, called the *H-κ* stacking method. The velocity structure of the crust and the uppermost mantle were inferred from a joint inversion of the receiver function data and Rayleigh-wave phase velocity dispersion measurements. The thickness of supracrustal basin rocks, crust, and mafic layer at the bottom of the crust, as well as the average shear-wave velocity (*Vs*) of these regions, were subsequently deduced from the velocity structure.

This chapter presents the results for each seismic station, including the basin and crustal thicknesses, crustal Poisson's ratio, and average shear-wave velocity of the crust and uppermost mantle. Subsequent to this, there will be a discussion and conclusion of the findings.

The material in this chapter has been published in a peer-reviewed journal, at the Geophysical Journal International (Appendix D), as: **Andriampenomanana, F., Nyblade, A.A., Wysession, M.E., Durrheim, R.J., Tilmann, F., Julià, J., Pratt, M.J., Rambolamanana, G., Aleqabi, G., Shore, P.J., and Rakotondraibe, T.**

(2017). The structure of the crust and uppermost mantle beneath Madagascar, *Geophysical Journal International*, 210 (3), 1525-1544, doi:10.1093/gji/ggx243.

3.2 Results

The *H-κ* stacking method was applied mainly to the lower-frequency receiver functions (*i.e.* those computed with a Gaussian width of 1.0). A starting *P*-wave velocity (*Vp*) of 6.5 km/s was used for the computation. Both low- and high-frequency receiver functions (*i.e.* computed with Gaussian widths of 1.0 and 2.5, respectively) were used in the joint inversion of receiver functions and Rayleigh-wave phase velocity dispersion.

In this section, results from the *H-κ* stacking method and joint inversion are presented separately. Then, estimates are grouped with regard to the geological location of the station and sorted by age in order to study their similarity and any variation with age of the crust and the uppermost mantle.

3.2.1 *H-κ* stacking method

The *H-κ* stacking procedure was generally performed for stations located in the crystalline basement of Madagascar and a few stations located in the eastern edge of the sedimentary basin where the intracrustal *Ps*-conversion phases are not dominant in the receiver function waveforms. Crustal thickness and *Vp/Vs* ratio for 29 seismic stations were obtained using a total of 491 traces. The Poisson's ratio at each seismic station was calculated from Equation (2.17).

Estimates, including the *Vp/Vs* ratio *(κ)* – Poisson's ratio *(ν)* – crustal thickness (*H)*, are summarized in Table 3.2 and Table 3. 3. The crustal thickness and Poisson's ratio are shown in contour maps in Figure 3.1.

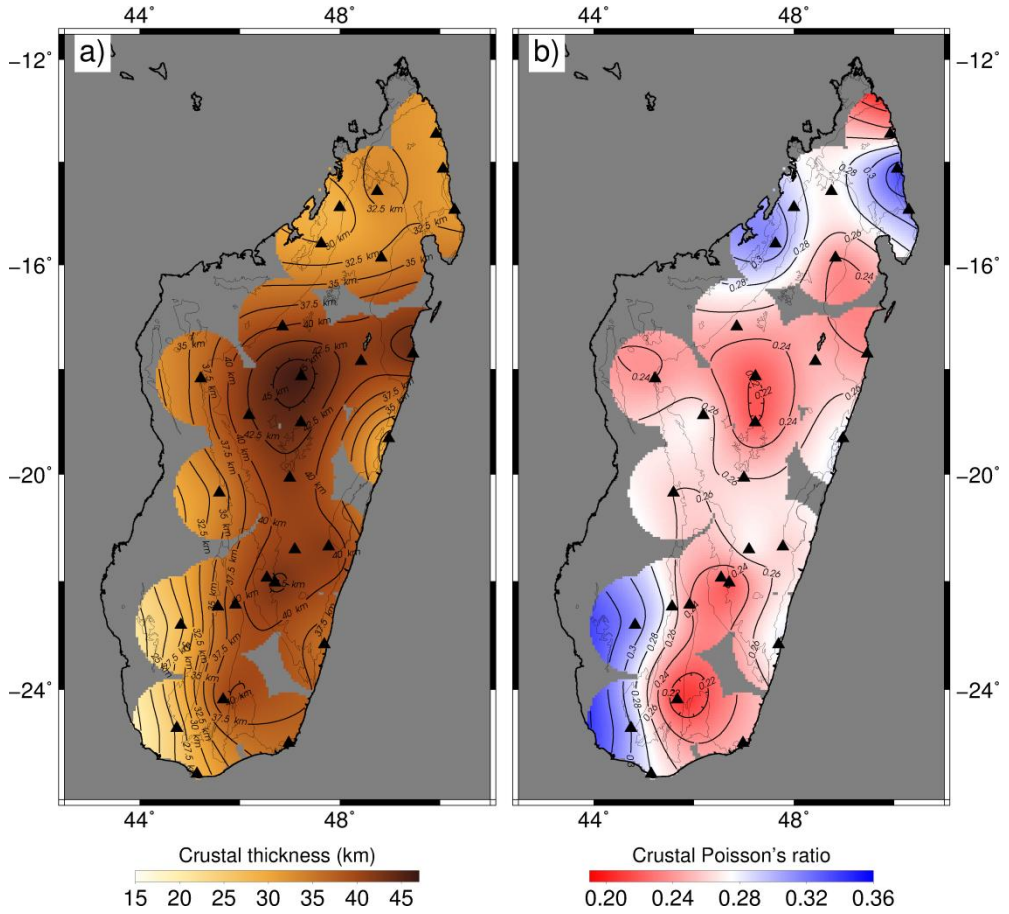

Figure 3.1: Contour maps of: (a) the crustal thickness and (b) Poisson's ratio, estimated from *H-κ* stacking method. Black squares mark the location of seismic stations. Also plotted are the major geological unit boundaries shown in Figure 1.4.

3.2.2 Join inversion method

A total of 653 receiver functions were used in the joint inversion to produce 37 new point estimates of crustal thickness and average shear-wave velocity of the basin and crust, and the average shear-wave velocity of the uppermost mantle.

The Karoo basin in the western part of Madagascar is constituted mainly of siltstones and sandstones. Previous studies (*e.g.* Castagna et al., 1985; Lee et al., 2003; Brocher, 2005) have shown that typical shear-wave velocities in

sedimentary rocks are less than 3.0 km/s. Table 3.1 shows examples of sedimentary rocks with their characteristic shear-wave velocity.

Table 3.1: Typical shear-wave velocity of sedimentary rocks (*e.g.* Castagna et al., 1985; Lee et al., 2003; Brocher, 2005).

Sedimentary rocks	Shear-wave velocity (km/s)
Porous clays and marls	0.1 – 2.7
Unconsolidated sediments	0.2 – 1.4
Shale	2.3 – 2.5
Siltstone	2.8 – 3.0
Sandstone	2.7 – 3.0

Therefore, the combined thickness of the layers in the uppermost crust with shear-wave velocity lower than 3.0 km/s were used as an estimate of the thickness of the sedimentary basin in the western region of Madagascar.

Laboratory experiments have shown that lower-crustal lithologies are characterized by shear-wave velocity lower than 4.3 km/s, while the mantle is dominated by rocks with typical shear-wave velocity above 4.3 km/s (Christensen and Mooney, 1995; Christensen, 1996). Following the approach from various studies that jointly inverted receiver functions and surface wave data in several parts of Africa (*e.g.* southern Africa by Kgaswane et al., 2009; western Africa by Tokam et al., 2010; eastern Africa by Tugume et al., 2013 and Kachingwe et al., 2015), the Moho was picked as the depth at which the shear-wave velocity is $\geq$ 4.3 km/s. At a few stations, the shear-wave velocity is slightly lower than 4.3 km/s (between 4.2-4.3 km/s) but the velocity model presents sharp change of shear-wave velocity. The Moho location at these stations was chosen at the depth corresponding to the jump, in velocity as the shear-wave velocity falls within the reported uncertainties of the estimates, ±0.1 km/s, in this study (see Section 2.5.5).

In addition, laboratory measurements have suggested that shear-wave velocity in lower-crust mafic lithologies, for example: garnet-free and garnet-bearing mafic gneisses and mafic granulites, or amphibolites, is higher than 3.9 km/s, while

intermediate-to-felsic lithologies are characterized by shear-wave velocity lower than 3.9 km/s (*e.g.* Holbrook *et al.* 1992; Christensen and Mooney, 1995; Rudnick and Fountain 1995). Consequently, layers at the bottom of the crust with shear-wave velocities between 4.0 km/s and 4.3 km/s were used to define the thickness of a mafic layer.

Estimates, including the thickness of the sedimentary basin, the crust, and the mafic lower crust, along with the average shear-wave velocity of the basin, the crust and uppermost mantle are shown in Table 3.2 and Table 3. 3. They are plotted in Figure 3.2 and Figure 3.3.

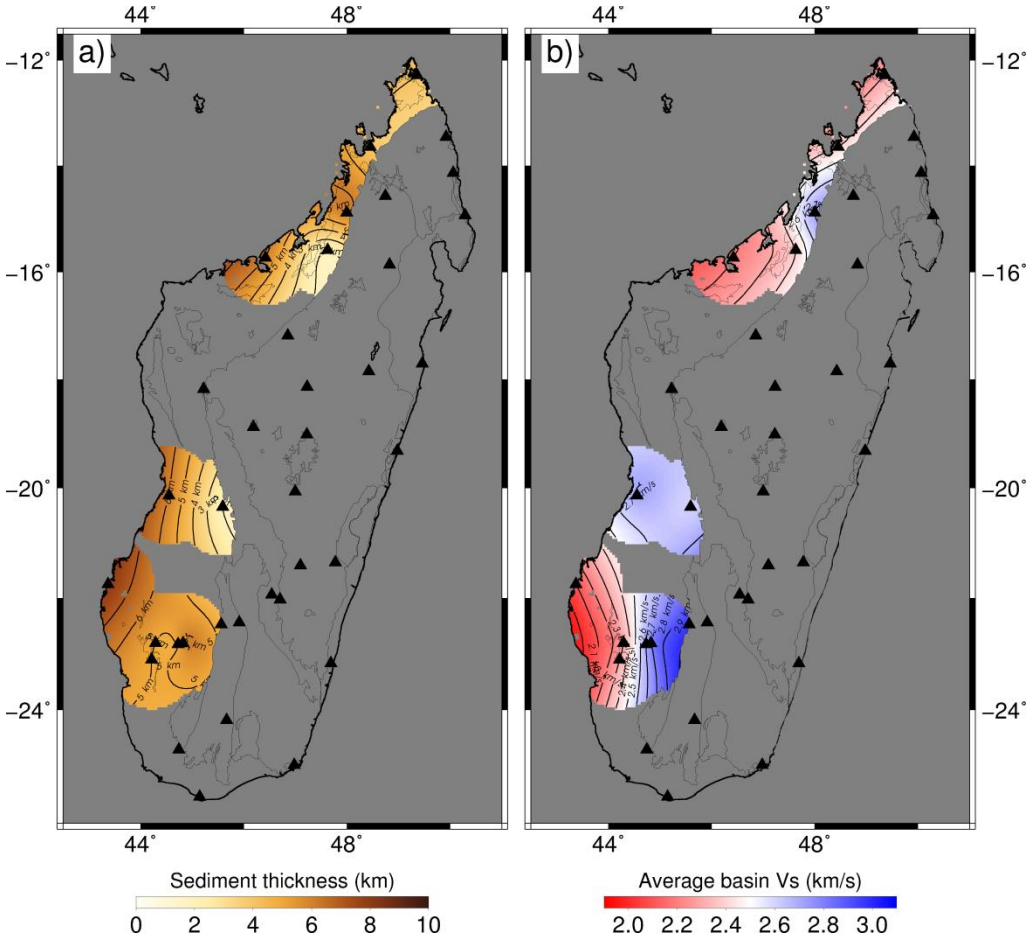

Figure 3.2: Maps showing (a) the thickness and (b) the average shear-wave velocity of the sedimentary basin beneath the basin stations. Also plotted are the major geological unit boundaries shown in Figure 1.4.

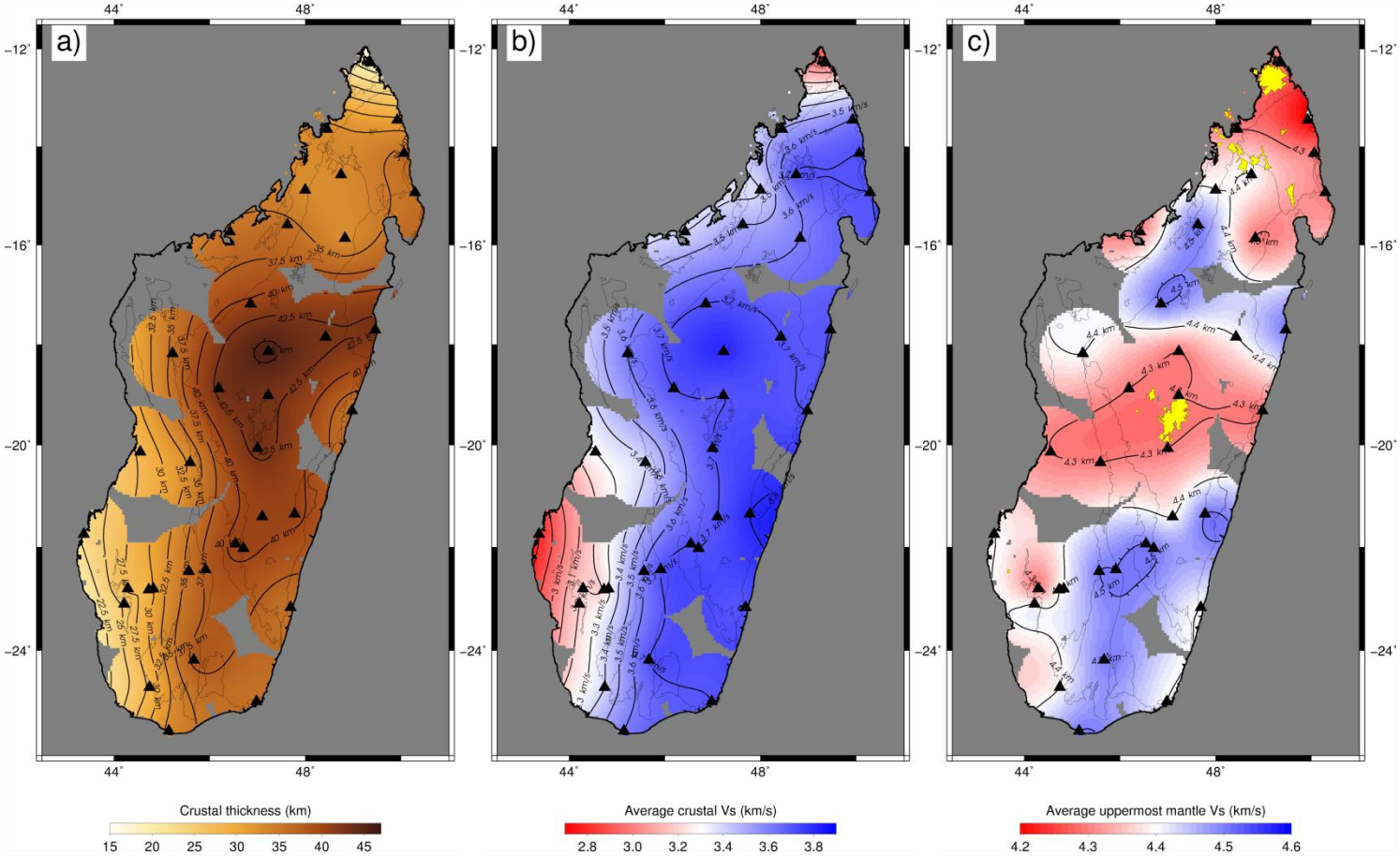

Figure 3.3: Contour maps showing (a) the crustal thickness, (b) the average crustal shear-wave velocity, and (c) the average uppermost mantle shear-wave velocity beneath Madagascar. Also plotted are the major geological unit boundaries shown in Figure 1.4.

3.2.3 Summary of estimates from *H-κ* stacking and joint-inversion method

Estimates from both methods are summarized in Table 3.2 and Table 3. 3 sorted by geological terrane and age. Table 3.2 and Table 3. 3 show results from the sedimentary basin and the Precambrian crust, respectively.

Note that the thickness of the crust obtained from the joint inversion technique is multiples of 2.5 due to the fact that the parameterization of the starting velocity model was a sequence of 2.5-km-thick layers.

Table 3.2: Summary of crustal structure for stations located in the Phanerozoic sedimentary basins. #Data is the number of traces used.

Station name	#Data	*H-κ* stacking		Joint inversion					
		Crustal thickness (km)	*Poisson's ratio*	*Sediment thickness (km)*	*Average sediment Vs (km/s)*	*Crustal thickness (km)*	*Average crustal Vs (km/s)*	*Average uppermost mantle Vs (km/s)*	*Mafic lower crust thickness (km)*
DGOS	34	-	-	4	2.3	18.0	3.0	4.3	0.0
BANJ	13	-	-	4	2.4	33.0	3.5	4.3	12.5
ANTS	22	28.6 ± 0.9	0.29 ± 0.02	6	2.7	33.0	3.4	4.4	5.0
BERG	20	30.1 ± 1.3	0.31 ± 0.01	2	2.4	35.5	3.5	4.5	5.0
MAJA	34	-	-	6	2.2	35.5	3.4	4.3	2.5
BAND	17	33.6 ± 1.7	0.26 ± 0.03	2	2.6	33.0	3.4	4.3	2.5
KIRI	19	-	-	6	2.7	28.0	3.3	4.3	2.5
MMBE	10	-	-	8	2.1	23.0	2.8	4.4	2.5
MS07	13	26.9 ± 2.4	0.31 ± 0.04	6	2.8	30.5	3.3	4.4	5.0
SKRH	8	-	-	5	2.7	28.0	3.2	4.4	0.0
LONA	30	-	-	5	2.3	28.0	3.2	4.3	0.0
MS04	13	-	-	5	2.3	25.5	3.2	4.4	2.5
CPSM	9	28.0 ± 1.0	0.28 ± 0.02	0	0.0	33.0	3.6	4.5	5.0
Average ± standard deviation		**29.4 ± 2.6**	**0.29 ± 0.02**	**4.5 ± 2.1**	**2.3 ± 0.7**	**29.5 ± 5.2**	**3.3 ± 0.2**	**4.4 ± 0.1**	**3.5 ± 3.3**

Table 3. 3: Summary of crustal structure for stations located within Precambrian terranes. #Data is the number of traces used.

Terrane (Age)	Station name	#Data	*H-κ* stacking		Joint inversion			
			Crustal thickness (km)	*Poisson's ratio*	*Crustal thickness (km)*	*Average crustal Vs (km/s)*	*Average uppermost mantle Vs (km/s)*	*Mafic lower crust thickness (km)*
Antongil-Masora (Paleoarchean. to Mesoarchean)	ANLA	24	43.5 ± 1.4	0.24 ± 0.02	43.0	3.7	4.5	15.0
Antananarivo (Neoarchean)	BAEL	24	33.5 ± 0.9	0.27 ± 0.02	33.0	3.7	4.4	2.5
	SOLA	9	33.0 ± 1.2	0.24 ± 0.02	33.0	3.6	4.3	2.5
	BARY	10	40.0 ± 2.5	0.25 ± 0.03	40.5	3.7	4.5	5.0
	ZAKA	16	41.4 ± 1.7	0.25 ± 0.01	43.0	3.7	4.4	2.5
	ZOBE	13	46.3 ± 2.1	0.22 ± 0.04	45.5	3.8	4.3	17.5
	BATG	12	42.3 ± 1.4	0.27 ± 0.02	43.0	3.7	4.3	7.5
	ABPO	59	43.9 ± 1.2	0.22 ± 0.01	43.0	3.7	4.3	5.0
	MAGY	14	28.9 ± 1.9	0.28 ± 0.04	35.5	3.7	4.3	5.0
	BITY	14	41.6 ± 2.4	0.26 ± 0.02	43.0	3.7	4.3	10.0
	MS19	15	40.8 ± 1.3	0.27 ± 0.01	40.5	3.7	4.4	2.5
	MS23	20	41.6 ± 2.9	0.26 ± 0.02	40.5	3.8	4.5	7.5
	MAHA	14	35.9 ± 0.9	0.28 ± 0.01	35.5	3.7	4.4	5.0
	VOI	8	43.1 ± 2.4	0.22 ± 0.04	40.5	3.7	4.5	4.5
Average ± standard deviation			**39.4 ± 5.0**	**0.25 ± 0.02**	**39.7 ± 4.1**	**3.7 ± 0.0**	**4.4 ± 0.1**	**5.9 ± 4.2**
Androyen-Anosyen (Paleoproterozoic)	MS12	9	39.1 ± 1.4	0.24 ± 0.02	38.0	3.7	4.5	5.0
	BKTA	11	39.5 ± 1.1	0.21 ± 0.02	38.0	3.7	4.5	5.0
	MS10	11	36.2 ± 1.1	0.27 ± 0.02	35.5	3.6	4.5	2.5
	FOMA	24	36.5 ± 1.6	0.25 ± 0.03	35.5	3.7	4.4	5.0
Average ± standard deviation			**37.8 ± 1.7**	**0.24 ± 0.03**	**36.8 ± 1.4**	**3.7 ± 0.1**	**4.5 ± 0.0**	**4.4 ± 1.3**

Table 3. 3 cont'd.

Terrane (Age)	Station name	#Data	*H-κ* stacking		Joint inversion			
			Crustal thickness (km)	*Poisson's ratio*	*Crustal thickness (km)*	*Average crustal Vs (km/s)*	*Average uppermost mantle Vs (km/s)*	*Mafic lower crust thickness (km)*
Ikalamavony (Mesoproterozoic)	VINA	24	36.2 ± 0.8	0.24 ± 0.01	35.5	3.6	4.4	5.0
	MS16	17	41.6 ± 0.8	0.23 ± 0.01	40.5	3.7	4.5	7.5
Average ± standard deviation			**38.9 ± 3.8**	**0.24 ± 0.01**	**38.0 ± 3.5**	**3.7 ± 0.1**	**4.5 ± 0.1**	**6.3 ± 1.8**
Bemarivo (Neoproterozoic)	SBV	20	31.1 ± 1.8	0.25 ± 0.03	30.5	3.6	4.2	2.5
	MKVA	10	31.3 ± 1.2	0.33 ± 0.01	35.5	3.7	4.3	2.5
	LAHA	26	31.1 ± 1.1	0.31 ± 0.01	33.0	3.7	4.3	0.0
Average ± standard deviation			**31.2 ± 0.1**	**0.30 ± 0.04**	**33.0 ± 2.5**	**3.7 ± 0.1**	**4.3 ± 0.1**	**1.7 ± 1.4**
Vohibory (Neoproterozoic)	AMPY	7	25.5 ± 2.4	0.30 ± 0.03	28.0	3.5	4.4	0.0

3.2.4 Comparison of crustal thickness estimates from *H-κ* stacking and the joint-inversion method

The modeling techniques employed in this chapter used different mathematical approaches, but both were based on receiver function analysis to estimate the crustal thickness beneath seismic stations. A plot of crustal thickness estimates from *H-κ* stacking method versus crustal thickness estimates from the joint-inversion method, all from Table 3.2 and Table 3. 3, is shown in Figure 3.4.

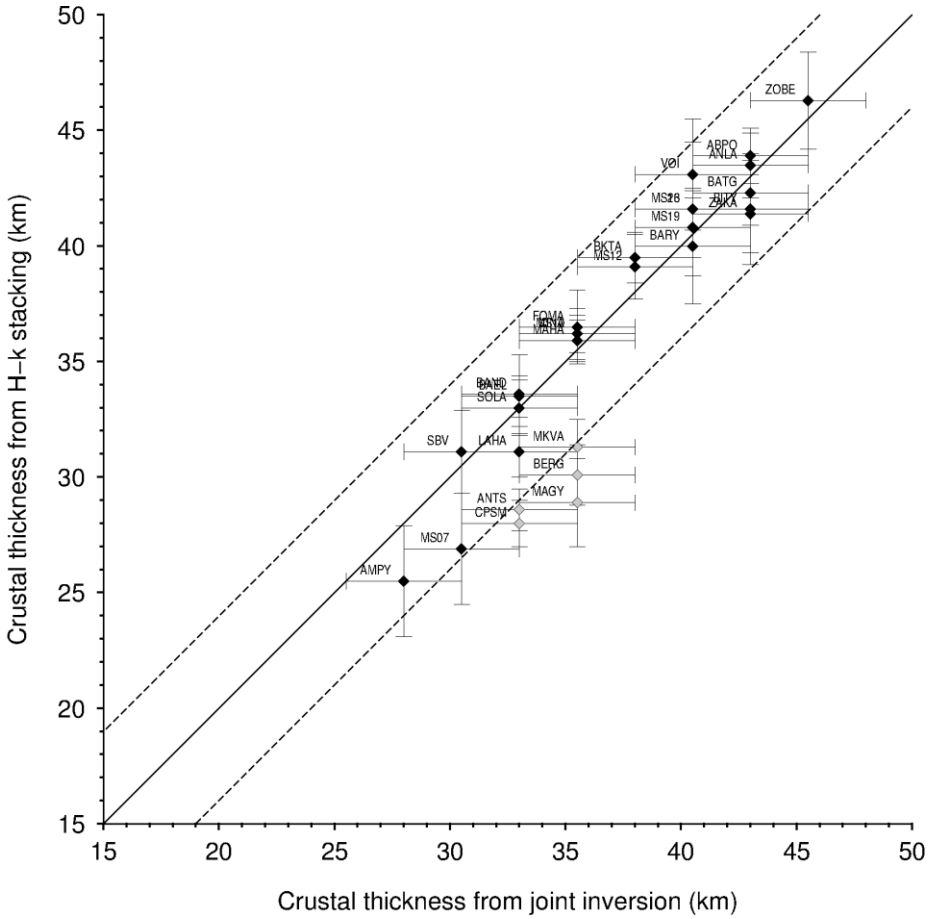

Figure 3.4: Crustal thickness values estimated from *H-κ* stacking versus the joint-inversion method for all stations in which both methods were applied. The solid line indicates a one-to-one correlation between the two estimates and the dashed lines show a difference of ±4 km. Stations represented in gray are outside of the ±4 km zone. Gray lines are error bars.

The vertical alignment of estimates at different depth in Figure 3.4 are due to the fact that the crustal thickness estimates from the joint inversion in this study is a multiple of 2.5 because of the parameterization of the starting model.

A one-to-one correlation between estimates from the *H-κ* stacking method and joint-inversion method is observed, within the reported uncertainties of the estimates, for all but a few stations (generally stations located in the sedimentary basin and along the east coast). Therefore, only estimates from the joint-inversion method were used to summarize the results for Moho depth. Besides, this technique was applied for all stations while the *H-κ* stacking method was only applied for a few of them.

3.2.5 Structure of the sedimentary basin

A total of 13 seismic stations (ANTS, BAND, BANJ, BERG, CPSM, DGOS, KIRI, LONA, MAJA, MMBE, MS04, MS07 and SKRH) are located in the western sedimentary basin of Madagascar. 242 receiver functions were gathered from these stations. *Vs* structures from all stations grouped by geological units are shown in Figure 3.5.

The joint inversion method shows that the thickest basin, about 6-8 km, is found especially along the west coast beneath the Morondava and Mahajanga basins. It thins out rapidly eastwards, around 2 km thick, along the eastern edge of the sedimentary basin. In addition, the thickness of the basin is thicker (~5-8 km) in southern part of the basin, *i.e.* Morondava and Mahajanga basin, compared to the northern part (~4 km), *i.e.* Antsiranana basin.

The average shear-wave velocity of the basin ranges from 2.1 to 2.7 km/s, with an average of 2.3 km/s, in the western regions of the basin, while between 2.4 and 2.8 km/s, with an average of 2.6 km/s, in the eastern regions.

The western sedimentary basin of Madagascar is characterized by a thin crust. It ranges between 18 and 36 km beneath the basin, with an average of 30 ± 5 km. The thinnest crust is found in the Antsiranana basin, ~18 km. It is between 23 and 33 km along the western and central regions of the basin, while between 31 and 36 km beneath its eastern region.

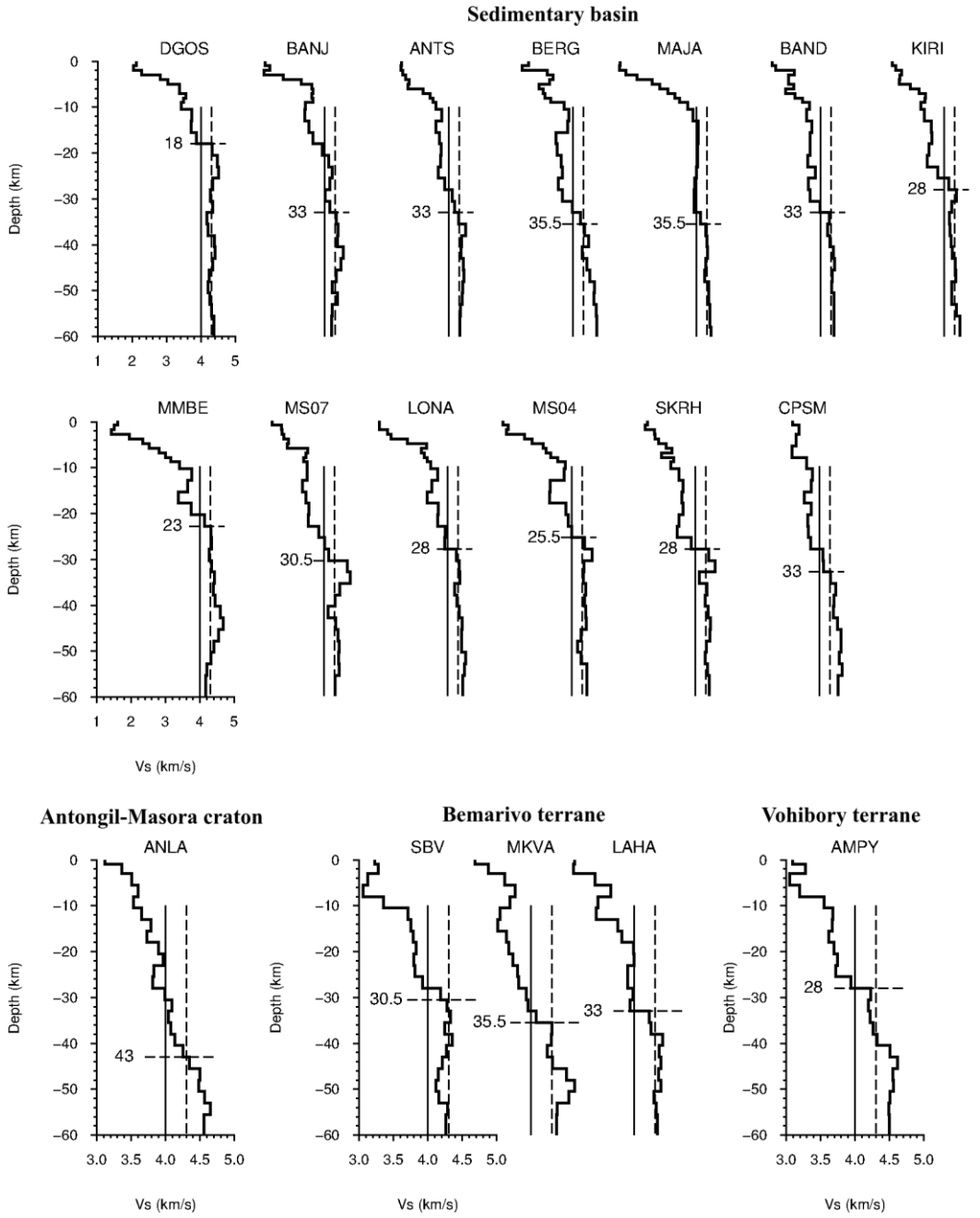

Figure 3.5: The crustal velocity profiles for seismic stations grouped by geological region. Vertical solid and dashed lines indicate shear-wave velocities of 4.0 km/s and 4.3 km/s, respectively. The horizontal dot-dashed lines with associated numbers are the Moho depths (in km).

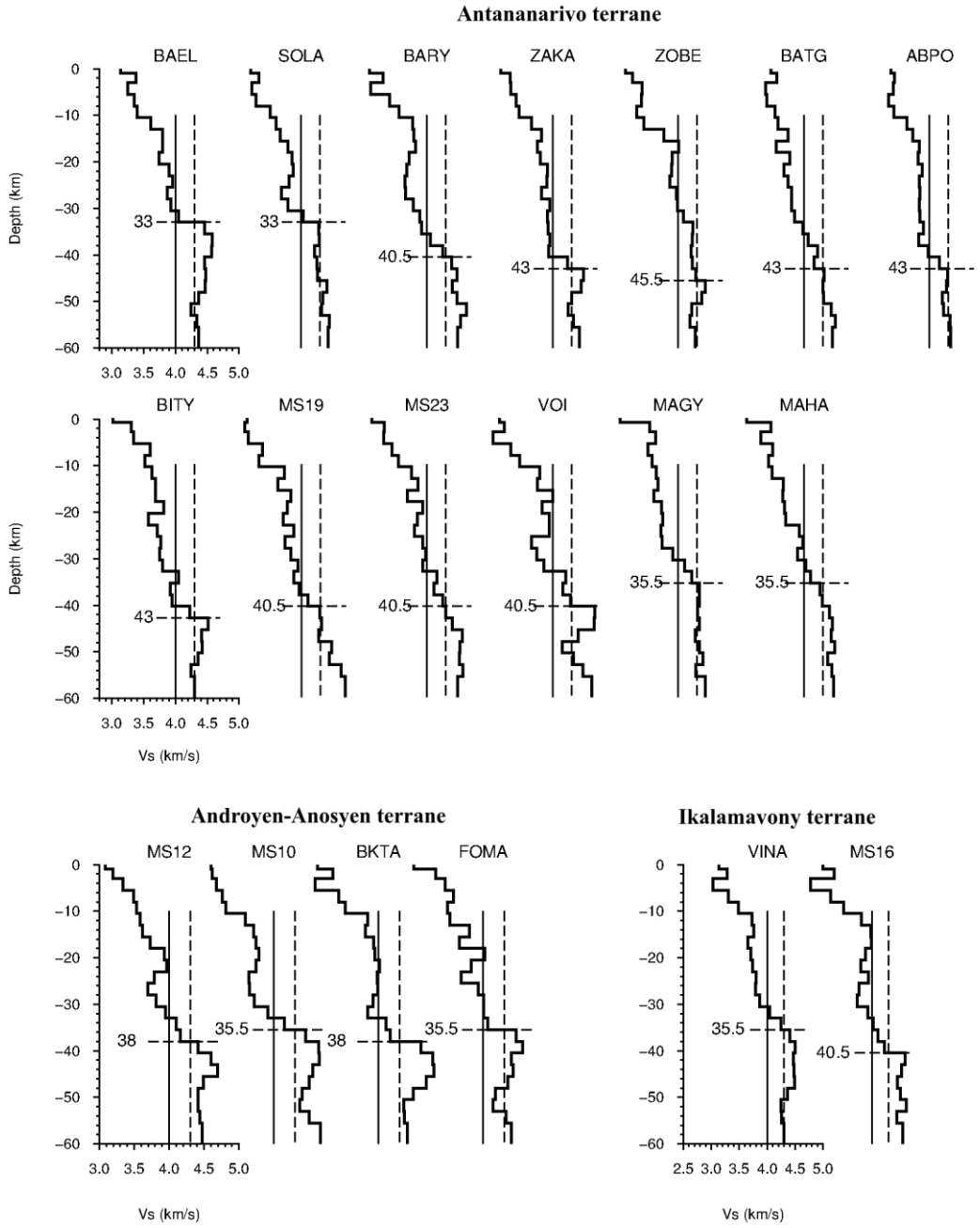

Figure 3.5 cont'd.

The crust beneath the western basin of Madagascar is characterized by slow shear-wave velocities. It ranges from 2.8 to 3.6 km/s, with an average of 3.3 ± 0.2 km/s. The bulk crustal Poisson's ratio, obtained from stations located mostly in the eastern regions of the basin, is somewhat high. It ranges from 0.26 to 0.31, with an average of 0.29 ± 0.02. The mafic layer at the bottom of the crust has a thickness between 3 and 13 km, with an average of 4 ± 3 km. The shear-wave velocity of the uppermost mantle ranges between 4.3 to 4.5 km/s (average 4.4 ± 0.1 km/s) beneath the basin. Slowest Vs (*i.e.* 4.3 km/s) are found beneath the Antsiranana basin (beneath DGOS and BANJ), Mahajanga basin (beneath MAJA station), and the Morondava basin (beneath KIRI and SKRH).

3.2.6 Structure of the Paleoarchean to Mesoarchean terrane

The age of the Antongil-Masora craton is between Paleoarchean to Mesoarchean. Only one seismic station, ANLA, is located in this craton in which a total of 24 receiver functions were obtained.

As expected, the crust beneath this old craton is thick, about 43 km (Figure 3.5) (as the craton is known as a fragment of the Western Dharwar Craton (WDC)). The crust is characterized by an average shear-wave velocity of 3.7 km/s and a bulk Poisson's ratio of 0.24. A 15-km-thick mafic layer is found at the bottom of the crust. The mantle lid beneath the craton is characterized by an average shear-wave velocity of 4.5 km/s.

3.2.7 Structure of the Neoarchean terrane

The Neoarchean terrane in Madagascar is the Antananarivo terrane, which occupies much of the central part of the island. 13 seismic stations (BAEL, SOLA, BARY, ZAKA, ZOBE, BATG, ABPO, MAGY, BITY, MS19, MS23, MAHA and VOI) are located in this terrane, and a total of 228 receiver functions were gathered.

The Antananarivo terrane has the thickest crust in Madagascar. The Moho depth in this terrane ranges between 33 and 46 km, with an average of 40 ± 4 km (Figure 3.5). The crust is thicker (> 40 km) around the central region of the terrane and tends to be thin (33-36 km) along its peripheral edges (the east coast and the northern region).

The crust is characterized by average *Vs* of 3.6-3.8 km/s, with an average of 3.7 ± 0.0 km/s, and a Poisson's ratio between 0.22 and 0.28 (with an average of 0.25 ± 0.02). The mafic layer at the lower crust generally ranges from 3 to 10 km thick. However, a thick mafic layer of ~18 km is observed beneath ZOBE stations. All of these give an average mafic layer thickness of 6 ± 4 km beneath the region. The average *Vs* of the uppermost mantle is between 4.3 and 4.5 km/s, with an average of 4.4 ± 0.1 km/s. The slowest uppermost mantle *Vs* (*i.e.* 4.3 km/s) are found beneath the following stations: SOLA, ZAKA, ZOBE, BATG, ABPO, MAGY, and BITY.

3.2.8 Structure of the Paleoproterozoic terrane

The Androyen-Anosyen terrane composes the Paleoproterozoic terrane of Madagascar and occupies the southern part of the Precambrian shield of the island. Four stations are located in the area, MS12, BKTA, MS10, and FOMA, where 55 receiver functions were obtained.

The thickness of the crust beneath this terrane ranges from 36 to 38 km, with an average of 37 ± 1 km (Figure 3.5). Similarly to the Antananarivo terrane, the central part of this terrane is thicker, ~38 km, compared to the eastern and western regions, ~36 km thick.

The average crustal shear-wave velocity of the terrane ranges between 36-3.7 km/s, with an average of 3.7 km/s. The bulk crustal Poisson's ratio is between 0.21-0.27, with an average of 0.24 ± 0.03. The thickness of the mafic layer in the lower crust is between 3 and 5 km. The mantle lid is characterized by a shear-wave velocity that ranges between 4.4-4.5 km/s.

3.2.9 Structure of the Mesoproterozoic terrane

The Ikalamavony terrane is the Mesoproterozoic terrane of Madagascar. Only two stations (VINA and MS16) are located in this terrane in which 41 receiver functions were obtained.

The two stations in this terrane are located far apart (~425 km) and have more in common with other stations near to them than with each other. VINA is located in the northernmost region of the terrane and the thickness of the crust beneath it is 36 km, which is roughly similar to the thickness found at BAND (~33 km). The station MS16 shows a strong similarity of crustal structure with its neighboring station VOI. The Moho depth beneath MS16 is 41 km (Figure 3.5).

The average crustal *Vs* of the terrane is between 3.6-3.7 km, with 3.7 ± 0.1 km/s of average. The Poisson's ratio of the crust is 0.23-0.24. The mafic lower crust beneath the terrane has a thickness of 5-8 km, with an average of 6 ± 2 km. The terrane is characterized by higher uppermost mantle *Vs* of 4.4-4.5 km/s.

3.2.10 Structure of the Neoproterozoic terrane

The Neoproterozoic terrane of Madagascar is composed of the Bemarivo terrane, in the north, and the Vohibory terrane, in the south. Four seismic stations (SBV, MKVA, LAHA and AMPY) are located in both terranes where 63 receiver functions were gathered.

The thickness of the crust beneath the Bemarivo terrane ranges between 31-36 km, with an average of 33 ± 3 km; while, from a single station, the thickness of the crust beneath the Vohibory terrane is 28 km (Figure 3.5).

The crust beneath the Bemarivo terrane is characterized by: an average *Vs* of 3.6-3.7 km/s (with an average of 3.7 ± 0.1 km/s), and a Poisson's ratio of 0.25-0.33 (with an average of 0.30 ± 0.04). The Vohibory terrane is characterized by a crustal *Vs* of 3.5 km/s and a Poisson's ratio of 0.30. The mafic lower crust is

between 0 and 3 km thick, with an average thickness of 2 ± 1 km, for the Bemarivo terrane and 0 km thick for the Vohibory terrane. Low uppermost mantle *Vs* is observed in the Bemarivo domain: between 4.2-4.3 km/s, with an average of 4.3 ± 0.1 km/s. The slowest *Vs* is found beneath SBV, 4.2 km/s, and LAHA-MKVA, 4.3 km/s. The uppermost mantle *Vs* is 4.4 km/s in the Vohibory terrane.

3.3 Discussion

Results from this study are broadly consistent with previous studies of the crustal structure in Madagascar. The main findings mirror the complex paleogeographic and tectonic history of Madagascar. To summarize, they reflect the northward and eastward opening of the western sedimentary basin and the thinning of the crust in this region. The crust beneath the central high plateau of the island is thicker compared to the peripheral regions. The seismic parameters show little evidence of secular variation in the crustal structure. Slow seismic velocity regions are found beneath the volcanic provinces of Madagascar.

In contrast to my findings, Paul and Eakin (2017) concluded that the crust beneath the central region of Madagascar is thinner compared to the eastern coast based on the analysis of records from the permanent stations ABPO in central Madagascar, and FOMA along the southern coast. The main discrepancy arises for FOMA, where their estimate of 44 km contrasts with my estimate of 36 km. Their high estimate is clearly due to their interpretation of a phase in the receiver functions, at ~6 s, as the direct Ps conversion from the Moho. However, this arrival could also be a multiple of an intra-crustal phase (at ~2 s). Note that Paul & Eakin (2017) only considered teleseismic events with back azimuths between 82° and 93°. However, looking at other backazimuth ranges a clear phase, presumably the Ps wave converted from the Moho discontinuity, is observed at ~4 s. This indicates thinner crust (~36 km) as reported in this study and earlier ones using receiver functions (*e.g.* Rindraharisaona et al., 2013, 2017), which used more than one station along the eastern coast and considered broader back azimuth ranges. In support of this interpretation, crustal thickness estimates from gravimetry imply

that the crust thins towards the eastern coast (Fourno and Roussel, 1994; Rakotondraompiana et al., 1999). Therefore, the balance of evidence points to the shallower Moho inferred in our joint inversion but the presence of the strong phase at 6 s for azimuths between ~60° and 130° points to lateral variability, which is beyond the scope of the current study to investigate further.

3.3.1 The western sedimentary basin: opening and seismic velocity

The basin margin in the western region of Madagascar is mainly due to the N30E, N85E, and N170E fracturing of the crust in the region during the fragmentation of West and East Gondwana between the Permian and Triassic Periods (Figure 1.5; Rajaomazava, 1992). Karoo deposits began to fill the deep grabens associated with the rifting of East Gondwana and Africa during this period of time and made up the western sedimentary basin of Madagascar.

Results in this study reveal that the thickness of the supracrustal strata in the western basin, in the sampled area, varies in two directions: from west to east, 6-8 km to 2 km thick, respectively, and from south to north, 5-8 km to 4 km thick, respectively (Figure 3.2). These findings relate the eastward and northward progressive opening and filling of the basin (Besairie, 1971; Piqué, 1999b) and are somewhat consistent with the direction of the fractures that made up the basin (Rajaomazava, 1992). The bidirectional opening of the basin has been mentioned in previous studies, for example Besairie (1971), Razafimbelo (1987), Coffin and Rabinowitz (1988), and Piqué (1999b), but is not as well described as in this study.

The shear-wave velocity of the eastern region of the basin is relatively faster, ~2.6 km/s, compared to the western region, which is ~2.3 km/s. The Karoo facies are mainly sandstones (see Section 1.3.4) (*e.g.* Besairie, 1967; Boast and Nairn, 1982) and crop out only along the eastern regions of the sedimentary basin (*e.g.* Wescott and Diggens, 1997; 1998). The higher shear-wave velocities (~2.6 km/s) in the eastern region of the basin likely indicate a greater proportion of sandstones and

siltstones, *i.e.* the Karoo facies, in the region (see Table 3.1). The lower shear-wave velocities in the western regions suggest that they are mainly influenced by the younger sediment deposits overlying the Karoo sequence.

3.3.2 Crustal stretching and thinning beneath the western sedimentary basin of Madagascar

Previous studies have located Madagascar adjacent to Tanzania and Kenya (Figure 1.1) (*e.g.* Du Toit, 1937; Norton and Sclater, 1979; Rabinowitz et al., 1983; Kusky et al., 2003) during Gondwana time. Therefore, it is reasonable to assume that, before the Mesozoic rifting events that led to the dislocation of Madagascar from Africa (*ca.* 160 Ma ago), the thickness of the crust beneath the western sedimentary basin of Madagascar was similar to the thickness of the crust in eastern Africa and the unrifted Precambrian crust of Madagascar to the east.

Previous studies conducted in eastern Africa have revealed that the thickness of the crust across the region has an average of 38-39 ± 3 km (Tugume et al., 2012, 2013; Kachingwe et al., 2015). This is comparable to the unrifted Precambrian crust of Madagascar found in this study, which has an average thickness of 38 ± 5 km. This suggests that the crust beneath the western sedimentary basin of Madagascar was stretched and thinned during the rifting from Africa. The continental-drift has thinned the crust by: ~20 km in the northernmost part of the island (*i.e.* 38 km vs. 18 km) and around ~12 km in the southwestern coast (*i.e.* 38 km vs. 23-26 km).

The average shear-wave velocities of the supracrustal strata in the western basin are slow. However, the shear-wave velocity structures of the lower crust beneath the basin stations (Figure 3.5) are similar to those of the stations located on the Precambrian crust stations. This suggests that the slow average crustal shear-wave velocities are due the contribution of the slow shear-wave velocities of the supracrustal basin sediments averaged together with the shear-wave velocity of the underlying Precambrian basement rocks.

3.3.3 Crustal thinning in the eastern coast of Madagascar

With the exception of the ANLA station, stations located along the east coast of Madagascar (SBV, MKVA, LAHA, ANLA, MAGY, MAHA and FOMA) show similar crustal thicknesses with an average of ~34 km. Compared to the thickness of crust of the central region (generally > 40 km), the crust beneath the eastern coast of Madagascar is thinner.

The sudden break-up of Madagascar/India block was linked with the passage of the block over the Marion hotspot about 95-85 Ma ago (Gnos et al., 1997). Hotspot reconstruction has located the Marion hotspot beneath the Madagascar/India block at this period of time (Raval and Veeraswamy, 2003). This likely interacted with the overriding plate and subsequently led to the separation of India and Madagascar (Storey et al., 1995; Torsvik et al., 1998; Raval and Veeraswamy, 2003). The heat associated with the Marion hotspot likely weakened and eroded the lithosphere beneath the eastern coast of Madagascar and resulted in the uplifting of the lithosphere. Therefore, the thinning of the crust along this region, about 5 km, can be explained as the result of the uplifting and thinning of the lithosphere when overriding the Marion hotspot.

In addition, the crustal thinning along the eastern coast of Madagascar reveals the different ways how the break-up in the western and eastern regions of Madagascar was accommodated. The crust in the western basin of the island was stretched and thinned, up to 20 km, due to the long and slow rifting processes that led to the separation of Madagascar from Africa; while the passage over the Marion hotspot caused the sudden separation from India, which likely thinned the crust for only about 5 km.

3.3.4 Evidence of little secular variation of the Precambrian crust

Several studies have investigated the relationship between crustal structure and age. For example, Durrheim and Mooney (1991; 1994) proposed that the Archean

crust is thinner compared to the Proterozoic one, ~35 km thick versus ~45 km thick, respectively. They interpreted the secular variation as the result of variation in composition of the upper mantle and thermal variation of the Earth's mantle during the Precambrian era. Conversely, other studies did not find any significant difference for both crusts (*e.g.* Rudnick and Fountain (1995), Zandt and Ammon (1995), and Tugume et al. (2012; 2013). Durrheim and Mooney (1991; 1994) suggested that the formation of the crust was above a hotter mantle in the Archean, while it was above a fertile mantle in the Proterozoic. Consequently, partial melting that usually associated with the fertile mantle produced mafic compounds which are likely underplating and thickened the Proterozoic crust. The mafic materials are not present in the Archean crust except if it had undergone post-Archean magmatic manifestations (Durrheim and Mooney, 1991; 1994).

Findings from this study show that the Archean crust of Madagascar has an average thickness of 40 ± 4 km (from 14 stations) while the Proterozoic crust is characterized by an average crustal thickness of 35 ± 4 km (from 10 stations). Archean and Proterozoic crusts are, respectively, characterized by Poisson's ratio of 0.25 ± 0.02 and 0.26 ± 0.04, average crustal shear-wave velocities of 3.7 ± 0.1 for both, mafic lower crust of 7 km and 4 km, and a similar uppermost mantle shear-wave velocity of 4.4 ± 0.1 km/s.

These show that the Archean crust is slightly thicker than the Proterozoic crust for Madagascar, which differs from the observation of Durrheim and Mooney (1991; 1994) but consistent with the results obtained in several regions of Africa (*e.g.* Tugume et al., 2012; 2013; Kachingwe et al., 2015). However, the seismic properties of both crusts are comparable.

There is little evidence of secular variation in the Precambrian crustal structure of Madagascar. This suggests that the pattern of secular variation, if there was any, may be erased by (1) the tectonic processes associated with the Mesozoic drifting of the island, or (2) by the Mesozoic and Cenozoic magmatic events in Madagascar.

3.3.5 Crustal lithologies of Madagascar

The variation in the crustal Poisson's ratio is a representative of the change in silicic compositions. Laboratory experiments (*e.g.* Christensen, 1996) have shown that granitic rocks with felsic composition have a Poisson's ratio of 0.24; intermediate lithologies, for example diorites, have a Poisson's ratio of 0.27; and mafic lithologies, for example gabbros, have Poisson's ratio of 0.30. Previous studies have suggested that Precambrian terranes are generally dominated by felsic to intermediate lithologies, with Poisson's ratio ranging between 0.25 and 0.27 for continental crusts.

In this study, the Precambrian terranes of Madagascar have a Poisson's ratio that ranges from 0.20 to 0.31, with an average of 0.26 ± 0.03. Overall, the crust of these terranes is representative of predominantly felsic to intermediate compositions.

However, the crust in the east coast of Madagascar is more mafic, with higher Poisson's ratio of 0.29 ± 0.04. It can be explained as the result of the syntectonic emplacement of rift basalts accompanying the separation of India and Madagascar (Storey et al., 1995), imparting a slightly more mafic composition in the crust. This phenomenon has been found, from other studies, in large continental rifts (Stein et al., 2016). The presence of a mafic layer with an average thickness of 6 ± 3 km may alternatively be considered.

Higher Poisson's ratios of 0.29 ± 0.02 are also observed along the eastern regions of the sedimentary basin. It can also be explained by the emplacement of rift basalts, with mafic composition in the crust, during the rifting of East Gondwana from Africa. An alternative explanation is that the higher Poisson's ratio is the contribution of the sedimentary basin in the uppermost crust.

3.3.6 Airy model of isostatic equilibrium

Under the Airy model of isostasy, the rock density of the crust is assumed to be equivalent, while the crustal blocks are characterized by varying thicknesses. In this model, higher mountains are believed to be compensated by deep roots to maintain the equilibrium of land masses. Generally, the variation in Moho depth should be approximately seven times the change in relief at the Earth's surface (*e.g.* Kearey et al., 2009).

A plot of the elevation versus the Moho depth, along an N-S profile across the length of Madagascar, is shown in Figure 3.6. Moho depths estimated from stations that are within a distance range between 0 and 60 km from the profile are plotted in this Figure. A very strong correlation between topography and crustal thickness is observed along the profile especially in the southern and central regions of Madagascar. An increase from 33 km to 46 km is observed for the crustal thickness, compared to a variation in elevation from 0 km to 1.6 km at the surface. This corresponds to a change in Moho depth about eight times greater than the corresponding change in the surface relief, suggesting that it can be fairly well explained by an Airy model of isostatic equilibrium.

However, this correlation breaks down in the northern part of the island, where elevations range from 1 to 2 km but crustal thicknesses are less than 35 km. Given that Madagascar has not undergone any tectonic activity in the past 85 Myr, some other mechanism is required to maintain this high elevation. One possibility is that the northern region is dynamically supported by the same thermal anomalies that have been the source of late Cenozoic volcanism in the north. In general, the pattern of isostatic equilibrium suggested by Figure 3.6 is superimposed upon a broad signature of uplift for the island. The average crustal thickness across all stations is 35 km while the average elevation of the stations is 496 m. This elevation is unusually high for the slightly thinner-than-average crustal thickness, suggesting that an additional factor is needed to explain the high elevations.

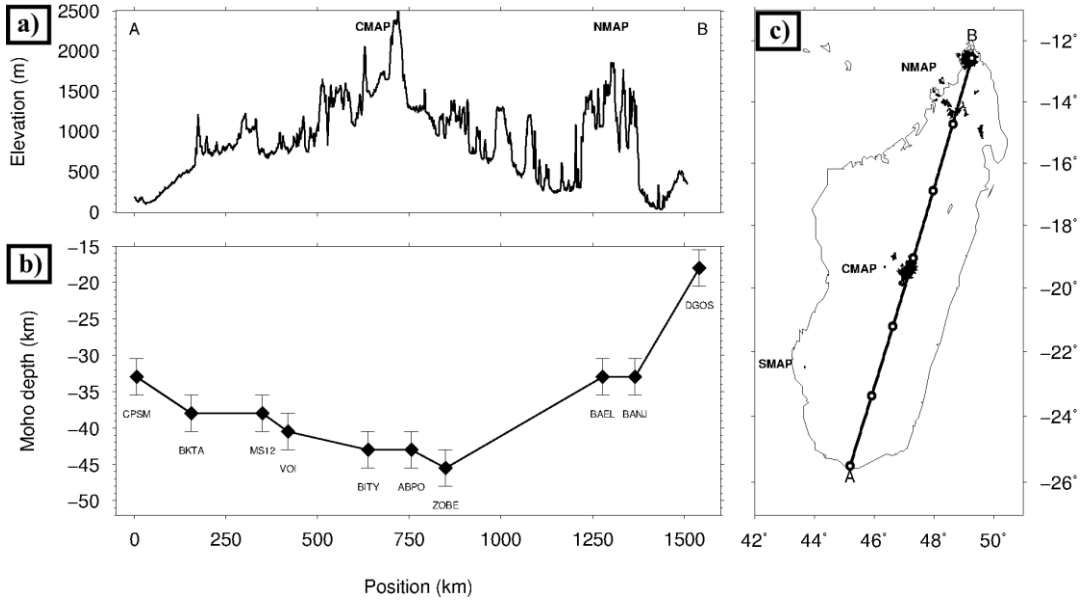

Figure 3.6: (a) Elevation of Madagascar (Amante and Eakins, 2009) along the profile A-B within the corresponding location of the Cenozoic volcanic provinces NMAP and CMAP, as shown in the figure on the right (in black). (b) Crustal thickness values for seismic stations along the same profile, along with accompanying error bars. White circles along the profile, in (c), are 250 km intervals from the 0 km position at A.

It is likely that the three large regions of seismically slow velocities in the upper mantle beneath the northern, central, and southwestern regions of Madagascar, imaged by Pratt et al. (2017), correspond to thermal anomalies that provide the buoyancy needed to maintain these high elevations. This is supported by observations of the erosion rates of river valleys and lavakas (erosional gullies), which suggest that Madagascar has been experiencing active uplift for at least the past 15 Myr (Cox et al. 2010; Roberts et al. 2012).

3.3.7 Evidence of thermal anomalies in the uppermost mantle

The average shear-wave velocity of the uppermost mantle beneath Madagascar ranges from 4.2 to 4.5 km/s, with an overall average of 4.4 ± 0.1 km/s (see Table 3.2 and Table 3. 3). Slow shear-wave velocities, between 4.2-4.3 km/s, are observed in particular areas: in the northern part (beneath seismic stations DGOS, BANJ, SOLA, SBV, and LAHA), in the central part (beneath seismic stations

ZAKA, ZOBE, BATG, ABPO, and BITY), in the eastern part (beneath seismic stations MAGY and FOMA), and in the western and southwestern part (beneath seismic stations MAJA, KIRI, BAND, and SKRH) (Figure 3.3: Contour maps showing (a) the crustal thickness, (b) the average crustal shear-wave velocity, and (c) the average uppermost mantle shear-wave velocity beneath Madagascar).

The slow uppermost mantle shear-wave velocities, 4.2-4.3 km/s, coincide with the three Cenozoic volcanic provinces of Madagascar (NMAP, CMAP, and SMAP) that have been found by Pratt et al. (2017). This is obvious, as the same surface wave data are used for the seismic tomography by Pratt et al. (2017) and this study for the joint inversion. They are interpreted to be the result of hot mantle-materials that gave rise to the Cenozoic volcanism.

3.4 Conclusion

The crustal and uppermost mantle seismic structure beneath Madagascar has been investigated in this study using 37 temporary and permanent broadband stations. Two techniques based on receiver functions modeling were used to estimate the thickness of the crust and the bulk crustal *Vp/Vs* ratio, from which the Poisson's ratio was obtained; and a joint inversion with surface wave data to obtain the velocity structure of the crust and uppermost mantle, and from it infer the thickness of the supracrustal sedimentary rocks and crust, the average shear-wave velocity of the curst and mantle, and the thickness mafic lower crust.

Results show a bidirectional thinning of the sedimentary basin in the western region of Madagascar (for the sampled area): from 5-8 km to 4 km, northward, and from 6-8 km to 2 km, eastward, reflecting the eastwardly and northwardly progressive opening and filling of the sedimentary basin.

The Mesozoic rifting from Africa thinned the crust beneath the western sedimentary basin of Madagascar by about ~12-20 km if compared to the unrifted crust in eastern Africa and in Madagascar.

A slight thinning of the crust is also found along the eastern coast of the island, between 31 and 36 km, compared to the thickness of the crust in the inland. This may have been caused by the lithosphere erosion that resulted in crustal uplift when Madagascar moved over the Marion hotspot in *ca.* 95-85 Ma ago and India broke away.

The crystalline crust of Madagascar is representative of predominantly felsic to intermediate compositions.

There is a little evidence of secular variation in the Precambrian crust in Madagascar. The Archean terranes are characterized by an average 40-km-thick crust, a Poisson's ratio of 0.25, an average crustal shear-wave velocity of 3.7 km/s, and an average thickness of mafic lower crust of 7 km; while the Proterozoic terranes have an average crustal thickness of 35 km, a Poisson's ratio of 0.26, an average crustal shear-wave velocity of 3.7 km/s, and an average thickness of mafic lower crust of 4 km.

A good correlation is observed between station elevation and crustal thickness across Madagascar, with about a 1 km change in elevation at the surface of Madagascar corresponding to a change of 8 km in Moho topography. However, surface elevations are anomalously high compared to crustal thicknesses, especially in the northern region, suggesting a source of dynamic topography that might be provided by mantle upwelling flows related to an upper mantle thermal anomaly. That would also explain the slow uppermost mantle shear-wave velocities of 4.2-4.3 km/s and episodes of Cenozoic volcanic activity in Madagascar.

Chapter 4

Uppermost mantle velocity and anisotropy beneath Madagascar from *Pn* tomography

4.1 Introduction

Volcanic activities in Madagascar can be grouped into two groups based on their age and lava compositions: the Cretaceous manifestations, which are mainly composed of tholeiitic basaltic lavas; and the Cenozoic manifestations, which are generally alkali basalt emissions (Besairie, 1973; Norton and Sclater, 1979).

The Cretaceous eruptions (*ca.* 95-85 Ma) are associated with the migration of the Madagascar/India block over the Marion hotspot, which subsequently broke up the overriding lithosphere and emitted large volumes of crustal-derived dacite/alkali rhyolite and mantle-derived tholeiitic basalt magmas (Storey et al., 1995; Torsvik et al., 1998; Raval and Veeraswamy, 2003). They are preserved all along the periphery of Madagascar: the eastern coast, the western sedimentary basin, and in the south along the Volcan de l'Androy (*e.g.* Mahoney et al., 1991; Rasamimanana, 1996; Storey et al, 1995).

Even though Madagascar was tectonically stable for the past 85 Myr and remote from tectonic plate boundaries, including the Indian mid-oceanic ridges in the east and the East African Rift (EAR) in the west, volcanic eruptions anomalously occurred in several parts of the island during the Cenozoic (*ca.* 50-0.5 Ma). The Cenozoic eruptions are not as voluminous as the Cretaceous manifestations and are mainly composed by alkali basalt magmas (Emerick and Duncan, 1982, 1983; Nougier et al., 1986; Rasaminanana, 1996; Collins, 2000; Bardintzeff et al., 2010). They are located principally in three regions: in the northern part of the island (the NMAP), in the central high plateau (the CMAP), and a small province in the southwestern region (the SMAP). The origin of the Cenozoic volcanism is controversial (see Section 1.3.6).

These phenomena make Madagascar a good candidate to investigate the origin of intraplate volcanism and the strain history of the mantle produced by rifting processes or flow of mantle materials. The seismic tomographic imaging is a powerful technique to investigate the lateral variation (*i.e. 2D*) or both lateral and vertical variations (*i.e. 3D*) of seismic properties (such as *P*-wave velocities, *S*-wave velocities, crustal attenuation…).

In this study, the uppermost mantle beneath Madagascar is investigated using *Pn* travel-time tomography in order to map out the lateral variation of *Pn*-wave velocity and the magnitude and direction of fast-polarization directions of *Pn* anisotropy in the uppermost mantle (*i.e.* the mantle lid). This is enabled by the existence of a dense seismic network in which 48 seismic stations were used. Findings from this part of the thesis, generally, shed new light on the origin of the intraplate Cenozoic volcanism of Madagascar, in particular the location of low-seismic-velocity zones and the direction of strains associated with it.

This chapter presents the results from the *Pn* tomography, followed by the discussion and conclusion of the findings. The material in this chapter is summarized and will be submitted for publication in a peer-reviewed journal in the manuscript (see Appendix E): **Andriampenomanana, F., Nyblade, A.A., Wysession, M.E., Durrheim, R.J., Rambolamanana, G., Tilmann, F., Aleqabi, G., Shore, P.J., Pratt, M.J., and Rakotondraibe, T. Uppermost mantle velocity and anisotropy beneath Madagascar from *Pn* tomography, to be submitted.**

4.2 Results

Results, including the lateral variations of *Pn*-wave velocities and magnitude and direction of *Pn* anisotropy fast-polarization directions, were inferred from 4541 *Pn* travel-times, obtained from 424 seismic events and 44 seismic stations.

4.2.1 *2D*-isotropic inversion

The effect of including the anisotropy in the inversion was assessed by turning off the anisotropy part in it. It means that an isotropic inversion is performed and that the anisotropic terms in Equation (2.32) were omitted in the inversion, but otherwise the same travel-time data and inversion parameters described in Section 2.7.5 were used.

After running the inversion for a number of iterations, the RMS error of the isotropic inversion was 1.00 s. A map presenting the lateral variation of the uppermost mantle isotropic *Pn*-velocity variations is shown in Figure 4.1.

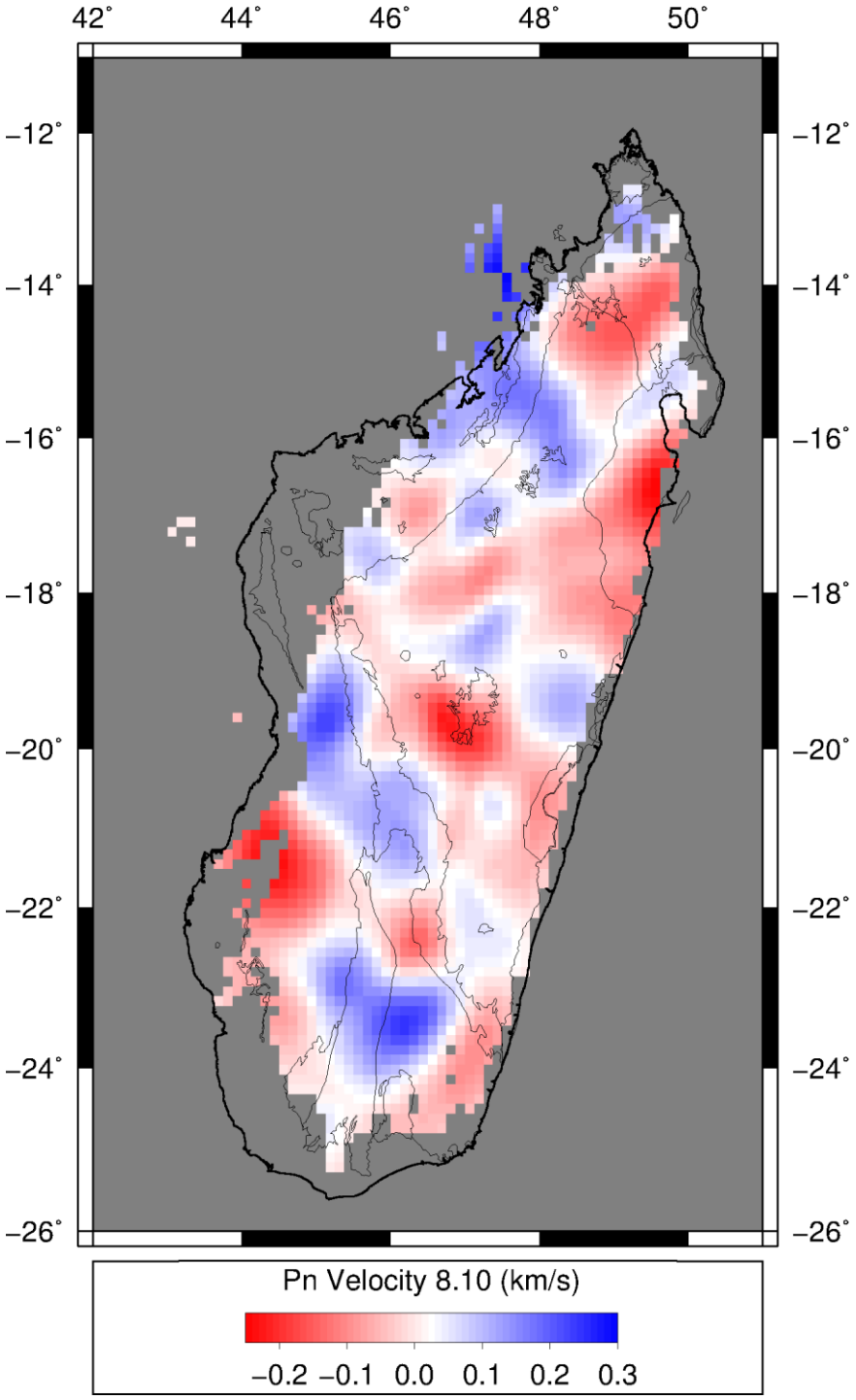

Figure 4.1: Uppermost mantle isotropic *Pn*-velocity variations, inverted without anisotropy. The velocity anomaly is nearly exactly the same as the inversion with anisotropy, with slight difference in magnitude. The average velocity is 8.10 km/s, and red and blue colors are high and low velocities, respectively. Also plotted are the major geological unit boundaries in Figure 1.4.

4.2.2 *2D*-anisotropic inversion

This time, the anisotropic terms in Equation (2.32) is included in the inversion. Consequently, both lateral variations of *Pn*-wave velocities and magnitude and direction of *Pn* anisotropy fast-polarization were obtained in the tomographic inversion.

As described in the Section 2.7.5, the damping parameters of 500 and 600 were used for the velocity and anisotropy for the inversion, respectively. The tomographic inversion was run for a number of iterations, which gave a RMS error of 0.60 s for the inversion.

Lateral variations of *Pn*-wave velocities and magnitude and direction of *Pn* anisotropy fast-polarization are shown in Figure 4.2 and Figure 4.3. In addition, location of thermal springs and shear-wave splitting results shown in these images will be used in the discussion sections.

Both isotropic and anisotropic inversions broadly yielded the same velocity anomaly patterns with slight differences in magnitudes. Therefore, the velocity map from the anisotropic inversion is considered for further interpretation as the anisotropy map was derived from it.

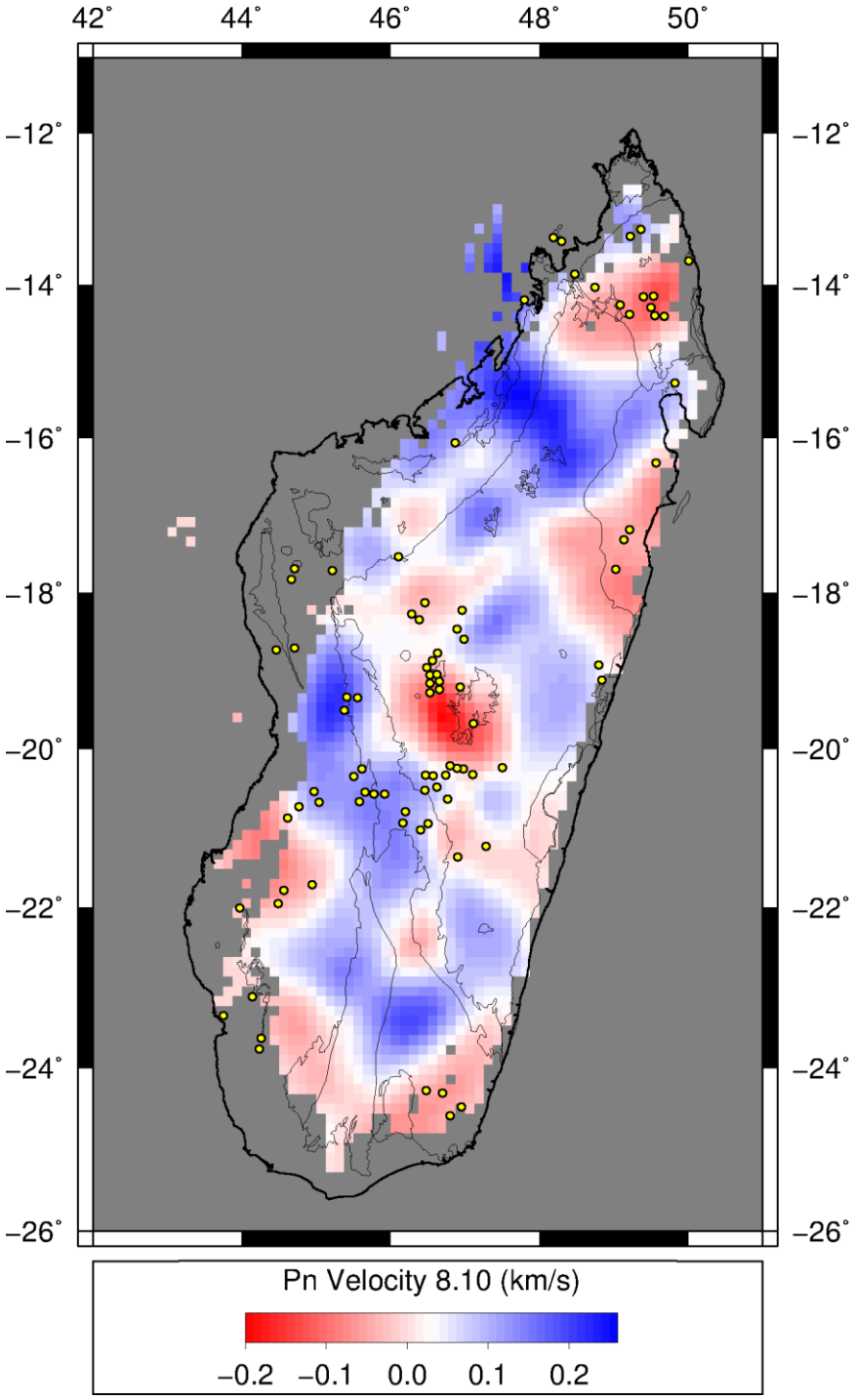

Figure 4.2: Uppermost mantle *Pn*-velocity variations, accounting for anisotropy. The isotropic velocity anomaly is nearly exactly the same, with only a slight difference in magnitude. The average velocity is 8.10 km/s, and red and blue colors show high and low velocity anomalies, respectively. Also plotted are the major geological unit boundaries from Figure 1.4 and and thermal spring locations (yellow dots) (Besairie, 1959).

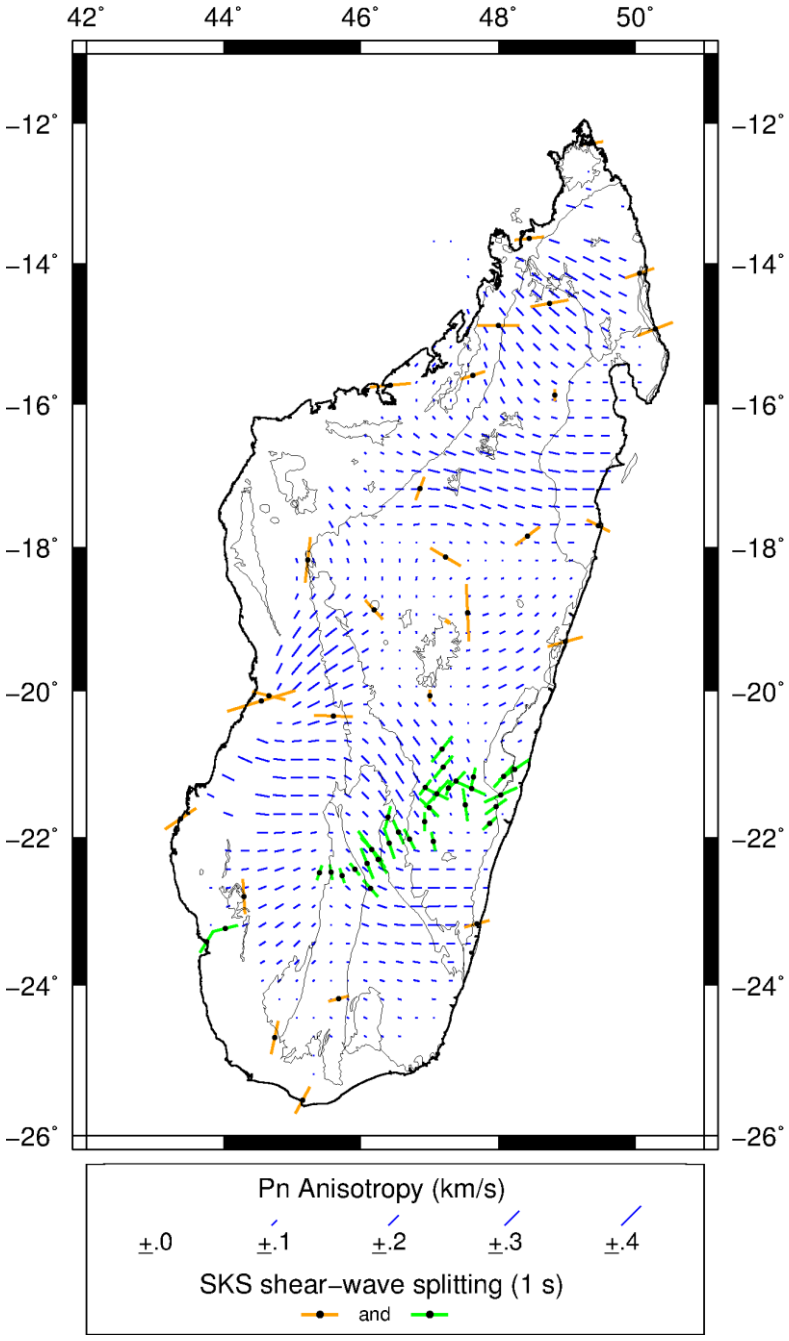

Figure 4.3: *Pn*-velocity anisotropy of the uppermost mantle obtained from *Pn* travel-time tomography. Blue bars indicate the fast *Pn*-anisotropy direction, and the length of the bars is proportional to the anisotropy magnitude. Orange and green bars are *SKS* shear-wave splitting measurements from the MACOMO and SELASOMA stations, respectively. The strike and length of the lines indicate the fast-velocity directions and the amount of splitting, respectively. Splitting measurements are obtained from Ramirez et al. (2015) and Reiss et al. (2016). Also plotted are the major geological unit boundaries shown in Figure 1.4.

4.2.3 Low-*Pn*-velocity regions in the uppermost mantle

Worldwide, the average for *Pn* velocities of continental lithosphere is known to be about 8.10 km/s (*e.g.* Mooney and Braille, 1989). In this study, the average *Pn* velocity beneath Madagascar is found to be 8.10 km/s. The *Pn* velocity varies between -0.20 km/s and +0.25 km/s from the average. Regions with *Pn* velocity slower than the global average were observed from the tomographic inversion. A cross-section showing the fluctuation of the *Pn*-velocity vis-à-vis to the average value (8.10 km/s) along an N-S profile across the length of Madagascar is presented in Figure 4.4. This profile cuts across the NMAP and CMAP volcanic provinces.

Several regions characterized by slow *Pn* velocity are observed in the uppermost mantle beneath Madagascar (Figure 4.2).

A low-*Pn*-velocity zone is observed in the uppermost mantle beneath the northernmost regions of the island, roughly between longitudes 48°E and 50°E and north of latitude 15°S. Its extension towards the north, west, and east is not well resolved due to poor ray path coverage in the region. The low-velocity-zone is directly beneath the known alkaline volcanic province in the region, the NMAP.

A prominent low-*Pn*-velocity zone is also observed in the uppermost mantle beneath the central part of Madagascar, approximately between latitudes 19-22°S and longitudes 46-48°E. The low-velocity zone lies beneath the CMAP volcanic province in the central part of the island. The region apparently extends southeastwards beneath the Masora craton.

A weak low-*Pn*-velocity zone is observed in the uppermost mantle beneath the southwestern parts of Madagascar, roughly west of the longitude 45°S and south of the latitude 20.5°S. The region is located beneath the southern part of the Morondava basin and possibly underlies the SMAP, although its extension westward is not well resolved due to poor coverage.

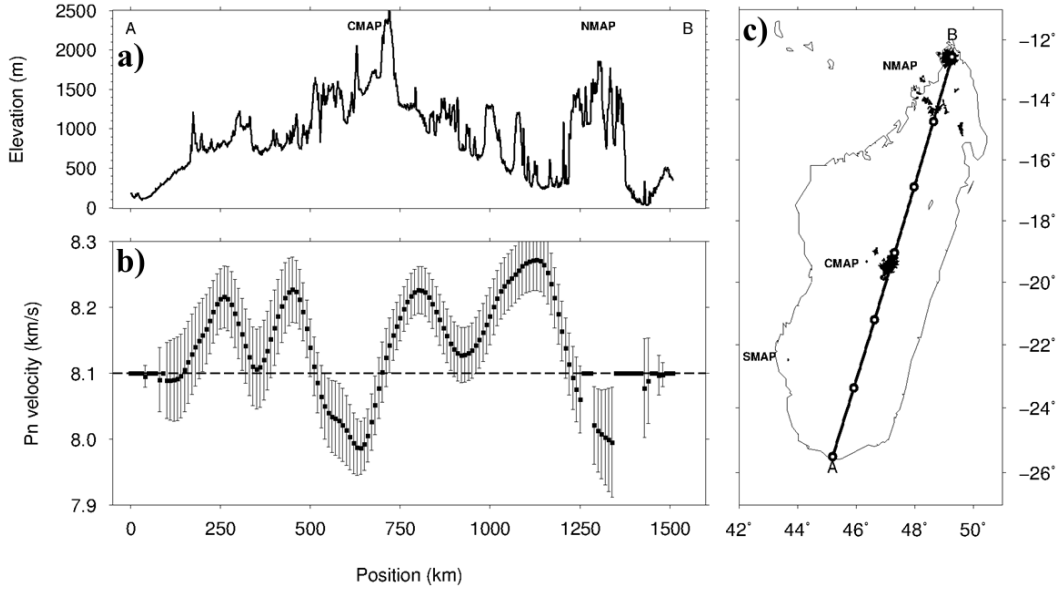

Figure 4.4: (a) Elevation of Madagascar (Amante and Eakins, 2009) along the profile A-B within the corresponding location of the NMAP and CMAP, as shown in the figure (c) (in black). (b) *Pn* velocity values along the same profile, along with accompanying error bars. White circles along the profile are 250 km intervals from the 0 km position at A. Dashed line is the global average *Pn* velocity (8.1 km/s). A *Pn* velocity of 8.1 km/s is assigned to un-sampled areas along the profile (*e.g.* around positions 0 km and between 1250-1500 km). The lowest *Pn* velocities are observed beneath NMAP and CMAP.

Lastly, a low-velocity zone is observed beneath the Antongil craton, between latitudes 17-19°S and longitudes 48-50°S. The eastward or northward limits of the low-velocity zone is not clearly resolved.

4.2.4 *Pn* anisotropy fast-polarization directions

The *Pn*-anisotropy perturbation ranges from 0 to 0.23 km/s (~3%) all over Madagascar. Two groups of *Pn* anisotropy fast-polarization direction are principally found from the anisotropic inversion: a NW-SE to E-W direction and a NE-SW direction (Figure 4.3).

A broad NW-SE direction of *Pn* anisotropy fast-polarization, with a maximum magnitude of 2.4%, is observed in the uppermost mantle beneath the northern regions of Madagascar underlying the NMAP, the northernmost part of the

Antananarivo terrane, the Bemarivo terrane, and the Antsiranana basin. The anisotropy direction rotates roughly to E-W in the south, particularly around the Antongil craton, and has a maximum magnitude of 2.5%.

Similarly to the anisotropic parameters in the northern regions, NW-SE directions with a maximum magnitude of 2.4% of *Pn* anisotropy fast-polarization are also observed in the uppermost mantle beneath the south-central part of Madagascar, underlying the CMAP, the southern part of the Antananarivo terrane, the central part of the Ikalamavony terrane, the Anosyen terrane, and the Ranotsara shear zone. The *Pn* anisotropy direction rotates also to E-W in the south, especially along the southeast coast.

The remaining part of the sampled area is characterized by *Pn* anisotropy with the fast-polarization in a NE-SW direction with a maximum magnitude of 2.8%. These anisotropy parameters are observed mainly in the eastern regions of the Antananarivo terrane and the Morondava basin.

4.2.5 Station static delays

The static delay reflects the structure of subsurface underlying the region. Positive station delays are representative of slower and/or thicker crust while negative delays present thinner and/or faster crust. The static delay variation of stations spanned ~0.9 s, from -0.52 s to +0.33 s, with a RMS station delay of 0.2 s. They are summarized in Table 4.1 and shown in Figure 4.5.

Table 4.1: Static station, number of event recorded per station, delay times, and errors.

Station	#Count	Delay(s)	Error(s)
ABPO	162	0.16	0.01
AMPY	46	-0.15	0.01
ANLA	144	0.23	0.00
ANTS	175	0.39	-0.02
BAEL	84	0.06	-0.02
BAND	166	0.21	0.02
BANJ	34	0.2	-0.05
BARY	165	0.13	0.01
BATG	137	0.02	0.00
BERG	182	0.17	0.01
BITY	52	-0.21	0.01
BKTA	57	0.01	0.02
CPSM	32	0.09	0.01
DGOS	39	-0.01	-0.01
FOMA	41	0.1	0.03
JNOV	38	-0.18	-0.01
KIRI	188	-0.3	-0.01
LAHA	141	-0.14	-0.01
LONA	84	-0.02	-0.02
MAGY	68	0.02	0.00
MAHA	111	-0.01	-0.02
MAJA	198	0.21	0.01
MAYO	29	-0.46	0.02
MKVA	59	-0.44	0.00
MMBE	35	0.16	-0.04
MS04	62	0.02	-0.03
MS07	107	-0.02	-0.01
MS10	142	0.08	0.00
MS12	144	-0.18	0.02
MS16	259	0.1	0.01
MS19	211	-0.19	0.00
MS23	237	0.19	0.00
RUM1	73	-0.02	-0.02
RUM2	99	0.03	-0.01
RUM3	39	-0.05	-0.01
RUM4	49	0.14	0.00
RUM5	43	0.29	0.02
SBVA	91	-0.4	0.04
SOLA	23	-0.24	0.02
TANS	32	-0.25	0.01
VINA	156	0.01	0.01
VOIA	257	0.16	0.00
ZAKA	197	0.27	0.01
ZOBE	100	-0.22	0.03

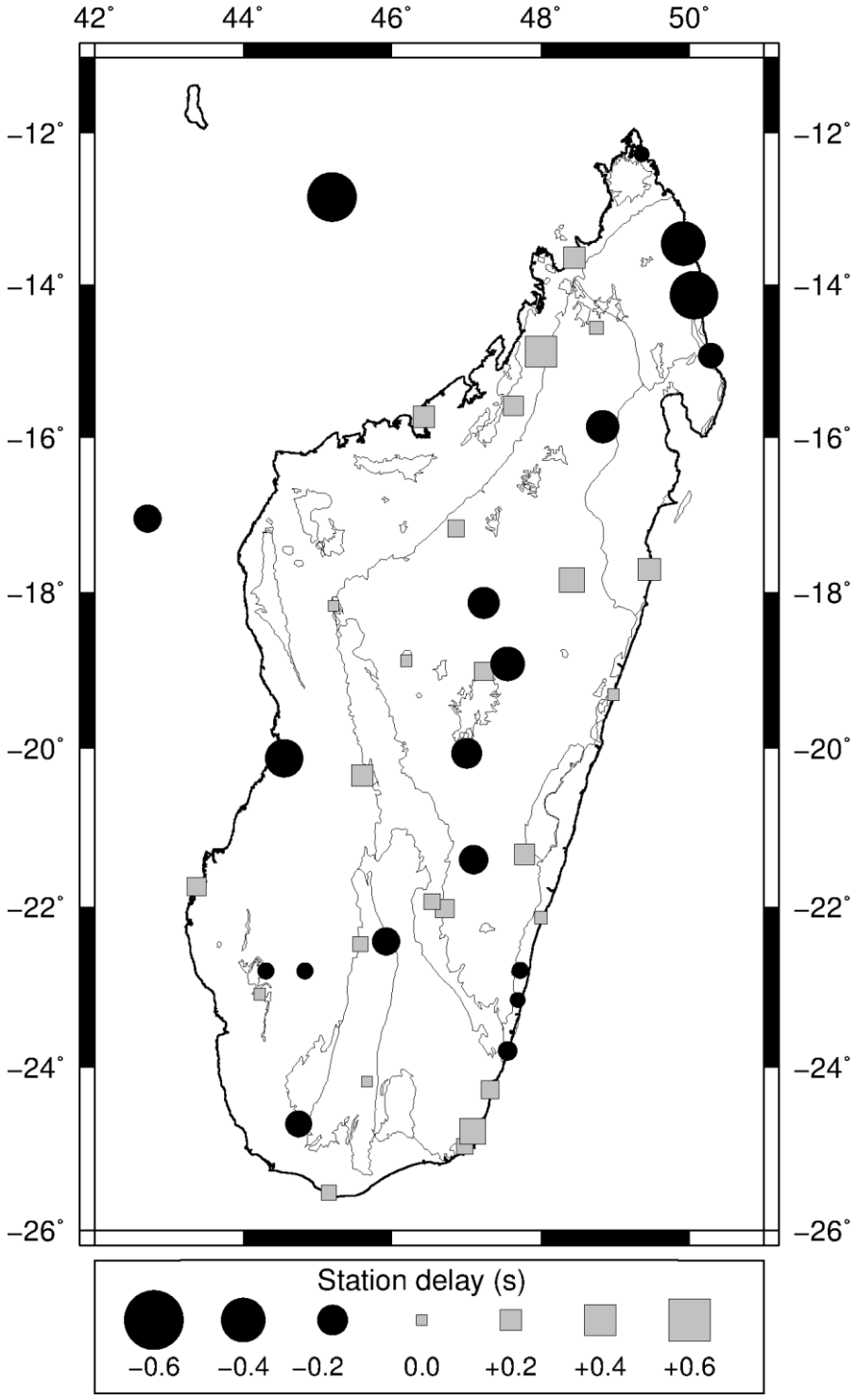

Figure 4.5: Station static delay times obtained from the inversion. Black circles and gray squares denote negative and positive delays. Also plotted are the major geological unit boundaries shown in Figure 1.4.

4.3 Discussion

Findings from this study reflect generally the heterogeneous geology of Madagascar. Lateral variations of *Pn* velocity and anisotropy in the uppermost mantle show correlation with the surface geology. To summarize, low-*Pn*-velocity zones, which correspond to upwelling of hot mantle materials, are observed in the uppermost mantle beneath Madagascar directly beneath the Cenozoic volcanic provinces. Compared to previous studies, general features of the low-velocity zones are comparable with those inferred from surface wave tomography (Pratt *et al.* 2017). Also, directions of *Pn* anisotropy fast-polarization of the uppermost mantle correlate with the measurement of upper mantle anisotropy derived from *SKS* shear-wave splitting technique (Reiss et *al.* 2016; Ramirez *et al.*, submitted), and present correlation with the orientation of some geological framework..

4.3.1 Low-*Pn*-velocity zones: focus of upwelling of hot mantle material and Cenozoic intraplate volcanism

Similar patterns of low-velocity zones are well resolved by the isotropic and anisotropic inversion (Figure 4.1 and Figure 4.2), despite the fact that a trade-off between anisotropy and velocity is observed in the test model. This trade-off is likely the cause of the slight difference (in terms of amplitude) for the two models.

Previous studies have suggested that prominent variations in seismic velocities observed within the upper mantle are typically related to thermal, pressure, or compositional variations (*e.g.* Karato and Jung, 1998; Goes and van der Lee, 2002; Perry et al., 2006). Black and Braille (1982) affirmed that they are, in most cases, linked with temperature variations. The upper mantle is known to be predominantly composed by peridotite. Laboratory measurements have confirmed that under high temperature and pressure, seismic wave velocities in peridotite decrease rapidly with increases in the temperature (*e.g.* Sato et al., 1989). Other studies have shown that high velocity is related to high pressure or low temperature (*e.g.* Matsushima and Akeni, 1977).

Following the approach of Sato et al. (1989), under high lithostatic pressure from the overlying rocks, the decrease in seismic velocities within the mantle is characteristic of hot mantle regions. Besides, the low-*Pn*-velocity zones directly beneath the Cenozoic alkaline volcanic provinces in the northern, central, and southwestern regions of Madagascar (NMAP, CMAP, and SMAP, respectively). These suggest that the low-*Pn*-velocity zones can be interpreted as hot mantle materials.

These low-velocity zones were previously identified by the surface wave tomography of Pratt et al. (2017). They confirmed that the negative shear-wave velocity anomaly zones, of about -4% relative to PREM, reach at least the depth of 150 km beneath the northern and central regions of Madagascar, and between depths of 50-150 km beneath the southwest region. Pratt et al. (2017) have interpreted these upper mantle low-velocity zones as upwelling asthenosphere that resulted in the anomalously high elevation and Cenozoic volcanism in Madagascar.

Geothermal systems in Madagascar are generally associated with volcano-tectonic or tectonic activity, and are located mainly in volcanic areas, fault zones, or sedimentary basins (Besairie, 1959; Andrianaivo and Ramasinoro, 2015). In Figure 4.2, the *Pn* tomography result shows a strong correlation between the location of thermal springs and low-velocity zones in Madagascar, supporting the presence of hot thermal anomaly beneath the regions.

However, in comparison with the model of Pratt et al. (2017), the uppermost mantle thermal perturbation inferred by the *Pn* tomography, in this present study, is more limited (Figure 4.2) beneath the regions where the Cenozoic alkaline volcanic provinces are observed. It accordingly suggests that these regions could be the focus of upwelling in the sublithospheric mantle as proposed by Pratt et al. (2017).

Torsvik et al. (1998) suggested that the mantle-derived materials that caused the Cenozoic volcanic eruption could be the remnants of the Marion hotspot that produced the Cretaceous eruptions. However, the high-elevated topography of

Madagascar is believed to be linked to the Cenozoic volcanism (Pratt et al., 2017). Several studies have found that this uplift is a recent phenomenon, as young as 15 Ma, from the observation of lavakas, seismicity, and the shape of river valleys (de Wit, 2003; Cox et al., 2010; Roberts et al., 2012). Thus, the low-velocity zones observed in this study are recent features, and cannot be linked to the Cretaceous events of Marion hotspot. This supports the observation of Bardintzeff et al. (2011) from the geochemical and isotopic (Sr-Nd) evidences, suggesting that the source of the CMAP and SMAP is different to the Cretaceous emission source.

In their interpretation, Pratt et al. (2017) have suggested that a removal of the mantle lithosphere is possibly observed beneath the CMAP, which was likely replaced by the upwelling asthenospheric mantle-derived materials. Furthermore, results inferred from the *Pn* tomography shows a negative velocity anomaly of about -2.5% relative to the PREM model beneath the CMAP. This value (around 7.9 km/s) is, however, apparently too high to be asthenosphere. Therefore, other techniques may be required to investigate the cause of the delamination of the lithosphere beneath CMAP as the resolution of the *Pn* tomography, here, is not sufficient to argue about the origin of such mechanism.

4.3.2 Seismic anisotropy signatures and tectonic framework

Several hypotheses were proposed to explain the unusual Cenozoic volcanic activities in Madagascar. Some authors have associated the volcanism to the complex past history of the island: for example, a reactivation of a very old and lithospheric-scale fracture zone during the Cenozoic era (Nougier et al., 1986). Moreover, links to neighboring regional tectonic events have been proposed: the Comoros hotspot in the northwest of Madagascar (Emerick and Duncan, 1982), hot asthenospheric-mantle-derived materials from the African Superplume (Ebinger and Sleep, 1998; Forte et al., 2010), or the conjectured extension of the EAR to Comoros and Madagascar (*e.g.* Calais et al., 2006, Saria et al., 2013; Stamps et al., 2014).

Laboratory experiment of Zhang and Karato (1995), conducted with upper-mantle rocks under high pressure and temperature, showed that the seismic anisotropy is generally due to lattice-preferred-orientation of olivine aggregates aligned by simple-shear strain (as the simple-shear strain is the principal deformation modes of rocks in the upper mantle). In their experiments, they observed that the orientation of the olivine fast-axis tended to be parallel to the flow direction. Silver and Chan (1988) hypothesized that the strain producing the seismic anisotropy on a continental scale can either be linked to the plate motion, stress in the crust, and the past or current tectonic history that defines the structure of the upper mantle. They also pointed out that the most recent tectonic activity in the upper mantle defines the fast-polarization direction of the anisotropy. Therefore, the flow direction of mantle-derived materials and strain history of the upper mantle can be tracked through the orientation of the seismic anisotropy.

Ray paths of *SKS* phases (*S* waves that cross the core as *P* waves and convert back into *S* waves at emergence) are approximately vertical and normal to the surface of the Earth. They best record the vertically integrated anisotropy of the fastest split-shear waves within the uppermost 200-300 km of the mantle (Savage and Silver, 1993). Previous studies revealed that there is a correlation between the fast-polarization directions of *Pn* anisotropy and *SKS* shear-wave splitting fast-polarization (*e.g.* Crampin, 1977; Christensen, 1984). Therefore, any difference reveals the depth variation of the anisotropy, which can be interpreted as the presence of different strain zones in the mantle.

I compared the *Pn* anisotropy observations with the orientation of *SKS* shear-wave splitting measurements that have been conducted in Madagascar (Reiss et al. 2016; Ramirez et al., submitted). The SELASOMA profile, which ran from the west to the east coast of Madagascar across the Ranotsara shear zone, found that the fast polarization direction changes from NW in the center to NE in the east and west (Reiss et al. 2016). A fast polarization direction of 50°, which is roughly aligned with the direction of absolute plate motion, was proposed to explain the NE orientation. The NW-oriented polarization was attributed to fossil anisotropy produced by a ~150-km-wide ductile deformation zone of ductile deformation

near the Ranotsara shear zone. Ramirez et al. (submitted), using the MACOMO data, have suggested that the ~EW-trending of the *SKS* fast-polarization direction in the northern region of Madagascar is the result of a NE-trending mantle flow guided by the African superplume or plate motion and subsequently reoriented by a SW-trending mantle flow from the Comoros hot spot. A circular pattern of anisotropy was observed around CMAP and the Antananarivo terrane by Ramirez et al. (submitted). They suggested that the origin of the circular feature could be the interaction between a NE-trending flow, which is likely from the African Superplume or the absolute plate motion, and the upwelling of the asthenospheric mantle beneath CMAP. Ramirez et al. (submitted) have attributed the N to NE-oriented anisotropy observed in the southwesten region of Madagascar to a small-scale flow in the asthenosphere. They have attributed the anisotropy in the southern area of Madagascar to a fossil anisotropy as it is aligned to the ~N-S direction of the shear zones in this region.

The fast-polarization of *Pn* anisotropy observed in the northern region of Madagascar, from this study, is oriented NW-SE (Figure 4.6). This is aligned to the orientation of the Tsaratanàna alkaline complex (*i.e.* the NMAP) and the Sandrakota shear zone. This suggests that the anisotropy in the uppermost mantle in this region can be attributed, also, to a fossil anisotropy. Note that the SKS anisotropy in Ramirez et al. (submitted) have observed a NE direction of anisotropy in this region and have attributed it to a NE-oriented mantle flow controlled by the African superplume or the absolute plate motion, which is modified by a SW-trending mantle flow from the Comoros hot spot. On the other hand, Silver and Chan (1988) have suggested that the most recent tectonic activity in the upper mantle defines the fast-polarization direction of the anisotropy in the region. Therefore, an alternative explanation is that the NE trending shown by the *SKS* could be overprinted, on top, by recent strain, which is likely the recent tectonic activity that is linked to the Cenozoic volcanic manifestation.

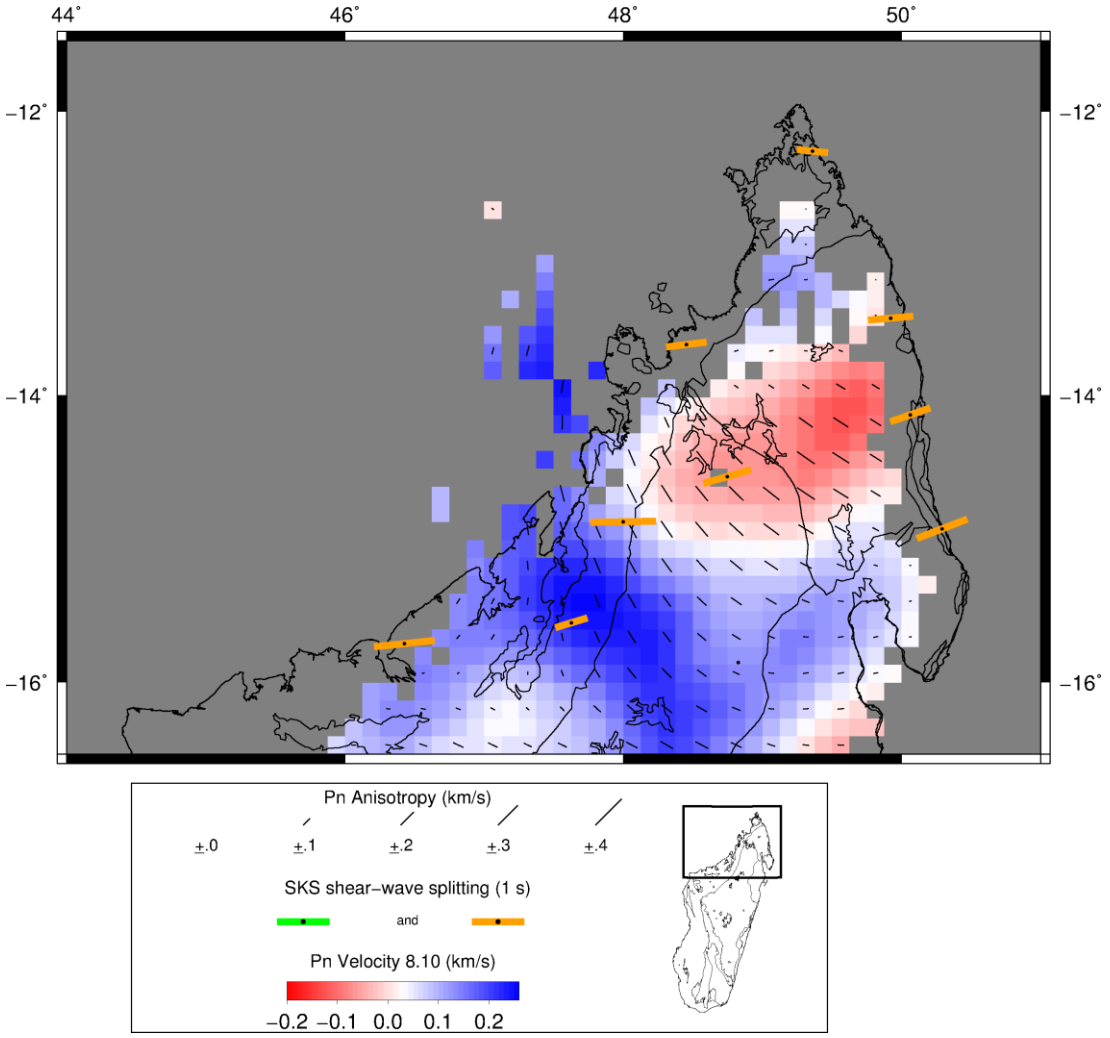

Figure 4.6: Map showing the lateral variation of *Pn* velocity (color scale), *Pn* anisotropy (black bars), and *SKS* shear-wave splitting (orange bars) (Ramirez et al., submitted) in the northern part of Madagascar. Red and blue colors correspond to low and high *Pn*-velocity, respectively. Black bars indicate the fast *Pn*-anisotropy direction, and the length of the bars is proportional to the anisotropy magnitude. The strike and length of the orange lines indicate the fast-velocity directions of SKS shear-wave splitting and the amount of splitting, respectively. Also plotted are the major geological unit boundaries and shear zones shown in Figure 1.4.

Both *Pn* and *SKS* anisotropies broadly present similar orientation, a NW-SE trending (Figure 4.7), in the area south to the CMAP. The area encompasses the southern portion of the Ikalamavony domain and aligns to the orientation of several shear zones (such as the Ranotsara, the Beraketa, the Ihosy, and the Zazafotsy shear zones) in this region. Reiss et al. (2016) and Ramirez et al. (submitted) have interpreted the NW orientation of the SKS fast polarization to be

the result of a fossil anisotropy, which is linked to a ~150-km-wide ductile deformation zone. Therefore, the *Pn* anisotropy can be, also, attributed to a fossil anisotropy for this region.

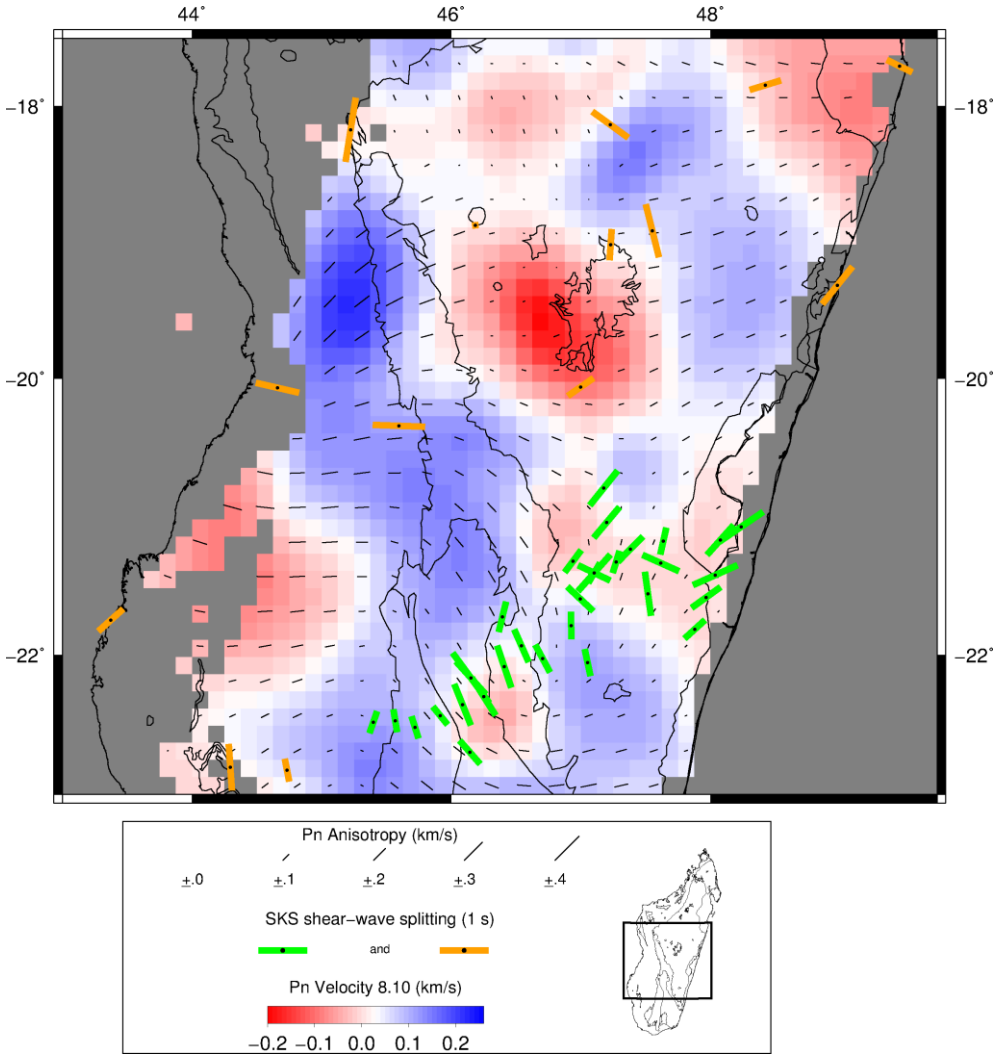

Figure 4.7: Map showing the lateral variation of *Pn* velocity (color scale), *Pn* anisotropy (black bars), and *SKS* shear-wave splitting (orange bars) (Ramirez et al., submitted) in the south-central part of Madagascar. Red and blue colors correspond to low and high *Pn*-velocity, respectively. Black bars indicate the fast *Pn*-anisotropy direction, and the length of the bars is proportional to the anisotropy magnitude. The strike and length of the orange lines indicate the fast-velocity directions of SKS shear-wave splitting and the amount of splitting, respectively. Also plotted are the major geological unit boundaries and shear zones shown in Figure 1.4

The *Pn* anisotropy is oriented from E-W to NE-SW along the western sedimentary basin, around the Morondava basin, of Madagascar. Reiss et al. (2016) interpreted the NE-trending along the western sedimentary as an influence of the mantle flow from plate motion; while Ramirez et al. (submitted), for the same region, have argued that it is a component of the circular pattern of anisotropy controlled by the upwelling astenosphere around CMAP. The orientation of the fast-polarization of *Pn* anisotropy for these regions can be, then, attributed either to the mantle flow from African superplume or the plate motion. However, as seen in Chapter 3, the lithosphere of this region has been subjected to a substantial deformation, streched and thinned, during the rifting from Africa. Consequently, the orientation of the *Pn* anisotropy, NE-SW-oriented, is likely portraying the strain from the rifting.

4.3.3 Implication to the formation of the Lwandle plate

The separation of the Somalian and Nubian plates initiates around the Afar region and extends to the south along the EARs. However, the trajectory of its southernmost extension is controversial. Analyses of geodesy, GPS data, seismicity, bathymetry, and tectonics in the surrounding regions suggest the formation of microplates, bounded by diffuse boundaries, connecting the EARs with the Southwest Indian Ridge (e.g., Chu and Gordon 1999; Calais et al., 2006, Saria et al., 2013; Stamps et al., 2014). It has been suggested that a diffuse plate boundary passes through the central part of Madagascar, detaching the Lwandle plate from the Somalian plate (Horner-Johnson et al., 2007; Saria et al., 2013; Stamps et al. 2014). In fact, this region of Madagascar is characterized by moderate seismicity and presents an E-W extensional stress (Bertil and Regnoult, 1998; Rindraharisaona et al., 2013; Rakotondraibe et al., in prep).

Our observation from the *Pn* anisotropy does not show strong evidence indicating the Lwandle plate edge. Also, the location of the low-*Pn*-velocity zone beneath the CMAP is distant to the presumed location of the edge of Lwandle plate.

4.3.4 Low-*Pn*-velocity in the Antongil craton

A low-*Pn*-velocity region is observed beneath the Antongil craton along its contact with the Antananarivo domain.

The Antongil craton contains the oldest rocks found in Madagascar, *ca.* 3.3 Ga (Tucker et al., 2011). The result from the joint inversion of receiver functions and surface wave data in the previous Chapter found that the crust beneath this craton is thicker than expected, about 43 km (as it is a fragment of the WDC), compared to the thickness of the crust elsewhere in the east coast, which has an average of 35 km. Consequently, the apparent low-*Pn*-velocity observed in this area could be explained as the result of time delays introduced by ray paths traveling through the deep crustal root.

An alternative explanation involves the presence of thermal springs in the area (Besairie, 1959), suggesting that the low-velocity zone actually exists and is related to high heat flow underlying the region. However, its origin is not clearly observed from the tomography in this study, even though a possible low-*Pn*-velocity zone is poorly resolved along the east coast of the Antongil craton (Figure 4.2). If it is not connected to NMAP or CMAP, another possibility is that the low-*Pn*-velocity zone is the remnant of the Marion hotspot that broke apart the WDC and left behind the Antongil craton during the separation of Madagascar and India in the Late Cretaceous (*ca.* 90 Ma) (Storey et al., 1995; Torsvik et al., 1998; Raval and Veeraswamy, 2003).

4.3.5 Crustal structure from static delays

Station static delays can be attributed either to local structure or velocity. Positive station delays are representative of slower and/or thicker crust, while negative delays indicate thinner and/or faster crust.

Hearn and Ni (1994) performed a *Pn* tomographic study in the Middle East and pointed out that a variation of 1 s in the station delay corresponded to either a

change of ~10.4 km in crustal thickness of a variation of ~1.6 km/s in crustal velocity (if the crustal thickness is fixed to 40 km). However, changes in station delays can also be introduced by errors related to the picking or clock drift of the station (Hearn, 1991; Hearn and Ni, 1994).

The variation of station static delays found in this study was ~0.9 s, which reflects the significant variation of the Moho location beneath Madagascar. This likely confirms the result from the joint inversion of receiver functions and surface wave data in the previous chapter (the thickness of the crust beneath Madagascar is between 18km and 46 km). The station delays are generally negative in the northern, southwestern, and southern parts of Madagascar, reflecting the thin crust in the region (Figure 4.5). The pattern of thicker crust in the central backbone of the island is generally shown by high positive station delays. However, a slight decrease in station delay, but still positive, is generally observed along the east coast compared to the central Precambrian region. This reflects the minor thinning of the crust in the region, which is previously interpreted as a thinning of the crust related to the passage of the Madagascar/India block over the Marion hotspot (about 95 – 85 Ma).

Neighboring stations present different delays in some regions; we associate these with systematic errors due to a low signal-to-noise ratio which contributed to a misidentification of seismic phases.

4.4 Conclusion

The lateral variation of the *Pn* velocity and anisotropy of the uppermost mantle beneath Madagascar were imaged in this study by inverting 4541 travel times of *Pn* phases refracted at the crust-mantle boundary.

The average *Pn* velocity of the uppermost mantle is approximately 8.1 km/s throughout the island, which ranges between 7.9 km/s to 8.3 km/s. A maximum value of *Pn* anisotropy of ~ 3% (0.23 km/s) is observed.

There is a strong correlation between the *Pn* velocity and anisotropy with the surface geology, tectonic history, and present-day tectonic framework of the island.

Significant low-*Pn*-velocity zones underlie the Cenozoic alkaline provinces in the northern and central parts of the island, respectively the NMAP and CMAP. These low-*Pn*-velocity zones are attributed to upwelling of hot mantle materials that gave rise to the Cenozoic volcanic activities in Madagascar. Compared to the observation from the surface-wave tomography in Pratt et al. (2017), the low-*Pn*-velocity zones in this study are more limited and located directly beneath the NMAP and CMAP. This likely suggests that these regions of low-*Pn*-velocity can be interpreted as the focus of the upwelling of asthenospheric mantle.

The orientation of the fast-polarisation of *Pn* anisotropy in the northern and south-central of Madagascar presents alignments to the existing geological framework, such as the alkaline volcanic complex, around the NMAP, and shear zones, in both regions. These likely suggest that the anisotropy in the uppermost mantle in these regions can be attributed to a fossil anisotropy. The *Pn* anisotropy in the western region, around the Morondava basin, can be attributed either to the mantle flow form the plate motion, the African superplume, or from the mark left by the stretching and thinning of the lithosphere during the Mesozoic rifting from Afica.

Results from this study do not show any substantial evidence of the formation of diffuse plate boundary, for the formation of Lwandle plate, cutting through the central region of Madagascar

The station static delays obtained in this study reflect the large variation of the thickness of the crust of Madagascar.

Chapter 5

Receiver function imaging of the mantle transition zone beneath Madagascar

5.1 Introduction

The origin of magmas that fed the Cenozoic volcanic eruptions in Madagascar is controversial. It has been linked to the fracture zone that developed during the Mesozoic rifting from Africa (Nougier et al., 1986), the Comoros hotspot, located northwest of the Madagascar (Emerick and Duncan, 1982, 1983), the mantle flow driven by the African Superplume (Forte et al., 2010; Hansen et al., 2012), and the development of an incipient plate boundary extending through Madagascar (Saria et al., 2013; Stamps et al., 2015; Michon, 2016). Bardintzeff et al. (2010) located the source of the Cenozoic activities in the lower part of the lithospheric mantle.

The investigation of the upper mantle beneath Madagascar from a surface wave tomography (Pratt et al., 2017) revealed low-velocity zones underlying the Cenozoic alkaline provinces. These low-velocity zones were attributed to upwelling of hot mantle materials, which are the origin of the Cenozoic eruptions. *Pn* tomography in Chapter 4 also mapped these low-velocity zones. The surface

wave tomography suggested that the low-velocity zones extend to depths at least 150 km, but their maximum depth extent remains uncertain.

In this study, the thickness of the mantle transition zone is estimated from the topography of the 410 km and 660 km discontinuities (they are referred to as the *410* and *660* in this manuscript). Briefly, the thickness of the mantle transition zone is thinner in a hot region and thicker in a cold mantle region. Therefore, it can be used as a "mantle thermometer" to identify any thermal anomaly in the upper mantle. The thermal anomaly underlying the Cenozoic alkaline provinces of Madagascar is then a good candidate to study its eventual depth extension.

This chapter presents the achieved results from the Receiver function imaging of the mantle transition zone, followed by the discussion and conclusion of the findings.

The material in this chapter is summarized and will be submitted for publication in a peer-reviewed journal in the manuscript (see Appendix F): **Andriampenomanana, F., Nyblade, A.A., Wysession, M.E., Durrheim, R.J., Rambolamanana, G., Tilmann, F., Aleqabi, G., Shore, P.J., Pratt, M.J., and Rakotondraibe, T. Receiver function imaging of the mantle transition zone beneath Madagascar, to be submitted.**

5.2 Results

The main objective of this study is the mapping of variations in the transition zone thickness. Consequently, receiver functions computed from a Gaussian width of 0.5 and 1.0 (equivalent to corner frequencies of 0.24 Hz and 0.5 Hz, respectively) were used (Owens, 2000). A total of 1028 receiver functions from 37 seismic stations were stacked from two different methods: the single-station stacking and the common-conversion point stacking methods.

5.2.1 Single-station stacking

Clear *P410s* and *P660s* phases from the 410 km and 660 km discontinuities can be observed for 16 stations, with good agreement between estimates of the mantle transition zone thickness from low- and high-frequency *P*-wave receiver functions (Table 5.1). The stacked traces obtained at each station, sorted from north to south, are shown in Figure 5.1.

Ps conversions from the 410 km discontinuity are located between 405 km and 445 km depths and between 635 km to 695 km depths for the Ps conversions from the 660 km discontinuity. The range in the transition zone thickness beneath the island from the 16 single-station stacks is 230 km and 260 km, with an average thickness is 247 ± 8 km (standard deviation).

Table 5.1: Summary of mantle transition zone thicknesses for the single-station stacking of *P* receiver functions computed from Gaussian widths of 0.5 and 1.0. *#Nb* is the number of trace stacked for each station, *#410* and *#660* columns are respectively the location of the 410 km and 660 km discontinuities with vertical errors, and *TZT* is the mantle transition zone thickness.

Station	**Gaussian width of 0.5**				**Gaussian width of 1.0**			
	#Nb	**#410**	**#660**	**TZT**	***#Nb***	**#410**	**#660**	**TZT**
ABPO	*212*	$425 \pm \frac{14}{10}$	$685 \pm \frac{12}{14}$	**260**	*212*	$425 \pm \frac{9}{10}$	$685 \pm \frac{10}{12}$	**260**
AMPY	*14*	$410 \pm \frac{18}{11}$	$660 \pm \frac{28}{19}$	**250**	*8*	$410 \pm \frac{9}{9}$	$660 \pm \frac{14}{8}$	**250**
ANLA	*25*	$430 \pm \frac{12}{15}$	$675 \pm \frac{29}{20}$	**245**	*15*	$425 \pm \frac{12}{5}$	$680 \pm \frac{16}{13}$	**255**
BAEL	*19*	$440 \pm \frac{26}{19}$	$685 \pm \frac{23}{21}$	**245**	*17*	$440 \pm \frac{22}{12}$	$680 \pm \frac{21}{20}$	**240**
BARY	*18*	$425 \pm \frac{20}{12}$	$670 \pm \frac{30}{20}$	**245**	*11*	$420 \pm \frac{13}{11}$	$655 \pm \frac{14}{15}$	**235**
BATG	*19*	$440 \pm \frac{23}{32}$	$690 \pm \frac{23}{19}$	**250**	*16*	$440 \pm \frac{23}{10}$	$685 \pm \frac{19}{12}$	**245**
BITY	*18*	$430 \pm \frac{23}{14}$	$660 \pm \frac{70}{24}$	**230**	*13*	$430 \pm \frac{11}{10}$	$650 \pm \frac{33}{12}$	**220**
DGOS	*30*	$445 \pm \frac{12}{12}$	$695 \pm \frac{15}{17}$	**250**	*15*	$455 \pm \frac{10}{35}$	$690 \pm \frac{17}{23}$	**235**
FOMA	*98*	$420 \pm \frac{10}{15}$	$660 \pm \frac{26}{25}$	**240**	*63*	$415 \pm \frac{8}{7}$	$680 \pm \frac{-}{21}$	**265**
LAHA	*44*	$430 \pm \frac{15}{17}$	$675 \pm \frac{18}{15}$	**245**	*32*	$435 \pm \frac{16}{21}$	$690 \pm \frac{13}{40}$	**255**
MAGY	*24*	$430 \pm \frac{14}{13}$	$680 \pm \frac{27}{28}$	**250**	*18*	$430 \pm \frac{17}{12}$	$675 \pm \frac{20}{13}$	**245**
MAJA	*20*	$415 \pm \frac{25}{32}$	$670 \pm \frac{19}{19}$	**255**	*17*	$420 \pm \frac{14}{10}$	$675 \pm \frac{11}{14}$	**255**
MS07	*14*	$430 \pm \frac{25}{15}$	$685 \pm \frac{21}{16}$	**255**	*11*	$435 \pm \frac{11}{13}$	$680 \pm \frac{19}{14}$	**245**
MS19	*18*	$405 \pm \frac{20}{43}$	$635 \pm \frac{19}{23}$	**230**	*17*	$430 \pm \frac{9}{9}$	$665 \pm \frac{10}{10}$	**235**
VOI	*33*	$405 \pm \frac{17}{13}$	$655 \pm \frac{22}{14}$	**250**	*20*	$420 \pm \frac{12}{-}$	$655 \pm \frac{11}{13}$	**235**
ZAKA	*25*	$435 \pm \frac{15}{20}$	$685 \pm \frac{26}{19}$	**250**	*16*	$435 \pm \frac{11}{11}$	$680 \pm \frac{32}{15}$	**245**

(-): is used when the limits in the confidence bounds are not clear in the wiggles.

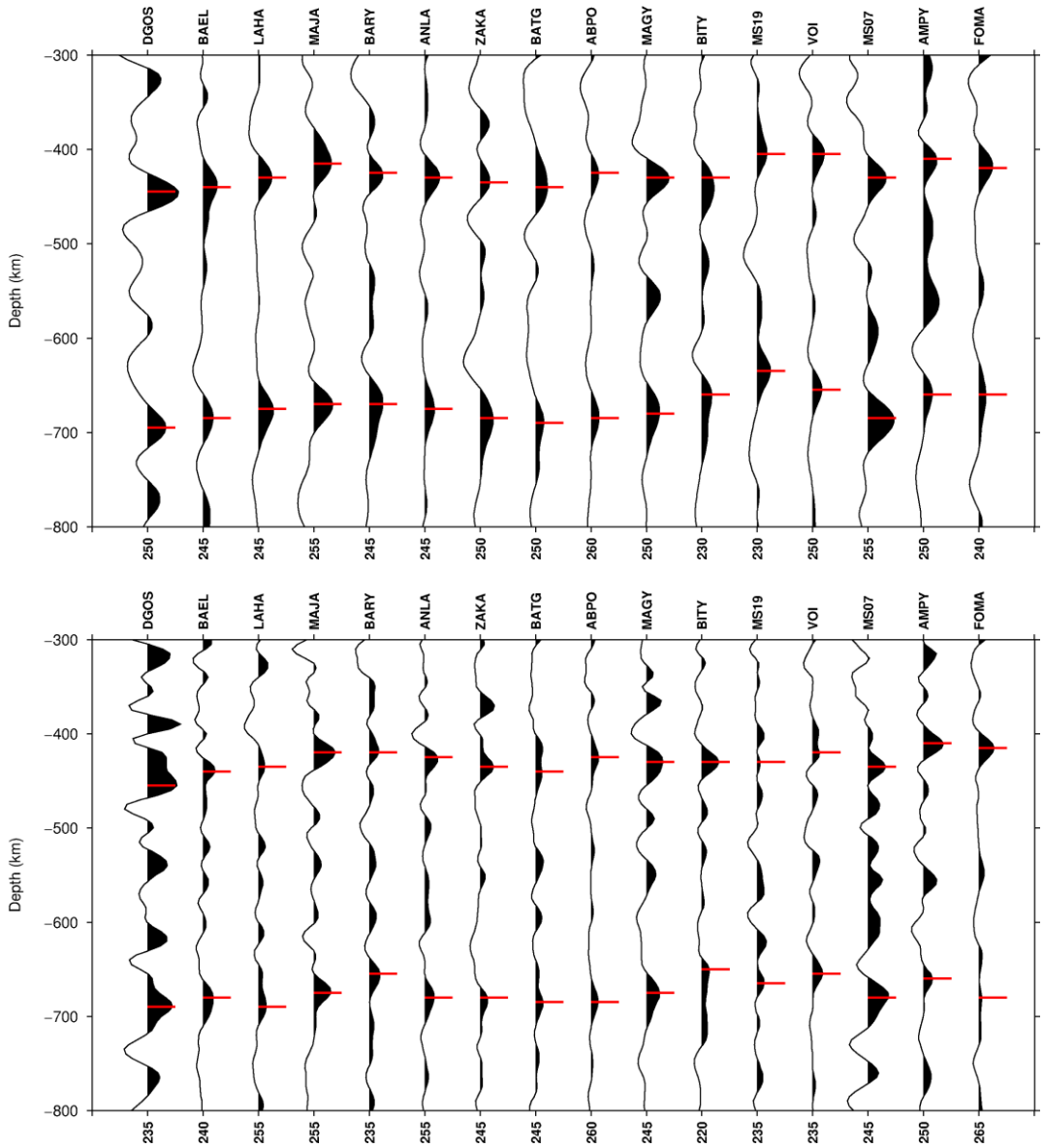

Figure 5.1: Single-station stacking of *P* receiver functions, for Gaussian factor of 0.5 (top) and 1.0 (bottom), for all stations used in this study sorted by latitude, from north (left) to south (right). *Ps* arrivals at the 410 km and 660 km discontinuities are generally observed at each station (black shade). Red lines show *Ps* conversions from the 410 km and 660 km discontinuities. Numbers at the bottom of each PRF wiggle are the transition zone thickness beneath each station.

5.2.2 Common-conversion point stacking

To compare to the single-station stacks, Table 5.2 lists the thickness of the transition zone beneath the 16 nodal points closest to the location of the 16 seismic stations listed in Table 5.2.

Several receiver function profiles with 0.25° node spacing are shown in Figure 5.3, Figure 5.4, Figure 5.5, and Figure 5.6. The locations of the profile are shown in Figure 5.2. For the northern profile A-A', the 410 km discontinuity ranges between 435 and 445 km depths and the 660 km discontinuity is between 675 km and 690 km depth (from Gaussian width of 0.5). This gives a range in the transition thicknesses of 235 to 250 km. In the north-central region of Madagascar along the B-B' and B1-B1' profiles, the transition zone thickness ranges from 240 km to 260 km. The transition zone ranges between 235 km and 260 km beneath the central part of Madagascar (C-C' and C1-C1' profiles). The east-west profile in the southern region (D-D' profile) shows a transition zone thickness varying between 245 km and 265 km. In the north-south profile D1-D1' the resolution is limited due to lack of receiver function traces in the bin and therefore no depth estimation of the discontinuities is made.

Table 5.2: Summary of mantle transition zone thicknesses for the common-conversion point stacking of *P* receiver functions computed from Gaussian widths of 0.5 and 1.0. *Lon* and *Lat* are respectively the longitude and latitude of a nodal point close to the seismic station listed in Table 5.1, *#410* and *#660* columns are respectively the location of the 410 km and 660 km discontinuities with vertical errors, and *TZT* is the mantle transition zone thickness.

Node		***Closest***	**Gaussian width of 0.5**			**Gaussian width of 1.0**		
Lon (°)	**Lat (°)**	***station***	**#410**	**#660**	**TZT**	**#410**	**#660**	**TZT**
47.25	**-19.00**	***ABPO***	435 ± 11 / 11	685 ± 25 / -	**250**	435 ± 11 / 16	665 ± 32 / 20	**230**
44.75	**-24.75**	***AMPY***	x x / x	x x / x	**x**	x x / x	x x / x	**x**
49.50	**-17.75**	***ANLA***	430 ± 14 / 14	675 ± 21 / 18	**245**	430 ± 12 / 12	675 ± 25 / 16	**245**
48.75	**-14.50**	***BAEL***	x x / x	x x / x	**x**	x x / x	x x / x	**x**
46.75	**-17.25**	***BARY***	425 ± 14 / 15	675 ± - / 21	**250**	425 ± - / 14	675 ± - / 19	**250**
46.25	**-18.75**	***BATG***	425 ± 20 / 19	675 ± 21 / 14	**250**	445 ± 28 / 34	670 ± 30 / x	**225**
47.00	**-20.00**	***BITY***	420 ± 15 / 11	655 ± 15 / 11	**235**	420 ± 16 / 16	665 ± 22 / 15	**245**
49.50	**-12.25**	***DGOS***	445 ± 11 / 11	680 ± 43 / 23	**235**	445 ± 17 / 16	680 ± 44 / 21	**235**
47.00	**-25.00**	***FOMA***	420 ± 18 / 16	650 ± 17 / 11	**230**	420 ± 16 / 16	660 ± 22 / 22	**240**
50.25	**-15.00**	***LAHA***	425 ± 22 / 13	660 ± 21 / 32	**235**	420 ± - / 8	660 ± 12 / 30	**240**
49.00	**-19.25**	***MAGY***	425 ± 11 / 11	690 ± 13 / 18	**265**	425 ± 15 / 12	690 ± 706 / 674	**265**
46.50	**-15.75**	***MAJA***	x x / x	x x / x	**x**	x x / x	x x / x	**x**
44.75	**-22.75**	***MS07***	430 - / 27	680 22 / 19	**250**	x x / x	x x / x	**x**
47.00	**-21.50**	***MS19***	415 ± 14 / 25	675 22 / 22	**260**	410 ± 20 / 17	675 ± 19 / 18	**265**
46.75	**-22.00**	***VOI***	x x / x	x x / x	**x**	410 ± 31 / 13	680 ± 30 / 19	**270**
48.50	**-17.75**	***ZAKA***	425 ± 19 / 28	680 ± 22 / 37	**255**	425 ± 16 / 11	675 ± 29 / 24	**250**

(x): high uncertainty.

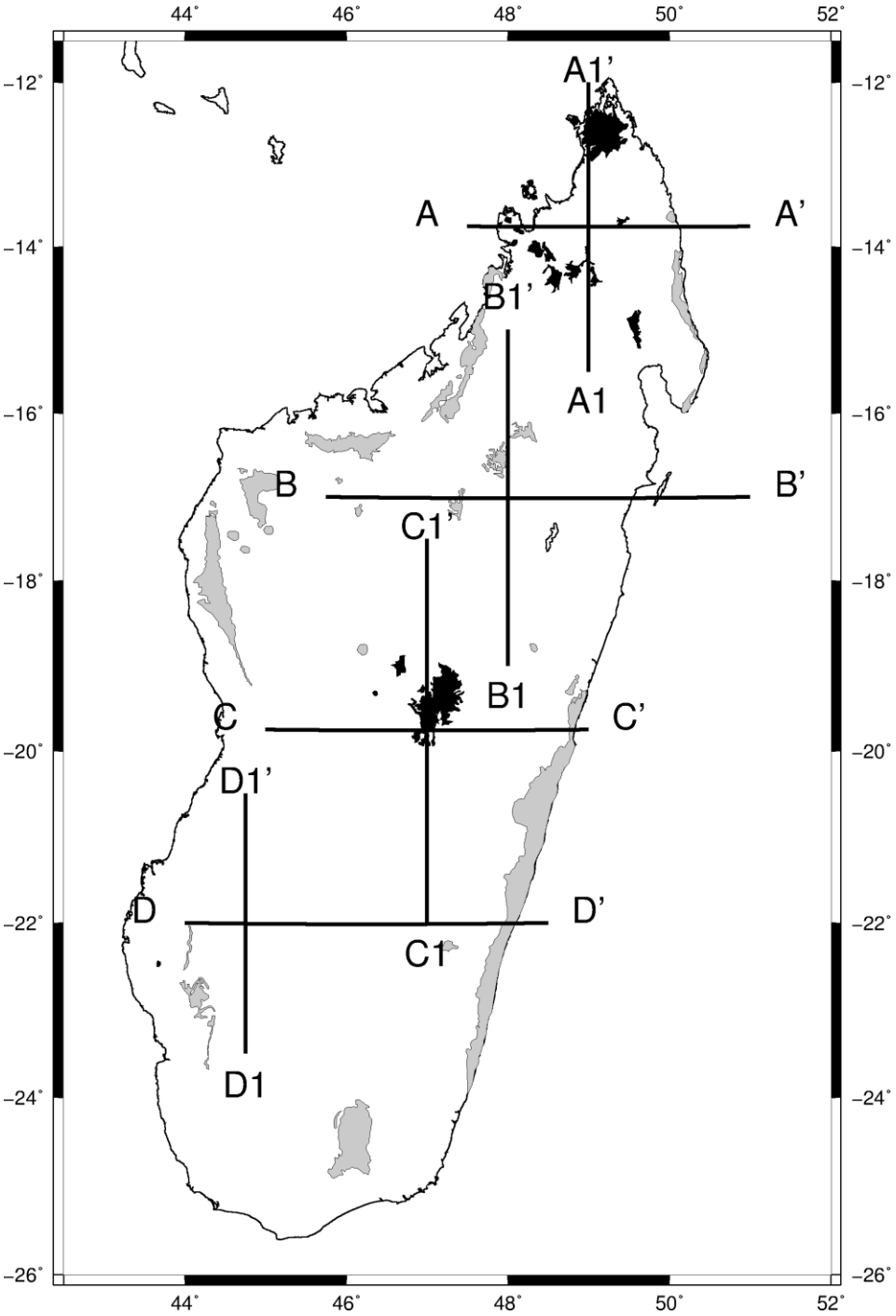

Figure 5.2: Map of Madagascar showing the location of Cretaceous (gray) and Cenozoic (black) volcanic provinces. Horizontal (A-A’, B-B’, C-C’, and D-D’) and vertical (A1-A1’, B1-B1’, C1-C1’, and D1-D1’) lines are profiles used to present the stacked receiver functions from common-conversion point stacking.

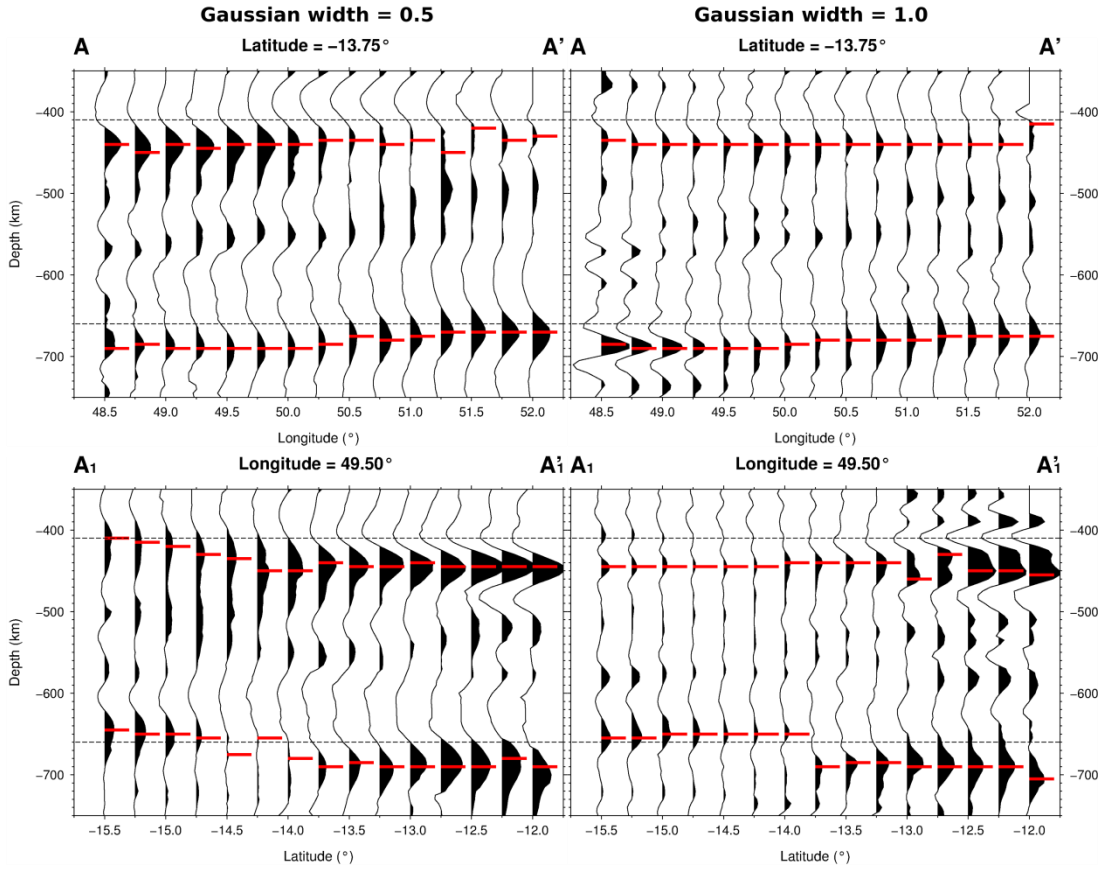

Figure 5.3: Results from common-conversion point stacking of *P* receiver function profiles along profiles A-A' (top) and A1-A1' (bottom) for *P* receiver function computed with Gaussian with of 0.5 (left) and 1.0 (right), beneath the northern region of Madagascar. Red lines are the maximum of *P410s* and *P660s* automatically picked around depths of 410 km and 660 km and correspond to the 410 km and 660 km discontinuities.

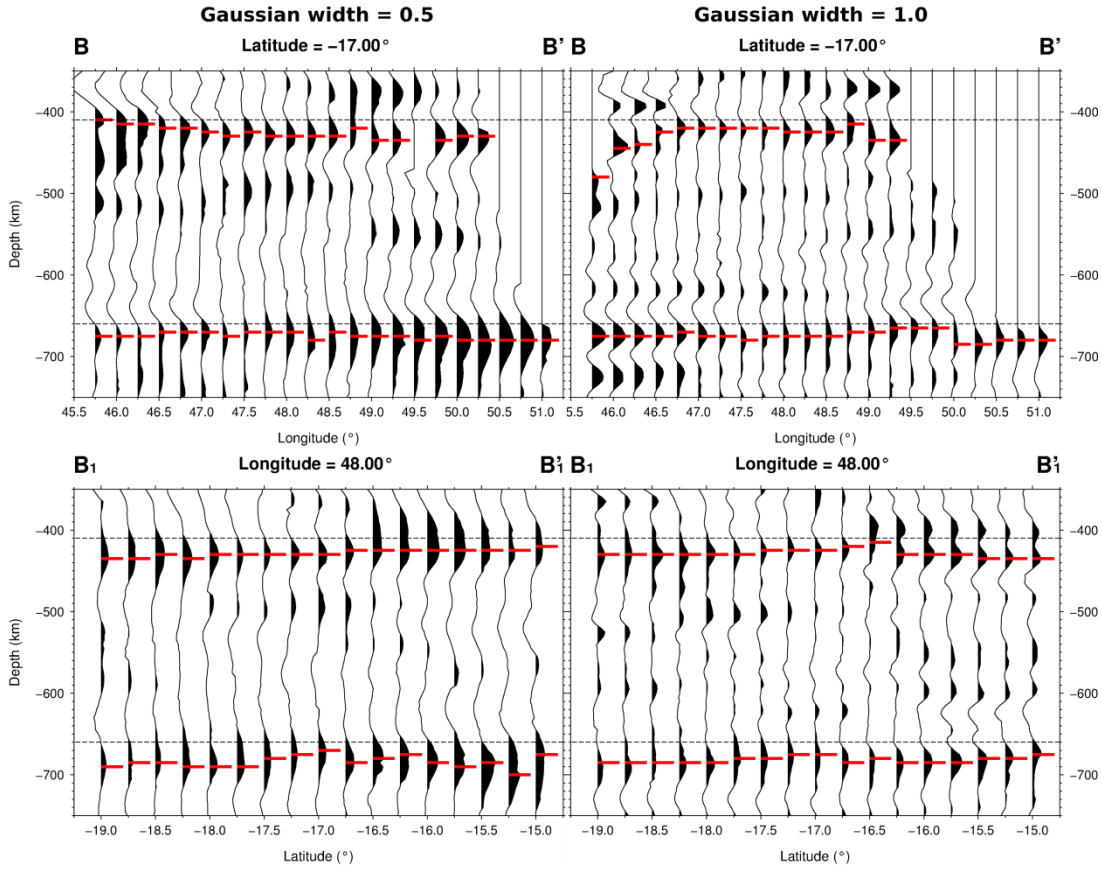

Figure 5.4: Results from common-conversion point stacking of *P* receiver function profiles along profiles B-B' (top) and B1-B1' (bottom) for *P* receiver function computed with Gaussian with of 0.5 (left) and 1.0 (right), beneath the north-central region of Madagascar. Red lines are the maximum of *P410s* and *P660s* automatically picked around depths of 410 km and 660 km and correspond to the 410 km and 660 km discontinuities.

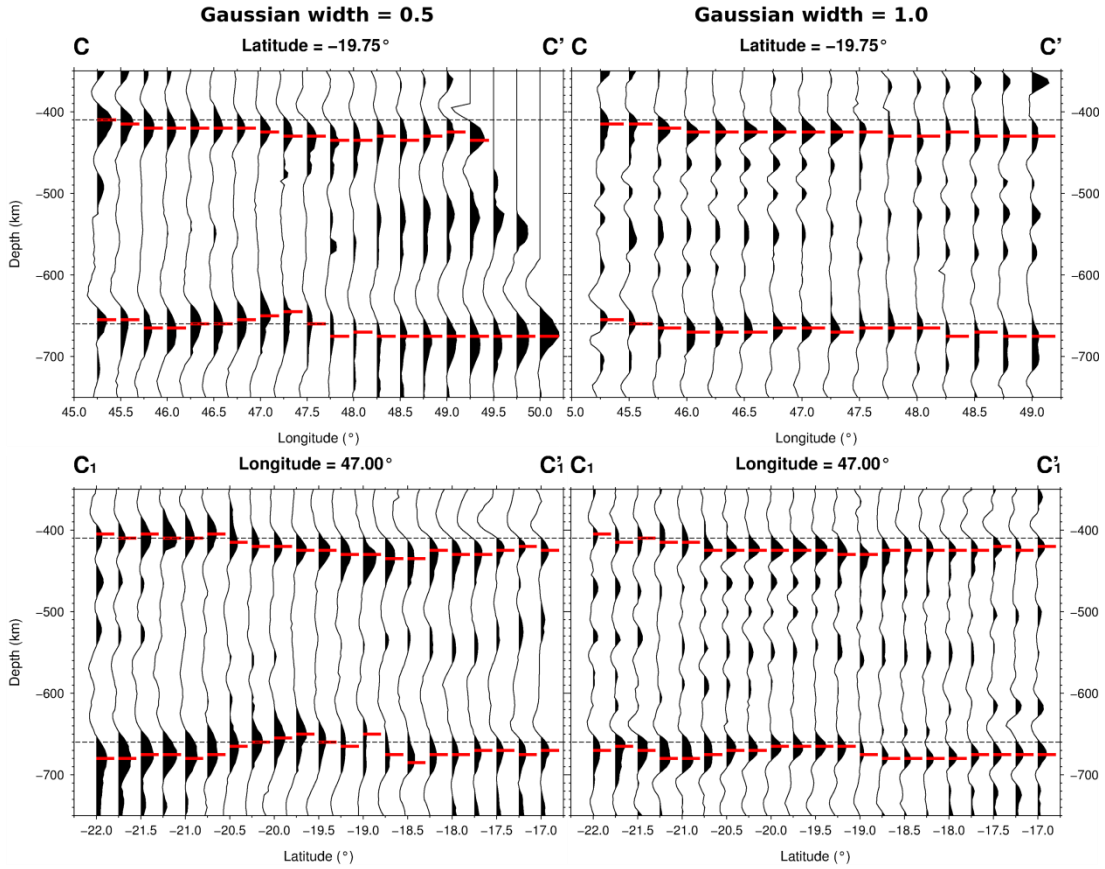

Figure 5.5: Results from common-conversion point stacking of *P* receiver function profiles along profiles C-C' (top) and C1-C1' (bottom) for *P* receiver function computed with Gaussian with of 0.5 (left) and 1.0 (right), beneath the central region of Madagascar. Red lines are the maximum of *P410s* and *P660s* automatically picked around depths of 410 km and 660 km and correspond to the 410 km and 660 km discontinuities.

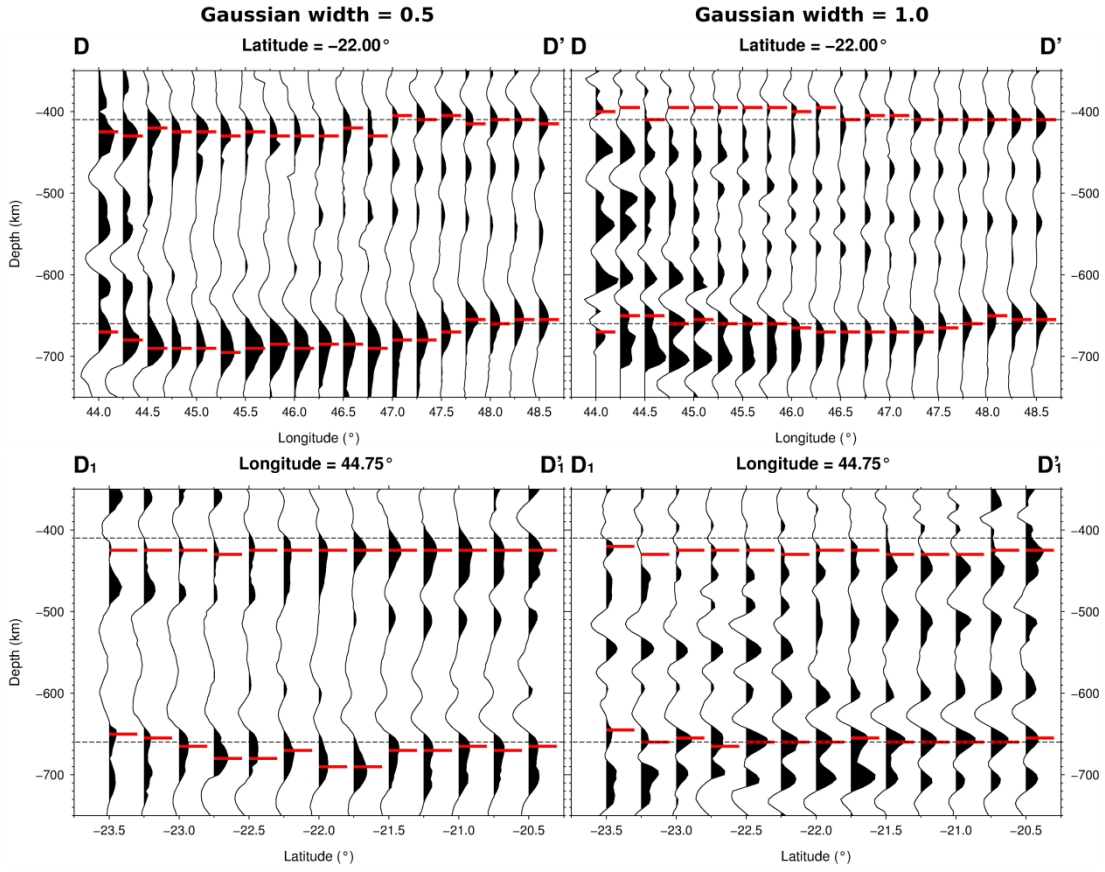

Figure 5.6: Results from common-conversion point stacking of *P* receiver function profiles along profiles D-D' (top) and D1-D1' (bottom) for *P* receiver function computed with Gaussian with of 0.5 (left) and 1.0 (right), beneath the central region of Madagascar. Red lines are the maximum of *P410s* and *P660s* automatically picked around depths of 410 km and 660 km and correspond to the 410 km and 660 km discontinuities.

5.3 Discussion

The main findings of this study are about the thicknesses of the transition zone beneath different region in Madagascar and their implication regarding the presence of volcanic activities in the island.

The topography of the transition zone discontinuities depends of the temperature of the surrounding region. The *410* is depressed in the vicinity of hot region, while the *660* is elevated. Consequently, the transition zone is thinner. Around a cold region, the *410* is elevated while the *660* is depressed. In this case, the transition zone is thicker (Bina and Helffrich, 1994). The mantle transition zone acts as "mantle thermometer" and is an important tool to probe the presence of any plume, slab, or water infiltration around the transition zone.

In summary, no significant topography of the 410 and 660 are observed beneath Madagascar and the thickness of the mantle transition zone is generally uniform, suggesting that no thermal anomalies are observed around the transition zone.

5.3.1 The mantle transition zone thickness

Both single-station and common-conversion point stacking methods show similar ranges in the depths of the mantle transition zone discontinuities. Overall, the 410 km discontinuity is located between depths of 410 km and 455 km and the 660 km discontinuity between depths of 660 km and 695 km.

When performing the depth migration of *P*-wave receiver functions, only the crustal part of the *1D* velocity model was replaced by the model obtained in the joint inversion of receiver functions and surface wave data in Chapter 3. However, the model of Pratt et al. (2017) suggests a negative shear-wave velocity anomaly of about -4 % (relative to PREM) in the upper mantle beneath the NMAP/CMAP/SMAP. This likely contributed to the late arrival of *P410s* and *P660s*, especially in these regions (*e.g.* profile A-A'). Therefore, depths of the discontinuities cannot be as easily used to infer the presence or absence of the

thermal anomalies as can the thickness of the transition zone. Temperature variations in the mantle transition zone can be more robustly determined from its thickness because it does not depend on the velocity structure in the upper mantle.

The transition zone thickness beneath Madagascar ranges between 230 km and 260 km, as determined from the single-station stacking. Estimates from the common-conversion point stacking are between 235 km and 265 km, consistent with those inferred from the single-station stacking. From the common-conversion stacking method, the northern region of Madagascar has a transition zone thickness that ranges between 235 km and 250 km while, it is around 235 km and 260 km across the central region and between 245 km and 265 km in the southern region. Compared to the global average, ~240-260 km (*e.g.* Shearer, 1991), the mantle transition zone thickness beneath Madagascar does not show a substantial deviation from it. Small differences, for example beneath the central region (~235 km) and southern region (~265 km), fall within the global average range when the ± 10 km uncertainty in our transition zone thickness estimates is considered. Therefore, there is no detectable thinning of the mantle transition zone beneath Madagascar.

5.3.2 Implication to the thermal anomaly beneath Madagascar

The uniformity of the transition zone thickness beneath Madagascar indicates an absence of a thermal anomaly in the region. This finding is not compatible with a superplume model (Forte et al., 2010; Hansen et al., 2012), which suggests large scale flow of hot material from the lower mantle to the upper mantle. Consequently, the results from this study do not support a superplume model to explain the origin of the Cenozoic volcanism in Madagascar. But the results support hypotheses linking the volcanism to geodynamic processes in the upper mantle as reviewed in the introduction Section 5.1.

This result contrasts with the study of Mulibo and Nyblade (2013) revealed a ~30-40 km of thinning of the transition zone beneath parts of eastern Africa, which

corresponds to a thermal anomaly of ~180-300° across the transition zone. Mulibo and Nyblade (2013) attributed this thermal anomaly to the African Superplume.

5.4 Conclusion

The mantle transition zone beneath Madagascar was investigated in this study by stacking P receiver functions. A total of 1809 P receiver functions were used for in single-station and common-conversion-point stacking to estimate the transition zone beneath the island. Both stacking techniques show uniform mantle transition zone thickness, varying between 230 km and 265 km beneath Madagascar, which is consistent with the global average of 240-260 km. Departures from the global average fall within the uncertainty of ± 10 km in the estimation of the depth of 410 km and 660 km discontinuities. There is no detectable thinning of the mantle transition zone and thus no evidence for the thermal anomaly in the mantle under Madagascar that extend on deep as the mantle transition zone. This finding supports an upper mantle origin for the Cenozoic volcanism in Madagascar.

While the resolution of this study is sufficient to rule out a large scale thermal anomaly in the transition zone under Madagascar, it is not sufficient to rule out the presence of a narrow anomaly as might arise from a plume tail. Therefore, although this study supports an upper mantle origin for the Cenozoic volcanism, a mantle plume origin cannot be ruled out.

Chapter 6

General discussion and conclusion

6.1 Introduction

Madagascar offers interesting and unusual geological framework to investigate geodynamic processes. However, prior to this study, very little is hitherto known about its deep structure, *i.e.* from the surface to the mantle. Several previous studies, mainly from geological approaches, have been conducted in Madagascar (*e.g.* Besarie, 1967; Rabinowitz et al., 1983; Piqué, 1999a; Collins, 2000; de Wit, 2003) and gave clue to the structure and origin of several perplexing geological features of the island, for example: the western sedimentary basin, the series of continental rifting, the anomalously high-elevated topography, and the Cenozoic intraplate volcanism. Due to the lack of data, geophysical approaches were applied only in small area (*e.g.* Rakotondrainibe, 1977; Rambolamanana et al., 1997; Rakotondraompiana et al., 1999; Rindraharisaona et al., 2013).

The recent temporary deployment of seismic stations over the whole island between 2011 and 2013 (Wysession et al., 2012; Tilmann 2012; Sigloch and Barruol, 2012), in addition to the existing permanent stations, enabled this study to investigate the crust, the uppermost mantle, and the mantle transition zone beneath Madagascar using a variety of techniques.

In this study, receiver functions were employed to investigate the basin, the crust, and the mantle transition beneath Madagascar using different approaches: such as, the *H-κ* stacking method of Zhu and Kanamori (2000), the joint inversion of receiver functions and surface wave data of Julià et al. (2000), and the single-station and common-conversion point stacking methods of Owens (2000). The travel time of *Pn* waves were used to perform a seismic tomography of the uppermost mantle beneath the island using the approach of Hearn (1996).

The main findings of this study mirror the complex geological framework of Madagascar which is controlled by the tectonic events that the island has undergone, starting from the amalgamation of Gondwana (*ca.* 570-510 Ma) until the present-day. They are generally about the crustal structure (including the thickness, shear-wave velocity structure, and Poisson's ratio), thermal anomaly beneath alkaline volcanic provinces, and the non-plume model to explain the volcanism in Madagascar.

This chapter presents the general discussion of findings from the three main projects of this research that are described in previous chapters. Then, a general conclusion of the research is presented.

6.2 General discussion

6.2.1 Thickness of the crust beneath Madagascar

The joint inversion of receiver functions and surface wave data in this study is in good agreement with previous estimates of crustal thickness. Thick crust (~40 km thick) is found beneath the central part of Madagascar, while it tends to be thinner (~33 km thick) towards the periphery of the island (Figure 3.1, Figure 3.3, Table 3.2, and Table 3. 3).

The present-day western basin of Madagascar was situated at the rift edge during the Permian-Triassic break-up of West and East Gondwana. Results from the joint inversion of receiver functions and surface wave data reveal that the rifted crust

beneath the sedimentary basin of Madagascar is thin (~18-36 km thick) compared to the unrifted crust beneath the Precambrian basement (with an average thickness of 38 ± 5 km). Previous studies have suggested that Madagascar was adjacent to present-day Tanzania and Kenya within Gondwana (Figure 1.1) (*e.g.* Du Toit, 1937; Norton and Sclater, 1979; Rabinowitz et al., 1983; Kusky et al., 2003). It is reasonable to assume that the thickness of the Precambrian crust beneath Madagascar and eastern Africa was similar prior to the rifting. Previous studies conducted in eastern Africa revealed that the crust beneath the region is about 38-39 ± 3 km thick (Tugume et al., 2012, 2013; Kachingwe et al., 2015), which is similar to the thickness of the unrifted crust beneath the eastern Precambrian basement of Madagascar. These likely suggest that the continental drift, separating the West and East Gondwana, stretched and thinned the crust beneath the western sedimentary basin of Madagascar by: ~20 km in the northernmost part of the island (*i.e.* 38 km vs. 18 km) and around ~12 km in the south-central coast (*i.e.* 38 km vs. 23-26 km) of the island.

A thinner-than-average crust (~34 km thick) is observed along the east coast of Madagascar, except beneath the Antongil craton (which is ~43 km thick). A hotspot reconstruction located the Marion hotspot beneath the Madagascar/India block about 95-85 Ma ago (Raval and Veeraswamy, 2003), which heated the overriding plate and subsequently weakened and eroded it. This likely caused an uplifting of the lithosphere, hence the thinning of the crust in the region, and fractured it, which caused the separation of India from Madagascar. As the Antongil craton is a fragment of the WDC, left behind when India split from Madagascar, the thick crust beneath the region is consistent with the crustal thickness of the WDC (*e.g.* Rai et al., 2013), which is ~46-54 km.

A north-south profile across the length of Madagascar shows that the crustal thickness varies from 33 km to 46 km while elevation varies from 0 km to 1.6 km (Figure 3.6). This corresponds to a change in Moho depth about eight times greater than the corresponding change in the surface relief, which is consistent to the Airy model of isostasy (*e.g.* Kearey et al., 2009).

The variation in thickness of the crust beneath Madagascar is portrayed by the significant change in station static delay (~0.9 s) in the *Pn* tomography. The thin crust across the western sedimentary basin is confirmed by a general negative static delay in contrast with the positive values for the central area. In addition, the slight thinning of the crust in the east coast is shown by positive but small amplitude of the station delays.

In contrast to my findings, Paul and Eakin (2017) concluded that the crust beneath the central region of Madagascar is thinner compared to the eastern coast based on the analysis of records from the permanent stations ABPO in central Madagascar, and FOMA along the southern coast. The main discrepancy arises for FOMA, where their estimate of 44 km contrasts with my estimate of 36 km. Their high estimate is clearly due to their interpretation of a phase in the receiver functions, at ~6 s, as the direct *Ps* conversion from the Moho. However, this arrival could also be a multiple of an intra-crustal phase (at ~2 s). Note that Paul and Eakin (2017) only considered teleseismic events with back azimuths between 82° and 93°. However, looking at other backazimuth ranges a clear phase, presumably the *Ps* wave converted from the Moho discontinuity, is observed at ~4 s. This indicates thinner crust (~36 km) as reported in this study and earlier ones using receiver functions (*e.g.* Rindraharisaona et al., 2013, 2017), which used more than one station along the eastern coast and considered broader back azimuth ranges. In support of this interpretation, crustal thickness estimates from gravimetry imply that the crust thins towards the eastern coast (Fourno and Roussel, 1994; Rakotondraompiana et al., 1999). Therefore, the balance of evidence points to the shallower Moho inferred in our joint inversion but the presence of the strong phase at 6 s for azimuths between ~60° and 130° points to lateral variability, which is beyond the scope of the current study to investigate further.

6.2.2 Crustal lithologies of Madagascar

The variation in the crustal Poisson's ratio is a representative of the change in silicic compositions. Previous studies have suggested that Precambrian terranes

are generally dominated by felsic to intermediate lithologies, with Poisson's ratio raging between 0.25 and 0.26 for continental crusts.

The Precambrian terranes of Madagascar are characterized by average crustal Poisson's ratios that range from 0.2 to 0.3 from this study, with an average of 0.26 ± 0.03. Overall, the crust of these terranes is representative of predominantly felsic to intermediate compositions.

However, the crust in the east coast is more mafic, with a higher Poisson's ratio (0.29 ± 0.04). This is likely the result of the syntectonic emplacement of rift basalts accompanying the separation of India and Madagascar (Storey et al., 1995), imparting a slightly more mafic composition in the crust. Similarly, higher Poisson's ratios of 0.29 ± 0.02 are also observed across the eastern regions of the sedimentary basin and can be explained by the emplacement of rift basalts with mafic composition in the crust, during the rifting of East Gondwana from Africa. However, the presence of high Poisson's ratio sediments in the basin in the uppermost crust is an alternative explanation.

6.2.3 Evidence of little secular variation from seismic properties

Several studies have investigated the relationship between crustal structure and age. For example in terms of thickness, Durrheim and Mooney (1991; 1994) proposed that the Archean crust is thinner compared to the Proterozoic one, ~35 km thick versus ~45 km thick, respectively. Also, they proposed that unlike Proterozoic crust, mafic materials are not present in the Archean crust except if it had undergone post-Archean magmatic manifestations.

The Archean crust of Madagascar has an average thickness of 40 ± 4 km (from 14 stations) while the Proterozoic crust is characterized by an average crustal thickness of 35 ± 4 km (from 10 stations). Archean and Proterozoic crusts are, respectively, characterized by Poisson's ratio of 0.25 ± 0.02 and 0.26 ± 0.04, average crustal shear-wave velocities of 3.7 ± 0.1 km/s for both, mafic lower crust

of 7 km and 4 km, and a similar uppermost mantle shear-wave velocity of 4.4 ± 0.1 km/s.

These estimates show that the Archean crust is slightly thicker than the Proterozoic crust for Madagascar which differs to the observation of Durrheim and Mooney (1991; 1994), but is consistent with the results obtained in several regions of Africa (*e.g.* Tugume et al., 2012; 2013; Kachingwe et al., 2015). However, the seismic properties of both crusts are similar. This suggests a little evidence of secular variation in the crustal structure of Madagascar. However, it is possible that the secular variations may be erased by the Mesozoic drifting of the island or by the volcanic activities during the Cretaceous and the Cenozoic.

6.2.4 Structure of the western sedimentary basin of Madagascar

The sedimentary basin in the western region of Madagascar was a result of the crustal fracturing and opening that preceded the Permian-Triassic break-up of West and East Gondwana. At this period of time, Karoo deposits began to fill the deep grabens associated with the rifting. Therefore, the basin is composed of basal formations consisting of Karoo sediments (that are mainly sandstones), from Late Carboniferous to Early Jurassic age, and younger sediment deposits on top.

The joint inversion of receiver functions and surface wave data in this study estimates the thickness of the western basin of Madagascar that varies in two direction (for the sampled area): from 6-8 km to 2 km, from west to east, and 5-8 km to 4 km from south to north (Figure 3.2). These findings mirror the bidirectional progressive opening to the east and north of the basin (Besairie, 1971; Piqué, 1999b). Rajaomazava (1992) confirmed that the opening of the pull-apart basins of Antsiranana, Mahajanga, and Morondava basins was predominantly controlled by groups of fractures with N85E and N170E orientations. This study presents a solid evidence of the eastward and northward progressive opening and filling of the basin, which was hypothesized by previous

geological studies (*e.g.* Besairie, 1971; Razafimbelo, 1987; Coffin and Rabinowitz, 1988; Piqué, 1999b).

The average shear-wave velocity of the basin is ~2.6 km/s in the eastern and ~2.3 km/s in the western region of the basin. The Karoo facies, which are mainly sandstones, crop out generally along the eastern region of the sedimentary basin (*e.g.* Besairie, 1967; Boast and Nairn, 1982; Wescott and Diggens, 1997; 1998). Therefore, the higher shear-wave velocity (*i.e.* 2.6 km/s) in the eastern region of the basin, which is the typical shear-wave velocity of sandstones and siltstones from laboratory experiments (*e.g.* Castagna et al., 1985; Lee et al., 2003; Brocher, 2005), is an indicator of the dominant Karoo facies. The slow average shear-wave velocity in the western region of the basin can be interpreted as an influence of the younger sediments that overlie the Karoo in the region.

6.2.5 Thermal anomalies and origin of the Cenozoic intraplate volcanism

Several hypotheses about the origin of the Madagascar intraplate volcanism have been proposed: a reactivation of a very old and lithosphere-scale fracture zone during the Cenozoic (Nougier et al., 1986), a link with the Comoros hotspot northwest of Madagascar (Emerick and Duncan, 1982), and hot asthenospheric mantle-derived materials from the African Superplume (Ebinger and Sleep, 1998; Forte et al., 2010), or extension of of the EAR to Comoros and Madagascar (*e.g.* Calais et al., 2006, Saria et al., 2013; Stamps et al., 2014).

Laboratory measurements have confirmed that under high temperature and pressure, the seismic velocities of peridotite, which is the predominant rock in the upper mantle, decrease rapidly if the temperature increases (*e.g.* Sato et al., 1989).

The *Pn* tomography reveals low-*Pn*-velocity (~7.9 km/s) zones in the uppermost mantle beneath Madagascar directly underlying the Cenozoic volcanic provinces in the northern, central, and southwestern region. Also, the joint inversion of

receiver functions and surface wave data found slow uppermost mantle shear-wave velocities (~4.2-4.3 km/s) beneath these regions. These low-seismic-velocity zones are attributed to hot asthenospheric-mantle-derived materials that gave rise to the Cenozoic volcanism in Madagascar.

These upper mantle low-seismic-velocity zones were previously observed by the surface wave tomography of Pratt et al. (2017) and are interpreted as upwelling asthenosphere that resulted in the anomalous high elevation and volcanic eruptions in Madagascar during the Cenozoic era.

However, in comparison with the model of Pratt et al. (2017), the uppermost mantle thermal perturbation inferred by the *Pn* tomography, in this present study, is more limited (Figure 4.2) beneath the regions where the Cenozoic alkaline volcanic provinces are observed. It accordingly suggests that these regions could be the focus of upwelling in the sublithospheric mantle as proposed by Pratt et al. (2017).

In addition, geothermal systems in Madagascar are generally associated with volcano-tectonic or tectonic activity, and are located mainly in volcanic areas, fault zones, or sedimentary basins (Besairie, 1959, Andrianaivo and Ramasinoro, 2015). Location of thermal springs in Madagascar correlates strongly with the low-seismic-velocity zones and supports the presence of hot thermal anomalies beneath these regions (Figure 4.2).

In summary, the Cenozoic volcanism in Madagascar is likely due to geodynamic processes in the upper mantle. This supports all hypotheses linking the volcanism to geodynamic processes in the upper mantle. For example, the link with Comoros hotspot, located northwest of the Madagascar (Emerick and Duncan, 1982, 1983), the lithospheric mantle source of Bardintzeff et al. (2010).

This is also supported by the absence of thinning of the mantle transition zone, obtained from previous chapter, which suggests no evidence for thermal anomalies in the mantle under Madagascar that extend on deep as the mantle transition zone. However, the resolution of this study is sufficient to rule out a

large scale thermal anomaly in the transition zone under Madagascar, but it is not sufficient to rule out the presence of a narrow anomaly as might arise from a plume tail. The low magnitude of *Pn* and *SKS* anisotropy suggesting a vertical flow beneath the low-velocity province around CMAP might be due to the presence of a narrow plume tail. Therefore, although this study supports an upper mantle origin for the Cenozoic volcanism, a narrow mantle plume origin cannot be ruled out.

6.2.6 Seismic anisotropy in the uppermost mantle beneath Madagascar

Previous studies have pointed out that the flow direction of mantle-derived materials and strain history of the upper mantle can be observed from the orientation of the seismic anisotropy (Zhang and Karato, 1995). Silver and Chan (1988) suggested that, on a continental scale, the most recent tectonic activity in the upper mantle defines the fast-polarization direction of the anisotropy. It can be observed from the anisotropy of *Pn* or *SKS* waves. Previous studies revealed that there is a correlation between the fast-polarization directions of *Pn* anisotropy, which best samples the uppermost mantle, and *SKS* shear-wave splitting, which best records the vertically integrated anisotropy of the fastest-split shear waves within the uppermost 200-300 km of the mantle, (*e.g.* Crampin, 1977; Christensen, 1984).

The SELASOMA profile, which ran from the west to the east coast of Madagascar across the Ranotsara shear zone, found that the fast polarization direction changes from NW in the center to NE in the east and west (Reiss et al. 2016). A fast polarization direction of 50°, which is roughly aligned with the direction of absolute plate motion, was proposed to explain the NE orientation. The NW-orientated polarization was attributed to fossil anisotropy produced by a ~150-km-wide ductile deformation zone of ductile deformation near the Ranotsara shear zone. Ramirez et al. (submitted), using the MACOMO data, have suggested that the EW-trending of the *SKS* fast-polarization direction in the northern region

of Madagascar is the result of a NE-trending mantle flow guided by the African superplume or plate motion and subsequently reoriented by a SW-trending mantle flow from the Comoros hot spot. A circular pattern of anisotropy was observed around CMAP and the Antananarivo terrane by Ramirez et al. (submitted). They suggested that the origin of the circular feature could be the interaction between a NE-trending flow, which is likely from the African Superplume or the absolute plate motion, and the upwelling of the asthenospheric mantle beneath CMAP. Ramirez et al. (submitted) have attributed the N to NE-oriented anisotropy observed in the southwesten region of Madagascar to a small-scale flow in the asthenosphere. They have attributed the anisotropy in the southern area of Madagascar to a fossil anisotropy as it is aligned to the ~N-S direction of the shear zones in this region.

The fast-polarization of *Pn* anisotropy observed in the northern region of Madagascar, from this study, is oriented NW-SE (Figure 4.6). This is aligned to the orientation of the Tsaratanàna alkaline complex (*i.e.* the NMAP) and the Sandrakota shear zone. This suggests that the anisotropy in the uppermost mantle in this region can be attributed, also, to a fossil anisotropy. Note that the SKS anisotropy in Ramirez et al. (submitted) have observed a NE direction of anisotropy in this region and have attributed it to a NE-oriented mantle flow controlled by the African superplume or the absolute plate motion, which is modified by a SW-trending mantle flow from the Comoros hot spot. On the other hand, Silver and Chan (1988) have suggested that the most recent tectonic activity in the upper mantle defines the fast-polarization direction of the anisotropy in the region. Therefore, an alternative explanation is that the NE trending shown by the *SKS* could be overprinted, on top, by recent strain, which is likely the recent tectonic activity that is linked to the Cenozoic volcanic manifestation.

Both *Pn* and *SKS* anisotropies broadly present similar orientation, a NW-SE trending (Figure 4.7), in the area south to the CMAP. The area encompasses the southern portion of the Ikalamavony domain and aligns to the orientation of several shear zones (such as the Ranotsara, the Beraketa, the Ihosy, and the Zazafotsy shear zones) in this region. Reiss et al. (2016) and Ramirez et al.

(submitted) have interpreted the NW orientation of the SKS fast polarization to be the result of a fossil anisotropy, which is linked to a ~150-km-wide ductile deformation zone. Therefore, the *Pn* anisotropy can be, also, attributed to a fossil anisotropy for this region.

The *Pn* anisotropy is oriented from E-W to NE-SW along the western sedimentary basin, around the Morondava basin, of Madagascar. Reiss et al. (2016) interpreted the NE-trending along the western sedimentary as an influence of the mantle flow from plate motion; while Ramirez et al. (submitted), for the same region, have argued that it is a component of the circular pattern of anisotropy controlled by the upwelling astenosphere around CMAP. The orientation of the fast-polarization of *Pn* anisotropy for these regions can be, then, attributed either to the mantle flow from African superplume or the plate motion. However, as seen in Chapter 3, the lithosphere of this region has been subjected to a substantial deformation, streched and thinned, during the rifting from Africa. Consequently, the orientation of the *Pn* anisotropy, NE-SW-oriented, is likely portraying the strain from the rifting.

The separation of the Somalian and Nubian plates initiates around the Afar region and extends to the south along the EARs. However, the trajectory of its southernmost extension is controversial. Analyses of geodesy, GPS data, seismicity, bathymetry, and tectonics in the surrounding regions suggest the formation of microplates, bounded by diffuse boundaries, connecting the EARs with the Southwest Indian Ridge (e.g., Chu and Gordon 1999; Calais et al., 2006, Saria et al., 2013; Stamps et al., 2014). It has been suggested that a diffuse plate boundary passes through the central part of Madagascar, detaching the Lwandle plate from the Somalian plate (Horner-Johnson et al., 2007; Saria et al., 2013; Stamps et al. 2014). In fact, this region of Madagascar is characterized by moderate seismicity and presents an E-W extensional stress (Bertil and Regnoult, 1998; Rindraharisaona et al., 2013; Rakotondraibe et al., in prep). Our observation from the *Pn* anisotropy does not show strong evidence indicating the Lwandle plate edge. Also, the location of the low-*Pn*-velocity zone beneath the CMAP is distant to the presumed location of the edge of Lwandle plate.

6.2.7 Island uplift: evidence of thermal buoyancy

The Airy model of isostatic equilibrium observed across the length of Madagascar (Figure 3.6) breaks down in the northern part of the island, where the crust is less than 35 km thick while the topography is > 1 km. Overall, the average thickness of the crust from all the stations is ~35 km while their average elevation is ~500 m. This elevation is anomalously high for this slightly thinner-than-average crustal thickness. Therefore, an additional mechanism is required to explain this broad signature of uplift, although the island had not undergone any tectonic activity in the past 85 Myr.

The anomalous uplift of Madagascar suggests a source of dynamic topography that might be provided by mantle upwelling flows related to the upper mantle thermal anomaly observed beneath the Cenozoic volcanic provinces.

Previous studies proposed an extensive uplift of Madagascar, at a rate of 0.4 mm/yr, since the Early Miocene (*ca.* 15 Ma). In these studies, the uplift was interpreted from: the high occurrence of lavakas that are surprisingly correlated with the seismicity, the normal faulting trending E-W direction, and the shape of river valleys (Grimison and Chen, 1988; Bertil and Regnoult, 1998; de Wit, 2003; Cox et al., 2010; Roberts et al., 2012; Rindraharisaona et al., 2013).

6.3 General conclusion

This study presents the first local-scale seismological study of the deep structure of the whole Madagascar, from the surface to the mantle transition zone. Briefly, the main goals of the research are: to study the structure of the deep structure of Madagascar, to infer the geodynamic links between the past tectonic histories and the inferred structure, and to evaluate candidate models for the origin of the Cenozoic volcanism. The main findings of the study reflect the strong contribution of the tectonic history of Madagascar to the current geology of the island.

In this study, the crust beneath Madagascar was investigated using two different receiver function techniques, a stacking procedure called the *H-κ* stacking method (Zhu and Kanamori, 2000), and a joint inversion of receiver functions and surface wave dispersion measurements (Julià et al., 2000). New point estimates of sedimentary basin and crustal thicknesses, shear-wave velocity structure, average crustal Poisson's ratio, and average shear-wave velocity of basin/crust/uppermost mantle were obtained. Then, seismic tomography was performed to image the lateral variation of both the velocity and anisotropy of *Pn* waves (Hearn, 1996) in the uppermost mantle beneath Madagascar. This technique identified the low-seismic-velocity zone directly underlying the Cenozoic alkaline volcanic provinces in Madagascar. Finally, the thickness of mantle transition zone beneath the island was estimated using two different stacking techniques (Owens, 2000): a single-station and a common-conversion point stacking of receiver functions. First, the depths of the *410* and *660* were discontinuities were determined. Variations in the thickness of the mantle transition zone are indicators of the presence or absence of anomalously hot or cold regions around the transition zone.

6.3.1 Crustal structure beneath Madagascar

The thickness of the crust beneath Madagascar ranges between 18 km to 46 km. This large range is reflected by the significant variation of the station static delays used in the tomographic study. The central part is characterized by thick crust (between 36-46 km with an average thickness of 42 km), the northern region has a crust that ranges between 31-36 km thick (average thickness of ~33 km), the thickness of the crust across the western basin ranges from 18 km to 36 km (average thickness of 30 km), and the crust along the east coast ranges between 31 to 43 km (average thickness of 36 km), and the southern region is characterized by crust between 36 km and 38 km (average of 37 km).

Results from the sampled area show a bidirectional thinning of the sedimentary basin in the western region of Madagascar: from 5-8 km to 4 km, northward, and

from 6-8 km to 2 km, eastward, reflecting the eastwardly and northwardly progressive opening and filling of the basin in the Permian-Triassic Periods. In addition, the Mesozoic Era rifting of Madagascar from Africa (*ca.* 165-130 Ma) stretched and thinned the crust beneath the sedimentary basin by 12 to 20 km, relative to the unrifted Precambrian crust of Madagascar and the eastern region of Africa.

The crust of Madagascar is representative of predominantly felsic to intermediate compositions. However, the crust is more mafic along the east coast and eastern region of the sedimentary basin, suggesting the syntectonic emplacement of rift basalts accompanying the Mesozoic rifting from Africa and India.

A slight thinning of the crust is also found along the eastern coast of the island (~36 km) compared to the thickness (~ 42 km) of the crust in the inland. This may have been caused by the erosion of lithosphere during the migration of Madagascar/India over the Marion hotspot (*ca.* 95-85 Ma) and India broke away which resulted in crustal uplift.

A little evidence of secular variation is observed for the Precambrian crust in Madagascar. The Archean terranes are characterized by an average 40-km-thick crust, an average Poisson's ratio of 0.25, an average crustal shear-wave velocity of 3.7 km/s, and an average thickness of mafic lower crust of 7 km; while the Proterozoic terranes have an average crustal thickness of 35 km, a Poisson's ratio of 0.26, an average crustal shear-wave velocity of 3.7 km/s, and an average thickness of mafic lower crust of 4 km.

A good correlation is observed between station elevation and crustal thickness across Madagascar, with about a 1 km change in elevation at the surface of Madagascar corresponding to a change of 8 km in Moho topography. However, surface elevations are anomalously high compared to crustal thicknesses, especially in the northern region, suggesting a source of dynamic topography that might be provided by mantle upwelling flows related to the upper mantle thermal anomaly. That would also explain the slow uppermost mantle *Pn* (~7.9 km/s) and

shear-wave (4.2-4.3 km/s) velocities and episodes of Cenozoic volcanic activity in Madagascar

6.3.2 *Pn* velocity and anisotropy: origin of the Cenozoic volcanism and tectonic framework

The uppermost mantle beneath Madagascar is characterized by average shear-wave velocity of ~4.4 km/s and *Pn* velocity of ~8.1 km/s. However, significant low-shear-wave-velocity (~4.2-4.3 km/s) and low-*Pn*-velocity (~7.9 km/s) zones underlie and coincide with the Cenozoic alkaline provinces in the northern, central, and northwestern region of the island, respectively the NMAP, CMAP, and SMAP. These low-seismic-velocity zones are attributed to upwelling of hot mantle materials that gave rise to the Cenozoic volcanic activities in Madagascar.

The orientation of the fast-polarisation of *Pn* anisotropy in the northern and south-central of Madagascar presents alignments to the existing geological framework, such as the alkaline volcanic complex, around the NMAP, and shear zones, in both regions. These likely suggest that the anisotropy in the uppermost mantle in these regions can be attributed to a fossil anisotropy. The *Pn* anisotropy in the western region, around the Morondava basin, can be attributed either to the mantle flow from the plate motion, the African superplume, or from the mark left by the stretching and thinning of the lithosphere during the Mesozoic rifting from Afica.

Mantle transition zone thickness varies between 230 km and 265 km beneath Madagascar, which is consistent with the global average of 240-260 km. Departures from the global average fall within the uncertainty of ± 10 km in the estimation of the depth of 410 km and 660 km discontinuities. There is no detectable thinning of the mantle transition zone and thus no evidence for the thermal anomaly in the mantle under Madagascar that extend on deep as the mantle transition zone. This finding supports an upper mantle origin for the Cenozoic volcanism in Madagascar. However, the resolution of this study is sufficient to exclude a large scale thermal anomaly in the transition zone under

Madagascar, but it is not sufficient to rule out the presence of a narrow anomaly as might arise from a plume tail.

6.4 Recommendations for future studies

I. A *S*-wave receiver functions analysis should be conducted to compare the result from the *P*-wave receiver functions. The *S-to-p* converted phases from any seismic discontinuities arrive earlier than the incident *S* wave and therefore are separated from the *S*-arrival and their multiples. The method is more appropriate for stations located in the sedimentary basin where multiple reverberations from the boundary basin-basement usually hide the actual *P-to-s* conversion from Moho for the *P*-wave receiver functions. It was also successfully applied for the mantle transition zone study.

II. The *3D* velocity model of Pratt et al. (2017) should be used in the mantle transition zone study when migrating receiver functions to depth before the stacking procedure to account for the low-velocity-zone (a negative shear-wave velocity anomaly of about -4 % relative to PREM) in the upper mantle beneath the Cenozoic volcanic provinces. This is to improve the estimation of the arrival time of the *P410s* and *P660s* conversions beneath these regions. Mulibo and Nyblade (2013) showed the significant effect of the *3D* velocity model in the estimation of the 410 km and 660 km discontinuities location compared with the previous study of Owens (2000) in the same region.

III. A body wave tomography of the whole mantle beneath Madagascar is recommended to be conducted to investigate the possible existence of a narrow thermal anomaly as might arise from a plume tail. This would not be resolved by the study of the mantle transition zone as this technique is mainly used to detect a large scale thermal anomaly.

References

Agrawal, P.K., Pandey, O.P., and Negi, J.G., 1992. Madagascar; a continental fragment of paleo-super Dharwar craton of India. *Geology*, 20, 543 - 546.

Akaogi, M., Ito, E., and Navrotsky, A., 1989. Olivine-modified spinel-spinel transitions in the system Mg_2SiO_4-Fe_2SiO_4: Calorimetric measurements, thermochemical calculation, and geophysical application. *Journal of Geophysical Research*, 94, 15671 - 15685.

Amante, C., and Eakins, B.W., 2009. ETOPO1 1 arc-minute global relief model: procedures, data sources and analysis. *NOAA Technical Memorandum NESDIS NGDC-24. National Geophysical Data Center, NOAA.*

Ammon, C.J., 1991. The isolation of receiver effects from teleseismic P waveforms. *Bulletin of the Seismological Society of America*, 81, 2504 - 2510.

Ammon C.J., 1997. An overview of receiver-function analysis. Department of Geosciences Pennsylvania State University. *Unpublished notes*.

Ammon, C.J., Randall, G.E., and Zandt, G., 1990. On the nonuniqueness of receiver function inversions. *Journal of Geophysical Research*, 95, 15303 - 15318.

Andrianaivo, L., and Ramasiarinoro, V.J., 2015. Geothermal energy resources of Madagascar – Country update. *Proceedings Word Geothermal Congrees 2015*, Australia.

Ashwal, L.D., Wiedenbeck, and M., Torvsik, T.H., 2017. Archaean zircons in Miocene oceanic hotspot rocks establish ancient continental crust beneath Mauritius. *Nature Communications*, 8, doi:10.1038/ncomms14086.

Backus, G. E., 1965. Possible forms of seismic anisotropy of the uppermost mantle under oceans. *Journal of Geophysical Research*, 70, 3429 - 3439.

Bagley, B., and Nyblade, A.A., 2013. Seismic anisotropy in eastern Africa, mantle flow, and the African superplume. *Geophysical Research Letters*, 40, 1500 - 1505.

Bamford, D., 1977. Pn velocity anisotropy in a continental upper mantle. *Geophysical Journal of the Royal Astronomical Society*, 49, 29 - 48.

Bardintzeff, J-M., Liegeois, J-P., Bonin, B., Bellon, H., and Rasamimanana, G., 2010. Madagascar volcanic provinces linked to the Gondwana break-up: Geochemical and isotopic evidences for contrasting mantle sources. *Gondwana Res*earch, 18, 295 - 314.

Bassin, C., Laske, G., and Masters, G., 2000. The current limits of resolution for surface wave tomography in North America. *EOS Transactions American Geophysical Union*, 81, F897.

Besairie, H., 1959. Contribution à l'étude des sources minérales et des eaux souterraines de Madagascar. *Document Bureau Géologique Madagascar n°92*,

Service Géologique, Antananarivo. Ministère de l'Industrie et des Mines, Direction des Mines et de l'Energie.

Besairie, H., 1967. La géologie du bassin de Morondava à Madagascar. *Document Bureau Géologique Madagascar n°175, Service Géologique de Madagascar*, v.2.

Besairie, H., 1968. Description géologique du massif ancien de Madagascar, Premier volume: Centre Nord et Centre Nord-Est, *Document Bureau Géologique Madagascar n°177a, Service Géologique*, Antananarivo. Ministère de l'Industrie et des Mines, Direction des Mines et de l'Energie, 117 pp.

Besairie, H., 1969. Description géologique du massif ancien de Madagascar, Deuxième volume: La regioncotière orientale entre le Mangoro et Vangaindrano. *Document Bureau Géologique Madagascar n°177b, Service Géologique*, Antananarivo. Ministère de l'Industrie et des Mines, Direction des Mines et de l'Energie, 67.

Besairie, H., 1971. Tectonique de Madagascar. Tectonique de l' Afrique. *Sciences de la Terre UNESCO Paris*, 549 - 558.

Besairie, H., 1972. Géologie de Madagascar. Les terrains sédimentaires. *Annual Géologique de Madagascar*, Antananarivo, 35.

Besairie, H., 1973. Brève revue de volcanisme à Madagascar. *Colloque sur les régions volcaniques tropicales, Pub. Ass. Géogr.*, Madagascar, 18.

Besse, J. and Courtillot, V., 1988. Paleogeographic maps of the Indian Ocean bordering continents since the Upper Jurassic. *Journal of Geophysical Research*, 93, 11791 - 11808.

Bertil, D., and Regnoult, J.M., 1998. Seismotectonics of Madagascar. *Tectonophysics*, 294, 57 - 74.

Bina, C.R., and Hellfrich, G., 1994. Phase transition Clapeyron slopes and transition zone seismic discontinuity topography. *Journal of Geophysical Research*, 99, 15853 - 15860.

Black, P.R., and Braille, L.W., 1982. Pn velocity and cooling of continental lithosphere. *Journal of Geophysical Research*, 87, 10557 - 10563.

Boast, J., and Nairn, A.E.M., 1982. An outline of the geology of Madagascar. In the Ocean basins and margins. *New York, Plenum Press*, 6, 649 - 696.

Bock, G., 1994. Synthetic seismogram images of upper mantle structure: No evidence for a 520-km discontinuity. *Journal of Geophysical Research*, 99, 15843 - 15851.

Brocher, T.A., 2005, Empirical relations between elastic wavespeeds and density in the Earth's crust. *Bulletin of the Seismological Society of America*, 95, 2081 - 2092.

Calais, E., Ebinger, C.J., Hartnady, C., and Nocquet, J.M., 2006. Kinematics of the East African rift from GPS and Earthquake slip vector data, in the afar volcanic province within the East African rift system, edited by Yirgu, G., Ebinger, C.J., and Maguire, P.K.H. *Geological Society Special Publication*, 259, 9 - 22.

Cassidy, J.F., 1992. Numerical experiments in broadband receiver function analysis. *Bulletin of the Seismological Society of America*, 82, 1453 - 1474.

Castagna, J.P., Batzle, M.L., and Eastwood, R.L., 1985. Relationships between compressional-wave and shear-wave velocities in clastic silicate rocks. *Geophysics*, 50, 571 - 581.

Christensen, N.I., 1984. The magnitude, symmetry and origin of upper mantle anisotropy based on fabric analyses of ultramafic tectonites. *Geophysical Journal of the Royal Astronomical Society,* 76, 89 - 111.

Christensen, N.I., 1996. Possion's ratio and crustal seismology. *Journal of Geophysical Research*, 101, 3139 - 3156.

Christensen, N.I., and Mooney, W.D., 1995. Seismic velocity structure and composition of the continental crust: a global view. *Journal of Geophysical Research*, 100, 9761 - 9788.

Coffin, M.F., and Rabinowitz, P.D., 1988. Evolution of the conjugate East African-Madagascan margins and the western Somali Basin. *Special Papers - Geological Society of America,* 226, 78.

Collins, A.S., 2000. The tectonic evolution of Madagascar: its place in the east African Orogen. *Gondwana Research.,* 3, 549 - 552.

Collins, A.S., 2006. Madagascar and the amalgamation of the central Gondwana. *Gondwana Research*, 9, 3 - 16.

Collins, A.S., and Pisarevsky, S.A., 2005. Amalgamating eastern Gondwana: The evolution of the circum-Indian orogens. *Earth-Science Reviews*, 71, 229 - 270, doi: 10.1016/j.earscirev.2005.02.004

Collins A.S., and Windley, B.F., 2002. The tectonic evolution of central and northern Madagascar and its place in the final assembly of Gondwana. *Journal of Geology,* 110, 325 - 340.

Cox, R., Zentner, D.B., Rakotondrazafy, A.M., and Rasoazanamparany, C.F., 2010. Shakedown in Madagascar: Occurrence of lavakas (erosional gullies) associated with seismic activity. *Geology*, 38, 179 - 182.

Crampin, S., 1977. A review of the effects of anisotropic layering on the propagation of seismic waves. *Geophysical Journal of the Royal Astronomical Society*, 49, 9 - 27.

Crotwell, H.P., Owens, T.J., and Ritsema, J., 1999. The TauP toolkit: Flexible seismic travel-time and ray-path utilities. *Seismological Research Letters,* 70, 154 - 160.

Darracott, B.W., 1974. On the crustal structure and evolution of southeastern Africa and the adjacent Indian Ocean. *Earth and Planetary Science Letters,* 24, 282 - 290.

Davis, J.P., Kind, R., and Sacks, I.S., 1989. Precursors to P'P' re-examined using broad-band data. *Geophysical Journal International,* 99, 595 - 604.

Deuss, A., and Woodhouse, J., 2001. Seismic observations of splitting of the mid-transition zone discontinuity in Earth's mantle. *Science*, 294, 354 - 357.

de Wit, M.J., Bowring S.A., Ashwal L.D., Randianasolo L.G., Morel V.P.I., and Rambeloson, R.A., 2001. Age and tectonic evolution of Neoproterozoic ductile shear zones in southwestern Madagascar, with implications for Gondwana studies. *Tectonics*, 20, 1 - 45.

de Wit, M.J., 2003. Madagascar: heads it's a continent, tails it's an island. Annual Review of Earth and Planetary Sciences, 31, 213 - 248.

Durrheim, R.J., and Mooney, W.D., 1991. Archean and Proterozoic crustal evolution: evidence from crustal seismology. *Geology*, 19, 606 - 609.

Durrheim, R.J., and Mooney, W.D., 1994. Evolution of the Precambrian lithosphere: seismological and geochemical constraints. *Journal of Geophysical Research*, 99, 15359 - 15374.

Du Toit., 1937. Our wandering continents. In: *Oliver Boyd, Edinburg*, 366p.

Dziewonski, A.M. and Anderson, D.L., 1981. Preliminary reference Earth model. *Physics of the Earth and Planetary Interiors*, 25, 297 - 356.

Ebinger, C.J., and Sleep, N.H., 1998. Cenozoic magmatism throughout east Africa resulting from impact of a single plume. *Nature*, 395, 788 - 791.

Efron, B., and Tibshirani, R., 1991. Statistical data analysis in the computer age. *Science*, 253, 390 - 395.

Emerick, C.M., and Duncan, R.A., 1982. Age progressive volcanism in the Comoros Archipelago, western Indian Ocean and implications for Somali plate tectonics. *Earth and Planetary Science Letters*, 60, 415 - 428.

Emerick, C.M., and Duncan, R.A., 1983. Errata. *Earth and Planetary Science Letters*, 62, 439.

Emry, E.L., Nyblade, A.A., Julià, J., Anandakrishnan, S., Aster, R.C., Wiens, D.A., Huerta, A.D., and Wilson, T.J., 2015. The mantle transition zone beneath West Antarctica: Seismic evidence for hydration and thermal upwellings. *Geochemistry, Geophysics, Geosystems*, 16, 40 - 58.

Forster, R., 1975. The geological history of the sedimentary basin of southem Mozambique, and some aspects of the origin of the Mozambique Channel. *Paleo (Geography-Climatology-Ecology),* 17, 267 - 287.

Forte, A.M., Quéré, S., Moucha, R., Simmons, N.A., Grand, S.P., Mitrovica, J.X., and Rowley, D.B. 2010. Joint seismic-geodynamic-mineral physical modelling of African geodynamics: A reconciliation of deep-mantle convection with surface geophysical constraints. *Earth and Planetary Science Letters*, 295, 329 - 341.

Fourno, J.P., and Roussel, J., 1994. Imaging of the Moho depth in Madagascar through the inversion of gravity data: geodynamic implications. *Terra Nova*, 6, 512 - 519.

Geiger, L., 1912. Probability method for the determination of Earthquake epicenters from the arrival time only (translated from Geiger's 1910 German article). *Bulletin of St. Louis University*, 8, 56 - 71.

Gnos, E., Immenhauser, A., and Peters, T., 1997. Late Cretaceous/early Tertiary convergence between the Indian and Arabian plates recorded in ophiolites and related sediments. *Tectonophysics*, 271, 1 - 19.

Goes, S., and van der Lee, S., 2002. Thermal structure of the North American uppermost mantle inferred from seismic tomography. *Journal of Geophysical Research*, 107, 10:1029/2000JB000049.

Gossler, J. and Kind, R., 1996. Seismic evidence for very deep roots of continents. *Earth and Planetary Science Letters*, 138, 1 - 13.

Grimison N.L., and Chen W.P., 1988. Earthquakes in the Davie Ridge-Madagascar region and the southern Nubian-Somalian plate boundary. *Journal of Geophysical* Research, 93, 10439 - 10450.

Gu, Y.J., Dziewonski, A.M., and Agee, C.B., 1998. Global de-correlation of the topography of transition zone discontinuities. Earth and Planetary Science Letters, 157, 57 - 67.

Gurrola, H., Minster, J.B., and Owens, T., 1994. The use of velocity spectrum for stacking receiver functions and imaging upper mantle discontinuities. *Geophysical Journal International*, 117, 427 - 440.

Hansen, S.E., Nyblade, A.A., and Benoit, M.H., 2012. Mantle structure beneath Africa and Arabia from adaptively parameterized P-wave tomography: Implications for the origin of Cenozoic Afro-Arabian tectonism. *Earth and Planetary Science Letters*, 319 - 320, 23 - 34.

Hearn, T.M., Beghoul, N., and Barazangi, M., 1991. Tomography of the western United States from regional arrival times. *Journal of Geophysical Research*, 96, 16369 - 16381.

Hearn, T.M., 1996. Anisotropic Pn tomography in the western United States. *Journal of Geophysical Research: Solid Earth*, 101, 8403 - 8414.

Hearn, T.M., and Ni, J.F., 1994. Pn velocities beneath continental collision zones: the Turkish-Iranian Plateau. *Geophysical Journal International*, 117, 273 - 283.

Hess, H. H., 1964. Seismic anisotropy of the uppermost mantle under oceans. *Nature*, 203, 629 - 631.

Holbrook, W.S., Mooney, W.D., and Christensen, N.I., 1992. The seismic velocity structure of the deep continental crust. In *Continental Lower Crust*, Chapter 1, 1 - 43, eds Fountain, D.M., Arculus, R., and Kay, R.W., Elsevier.

Horner-Johnson, B.C., Gordon, R.G., and Argus, D.F., 2007. Plate kinematic evidence for the existence of a distinct plate between the Nubian and Somalian plates along the Southwest Indian Ridge. *Journal of Geophysical Research*, 112, B05418.

Huerta, A.D., Nyblade, A.A., and Reusch, A.M., 2009. Mantle transition zone structure beneath Kenya and Tanzania: more evidence for a deep-seated thermal upwelling in the mantle. *Geophysical Journal International*, 177, 1249 - 1255.

Jöns, N., and Schenk, V., 2008. Relics of the Mozambique Ocean in the central East African Orogen: evidence from the Vohibory Block of southern Madagascar. *Journal of Metamorphic Geology*, 26, 17 - 28.

Julià J., and Mejía J., 2004. Thickness and *Vp*/*Vs* ratio variation in the Iberian crust. *Geophysical Journal International*, 156, 59 - 72.

Julià, J., Ammon, C.J., and Herrmann, R.B., 2003. Lithospheric structure of the Arabian Shield from the joint inversion of receiver functions and surface wave group velocities. *Tectonophysics*, 371, 1 - 21.

Julià, J., Ammon, C.J., Herrmann, R.B., and Correig, A.M., 2000. Joint inversion of receiver function and surface wave dispersion observations. *Geophysical Journal International*, 143, 99 - 112.

Julià, J., Ammon, C.J., and Nyblade, A.A., 2005. Evidence for mafic lower crust in Tanzania, East Africa, from joint inversion of receiver functions and Rayleigh wave dispersion velocities. *Geophysical Journal International*, 162, 555 - 562.

Julià, J., Assumpção, M., and Rocha, M.P., 2008. Deep crustal structure of the Paranã Basin from receiver functions and Rayleigh-wave dispersion: evidence for a fragmented cratonic root. *Journal of Geophysical Research*, 113, B08318.

Kachingwe, M., Nyblade, A., and Julià, J., 2015. Crustal structure of Precambrian terranes in the southern African subcontinent with implications for secular variation in crustal genesis. *Geophysical Journal International*, 202, 533 - 547.

Karato, S.I., and Jung, H., 1998. Water, partial melting and the origin of the seismic low velocity and high attenuation zone in the upper mantle. *Earth and Planetary Science Letters*, 157, 193 - 207.

Karato, S., and Wu, P., 1993. Rheology of the upper mantle: A synthesis. *Science*, 260, 771 - 778.

Kearey, P., Klepeis, K.A., and Vine, F.J., 2009. In: Global Tectonics (3rd edition), *Chichester*, Wiley-Blackwell.

Kennett, B.L.N., and Engdahl, E.R., 1991. Travel times for global Earthquake location and phase identification. *Geophysical Journal International*, 105, 429 - 465.

Kennett, B.L.N., Engdahl, E.R., and Buland, R., 1995. Constraints on seismic velocities in the Earth from travel times. *Geophysical Journal International*, 122, 108 - 124.

Kgaswane, E.M., Nyblade, A.A., Julià, J., Dirks, P.H.G.M., Durrheim, R.J., and Pasyanos, M.E., 2009. Shear wave velocity structure of the lower crust in Southern Africa: evidence composition heterogeneity within the Archean and Proterozoic terrains. *Journal of Geophysical Research*, 114, B12304.

Kind, R., and Vinnik, L.P., 1988. The upper mantle discontinuities underneath the GRF array from P-to-S conversed phases. *Journal of Geophysics*, 62, 138 - 147.

Kusky, T.M., Abdelsalam, M.G., Tucker, R.D., Stern, R.J., 2003. Evolution of the East African and related Orogens, and the assembly of Gondwana. *Precambrian Research*, 123, 81 - 337.

Kusky, T.M., Toraman, E., and Raharimahefa, T., 2007. The Great Rift Valley of Madagascar: An extension of the Africa-Somali diffusive plate boundary? *Gondwana Research*, 11, 577 - 579.

Lahr, J.C, 1984. Description of the weighted regression and quality estimation used in the Earthquake location program HYPOELLIPSE. *Open-File Report*, 84 - 766.

Langston, C.A., 1979. Structure under Mount Rainier, Washington, inferred from teleseismic body waves. *Journal of Geophysical Research*, 84, 4749 - 4762.

Lawrence, J.F., and Shearer, P.M., 2006. A global study of transition zone thickness using receiver functions. *Journal of Geophysical Research*, 111, B06307.

Lee, W.H.K., Kanamori, H., Jennings, P.C., and Kisslinger, C., 2003. International Handbook of Earthquake & Engineering Seismology: London, *Academic Press*, 1591 p.

Ligorria, J.P., and Ammon, C.J., 1999. Iterative deconvolution and receiver function estimation. *Bulletin of the Seismological Society of America*, 89, 1395 - 1400.

Long, M.D., and Silver, P.G., 2009. Shear wave splitting and mantle anisotropy: Measurements, interpretations, and new directions. *Surveys in Geophysics*, 30, 407 - 461.

Lowrie, W., 2007. In: Fundamentals of geophysics. Cambridge, *Cambridge University Press*, p191.

Mahoney, J., Nicollet, C., and Dupuy, C., 1991. Madagascar basalts: tracking oceanic and continental sources. *Earth and Planetary Science Letters*, 104, 350 - 363.

Martelat, J.-E., Lardeaux, J.-M., Nicollet, C., and Rakotondrazafy, R., 2000. Strain pattern and Late Precambrian deformation history in southern Madagascar. *Precambrian Research*, 102, 1 - 20.

Martelat, J.-E., Randrianasolo, B., Schulmann, K., Lardeaux, J.-M., and Devidal, J.-L., 2014. Airborne magnetic data compared to petrology of crustal scale shear zones from southern Madagascar: A tool for deciphering magma and fluid transfer in orogenic crust. *Journal of African Earth Sciences*, 94, 74 - 85.

Mascle, J., Mougenot, D., Blarez, E., Marinho, M., and Virlogeux, P., 1987. African transform continental margins: examples from Guinea, the Ivory Coast and Mozambique. *Geological Journal*, 22, 537 - 567.

Matsushima, S., and Akeni, K., 1977. Elastic wave velocities in the ichinome-gata ultramafic nodules: composition of the uppermost mantle [A]. In: *High-pressure Research: Application in Geophysics [C]*, eds Murli H. Manghnani and Syun-iti Akimoto., New York: Academic Press, 65 - 76.

Melbourne, T., and Helmberger, D., 1998. Fine structure of the 410-km discontinuity. Journal of Geophysical Research, 103, 10091 - 10102.

Menke, W., 1984. Geophysical data analysis: discrete inverse theory. *Academic Press*, Orlando.

Michon, L., 2016. The volcanism of the Comores archipelago integrated at a regional scale. In: Bachelery, P., Lenat, J.-F., Di Muro, A., Michon, L. (Eds.), *Active Volca-noes of the Southwest Indian Ocean: Piton de la Fournaise and Karthala. Active Volcanoes of the World*. Springer-Verlag, Berlin, Heidelberg, 333 - 344.

Mooney, W.D., and Braille, L.W., 1989. The seismic structure of the continental crust and upper mantle of North America. In: The Geology of North America-An *Overview*, Vol. A, pp. 39-52, eds Bally, A.W., and Palmer, A.R., *Geol. SOC. Am.*, Boulder, CO.

Mulibo, G.D., and Nyblade, A.A, 2013. Mantle transition zone thinning beneath eastern Africa: Evidence for a whole-mantle superplume structure. *Geophysical Research Letter*, 40, doi:10.1002/grl.50694.

Nédélec, A., Ralison , B., Bouchez, J. L., and Grégoire, V., 2000. Structure and metamorphism of the granitic basement around Antananarivo: a key to the Pan-African history of central Madagascar and its Gondwana connections. *Tectonics*, 19, 997 - 1020.

Nicollet, C., 1990. Crustal evolution of the granulites of Madagascar. *In: Vielzeuf, D. and Vidal, Ph. (Eds.), Granulites and crustal evolution*, 291 - 310.

Norton, I.O., and Sclater, J.G., 1979. A model for the evolution of the Indian Ocean and the breakup of Gondwanaland. *Journal of Geophysical Research*, 84, 6803 - 6830.

Nougier, J., Cantagrel, J.M., and Karche, J.P., 1986. The Comoros archipelago in the western Indian Ocean: volcanology, geochronology and geodynamic setting. *Journal of African Earth Sciences*, 5, 135 - 144.

Owens, T.J., and Zandt, G., 1985. The response of the continental crust-mantle boundary observed on broadband teleseismic receiver functions. *Geophysical Research Letters*, 12, 705 - 708.

Owens, T.J., Zandt, G., and Taylor, S.R., 1984. Seismic evidence for an ancient rift beneath the Cumberland Plateau, Tennessee; a detailed analysis of broadband teleseismic P-waveforms. *Journal of Geophysical Research*, 89, 7783 - 7795.

Owens, T.J., Nyblade, A.A., Gurrola, H., and Langston, C.A., 2000. Mantle transition zone structure beneath Tanzania, East Africa. *Geophysical Research Letters*, 27, 827 - 830.

Paige, C.C., and Saunders, M.A., 1982. Algorithm 583: LSQR: Sparse linear equations and least squares problems. *ACM Transactions on Mathematical Software (TOMS)*, 8, 195 - 209.

Paige, C.C., and Saunders, M.A., 1982. LSQR: An algorithm for sparse linear equations and sparse least squares. *ACM Transactions on Mathematical Software (TOMS)*, 8, 43 - 71.

Pasyanos, M.E., and Nyblade, A.A., 2007. A top to bottom lithospheric study of Africa and Arabia. Tectonophysics, 444, 27 - 44.

Paul, J.D., and Eakin, C.M., 2017. Mantle upwelling beneath Madagascar: evidence from receiver function analysis and shear wave splitting. *Journal of Seismology*, 21, 825 - 836.

Pearson, D.G., Brenker, F.E., Nestola, F., McNeill, J., Nasdala, L., Hutchison, M.T., Matveev, S., Mather K., Silversmit G., Schmitz S, Vekemans B., and Vincze L., 2014. Hydrous mantle transition zone indicated by ringwoodite included within diamond. *Nature*, 507, 221 - 224.

Perry, H.K.C., Jaupart, C., Mareschal, J.-C., and Shapiro, N.M., 2006. Upper mantle velocity-temperature conversion and composition determined from seismic refraction and heat flow. *Journal of Geophysical Research,* 111, B07301.

Piqué, A., 1999a. The geological evolution of Madagascar: an introduction. *Journal of African Earth Sciences*, 28, 919 - 930.

Piqué, A., 1999b. The initiation and development of the Morondava Basin (Madagascar) from the Late Carboniferous to the Middle Jurassic: sedimentary, palaeontological and structural data. *Journal of African Earth Sciences*, 28, 931 - 948.

Powell, C.M., Li, Z.X., McElhinny, M.W., Meert, J.G., and Park, J.K., 1993. Paleomagnetic constraints on timing of the Neoproterozoic breakup of Rodinia and the Cambrian formation of Gondwana. *Geology*, 21, 889 - 892.

Pratt, M.J., Wysession, M.E., Aleqabi, G.I., Wiens, D.A., Nyblade, A.A, Shore, P. J., Rambolamanana, G., Andriampenomanana, F., Rakotondraibe, T., Tucker, R.D., Barruol, G., and Rindraharisaona, E., 2017. Shear-velocity structure of the crust and uppermantle of Madagascar derived from surface wave tomography. *Earth and Planetary Science Letters*, 458, 405 - 417.

Rabinowitz, P.D., Coffin, M.F., and Falvey, D., 1983. The separation of Madagascar and Africa. *Science*, 220, 67 - 69.

Raharimahefa, T., and Kusky. T.M., 2010. Environmental monitoring of Bombetoka Bay and the Betsiboka estuary, Madagascar, using multi-temporal satellite data. *Journal of Earth Science*, 21, 210 - 226.

Raharimahefa T., Kusky. T.M., Toraman, E., Rasoazanamparany, C., and Rasaonina, I., 2013. Geometry and kinematics of the late Proterozoic Angavo shear zone, central Madagascar: Implication for Gondwana assembly. *Tectonophysics*, 592, 113 - 129.

Rai, A., Gaur, V.K., Rai, S.S., and Priestley, K., 2009. Seismic signatures of the Pan African orogeny: implications for southern Indian high grade terranes. *Geophysical Journal International*, 176, 518 - 528.

Rai, S.S., Borah, K., Das, R., Gupta, S., Srivastava, S., Prakasam, K.S., Sivaram, K., Kumar, S., and Meena, R., 2013. The South India Precambrian crust and shallow lithospheric mantle: Initial results from the India Deep Earth Imaging Experiment (INDEX). *Journal of Earth System Science*, 122, 1435 - 1453.

Rajaomazava, F., 1992. Etude de la subsidence du bassin sédimentaire de Morondava (Madagascar) dans le cadre de l'évolution géodynamique de la marge Est-Africaine. *PhD Thesis*, Univ. Montpellier, France.

Rakotondraibe, T., Nyblade, A.A., Wysession, M.E., Durrheim, R.J., Rambolamanana, G., Aleqabi, G., Shore, P.J., Pratt, M.J., Andriampenomanana, F., Rumpker, G., and Rindraharisaona, E., in prep. Seismostectonic study for Madagascar.

Rakotondrainibe, 1977. Contribution à l'étude de la séismicité de Madagascar. *PhD Thesis*, University of Antananarivo, Madagascar.

Rakotondraompiana, S.A., Albouy, Y., and Piqué, A., 1999. Lithospheric model of the Madagascar Island (western Indian Ocean): a new interpretation of the gravity data. *Journal of African Earth Sciences*, 28, 961 - 973.

Rambolamanana, G., Suhadolc, P., and Panza, G.F., 1997. Simultaneous inversion of hypocentral parameters and structure velocity of the central region of Madagascar as a premise for the mitigation of seismic hazard in Antananarivo. *Pure Applied Geophysics*, 149, 707 - 730.

Ramirez, C., Nyblade, A.A., Wysession, M.E., Andriampenomanana, F., and Rakotondraibe, T., (Submitted). Complex seismic anisotropy in Madagascar revealed by shear wave splitting measurements, *Earth and Planetary Science Letters*.

Rasamimanana, G., 1996. Caractérisations géochimiques et géochronologiques de trois épisodes magmatiques (Crétacé, Miocène terminal et Quaternaire) à Madagascar, associés aux phénomènes de rifting. *PhD Thesis*, University of Paris-Sud, Orsay, 234 p.

Raval, U., and Veeraswamy, K., 2003. India-Madagascar separation: breakup along a pre-existing mobile belt and chipping of the craton. *Gondwana Research*, 6, 467 - 485.

Razafimbelo, M.E., 1987. Le bassin de Morondava (Madagascar) synthèse géologique et structurale. *PhD Thesis*, Univerity of Louis-Pasteur, France.

Reeves, C., 2014. The position of Madagascar within Gondwana and its movements during Gondwana dispersal. *Journal of African Earth Sciences*, 94, 45 - 57.

Reiss, M.C., Rümper, G., Tilmann, F., Yuan, X., Giese, J., and Rindraharisaona, E.J., 2016. Seismic anisotropy of the lithosphere and asthenosphere beneath southern Madagascar from teleseismic shear wave splitting analysis and waveform modeling. *Journal of Geophysical Research: Solid Earth*, 121, B013020.

Reusch, A.M., Nyblade, A.A., Wiens, D.A., Shore, P.J., Ateba, B., Tabod, C.T., and Nnange, J.M., 2010. Upper mantle structure beneath Cameroon from body wave tomography and the origin of the Cameroon Volcanic Line.

Geochemistry, Geophysics, Geosystems, 13, 11, Q10W07, doi:10.1029/2010GC003200.

Reusch, A.M., Nyblade, A.A., Tibi, R., Wiens, D.A., Shore, P.J., Ateba, B., Tabod, C.T., and Nnange, J.M., 2011. Mantle transition zone thickness beneath Cameroon: evidence for an upper mantle origin for the Cameroon Volcanic Line. *Geophysical Journal International*, doi: 10.1111/j.1365-246X.2011.05239.x.

Revenaugh, J., and Jordan, T.H., 1991. Mantle layering from ScS reverberations (3) The upper mantle. *Journal of Geophysical Research*, 96, 19781 - 19810.

Rigden, S.M., Gwanmesia, G.D., Fitz Gerald, J.D., Jackson, I., and Liebermann, R.C., 1991. Spinel elasticity and seismic structure of the transition zone of the mantle. *Nature*, 354, 143 - 145.

Rindraharisaona, E.J., Guidarelli, M., Aoudia, A., and Rambolamanana, G., 2013. Earth structure and instrumental seismicity of Madagascar: Implications on the seismotectonics. *Tectonophysics*, 594,165 - 181.

Rindraharisaona, E.J, Tilmann, F., Yuan, X., Rümper, G., Giese, J., Rambolamanana, G., and Barruol, G., 2017. Crustal structure of southern Madagascar from receiver functions and ambient noise correlation: Implications for crustal evolution. *Journal of Geophysical Research: Solid Earth*, 122, B013565.

Ringwood, A.E., 1975. *Composition and Petrology of the Earth's Mantle*, McGraw-Hill, New York.

Roberts, G.G., Paul, J.D., White, N., and Winterbourne, J., 2012. Temporal and spatial evolution of dynamic support from river profiles: A framework for Madagascar. *Geochemistry Geophysics Geosystems*, 13, Q04004.

Rudnick, R.L., and Fountain, D.M., 1995. Nature and composition of the continental crust the continental crust: a lower crustal perspective. *Reviews of Geophysics*, 33, 267 - 309.

Ryberg, T., Wenzel, F., Egorkin, A.V., and Solodilov, L., 1997. Short-period observation of the 520 km discontinuity in northern Eurasia. *Journal of Geophysical Research*, 102, 5413 - 5422.

Saikia, A., Frost, D.J., and Rubie, D.C., 2008. Splitting of the 520-kilometer seismic discontinuity and chemical heterogeneity in the mantle. *Science*, 319, 1515 - 1518.

Saria, E., Calais, E., Altmamini, Z., Pascal, P., and Farah, H., 2013. A new velocity field for Africa from combined GPS and Doris: Contribution to African reference frame. *Journal of Geophysical Research: Solid Earth*, 118, 1677 - 1697.

Sato, H., Sacks, I.S., and Murase, T., 1989. The use of laboratory velocity data for estimating temperature and partial melt fraction in the low-velocity zone: comparison with heat flow and electrical conductivity studies. *Journal of Geophysical Research*, 94, 5689 – 5704. doi:10.1029/JB094iB05p05689.

Savage, M.K., 1999. Seismic anisotropy and mantle deformation: What have we learned from shear wave splitting? *Reviews of Geophysics*, 37, 65 - 106.

Savage, M.K., and Silver, P.G., 1993. Mantle deformation and tectonics: Constraints from seismic anisotropy in the western United States. *Physics of the Earth and Planetary Interiors*, 78, 207 - 228.

Scheidegger, A. E., and Willmore, P. L., 1957. The use of a least squares method for the interpretation of data from seismic surveys. *Geophysics*, 9 - 21.

Schlich, R., 1975. Structure et âge de l'océan Indien occidental. *Mémoires de la Société géologique de France*, 6, 102.

Schreurs, G., Giese, J., Berger, A., and Gnos, E., 2010. A new perspective on the significance of the Ranotsara shear zone in Madagascar. *International Journal of Earth Sciences*, 99, 1827 - 1847.

Sigloch, K., and Barruol, G., 2012. RHUM-RUM investigates La Réunion mantle plume from crust to core. *AGU Fall Meeting Abstract*.

Silver, P.G., 1996. Seismic anisotropy beneath the continents: Probing the depths of geology. *Annual Review of Earth and Planetary Sciences*, 24, 385 - 432.

Silver, P.G., and Chan, W.W., 1991. Shear wave splitting and subcontinental mantle deformation. *Journal of Geophysical Research.*, 96, 16429 - 16454.

Shearer, P.M., 1990. Seismic imaging of upper-mantle structure with new evidence for a 520-km discontinuity. *Nature*, 344, 121 - 126.

Shearer, P.M., 1991. Constraints on upper mantle discontinuities from observations of long-period reflected and converted phases. *Journal of Geophysical Research*, 96, 18147 - 18182.

Shearer, P.M., 1996. Transition zone velocity gradients and the 520-km discontinuity. *Journal of Geophysical Research*, 101, 3053 - 3066.

Shearer, P. M., 2000. Upper mantle seismic discontinuities, in Earth's deep interior: mineral physics and tomography from the atomic to the global scale (eds S.-I. Karato, A. Forte, R. Liebermann, G. Masters and L. Stixrude). *American Geophysical Union*, Washington, D. C.

Shearer, P.M., and Flanagan, M.P., 1999. Seismic velocity and density jumps across the 410- and 660-kilometer discontinuities. *Science*, 285, 1545 - 1548.

Smith, A.G., and Hallam, A., 1970. The fit of southern continents. *Nature*, v225, 10, 139 - 145.

Stamps, D. S., Flesch, L. M., Calais, E., and Ghosh, A., 2014. Current kinematics and dynamics of Africa and the East African Rift System. *Journal of Geophysical Research. Solid Earth*, 119, 5161 - 5186.

Stamps, D.S., Iaffaldano, G., and Calais, E., 2015. Role of mantle flow in Nubia–Somalia divergence. *Geophysical Research Letters*, 42, 290 - 296.

Stein, S., Brown, E., Darbyshire, F., Frederiksen, A., Jurdy, D., Kley, J., Moucha, R., Stein, C.A., Tyrone, R., Wiens, D., and Wysession, M, E, 2016. New insights into North America's Midcontinent Rift. *Eos*, 97. doi:10.1029/2016EO056659.

Stein, S., and Wysession, M., 2003. An Introduction to Seismology, Earthquakes and Earth Structure. *Blackwell*, Malden, MA.

Steinberger, B., and Torsvik, T., 2012. A geodynamic model of plumes from the margins of Large Low Shear Velocity Provinces. *Geochemistry, Geophysics, Geosystems*, 13, doi:10.1029/2011GC003808.

Stern, R.J., 1994. Arc assembly and continental collision in the Neoproterozoic East African Orogen: implications for the consolidation of Gondwanaland. *Annual Reviews Earth Planetary Sciences*, 22, 319 - 351.

Storey, M., Mahoney, J.J., Saunders, A.D., Duncan, R.A., Kelley, S.P., and Coffin, M.F., 1995. Timing of hotspot related volcanism and breakup of Madagascar and India. *Science*, 267, 852 - 855.

Tarling, D.H., 1971. Gondwanaland, paleomagnetism and continental drift. *Nature*, 229, 17 - 21.

Tedla, G.E, Van der Meijde, M., Nyblade, A.A., and Van der Meer, F. D., 2011. A crustal thickness map of Africa derived from a global gravity field model using Euler deconvolution. *Geophysical Journal International*, 187, 1 - 9.

Thomas, R.J., De Waele, B., Schofield, D.I., Goodenough, K.M., Horstwood, M., Tucker, R., Bauer, W., Annells, R., Howard, K., Walsh, G., Rabarimanana, M., Rafahatelo, J.M., Ralison, A.V., and Randriamananjara, T., 2009. Geological evolution of the Neoproterozoic Bemarivo Belt, northern Madagascar. *Precambrian Research*, 172, 279 - 300.

Tilmann, F., Yuan, X., Rümpker, G., and Rindraharisaona, E., 2012. SELASOMA Project, Madagascar 2012-2014, DeutschesGeoForschungsZentrum GFZ, Seismic Network. doi:10.14470/MR7567431421.

Tokam, A-P.K., Tabod, C.T., Nyblade, A.A., Julià, J., Wiens, D.A., and Pasyanos, M.E., 2010. Structure of the crust beneath Cameroon, West Africa, from joint inversion of Rayleigh wave group velocities and receiver functions. *Geophysical Journal International*, 183, 1061 - 1076.

Torsvik, T.H., Tucker, R.D., Ashwal, L.D., Eide, E.A., Rakotosolofo, N.A., and de Wit, M.J., 1998. Late Cretaceous magmatism in Madagascar: paleomagnetic evidence for a stationary Marion hotspot. *Earth and Planetary Science Letters*, 64, 221 - 232.

Tucker, R.D., Kusky, T.M., Buchwaldt, R., and Handke, M.J., 2007. Neoproterozoic nappes and superposed folding of the Itremo Group, west-central Madagascar. *Gondwana Research*, 12, 356 - 379. doi:10.1016/j.gr.2006.12.001.

Tucker, R.D., Peters, S.G., Roig, J.Y., Théveniaut, H., and Delor, C., 2012. Notice explicative des cartes géologique et métallogéniques de la République de Madagascar à 1/1000000. *Ministère des Mines, PGRM*, Antananarivo, République de Madagascar.

Tucker, R.D., Roig, J.Y., Delor, C., Amelin, Y., Goncalves, P., Rabarimanana, M.H., Ralison, A.V., and Belcher, R.W., 2011. Neoproterozoic extension in the Greater DharwarCraton: a reevaluation of the Betsimisaraka “suture” in Madagascar. *Canadian Journal of Earth Sciences*, 48, 389 - 417.

Tugume, F., Nyblade, A., and Julià, J., 2012. Moho depths and Poisson's ratios of Precambrian crust in East Africa: evidence for similarities in Archean and Proterozoic crustal structure. *Earth and Planetary Science Letters*, 355 - 356, 73 - 81.

Tugume, F., Nyblade, A., Julià, J., and van de Meijde, M., 2013. Precambrian crustal structure in Africa and Arabia: evidence lacking for secular variation. *Tectonophysics*, 609, 250 - 266.

Vidale, J.E., and Benz, H.M., 1992. Sharpness of upper-mantle discontinuities determined from high-frequency reflections. *Nature*, 356, 678 - 683.

Vinnik, L., Chevrot, S., Montagner, J-P., 1977. Evidence for a stagnant plume in the transition zone? *Geophysical Research Letters*, 24, 1007 - 1010.

Wegner, A., 1924. La genèse des continents et des océans. Théories des translations continentals. *Nizet et Bastard Eds.*, *Paris*, 236.

Wescott, W.A., and Diggens, J.N., 1997. Depositional history and stratigraphical evolution of the Sakoa Group (Lower Karoo Supergroup) in the southern Morondava Basin, Madagascar. *Journal of African Earth Sciences*, 24, 585-601.

Wescott, W.A., and Diggens, J.N., 1998. Depositional history and stratigraphical evolution of the Sakamena Group (Middle Karoo Supergroup) in the southern Morondava Basin, Madagascar. *Journal of African Earth Sciences*, 27, 461 - 479.

Wessel, P., and Smith, W.H.F., 1998. New, improved version of Generic Mapping Tools released. *EOS Transactions American Geophysical Union*, **79**, 579.

Wüstefeld, A., Bokelmann, G.H.R., Barruol, G., and Montagner, J.-P., 2009. Identifying global seismic anisotropy patterns by correlating shear-wave splitting and surface waves data. *Physics of the Earth and Planetary Interiors*, 176, 198 - 212.

Wysession, M., Wiens, D., Nyblade, A., and Rambolamanana, G., 2012. Investigating mantle structure with broadband seismic arrays in Madagascar and Mozambique. *AGU Fall Meeting Abstract*, p. B2591.

Yu, Y., Gao, S. S., Moidaki, M., Reed, C. A., and Liu, K. H., 2015. Seismic anisotropy beneath the incipient Okavango rift: Implications for rifting initiation. *Earth and Planetary Science Letters*, 430, 1 - 8, doi:10.1016/j.epsl.2015.08.009.

Zandt, G., and Ammon, C.J., 1995. Continental crust composition constrained by measurements of crustal Poisson's ratio. *Nature*, 374, 152 - 154.

Zhu, L., and Kanamori, H., 2000. Moho depth variation in Southern California from teleseismic receiver functions. *Journal of Geophysical Research*, 105, 2969 - 2980.

Zhang, S., and Karato, S., 1995. Lattice preferred orientation of olivine deformed in simple shear. *Nature*, 375, 774 - 777.

Appendices

Appendix A

Table A.1: List of teleseismic events used to compute receiver functions.

Date	Time	Lat (º)	Lon (º)	Depth (km)	Magnitude
2007/08/08	17:04:58	-6.089	107.584	293.8	7.5
2007/08/20	13:46:19	6.11	127.446	23.8	6.4
2007/09/30	05:23:34	-49.247	164.194	10	7.4
2007/09/30	09:47:53	-49.17	164.423	18	6.6
2007/11/25	16:02:18	-8.352	118.337	35.5	6.5
2007/11/25	19:53:08	-8.226	118.526	31.6	6.5
2007/12/15	09:39:54	-6.656	131.128	65.1	6.4
2008/04/12	00:30:12	-55.591	158.542	10	7.1
2008/05/12	06:27:59	31.064	103.372	7.6	7.9
2008/05/31	04:37:54	-41.253	80.485	0.5	6.4
2008/06/01	01:57:24	20.147	121.371	33.2	6.2
2008/06/08	12:25:29	37.961	21.449	15.8	6.2
2008/10/29	11:32:41	30.497	67.563	2.9	6.2
2008/12/08	18:39:09	-53.02	106.803	10	6.3
2008/12/13	08:45:35	-49.087	123.427	0.1	5.9
2008/12/25	03:20:29	5.776	125.523	209.3	6.3
2009/01/03	22:33:42	-0.709	133.312	34.4	7.2
2009/02/11	17:34:51	3.775	126.499	24.2	7.1
2009/03/16	14:15:56	3.725	126.622	34	6.3
2009/06/16	20:05:58	-54.404	5.869	16	6.1
2009/08/10	19:55:39	14.052	92.868	30.7	7.5
2009/08/28	01:51:19	-7.202	123.461	640.1	6.9
2009/09/02	07:55:01	-7.735	107.411	57.8	7
2009/09/30	10:16:10	-0.707	99.968	90.2	7.6
2009/11/08	19:41:45	-8.284	118.667	32.1	6.6
2009/11/10	02:48:46	8.028	91.951	22.7	6
2009/11/28	06:04:25	-10.359	118.843	38.7	6
2010/01/05	04:55:38	-58.464	-14.859	10	6.8
2010/02/07	06:10:00	23.436	123.691	23	6.3
2010/02/27	06:34:13	-36.148	-72.933	28.1	8.8
2010/03/04	00:18:52	22.93	120.8	27	6.3
2010/05/09	05:59:42	3.733	96.028	42.3	7.3
2010/06/12	19:26:50	7.851	91.955	31.4	7.5
2010/07/18	13:04:11	-5.981	150.516	45.8	6.9
2011/01/02	20:20:18	-38.391	-73.399	24.4	7.1
2011/01/18	20:23:25	28.683	63.995	79.9	7.2
2011/02/10	14:39:28	4.13	123.062	532.8	6.5
2011/03/06	14:32:36	-56.386	-27.025	92	6.5
2011/03/10	17:08:37	-6.857	116.73	518.6	6.6
2011/03/24	13:55:13	20.63	99.918	12.8	6.8
2011/04/01	13:29:11	35.732	26.547	75.5	6.1
2011/04/03	20:06:43	-9.734	107.769	31.9	6.7
2011/08/30	06:57:41	-6.359	126.75	467.2	6.9
2011/10/23	10:41:22	38.729	43.446	7.6	7.1
2011/10/23	20:45:37	38.589	43.117	10.1	6
2011/11/01	00:21:27	43.626	82.414	26.2	5.6
2011/11/08	02:59:08	27.25	125.723	228.2	6.9
2011/11/14	04:05:12	-0.953	126.88	24.4	6.4
2011/11/28	09:13:11	-7.034	116.965	623.6	5.8
2011/11/30	00:27:06	15.455	118.999	21.1	6
2011/11/30	19:42:37	7.778	93.823	39.2	5.6
2011/12/11	09:54:56	-56.049	-28.213	130.6	6.3
2011/12/14	05:04:57	-7.528	146.814	128.5	7.1
2011/12/27	15:21:57	51.835	95.964	12.8	6.7
2012/01/01	05:27:55	31.468	138.183	359.7	6.8
2012/01/10	18:36:59	2.433	93.21	20.9	7.2
2012/01/15	13:40:19	-60.948	-56.113	10	6.6
2012/01/22	05:53:42	-56.759	-25.147	18.7	6
2012/02/06	03:49:13	9.919	123.217	17.5	6.7
2012/02/06	10:10:19	9.9	123.175	12.6	6
2012/02/06	11:33:38	9.81	123.089	23.4	5.9
2012/02/26	06:17:19	51.801	95.98	13	6.7
2012/03/20	17:56:19	-3.833	140.263	69.2	6.3
2012/03/21	22:15:05	-6.223	146.008	117.7	6.6
2012/04/11	08:38:37	2.238	93.014	26.3	8.6
2012/04/11	10:43:10	0.767	92.428	21.6	8.2
2012/04/14	10:56:18	-57.576	-65.372	8.4	6.2
2012/04/15	05:57:40	2.581	90.336	25	6.3

2012/04/17	07:13:49	-5.534	147.125	208.2	6.9
2012/05/20	02:03:52	44.89	11.23	6.3	6
2012/05/24	22:47:46	72.96	5.683	10	6.2
2012/06/10	12:44:16	36.42	28.88	35	6
2012/06/23	04:34:53	3.009	97.896	95	6.1
2012/06/29	21:48:52	43.433	84.7	18	6.3
2012/07/25	00:27:45	2.707	96.045	22	6.4
2012/08/11	13:03:10	38.329	46.826	11	6.4
2012/08/12	10:47:06	35.661	82.518	13	6.3
2012/08/26	15:05:37	2.19	126.837	91.1	6.6
2012/08/31	12:47:33	10.811	126.638	28	7.6
2012/09/03	18:23:05	-10.708	113.931	14	6.1
2012/09/14	04:51:47	-3.319	100.594	19	6.2
2012/10/08	11:43:31	-4.472	129.129	10	6.3
2012/10/12	00:31:28	-4.892	134.03	13	6.5
2012/11/02	18:17:32	9.219	126.161	37	6.1
2012/11/06	06:17:27	9.963	57.203	10	5.6
2012/11/11	01:12:38	23.005	95.885	13.7	6.8
2012/12/05	17:08:13	33.506	59.571	14.4	5.8
2012/12/10	16:53:08	-6.533	129.825	155	7.1
2012/12/11	06:18:27	0.533	126.231	30	6
2012/12/17	09:16:30	-0.649	123.807	44.2	6.1
2013/01/10	13:47:03	4.72	95.095	38	5.7
2013/01/21	22:22:52	4.966	95.856	11.6	6.1
2013/01/28	16:38:53	42.605	79.708	15	6.1
2013/02/16	04:37:36	5.812	125.748	105	6.1
2013/03/07	03:36:47	24.268	121.428	9.6	5.5
2013/03/19	03:29:00	-58.915	-24.409	31.3	5.9
2013/03/27	02:03:20	23.827	121.221	21.4	5.9
2013/04/06	04:42:35	-3.513	138.477	66	7
2013/04/09	11:52:50	28.5	51.591	10	6.4
2013/04/16	10:44:20	28.107	62.053	82	7.7
2013/04/16	22:55:27	-3.218	142.543	13	6.6
2013/04/20	00:02:47	30.308	102.888	14	6.6
2013/04/30	06:25:23	37.655	-25.007	10	5.8
2013/05/11	02:08:08	26.56	57.77	15	6.1
2013/05/18	04:05:42	-53.09	22.08	10	5.6
2013/05/26	06:08:15	39.931	67.345	15.8	5.7
2013/06/02	05:43:03	23.794	121.133	17	6.2
2013/06/13	16:47:23	-9.998	107.243	8.6	6.7
2013/06/15	16:11:00	34.449	25.044	10	6.2
2013/06/16	21:39:04	34.27	25.114	26	6
2013/07/02	07:37:02	4.698	96.687	10	6.1
2013/07/02	13:55:41	4.654	96.706	31.8	5.5
2013/07/06	05:05:06	-3.249	100.567	19.7	6
2013/07/15	14:03:43	-60.868	-25.144	31	7.3
2013/07/21	23:45:56	34.499	104.243	9.8	5.9
2013/07/22	07:01:42	-46.042	34.826	10	6.1
2013/07/26	21:32:59	-57.915	-23.841	13	6.2
2013/08/12	00:53:43	-7.135	129.809	95	6
2013/09/01	11:52:29	-7.44	128.221	112	6.5
2013/09/24	11:29:47	26.951	65.501	15	7.7
2013/09/28	07:34:06	27.183	65.505	12	6.8
2013/10/04	17:26:13	-38.606	78.369	12.7	6.4
2013/10/12	13:11:53	35.514	23.252	40	6.6
2013/10/15	00:12:32	9.88	124.117	19	7.1
2013/11/16	03:34:31	-60.263	-47.062	10	6.9
2013/11/17	09:04:55	-60.274	-46.401	10	7.7
2013/11/25	06:27:33	-53.945	-55.003	11.8	7
2013/12/01	01:24:13	-7.027	128.379	9.9	6.4
2014/02/03	03:08:46	38.264	20.39	5	6
2014/03/21	13:41:09	7.745	94.334	21.5	6.4
2014/04/15	03:57:01	-53.497	8.722	11.2	6.8
2014/11/15	02:31:41	1.893	126.522	45	7.1
2014/11/21	10:10:19	2.3	127.056	35	6.5
2014/11/26	14:33:43	1.96	126.575	39	6.8
2014/12/06	22:05:10	-6.11	130.483	116	6
2014/12/17	06:10:05	-3.83	100.143	10	5.9
2015/03/17	22:12:28	1.669	126.522	44	6.2
2015/04/25	06:11:25	28.231	84.731	8.2	7.8
2015/04/26	07:09:10	27.771	86.017	22.9	6.7
2015/05/12	07:05:19	27.809	86.065	15	7.3
2015/06/17	12:51:32	-35.364	-17.16	10	7
2015/07/27	21:41:21	-2.643	138.519	48	7
2015/09/24	15:53:27	-0.621	131.262	18	6.6

Figure A.1: Receiver functions for all stations. The four-column figure shows the radial and tangential calculated from Gaussian parameter 1.0 and 2.5 respectively.

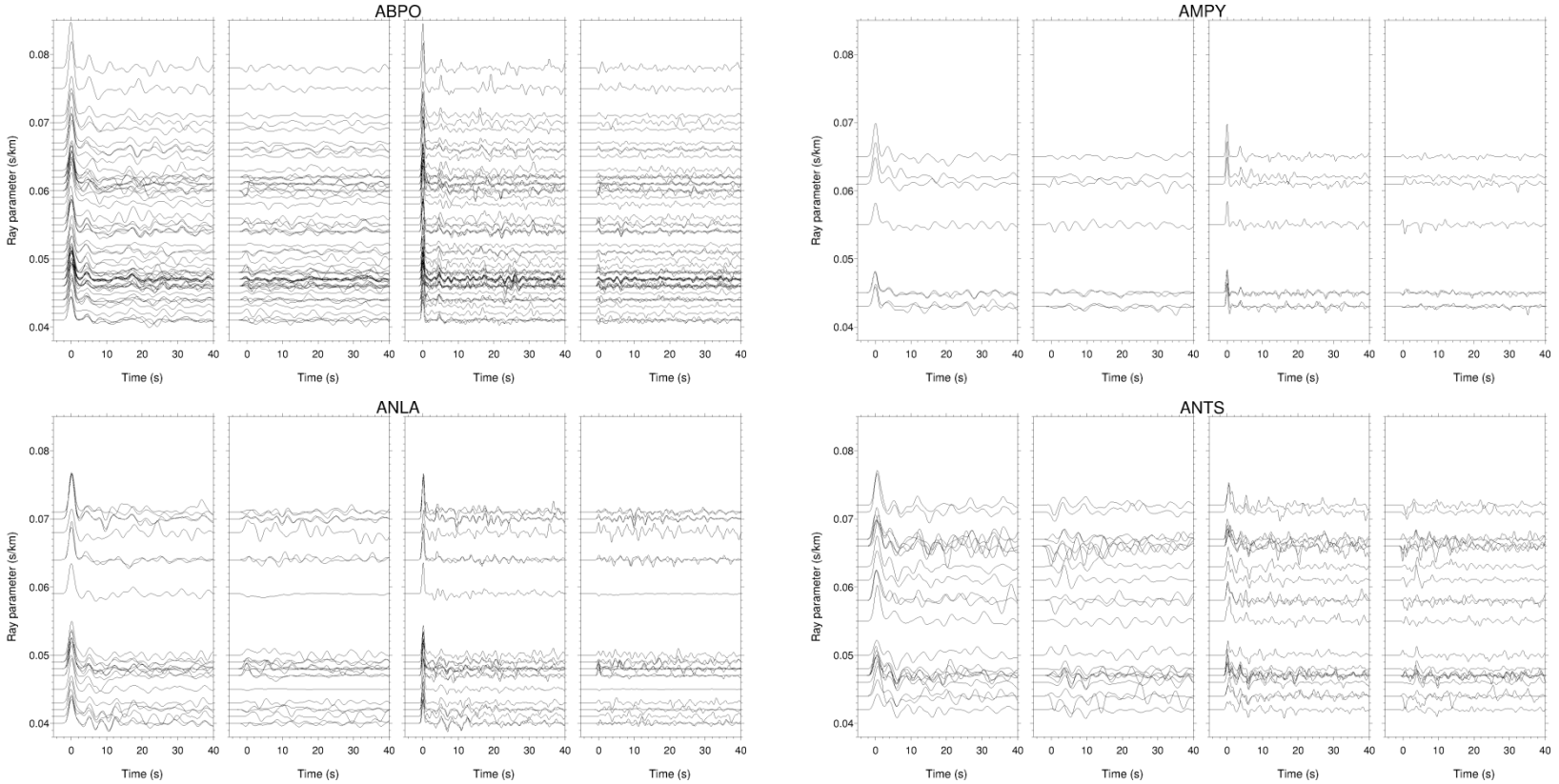

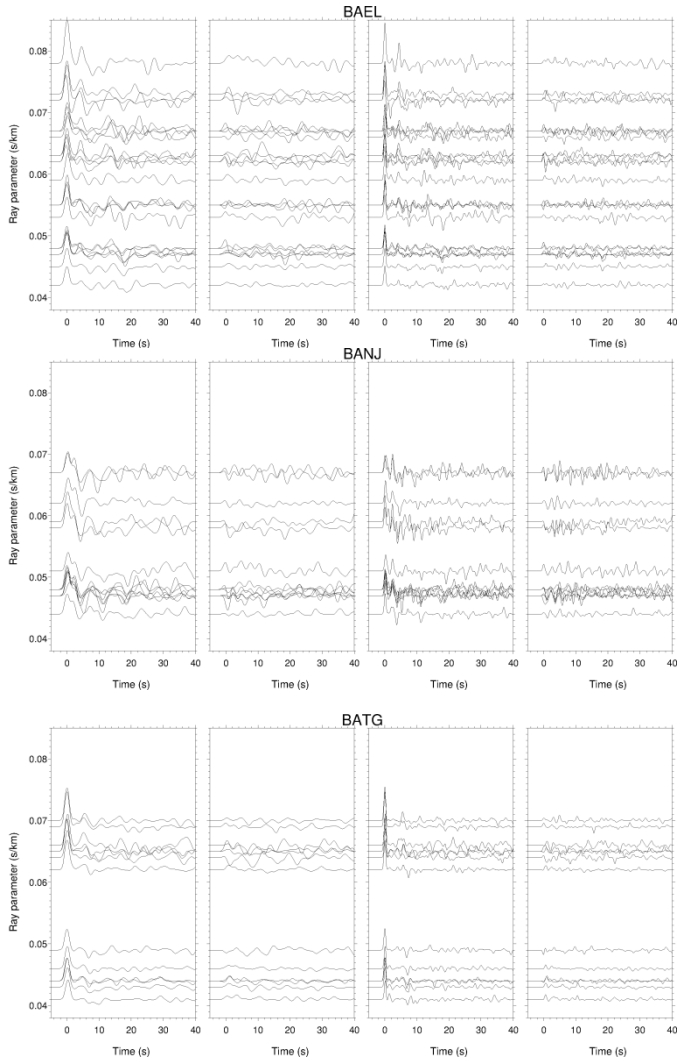
BAEL
BANJ
BATG
Ray parameter (s/km)
0.04
0.05
0.06
0.07
0.08
Time (s)
0
10
20
30
40

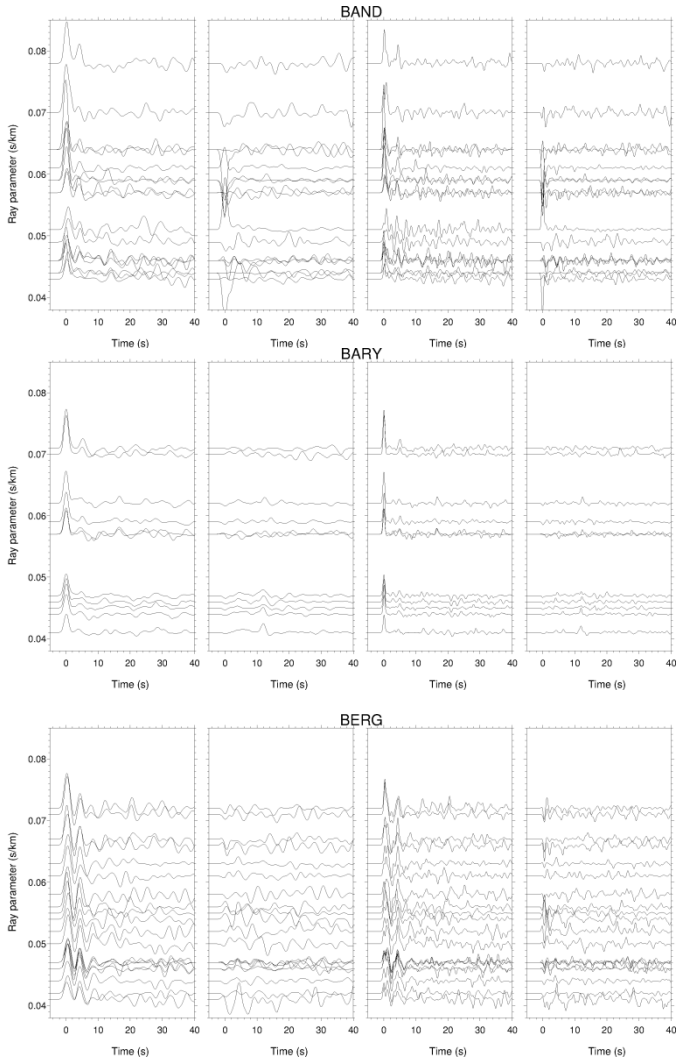
BAND
BARY
BERG
Ray parameter (s/km)
0.04
0.05
0.06
0.07
0.08
Time (s)
0
10
20
30
40

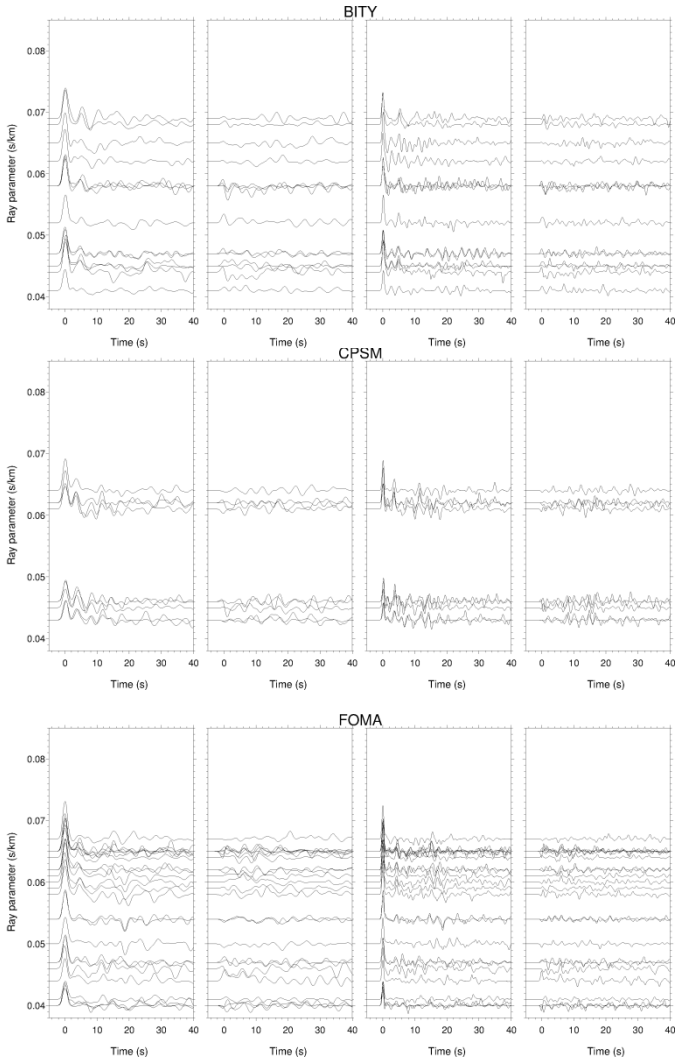
BITY
CPSM
FOMA
Ray parameter (s/km)
0.04
0.05
0.06
0.07
0.08
Time (s)
0
10
20
30
40

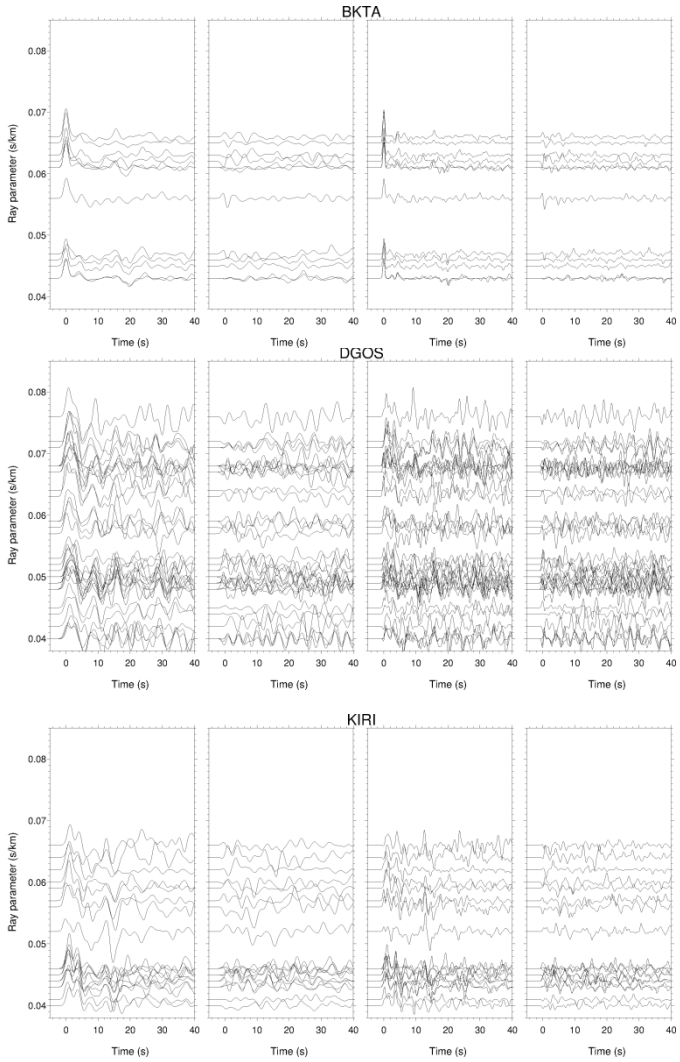
BKTA
DGOS
KIRI
Ray parameter (s/km)
0.04
0.05
0.06
0.07
0.08
Time (s)
0
10
20
30
40

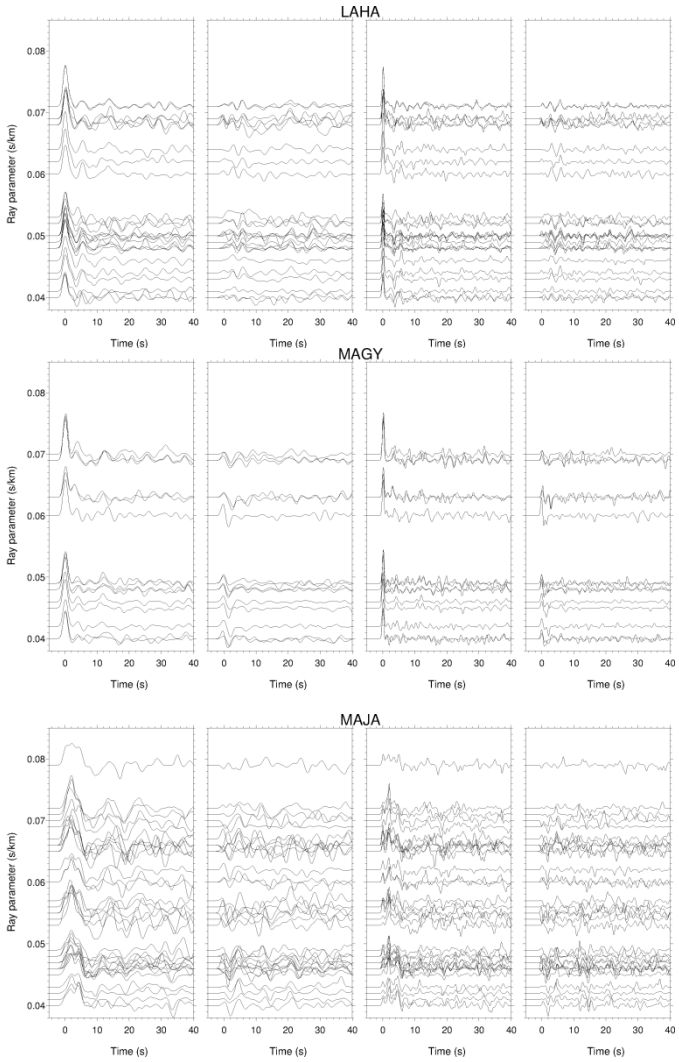
LAHA
MAGY
MAJA
Ray parameter (s/km)
Time (s)

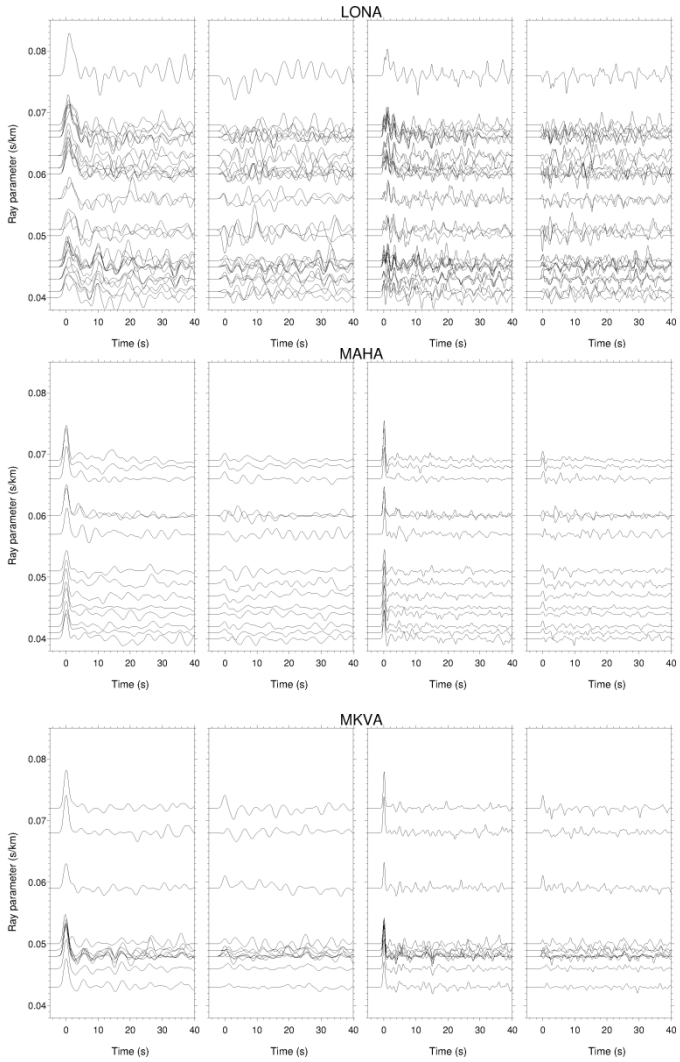
LONA
MAHA
MKVA
Ray parameter (s/km)
Time (s)

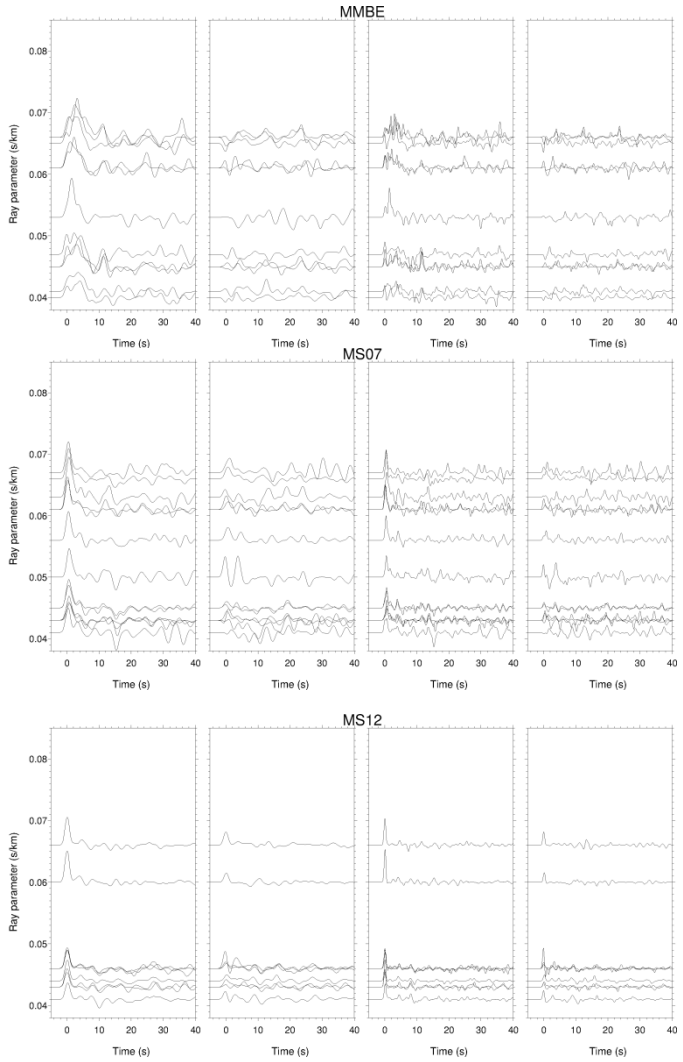
MMBE
MS07
MS12
Ray parameter (s/km)
0.08
0.07
0.06
0.05
0.04
0 10 20 30 40
Time (s)

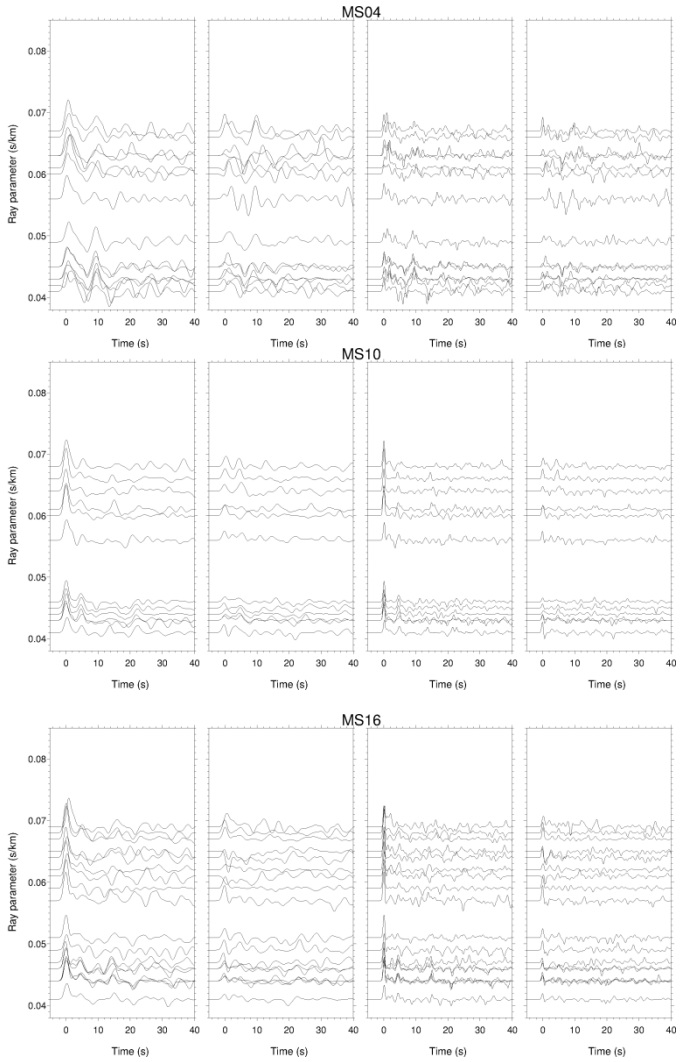
MS04
MS10
MS16
Ray parameter (s/km)
0.08
0.07
0.06
0.05
0.04
0 10 20 30 40
Time (s)

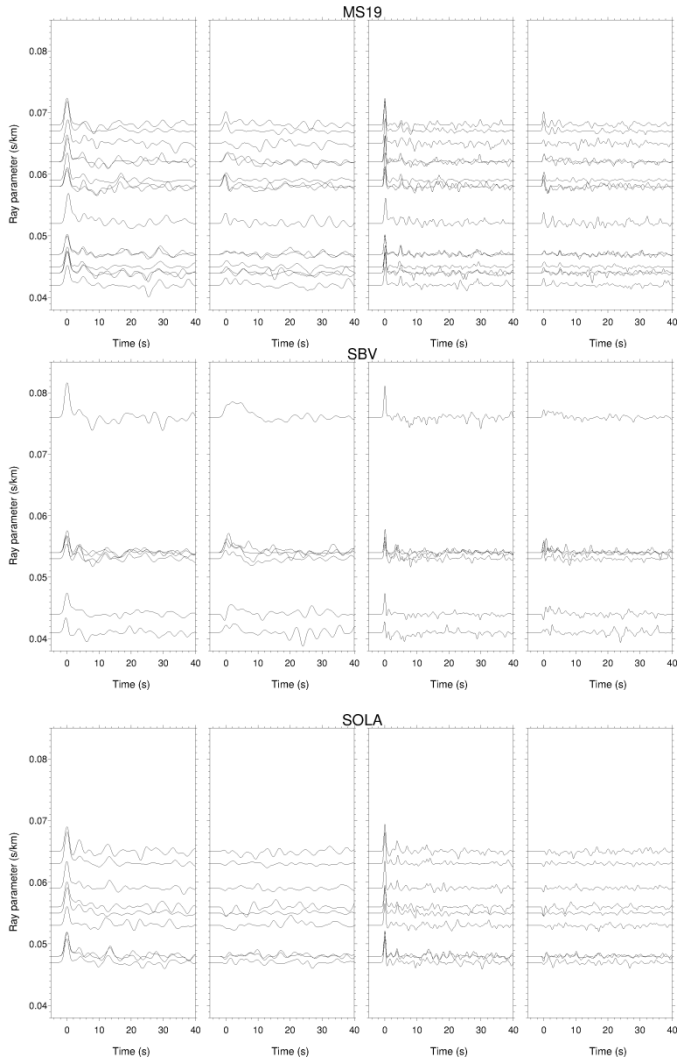
MS19
SBV
SOLA
Ray parameter (s/km)
Time (s)

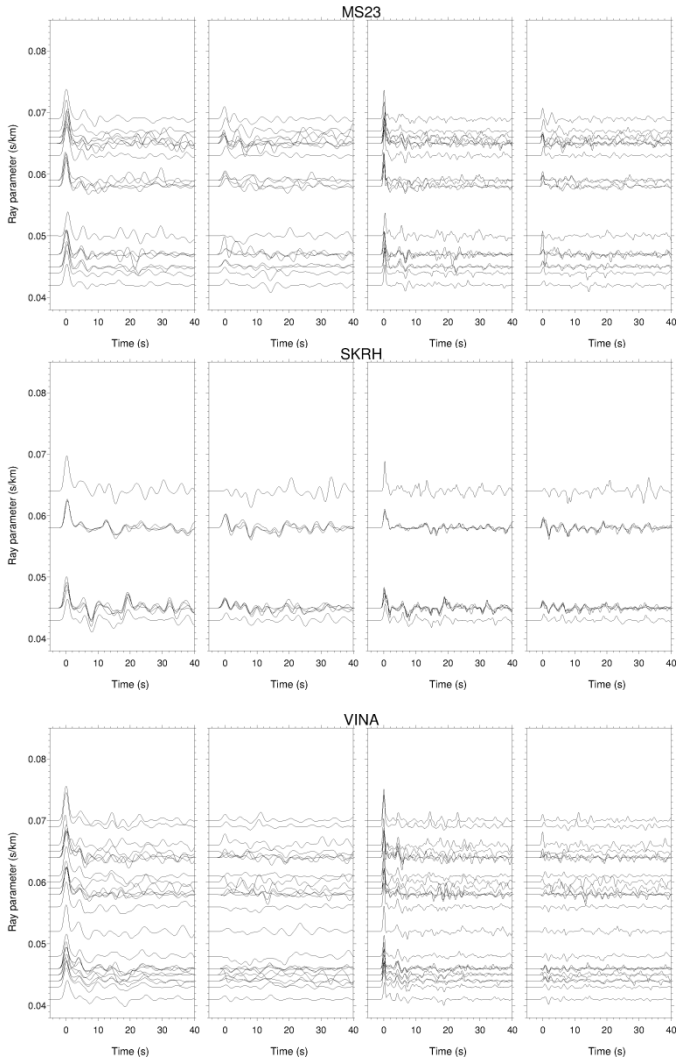
MS23
SKRH
VINA
Ray parameter (s/km)
Time (s)

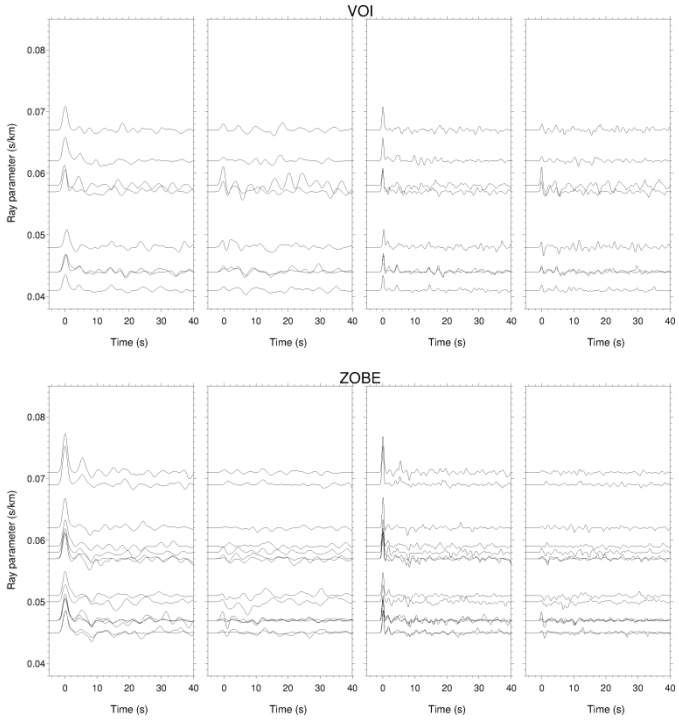
VOI
ZOBE
Ray parameter (s/km)
0.08
0.07
0.06
0.05
0.04
0 10 20 30 40
Time (s)

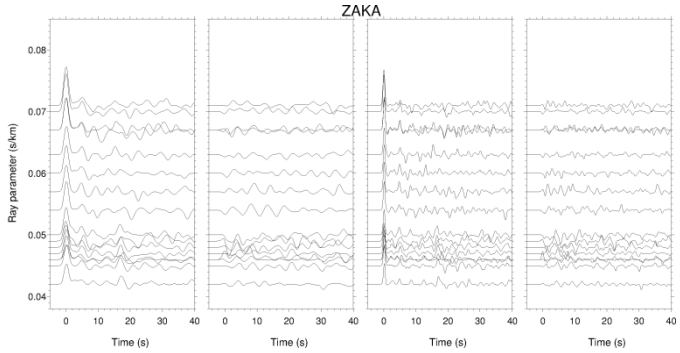
ZAKA
Ray parameter (s/km)
0.08
0.07
0.06
0.05
0.04
0 10 20 30 40
Time (s)

Box A.1. This appendix shows how the bootstrapping procedure works.

8 good receiver functions were obtained in the seismic station AMPY. For the bootstrapping technique, they were labeled as 1, 2, .., 8:

Label	Receiver function's file name
1	2012239151255.10.AMPY.td.1.0.eqr
2	2012244125516.10.AMPY.td.1.0.eqr
3	2012286003914.10.AMPY.td.1.0.eqr
4	2012316011840.10.AMPY.td.1.0.eqr
5	2012345170015.10.AMPY.td.1.0.eqr
6	2013106104843.10.AMPY.td.1.0.eqr
7	2013164165236.10.AMPY.td.1.0.eqr
8	2013196140839.10.AMPY.td.1.0.eqr

200 replications of bootstrap sample were used. The following lines show the selected receiver functions for a sample followed by the estimation of κ and H.

Example : 2 7 2 6 1 8 8 1 : receiver functions randomly selected.

1.91 24.7 : κ and H, respectively.

2 7 2 6 1 8 8 1 1.91 24.7	1 7 1 6 2 6 8 1 1.90 24.8	4 6 5 4 7 3 8 7 1.82 26.3	5 5 3 5 2 6 5 3 1.90 24.8	2 7 5 3 1 3 4 2 1.88 25.2
3 1 6 3 1 3 1 2 1.85 25.5	7 2 4 3 1 5 5 7 1.91 24.9	7 2 7 3 3 7 5 3 1.86 25.1	8 5 7 1 1 2 2 8 1.95 24.3	8 8 2 4 7 5 4 5 1.86 26.0
3 7 4 2 3 8 4 4 1.78 27.0	2 4 5 3 5 7 3 8 1.86 25.5	4 5 4 7 1 2 5 6 1.86 25.8	3 8 7 4 8 2 3 1 1.85 25.7	8 6 4 6 7 8 7 1 2.01 20.5
3 6 1 1 6 4 6 1 1.84 25.8	6 2 5 2 5 2 3 4 1.89 25.1	4 5 2 6 4 4 6 8 1.80 26.9	3 6 5 3 4 6 6 2 1.81 25.8	6 4 4 2 6 6 3 8 2.01 20.5
6 4 6 3 8 5 1 3 1.83 25.9	7 3 8 1 8 2 8 6 1.87 25.2	6 5 8 6 4 3 4 2 1.82 26.2	6 7 5 4 3 5 5 8 1.88 25.3	6 3 4 7 5 4 2 7 1.83 26.1
3 1 3 7 5 7 7 1 1.91 24.7	4 8 7 8 5 2 1 4 1.86 26.1	5 6 7 3 3 4 2 3 1.81 25.9	8 4 4 6 1 2 7 3 1.82 26.4	8 3 1 8 7 7 6 8 1.86 25.2
8 1 6 2 4 5 3 8 1.86 25.6	6 3 5 2 8 2 4 6 1.85 25.5	1 8 8 7 7 5 1 1.94 24.4	1 4 2 8 2 7 5 2 1.93 24.7	2 2 7 6 8 2 1 2 1.93 24.2
2 1 4 4 6 8 3 2 1.82 26.4	6 7 2 7 5 5 2 1 1.95 24.1	7 4 4 1 1 7 2 5 1.87 25.7	2 1 4 2 5 1 1 5 1.97 24.2	2 3 4 6 1 2 1 1 1.88 25.4
2 4 3 1 4 3 7 6 1.80 26.5	7 6 8 1 6 2 2 1 1.91 24.5	6 7 6 6 6 5 1 7 2.00 20.5	3 6 7 3 7 8 2 1 1.86 25.1	8 5 8 6 8 1 7 6 2.00 20.5
7 7 5 1 3 7 1 2 1.95 24.2	8 1 5 2 6 2 2 8 1.95 24.2	7 3 1 1 1 8 7 8 1.90 25.0	3 2 8 2 1 2 3 4 1.86 25.4	3 1 7 2 6 6 7 3 1.83 25.4
6 6 8 1 4 2 6 2 2.00 20.5	1 1 3 5 6 6 8 8 1.86 25.4	7 6 5 2 7 3 2 1 1.91 24.4	4 2 6 3 4 7 2 1 1.83 26.2	7 4 8 3 3 2 3 6 1.81 25.8
7 8 3 4 7 2 6 4 1.82 26.2	6 6 5 5 7 3 8 7 1.87 24.9	4 7 5 1 5 6 5 8 1.88 25.4	3 4 3 4 4 6 4 5 1.76 27.5	8 4 1 2 8 4 8 8 1.83 26.7
6 3 4 4 1 3 5 5 1.82 26.2	2 1 3 3 4 4 4 4 1.76 27.6	5 8 7 2 2 3 7 3 1.91 24.5	8 4 3 6 7 7 4 1 1.82 26.4	7 2 4 8 7 6 4 6 2.02 20.5
4 7 8 3 1 6 4 8 1.82 26.5	4 4 3 3 7 3 6 3 1.74 26.9	5 4 7 7 3 1 3 2 1.87 25.4	6 2 8 5 2 6 4 8 2.01 20.5	5 2 8 4 3 4 8 1 1.84 26.3
4 4 1 2 4 7 1 4 1.77 27.5	1 7 5 3 2 8 1 7 1.94 24.4	8 3 4 3 3 2 1 1 1.84 25.8	3 5 8 6 2 7 5 1 1.90 24.7	1 7 1 8 8 4 8 3 1.86 25.8
7 8 3 6 6 2 3 5 1.83 25.3	8 2 3 6 2 8 6 5 1.87 24.9	4 6 3 3 4 6 8 7 1.79 26.5	6 6 6 1 8 4 4 2 2.00 20.5	7 6 2 4 7 5 2 8 1.89 24.9

6 6 7 6 1 3 2 6 2.01 20.5	3 7 8 8 7 2 1 6 1.87 25.0	7 4 2 5 7 4 4 6 1.81 26.7	1 6 5 8 4 2 2 7 1.89 25.1	5 5 3 5 8 7 1 6 1.90 24.8
8 5 8 1 8 6 5 7 1.89 25.0	4 7 8 8 5 6 6 4 2.00 20.5	7 5 4 6 2 4 6 3 1.81 26.4	7 3 3 5 4 8 8 6 1.84 25.8	8 7 3 4 7 8 1 7 1.86 25.6
8 2 7 8 7 1 6 2 1.92 24.4	2 3 6 7 1 5 4 1 1.88 25.3	5 4 7 5 5 5 8 4 1.89 25.5	7 2 7 3 3 5 1 2 1.91 24.6	6 2 4 4 3 3 1 7 1.80 26.5
6 6 8 8 3 3 7 7 1.83 25.3	1 4 7 2 5 5 6 3 1.88 25.2	6 6 7 2 4 4 5 3 1.81 26.4	7 7 6 2 8 4 8 3 1.85 25.5	8 2 7 2 4 6 3 7 1.86 25.3
7 1 6 5 4 5 1 4 1.86 25.9	8 4 5 8 4 7 4 7 1.82 26.9	4 2 1 6 4 5 4 1 1.81 26.8	3 8 8 4 4 4 7 6 1.78 27.2	2 7 7 6 6 5 2 3 1.88 24.5
1 3 6 6 8 8 6 5 1.86 25.2	3 4 2 5 8 8 1 5 1.88 25.4	8 7 6 5 4 4 3 2 1.82 26.3	2 8 5 1 2 7 2 1 1.99 23.8	4 1 1 2 3 4 7 6 1.82 26.3
6 5 1 3 4 3 5 1 1.86 25.6	8 4 1 4 3 1 5 8 1.83 26.5	7 8 3 4 6 4 6 5 1.80 26.5	5 6 6 8 7 8 8 5 2.01 20.5	5 4 6 1 1 2 7 2 1.90 25.0
3 8 6 2 7 1 5 4 1.86 25.5	1 7 8 5 4 6 4 4 1.80 27.0	7 6 2 2 5 6 8 8 1.89 24.5	2 3 1 8 5 8 6 7 1.90 24.8	2 4 1 7 2 2 2 3 1.91 24.7
3 2 5 1 1 2 7 6 1.91 24.6	4 4 2 6 3 5 4 2 1.79 26.8	8 7 8 7 8 1 7 1 1.91 24.8	1 3 8 3 5 2 1 6 1.89 25.0	3 4 7 7 3 5 5 7 1.86 25.4
1 3 4 8 4 3 2 6 1.80 26.5	4 7 5 5 7 8 4 2 1.87 25.7	3 3 3 2 3 8 2 5 1.82 25.6	4 7 3 3 4 1 4 5 1.79 26.9	2 8 3 8 4 8 4 1 1.82 26.7
5 8 4 8 2 7 4 1 1.86 26.1	7 4 8 2 3 6 7 4 1.82 26.2	3 8 8 2 2 2 4 1 1.88 25.3	2 7 4 5 7 6 1 3 1.86 25.4	1 1 7 8 8 5 8 2 1.94 24.4
6 4 1 2 5 2 4 4 1.81 26.8	7 3 6 2 2 6 1 3 1.84 25.3	5 6 2 1 6 6 1 2 1.90 24.7	6 3 3 6 3 1 4 2 1.80 26.1	3 5 2 2 3 4 5 2 1.89 25.1
4 2 2 8 8 7 2 3 1.89 25.1	1 1 1 6 8 1 1 3 1.89 25.1	4 2 8 3 5 8 2 8 1.88 25.4	4 4 5 7 7 5 5 1 1.89 25.5	4 1 6 6 8 6 4 1 2.00 20.5
1 7 2 7 8 6 4 3 1.85 25.5	8 3 5 8 1 5 6 6 1.86 25.3	2 6 3 8 7 7 6 5 1.88 24.7	2 8 8 6 6 6 4 3 2.00 20.5	1 5 2 7 7 3 7 2 1.95 24.1
8 3 7 8 2 4 2 1 1.88 25.4	2 4 5 5 1 3 3 1 1.88 25.4	7 5 7 7 1 2 4 5 1.94 24.4	5 3 5 6 8 7 2 5 1.91 24.7	5 2 3 4 8 3 8 8 1.84 25.8
4 8 7 2 3 4 2 7 1.84 26.0	2 5 1 6 8 1 7 7 1.94 24.2	1 3 7 1 4 1 3 1 1.87 25.5	8 8 2 3 4 6 5 3 1.84 25.7	7 5 1 4 7 4 6 1 1.86 25.9
4 3 6 8 1 4 5 5 1.82 26.4	2 3 5 7 6 4 8 7 1.85 25.4	3 8 3 4 5 5 8 2 1.87 25.5	1 6 2 1 7 4 7 5 1.89 25.1	4 7 4 6 8 7 3 8 1.82 26.4
1 6 4 5 4 3 1 5 1.84 26.1	5 5 4 5 3 6 3 2 1.84 25.7	4 6 3 1 1 4 8 4 1.78 27.2	8 3 7 6 6 7 5 2 1.88 24.7	6 6 2 7 2 2 4 1 1.86 25.2
7 1 2 3 2 6 2 5 1.91 24.4	5 3 5 6 6 7 4 2 1.85 25.5	2 8 3 3 8 1 3 3 1.82 25.7	3 4 1 3 5 8 7 8 1.84 25.8	1 6 2 7 2 4 8 7 1.89 25.1
8 5 1 2 2 6 3 8 1.90 24.8	7 8 6 3 5 1 1 3 1.86 25.3	5 7 3 1 1 1 6 4 1.87 25.5	1 7 4 7 4 3 3 1 1.82 26.3	2 2 3 8 8 3 2 8 1.87 25.0
2 6 2 7 8 2 8 7 1.93 24.1	2 3 4 6 5 2 2 4 1.83 26.1	7 8 8 5 1 2 1 6 1.93 24.6	7 7 4 1 6 8 1 7 1.87 25.5	1 3 4 1 2 7 2 5 1.92 24.8
1 1 3 1 8 8 1 4 1.87 25.7	3 2 6 7 5 1 4 6 1.85 25.5	8 1 4 8 7 6 6 4 2.00 20.5	2 4 6 1 6 3 4 5 1.82 26.2	6 4 4 3 5 1 5 7 1.83 26.2
4 5 8 3 7 6 3 6 1.81 26.1	3 3 4 8 4 8 3 4 1.77 27.1	2 1 1 6 3 4 8 7 1.86 25.6	1 5 1 5 6 5 4 1 1.92 24.9	1 2 3 8 2 2 6 1 1.90 24.7
3 5 8 1 5 3 4 2 1.88 25.4	4 1 4 7 2 1 7 6 1.84 26.1	3 1 3 7 2 1 1 2 1.94 24.4	8 1 3 2 2 5 1 6 1.90 24.7	8 6 8 3 1 7 2 6 1.86 25.1

The average and error of these values are: H = 25.5 ± 2.4 km and Vp/Vs = 1.86 ± 0.10.

Figure A.2: H-κ stacking results from all the considered seismic stations. (These supplementary figures are printed here in Black and White)

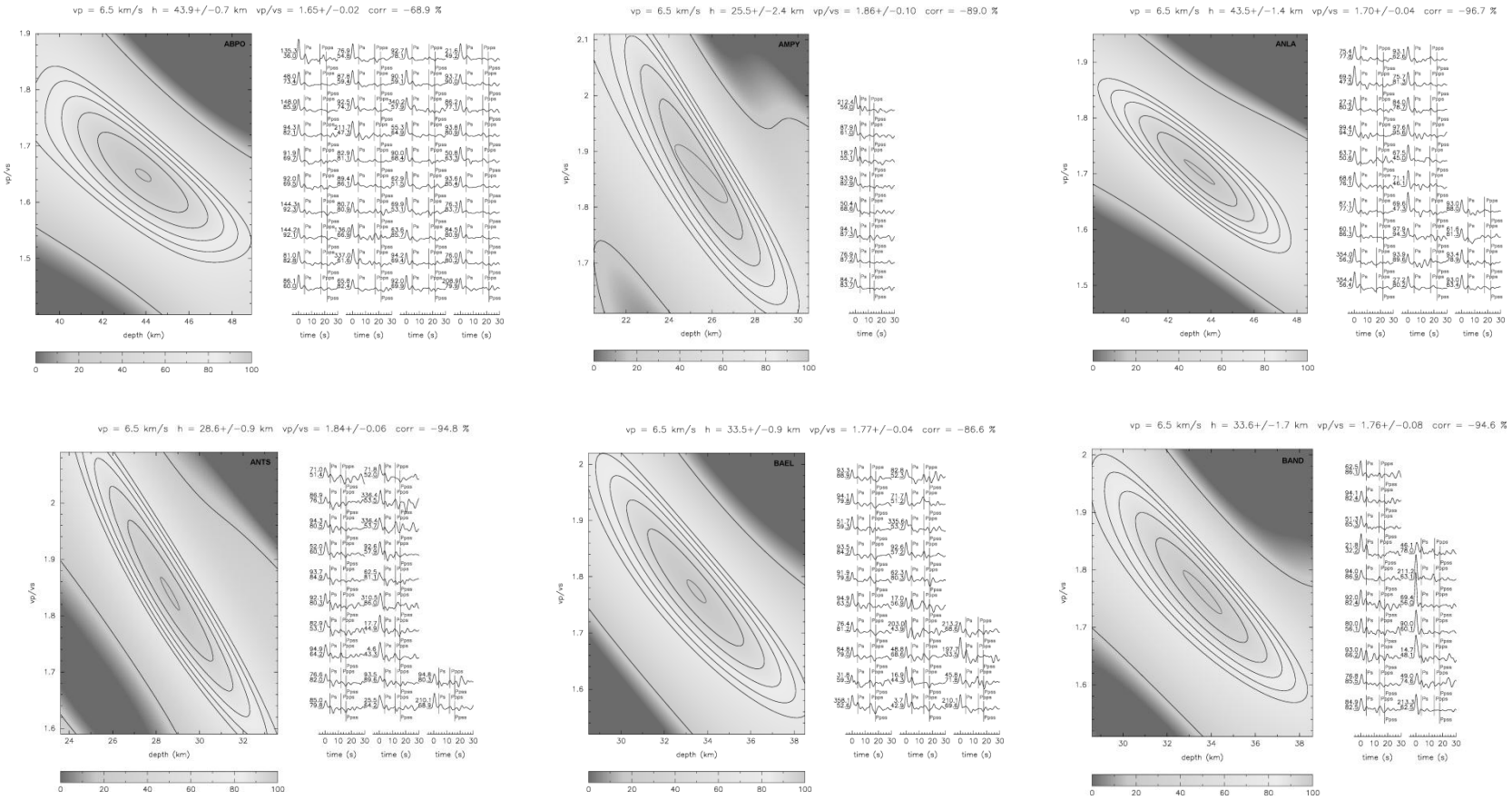

vp = 6.5 km/s h = 40.0+/−2.5 km vp/vs = 1.74+/−0.08 corr = −97.0 %

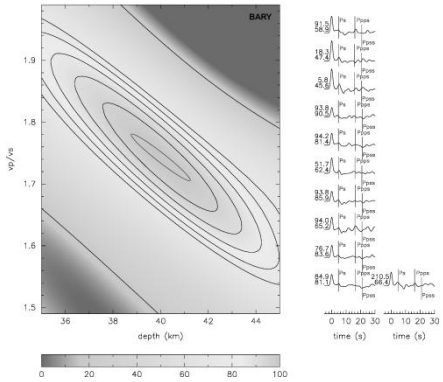

vp = 6.5 km/s h = 42.3+/−1.4 km vp/vs = 1.77+/−0.05 corr = −98.0 %

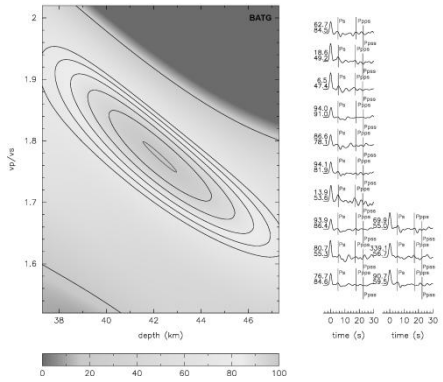

vp = 6.5 km/s h = 30.1+/−1.3 km vp/vs = 1.89+/−0.04 corr = −95.1 %

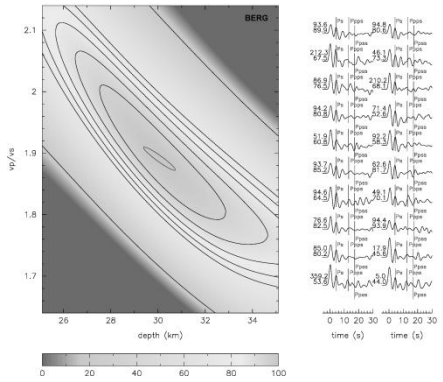

vp = 6.5 km/s h = 41.6+/−2.4 km vp/vs = 1.75+/−0.06 corr = −94.1 %

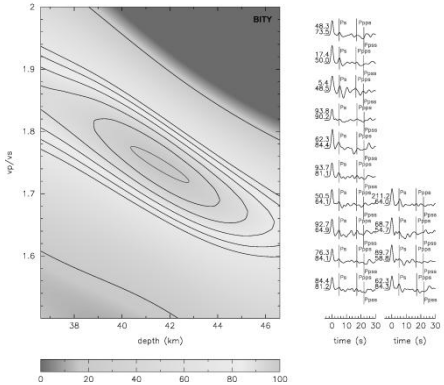

vp = 6.5 km/s h = 39.5+/−1.1 km vp/vs = 1.65+/−0.04 corr = −95.3 %

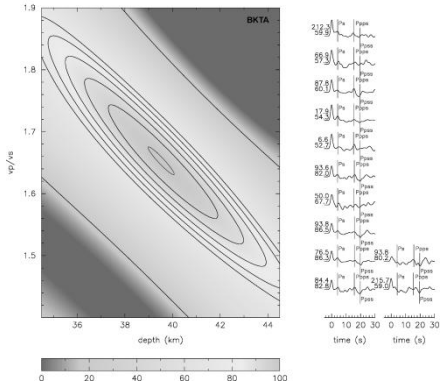

vp = 6.5 km/s h = 28.0+/−1.0 km vp/vs = 1.82+/−0.07 corr = −98.3 %

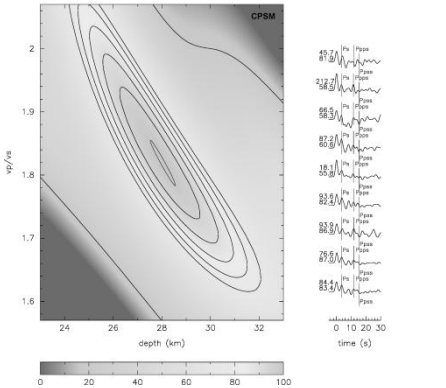

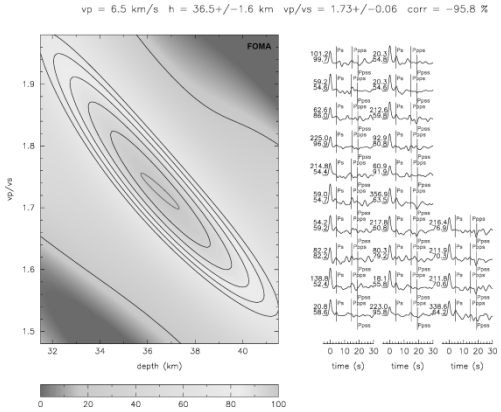
vp = 6.5 km/s h = 36.5+/−1.6 km vp/vs = 1.73+/−0.06 corr = −95.8 %
FOMA
vp/vs
depth (km)
time (s)

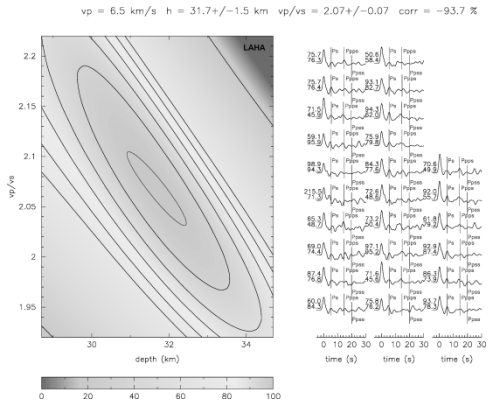
vp = 6.5 km/s h = 31.7+/−1.5 km vp/vs = 2.07+/−0.07 corr = −93.7 %
LAHA
vp/vs
depth (km)
time (s)

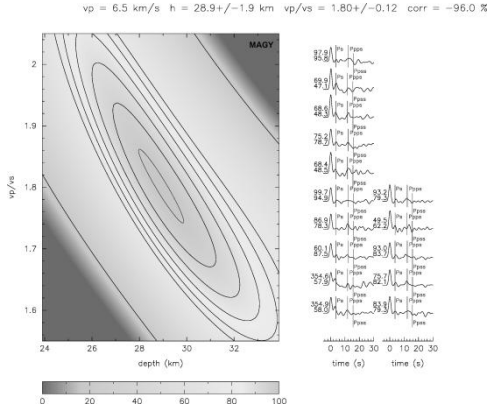
vp = 6.5 km/s h = 28.9+/−1.9 km vp/vs = 1.80+/−0.12 corr = −96.0 %
MAGY
vp/vs
depth (km)
time (s)

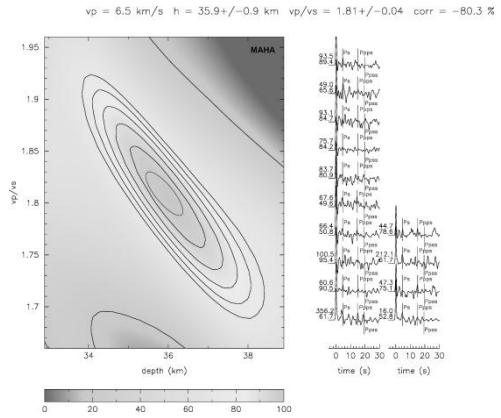
vp = 6.5 km/s h = 35.9+/−0.9 km vp/vs = 1.81+/−0.04 corr = −80.3 %
MAHA
vp/vs
depth (km)
time (s)

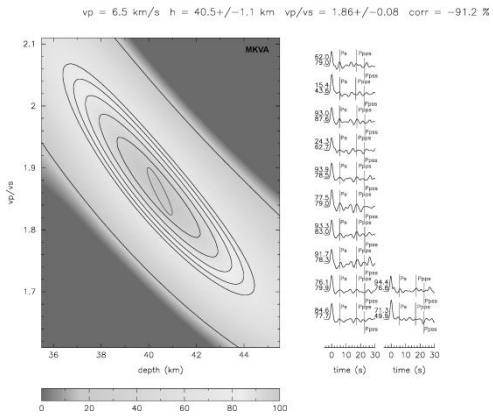
vp = 6.5 km/s h = 40.5+/−1.1 km vp/vs = 1.86+/−0.08 corr = −91.2 %
MKVA
vp/vs
depth (km)
time (s)

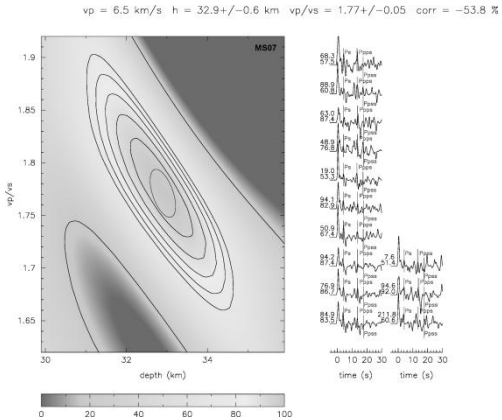
vp = 6.5 km/s h = 32.9+/−0.6 km vp/vs = 1.77+/−0.05 corr = −53.8 %
MS07
vp/vs
depth (km)
time (s)

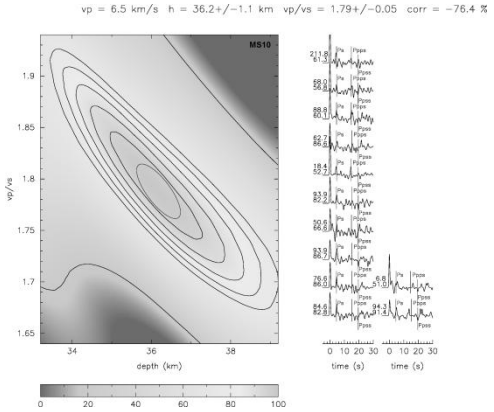
vp = 6.5 km/s h = 36.2+/−1.1 km vp/vs = 1.79+/−0.05 corr = −76.4 %
MS10
vp/vs
depth (km)
time (s)
time (s)

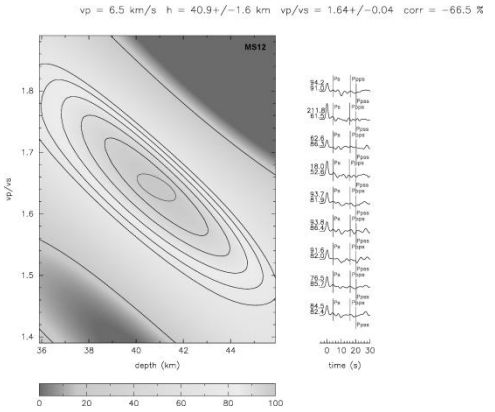
vp = 6.5 km/s h = 40.9+/−1.6 km vp/vs = 1.64+/−0.04 corr = −66.5 %
MS12
vp/vs
depth (km)
time (s)

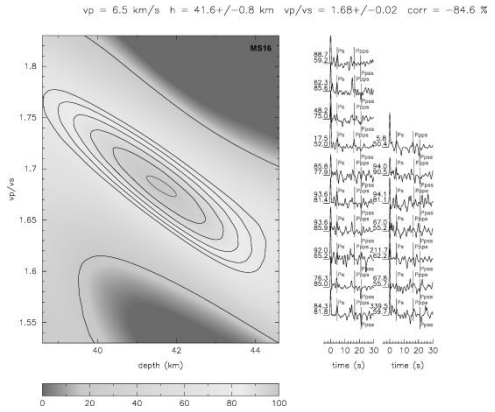
vp = 6.5 km/s h = 41.6+/−0.8 km vp/vs = 1.68+/−0.02 corr = −84.6 %
MS16
vp/vs
depth (km)
time (s)
time (s)

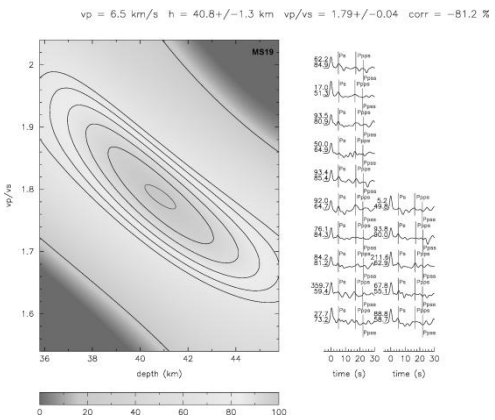
vp = 6.5 km/s h = 40.8+/−1.3 km vp/vs = 1.79+/−0.04 corr = −81.2 %
MS19
vp/vs
depth (km)
time (s)
time (s)

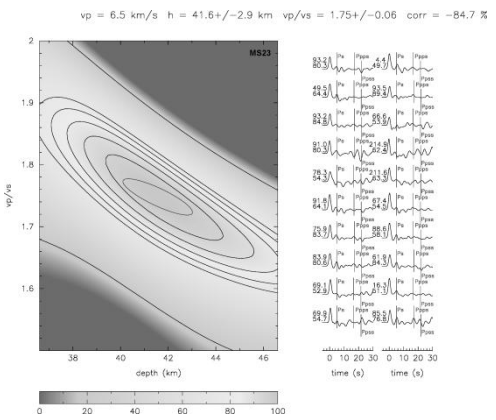
vp = 6.5 km/s h = 41.6+/−2.9 km vp/vs = 1.75+/−0.06 corr = −84.7 %
MS23
vp/vs
depth (km)
time (s)
time (s)

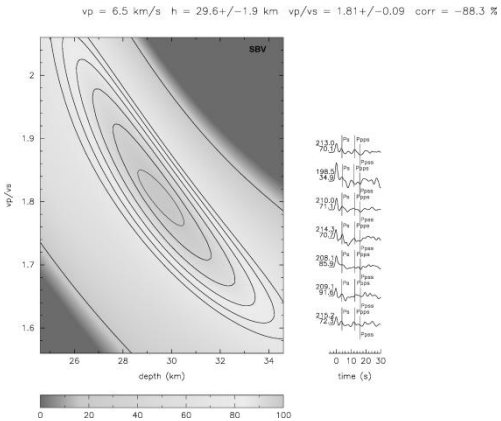
vp = 6.5 km/s h = 29.6+/−1.9 km vp/vs = 1.81+/−0.09 corr = −88.3 %
SBV
vp/vs
depth (km)
time (s)

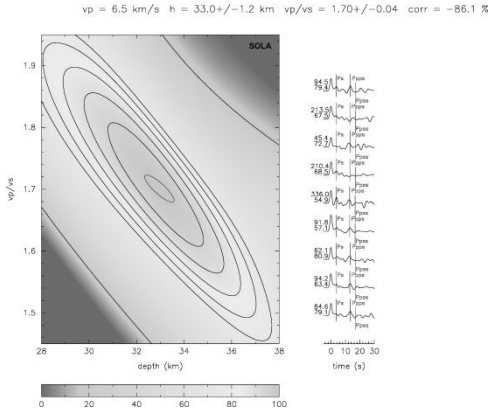
vp = 6.5 km/s h = 33.0+/−1.2 km vp/vs = 1.70+/−0.04 corr = −86.1 %
SOLA
vp/vs
depth (km)
time (s)

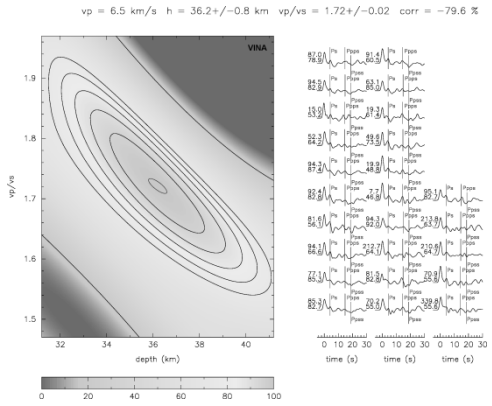
vp = 6.5 km/s h = 36.2+/−0.8 km vp/vs = 1.72+/−0.02 corr = −79.6 %
VINA
vp/vs
depth (km)
time (s)

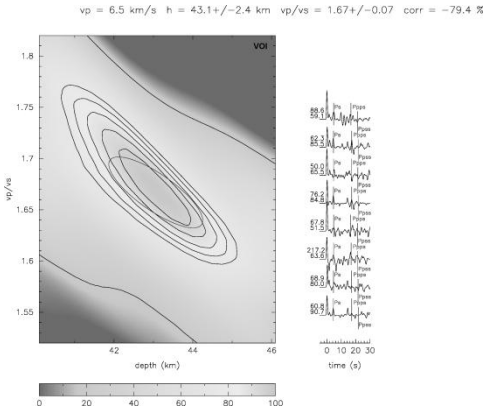
vp = 6.5 km/s h = 43.1+/−2.4 km vp/vs = 1.67+/−0.07 corr = −79.4 %
VOI
vp/vs
depth (km)
time (s)

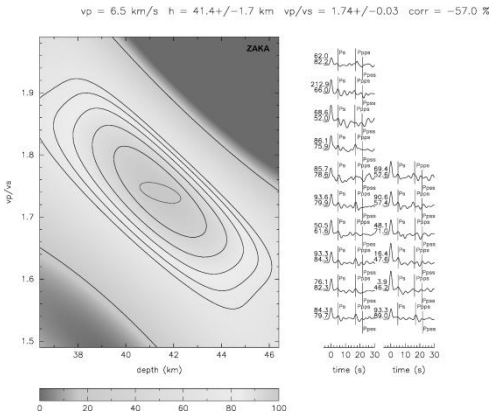
vp = 6.5 km/s h = 41.4+/−1.7 km vp/vs = 1.74+/−0.03 corr = −57.0 %
ZAKA
vp/vs
depth (km)
time (s)

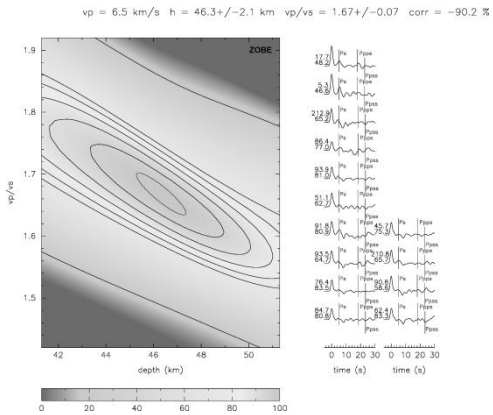
vp = 6.5 km/s h = 46.3+/−2.1 km vp/vs = 1.67+/−0.07 corr = −90.2 %
ZOBE
vp/vs
depth (km)
time (s)

Figure A.3: Joint inversion results from all stations used in the study.

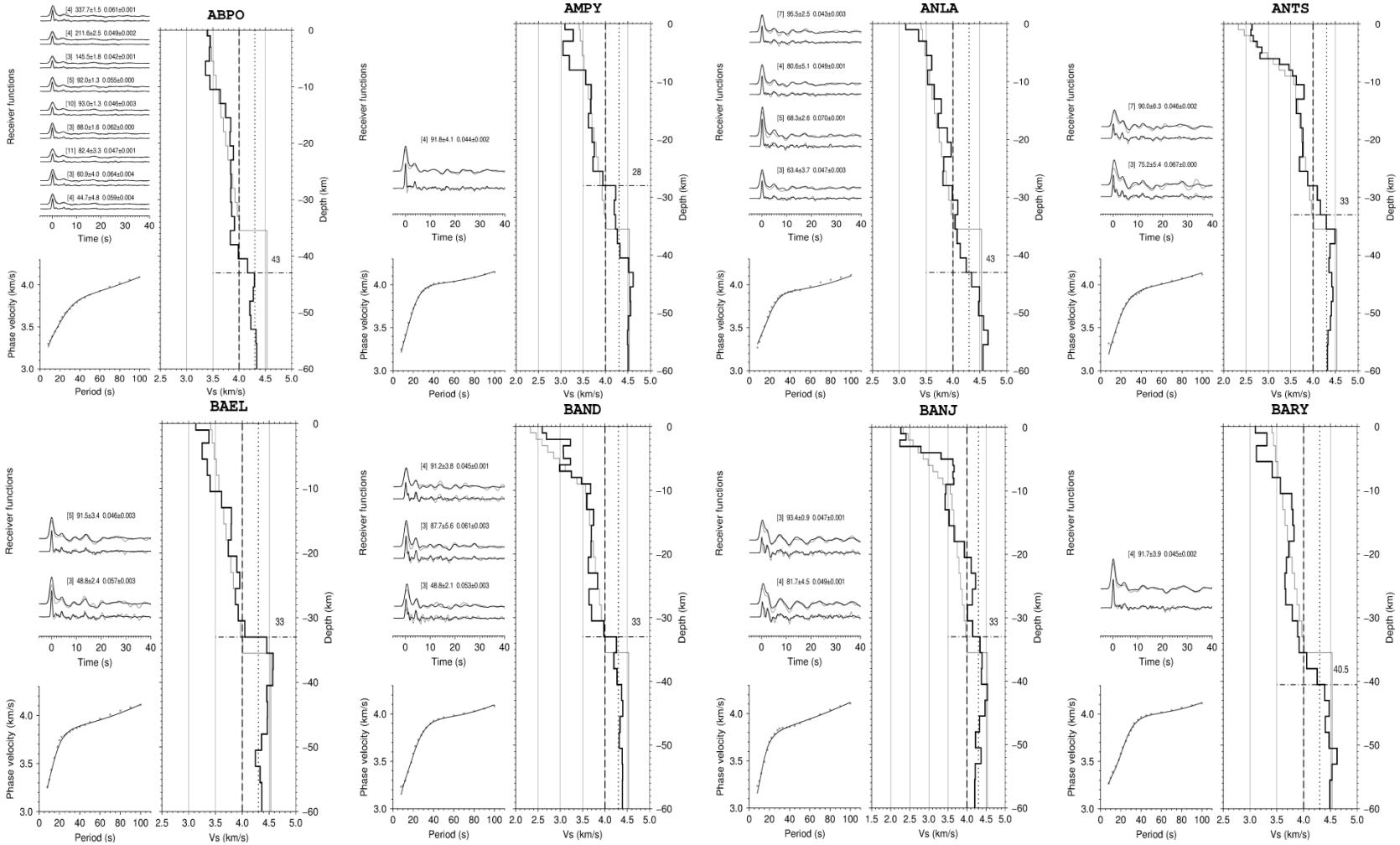

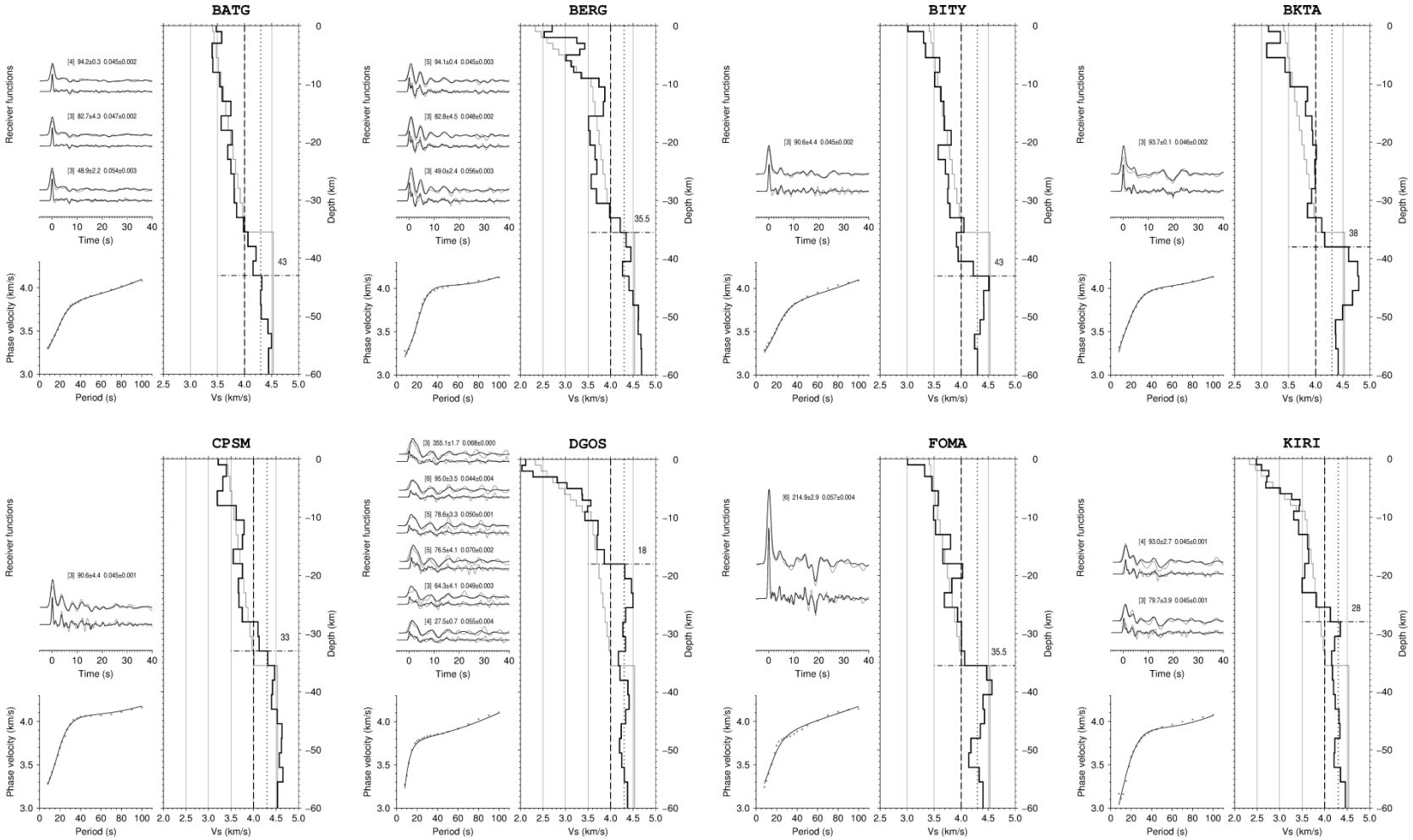
BATG
[4] 94.2±0.3 0.045±0.002
[3] 82.7±4.3 0.047±0.002
[3] 48.9±2.2 0.054±0.003
43
BERG
[5] 94.1±0.4 0.045±0.003
[3] 82.8±4.5 0.048±0.002
[3] 49.0±2.4 0.056±0.003
35.5
BITY
[3] 90.6±4.4 0.045±0.002
43
BKTA
[3] 93.7±0.1 0.046±0.002
38
CPSM
[3] 90.6±4.4 0.045±0.001
33
DGOS
[3] 355.1±1.7 0.068±0.000
[6] 95.0±3.5 0.044±0.004
[5] 78.6±3.3 0.050±0.001
[5] 76.5±4.1 0.070±0.002
[3] 64.3±4.1 0.049±0.003
[4] 27.5±0.7 0.055±0.004
18
FOMA
[6] 214.9±2.9 0.057±0.004
35.5
KIRI
[4] 93.0±2.7 0.045±0.001
[3] 79.7±3.9 0.045±0.001
28
Receiver functions
Time (s)
Phase velocity (km/s)
Period (s)
Vs (km/s)
Depth (km)

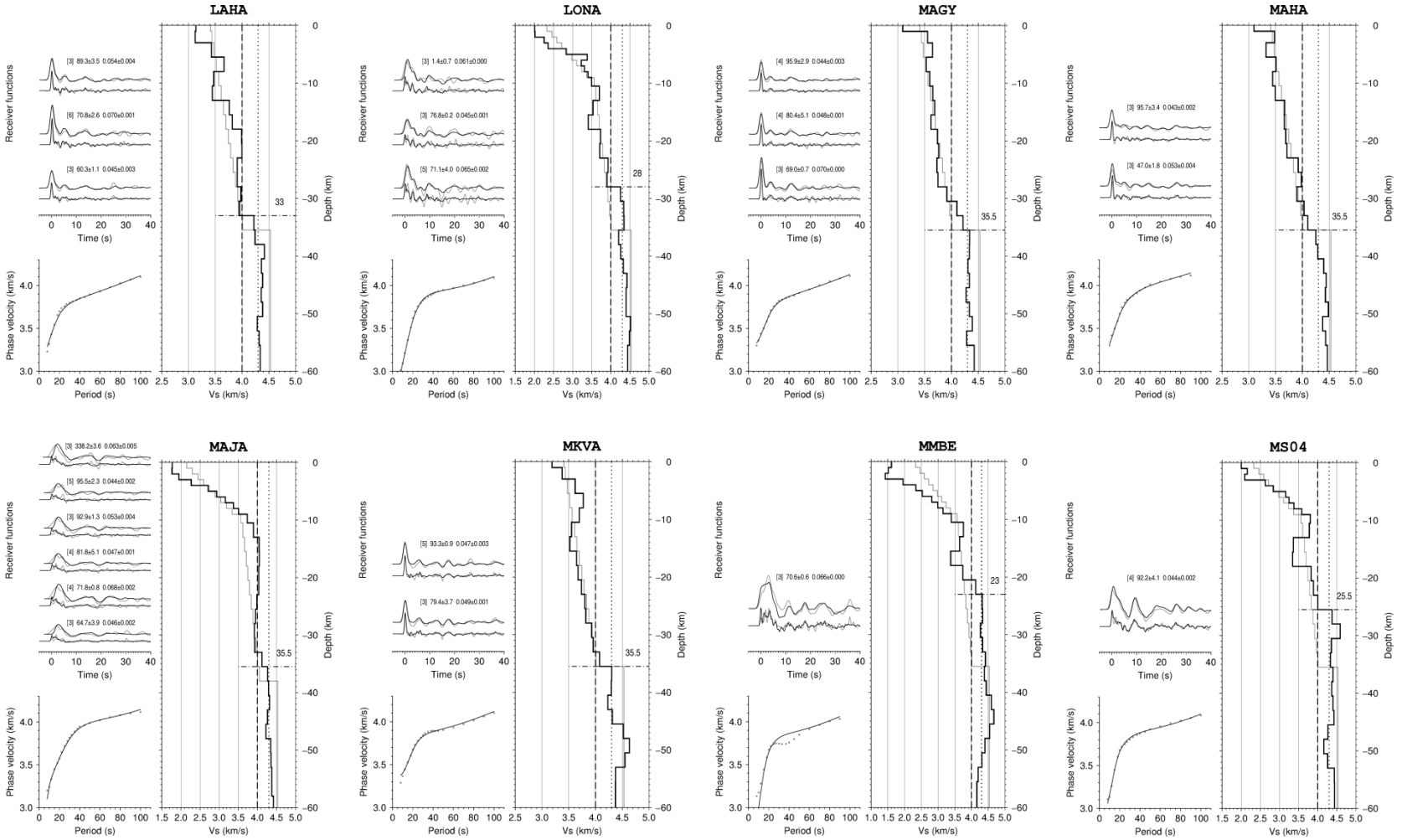
LAHA
LONA
MAGY
MAHA
MAJA
MKVA
MMBE
MS04
Receiver functions
Time (s)
Phase velocity (km/s)
Period (s)
Vs (km/s)
Depth (km)
33
28
35.5
23
25.5

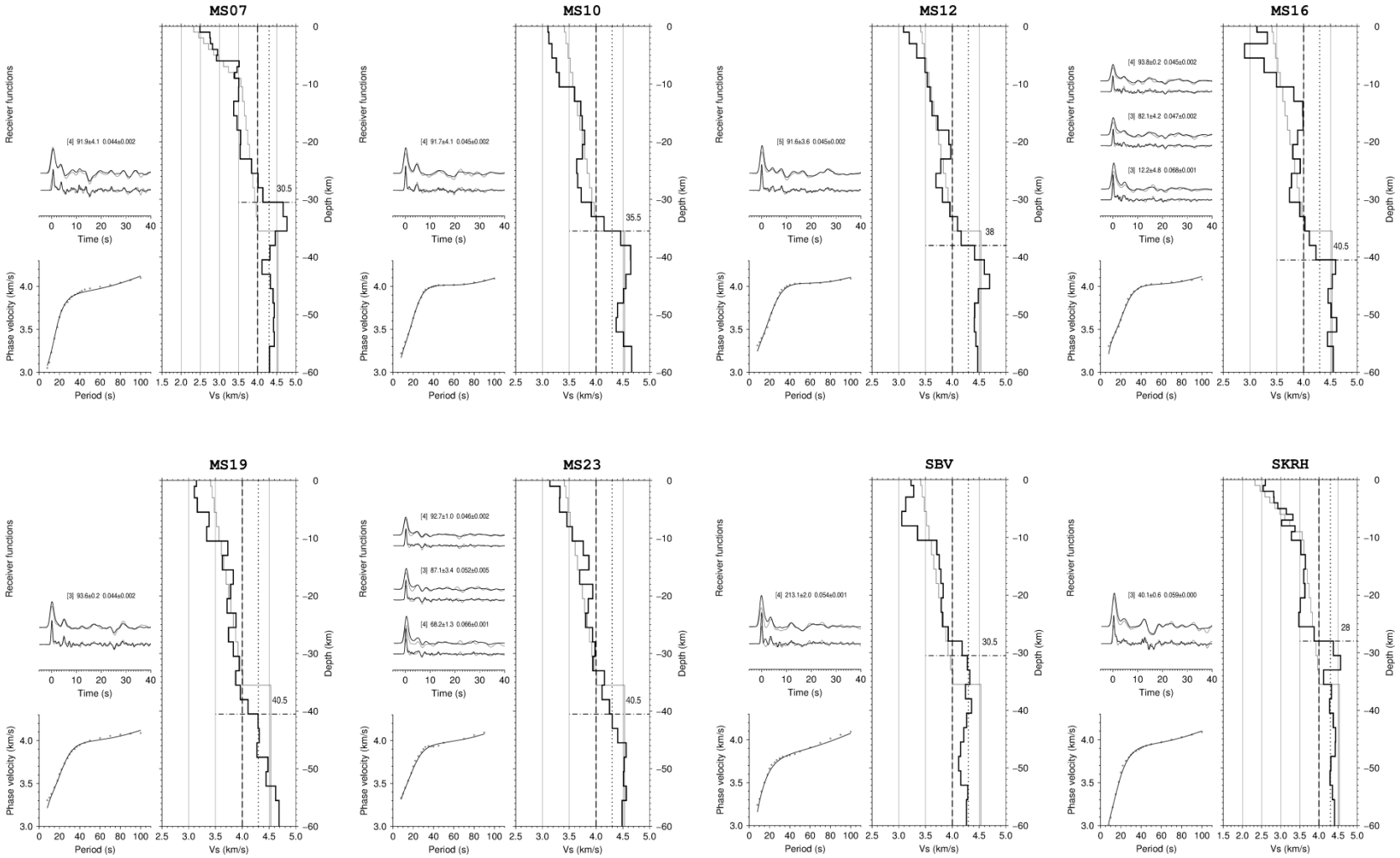
MS07
MS10
MS12
MS16
MS19
MS23
SBV
SKRH
Receiver functions
Time (s)
Phase velocity (km/s)
Period (s)
Vs (km/s)
Depth (km)
30.5
35.5
38
40.5
40.5
30.5
28

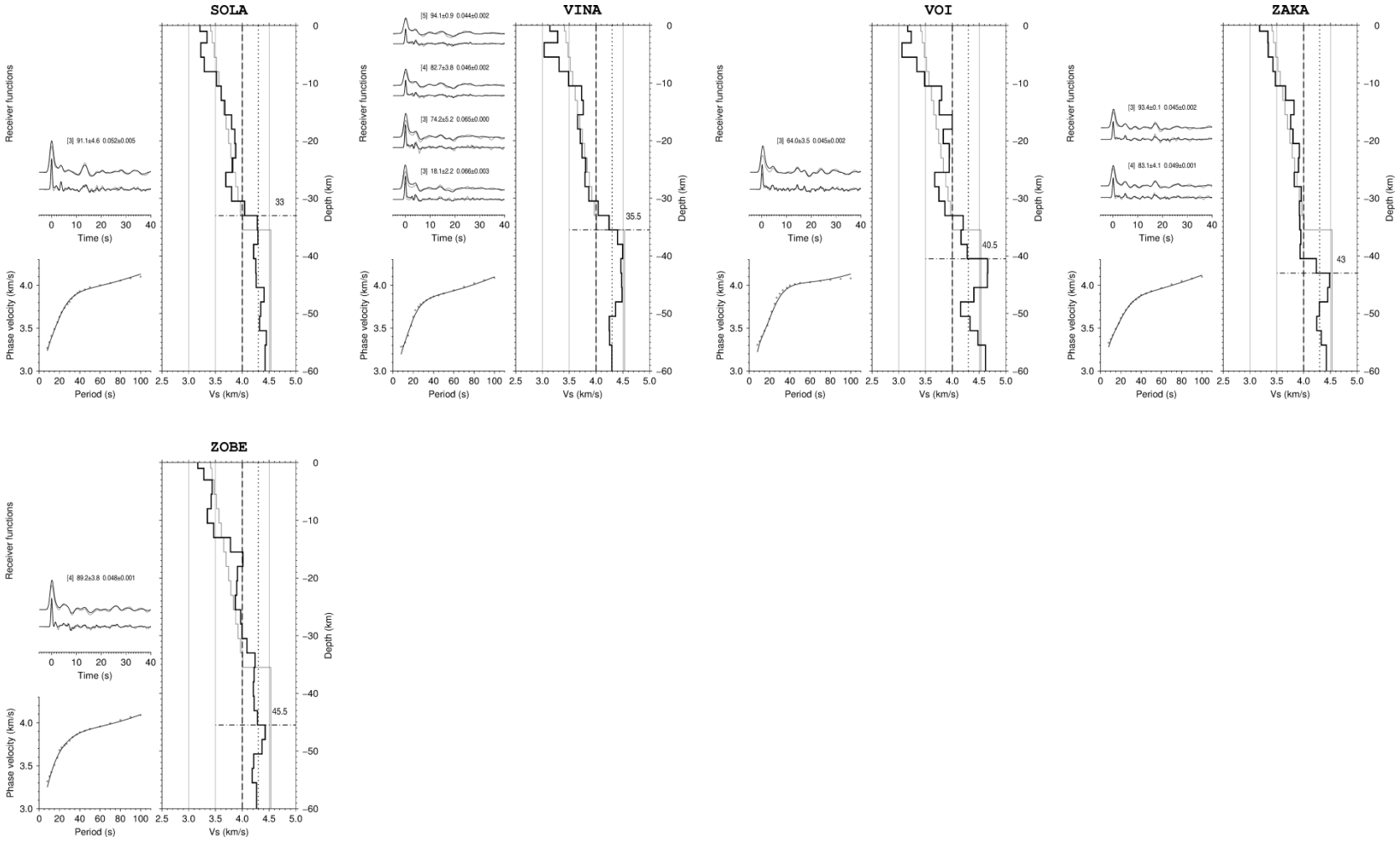
SOLA
[3] 91.1±4.6 0.052±0.005
33
VINA
[5] 94.1±0.9 0.044±0.002
[4] 82.7±3.8 0.046±0.002
[3] 74.2±5.2 0.065±0.000
[3] 18.1±2.2 0.066±0.003
35.5
VOI
[3] 64.0±3.5 0.045±0.002
40.5
ZAKA
[3] 93.4±0.1 0.045±0.002
[4] 83.1±4.1 0.049±0.001
43
ZOBE
[4] 89.2±3.8 0.048±0.001
45.5
Receiver functions
Time (s)
Phase velocity (km/s)
Period (s)
Vs (km/s)
Depth (km)

Appendix B

Table B.1: List of local and regional Earthquakes obtained from HYPOELLIPSE. Columns Date, Time, Lat, Lon, D, and M indicate the date, time, latitude, longitude, depth, and magnitude of the events, respectively.

Date	Time	Lat (°)	Lon (°)	D (km)	M
2011-10-24	22:24:19	-21.642	48.2192	3	1.6
2011-11-07	05:33:39	-19.167	49.6722	10	2.9
2011-11-13	10:54:56	-16.3807	46.8212	40	2.5
2011-11-13	11:26:31	-17.266	48.5332	23	2.7
2011-11-21	06:43:16	-18.123	47.7328	25	2.7
2011-11-21	23:24:56	-18.0083	49.0365	39	2.7
2011-11-24	00:04:29	-19.3725	46.2755	16	1.6
2011-11-24	13:33:45	-16.8693	49.0298	32	3.2
2011-11-25	06:35:05	-17.9702	48.51	10	3
2011-11-26	12:50:50	-18.0402	48.7883	8	3
2011-12-08	23:16:45	-16.8553	47.832	44	3.3
2011-12-23	17:34:50	-17.5392	47.7447	21	3
2011-12-30	06:31:07	-17.566	48.6633	45	3.3
2011-12-31	05:06:26	-14.9055	49.5288	15	2.7
2011-12-31	20:57:57	-18.1322	48.6437	12	3.2
2012-01-05	13:28:04	-17.5848	48.9803	15	2
2012-01-06	19:16:12	-16.4635	48.342	32	2.2
2012-01-09	03:36:21	-18.539	48.4108	15	3.2
2012-01-09	22:13:52	-18.7087	48.8858	15	2.6
2012-01-24	20:59:25	-15.6505	49.945	0	1.1
2012-01-28	08:52:53	-16.8375	48.6085	15	2.2
2012-01-28	14:16:02	-17.3345	48.525	9	2.7
2012-01-29	02:28:02	-17.787	47.9625	12	2.3
2012-01-31	18:41:48	-17.3365	48.6577	10	3.9
2012-02-01	22:16:56	-16.7583	48.5675	13	2.4
2012-02-02	13:29:17	-16.545	47.9222	0	2.5
2012-02-06	14:57:04	-14.6278	49.4065	8	2.5
2012-02-07	00:49:18	-24.6252	47.1657	10	3.1
2012-02-11	23:30:55	-19.3297	47.0062	15	1.5
2012-02-12	06:32:22	-21.0682	47.4532	15	1.3
2012-02-12	15:49:55	-17.2903	48.5257	12	3.5
2012-02-12	19:34:38	-18.1048	48.6703	30	2.4
2012-02-26	08:23:49	-19.0145	47.1862	12	2.3
2012-03-15	00:54:09	-14.3097	49.1123	55	3.7
2012-03-16	11:56:56	-17.5407	48.355	13	4.3
2012-03-16	23:29:41	-17.6688	48.5443	16	3.2
2012-03-20	23:37:18	-19.2365	47.531	10	2.6
2012-03-22	00:09:54	-18.3017	48.521	28	3
2012-03-30	08:26:25	-18.4185	47.8728	0	3.7
2012-04-05	01:52:35	-19.9055	47.0212	10	3.6
2012-04-10	00:58:36	-18.2938	47.5985	21	3.1
2012-04-21	19:24:43	-15.8993	48.4238	24	3
2012-04-23	21:13:15	-16.8972	45.5873	28	4
2012-04-29	20:31:12	-18.7678	47.609	10	3
2012-05-02	07:46:24	-21.034	45.8987	10	2.6
2012-05-12	02:12:52	-16.8523	45.6672	7	3.8
2012-05-14	11:57:50	-14.9695	49.3692	21	3.4
2012-05-29	13:50:37	-13.9058	49.494	30	3.8
2012-06-06	22:12:02	-23.7415	44.9128	22	2.9
2012-06-17	01:08:09	-16.4653	49.2023	5	2.8
2012-06-17	10:11:35	-16.5207	49.2263	15	3.2
2012-06-17	16:48:51	-15.8123	50.4517	6	3.1
2012-06-22	16:38:33	-16.817	47.9253	15	2.4
2012-06-23	11:18:27	-20.039	46.5087	16	3.4
2012-06-25	10:56:08	-17.4405	48.6612	10	3.4
2012-06-26	00:10:50	-21.3817	45.8382	25	3.7
2012-06-26	01:34:44	-17.8255	49.1072	25	3.4
2012-07-03	06:58:24	-21.6757	47.5223	57	2.4
2012-07-04	15:28:04	-16.1727	46.139	5	4
2012-07-04	18:25:38	-16.1932	49.1858	0	3
2012-07-10	04:06:38	-17.8858	48.2843	10	2.6
2012-07-11	12:53:50	-14.1095	48.6803	18	2.7
2012-07-15	18:17:32	-16.1695	48.8885	10	3.2
2012-07-17	10:13:51	-20.9892	41.4405	11	2.8
2012-07-18	17:21:43	-18.9963	47.3463	11	2.9
2012-07-24	00:44:43	-22.6318	45.8355	14	3.7
2012-07-26	04:41:42	-17.7343	48.5703	15	3
2012-07-29	20:36:24	-14.0943	49.4173	10	2.1
2012-07-30	16:45:51	-23.5785	45.0288	9	3.7
2012-08-03	10:27:42	-18.5195	48.7302	14	2.7
2012-08-03	18:24:14	-15.395	50.7932	26	2.8
2012-08-05	18:07:10	-16.4117	47.5842	12	2.4
2012-08-06	02:25:12	-18.0475	48.4152	23	2.8
2012-08-06	23:54:29	-19.125	47.0693	5	3
2012-08-07	02:02:57	-19.1808	47.1688	10	2.6
2012-08-08	05:11:13	-20.2323	47.1507	28	3.2
2012-08-08	08:07:33	-17.6642	48.7412	32	2.9
2012-08-09	17:14:16	-18.2713	45.9958	15	1.3
2012-08-10	07:46:07	-18.1122	47.9817	30	2.5
2012-08-11	13:57:06	-20.1305	46.8315	27	2.2
2012-08-11	23:32:12	-15.5098	48.073	24	4.3
2012-08-12	01:05:03	-15.3675	48.0042	24	3.1
2012-08-12	17:55:15	-17.5478	48.6962	18	2.6
2012-08-18	07:05:34	-18.6778	45.8137	10	3.9
2012-08-18	20:00:38	-15.428	48.1155	23	1.2
2012-08-19	21:16:00	-18.8467	46.6445	0	2.9
2012-08-21	09:06:24	-18.8825	46.7463	17	2
2012-08-21	10:07:32	-14.1435	48.654	18	1.4
2012-08-21	20:34:48	-18.948	46.6645	17	1.6
2012-08-22	00:35:11	-14.3012	48.6183	23	3.4
2012-08-22	23:25:57	-24.2323	45.5683	0	1.8
2012-08-23	21:47:11	-19.0348	46.7478	12	1.8
2012-08-24	01:31:31	-17.5645	48.3463	25	2.4
2012-08-24	04:10:40	-19.0325	46.7177	19	1.8
2012-08-25	00:24:06	-19.1357	46.7905	27	1.9
2012-08-25	07:05:26	-16.4783	49.8902	43	1.7
2012-08-25	14:51:21	-17.3982	48.7248	2	2.3
2012-08-26	02:03:43	-19.0528	46.6887	30	1.4
2012-08-27	21:46:44	-19.0637	46.7602	29	1.5
2012-08-28	08:39:36	-17.284	48.0477	25	2.4
2012-08-29	18:31:38	-19.0032	46.692	8	2.6
2012-08-30	07:02:53	-17.7522	48.1622	13	3.6
2012-08-30	09:32:12	-19.0182	46.6193	21	1.9

2012-09-01	00:07:51	-17.8525	48.1322	24	2.5
2012-09-01	10:10:10	-23.1958	43.582	26	3
2012-09-01	18:34:16	-19.021	46.737	4	2.4
2012-09-01	19:06:42	-18.1338	46.559	23	2.1
2012-09-01	23:31:12	-19.223	46.6662	25	3.9
2012-09-02	07:22:43	-18.9458	46.6833	23	2.1
2012-09-02	12:20:08	-18.999	46.7182	19	1.7
2012-09-02	20:19:11	-18.9712	46.711	6	2.3
2012-09-03	12:40:32	-16.0078	47.8328	28	3.8
2012-09-03	15:25:29	-17.372	48.022	30	2.5
2012-09-03	23:27:39	-19.8672	46.3643	10	3.5
2012-09-04	20:34:25	-19.2347	46.7073	25	3
2012-09-04	21:31:50	-18.92	46.7132	21	1.6
2012-09-05	04:10:42	-18.8763	46.7463	36	1.7
2012-09-05	10:44:51	-23.95	46.4798	8	2.6
2012-09-06	11:52:29	-19.1918	46.6933	9	3
2012-09-06	13:10:20	-23.6855	45.2078	17	2.3
2012-09-07	20:34:27	-18.9033	46.7525	5	2
2012-09-08	20:03:58	-18.5025	46.8252	28	2
2012-09-09	08:07:38	-18.761	45.964	21	1.5
2012-09-09	11:12:21	-17.8195	48.0245	3	2.9
2012-09-09	12:03:43	-18.9935	46.6612	20	2.3
2012-09-09	14:46:28	-18.9232	46.7375	18	2.1
2012-09-10	12:52:58	-18.9682	46.6908	21	2.9
2012-09-11	01:04:16	-13.5722	48.943	27	2.6
2012-09-11	03:53:49	-18.7385	46.4257	20	2.1
2012-09-12	23:56:16	-19.1985	47.1692	22	2.5
2012-09-13	23:42:36	-14.3963	49.449	14	2.3
2012-09-14	13:11:03	-23.4898	47.0065	18	2.5
2012-09-14	20:12:41	-20.713	47.8262	1	2.6
2012-09-15	20:02:00	-18.271	47.6858	17	2.5
2012-09-16	20:44:36	-14.2893	48.6628	10	2.3
2012-09-17	00:46:49	-18.7287	46.9418	0	2.3
2012-09-17	12:45:45	-17.3243	48.4733	17	2.9
2012-09-17	19:25:59	-18.7677	47.5028	16	1.2
2012-09-18	03:32:08	-18.6137	47.6098	8	3
2012-09-18	14:58:02	-20.5777	45.239	40	2.4
2012-09-18	16:33:39	-19.2405	48.415	28	2.9
2012-09-19	05:17:48	-24.5003	45.0925	12	1.9
2012-09-19	07:53:53	-17.7002	46.6132	21	2.7
2012-09-20	10:26:06	-18.8875	46.7232	10	2.9
2012-09-20	11:13:21	-18.9103	46.7167	47	2.3
2012-09-21	21:52:16	-18.2265	46.3982	10	1
2012-09-22	06:21:36	-20.0608	46.8787	31	3.9
2012-09-23	18:55:12	-16.8408	49.2403	25	2.6
2012-09-23	20:39:37	-18.7868	46.7373	22	2.8
2012-09-23	23:37:07	-18.3962	47.9043	26	1.8
2012-09-24	09:12:55	-18.9545	46.754	14	1
2012-09-25	22:47:05	-18.2233	46.3503	31	1.6
2012-09-26	14:17:43	-19.8423	46.8112	0	2
2012-09-27	16:41:06	-16.2895	45.4213	8	2.7
2012-09-27	23:17:37	-18.9655	46.7392	17	2.7
2012-09-28	12:59:55	-18.9733	46.7122	17	1.7
2012-09-29	09:55:01	-19.2757	47.7032	27	3.8
2012-09-29	16:13:56	-19.3788	46.9172	16	3.2
2012-09-29	22:07:54	-17.5388	48.3378	16	2.4
2012-09-30	06:08:15	-14.9487	49.5858	9	3.9
2012-09-30	08:18:23	-16.667	46.1885	39	3
2012-09-30	15:38:56	-18.7632	46.1337	15	1.2
2012-09-30	19:43:28	-14.9102	49.5225	7	2.4
2012-10-01	19:06:12	-17.969	47.8388	7	3
2012-10-01	23:47:43	-20.9133	46.5897	11	2.3
2012-10-03	12:37:37	-18.9585	46.8422	34	1.1
2012-10-03	21:45:11	-19.0207	46.8237	30	2.4
2012-10-04	11:15:42	-17.6158	48.4695	26	2.9
2012-10-05	19:43:32	-13.8795	49.0825	8	2.5
2012-10-06	22:36:04	-13.8365	47.8612	9	2.6
2012-10-08	05:33:47	-17.4528	48.5273	33	2.9
2012-10-09	00:46:51	-14.4325	49.4783	25	2.4
2012-10-10	04:11:24	-18.64	47.5725	37	3.6
2012-10-10	05:53:48	-18.9592	46.7178	15	2.3
2012-10-10	09:21:22	-18.7875	46.7552	28	2.3
2012-10-10	18:42:53	-19.1245	46.781	19	2.5
2012-10-11	20:49:00	-14.9452	49.7092	20	2.8
2012-10-13	09:32:15	-14.9158	49.771	31	2.4
2012-10-14	00:52:04	-18.397	46.7807	1	1.8
2012-10-15	18:35:08	-18.8935	46.6533	34	1.9
2012-10-16	16:51:47	-19.0573	46.7125	12	2.5
2012-10-16	22:54:00	-18.9417	46.7625	20	2
2012-10-17	00:22:43	-18.9212	46.7237	0	2.1
2012-10-17	01:51:26	-19.3237	46.6895	4	2.7
2012-10-17	08:37:16	-14.3258	49.432	33	3
2012-10-17	13:47:13	-20.1787	46.161	20	2.3
2012-10-17	16:24:13	-18.544	46.5078	40	2
2012-10-18	10:42:26	-19.0665	46.6972	21	2.7
2012-10-18	11:58:05	-14.9987	49.3445	27	3
2012-10-18	12:44:24	-20.27	47.0393	33	2.6
2012-10-18	16:12:48	-16.8027	49.7422	32	3.3
2012-10-18	17:36:05	-19.8467	46.9198	26	2.2
2012-10-18	18:42:23	-19.0118	46.7008	17	2
2012-10-18	23:39:39	-14.3562	49.4022	40	2.4
2012-10-19	01:39:23	-14.3587	49.4353	19	2.1
2012-10-20	08:52:02	-22.9135	45.3048	27	2.1
2012-10-20	10:34:11	-17.9122	47.0497	31	1.7
2012-10-20	18:19:41	-18.5415	46.6318	19	1.7
2012-10-21	20:50:40	-14.338	49.456	9	2.4
2012-10-23	05:06:15	-20.556	45.435	18	2.5
2012-10-23	11:29:44	-19.0038	46.7232	36	1.2
2012-10-25	05:53:25	-18.2177	47.54	27	2.6
2012-10-25	10:25:46	-23.4245	45.0212	27	2.3
2012-10-25	12:42:29	-14.3732	49.4578	32	2.9
2012-10-26	17:18:14	-18.5957	45.8223	19	3
2012-10-26	20:15:04	-18.89	46.7673	4	1.1
2012-10-27	05:40:38	-18.9602	46.7408	15	1.3
2012-10-28	12:58:13	-17.3093	45.6313	10	2.7
2012-10-31	00:32:00	-18.0483	47.7547	8	2.4
2012-10-31	10:11:29	-18.4165	47.2405	32	1.9
2012-11-01	00:19:27	-17.2627	49	43	4.7
2012-11-01	23:40:50	-18.9198	46.6483	20	1.4
2012-11-02	20:13:39	-17.724	48.5027	12	2.5
2012-11-02	21:57:56	-17.7145	46.2078	24	2.9
2012-11-03	03:03:57	-18.6707	46.1497	22	3
2012-11-04	01:22:34	-19	46.729	12	2.7
2012-11-04	01:58:42	-19.1252	46.7072	20	2.5
2012-11-04	10:05:12	-18.2267	47.7903	23	2.6
2012-11-04	12:49:25	-24.4338	44.9608	28	3.1
2012-11-05	16:08:38	-19.242	46.4258	16	2.4
2012-11-06	08:11:44	-16.1087	47.4305	26	3.1
2012-11-07	00:51:43	-18.5822	47.7022	24	1.8
2012-11-07	01:50:34	-15.3942	47.1542	2	2.7

2012-11-08	05:29:13	-25.417	45.0412	9	1.9
2012-11-08	17:25:58	-17.3147	48.4552	19	2.5
2012-11-11	12:00:31	-13.8735	48.4852	26	2.9
2012-11-13	00:01:51	-19.0268	46.8263	15	2.7
2012-11-13	16:13:47	-19.3612	48.6043	12	2.6
2012-11-14	20:15:15	-18.2133	47.7377	10	1.4
2012-11-16	16:40:27	-18.1557	45.5207	10	2.3
2012-11-20	00:00:51	-20.4455	45.5243	30	3
2012-11-20	08:02:57	-18.292	45.493	35	2.4
2012-11-21	23:17:06	-17.3228	47.983	0	2.6
2012-11-22	09:46:34	-19.5865	46.919	25	2.6
2012-11-23	00:22:51	-15.0187	49.2763	32	2.8
2012-11-23	10:27:09	-18.894	46.757	19	2.1
2012-11-26	06:18:33	-19.8982	47.2388	28	2.3
2012-11-27	00:40:11	-20.5035	46.661	29	2.1
2012-11-27	09:34:19	-17.9158	48.3493	16	3
2012-11-27	20:22:35	-18.3145	46.5178	34	2
2012-11-30	20:07:23	-17.4887	48.4933	28	2.6
2012-12-02	15:55:35	-19.2625	46.683	34	2.1
2012-12-03	18:06:22	-19.0048	46.8228	15	2.6
2012-12-05	04:47:38	-18.5747	46.7165	34	1.9
2012-12-06	07:14:40	-17.5245	49.4947	29	3.1
2012-12-08	11:26:05	-19.061	46.707	7	1.8
2012-12-09	09:34:19	-24.263	47.5237	10	1.8
2012-12-10	03:52:20	-20.294	45.5223	17	1.1
2012-12-10	23:52:41	-15.5575	49.9012	18	3.4
2012-12-11	01:08:48	-18.8793	46.7363	22	2.4
2012-12-11	21:40:54	-20.1148	47.0828	21	2.1
2012-12-12	07:03:39	-17.8912	45.9868	6	2
2012-12-12	16:22:44	-18.5132	44.7132	4	1.9
2012-12-13	05:54:43	-22.539	47.4767	5	3.7
2012-12-13	20:20:00	-14.2973	48.5507	15	1.3
2012-12-16	17:33:10	-18.9063	46.7338	30	1.9
2012-12-16	23:33:50	-18.9075	46.773	13	1.7
2012-12-17	03:39:29	-19.0602	46.7317	20	2.2
2012-12-20	07:04:53	-18.9853	46.7422	23	2.3
2012-12-21	00:44:46	-18.99	46.751	16	2.3
2012-12-21	23:47:34	-19.0047	46.6932	15	3
2012-12-22	00:17:16	-18.9357	46.8125	35	1.1
2012-12-22	08:19:47	-19.0418	46.7057	21	2
2012-12-22	21:55:24	-18.9663	46.72	6	2.1
2012-12-23	04:48:13	-18.923	46.6603	18	1.4
2012-12-23	12:30:40	-19.0528	46.7225	25	2.4
2012-12-24	12:17:16	-19.0372	46.7315	18	2.8
2012-12-26	16:41:54	-20.3245	47.1163	32	2.1
2012-12-27	01:31:01	-17.7022	48.5963	33	3.3
2012-12-27	02:58:11	-14.2712	48.667	18	3
2012-12-28	16:49:00	-20.039	46.4197	8	2.3
2012-12-29	00:56:43	-17.7347	48.6678	12	2.8
2012-12-29	22:56:05	-16.402	48.746	17	2.8
2012-12-30	01:26:38	-18.0463	46.2585	32	3.6
2012-12-30	18:40:54	-23.782	46.4213	20	2.2
2012-12-30	22:58:21	-18.9927	46.7265	20	2.6
2013-01-01	04:43:16	-18.9255	46.7067	7	2.4
2013-01-01	08:39:55	-18.9303	46.7062	29	2.2
2013-01-01	10:35:37	-19.0285	46.6845	26	1.6
2013-01-01	17:54:45	-19.1287	46.7498	34	2.1
2013-01-01	21:53:35	-18.729	46.318	31	2
2013-01-01	23:16:09	-18.7515	46.6605	15	1.9
2013-01-02	06:46:32	-18.9775	46.6977	33	1.3
2013-01-02	10:15:14	-24.1883	44.8145	31	2.6
2013-01-03	23:13:02	-14.3868	48.7047	18	2.3
2013-01-04	06:35:14	-24.471	44.1872	23	3.4
2013-01-06	05:33:15	-19.1158	46.7075	22	1.9
2013-01-08	12:02:12	-18.9565	46.7685	26	2.7
2013-01-08	16:01:19	-18.9665	46.8122	26	2.7
2013-01-08	21:59:29	-18.9975	46.7155	5	2.4
2013-01-09	23:54:39	-16.9527	45.7065	24	2.8
2013-01-10	00:50:09	-14.8833	49.505	26	2
2013-01-10	17:32:11	-18.9195	46.728	13	1.9
2013-01-13	13:24:54	-18.6865	45.9267	23	4.8
2013-01-15	15:44:11	-19.029	46.7092	20	3.4
2013-01-15	19:10:20	-18.0533	46.4677	26	2.3
2013-01-15	21:55:02	-17.287	47.7622	28	2.5
2013-01-18	09:25:52	-18.922	46.6277	31	2.1
2013-01-18	10:14:58	-18.9652	46.6293	30	2.2
2013-01-19	04:19:03	-22.1372	47.0388	25	3.2
2013-01-19	14:40:32	-17.4625	48.6482	21	1.8
2013-01-20	12:09:02	-18.6827	46.1128	24	3.1
2013-01-21	06:58:38	-18.7498	45.9875	30	2.2
2013-01-21	16:04:27	-17.3882	47.7385	26	2.3
2013-01-21	17:22:04	-18.7425	46.588	27	2
2013-01-22	09:26:43	-17.0973	49.8408	18	3
2013-01-23	02:16:03	-18.502	45.7528	20	2.6
2013-01-24	00:44:46	-14.269	48.7162	39	2.3
2013-01-24	13:36:48	-24.5547	44.7708	11	2
2013-01-25	01:00:55	-24.481	45.0642	19	2.5
2013-01-26	19:57:13	-19.6118	46.9463	33	2.8
2013-01-28	15:08:48	-18.3912	45.4923	29	1.6
2013-01-28	23:54:34	-23.721	45.6468	21	3.6
2013-01-29	01:43:30	-23.8175	44.5862	33	1.7
2013-01-29	17:11:34	-14.5573	49.5095	25	2.4
2013-02-01	12:37:11	-22.6375	47.8622	18	2.9
2013-02-02	06:24:45	-19.0208	46.7652	29	1.3
2013-02-03	04:29:49	-22.6063	44.3543	4	2.5
2013-02-03	07:01:40	-14.1375	48.1962	18	2.4
2013-02-03	20:57:57	-15.829	47.8178	3	1.3
2013-02-04	09:21:52	-18.1317	46.6945	30	2
2013-02-04	20:19:51	-20.0968	46.438	16	2.9
2013-02-05	23:16:47	-18.289	46.4423	36	1.2
2013-02-08	02:11:44	-18.6562	47.686	36	2.5
2013-02-08	17:48:35	-17.2993	48.6083	0	3.2
2013-02-08	22:15:05	-18.3592	47.6505	25	2.2
2013-02-10	01:36:26	-17.9903	46.2158	15	1.5
2013-02-11	11:03:34	-18.6295	46.3573	8	1.5
2013-02-11	21:47:50	-17.5922	48.654	19	2.5
2013-02-11	23:02:50	-18.9683	46.7018	20	1.8
2013-02-13	14:00:48	-18.2467	48.1553	29	2.5
2013-02-14	00:35:03	-14.5393	49.0313	22	2.1
2013-02-14	13:03:40	-13.8348	49.4443	36	2.5
2013-02-15	13:52:03	-18.1168	46.5158	38	3.1
2013-02-18	04:06:33	-22.7135	47.5222	30	4.2
2013-02-18	15:19:48	-17.3317	48.4108	27	2.9
2013-02-20	14:12:13	-18.6717	44.8002	0	2.9
2013-02-20	16:43:44	-19.0222	46.7377	29	2.3
2013-02-21	07:27:14	-18.3948	46.5802	14	2.7
2013-02-21	23:36:07	-18.9628	46.7443	18	2.6
2013-02-22	01:21:06	-18.971	46.7828	18	3.1
2013-02-23	17:55:53	-16.8253	45.6485	40	3.7
2013-02-24	01:31:49	-17.7443	48.3037	26	2.3

2013-02-25	02:15:18	-21.2148	47.988	15	1
2013-02-25	23:23:32	-14.627	49.0757	13	2.2
2013-02-26	00:53:23	-18.8952	46.765	29	1.7
2013-02-27	02:23:13	-18.1953	45.8253	29	3.1
2013-02-28	11:56:25	-24.5067	46.5773	0	1.9
2013-03-01	00:26:14	-17.2155	48.9628	23	3
2013-03-01	11:03:06	-17.7848	47.0577	25	1.9
2013-03-02	16:47:06	-25.0085	46.5967	21	2.3
2013-03-02	18:38:38	-18.986	46.6757	32	2
2013-03-03	11:12:10	-17.7447	46.1715	21	2.9
2013-03-03	18:04:31	-19.3057	47.0157	9	2.9
2013-03-04	07:57:45	-20.257	46.7745	26	2.4
2013-03-04	21:51:17	-17.366	48.921	10	2.9
2013-03-05	04:03:20	-19.0088	46.726	30	2.7
2013-03-05	05:27:46	-18.6668	46.7432	12	2.1
2013-03-06	17:46:54	-19.46	46.566	28	2.7
2013-03-07	15:17:50	-13.4955	48.4495	15	2.9
2013-03-08	14:25:37	-13.9603	48.5948	13	2.7
2013-03-08	19:14:55	-18.0355	47.8795	0	3
2013-03-08	20:48:03	-19.306	46.7048	19	2.2
2013-03-09	00:46:47	-13.948	48.6112	27	2.5
2013-03-09	23:32:38	-18.4175	47.805	38	2.8
2013-03-10	00:38:30	-14.9895	49.3065	29	3.2
2013-03-11	07:12:29	-17.5788	48.3662	8	2.6
2013-03-11	13:18:36	-17.8223	48.495	28	2.8
2013-03-11	14:23:13	-16.6683	48.3455	10	2.6
2013-03-11	17:42:18	-18.1773	46.1453	19	2.6
2013-03-14	20:10:31	-15.6493	49.6792	26	2.9
2013-03-17	04:57:04	-20.8165	48.0823	8	3.9
2013-03-18	21:50:53	-16.4428	48.0303	19	2.8
2013-03-19	01:20:01	-20.8742	47.9695	10	2.5
2013-03-20	04:15:19	-17.7517	48.4178	9	2.4
2013-03-20	18:26:29	-19.1955	46.6972	15	1
2013-03-21	02:08:04	-17.3372	48.5547	18	2.9
2013-03-21	08:26:01	-17.365	48.646	40	3.8
2013-03-23	01:58:40	-24.7872	45.6498	0	3.5
2013-03-24	03:25:55	-18.2395	48.7105	5	2.4
2013-03-24	17:44:53	-14.7395	49.6203	23	2.8
2013-03-24	21:44:08	-19.9152	47.0593	21	2.2
2013-03-26	09:48:39	-24.2563	44.5075	30	4.7
2013-03-26	11:58:16	-24.3118	44.564	16	1
2013-03-26	23:02:12	-24.3228	44.606	22	2.2
2013-03-26	23:29:54	-24.2973	44.6142	22	1.8
2013-03-27	05:00:20	-23.3432	45.2078	10	2.2
2013-03-27	20:26:42	-24.2795	44.5498	25	2.3
2013-03-28	03:59:25	-18.3855	47.632	15	2.6
2013-03-28	04:48:18	-17.4357	47.656	21	2.4
2013-03-29	08:53:41	-17.9283	48.3783	21	2.2
2013-03-29	10:13:01	-19.2808	46.746	15	1.5
2013-03-29	16:22:19	-19.269	46.7317	15	2.8
2013-03-30	12:52:06	-19.2015	46.6098	23	3.5
2013-03-30	18:21:19	-24.8067	45.6503	10	2
2013-04-02	09:45:45	-24.2085	45.5565	12	2.6
2013-04-03	00:28:13	-13.0383	48.8613	11	2.4
2013-04-03	03:02:00	-18.2985	45.2452	17	2
2013-04-03	21:46:42	-19.3748	46.9922	28	1.2
2013-04-04	16:40:42	-18.8425	46.789	16	1.8
2013-04-05	02:33:54	-18.1053	46.432	33	3.9
2013-04-05	21:14:39	-24.2487	44.5815	15	2.2
2013-04-06	01:22:43	-20.0353	47.0263	10	2.4
2013-04-06	09:07:54	-19.0155	46.976	10	1.5
2013-04-06	09:55:22	-18.3848	46.4712	10	3
2013-04-06	11:40:36	-19.0567	46.7277	19	3.4
2013-04-06	12:33:13	-16.9588	48.4002	0	3.1
2013-04-06	19:33:12	-18.6392	48.0505	21	1.8
2013-04-06	22:05:08	-17.6118	48.468	16	2.3
2013-04-07	18:29:29	-18.5788	44.7108	0	1.9
2013-04-07	21:09:31	-17.511	48.2295	0	2
2013-04-08	01:41:33	-17.7402	48.237	9	2.2
2013-04-08	06:24:09	-18.4162	46.8797	11	3.2
2013-04-10	01:21:10	-18.4615	44.6138	24	2.3
2013-04-10	03:58:21	-17.877	47.9468	33	2.4
2013-04-10	14:02:35	-18.4745	46.6903	19	2.2
2013-04-10	22:11:07	-19.5607	46.9065	29	2.3
2013-04-11	11:07:03	-19.6818	47.2067	10	1.3
2013-04-11	14:37:17	-18.5443	44.6907	3	3.2
2013-04-11	22:38:14	-14.6865	49.5388	10	2.5
2013-04-12	05:22:44	-24.9357	44.9542	22	2.7
2013-04-13	02:26:08	-17.1128	47.9807	23	2.5
2013-04-13	03:47:10	-18.6153	46.1917	32	2.2
2013-04-14	08:09:22	-24.2703	44.4308	27	3.1
2013-04-18	00:09:36	-19.0368	46.5908	23	2.4
2013-04-18	08:54:44	-19.3738	46.8835	39	1.8
2013-04-19	00:02:24	-17.6472	45.3515	6	1.8
2013-04-19	10:49:57	-18.7988	46.1047	17	3
2013-04-19	22:02:23	-17.7777	48.3893	14	1.9
2013-04-19	22:02:24	-17.76	48.3055	40	1.9
2013-04-20	06:20:09	-20.6762	48.8035	1	2.4
2013-04-20	22:50:26	-18.939	46.77	34	1.5
2013-04-21	01:09:07	-19.0477	46.7192	5	2.5
2013-04-21	04:32:14	-19.0513	46.7345	6	2.3
2013-04-22	21:27:17	-15.139	49.9983	13	2
2013-04-23	13:21:24	-19.215	46.8367	10	1.9
2013-04-23	15:29:54	-18.985	46.7547	5	2.4
2013-04-24	07:10:24	-18.3787	46.5072	10	1.8
2013-04-24	15:05:34	-18.9462	46.7497	6	1.3
2013-04-24	18:49:55	-19.0287	46.739	10	1.8
2013-04-25	14:35:00	-18.9678	47.014	10	2.9
2013-04-26	13:12:19	-15.2695	49.5882	32	2.7
2013-04-27	06:20:47	-19.8455	46.2372	10	2.6
2013-04-29	17:36:14	-18.4383	47.636	34	2
2013-05-01	22:49:31	-19.9413	46.8495	8	2.6
2013-05-04	04:29:02	-18.956	46.7063	13	1.3
2013-05-04	15:33:46	-17.4878	48.3988	3	3.1
2013-05-05	18:23:32	-19.0247	46.9798	41	1.3
2013-05-06	01:36:19	-15.5345	49.7215	26	2.2
2013-05-06	22:31:16	-17.7218	48.4132	32	2.2
2013-05-07	13:46:23	-18.976	46.7722	27	2.4
2013-05-10	01:18:04	-19.0858	44.6177	31	1.3
2013-05-10	23:22:31	-18.3295	46.3127	31	2
2013-05-11	23:05:46	-19.8773	47.1255	11	1.1
2013-05-13	14:40:15	-19.0483	46.7335	20	2.7
2013-05-14	04:10:23	-17.5042	48.3787	25	1
2013-05-14	09:50:40	-15.4617	49.8397	28	2.7
2013-05-14	15:43:11	-21.5923	47.3072	29	2.5
2013-05-14	20:59:06	-19.2192	46.8602	15	1.9
2013-05-15	08:16:26	-19.2597	46.127	10	1.8
2013-05-15	22:52:57	-14.5455	48.771	24	2.1
2013-05-16	00:06:47	-14.8817	49.551	32	2.3
2013-05-16	00:44:11	-14.2795	49.3585	29	2.1

2013-05-16	03:51:49	-14.9018	49.5998	19	2.8
2013-05-17	06:39:54	-18.701	46.1908	35	4
2013-05-17	09:53:46	-17.8565	47.6983	23	2
2013-05-17	22:22:47	-18.3535	46.4475	31	2
2013-05-18	23:47:06	-16.9052	45.0428	15	2.4
2013-05-19	20:42:08	-21.7925	43.384	18	2.7
2013-05-19	22:53:50	-17.405	47.7058	17	2
2013-05-22	02:35:03	-20.8747	47.7322	10	2.3
2013-05-23	00:17:03	-19.149	46.651	28	2.7
2013-05-23	02:22:11	-17.419	46.0983	36	2.4
2013-05-23	04:53:56	-19.594	46.9992	11	2.4
2013-05-24	02:34:25	-18.6558	48.2217	13	3.8
2013-05-24	14:25:29	-22.5315	46.0147	20	2.4
2013-05-25	13:43:27	-19.939	44.9382	25	2.6
2013-05-25	17:29:09	-18.2027	46.072	24	2
2013-05-27	02:49:21	-19.3903	46.7073	18	1.9
2013-05-27	03:17:21	-19.077	46.7387	15	2.3
2013-05-27	06:31:39	-18.9645	46.7428	22	2.9
2013-05-27	13:02:42	-17.8453	47.7552	22	2.4
2013-05-27	16:33:19	-22.859	45.1902	0	2.2
2013-05-29	01:54:01	-17.6758	45.474	10	1.7
2013-05-29	20:15:55	-19.2515	46.7252	28	1.9
2013-05-30	02:51:07	-23.54	45.344	25	2
2013-05-30	21:31:07	-18.6162	46.0455	15	1.2
2013-05-31	06:12:38	-18.2045	46.6732	28	1.7
2013-05-31	11:02:19	-17.68	47.8287	27	1.2
2013-05-31	16:27:17	-18.4303	45.4373	15	1.1
2013-06-02	20:08:39	-16.9545	49.7738	30	3.1
2013-06-04	02:01:33	-18.8405	46.17	33	2
2013-06-04	16:00:43	-18.3113	47.4607	4	2.7
2013-06-04	17:57:32	-17.2632	46.0872	28	2.6
2013-06-05	14:07:11	-20.5918	46.1457	17	2.6
2013-06-06	20:49:31	-17.2665	47.9807	11	2.5
2013-06-07	21:53:54	-24.6397	45.0297	32	2.1
2013-06-08	02:59:25	-17.8848	45.8125	9	1.9
2013-06-09	02:24:02	-17.8452	45.7722	10	2.5
2013-06-09	19:05:56	-17.9173	45.854	22	3.3
2013-06-09	23:34:11	-19.6725	45.8513	10	2.2
2013-06-10	06:25:49	-17.9145	47.9363	21	3
2013-06-11	23:16:10	-19.3663	47.003	20	2.5
2013-06-13	20:29:39	-18.492	44.7237	26	1.7
2013-06-14	11:21:43	-23.5113	46.4605	25	1.7
2013-06-15	13:00:08	-18.9312	46.7617	15	2.4
2013-06-15	15:03:16	-19.1723	48.3812	0	2.1
2013-06-16	10:12:14	-18.2013	47.394	37	2.1
2013-06-17	03:54:19	-20.6085	45.749	27	2.4
2013-06-20	05:13:03	-18.6865	45.3823	23	1.7
2013-06-22	04:15:15	-20.3363	46.5442	47	1.9
2013-06-22	21:32:56	-17.8793	45.8567	18	1.9
2013-06-28	02:39:45	-18.2683	46.504	32	3
2013-07-01	16:55:00	-18.9487	46.6895	31	1.8
2013-07-04	13:40:59	-24.4715	45.1083	20	3.1
2013-07-06	02:03:15	-15.6153	49.5535	25	1.6
2013-07-06	11:25:47	-17.9005	45.8293	8	2.3
2013-07-08	23:59:20	-17.5977	48.587	33	2.4
2013-07-10	05:23:39	-16.2653	47.9517	27	4.5
2013-07-10	19:13:04	-19.144	46.7992	34	2.9
2013-07-10	19:43:10	-18.3905	47.6723	38	3.2
2013-07-11	03:40:03	-18.4152	47.9678	39	2.2
2013-07-12	11:49:20	-17.2763	47.6565	28	3.3
2013-07-16	07:10:19	-17.0137	47.9267	22	3
2013-07-17	20:11:47	-15.025	49.6098	21	2
2013-07-17	23:45:34	-18.3653	46.4345	39	1.7
2013-07-19	03:05:29	-19.062	46.724	22	1.7
2013-07-20	10:50:24	-20.1093	47.2382	29	3.1
2013-07-23	18:57:10	-18.3873	47.6662	27	2.9
2013-07-25	15:27:14	-24.1547	44.5665	21	2.4
2013-07-27	05:43:39	-20.676	45.3472	23	2.9
2013-07-28	05:02:34	-19.0448	46.6742	22	2.6
2013-07-28	19:24:06	-17.3783	48.634	28	3.3
2013-08-02	15:47:00	-19.5847	46.1508	34	1.8
2013-08-02	23:42:41	-18.721	46.9853	22	3.2
2013-08-03	06:35:04	-18.9983	46.7117	16	1.5
2013-08-03	21:15:08	-18.4828	45.5458	13	2.7
2013-08-04	20:10:28	-18.5703	45.9195	24	2
2013-08-04	22:32:18	-14.8497	49.0432	23	2.4
2013-08-05	15:39:06	-17.829	48.247	35	3.1
2013-08-10	22:59:56	-14.6703	49.9125	32	2.4
2013-08-11	03:06:25	-23.2383	45.877	26	3.2
2013-08-11	04:00:46	-19.022	46.65	15	1.5
2013-08-18	09:05:57	-17.5782	48.8155	49	3.2
2013-08-22	21:27:14	-17.5117	48.3285	10	3
2013-08-23	01:42:55	-17.4255	48.6348	15	2.5
2013-08-23	20:01:04	-17.2542	48.4563	27	2.7
2013-08-24	06:39:05	-18.0543	47.85	32	2.3
2013-08-24	12:35:28	-16.2753	49.0838	5	3
2013-08-25	04:34:39	-18.0243	47.2967	5	1.9
2013-08-27	02:59:28	-19.9263	47.1783	10	2.5
2013-08-27	05:58:31	-23.4398	44.9262	0	2.8
2013-08-27	10:26:28	-17.7738	47.3448	25	1.7
2013-08-27	16:15:15	-19.945	47.3258	19	2.7
2013-08-30	22:25:11	-19.3885	46.9242	24	2.6
2013-08-31	03:47:54	-19.3663	47.0443	35	3.1

Appendix C

Figure C.1: Single station stacking of *P* receiver functions observed for all seismic station for Gaussian factor 0.5 (left) and 1.0 (right). Dashed lines are 410 km, 520 km and 660 km depths.

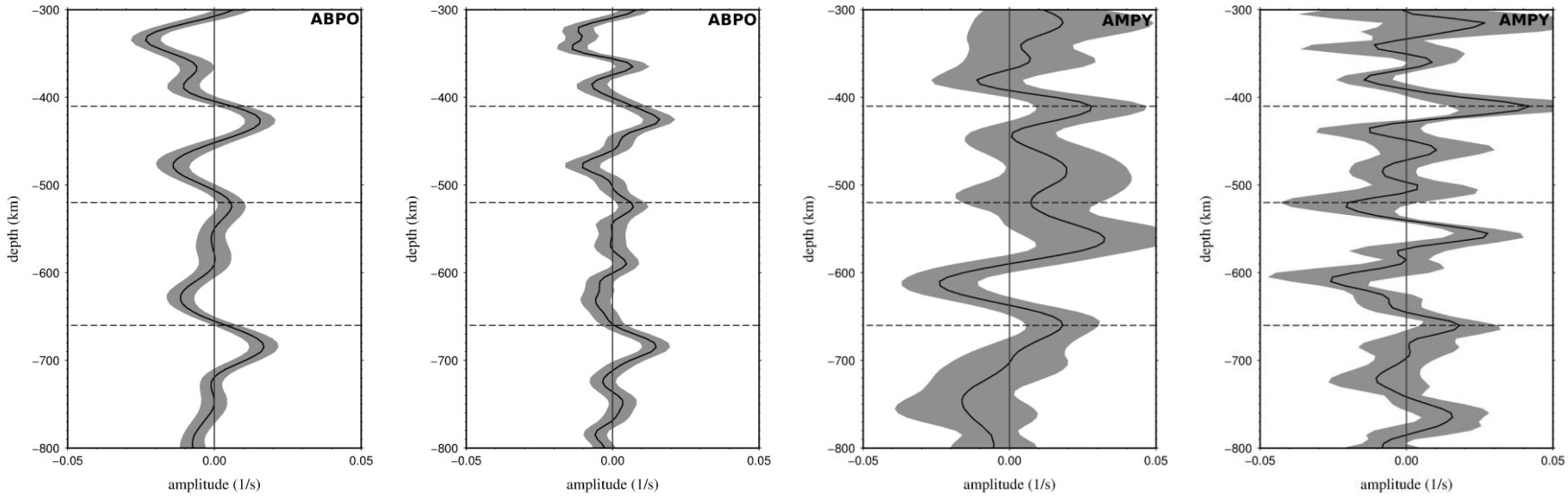

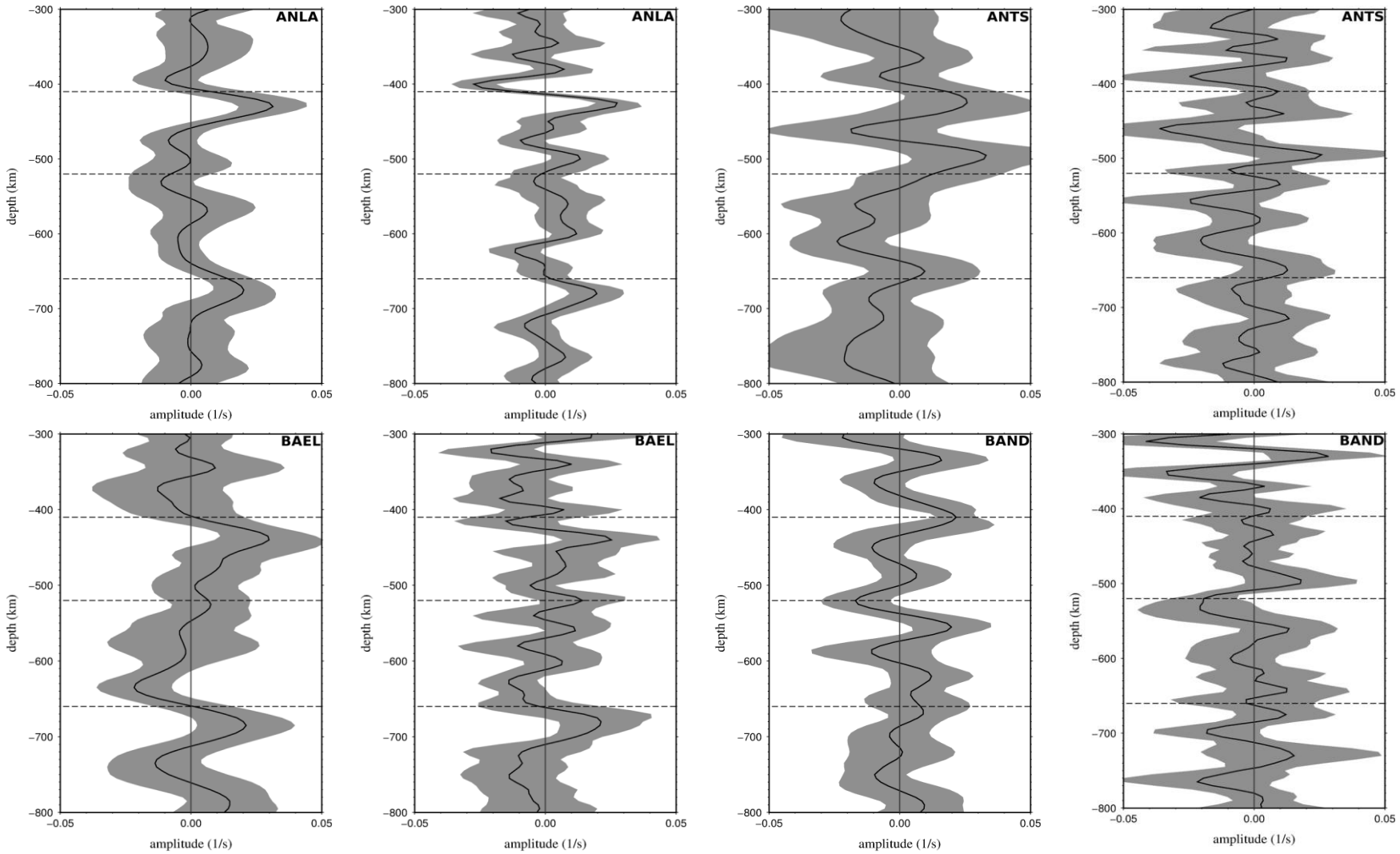
ANLA
ANLA
ANTS
ANTS
BAEL
BAEL
BAND
BAND
depth (km)
amplitude (1/s)
−300
−400
−500
−600
−700
−800
−0.05
0.00
0.05

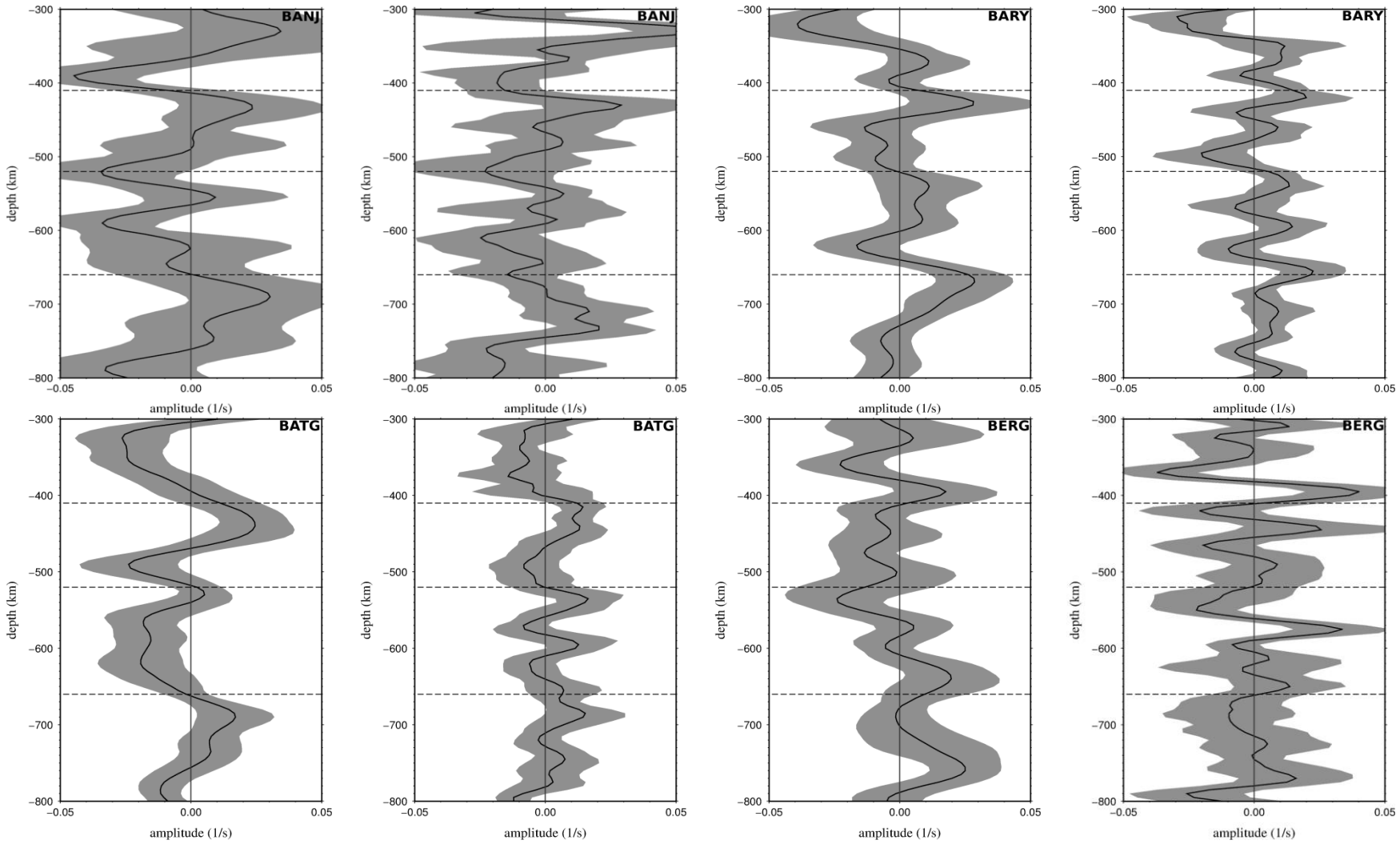
BANJ
BANJ
BARY
BARY
BATG
BATG
BERG
BERG
depth (km)
amplitude (1/s)
−300
−400
−500
−600
−700
−800
−0.05
0.00
0.05

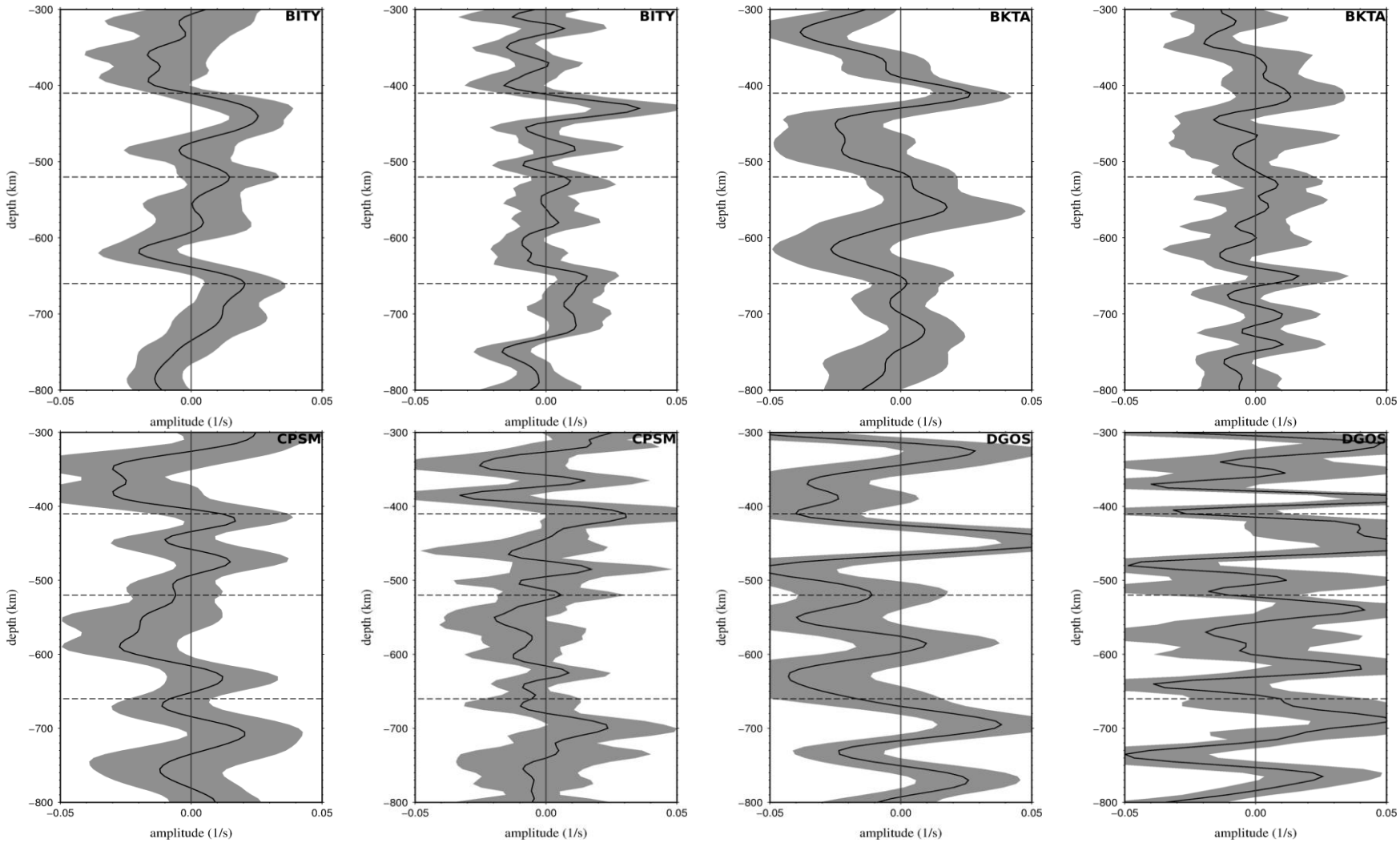
BITY
BITY
BKTA
BKTA
CPSM
CPSM
DGOS
DGOS
depth (km)
amplitude (1/s)
−300
−400
−500
−600
−700
−800
−0.05
0.00
0.05

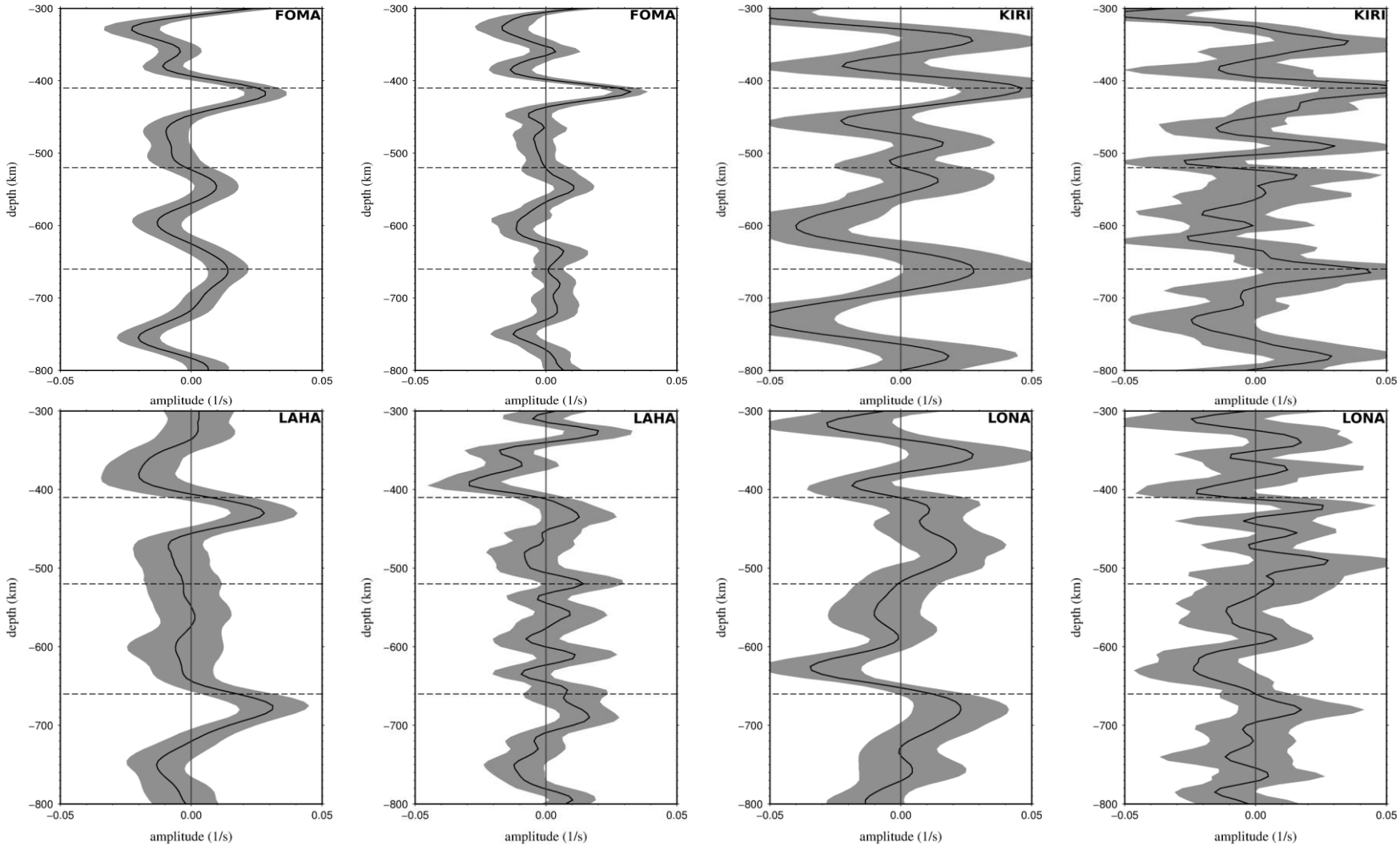
FOMA
FOMA
KIRI
KIRI
LAHA
LAHA
LONA
LONA
depth (km)
amplitude (1/s)
−300
−400
−500
−600
−700
−800
−0.05
0.00
0.05

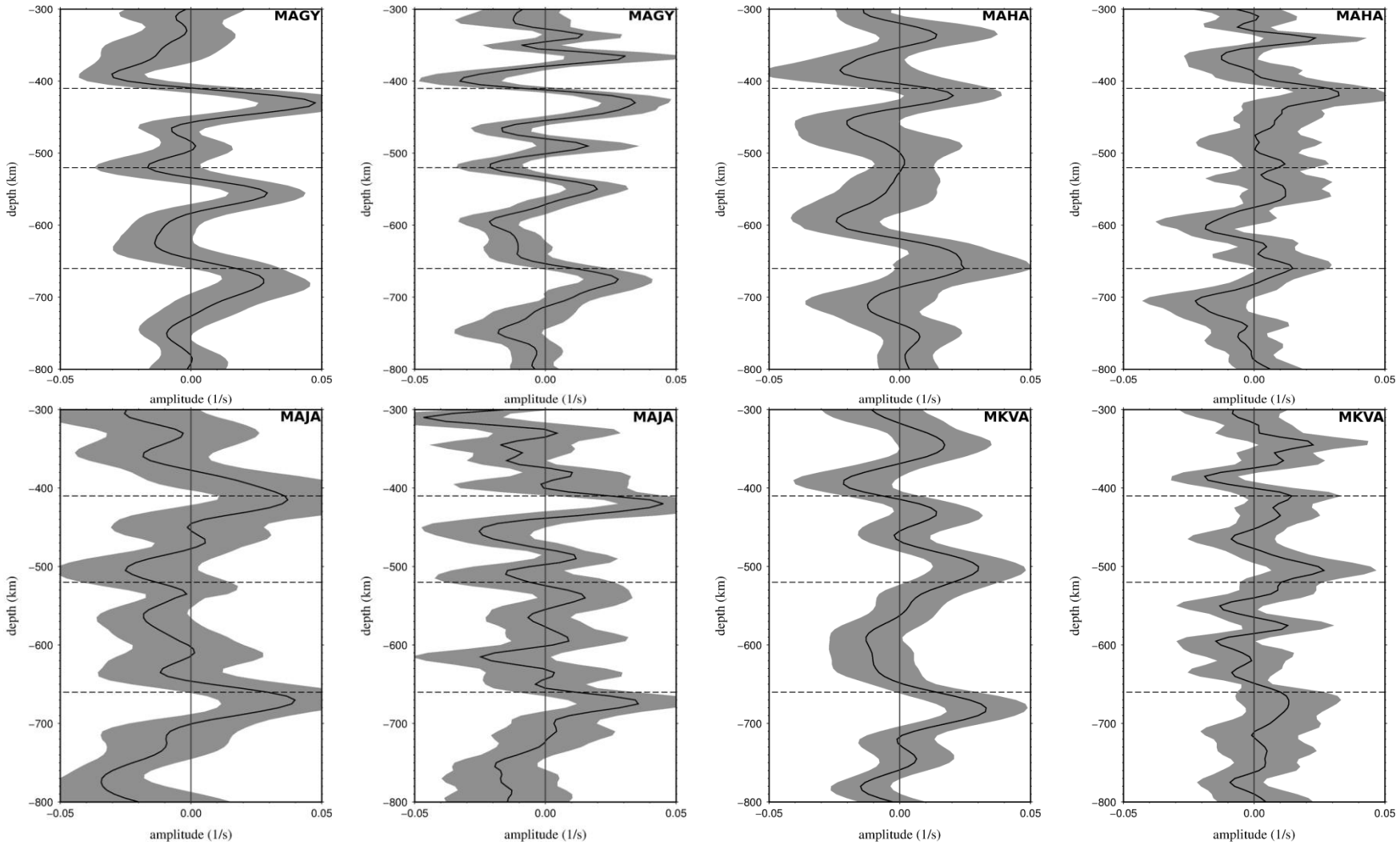
MAGY
MAGY
MAHA
MAHA
MAJA
MAJA
MKVA
MKVA
depth (km)
amplitude (1/s)
−300
−400
−500
−600
−700
−800
−0.05
0.00
0.05

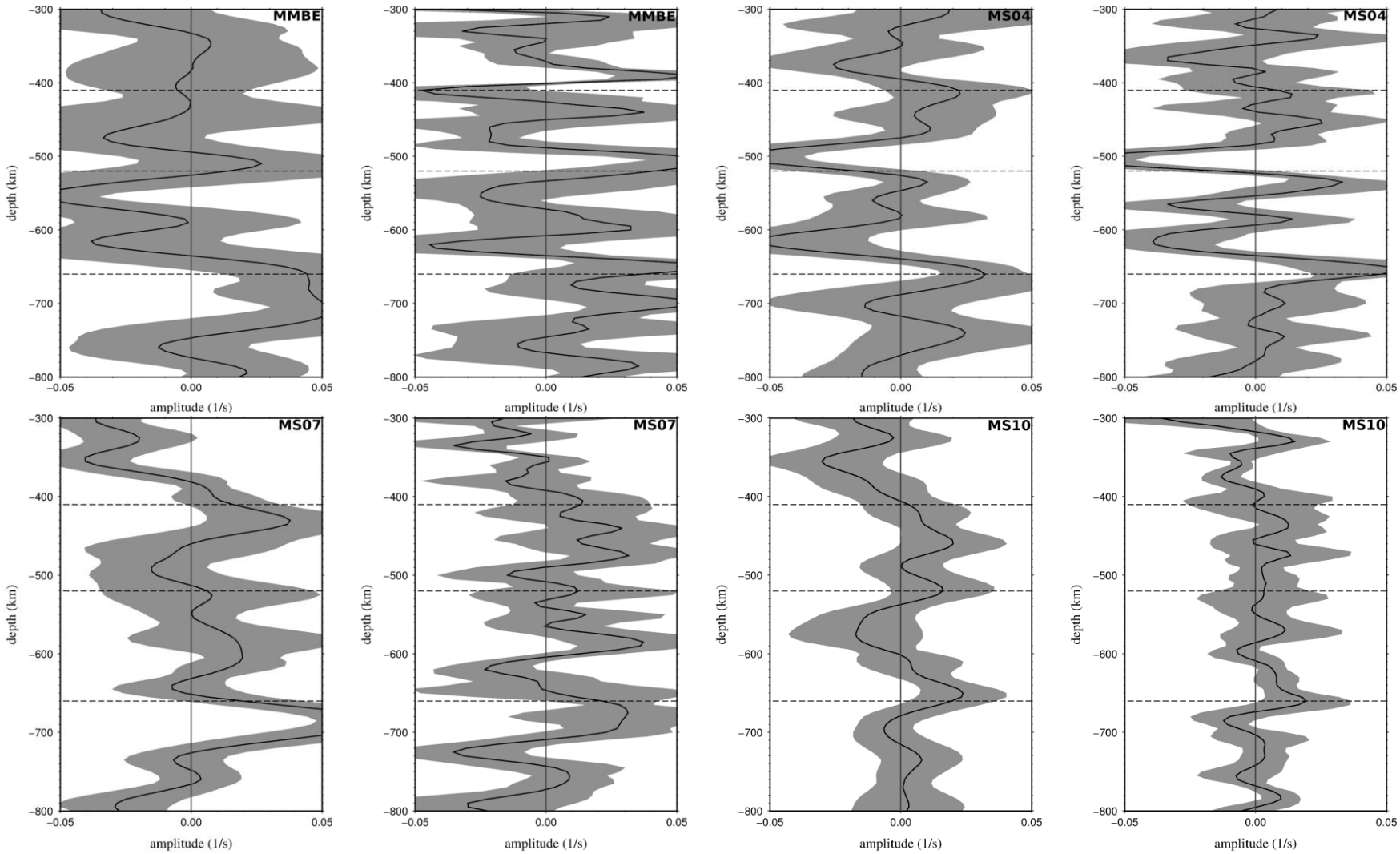
MMBE
MMBE
MS04
MS04
MS07
MS07
MS10
MS10
depth (km)
amplitude (1/s)
−300
−400
−500
−600
−700
−800
−0.05
0.00
0.05

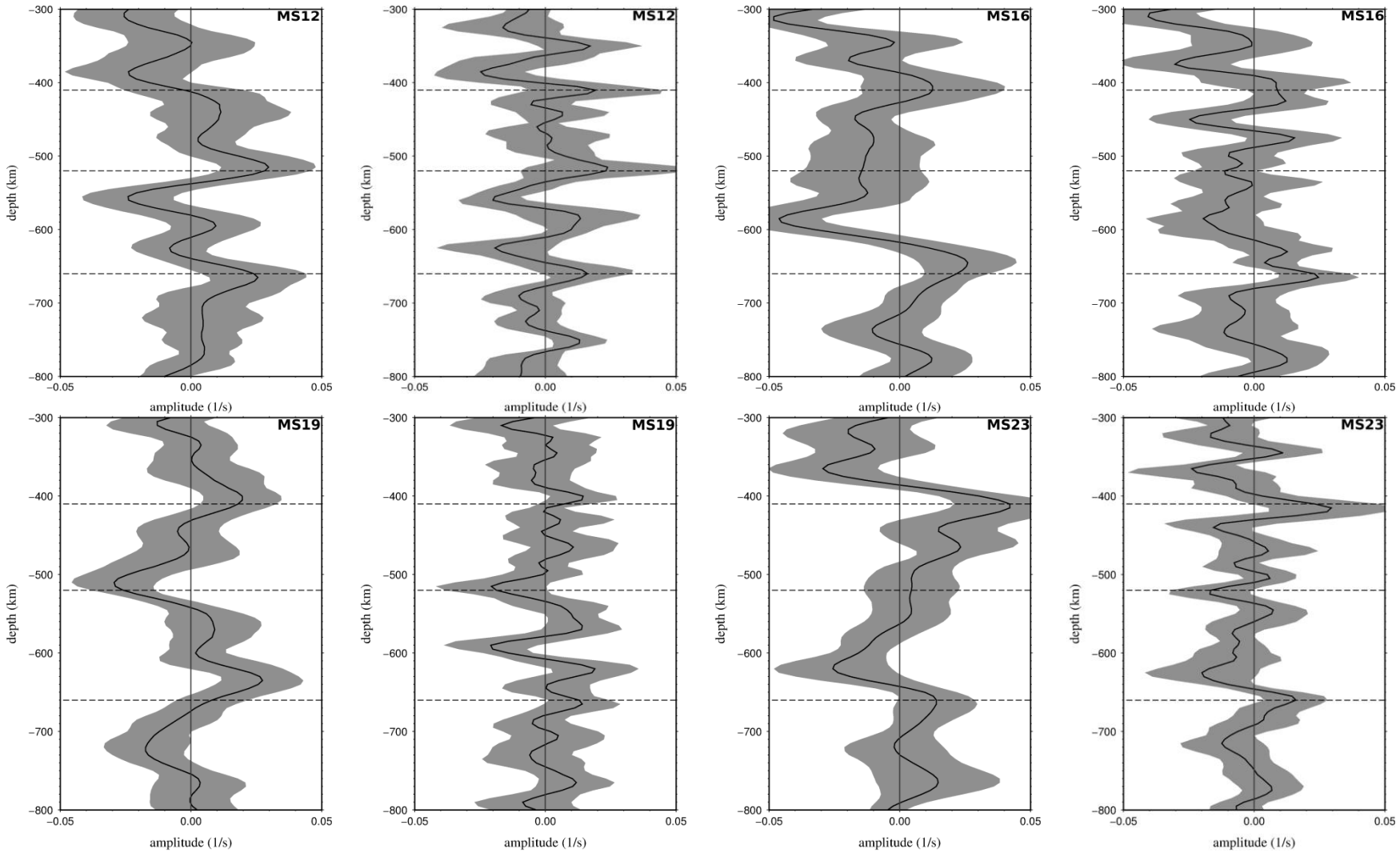
MS12
MS12
MS16
MS16
MS19
MS19
MS23
MS23
depth (km)
amplitude (1/s)
−300
−400
−500
−600
−700
−800
−0.05
0.00
0.05

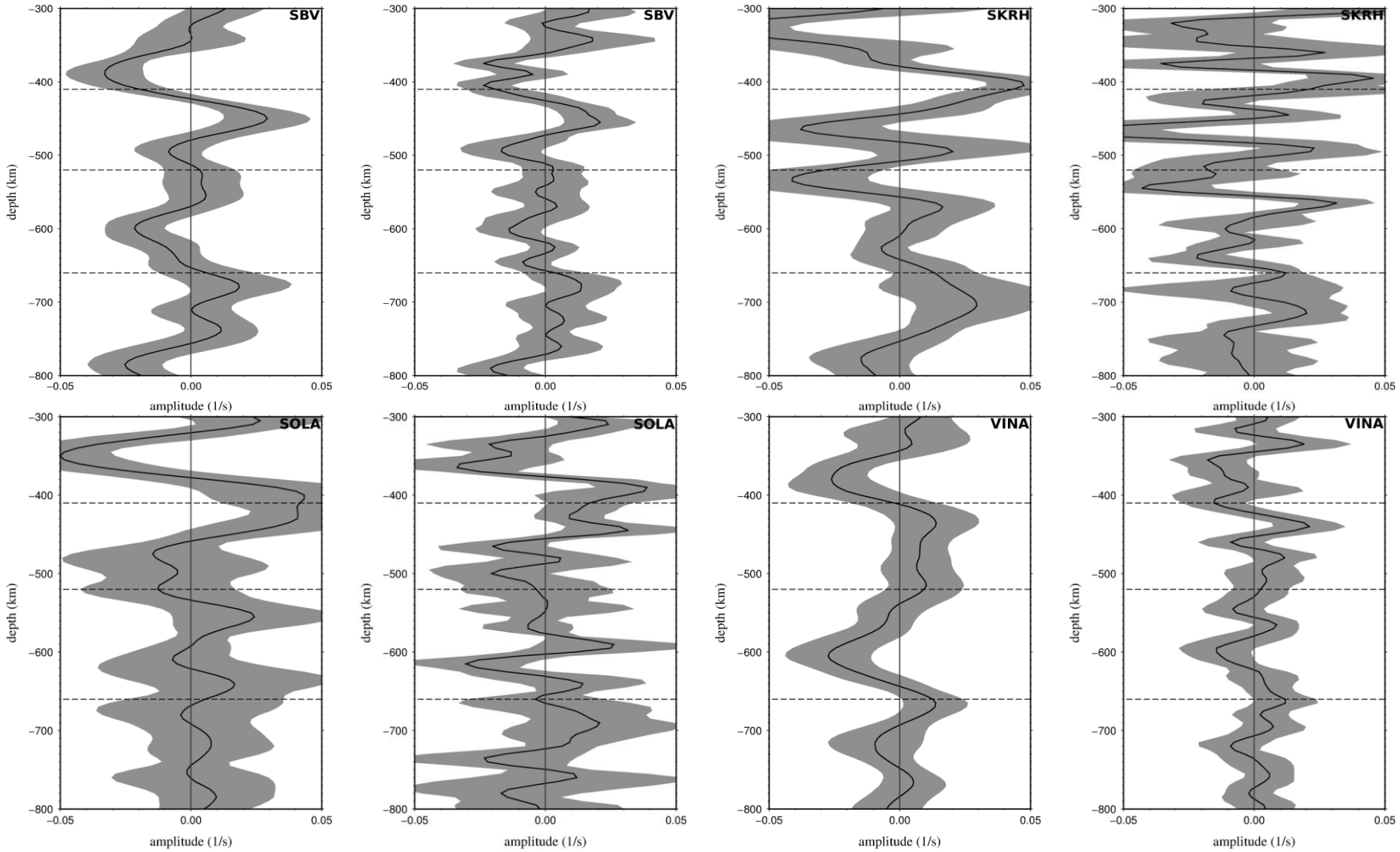
SBV
SBV
SKRH
SKRH
SOLA
SOLA
VINA
VINA
depth (km)
amplitude (1/s)
−300
−400
−500
−600
−700
−800
−0.05
0.00
0.05

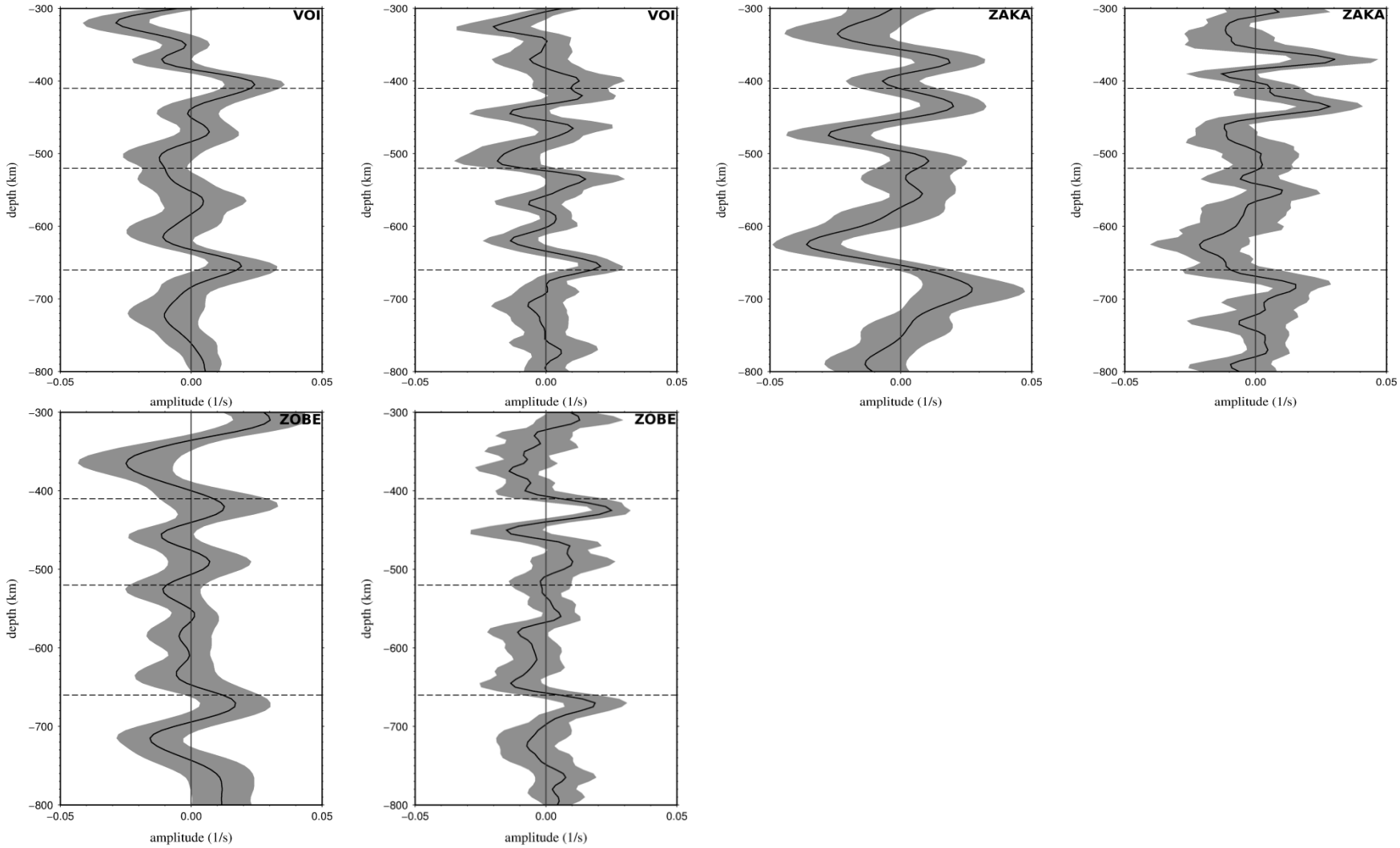
VOI
VOI
ZAKA
ZAKA
ZOBE
ZOBE
depth (km)
amplitude (1/s)
−300
−400
−500
−600
−700
−800
−0.05
0.00
0.05

Figure C.2: Single station stacking of *P* receiver functions observed for a few nodes for Gaussian factor 0.5. Dashed lines are 410 km, 520 km and 660 km depths.

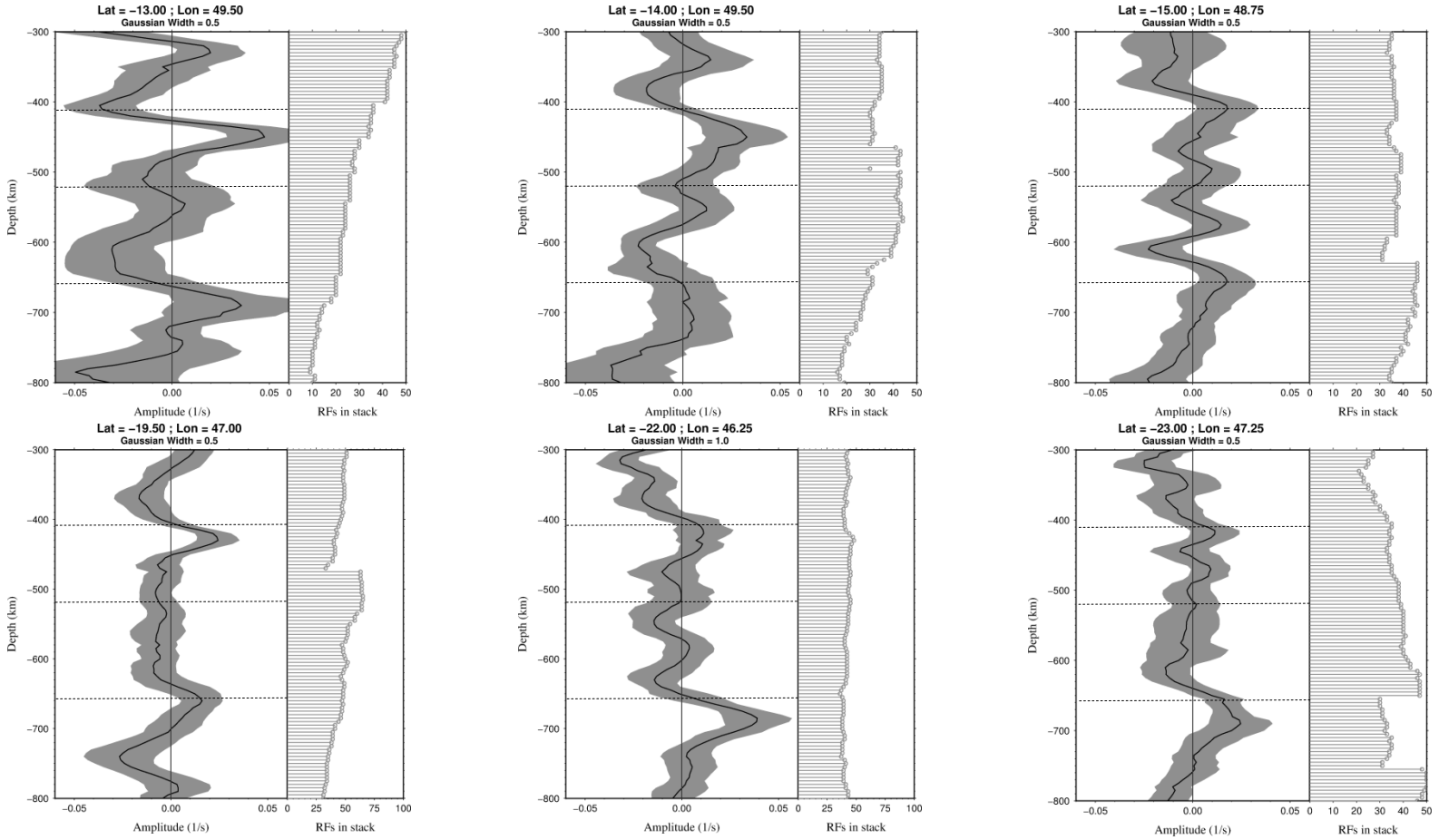

Appendix D

Geophysical Journal International

Geophys. J. Int. (2017) **210,** 1525–1544
Advance Access publication 2017 June 3
GJI Seismology

doi: 10.1093/gji/ggx243

The structure of the crust and uppermost mantle beneath Madagascar

Fenitra Andriampenomanana,[1,2] Andrew A. Nyblade,[1,3] Michael E. Wysession,[4] Raymond J. Durrheim,[1] Frederik Tilmann,[5] Jordi Julià,[6] Martin J. Pratt,[4] Gérard Rambolamanana,[2] Ghassan Aleqabi,[4] Patrick J. Shore[4] and Tsiriandrimanana Rakotondraibe[1,2]

[1] *School of Geosciences, University of the Witwatersrand, Private Bag* 3 - 2050 *Wits, Johannesburg, South Africa. E-mail: nyonyfenitra@gmail.com*
[2] *Institut et Observatoire de Géophysique d'Antananarivo, Université d'Antananarivo, Ambohidempona - B.P* 3843, *Antananarivo* 101, *Madagascar*
[3] *Department of Geosciences, Penn State University,* 503 *Deike Building, University Park, PA* 16802, *USA*
[4] *Department of Earth and Planetary Sciences, Washington University in St. Louis, Campus Box* 1169, 1 *Brookings Dr, Saint Louis, MO* 63130-4899, *USA*
[5] *Deutsches GeoForschungsZentrum (GFZ), Telegrafenberg, D-*14473 *Potsdam, Germany*
[6] *Departamento de Geofisica & Programa de Pós-Graduação em Geodinâmica e Geofisica, Universidade Federal do Rio Grande do Norte, Natal, Brazil*

Accepted 2017 June 1. Received 2017 May 15; in original form 2016 November 12

SUMMARY

The lithosphere of Madagascar was initially amalgamated during the Pan-African events in the Neoproterozoic. It has subsequently been reshaped by extensional processes associated with the separation from Africa and India in the Jurassic and Cretaceous, respectively, and been subjected to several magmatic events in the late Cretaceous and the Cenozoic. In this study, the crust and uppermost mantle have been investigated to gain insights into the present-day structure and tectonic evolution of Madagascar. We analysed receiver functions, computed from data recorded on 37 broad-band seismic stations, using the H–κ stacking method and a joint inversion with Rayleigh-wave phase-velocity measurements. The thickness of the Malagasy crust ranges between 18 and 46 km. It is generally thick beneath the spine of mountains in the centre part (up to 46 km thick) and decreases in thickness towards the edges of the island. The shallowest Moho is found beneath the western sedimentary basins (18 km thick), which formed during both the Permo-Triassic Karro rifting in Gondwana and the Jurassic rifting of Madagascar from eastern Africa. The crust below the sedimentary basin thickens towards the north and east, reflecting the progressive development of the basins. In contrast, in the east there was no major rifting episode. Instead, the slight thinning of the crust along the east coast (31–36 km thick) may have been caused by crustal uplift and erosion when Madagascar moved over the Marion hotspot and India broke away from it. The parameters describing the crustal structure of Archean and Proterozoic terranes, including average thickness (40 km versus 35 km), Poisson's ratio (0.25 versus 0.26), average shear-wave velocity (both 3.7 km s^{-1}), and thickness of mafic lower crust (7 km versus 4 km), show weak evidence of secular variation. The uppermost mantle beneath Madagascar is generally characterized by shear-wave velocities typical of stable lithosphere (~4.5 km s^{-1}). However, markedly slow shear-wave velocities (4.2–4.3 km s^{-1}) are observed beneath the northern tip, central part and southwestern region of the island where the major Cenozoic volcanic provinces are located, implying the lithosphere has been significantly modified in these places.

Key words: Joint inversion; Sedimentary basin processes; Crustal structure.

1 INTRODUCTION

Madagascar displays a complex geological framework resulting from several tectonic events that span more than 2.5 billion years of Earth's history. The Malagasy lithosphere was originally amalgamated and reworked by the Neoproterozoic Pan-African Orogeny and later modified by a series of extensional events that lead to continental break-up from Africa in the Jurassic and from India during the Cretaceous (e.g. Rabinowitz *et al.* 1983; Coffin & Rabinowitz 1987; Collins 2006). In the Cenozoic, the tectonic evolution of Madagascar was marked by a series of magmatic events (e.g. Mahoney *et al.* 1991; Storey *et al.* 1995). Although Madagascar offers a unique geological framework to investigate how the continental crust is formed and then modified by extensional and

© The Authors 2017. Published by Oxford University Press on behalf of The Royal Astronomical Society.

magmatic processes, little is known about its deep structure and composition.

In this paper, we contribute to the growing body of seismic constraints on crustal structure by investigating crustal structure across Madagascar. Teleseismic *P*-wave receiver functions have been used together with surface wave phase-velocity measurements to obtain 37 new point estimates of crustal thickness, shear-velocity structure, and Poisson's ratio spanning the island, along with estimates of uppermost mantle shear-wave velocity. These results were obtained using broadband seismic data recorded on both permanent and temporary seismic stations in Madagascar, modelled with two different methods, H–κ stacking of receiver functions (Zhu & Kanamori 2000) and a joint inversion of receiver functions and Rayleigh wave phase velocities (Julià *et al*. 2000, 2003). The temporary stations were part of two networks, the Madagascar-Comoros-Mozambique (MACOMO) network (Wysession *et al*. 2011), and the Seismological Signatures in the Lithosphere/Asthenosphere system of Southern Madagascar (SELASOMA) network (Tilmann *et al*. 2012). The ensemble of seismic stations enables us to examine crustal structure in each tectonic region of the island, and thus to gain insights into several processes that have formed and subsequently modified the crust and uppermost mantle beneath Madagascar.

Our findings shed new lights on the opening of rift basins and related thinning of the crust, the origin of high elevations across the island, crustal composition, secular variation in Precambrian crustal genesis, and geodynamic links between regions of low mantle seismic velocities and crustal structure. These results relate the different styles of separation from Africa and India to the different response of the crust, that is a large degree of crustal thinning is observed in the west related to the opening of the rift basins, whereas only very localized minor thinning is observed along the east coast following the separation from India. To first order, Archean and Proterozoic crust is observed to be similar. Low seismic velocities in the uppermost mantle beneath the northern, central, and southwestern parts of Madagascar are correlated with locations of Cenozoic volcanism.

2 TECTONIC SETTING

The geology of Madagascar can be divided into two major structural zones (Fig. 1). The western third of the island is covered by Late Carboniferous to Quaternary age sedimentary basins that consist of recent deposits lying on top of a Karoo sequence, while the remaining two-thirds of the island, on the eastern side, consist predominantly of Precambrian and Early Palaeozoic rocks that have been reworked during the Pan-African Orogeny (e.g. Nicollet 1990; de Wit 2003). Mesozoic and Cenozoic volcanic provinces are also found in several locations on the island (Fig. 1).

2.1 Sedimentary basins

The sedimentary basins along the western side of Madagascar formed during the separation of Madagascar from Africa, which started in the Late Paleaozoic and was complete by the Late Jurassic and Early Cretaceous (Rabinowitz *et al.* 1983; Piqué 1999a). During this separation, the East Gondwana Plate (Madagascar–India–Seychelles–Antarctica–Australia) moved south–southeasterly along a transform fault, which is currently known as the Davie Ridge (Segoufin & Patriat 1980; Coffin & Rabinowitz 1987; Cochran 1988; Piqué 1999a). A hotspot reconstruction places the southeastern region of Madagascar above the Marion hotspot during the Late Cretaceous (~90 Ma), which led to the separation of India–Seychelles from Madagascar (Storey *et al.* 1995; Torsvik *et al.* 1998; Piqué 1999a; Raval & Veeraswamy 2003). This separation was accompanied by significant magmatic activity along both the east and west coasts of Madagascar (Schlich 1975; Norton & Sclater 1979; Mahoney *et al.* 1991). Madagascar completely separated from India by the end of the Cretaceous (Dyment 1991).

While Madagascar was part of Gondwana, from the Carboniferous through the Early Triassic, Karoo sediments began accumulating in depressions that would eventually develop into the Antsiranana, Mahajanga and Morondava rift basins along the western part of the island (Fig. 1). The sedimentary rocks in these basins range in age from the Carboniferous to the present, with the basal formations consisting of Karoo sediments. The filling of the basins proceeded from south to north and from west to east, accompanying the northward progression of the opening of the basins (Besairie 1971; Piqué 1999a). Early studies of the western sedimentary basins of Madagascar suggested a sediment thickness of more than 10 km in the south, thinning out towards the north and east (Besairie 1971; Boast & Nairn 1982; Coffin & Rabinowitz 1988).

2.2 Precambrian basement

The Precambrian basement of Madagascar can be divided into six major units, approximately in order of decreasing age: Antongil-Masora craton, and the Antananarivo, Anosyen-Androyen, Ikalamavony, Vohibory and Bemarivo terranes (Fig. 1).

(1) *Palaeoarchean to Mesoarchean:* The Antongil-Masora craton is located along the east coast of Madagascar in two locations, the Antongil terrane in the mid-north and the Masora terrane in the mid-south. This craton contains the oldest rocks (~3.3 Ga) in Madagascar (Tucker *et al.* 2011) and is composed mainly of Palaeoarchean to Mesoarchean migmatic gneiss suites (Besairie 1968, 1969; Hottin 1976). It is usually interpreted as a fragment of the cratonic lithosphere of the Western Dharwar Craton in India (e.g. Raval & Veeraswamy 2003).

(2) *Neoarchean:* The Antananarivo terrane occupies the major portion of the Precambrian shield of Madagascar and its central high plateau. It is composed mostly of Neoarchean (~2.5 Ga) orthogneisses and paragneisses that grade from greenschist to granulite facies (Tucker *et al*. 2011, 2012).

(3) *Palaeoproterozoic:* The Anosyen-Androyen terrane constitutes the southernmost part of the Precambrian shield of Madagascar (Tucker *et al.* 2012). Geochronological data and common geological characteristics, such as a Palaeoproterozoic (~2.0–1.8 Ga) gneissic basement and sequences of Neoarchean and Palaeoproterozoic platform sediments, point to similarities between the Anosyen and Androyen subdomains, leading to their consideration as a single terrane.

(4) *Mesoproterozoic:* The Ikalamavony terrane forms a narrow NNW–SSE striking zone between the older Anosyen-Androyen and Antananarivo terranes. It is dominated by the Ikalamavony Group (~1.08–0.98 Ga), which includes higher-grade Mesoproterozoic metasedimentary and meta-igneous rocks (Cox *et al.* 2004; Tucker *et al.* 2007).

(5) *Neoproterozoic:* The Bemarivo terrane of northern Madagascar comprises Neoproterozoic (~758–708 Ma) intrusive granitic and volcanosedimentary rocks (Thomas *et al.* 2009; Tucker *et al.* 2012). The Vohibory terrane is located west of the Anosyen-Androyen terrane. It is an oceanic terrane of early Neoproterozoic

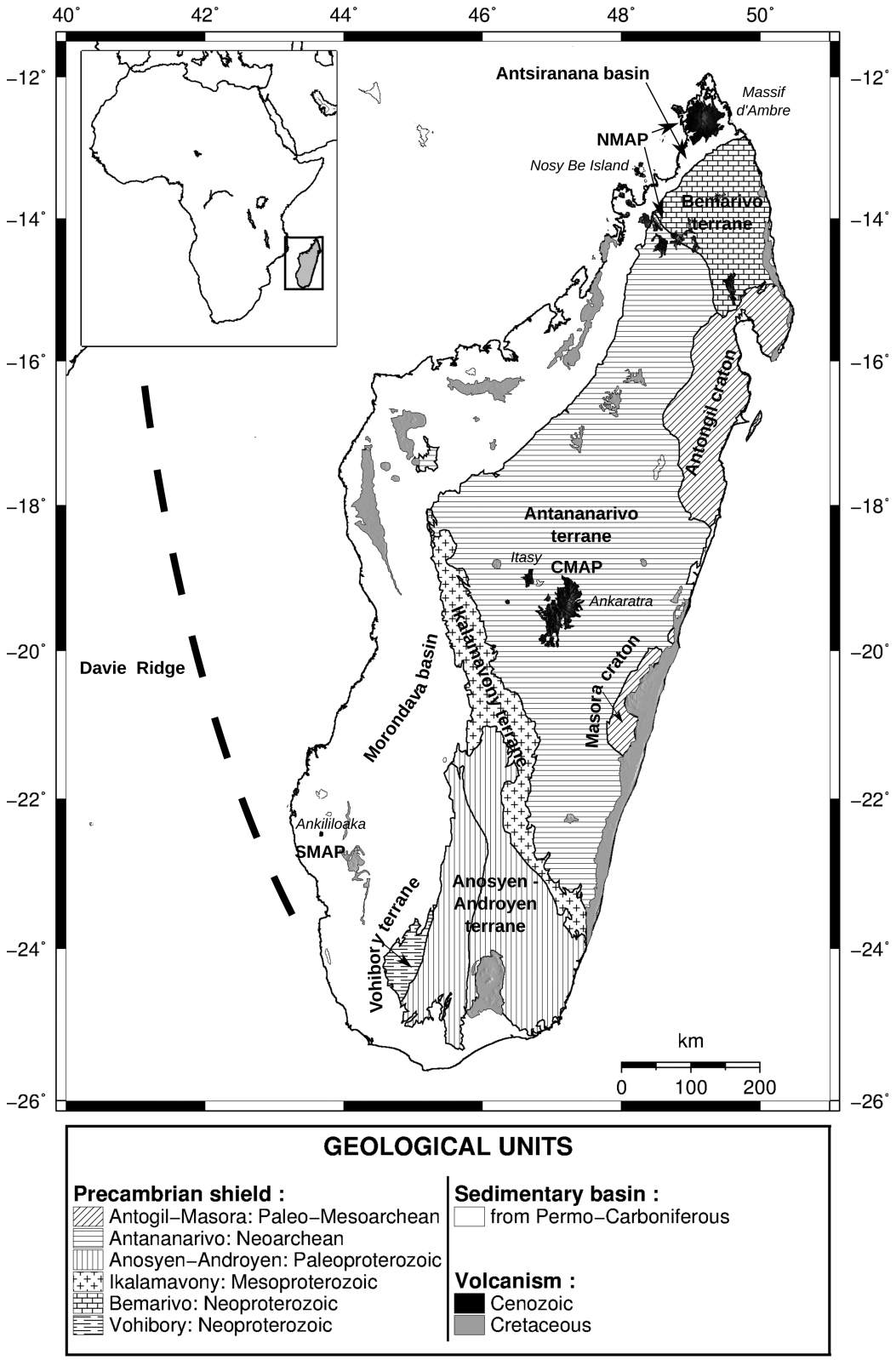

Figure 1. A simplified geological map of Madagascar showing the different geological units that are found in the study area (modified from Tucker *et al.* 2012) and locations of Cretaceous and Cenozoic volcanic provinces (NMAP/CMAP/SMAP).

age (~850 Ma), and is composed of intercalations of metabasalts, acidic volcanic rocks, and chemical metasedimentary rocks (GAF-BGR 2008; Jöns & Schenk 2008).

2.3 Volcanic provinces of Madagascar

Evidence of magmatism in Madagascar is characterized mainly by Cretaceous and Cenozoic eruptions (Besairie 1973). Intense fissural volcanism was associated with the dislocation of the East Gondwana Plate from the rest of Gondwana during the Permo-Triassic, as well as by the breaking apart of India, the Seychelles, Australia and Antarctica in the Cretaceous (~95–85 Ma) (Schlich 1975; Norton & Sclater 1979). As the latter volcanism coincided with the passage of Madagascar over the Marion hotspot, this resulted in the emplacement of mantle-derived tholeiitic basalts and crustal-derived dacite/alkali rhyolite magmas. Though these lavas may have once covered most of Madagascar, they are largely found today along the western, eastern and southern perimeter of the island (Storey *et al.* 1995; Torsvik *et al.* 1998).

Significant localized Cenozoic volcanic activity also occurred in several parts of Madagascar, as recently as the Quaternary (<1 Ma), such as in the Massif d'Ambre, Nosy Be Island, at the northern tip of Madagascar and in the Ankaratra and Itasy volcanic areas of the central highlands (Fig. 1). In general, Cretaceous volcanism was dominated by eruptions of tholeiitic basaltic lavas, while the Cenozoic volcanism primarily consisted of alkali basalt eruptions. A seismic analysis of the mantle roots of these volcanic terranes using surface waves revealed three large distinct seismic low-velocity regions that extend through the lithosphere and well into the asthenosphere beneath the northern (NMAP: Northern Madagascar Alkaline Province), central (CMAP: Central Madagascar Alkaline Province) and southwestern (SMAP: Southern Madagascar Alkaline Province) volcanic regions (Pratt *et al.* 2017; Fig. 1).

2.4 Previous studies of the crust of Madagascar

Although geological studies of Madagascar date back to the 1960s, very little is known about its deeper crustal structure. Previous studies have used local gravimetric data to model crustal thicknesses. Fourno & Roussel (1994) and Rakotondraompiana *et al.* (1999) reported a range of Moho depths from 25 to 40 km and 25 to 35 km, respectively. Rajaomazava (1992) used gravity data to model the crustal thickness beneath the Morondava basin and the central part of the island, reporting crustal thicknesses of 32–36 km and 32–38 km, respectively. Crustal thickness models for Africa, obtained from modelling satellite gravity data, show Madagascar Moho depths ranging between 35 and 42 km (Tedla *et al.* 2011; Tugume *et al.* 2013).

Because of a lack of seismic recording stations, there have been few seismological studies of the crust in Madagascar. Rakotondrainibe (1977) used traveltime analysis of body waves recorded at an array of short-period seismometers in the centre of Madagascar maintained by IOGA (Institut et Observatoire de Géophysique d'Antananarivo), and found a 36-km-thick crust beneath the central plateau. In the same region, Rambolamanana *et al.* (1997) used a simultaneous inversion of hypocentral parameters and crustal velocities to obtain a thickness of 42 km, and Rai *et al.* (2009) inferred a thickness of 38 km from receiver functions. A more recent study by Rindraharisaona *et al.* (2013), using a joint inversion of receiver functions and surface wave dispersion measurements from the four permanent broad-band seismic stations in Madagascar, found crustal thicknesses of 35 km beneath station SBV (in the north) and FOMA (in the south), 42 km beneath station ABPO (centre), and 39 km beneath station VOI (southcentral). The surface-wave tomography study of Pasyanos & Nyblade (2007) found crustal thicknesses in Madagascar to vary between 25 and 35 km, and the global CRUST 1.0 model shows crustal thicknesses ranging from 36 to 45 km (Laske *et al.* 2013). Recently, the crust in the southern part of Madagascar was investigated by Rindraharisaona *et al.* (2017) using the full SELASOMA data set, as well as data from additional stations in southern Madagascar. Using joint inversion of receiver functions and ambient-noise derived surface waves, they revealed a thinning of the crystalline crust to 13 km in the Morondava basin, and a slightly greater thickness of the Archean crust (~39 km) compared to the Proterozoic crust (~35 km). They also reported moderately thin crust (~30 km) along the eastern coast.

These studies suggest generally thick crust beneath the spine of mountains in the centre part of the island with a decrease in thickness towards the edges of the island, particularly towards the west. However, another study by Paul & Eakin (2017), from receiver function analysis beneath two permanents stations, suggested otherwise. In fact, they found that the central part of Madagascar is thinner (~39 km) than the eastern coast (~44 km). Additional information on crustal structure comes from a recent study of SKS splitting along the SELASOMA profile showing strong crustal anisotropy of up to 12 per cent in a 150 km broad zone located along the shear zones in southern Madagascar (Reiss *et al.* 2016).

3 DATA AND METHODS

3.1 Data

Most of the seismic data used in this study were collected from a recent deployment of 26 temporary broad-band seismic stations in Madagascar through the Madagascar–Comoros–Mozambique (MACOMO) project (Wysession *et al.* 2011; Fig. 2). Each seismic station was equipped with a 24-bit data logger (Quanterra Q330), a broad-band sensor (Guralp CMG-3T, Streckeisen STS-2, or Nanometrics Trillium 120PA), and a GPS clock. The data were recorded continuously at both 1 and 40 samples per second. These stations were deployed throughout the island between 2011 and 2013 in two parts: 10 seismic stations were installed mostly along the coasts in September, 2011. The remaining 16 stations were deployed in September, 2012, and all of the stations were removed from the field in August–September 2013.

In addition to MACOMO data, seismic data from five additional broad-band seismic stations were used: SKRH (AFRICAARRAY), ABPO (IRIS/GSN), FOMA (GEOSCOPE) and VOI and SBV (GEOFON). A further seven seismic stations were used from the SELASOMA experiment (Tilmann *et al.* 2012), which included a linear deployment of temporary broad-band seismic stations across the southern part of Madagascar (Fig. 2). In summary, a total of 37 temporary and permanent seismic stations were used in this study (listed in Table S1). Rayleigh wave phase-velocity measurements derived from ambient-noise analysis and teleseismic surface wave tomography have been taken from Pratt *et al.* (2017).

3.2 Receiver functions

Receiver functions are time series composed of *P*-to-*S* converted phases generated after the interaction of a

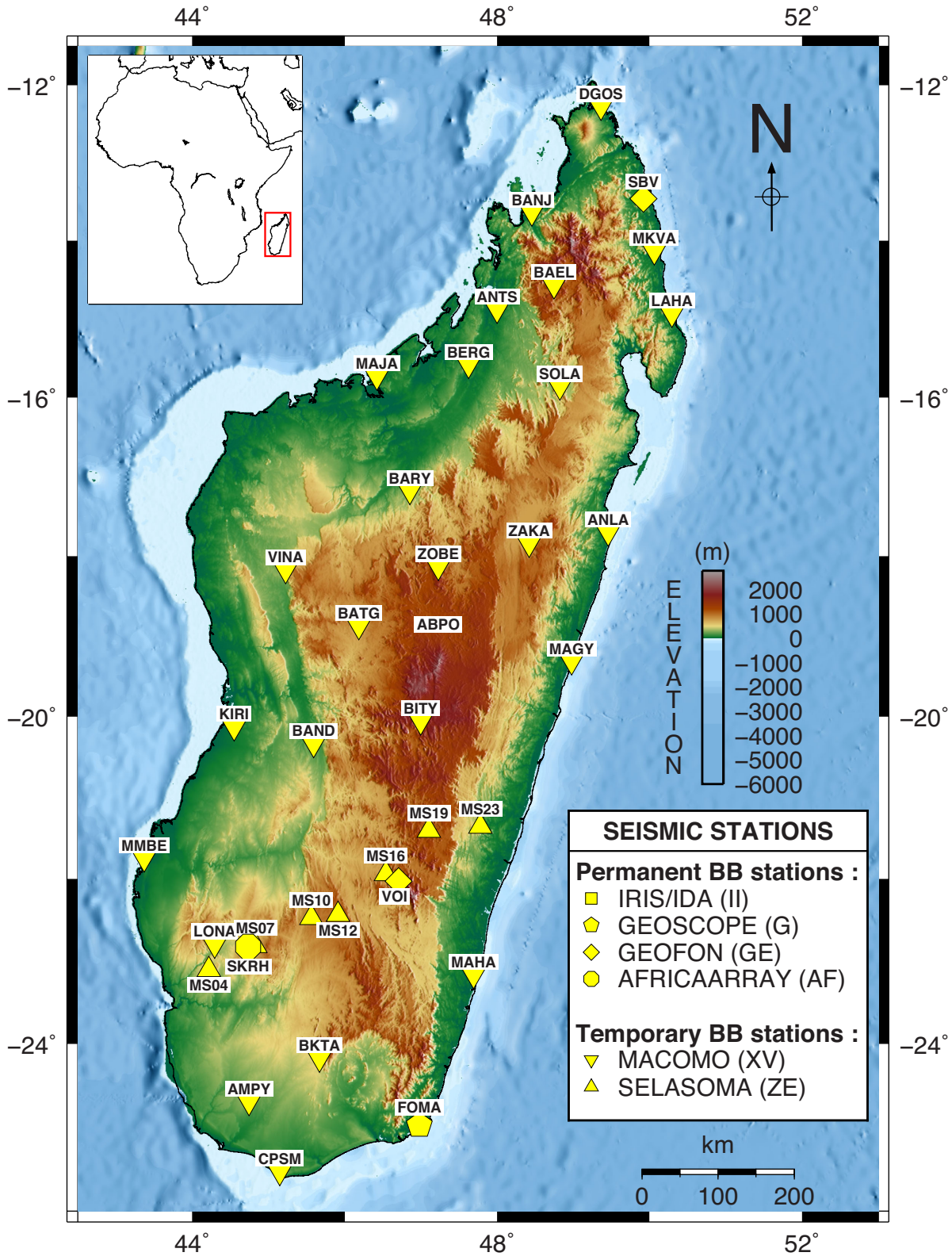

Figure 2. Topographic map of Madagascar showing the distribution of temporary and permanent seismic stations used in this study.

teleseismic *P*-wave front with subsurface discontinuities local to the recording station (Fig. 3). The main phases include the *P*-to-*S* conversion upon refraction (Ps) and the multiple reverberations between the free-surface and the discontinuity (PpPs and PsPs+PpSs). The time and amplitude of the *P*-to-*S* conversions are mainly controlled by the *S*-velocity contrasts and the corresponding *S*-*P* traveltimes, and are commonly utilized to determine the *S*-velocity structure under the recording sites (Langston 1979; Owens *et al.* 1984; Ammon *et al.* 1990; Cassidy 1992).

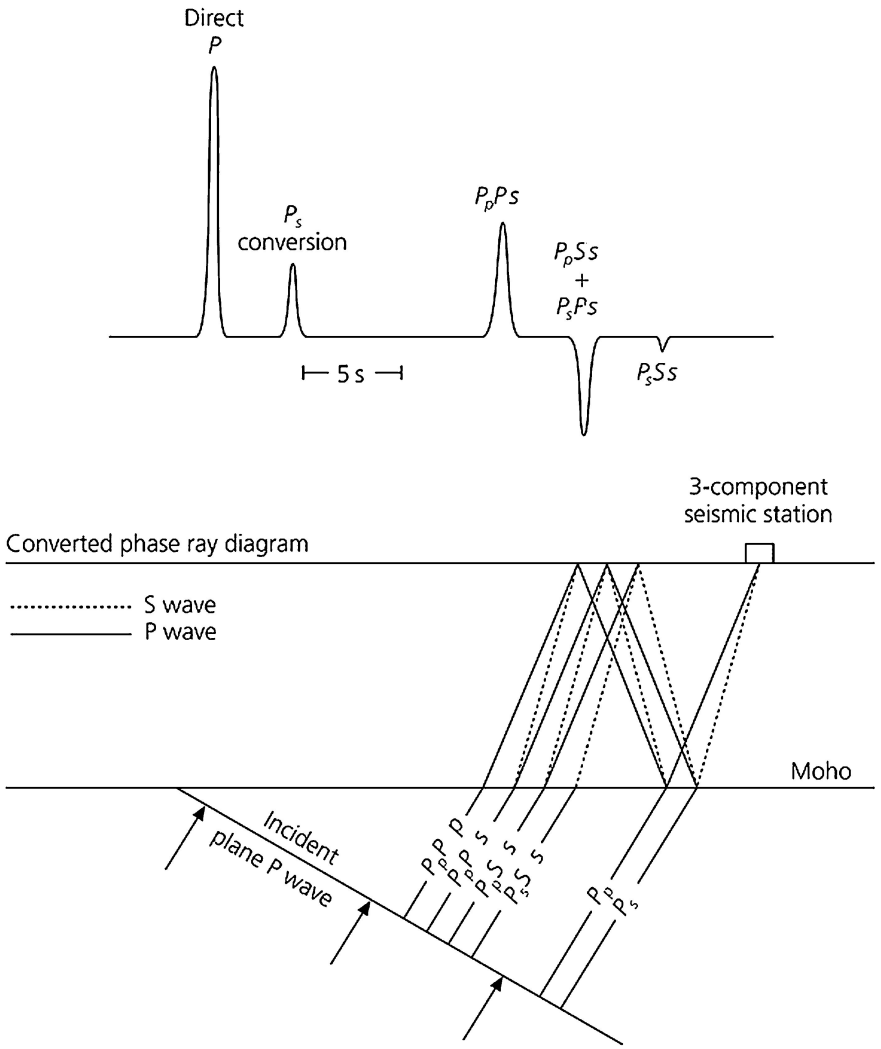

Figure 3. Top panel: synthetic radial receiver function waveform. Bottom panel: corresponding seismic ray diagram of *P*-to-*S* converted phases that contain the receiver function of a single layer over a half-space (taken from Stein & Wysession 2003).

A total of 143 teleseismic events with moment magnitude $M_w \geq 5.5$ and epicentral distances between 30° and 95° were used to compute radial and tangential receiver functions through the iterative time-domain deconvolution procedure of Ligorría & Ammon (1999) (Fig. 4 and listed in Table S2). The original waveforms were windowed 10 s before and 100 s after the *P*-wave arrival, de-trended, tapered and band-pass filtered between 0.05 Hz (to remove low-frequency noise) and 4 Hz (to avoid aliasing), before decimation to 10 samples per second. Horizontal components were then rotated along the great-circle path into radial and transverse components. Finally, *P*-wave radial and tangential receiver functions were obtained by deconvolving the vertical component from the corresponding radial and tangential components. Receiver functions were computed at two overlapping frequency bands with corner frequencies of 0.5 and 1.25 Hz, corresponding to Gaussian filter widths of 1.0 and 2.5, respectively. Receiver function amplitudes are frequency-dependent when second-order discontinuities are present under the station, so the use of overlapping frequency bands helps to discriminate sharp discontinuities from gradational transitions (Julià 2007).

To assess the quality of the receiver functions, each radial receiver function was convolved with its corresponding observed vertical-component seismogram to reconstruct the radial-component seismogram, and only radial receiver functions that recovered ≥85 per cent of the observed radial-component seismogram were selected for further analysis (Ligorría & Ammon 1999). In addition, data from events with large tangential receiver functions were discarded. Tangential receiver functions can be used to estimate the degree of heterogeneity and anisotropy of the propagating medium (Cassidy 1992), with small amplitudes on the tangential receiver functions indicating a predominantly 1-D and isotropic medium beneath a receiver. Fig. 5 shows examples of radial receiver functions computed for a Gaussian filter width of 1.0 for a permanent and a temporary seismic station, ABPO and ZAKA, respectively. Receiver functions for all stations are given in Fig. S1.

3.3 *H–κ* stacking method

The *H–κ* stacking method developed by Zhu & Kanamori (2000) was used to estimate crustal thickness (*H*) and *Vp*/*Vs* ratio (*κ*) beneath each station using receiver functions that have clear Ps waves and one or more multiple reverberations (PpPs, PsPs +PpSs, PsSs). The technique applies a grid search through *H* and *κ* parameter



Figure 4. Distribution of earthquakes (black dots) centred on the middle of the seismic network (black star). The two grey lines indicate the minimum (30°) and maximum (95°) event-station distances, in degrees, used in the receiver-function computations.

space that stacks the receiver function amplitudes along the corresponding phase-moveout curves according to

$$s(H,\kappa) = \sum_{j=1}^{N} w_1\, r_1\,(t_1) + w_2 r_2\,(t_2) - w_3 r_3\,(t_3)\,, \qquad (1)$$

where w_1, w_2 and w_3 are *a priori* weights assigned to the Ps, PpPs and PsPs+PpSs phases, respectively; r_j is the amplitude of the radial receiver function; t_1, t_2 and t_3 are the arrival times of the phases, and N is the number of receiver functions used. The best estimates of H and κ correspond to a maximum of the $s(H,\kappa)$ surface, which in turn matches the arrival times of the Ps, PpPs and PsPs+PpSs phases. The stacking procedure requires the assumption of an average Vp for the crust, which was fixed at the continental average of 6.5 km s^{-1} (e.g. Christensen & Mooney 1995).

When applying the stacking procedure to the data set, weights for the Ps, PpPs and PsPs+PpSs phases are usually selected depending upon the clarity of the phases. When all three phases were distinctly seen in the receiver-function waveforms, weighting factors of $w_1 = 0.4$, $w_2 = 0.3$ and $w_3 = 0.3$ were chosen. However, when the PpPs and PsPs+PpSs phases were less clear than the Ps phase, a higher weight of 0.6 was given to the Ps phase, and smaller but equal weights of 0.2 to the PpPs and PsPs+PpSs phases. Receiver functions computed with a Gaussian filter width of 1.0 were used for most of the stations, and receiver functions computed with a Gaussian filter width of 2.5 were used to check for consistency. However, for stations ABPO, MAHA, MS10, MS12, MS16, SBV and VOI the Ps and converted phases on the receiver functions computed using a Gaussian filter width of 2.5 were more easily identified, and therefore the results reported for these stations are from the H–κ stacking of the higher-frequency receiver functions. In addition, in sedimentary basins, reverberations from the sediment-basement interface can make the Ps and Moho reverberations difficult to identify, so the H–κ stacking technique was not used for some of the seismic stations in the sedimentary basins.

The approach of Julià & Mejía (2004) was used to estimate the uncertainty in the results from the H–κ stacking method. This approach employs a bootstrap resampling technique (Efron & Tibshirani 1991) to compute a one-standard-deviation error around the best-estimated values of H and κ. This involved resampling the receiver-function data sets with replacement 200 times for each station, applying the H–κ stacking procedure to the resampled data set, and computing the average and standard deviations from the resulting 200 estimates. In addition, to evaluate uncertainties

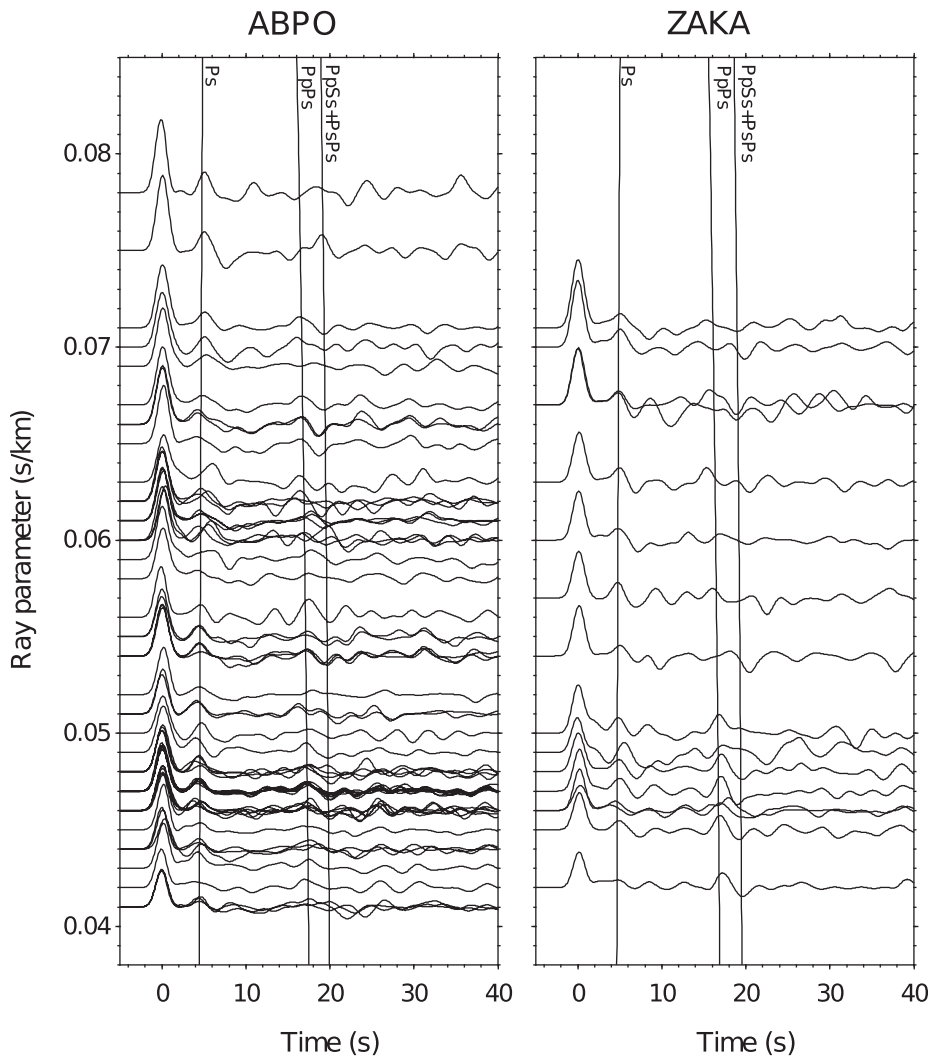

Figure 5. A plot of the radial receiver functions from a permanent seismic station, ABPO (left-hand panel), and a temporary station, ZAKA (right-hand panel), versus ray parameters estimated using a Gaussian filter width of 1.0. The three vertical lines show the predicted Ps, PpPs and PsPs+PpSs phase arrival times.

resulting from the choice of an average crustal *Vp*, the stacking procedure was applied using a range of *Vp* between 6.3 and 6.8 km s^{-1}. Overall uncertainties in H and κ were obtained by combining the formal uncertainties from the bootstrap method with the range of H and κ values obtained when using different *Vp* values. The overall uncertainties for each station are ±1–3 km for the Moho depth and ±0.02 for κ. An example of H–κ stacking for station VINA is shown in Fig. 6, and the results for all stations using an average crustal *Vp* of 6.5 km s^{-1} are summarized in Tables 1 and 2 and given in Fig. S2.

3.4 Joint inversion of receiver functions with the dispersion of Rayleigh wave phase velocities

For obtaining estimates of crustal thickness and crustal shear-wave velocities, the method developed by Julià *et al.* (2000, 2003) was used, which involves jointly inverting the receiver functions and surface-wave dispersion curves using an iterative, least-squares algorithm with a roughness norm. The input for the joint inversion consists of an initial velocity model, the observed receiver functions, and the Rayleigh-wave phase-velocity curves. An influence factor is used to control the trade-off between fitting the receiver functions and the phase-velocity dispersion curves, and equal contributions of receiver functions and dispersion data were used. Velocity models are parameterized as a stack of thin layers of fixed thickness and uniform velocity, so a smoothness parameter is needed to regularize the inversion by controlling the trade-off between fitting the observations and smoothing the velocity model. Rayleigh-wave phase velocities from 8 to 100 s, taken from the surface-wave tomography studies of Madagascar by Pratt *et al.* (2017), were used after applying a 3-point running average to smooth the dispersion curve.

The starting model used in the joint inversions consisted of an isotropic medium with a 35.5-km-thick crust and a linear shear-wave-velocity increase across the crust of 3.4–4.0 km s^{-1}, overlying a flattened PREM (Preliminary Reference Earth Model) structure for the mantle (Dziewonski & Anderson 1981). The crustal Poisson's ratio was set to the value obtained from the H–κ stacking at each station and crustal densities were obtained from the values of *Vp* using the empirical relationship of Berteussen (1977). The preset thicknesses of the first and second layers were, respectively, 1 and 2 km, and the layer thickness increased to 2.5 km for depths between 3 and 60.5 km, 5 km for depths between 60.5 and 260.5 km, and 10 km below 260.5 km depth. The velocity structure from the inversion is fixed to the PREM-like values for depths below 200 km.

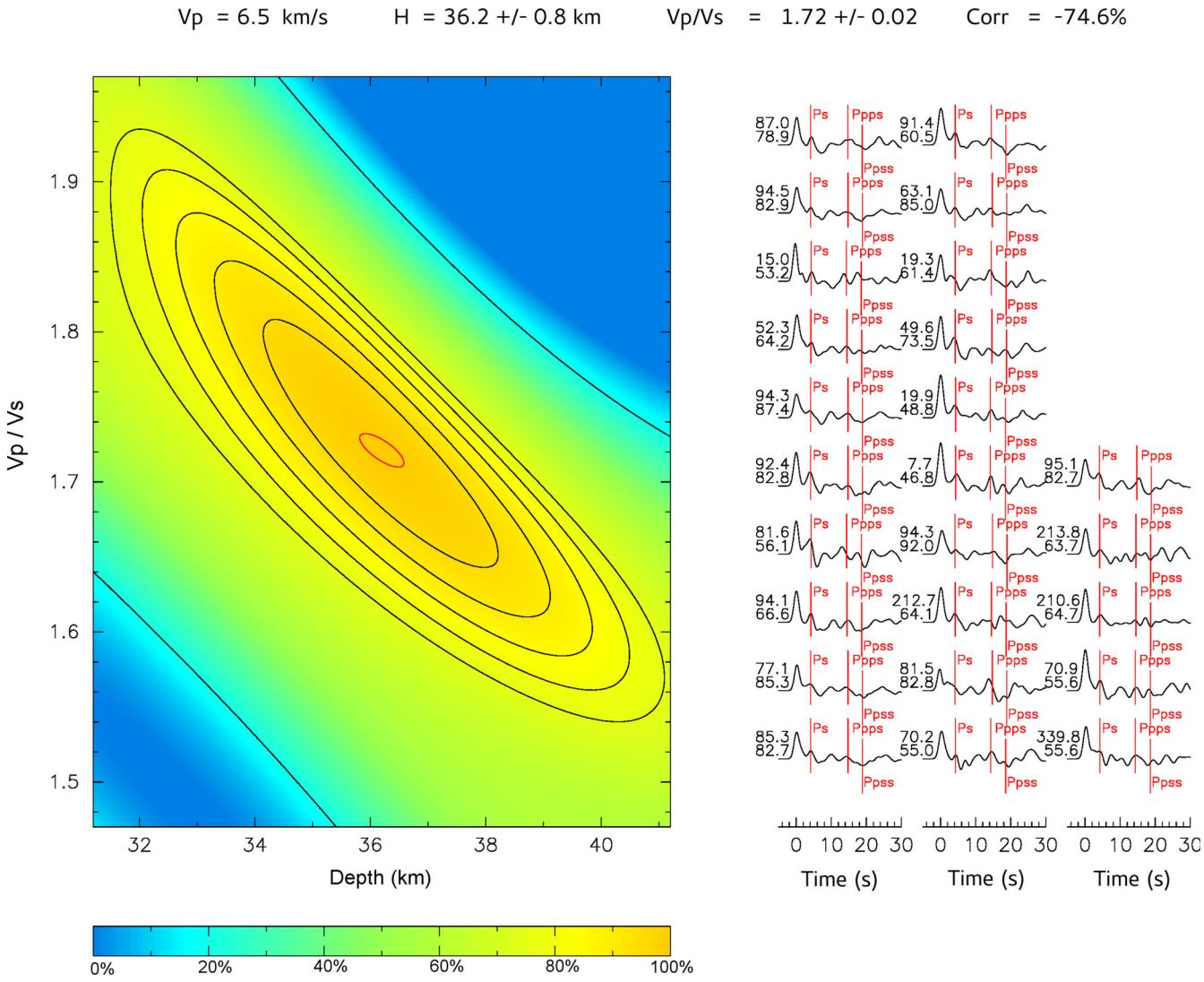

Figure 6. *H–κ* stacking results for seismic station VINA. Left-hand panel: *H–κ* parameter space with the optimal values for *H* and *κ* (centre of red ellipse). The black contours map out the percentage values, in the colour scale bar, of the normalized objective function given in eq. (1). Right-hand panel: receiver functions labelled by the event backazimuth (top number) and epicentral distance (bottom number), both in degrees. The optimal results for *H* and *κ* obtained are summarized along the top, along with their formal uncertainties, and shown with the red contour on the left panel.

The starting model for the seismic stations installed in the sedimentary basins was slightly different. The top 10 km of the sedimentary basin was characterized by a linear shear-wave velocity structure increasing from 2.2 to 3.6 km s^{-1} with a layer thickness of 1 km. Poisson's ratio was set to 0.35 for the top 3 km and then 0.29 for the remaining 7 km. Again, the densities were determined using the velocity–density relationship from Berteussen (1977).

The radial receiver functions were grouped by backazimuth and ray parameter before the joint inversion to account for laterally varying structures (Julià *et al.* 2008). Both high- and low-frequency receiver functions were binned into groups in which bounds in backazimuth and ray parameter were limited to maximum variations of 10° and 0.01 s km^{-1}, respectively. A minimum of three receiver functions was required to compute an average. Inversion results for each group yielded similar velocity structures for each station, indicating minimal lateral variations in crustal structure below each station. Consequently, all of the groups of receiver functions were inverted together to obtain an average velocity model for each station. An example of the joint inversion for station VINA is shown in Fig. 7, with the crustal structure for all stations summarized in Tables 1 and 2. The inversion results for the other stations are provided in Fig. S3.

Uncertainties in the velocity models were estimated by applying the approach of Julià *et al.* (2005) of repeating the inversion for a range of inversion parameters and Poisson's ratios. Doing this, we estimate an uncertainty of approximately 0.1 km s^{-1} for the velocity in each layer, which translates into an uncertainty of ±2.5 km in the depth of any crustal boundary observed in the model, including the Moho.

4 RESULTS

A correlation of *H–κ* stacking (for basement stations) with the joint inversion results shows a generally comparable estimation of crustal thickness for all seismic stations (Fig. 8). Consequently, only results from the joint inversion method are used to summarize the results for

Table 1. Summary of crustal structure parameters for stations located in the sedimentary basins along the western side of Madagascar.

Station name	Network code	#Events	*H–κ* stacking		Joint inversion					
			Crustal thickness (km)	Poisson's ratio	Sediment thickness (km)	Average sediment *Vs* (km s^{-1})	Crustal thickness (km)	Average crustal *Vs* (km s^{-1})	Average uppermost mantle *Vs* (km s^{-1})	Mafic lower crust (km)
DGOS	XV	34	–	–	4	2.3	18.0	3	4.3	0.0
BANJ	XV	13	–	–	4	2.4	33.0	3.5	4.3	12.5
ANTS	XV	22	28.6 ± 0.9	0.29 ± 0.02	6	2.7	33.0	3.4	4.4	5.0
BERG	XV	20	30.1 ± 1.3	0.31 ± 0.01	2	2.4	35.5	3.5	4.5	5.0
MAJA	XV	34	–	–	6	2.2	35.5	3.4	4.3	2.5
BAND	XV	17	33.6 ± 1.7	0.26 ± 0.03	2	2.6	33.0	3.4	4.3	2.5
KIRI	XV	19	–	–	6	2.7	28.0	3.3	4.3	2.5
MMBE	XV	10	–	–	8	2.1	23.0	2.8	4.4	2.5
MS07	ZE	13	26.9 ± 2.4	0.31 ± 0.04	6	2.8	30.5	3.3	4.4	5.0
SKRH	AF	8	–	–	5	2.7	28.0	3.2	4.4	0.0
LONA	XV	30	–	–	5	2.3	28.0	3.2	4.3	0.0
MS04	XV	13	–	–	5	2.3	25.5	3.2	4.4	2.5
CPSM	XV	34	28.0 ± 1.0	0.28 ± 002	0	0.0	33.0	3.6	4.5	5.0
Average ± standard deviation			**29.4 ± 2.6**	**0.29 ± 0.02**	**4.5 ± 2.1**	**2.3 ± 0.7**	**29.5 ± 5.2**	**3.3 ± 0.2**	**4.4 ± 0.1**	**3.5 ± 3.3**

Note the crustal thickness and average properties represent the total crust, that is sedimentary layers plus crystalline basement.

Table 2. Summary of crustal structure parameters for stations located within Precambrian terranes.

Terrane (age)	Station name	Net. code	#Events	*H–κ* stacking		Joint inversion			
				Crustal thickness (km)	Poisson's ratio	Crustal thickness (km)	Average crustal *Vs* (km s^{-1})	Average uppermost mantle *Vs* (km s^{-1})	Mafic lower crust (km)
Antongil-Masora (Palaeoarchean to Mesoarchean)	ANLA	XV	24	43.5 ± 1.4	0.24 ± 0.02	43.0	3.7	4.5	15.0
	BAEL	XV	24	33.5 ± 0.9	0.27 ± 0.02	33.0	3.7	4.4	2.5
	SOLA	XV	9	33.0 ± 1.2	0.24 ± 0.02	33.0	3.6	4.3	2.5
	BARY	XV	10	40.0 ± 2.5	0.25 ± 0.03	40.5	3.7	4.5	5.0
	ZAKA	XV	16	41.4 ± 1.7	0.25 ± 0.01	43.0	3.7	4.4	2.5
	ZOBE	XV	13	46.3 ± 2.1	0.22 ± 0.04	45.5	3.8	4.3	17.5
Antananarivo	BATG	XV	12	42.3 ± 1.4	0.27 ± 0.02	43.0	3.7	4.3	7.5
(Neoarchean)	ABPO	II	59	43.9 ± 1.2*	0.22 ± 0.01*	43.0	3.7	4.3	5.0
	MAGY	XV	14	28.9 ± 1.9	0.28 ± 0.04	35.5	3.7	4.3	5.0
	BITY	XV	14	41.6 ± 2.4	0.26 ± 0.02	43.0	3.7	4.3	10.0
	MS19	ZE	15	40.8 ± 1.3	0.27 ± 0.01	40.5	3.7	4.4	2.5
	MS23	ZE	20	41.6 ± 2.9	0.26 ± 0.02	40.5	3.8	4.5	7.5
	MAHA	XV	14	35.9 ± 0.9*	0.28 ± 0.01*	35.5	3.7	4.4	5.0
	VOI	GE	8	43.1 ± 2.4*	0.22 ± 0.04*	40.5	3.7	4.5	4.5
Average ± standard deviation				**39.4 ± 5.0**	**0.25 ± 0.02**	**39.7 ± 4.1**	**3.7 ± 0.0**	**4.4 ± 0.1**	**5.9 ± 4.2**
	MS12	ZE	9	39.1 ± 1.4*	0.24 ± 0.02*	38.0	3.7	4.5	5.0
Anosyen-Androyen	BKTA	XV	11	39.5 ± 1.1	0.21 ± 0.02	38.0	3.7	4.5	5.0
(Palaeoproterozoic)	MS10	ZE	11	36.2 ± 1.1*	0.27 ± 0.02*	35.5	3.6	4.5	2.5
	FOMA	G	24	36.5 ± 1.6	0.25 ± 0.03	35.5	3.7	4.4	5.0
Average ± standard deviation				**37.8 ± 1.7**	**0.24 ± 0.03**	**36.8 ± 1.4**	**3.7 ± 0.1**	**4.5 ± 0.0**	**4.4 ± 1.3**
Ikalamavony	VINA	XV	24	36.2 ± 0.8	0.24 ± 0.01	35.5	3.6	4.4	5.0
(Mesoproterozoic)	MS16	ZE	17	41.6 ± 0.8*	0.23 ± 0.01*	40.5	3.7	4.5	7.5
Average ± standard deviation				**38.9 ± 3.8**	**0.24 ± 0.01**	**38.0 ± 3.5**	**3.7 ± 0.1**	**4.5 ± 0.1**	**6.3 ± 1.8**
Bemarivo (Neoproterozoic)	SBV	GE	20	31.1 ± 1.8*	0.25 ± 0.03*	30.5	3.6	4.2	2.5
	MKVA	XV	10	31.3 ± 1.2	0.33 ± 0.01	35.5	3.7	4.3	2.5
	LAHA	XV	26	31.1 ± 1.1	0.31 ± 0.01	33.0	3.7	4.3	0.0
Average ± standard deviation				**31.2 ± 0.1**	**0.30 ± 0.04**	**33.0 ± 2.5**	**3.7 ± 0.1**	**4.3 ± 0.1**	**1.7 ± 1.4**
Vohibory (Neoproterozoic)	AMPY	XV	7	25.5 ± 2.4	0.30 ± 0.03	28.0	3.5	4.4	0.0

*Results obtained from receiver functions computed using a Gaussian filter width of 2.5.

Moho depth. Moreover, this technique was applied for all seismic stations (37 stations) while the *H–κ* stacking could only be applied for stations located in the basement and a few in the basin (29 stations in total). Results from *H–κ* stacking and the joint inversion of receiver functions and Rayleigh-wave phase-velocity dispersion measurements are summarized in Tables 1 and 2 and illustrated in Figs 9–13.

2-D contour maps were generated by interpolating the point measurements from the *H–κ* stacking and the joint inversion methods using the surface routine of the Generic Mapping Tools (GMT;

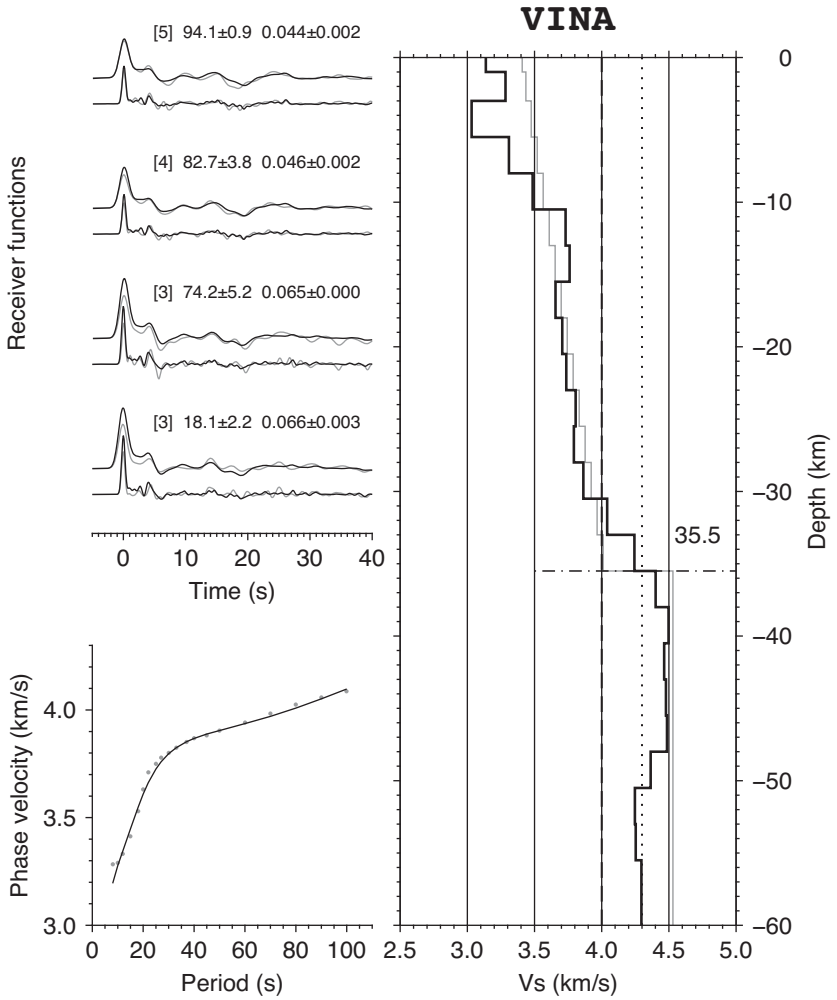

Figure 7. Joint inversion of Rayleigh wave phase velocities and receiver functions for station VINA. Top left-hand panel: grey and black lines are the observed and predicted radial receiver functions, respectively, estimated for Gaussian filter widths of 1.0 (top panel) and 2.5 (bottom panel). The numbers on top of the waveforms are the number of receiver functions stacked (in the square bracket), the average back azimuth (± one standard deviation), and the average ray parameter (±1 standard deviation) for the stack. Bottom left-hand panel: the observed and predicted dispersion curves of the phase velocity, shown with grey dots and a black line, respectively. Right-hand panel: the starting velocity model (grey line) and predicted velocity structure (black line). The horizontal dash-dot line and number indicate the Moho depth (in km). The vertical dashed and dotted lines correspond to *Vs* values of 4.0 and 4.3 km s^{-1}.

Wessel & Smith 1998). Only interpolated values within a 1°-radius distance from the point measurements are shown in the maps. Fig. 9 shows the sediment thickness from joint inversion, and Figs 10 and 11 show the Moho depth and Poisson ratio or average crustal *Vs* derived from *H–κ* stacking and joint inversion, respectively. Fig. 12 shows topography and crustal thickness along a south-to-north profile across Madagascar. Fig. 13 shows the correlation of the shear-wave velocity distribution in the uppermost mantle from the surface-wave tomography of Pratt *et al.* (2017) with that obtained from the joint inversion technique in this study.

A number of the parameters provided in Tables 1 and 2 have been interpreted from the shear-wave velocity profiles. Previous studies (e.g. Holbrook *et al.* 1992; Christensen & Mooney 1995; Rudnick & Fountain 1995; Rudnick & Gao 2003) have shown that lower crustal mafic lithologies such as amphibolites, garnet-bearing and garnet-free mafic granulites, and mafic gneisses typically have shear-wave velocities that are higher than 3.9 km s^{-1}. Therefore, to determine the thickness of the mafic lower crust we use the thickness of layers in the lowermost crust with velocities between 4.0 and 4.3 km s^{-1}. The depth where the shear-wave velocity is ≥4.3 km s^{-1} is taken as the Moho. For most stations, at this depth there is also a recognizable step increase or discontinuity in the shear-wave velocity.

Previous studies have shown that typical shear-wave velocities in sedimentary rocks are less than 3.0 km s^{-1} (e.g. Castagna *et al.* 1985; Brocher 2005). Therefore, the combined thickness of the layers with shear-wave velocity lower than 3.0 km s^{-1} were used as an estimate of the thickness of the sedimentary basin in the western region of Madagascar.

4.1 Sedimentary basins

Thirteen seismic stations (ANTS, BAND, BANJ, BERG, CPSM, DGOS, KIRI, LONA, MAJA, MMBE, MS04, MS07 and SKRH) are located in the western sedimentary basins. Our results show that the thickest sedimentary sections are observed beneath the western parts of the basins: about 6–8 km along the west coast beneath the Morondava and Mahajanga basins, thinning out rapidly eastward to only 2 km near the eastern edge of the basin. A variation in maximum sediment layer thickness is also observed along the north-south direction, from 5 to 8 km in the south to 4 km in the north.

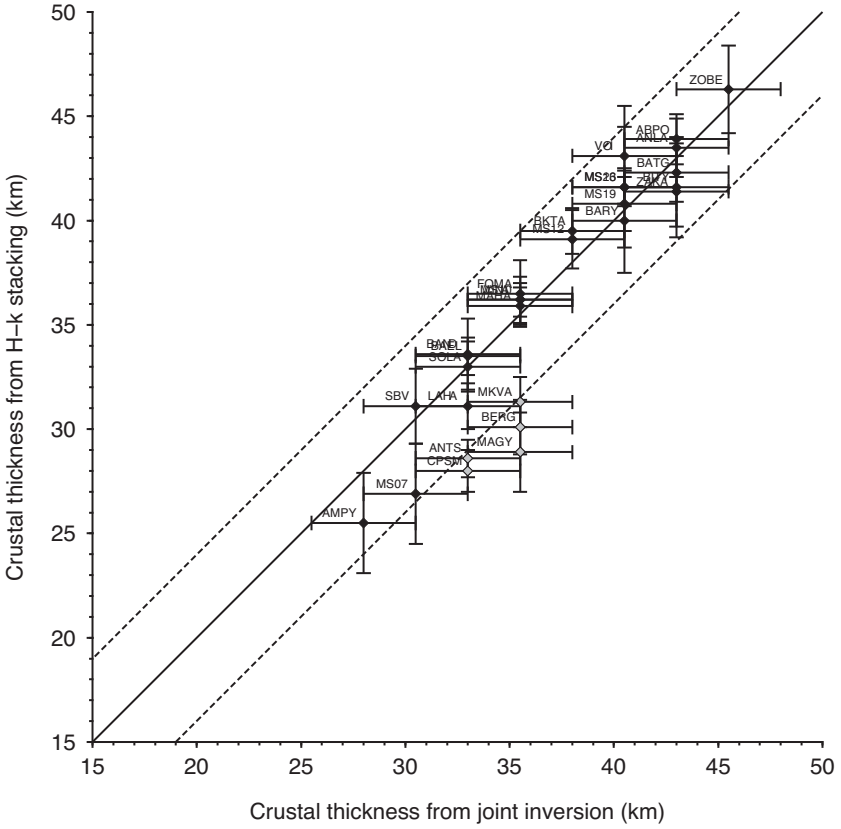

Figure 8. Crustal thickness values estimated from *H–κ* stacking techniques versus the joint-inversion method. The solid line indicates a one-to-one correlation between the two estimates and the dashed lines show a difference of ±4 km. Stations represented in grey are outside of the ±4 km zone and are either from stations in the sedimentary basins where crustal thickness is more difficult to constrain because of reverberations from the sediment-basement interface (BERG), or stations that generally present a gradational Moho in the velocity structure (CPSM, ANTS, MAGY and BERG).

The shear-wave velocities of the sedimentary layers range from 2.1 to 2.7 km s^{-1} in the western regions of the basins, with an average of 2.3 km s^{-1}, and from 2.4 to 2.8 km s^{-1} in the eastern regions, with an average of 2.6 km s^{-1}.

The basins are also characterized by a thin crust, with the Moho at depths between 18 and 36 km under the stations in the sedimentary basin, with an average of 30 ± 5 km. The total crustal thickness, i.e. sediments and basement, ranges from 23 to 33 km in the central and western parts of the basins and between 31 and 36 km in the eastern part of the basins. The northernmost part of the basin region has the thinnest crust, characterized by a Moho at 18 km depth. The crust is also characterized by slow average shear-wave velocities, which vary from 2.8 to 3.6 km s^{-1}, with an average of 3.3 ± 0.2 km s^{-1}. Poisson's ratios for the whole crust range from 0.26 to 0.31, with values generally increasing with distance from the Precambrian terranes of Madagascar, and an average of 0.29 ± 0.02. The thickness of the mafic layer at the bottom of the crust varies between 3 and 13 km for all of the basin stations, with an average of 4 ± 3 km, and uppermost mantle shear-wave velocities that range from 4.3 to 4.5 km s^{-1}.

4.2 Palaeoarchean to Mesoarchean terrane

The crust beneath the Antongil-Masora craton is 43 km thick, although only one station was located in this terrane. The crust is characterized by an average crustal shear-wave velocity of 3.7 km s^{-1}, a Poisson's ratio of 0.24, and a 15-km-thick mafic lower crust. The average shear-wave velocity of the uppermost mantle here is 4.5 km s^{-1}.

4.3 Neoarchean terrane

The Moho beneath the Antananarivo terrane ranges in depth from 33 to 46 km, with an average depth of 40 km. The crust of the northernmost part of the terrane is the thinnest, with a Moho depth of 33 km. The crust is thicker, with a Moho depth between 41 and 46 km, beneath the central and southern parts of the terrane, and thins to 36 km along the east coast. The average shear-wave velocity of the crust for this region is 3.7 km s^{-1}, the average crustal Poisson's ratio is 0.25, and the average thickness of the mafic lower crust is 6 km. The average shear-wave velocity of the uppermost mantle is 4.4 km s^{-1}.

4.4 Palaeoproterozoic terrane

The crustal thickness beneath the Anosyen-Androyen terrane ranges from 36 to 38 km, with an average of 37 km. The crust is characterized by an average shear-wave velocity of 3.7 km s^{-1}, an average Poisson's ratio of 0.24, and an average thickness of the mafic lower crust of 4 km. The average uppermost mantle shear-wave velocity is 4.5 km s^{-1}.

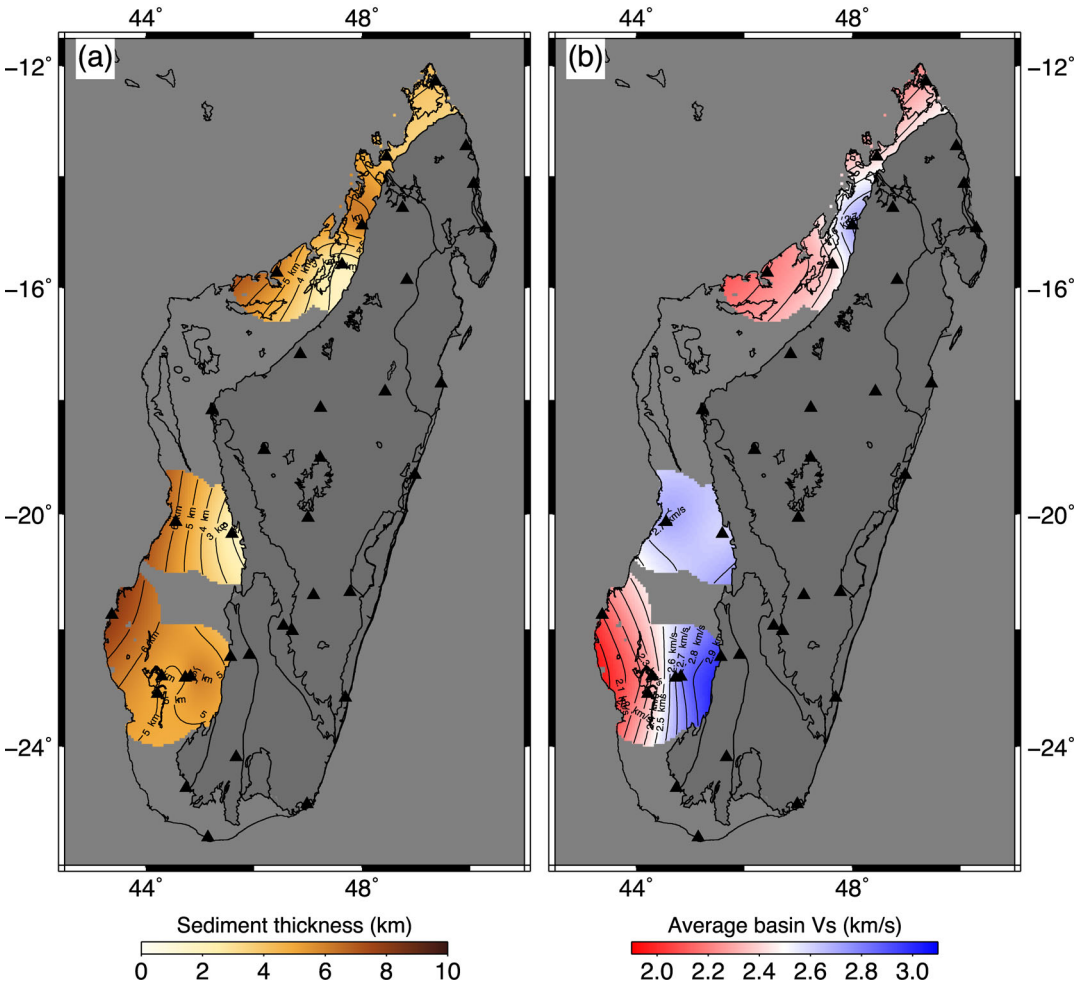

Figure 9. Contour maps of (a) basin thicknesses and (b) average basin shear-wave velocities using seismic stations located in the sedimentary basin. All are interpolated from the point estimates of the station values. Also plotted are the major geological unit boundaries shown in Fig. 1 and station locations (black triangles).

4.5 Mesoproterozoic terrane

The two stations in the Ikalamavony terrane are located far apart and have more in common with other stations near to them than with each other. Station VINA is at the north end of the terrane bordering the sedimentary basin and its crustal thickness of 36 km is similar to the 33-km-thick crust under station BAND. Beneath station MS16, which is located between the Antananarivo and Anosyen-Androyen terranes, the crust is 41 km thick, similar to the thickness of the crust found under station VOI. For both stations the average crustal shear-wave velocity is 3.7 km s^{-1}, Poisson's ratios are 0.23 and 0.24, and the thickness of the mafic lower crust is 5–8 km. The uppermost mantle has shear-wave velocities of 4.4–4.5 km s^{-1}.

4.6 Neoproterozoic terrane

The crustal thicknesses beneath the Bemarivo terrane range from 31 to 36 km, with an average of 33 km. For the Vohibory terrane, the crustal thickness determined from a single station is 28 km. The crust of both terranes is characterized by averaged shear-wave velocities of 3.5–3.7 km s^{-1}. The average Poisson's ratio for both terranes is 0.30. The thickness of the mafic lower crust is 2 km thick on average beneath the Bemarivo terrane and 0 km thick under the Vohibory terrane. The shear-wave velocity of the uppermost mantle under the Bemarivo terrane is 4.2 to 4.3 and 4.4 km s^{-1} under the Vohibory terrane.

5 DISCUSSION

The main findings of this study reflect the complex geological history of the island and are broadly consistent with previous estimates of crustal structure, where such estimates exist. To summarize, sedimentary basin thickness decreases northwards and eastwards. The average crustal shear-wave velocities increase from west to east, mostly as a result of the diminishing effect of thinner sedimentary layers. The crust beneath the high plateau that runs along the central spine of Madagascar is noticeably thicker than most of the peripheral regions. This region correspondingly contains the oldest basement rocks of Madagascar, and is representative of the fact that the crustal thickness and other seismic parameters of different regions of Madagascar are strongly representative of its Palaeogeographic and tectonic history. Results also show variable architecture of the Moho discontinuity, that is sharp or gradational, for the Precambrian terranes of Madagascar.

The thinning of the basins (Fig. 9a), which reflects both the eastward and northward progression in the rifting that formed the basins, has been mentioned previously in several studies, including Besairie (1971), Razafimbelo (1987), Coffin & Rabinowitz (1988)

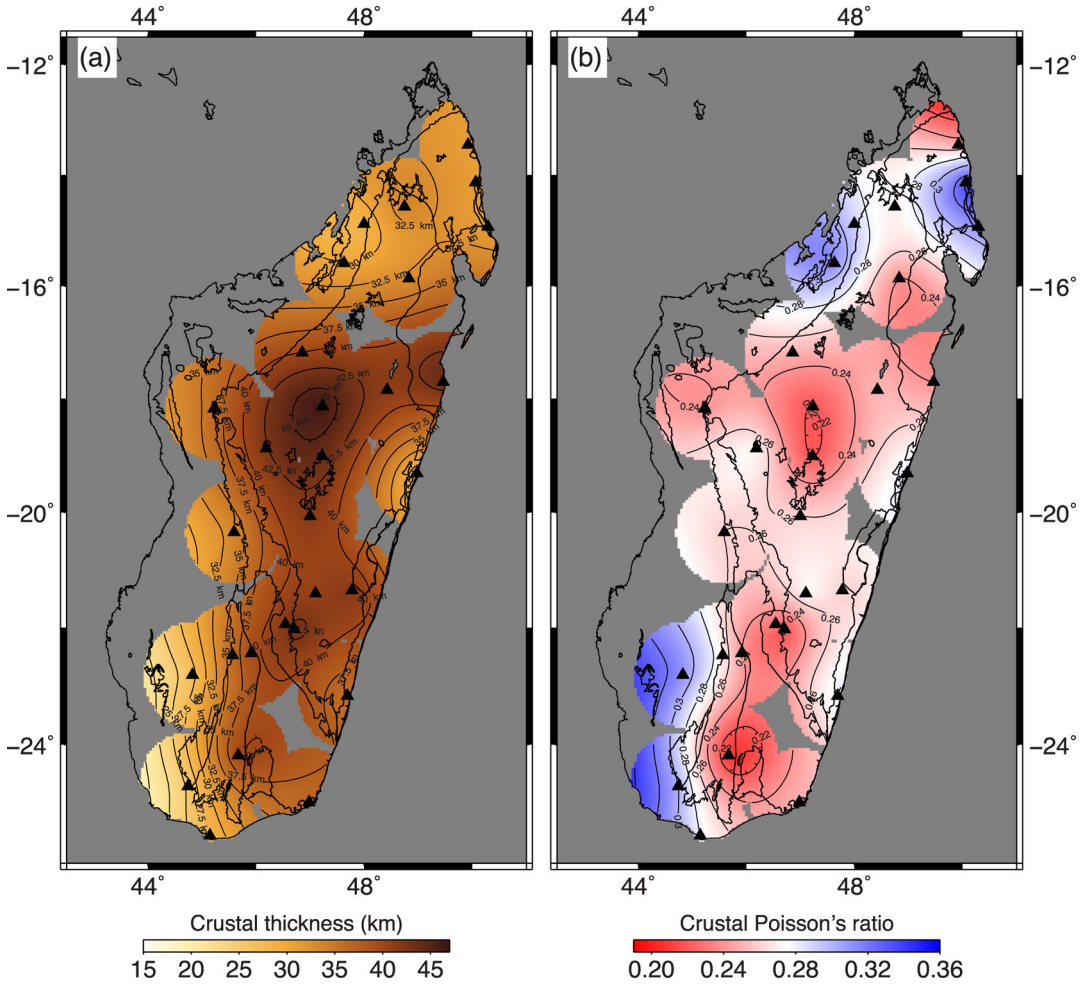

Figure 10. Contour maps of (a) crustal thicknesses and (b) Poisson's ratio using 29 stations from which the H–κ stacking technique was applied. All are interpolated from the point estimates of the station values. Also plotted are the major geological unit boundaries shown in Fig. 1 and station locations (black triangles).

and Piqué (1999b), but is not as well characterized as in this study. In terms of seismic shear-wave velocities, the western parts of the basins are slower, at ∼2.3 km s^{-1}, compared to ∼2.6 km s^{-1} for the eastern parts (Fig. 9b). The higher velocities observed in the eastern parts of the basins can be explained by the fact that the Karoo facies, which are mainly sandstones, outcrop only in the eastern parts of the basin (Wescott & Diggens 1997, 1998), suggesting that the shear-wave velocities in the western part of the basin are influenced by the younger deposits overlying the Karoo sequence.

It is reasonable to assume that before Madagascar rifted away from Africa the thickness of the crust along the western parts of Madagascar was similar to the thickness of unrifted Precambrian crust both to the east, found in this study to be 38 ± 5 km, and in eastern Africa, found by Kachingwe *et al.* (2015) to be 38–39 ± 3 km. Given this, and the thickness of the crust beneath the western rifted margin of Madagascar, the amount of crustal thinning beneath the sedimentary basins can be estimated. In the northernmost part of the island, it thus appears that the crust has been thinned by ∼20 km (i.e. 38 km versus 18 km), and along the west-central and south-central edges of the island, it appears that the crust has been thinned by ∼12 km (i.e. 38 km versus 23–26 km).

The crust on the east coast of Madagascar is also observed to be thinner than in the central highland plateau of the island, but not nearly as thin as beneath the west coast (Figs 10a and 11a). With the exception of station ANLA (in the Palaeoarchean Antongil craton), the east-coast stations of SBV, MKVA, LAHA, MAGY, MAHA and FOMA display crustal thicknesses that are similar, with an average thickness of 34 km. The differences in crustal structure between the east and west coasts can be understood from the different ways in which breakup was accommodated. Along the east coast, India moved northward along what was primarily a transform fault, so there was not the same development of extensional basins as found along the west side of the island.

The separation of India from Madagascar was likely influenced by the passage of the Greater India block over the Marion hotspot about 95–85 Ma, when the extensive floods basalts covered much of the island (Storey *et al.* 1995; Torsvik *et al.* 1998). The thermal anomaly associated with the hotspot likely weakened and thinned Madagascar's lithosphere, facilitating the break-away of the Greater India block along the edge of the Western Dharwar Craton (Raval & Veeraswamy 2003). The slight thinning of the crust found along the east coast of Madagascar could be the result of uplifting and erosion of the crust due to the Marion plume, as opposed to or in addition to a minimal component of rifting.

In contrast to our findings, Paul & Eakin (2017) concluded that the crust beneath the central region of Madagascar is thinner compared to the eastern coast based on the analysis of records from the permanent stations ABPO in central Madagascar, and FOMA

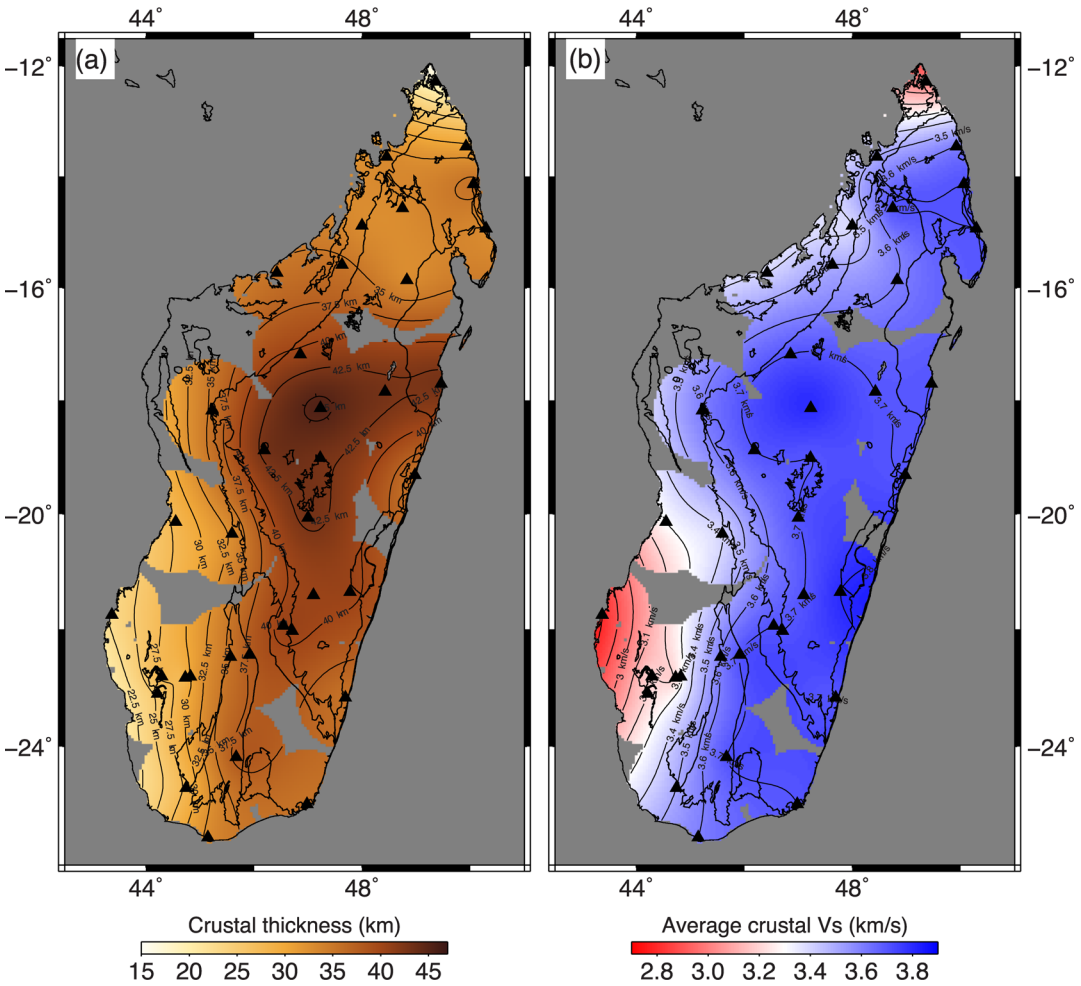

Figure 11. Contour maps of (a) crustal thicknesses and (b) average crustal shear-wave velocities using 37 stations from which the joint receiver function inversion method was applied. All are interpolated from the point estimates of the station values. Also plotted are the major geological unit boundaries shown in Fig. 1 and station locations (black triangles).

along the southern coast. The main discrepancy arises for FOMA, where their estimate of 44 km contrasts with our estimate of 36 km. Their high estimate is clearly due to their interpretation of a phase in the receiver functions, at ∼6 s, as the direct Ps conversion from the Moho. However, this arrival could also be a multiple of an intra-crustal phase (at ∼2 s; see Fig. S4). Note that Paul & Eakin (2017) only considered teleseismic events with back azimuths between 82° and 93°. However, looking at other backazimuth ranges (Fig. S4, in this study), a clear phase, presumably the Ps wave converted from the Moho discontinuity, is observed at ∼4 s. This indicates thinner crust (∼36 km) as reported in this study and earlier ones using receiver functions (e.g. Rindraharisaona *et al*. 2013, 2017), which used more than one station along the eastern coast and considered broader back azimuth ranges. In support of this interpretation, crustal thickness estimates from gravimetry imply that the crust thins towards the eastern coast (Fourno & Roussel 1994; Rakotondraompiana *et al.* 1999). Therefore, the balance of evidence points to the shallower Moho inferred in our joint inversion but the presence of the strong phase at 6 s for azimuths between ∼60° and 130° points to lateral variability, which is beyond the scope of the current study to investigate further.

Several studies have investigated variations in crustal structure with age in order to assess secular variation in the continental crust. Some studies have reported that Archean crust is thinner than Proterozoic crust (e.g. Durrheim & Mooney 1991, 1994; Thompson *et al.* 2010), while others have found little evidence for age-dependent differences (e.g. Rudnick & Fountain 1995; Zandt & Ammon 1995; Tugume *et al*. 2012, 2013; Kachingwe *et al.* 2015). Crustal thicknesses obtained in this study suggest that the Archean crust (40 ± 4 km) in Madagascar is on average slightly thicker than the Proterozoic crust (35 ± 4 km). In contrast, there are no significant differences in Poisson's ratio between the Archean crust (0.25 ± 0.02) and Proterozoic crust (0.26 ± 0.04) or in average shear wave velocities (3.7 km s^{-1} for both), though the average thickness of the mafic lower crust is slightly greater for Archean terranes (7 km) than it is for Proterozoic terranes (4 km). Our results are in broad agreement with Rindraharisaona *et al.* (2017). They concluded that the Archean crust is also slightly thicker (38–43 km) compared to the Proterozoic crust (33–38 km). They attributed the difference to the absence of a mafic lower crustal underplate in the Proterozoic terranes, and suggested that the underplated layer may have delaminated due to the high-temperature metamorphism that affected the areas, a process described by Martelat *et al.* (2000); Jöns & Schenk (2011), and Horton *et al.* (2016).

The observed variations in the crustal Poisson's ratio can be interpreted as the result of changes in silicic compositions. Laboratory measurements (e.g. Christensen 1996) have demonstrated that Poisson's ratio is 0.24 for felsic granitic rocks, 0.27 for

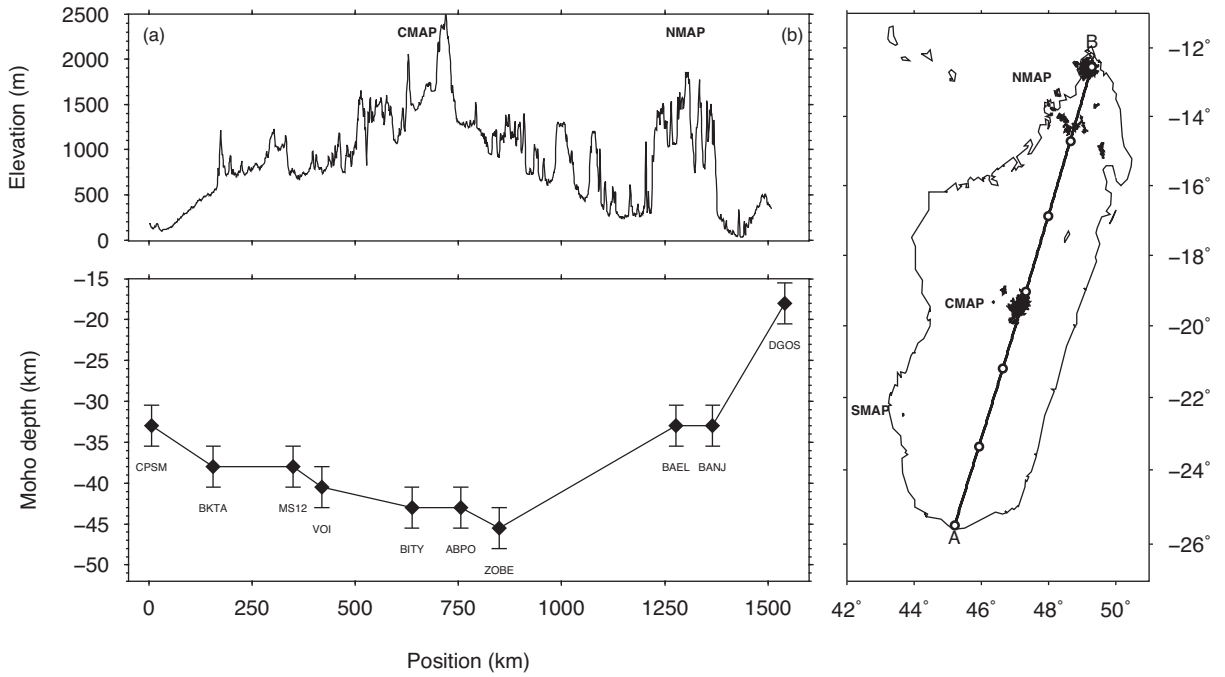

Figure 12. Top panel: elevation of Madagascar (Amante & Eakins 2009) along the profile A–B. The Cenozoic volcanic provinces NMAP and CMAP are shown in the figure at right (in black). Bottom panel: crustal thickness values for seismic stations along the same profile. Right-hand panel: white circles along the profile are 250 km intervals from the 0 km position at A.

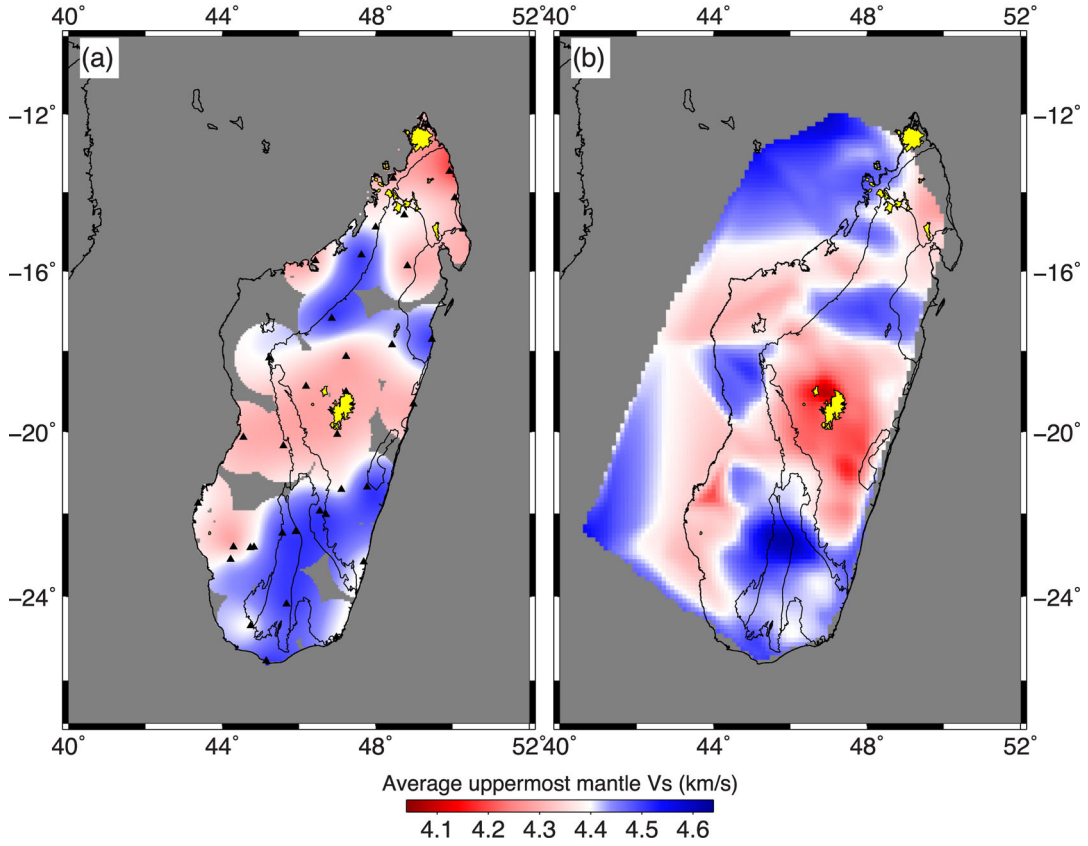

Figure 13. Maps showing (a) the average uppermost mantle shear-wave velocities, interpolated from the point estimates of the station values from this study and (b) the shear velocities at 50 km depth from the surface-wave tomography in Pratt *et al.* (2017). Also plotted are the major geological unit boundaries shown in Fig. 1, the locations of the NMAP/CMAP/SMAP provinces (Northern, Central and Southern Madagascar Alkaline Provinces, respectively) (in yellow), and station locations (black triangles). The regions where the uppermost mantle shear-wave velocities are anomalously low correspond very well with regions of Cenozoic volcanic activity and with low-velocity mantle anomalies determined from the surface-wave study of Pratt *et al.* (2017).

intermediate lithologies (such as diorite), and 0.30 for mafic gabbros. We found the Archean and Proterozoic terranes to have a Poisson's ratio that ranged from 0.2 to 0.3 with, an average of 0.26 ± 0.03 (Fig. 10b). Overall, the crust of these terranes is representative of predominantly felsic to intermediate compositions. In contrast, the eastern regions of the west-coast sedimentary basins have higher crustal Poisson's ratio of 0.29 ± 0.02. It is possible that this reflects the syntectonic emplacement of rift basalts while the Greater India block was rifting away from Africa, as has been found at other large continental rifts (Stein *et al.* 2016), imparting a slightly more mafic composition to the crust. However, this interpretation is not supported by the low average crustal shear-wave velocities (3.3 km s^{-1}) or the thin mafic lower crust (4 km) under the basins. An alternative and maybe more likely possibility is that the higher Poisson's ratio results simply from the contribution of the sediments in the basin, which can have a higher Poisson's ratio than crystalline rocks.

As can be seen in Fig. 12, which shows a N–S profile across the length of Madagascar, there is a very strong correlation between elevation and crustal thickness. An increase from 33 to 46 km is observed for the crustal thickness of Madagascar, compared to a corresponding variation of 0–1.6 km in elevation at the surface. A comparison of the two curves reveals a change in Moho depth that is approximately eight times greater than the corresponding change in surface relief, suggesting that it can be fairly well explained by an Airy model of isostatic equilibrium.

However, this correlation breaks down in the northern part of the island, where elevations range from 1 to 2 km but crustal thicknesses are less than 35 km. Given that Madagascar has not undergone any tectonic activity in the past 85 Myr, some other mechanism is required to maintain this high elevation. One possibility is that the northern region is dynamically supported by the same thermal anomalies that have been the source of late Cenozoic volcanism in the north. In general, the pattern of isostatic equilibrium suggested by Fig. 12 is superimposed upon a broad signature of uplift for the island. The average crustal thickness across all stations is 35 km while the average elevation of the stations is 496 m. This elevation is unusually high for the slightly thinner-than-average crustal thickness, suggesting that an additional factor is needed to explain the high elevations. It is likely that the three large regions of seismically slow velocities in the upper mantle beneath the northern, central, and southwestern regions of Madagascar, imaged by Pratt *et al.* (2017; Fig. 13), correspond to thermal anomalies that provide the buoyancy needed to maintain these high elevations. This is supported by observations of the erosion rates of river valleys and lavakas (erosional gullies), which suggest that Madagascar has been experiencing active uplift for at least the past 15 Myr (Cox *et al.* 2010; Roberts *et al.* 2012).

The uppermost mantle beneath Madagascar is generally characterized by average shear-wave velocities that range from 4.2 to 4.5 km s^{-1}, with an overall average of 4.4 ± 0.1 km s^{-1} (Fig. 13). The shear velocity of the uppermost mantle drops to values of 4.2–4.3 km s^{-1} in the northern part (beneath seismic stations DGOS, BANJ, SBV, MKVA and LAHA), central part (beneath stations ZOBE, ABPO, BATG, BITY and MAGY), and western and southwestern parts (beneath stations MAJA, BAND, KIRI and LONA). These slow mantle velocities of 4.2–4.3 km s^{-1} coincide with the three major volcanic provinces in Madagascar (NMAP, CMAP and SMAP) that are observed to have upper mantle low-shear-velocity anomalies from surface wave tomography (Pratt *et al.* 2017; see Figs 13a and b). The anomalies in the northern and central parts correspond to locations of Cenozoic volcanic activity within the past 1 Ma (Tucker & Conrad 2008), while the slow upper mantle *Vs* in the western, southwestern, and eastern parts correspond to Cretaceous surface volcanism, and also 9-Ma-old volcanics in the southwestern region of Ankililoaka (Bardintzeff *et al.* 2010).

6 CONCLUSIONS

The seismic structure of the crust and uppermost mantle of Madagascar has been investigated using broadband data recorded on 37 temporary and permanent broad-band seismic stations. We applied the H–κ stacking procedure to seismic stations deployed on the Precambrian basement and the easternmost parts of the sedimentary basins to calculate the crustal thickness (H) and bulk crustal Vp/Vs ratio (κ), from which Poisson's ratio was determined. Receiver functions were jointly inverted with Rayleigh-wave phase-velocity dispersion measurements to image the Moho and obtain vertical profiles of shear-wave velocities.

Our results reveal that basins along the west coast thin both eastward, from depths of 6–8 to 2 km, and northward, from depths of 5–8 to 4 km, reflecting the eastwardly and northwardly progressive opening and filling of the sedimentary basins. The thickness of Madagascar's crust ranges between 18 and 46 km. Beneath the western basins the crust is thinner (18–36 km thick) because of the Mesozoic rifting of Madagascar from eastern Africa. In comparison to estimates of the thickness of nearby unrifted crust, it appears that the rifted crust has been vertically thinned by as much as ∼12 to 20 km.

There is a weak evidence for secular variation in the structure of the Precambrian crust in Madagascar. The Archean terranes have an average crustal thickness of 40 km and average Poisson's ratio of 0.25, and the Proterozoic terranes have an average crustal thickness of 35 km and average Poisson's ratio of 0.26. The thickness of the mafic lower crust is great for Archean terranes (7 km) than for Proterozoic terranes (4 km), but both have similar average crustal shear-wave velocities (3.7 km s^{-1}).

Crustal thickness beneath the Precambrian terranes along the east coast of Madagascar ranges from 31 to 36 km, somewhat thinner than beneath the interior of the island. The small amount of thinning may have been caused by crustal uplift and erosion when Madagascar moved over the Marion hotspot and India broke away.

The uppermost mantle beneath Madagascar is generally characterized by average shear-wave velocities that range from 4.2 to 4.5 km s^{-1}, with an overall average of 4.4 ± 0.1 km s^{-1}. The shear-wave velocity of the uppermost mantle drops to values of 4.2–4.3 km s^{-1} in the northern, central, and southern parts of the island, coincident with the three major volcanic provinces in Madagascar.

There is a fairly good correlation between station elevation and the underlying crustal thickness across Madagascar, with about a 1 km change in elevation at the surface of Madagascar corresponding to a change of 8 km in Moho topography. However, in the northern part of the island, surface elevations are anomalously high compared to crustal thicknesses, suggesting a source of dynamic topography that might be provided by an upper mantle thermal anomaly that would also explain the slow uppermost mantle shear-wave velocities of 4.2–4.3 km s^{-1} and episodes of recent volcanic activity.

ACKNOWLEDGEMENTS

We gratefully acknowledge the field support from IRIS-PASSCAL, which provided the seismic equipment for the MACOMO project (FDSN code: XV 2011–2013, Wysession *et al.* 2011);

SELASOMA project (FDSN code: ZE2012–2014, Tilmann *et al.* 2012), IRIS (FDSN code: II, Scripps Institution of Oceanography 1986), AFRICAARRAY (FDSN code: AF, Penn State University 2004), GEOFON (FDSN code: GE, GEOFON Data Centre 1993) and GEOSCOPE (FDSN code: G, Institut de Physique du Globe de Paris (IPGP) & Ecole et Observatoire des Sciences de la Terre de Strasbourg (EOST) 1982) for additional seismic data. Figures in this paper have been produced with GMT (Wessel & Smith 1998). This research was funded by the National Science Foundation, through grants EAR-0838426 and 0838387. We thank E. Rindraharisaona for her constructive comments and discussion. We also thank an anonymous reviewer and Stewart Fishwick for providing insightful reviews which helped to improve the paper.

REFERENCES

Amante, C. & Eakins, B.W., 2009. ETOPO1 1 arc-minute global relief model: procedures, data sources and analysis, NOAA Technical Memorandum NESDIS NGDC-24, National Geophysical Data Center, NOAA. doi:10.7289/V5C8276M.

Ammon, C.J., Randall, G.E. & Zandt, G., 1990. On the nonuniqueness of receiver function inversions, *J. geophys. Res.,* **95,** 15 303–15 318.

Bardintzeff, J-M., Liegeois, J-P., Bonin, B., Bellon, H. & Rasamimanana, G., 2010. Madagascar volcanic provinces linked to the Gondwana breakup: geochemical and isotopic evidences for contrasting mantle sources, *Gondwana Res.,* **18,** 295–314.

Berteussen, K.A., 1977. Moho depth determinations based on spectral ratio analysis of NORSAR long-period P waves, *Phys. Earth planet. Int.,* **31,** 313–326.

Besairie, H., 1968. Description géologique du massif ancien de Madagascar, Premier volume: Centre Nord et Centre Nord-Est, Doc. Bur. Geol. n°177a, Service Géologique, Antananarivo. Ministère de l'Industrie et des Mines, Direction des Mines et de l'Energie, 117 pp.

Besairie, H., 1969. Description géologique du massif ancien de Madagascar, Deuxième volume: La regioncotière orientale entre le Mangoro et Vangaindrano. Doc. Bur. Geol. n°177b, Service Géologique, Antananarivo. Ministère de l'Industrie et des Mines, Direction des Mines et de l'Energie, 67 pp.

Besairie, H., 1971. Tectonique de madagascar. Tectonique de l' Afrique. *Sciences de la Terre UNESCO Paris,* 549–558.

Besairie, H., 1973. Brève revue de volcanisme à Madagascar. Colloque sur les régions volcaniques tropicales, *Pub. Ass. Géogr., Madagascar,* 18 pp.

Boast, J. & Nairn, A.E.M., 1982. An outline of the geology of Madagascar, in *The Ocean Basins and Margins,* pp. 649–696, eds Nairn, A.E.M. & Stehli, F.G., Plenum Press.

Brocher, T.A., 2005. Empirical relations between elastic wavespeeds and density in the Earth's crust, *Bull. seism. Soc. Am.,* **95,** 2081–2092.

Cassidy, J.F., 1992. Numerical experiments in broadband receiver function analysis, *Bull. seism. Soc. Am.,* **82,** 1453–1474.

Castagna, J.P., Batzle, M.L. & Eastwood, R.L., 1985. Relationships between compressional-wave and shear-wave velocities in clastic silicate rocks, *Geophysics,* **50,** 571–581.

Christensen, N.I., 1996. Poisson's ratio and crustal seismology, *J. geophys. Res.,* **101,** 3139–3156.

Christensen, N.I. & Mooney, W.D., 1995. Seismic velocity structure and composition of the continental crust: a global view, *J. geophys. Res.,* **100,** 9761–9788.

Cochran, J.R., 1988. Somali Basin, Chain Ridge and the origin of the Northern Somali Basin gravity and geoid low, *J. geophys. Res.,* **93,** 11 985–12 008.

Coffin, M.F. & Rabinowitz, P.D., 1987. Reconstruction of Madagascar and Africa: evidence from the Davie fracture zone and Western Somali Basin, *Geophys. Res. Lett.,* **92,** 9385–9406.

Coffin, M.F. & Rabinowitz, P.D., 1988. Evolution of the conjugate East African-Madagascan margins and the western Somali Basin, *Spec. Pap. Geol. Soc. Am.,* **226,** 78.

Collins, A.S., 2006. Madagascar and the amalgamation of Central Gondwana, *Gondwana Res*., **9,** 3–16.

Cox, R., Coleman, D.S., Chokel, C.B., DeOreo, S.B., Wooden, J.L., Collins, A.S., Kröner, A. & DeWaele, B., 2004. Proterozoic tectonostratigraphy and paleogeography of central Madagascar derived from detrital zircon U-Pb age populations, *J. Geol.,* **112,** 379–399.

Cox, R., Zentner, D.B., Rakotondrazafy, A.M. & Rasoazanamparany, C.F., 2010. Shakedown in Madagascar: occurrence of lavakas (erosional gullies) associated with seismic activity, *Geology,* **38,** 179–182.

de Wit, M.J., 2003. Madagascar: heads it's a continent, tails it's an island, *Ann. Rev. Earth planet. Sci,* **31,** 213–248.

Durrheim, R.J. & Mooney, W.D., 1991. Archean and Proterozoic crustal evolution: evidence from crustal seismology, *Geology,* **19,** 606–609.

Durrheim, R.J. & Mooney, W.D., 1994. Evolution of the Precambrian lithosphere: seismological and geochemical constraints, *J. geophys. Res.,* **99,** 15 359–15 374.

Dyment, J., 1991. Structure et évolution de la lithosphère océanique dans l'Océan Indien: apport des données magnétiques, *PhD thesis*, Univ. Strasbourg, 374 pp.

Dziewonski, A.M. & Anderson, D.L., 1981. Preliminary reference earth model, *Phys. Earth planet. Inter.,* **25,** 297–356.

Efron, B. & Tibshirani, R., 1991. Statistical data analysis in computer age, *Science,* **253,** 390–395.

Fourno, J.P. & Roussel, J., 1994. Imaging of the Moho depth in Madagascar through the inversion of gravity data: geodynamic implications, *Terra Nova,* **6,** 512–519.

GAF-BGR, 2008. Final report. Explanatory notes for the Vohibory Domain southwest Madagascar. Réalisation des travaux de cartographie géologique de Madagascar, révision approfondie de la cartographie géologique et minière aux échelles 1/100000 et 1/500000 zone Sud. République de Madagascar, Ministère de L'Energie et des Mines (MEM/SG/DG/UCP/PGRM), 85 pp.

Holbrook, W.S., Mooney, W.D. & Christensen, N.I., 1992. The seismic velocity structure of the deep continental crust, in *Continental Lower Crust,* chapt. 1, pp. 1–43, eds Fountain, D.M., Arculus, R. & Kay, R.W., Elsevier.

Horton, F., Hacker, B., Kylander-Clark, A., Holder, R. & Jöns, N., 2016. Focused radiogenic heating of middle crust caused ultrahigh temperatures in southern Madagascar, *Tectonics,* **35,** 293–314.

Hottin, G., 1976. Présentation et essai d'interprétation du Précambrien de Madagascar, *Bulletin du Bureau de Recherches Géologiques et Minières,* 2nd série, Vol. IV, 117–153.

Institut de Physique du Globe de Paris (IPGP), & Ecole et Observatoire des Sciences de la Terre de Strasbourg (EOST)., 1982. GEOSCOPE, French Global Network of broad band seismic stations, Institut de Physique du Globe de Paris (IPGP), https://doi.org/10.18715/GEOSCOPE.G.

Jöns, N. & Schenk, V., 2008. Relics of the Mozambique Ocean in the central East African Orogen: evidence from the Vohibory Block of southern Madagascar, *J. Metamorph. Geol.,* **26,** 17–28.

Jöns, N. & Schenk, V., 2011. The ultrahigh temperature granulites of southern Madagascar in a polymetamorphic context: Implications for the amalgamation of the Gondwana supercontinent, *Eur. J. Mineral.,* **23,** 127–156.

Julià, J., 2007. Constraining velocity and density contrasts across the crust-mantle boundary with receiver function amplitudes, *Geophys. J. Int.,* **171,** 286–301.

Julià, J. & Mejía, J., 2004. Thickness and *Vp*/*Vs* ratio variation in the Iberian crust, *Geophys. J. Int.,* **156,** 59–72.

Julià, J., Ammon, C.J. & Herrmann, R.B., 2003. Lithospheric structure of the Arabian Shield from the joint inversion of receiver functions and surface-wave group velocities, *Tectonophysics,* **371,** 1–21.

Julià, J., Ammon, C.J. & Nyblade, A.A., 2005. Evidence for mafic lower crust in Tanzania, East Africa, from joint inversion of receiver functions and Rayleigh wave dispersion velocities, *Geophys. J. Int.,* **162,** 555–562.

Julià, J., Assumpção, M. & Rocha, M.P., 2008. Deep crustal structure of the Paranã Basin from receiver functions and Rayleigh-wave dispersion: evidence for a fragmented cratonic root, *J. geophys. Res.,* **113,** B08318. doi:10.1029/2007JB005374.

Julià, J., Ammon, C.J., Herrmann, R.B. & Correig, A.M., 2000. Joint inversion of receiver function and surface wave dispersion observations, *Geophys. J. Int.,* **143,** 99–112.

Kachingwe, M., Nyblade, A.A. & Julià, J., 2015. Crustal structure of Precambrian terranes in the southern African subcontinent with implications for secular variation in crustal genesis, *Geophys. J. Int.,* **202,** 533–547.

Langston, C.A., 1979. Structure under Mount Rainier, Washington, inferred from teleseismic body waves, *J. geophys. Res.,* **84,** 4749–4762.

Laske, G., Masters, G., Ma, Z. & Pasyanos, M., 2013. Update on CRUST1.0 - A 1-degree Global Model of Earth's Crust, *Geophys. Res. Abstr.,* **15,** Abstract EGU2013-2658.

Ligorría, J.P. & Ammon, C.J., 1999. Iterative deconvolution and receiver function estimation, *Bull. seism. Soc. Am.,* **89,** 1395–1400.

Mahoney, J., Nicollet, C. & Dupuy, C., 1991. Madagascar basalts: tracking oceanic and continental sources, *Earth planet. Sci. Lett.,* **104,** 350–363.

Martelat, J.-E., Lardeaux, J.-M., Nicollet, C. & Rakotondrazafy, R., 2000. Strain pattern and late Precambrian deformation history in southern Madagascar, *Precambrian Res*., **102,** 1–20.

Nicollet, C., 1990. Crustal evolution of the granulites of Madagascar, in: *Granulites and Crustal Evolution*, pp. 291–310, eds Vielzeuf, D. & Vidal, P.H.

Norton, I.O. & Sclater, J.G., 1979. A model for the evolution of the Indian Ocean and the breakup of Gondwanaland, *J. geophys. Res.,* **84,** 6803–6830.

Owens, T.J., Zandt, G. & Taylor, S.R., 1984. Seismic evidence for an ancient rift beneath the Cumberland Plateau, Tennessee; a detailed analysis of broadband teleseismic P-waveforms, *J. geophys. Res.,* **89,** 7783–7795.

Pasyanos, M.E. & Nyblade, A.A., 2007. A top to bottom lithospheric study of Africa and Arabia, *Tectonophysics,* **444,** 27–44.

Paul, J.D. & Eakin, C.M., 2017. Mantle upwelling beneath Madagascar: evidence from receiver function analysis and shear wave splitting, *J. Seismol,* 1–12.

Penn State University, 2004. AfricaArray. International Federation of Digital Seismograph Networks, *Other/Seismic Network*. doi:10.7914/SN/AF.

Piqué, A., 1999a. The geological evolution of Madagascar: an introduction, *J. Afr. Earth Sci.,* **28,** 919–930.

Piqué, A., 1999b. The initiation and development of the Morondava Basin (Madagascar) from the Late Carboniferous to the Middle Jurassic: sedimentary, palaeontological and structural data, *J. Afr. Earth Sci.,* **28,** 931–948.

Pratt, M.J. *et al.*, 2017. Shear-velocity structure of the crust and upper mantle of Madagascar derived from surface wave tomography, *Earth planet. Sci. Lett.,* **458,** 405–417.

Rabinowitz, P.D., Coffin, M.F. & Falvey, D., 1983. The separation of Madagascar and Africa, *Science,* **220,** 67–69.

Rai, A., Gaur, V.K., Rai, S.S. & Priestley, K., 2009. Seismic signatures of the Pan African orogeny: implications for southern Indian high grade terranes, *Geophys. J. Int.,* **176,** 518–528.

Rajaomazava, F., 1992. Etude de la subsidence du bassin sédimentaire de Morondava (Madagascar) dans le cadre de l'évolution géodynamique de la marge Est-Africaine, *PhD thesis*, Univ. Montpellier, France.

Rakotondrainibe, 1977. Contribution à l'étude de la séismicité de Madagascar, *PhD Thesis*, Univ. Antananarivo, Madagascar.

Rakotondraompiana, S.A., Albouy, Y. & Piqué, A., 1999. Lithospheric model of the Madagascar island (western Indian Ocean): a new interpretation of the gravity data, *J. Afr. Earth Sci.,* **28,** 961–973.

Rambolamanana, G., Suhadolc, P. & Panza, G.F., 1997. Simultaneous inversion of hypocentral parameters and structure velocity of the central region of Madagascar as a premise for the mitigation of seismic hazard in Antananarivo, *Pure appl. Geophys.,* **149,** 707–730.

Raval, U. & Veeraswamy, K., 2003. India-Madagascar separation: breakup along a pre-existing mobile belt and chipping of the craton, *Gondwana Res.,* **6,** 467–485.

Razafimbelo, M.E., 1987. Le bassin de Morondava (Madagascar) synthèse géologique et structurale, *PhD thesis*, Univ. Louis-Pasteur, France.

Reiss, M.C., Rümpker, G., Tilmann, F., Yuan, X., Giese, J. & Rindraharisaona, E.J., 2016. Seismic anisotropy of the lithosphere and asthenosphere beneath southern Madagascar from teleseismic shear wave splitting analysis and waveform modeling, *J. geophys. Res.,* **121,** doi:10.1002/2016JB013020.

Rindraharisaona, E.J., Guidarelli, M., Aoudia, A. & Rambolamanana, G., 2013. Earth structure and instrumental seismicity of Madagascar: implications on the seismotectonics, *Tectonophysics,* **594,** 165–181.

Rindraharisaona, E.J., Tilmann, F., Yuan, X., Rümper, G., Giese, J., Rambolamanana, G. & Barruol, G., 2017. Crustal structure of southern Madagascar from receiver functions and ambient noise correlation: implications for crustal evolution, *J. geophys. Res.,* **122**(2), 1179–1197.

Roberts, G.G., Paul, J.D., White, N. & Winterbourne, J., 2012. Temporal and spatial evolution of dynamic support from river profiles: a framework for Madagascar, *Geochem. Geophys. Geosyst.,* **13,** Q04004, doi:10.1029/2012GC004040.

Rudnick, R.L. & Fountain, D.M., 1995. Nature and composition of the continental crust the continental crust: a lower crustal perspective, *Rev. Geophys.,* **33,** 267–309.

Rudnick, R.L. & Gao, S., 2003. Composition of the continental crust, in *Treatise on Geochemistry*, Vol. 3, Elsevier, 64 pp.

Schlich, R., 1975. Structure et âge de l'océan Indien occidental, *Mem. Soc. Geol. Fr.,* **6,** 102.

Scripps Institution of Oceanography, 1986. IRIS/IDA Seismic Network. International Federation of Digital Seismograph Networks. Other/Seismic Network. doi:10.7914/SN/II.

Segoufin, J. & Patriat, P., 1980. Existence d'anomalies mésozoïques dans le bassin de Somalie. Implications pour les relations Afrique-Antarctique-Madagascar, *C.R. Acad. Sci.,* Paris, **291,** 85–88.

Stein, S. *et al.*, 2016. New insights into North America's Midcontinent Rift, *Eos,* **97,** doi:10.1029/2016EO056659.

Stein, S. & Wysession, M., 2003. *An Introduction to Seismology, Earthquakes and Earth Structure,* Blackwell, Malden, MA.

Storey, M., Mahoney, J.J., Saunders, A.D., Duncan, R.A., Kelley, S.P. & Coffin, M.F., 1995. Timing of hotspot related volcanism and breakup of Madagascar and India, *Science,* **267,** 852–855.

Tedla, G.E, Van der Meijde, M., Nyblade, A.A. & Van der Meer, F.D., 2011. A crustal thickness map of Africa derived from a global gravity field model using Euler deconvolution, *Geophys. J. Int.,* **187,** 1–9.

Thomas, R.J. *et al.*, 2009. Geological evolution of the Neoproterozoic Bemarivo Belt, northern Madagascar, *Precambrian Res.,* **172,** 279–300.

Thompson, D.A., Bastow, I.D., Helffrich, G., Kendall, J.M., Wookey, J., Snyder, D.B. & Eaton, D.W., 2010. Precambrian crustal evolution: seismic constraints from the Canadian Shield, *Earth Planet. Sci. Lett.,* **297,** 655–666.

Tilmann, F., Yuan, X., Rümpker, G. & Rindraharisaona, E., 2012. SELASOMA Project, Madagascar 2012–2014, DeutschesGeoForschungsZentrum GFZ, Seismic Network, doi:10.14470/MR7567431421.

Torsvik, T.H., Tucker, R.D., Ashwal, L.D., Eide, E.A., Rakotosolofo, N.A. & de Wit, M.J., 1998. Late Cretaceous magmatism in Madagascar: paleomagnetic evidence for a stationary Marion hotspot, *Earth Planet. Sci. Lett.,* **64,** 221–232.

Tucker, R.D. & Conrad, J., 2008. 40Ar/39Ar geochronology of Mesozoic and younger igneous rocks of central and northern Madagascar, in *Final Report of the BGS-USGS Consortium to the Government of Madagascar,* World Bank Project UK-04-0100, Chapter 7.

Tucker, R.D., Kusky, T.M., Buchwaldt, R. & Handke, M.J., 2007. Neoproterozoic nappes and superposed folding of the Itremo Group, west-central Madagascar, *Gondwana Res.,* **12,** 356–379.

Tucker, R.D., Peters, S.G., Roig, J.Y., Théveniaut, H. & Delor, C., 2012. Notice explicative des cartes géologique et métallogéniques de la République de Madagascar à 1/1000000, Ministère des Mines, PGRM, Antananarivo, République de Madagascar.

Tucker, R.D., Roig, J.Y., Delor, C., Amelin, Y., Goncalves, P., Rabarimanana, M.H., Ralison, A.V. & Belcher, R.W., 2011. Neoproterozoic extension in the Greater Dharwar Craton: a reevaluation of the Betsimisaraka "suture" in Madagascar, *Can. J. Earth Sci.,* **48,** 389–417.

Tugume, F., Nyblade, A. & Julià, J., 2012. Moho depths and Poisson's ratios of Precambrian crust in East Africa: evidence for similarities in Archean

and Proterozoic crustal structure, *Earth Planet. Sci. Lett.,* **355–356,** 73–81.

Tugume, F., Nyblade, A., Julià, J. & van de Meijde, M., 2013. Precambrian crustal structure in Africa and Arabia: evidence lacking for secular variation, *Tectonophysics,* **609,** 250–266.

Wescott, W.A. & Diggens, J.N., 1997. Depositional history and stratigraphical evolution of the Sakoa Group (Lower Karoo Supergroup) in the southern Morondava Basin, Madagascar, *J. Afr. Earth Sci.,* **24,** 585–601.

Wescott, W.A. & Diggens, J.N., 1998. Depositional history and stratigraphical evolution of the Sakamena Group (Middle Karoo Supergroup) in the southern Morondava Basin, Madagascar, *J. Afr. Earth Sci.,* **27,** 461–479.

Wessel, P. & Smith, W.H.F., 1998. New, improved version of Generic Mapping Tools released, *EOS T. Am. Geophys. Un.,* **79,** 579.

Wysession, M., Wiens, D. & Nyblade, A., 2011. Investigation of Sources of Intraplate Volcanism Using PASSCAL Broadband Instruments in Madagascar, the Comores, and Mozambique, International Federation of Digital Seismograph Networks. Other/Seismic Network. doi:10.7914/SN/XV_2011.

Zandt, G. & Ammon, C.J., 1995. Continental crust composition constrained by measurements of crustal Poisson's ratio, *Nature,* **374,** 152–154.

Zhu, L. & Kanamori, H., 2000. Moho depth variation in Southern California from teleseismic receiver functions, *J. geophys. Res.,* **105,** 2969–2980.

SUPPORTING INFORMATION

Supplementary data are available at *GJI* online.

Figure S1. Receiver functions for all stations. The four-column figure shows the radial and tangential calculated from Gaussian parameter 1.0 and 2.5, respectively.

Figure S2. Results from the *H–k* stacking method for all stations. Left-hand panel: H–κ parameter space with the optimal values for H and κ (centre of red ellipse). The black contours map out the percentage values, in the colour scale bar, of the normalized objective function given in eq. (1). Right-hand panel: receiver functions labelled by the event backazimuth (top number) and epicentral distance (bottom number), both in degrees. The optimal results for H and κ obtained are summarized along the top, along with their formal uncertainties, and shown with the red contour on the left-hand panel.

Figure S3. Results from the joint inversion of receiver functions and Rayleigh wave phase-velocity dispersion. Top left-hand panel: grey and black lines are the observed and predicted radial receiver functions, respectively, estimated for Gaussian filter widths of 1.0 (top panel) and 2.5 Hz (bottom panel). The numbers on top of the waveforms are the number of receiver functions stacked (in the square bracket), the average back azimuth (±1 standard deviation), and the average ray parameter (±1 standard deviation) for the stack. Bottom left-hand panel: the observed and predicted dispersion curves of the phase velocity, shown with grey dots and a black line, respectively. Right-hand panel: the starting velocity model (grey line) and predicted velocity structure (black line). The horizontal dash–dotted line and number indicate the Moho depth (in km). The vertical dashed and dotted lines correspond to *Vs* values of 4.0 and 4.3 km s^{-1}.

Figure S4. Receiver functions used (a) in this study and (b) in Paul & Eakin (2017) for the station FOMA. Both figures show Ps conversions at ∼2, ∼4 and ∼6 s. The Ps conversion at ∼2 s likely presents an intracrustal discontinuity. The one at ∼4 s is interpreted as the Moho Ps conversion in this study, which suggests a shallower Moho (∼36 km) than reported in Paul & Eakin (2017). The Ps conversion at ∼6 s was interpreted as the Moho Ps by Paul & Eakin (2017) and yielded a deeper Moho. Note that the arrival at ∼6 s is only strong for northeastern and eastern azimuths.

Table S1. List of seismic stations used in this study.

Table S2. List of seismic events used in this study.

Please note: Oxford University Press is not responsible for the content or functionality of any supporting materials supplied by the authors. Any queries (other than missing material) should be directed to the corresponding author for the paper.

Appendix E

Uppermost mantle velocity and anisotropy beneath Madagascar from *Pn* tomography

Fenitra Andriampenomanana[1,4], Andrew A. Nyblade[1,2], Michael E. Wysession[3], Raymond J. Durrheim[1], Gérard Rambolamanana[4], Frederik Tilmann[5], Ghassan Aleqabi[3], Patrick J. Shore[3], Martin J. Pratt[3], and Tsiriandrimanana Rakotondraibe[1,4].

1. School of Geosciences, University of the Witwatersrand, Private Bag 3 - 2050 Wits, Johannesburg, South Africa. E-mail: nyonyfenitra@gmail.com
2. Department of Geosciences, Penn State University, 503 Deike Building, University Park, PA 16802, USA.
3. Department of Earth and Planetary Sciences, Washington University in St. Louis, Campus Box 1169, 1 Brookings Dr., Saint Louis, MO 63130-4899, USA.
4. Institut et Observatoire de Géophysique d'Antananarivo, Université d'Antananarivo, Ambohidempona - B.P 3843, Antananarivo 101, Madagascar.
5. Deutsches GeoForschungsZentrum (GFZ), Telegrafenberg, 14473 Potsdam, Germany.

Abstract

We present a *Pn* tomography study in which 4541 *Pn* travel times, derived from 44 seismic stations and 424 seismic events, were inverted to determine the lateral variations in the velocity and anisotropy of the uppermost mantle beneath Madagascar. Results show an average uppermost mantle *Pn*-velocity of 8.1 km/s beneath the island. However, low-*Pn*-velocity zones (~7.9 km/s) are found underlying the Cenozoic volcanic provinces in the northern, central, and southwestern region of the island, which are attributed to thermal anomalies that associated with upwelling of hot mantle materials. Direction of *Pn* anisotropy shows a dominant NW-SE direction of fast-polarization in the northern region (around NMAP), which we attribute to a fossil anisotropy or an overprinting of the anisotropy in the upper mantle by recent tectonic activity. A similar orientation of *Pn* anisotropy is observed around the Ranotsara shear zone, south to the CMAP, which we similarly interpret as a fossil anisotropy. Our observation does not show any strong evidence linking the *Pn* velocity or anisotropy with the formation of the Lwandle plate.

1. INTRODUCTION

The lithosphere of Madagascar is characterized by complex continental deformations during the Neoproterozoic Pan-African Orogeny (e.g., Collins 2000). It was subsequently reshaped by a series of extensional events associated with the fragmentation from Africa and India in the Jurassic and Cretaceous, respectively (e.g., Rabinowitz *et al.* 1983; Coffin & Rabinowitz 1987; Collins 2006). They were simultaneously accompanied by voluminous eruptions of tholeiitic basaltic lavas (Schlich 1975; Norton & Sclater 1979; Mahoney *et al.* 1991) and formed the volcanic provinces presently observed along the east and west coasts and the southern region of Madagascar. Yet, the most intriguing tectonic event that occurred in Madagascar is the eruption of alkaline intraplate volcanic rocks in the northern, central, and southwestern regions of the island during the Cenozoic (<50 Ma), albeit the island has largely been tectonically stable since 85 Ma (Emerick & Duncan, 1982, 1983; Nougier *et al.* 1986; Tucker & Conrad 2008; Bardintzeff *et al.* 2010). Therefore, Madagascar is a particularly interesting place to study tectonic evolution associated with rifting and the origin of intraplate volcanism and its implication for the kinematics and dynamics of the lithosphere.

Debate on the origin of the Cenozoic volcanism of Madagascar is controversial. This present study mainly contributes to the growing understanding of such anomalous tectonic event by conducting a *Pn* tomographic imaging of the uppermost mantle velocity and anisotropy. Studies of lateral variations in *Pn* velocity in the uppermost mantle have long been used to investigate regional tectonics and other thermally related phenomena (e.g., Scheidegger & Willmore 1957; Backus 1965). Isotropic variations in the *Pn* velocity are principally attributed to variations in pressure, temperature, and composition in the upper mantle, while anisotropic changes in the *Pn* velocity could reveal the strain history (e.g., Black & Braile 1982; Goes & van der Lee 2002; Perry *et al.* 2006). The fast *Pn* anisotropy directions are actually associated with the orientation of olivine crystals due to stress, strain, creep and flow, or the alignment of features such as dikes and melt-filled lenses within the upper mantle (e.g., Silver 1996; Savage 1999; Walker *et al.* 2004). In general, seismic anisotropy is linked to the orientation of olivine fast axes (*a* axes) parallel to the direction of the maximum shearing strain under simple shear conditions, with the slow axes (*b* axes) perpendicular to it (e.g., Ribe 1992; Karato & Wu 1993). However, it should be noted that in the case of pure shear deformation the slow axes tend to be parallel to the flow plane and the fast axis in the plane normal to it (Kaminski & Ribe 2001).

We use *Pn* travel-time residuals of regional seismic events to infer variations in the *Pn* velocity and anisotropy in the mantle lid beneath Madagascar. This study was enabled by the recent expansion of seismic monitoring in Madagascar. For this study we mostly used seismic data gathered by four permanent broadband stations and the 26 broadband stations of the Madagascar-Comoros-Mozambique (MACOMO) project (Wysession *et al.* 2011), supplemented by data from seven temporary broadband stations from the Seismological Signatures in the Lithosphere/Asthenosphere system of Southern Madagascar (SELASOMA) experiment (Tilmann *et al.* 2012) and 10 temporary

broadband stations from the Réunion Hotspot and Upper Mantle – Réunions Unterer Mantel (RHUM-RUM) project (Sigloch & Barruol 2012).

Our findings primarily attribute slow *Pn* velocities beneath the Cenozoic intraplate volcanic provinces and observed complex anisotropic patterns throughout Madagascar but somehow correlate with the geological aspect of some regions.

2. TECTONIC BACKGROUND

The Precambrian crust of Madagascar was first formed/reworked during the amalgamation of Gondwana in the Late Neoproterozoic and Early Cambrian (*ca.* 570-510 Ma) (Powell *et al.* 1993; Shackleton 1996). The rift system associated with the breakup of Gondwana, during the Late Jurassic and Early Cretaceous (~150 Ma) (Rabinowitz *et al.* 1983; Piqué 1999), has reshaped the lithosphere, created the sedimentary basins in the western part, and led to the isolation of the island. Around ~130 Ma Antarctica-Australia separated from Madagascar-India-Seychelles. The passage of Madagascar-India-Seychelles over the Marion hot spot in the Late Cretaceous (~90 Ma) weakened and fractured the lithosphere near the eastern margin and Madagascar split from India-Seychelles (~95-84 Ma) (Storey *et al.* 1995; Gnos *et al.* 1997; Torsvik *et al.* 1998). Mantle-derived tholeiitic basalts and crustal-derived dacite/alkali rhyolite magmas were emplaced over most of Madagascar, but are currently preserved mainly along the western, eastern, and southern (Anosy volcanic province) perimeters of the island (Storey *et al.* 1995; Torsvik *et al.* 1998). During the break-away of India from Madagascar, the western part of the Dharwar Craton of India split from the once-connected Antongil-Masora craton on the eastern coast of Madagascar.

Since the Late Cretaceous, Madagascar has been remote from tectonic plate boundaries, including the Indian mid-oceanic ridges in the east and the East African Rift system (EARs) in the west. The Comoros and Mascarene Archipelago (Réunion, Mauritius, etc) are located northeast and east of Madagascar, respectively. Though Madagascar had not experienced any major tectonic activities for the past 85 Myr, Cenozoic volcanic provinces, as young the Quaternary (<1 Ma), are found in (1) Nosy Be Island and the Massif d'Ambre in the northern region, (2) around Itasy and Ankaratra in the central region (Emerick & Duncan, 1982, 1983; Nougier *et al.* 1986; Tucker & Conrad 2008), and (3) around Ankililoaka in the southwestern region of Madagascar (Bardintzeff *et al.* 2010) (Figure 1.4). These three young volcanic provinces consist mainly of alkali basalts that erupted between *ca.* 50 and 1 Ma (Emerick & Duncan, 1982, 1983; Nougier *et al.* 1986; Collins 2000; Tucker & Conrad 2008), and are known as the Northern Madagascar Alkaline Province (NMAP), the Central Madagascar Alkaline Province (CMAP), and the Southern Madagascar Alkaline Province (SMAP), respectively. The origin of the Madagascar's intraplate volcanism has long been debated. Most researchers have related the volcanism to past tectonic history. For example, Nougier *et al.* (1986) associated the volcanism to fracture zones that accompanied the Mesozoic rifting of Madagascar. On the other hand, connections to neighboring tectonic events have also been proposed: for example, the currently active Comoros volcanic provinces northwest of Madagascar (Emerick & Duncan, 1982); hot asthenospheric mantle associated with the lower mantle African Superplume (Ebinger & Sleep 1998; Forte *et al.* 2010); or the

extension of the East Africa Rift separating the African plate into the Nubian and Somalian plates (e.g., Saria *et al.* 2013; Stamps *et al.* 2015; Michon 2016).

The geological aspect observed at the surface of Madagascar shows distinctly two main regions. The western third of the island consists of a Carboniferous-to-present-day sedimentary basin. It is, in turn, divided into three major basins: the Antsiranana, the Mahajanga, and the Morondava basin. Precambrian basement crops out over the remaining eastern two-thirds of the island. It is divided into six units with Paleoarchean to Neoproterozoic ages: the Bemarivo, Antananarivo, Ikalamavony, Anosyen-Androyen and Vohibory domains, and the Antogil-Masora cratons (Figure 1.4) (e.g., Collins & Windley 2002; Collins 2006; Tucker *et al.* 2011).

Madagascar is cut by several N-S or NW-SE trending crustal-scale shear zones (Figure 1.4). They frequently mark the boundaries of major geological domains (e.g., the Sandrakota, Ranotsara, Beraketa, and Ampanihy shear zones), although some lie within domains (e.g., the Angavo-Ifanadiana, Zazafotsy, Ihosy, and Ejeda shear zones) (Martelat *et al.* 2000, 2014; Raharimahefa & Kusky 2010). Some of these shear zones are rooted in the mantle. In the northern part of the island, the Sandrakota shear zone, a 50-km-wide and 100-km-long high-strain zone with a NW-SE trend, is observed along the contact between the northernmost part of the Antananarivo domain and the southern part of the Bemarivo domain (Thomas *et al.* 2009). In the central part of Madagascar, the Angavo-Ifanadiana shear zone, a N-S trending highly-strained zone that is 20 to 60 km wide and 800 km long, traverses the eastern edge of the Antananarivo domain. It is a major strike-slip shear zone (Nédélec *et al.* 2000) and is very similar to the Achankovil shear zone of India (Raharimahefa *et al.* 2013). In the southern part of the island, the Ranotsara shear zone, a N-S to NW-SE trending strike-slip shear zone that is 20 km wide and 350 km long, marks the contact between the Anosyen-Androyen domains with the Ikalamavony domain. It was active during the late stages of the East African Orogeny (de Wit *et al.* 2001) and was used to position Madagascar within Gondwana (e.g., Müller 2000; Collins & Windley 2002). Recent studies found that the Ranotsara shear zone is a heterogeneous structure with a ductile deflection zone in its central segment and NW-SE trending brittle normal faults along its length (Schreurs *et al.* 2010). The Ihosy and Zazafotsy shear zones are parallel, N-S trending, highly strained, 5- to 15-km-wide and 350-km-long ductile shear zones within the northernmost portion of the Anosyen domain (Martelat *et al.* 2000, 2014). Three 20-km-wide and N-S trending (between N0 and N15) major shear-zones are identified in the southern part of the Malagasy Precambrian crust. The Beraketa shear zone is a 250-km-long strike-slip shear zone, mainly N-S trending except in its northern part, which is oriented parallel to the N140 Ranotsara shear zone. The Beraketa shear zone constitutes the contact between the Anosyen and Androyen subdomains (de Wit *et al.*, 2001; Martelat *et al.*, 2000, 2014). The Ampanihy shear zone separates the Androyen subdomain with the Vohibory domain and trends N-S parallel to the Beraketa shear zone. The Ejeda shear zone is located in the western part of the Vohibory domain. The lengths of the Ejeda and Ampanihy shear zones are not well defined, as they extend under the sedimentary cover.

The crust and the upper mantle of Madagascar have recently been the subject of intensive investigations using seismological approaches due to the

expansion of seismic network all over the island. Pratt *et al.* (2017) conducted a shear-wave tomography from surface waves of Madagascar, which revealed upper mantle low-shear-velocity zones that reach a depth of at least 150 km beneath NMAP and CMAP and depths 50-150 km beneath SMAP. These low velocity zones were interpreted to be asthenospheric upwellings that caused the Cenozoic volcanic activities. A delamination of mantle lithosphere was also proposed beneath the CMAP, which likely caused the uplift in the region. A few previous seismological studies have also noted the presence of low seismic velocity regions beneath these regions. A joint inversion of receiver functions and surface wave data by Rindraharisaona *et al.* (2013) and Andriampenomanana *et al.* (2017) revealed a seismically slow upper mantle beneath NMAP/CMAP/SMAP. In addition, a good correlation between topography and crustal thickness was observed along a south-to-north profile across Madagascar in Andriampenomanana *et al.* (2017), except in the northern part where the surface elevation is high compared to crustal thickness, suggesting a source of dynamic topography that could correlate with a slow upper mantle thermal anomaly.

A recent study of teleseismic shear-wave splitting beneath Madagascar using MACOMO data revealed a complex pattern of anisotropy in the upper mantle of the island (Ramirez et al. in prep). This study has not interpreted the anisotropy as the result of a mantle flow from the African superplume or the absolute plate motion but has included the presence of upwelling asthenosphere from the model of Pratt et al. (2017) in theis interpretation. The SELASOMA profile, which ran from the west to the east coast of Madagascar across the Ranotsara shear zone, found that the fast polarization direction changes from NW in the center to NE in the east and west (Reiss *et al.* 2016). A fast polarization direction of 50°, which is roughly aligned with the direction of absolute plate motion, was proposed to explain the NE orientation. The NW-orientated polarization was attributed to crustal anisotropy produced by a zone of ductile deformation near the Ranotsara shear zone. Lastly, for the regional surrounding, shear-wave splitting beneath the Seychelles and Réunion islands is attributed to mantle flow resulting from plate motions and density-driven flow linked to the African Superplume (Hammond *et al.* 2005; Barruol & Fontaine 2013).

3. DATA

The data consist of *Pn* first-arrival times obtained from local earthquakes that occurred within Madagascar between September 2011 and September 2013. Recording stations were generally from the Madagascar-Comoros-Mozambique (MACOMO) project (XV Network: Wysession *et al.* 2011). A total of 26 broadband seismic stations were temporarily deployed in Madagascar between 2011 and 2013 for the MACOMO project, 10 of the stations collected seismic data for two years starting in September 2011, while the remaining 16 were deployed for one year, starting in September 2012. Each seismic station was equipped with a 24-bit data logger (Quanterra Q330), a broadband sensor (Guralp CMG-3T, Streckeisen STS-2, or NanometricsTrillium 120PA), and a GPS clock.

Data from four permanent broadband stations were also used: ABPO (IRIS/GSN, II Network, from September 2011 to November 2013), FOMA (GEOSCOPE, G Network, from September 2011 to November 2013), and VOI and SBV (GEOFON, GE Network, from October 2011 to September 2013).

In addition, several temporary broadband stations from two other simultaneous experiments were used to fill the gap in the southern part of Madagascar: seven broadband stations from the Seismological Signatures in the Lithosphere/Asthenosphere system of Southern Madagascar (SELASOMA) experiment (ZE Network: Tilmann *et al.* 2012; from May 2012 to September 2013), which aims to study the lithosphere in southern Madagascar around the Ranotsara shear-zone; and 10 broadband stations from the Réunion Hotspot and Upper Mantle – Réunions Unterer Mantel (RHUM-RUM) project (YV Network: Sigloch & Barruol 2012; from April 2011 to December 2013), where five stations were deployed near the southeastern coast of Madagascar and five stations on the Iles Eparses (islands around Madagascar), with the aim of imaging any mantle plume under the Réunion hotspot.

In summary, a total of 47 broadband stations, well-distributed across Madagascar, were considered in this study (Figure 2.9). Seismic events were located using the earthquake location program HYPOELLIPSE (Lahr 1999) in which the Earth model from Andriampenomanana *et al.* (2017) was used. As a result, a total of 8325 first arrivals were obtained from 647 regional earthquakes recorded at the 47 seismic stations.

In order to ensure that we only have *Pn* first arrivals in our inversion and also to guarantee the quality of the solution, the following criteria were iteratively applied: (1) seismic events must be inside the seismic network, (2) a correction for the receiver topography was applied to each travel time by assuming a *P* velocity of 5.5 km/s for the surface, (3) the epicentral distance was between 200 km (the *Pg-Pn* crossover distance for a 35-km-thick crust, the average crustal thickness of Madagascar (Andriampenomanana *et al.* 2017)) and the maximum recorded epicentral distance of ~1500 km, (4) each seismic station recorded at least five seismic events, (5) each seismic event was recorded at least by five seismic stations, (6) the travel-time data versus the epicentral distance was fitted to a straight line using an iterative least-squares algorithm, and (7) travel-time residuals larger than 6 s relative to the best-fit line were discarded. The mean *Pn* velocity, 8.10 km/s, was obtained from the inverse of the slope of the best-fit line, while the mean crustal delay, 6.2 s, was given by its intercept.

The selection criteria left 4541 *Pn* travel times from 424 seismic events recorded by 44 seismic stations. *Pn* ray paths between the selected seismic events and stations are shown in Figure 2.30. As expected, the ray paths present a good coverage mostly along the Precambrian basement of Madagascar. The extreme northern, western, and southern parts of the island are poorly covered. The travel-time plot versus distance and the travel-time residuals relative to the straight-line fit are shown in Figure 4.

4. *Pn* TOMOGRAPHY METHOD

Pn phases are waves that are refracted at the crust-mantle boundary. As a refracted ray, *Pn* ray paths are the combination of three portions: (1) the source-to-mantle path through the crust, (2) the passage through the uppermost mantle (the lid), and (3) the up-going mantle-to-receiver path back through the crust. A technique developed by Hearn (1996) was used to tomographically invert the *Pn* travel times to infer the variation of the uppermost mantle velocity, which is

obtained from the inverse of the slowness, and the seismic anisotropy, which is described by the magnitude and direction of the fastest wave propagation.

In this approach, the mantle-lid surface is divided into a two-dimensional set of cells for which the uppermost mantle velocity and anisotropy variations are calculated. The travel time residuals, t_{ij}, of the ray between station i and earthquake j are described as:

$$t_{ij} = a_i + b_j + \sum d_{ijk}\,(s_k + A_k cos2\phi + B_k sin2\phi), \qquad (1)$$

where a_i is the static delay for station i, b_j is the static delay for event j, ϕ is the back azimuth angle, d_{ijk} is the distance traveled by the ray ij in mantle cell k, and s_k is the slowness perturbation (the inverse of velocity), and A_k and B_k are two anisotropic coefficients (Hearn, 1996).

A regularized least-squares method is used when solving the set of travel-time equations in Equation (1). These multiple travel-time equations are obtained from all the rays, between event-station pair, in which the unknowns are the station and event delays (a_i and b_j), the mantle-lid slowness (s_k), and the two anisotropic coefficients (A_k and B_k). The anisotropy parameters, the magnitudes and directions of the fastest wave propagation, within the cell k are estimated by $\sqrt{A_k^2 + B_k^2}$ and $\frac{1}{2} arctan\left(\frac{B_k}{A_k}\right)$, respectively.

Laplacian damping equations are introduced to regularize the solution of Equation (1). Accordingly, the solution is controlled by the damping coefficients. The velocity and the anisotropy are separately regularized in the inversion by two damping constants. The smoothness of the velocity is controlled by damping the slowness s_k and the smoothness of the anisotropy is controlled by damping the two anisotropy coefficients, A_k and B_k. The damping coefficients control the trade-off between errors and resolution: typically, low values provide good resolution but large errors, and high damping gives poor resolution but small errors.

By assuming a constant velocity of the crust, the static delays can be expressed as:

$$a_i = z_i \sqrt{\frac{1}{V_{crust}^2} - \frac{1}{V_{mantle}^2}} \qquad (2)$$

where z_i and V_{crust} are the thickness and the average P-wave velocity of the crust, and V_{mantle} is the average mantle P-wave velocity. The crustal thickness term is replaced by the crustal thickness minus the depth of the event for the event delays. Station static delays, a_i, are functions of the crustal thickness, the crustal seismic velocity, and the mantle seismic velocity. Event static delays, b_i, are function of these parameters plus the certainty in source parameters (e.g., event depth and origin time).

The thickness of the crust in the initial model was set to 35 km, which was obtained from the intercept of the linear fit to the traveltime-distance curve. An average crustal velocity of 6.4 km/s is used for the starting model (from Andriampenomanana *et al.*, 2017).

5. REGULARIZATION OF VELOCITY-ANISOTROPY TRADE-OFF

Selecting the best appropriate damping parameter is crucial in the regularized least-square inversion as it controls the trade-off between errors and resolution. The damping coefficient of the velocity was set first through trial and error by turning off the anisotropy part in the inversion. The coefficient was

chosen according to the resolution of the obtained structure, the error observation, and, of course, the consistency with the geology to avoid over- or under-damping. The surface of the uppermost mantle was gridded into 1/8-degree square cells (0.125° x 0.125°) when attempting to solve the set of travel-time equations, and the inversion algorithm was run for a number of iterations. After a number of assessments, the structure obtained from a damping coefficient of 500 appeared to be acceptable for the velocity variation (Figure 2.32).

Following the approach of Hearn (1996), the relative trade-off between the velocity variations and the anisotropy variations was examined in order to choose the best damping coefficient for the anisotropy. This involved building two sets of synthetic checkerboard models: the first model was characterized by laterally varying sinusoidal perturbations of velocity with no anisotropy variations, and the second model included sinusoidal variations in anisotropy parameters without velocity variations. The models were inverted using the travel times and ray paths that were used for the real data with a velocity damping coefficient fixed at 500, as previously found, while the damping coefficient for the anisotropy calculation was changed. The root-mean-square (rms) of the anisotropy magnitude and the velocity perturbations were subsequently measured. The best value of the anisotropy damping constant would equalize the velocity-to-anisotropy trade-off, the ratio of rms(anisotropy only)/rms(velocity only), as well as the anisotropy-to-velocity trade-off, the ratio of rms(velocity only)/rms(anisotropy only). After a number of inversions, the two curves intersected at a value of ~600 for the anisotropy damping coefficient (Figure 2.33).

Therefore, damping coefficients of 500 and 600 were chosen for the velocity and anisotropy, respectively, for further computation and interpretation. Only grid cells that were crossed by at least 20 ray paths were considered, so that cells with a high-path density were not masked.

6. ERROR ESTIMATION

A bootstrap resampling technique (Koch, 1992) was used to evaluate the standard error of the tomographic inversion. In this technique, *Pn* travel-time datasets are randomly resampled and inverted 100 times (Hearn and Ni, 1994), and the one-standard-deviation error is computed from the resulting bootstrap sample solutions. The rms error of the residuals is 0.7 s, which is probably related to systematic errors: for example, uncertainties in stations and event locations. Standard errors of both velocity and anisotropy are generally less than 0.08 km/s and 0.06 km/s, respectively (Figure 2.34). However, the highest errors in velocity (>0.1 km/s) and anisotropy magnitude estimations are observed in regions where the ray-path density is the lowest, especially along the edge of the sampled area and in the northernmost and southernmost parts of Madagascar. The error is lower than 0.05 km/s for both velocity and anisotropy across the areas that have a high density of ray paths.

7. RESOLUTION ANALYSIS

Sinusoidal checkerboards were built to assess the influence of ray coverage on the spatial resolution of the tomography. This involved creating a checkerboard sinusoidal test model with velocity varying between -0.30 km/s and +0.30 km/s relative to the average *Pn* velocity, 8.1 km/s, of both velocity and

anisotropy amplitudes. The anisotropy direction was set to be a succession of N-S and E-W trends. *Pn* ray paths, seismic stations, and seismic events used for the tomographic inversion of the real data were utilized to compute synthetic *Pn* arrival times. We added Gaussian noise to the synthetic travel times with a standard deviation of 0.7 s, which is equivalent to the rms error of the residuals obtained from the actual inversion. The synthetic travel times were inverted by considering identical inversion parameters as the real data and different checkerboard sizes (1.00° x 1.00°, 1.25° x 1.25°, 1.50° x 1.50°, 1.75° x 1.75°, 2.0° x 2.0°, 2.25° x 2.25°, 2.50° x 2.50°, 2.75° x 2.75°, and 3.00° x 3.00°) to recover the checkerboard pattern (Figure 2.35 and Figure 2.36). The tests indicate that *Pn* velocities with 1.25° x 1.25° cell sizes can be resolved for most of the regions, but the resolution can reach as small as 1.00° x 1.00° in the center part of the island, mostly around the Antananarivo domain, where the density of ray paths is highest. However, the resolution weakens around the edge of the sampled area. The *Pn* anisotropy also can be resolved for a grid size of 1.25° x 1.25°.

8. RESULTS

A total of 4541 *Pn* travel times were tomographically inverted. The effect of including the anisotropy in the inversion was assessed by turning off the anisotropy part in it. It means that an isotropic inversion is performed and that the anisotropic terms in Equation (1) were omitted in the inversion, but otherwise used the same travel-time data and inversion parameters. We inverted the *Pn* travel times for velocity variations only (Figure 4.1) and for both velocity and anisotropy variations (Figure 4.2 and Figure 4.3). The rms errors are 1.00 s for the velocity-only inversion and 0.60 s for the simultaneous velocity-anisotropy inversion. The inversions broadly yielded to the same velocity anomaly patterns with slight differences in magnitudes. Station static delays are plotted in Figure 9.

8.1. Pn velocity variations

Worldwide, the average *Pn* velocity of continental lithosphere is known to be about 8.10 km/s (e.g., Mooney & Braille 1989). In this study, the average *Pn* velocity beneath Madagascar is found to be 8.10 km/s and varies between -0.20 km/s and +0.25 km/s from it. Several regions characterized by *Pn* velocity <8.0 km/s are observed in the uppermost mantle beneath Madagascar.

A low-Pn-velocity zone is observed in the uppermost mantle beneath the northernmost regions of the island, roughly between longitudes 48°E and 50°E and north of latitude 15°S. Its extension towards the north, west, and east is not well resolved due to poor ray path coverage in the region. However, the low-velocity-zone is directly beneath the known alkaline volcanic province in the region, the NMAP. A prominent low-*Pn*-velocity zone is also observed in the uppermost mantle beneath the central part of Madagascar, approximately between latitudes 19-22°S and longitudes 46-48°E. The low-velocity zone lies beneath the CMAP volcanic province in the central part of the island. The region apparently extends southeastwards. Weak low-*Pn*-velocity regions are observed in the uppermost mantle beneath the southwestern parts of Madagascar, roughly west of the longitude 45°S and south of the latitude 20.5°S. The region is located beneath the southern part of the Morondava basin and possibly underlies the SMAP, although its extension westward is not well resolved due to poor coverage. Lastly,

a low-velocity zone is observed beneath the Antongil craton, between latitudes 17-19°S and longitudes 48-50°S. The eastward or northward limit of the low-velocity zone is not clearly resolved.

8.2. Pn anisotropy variations

The *Pn*-anisotropy perturbation ranges from 0 to 0.23 km/s (~3%) all over Madagascar. Two groups of *Pn* anisotropy fast-polarization direction are principally found from the anisotropic inversion: a NW-SE to E-W direction and a NE-SW direction.

A broad NW-SE direction of *Pn* anisotropy fast-polarization, with a maximum magnitude of 2.4%, is observed in the uppermost mantle beneath the northern regions of Madagascar underlying the NMAP, the northernmost part of the Antananarivo terrane, the Bemarivo terrane, and the Antsiranana basin. The anisotropy direction rotates roughly to E-W in the south, particularly around the Antongil craton, and reduces in magnitude. Similarly to the anisotropic parameters in the northern regions, NW-SE directions with a maximum magnitude of 2.4% of *Pn* anisotropy fast-polarization are also observed in the uppermost mantle beneath the south-central part of Madagascar, south of the CMAP, the central part of the Ikalamavony terrane, and the Ranotsara shear zone. The *Pn* anisotropy direction rotates also to E-W in the south, especially along the southeast coast. The remaining part of the sampled area is characterized by *Pn* anisotropy with the fast-polarization in a NE-SW direction with a maximum magnitude of 2.8%. These anisotropy parameters are observed mainly in the eastern regions of the Antananarivo terrane and the Morondava basin.

9. DISCUSSION

Findings from this study reflect generally the heterogeneous geology of Madagascar. Lateral variations of *Pn* velocity and anisotropy in the uppermost mantle show correlation with the surface geology. To summarize, low-*Pn*-velocity zones, which correspond to upwelling of hot mantle materials, are observed in the uppermost mantle beneath Madagascar directly beneath the Cenozoic volcanic provinces. Compared to previous studies, general features of the low-velocity zones are comparable with those inferred from surface wave tomography (Pratt *et al.* 2017). Also, directions of *Pn* anisotropy fast-polarization of the uppermost mantle correlate with the measurement of upper mantle anisotropy derived from *SKS* shear-wave splitting technique (Reiss et *al.* 2016; Ramirez *et al.*, submitted), and present correlation with the orientation of some geological framework..

The surface-wave tomography of Pratt *et al.* (2017) identified low shear-wave velocity regions in the upper mantle beneath the northern, central, and southwestern regions of Madagascar. They suggested that the negative shear-wave velocity anomaly zones, of about -4% relative to PREM, reach at least the depth of 150 km beneath the northern and central regions while between depths of 50-150 km beneath the southwest region. Although, the tomography of *Pn* waves samples mainly the region neighboring the Moho discontinuity, the pattern of these low velocity areas are well characterized, for the same regions, in this present study. Pratt *et al.* (2017) have interpreted these anomalous low-velocity zones as an upwelling asthenosphere. In comparison with the model of Pratt *et al.* (2017), the uppermost mantle thermal perturbation inferred by the *Pn*

tomography, in this present study, is more limited (Figure 4.6 and Figure 4.7) beneath the regions where the Cenozoic alkaline volcanic provinces are observed. The pattern shows that the regions of low-*Pn*-velocity are mainly underlying the NMAP and CMAP. It accordingly suggests that these regions could be the focus of upwelling in the sublithospheric mantle as proposed by Pratt *et al.* (2017).

In their interpretation, Pratt *et al.* (2017) have suggested that a removal of the mantle lithosphere is possibly observed beneath the CMAP, which was likely replaced by the upwelling asthenospheric mantle-derived materials. Furthermore, results inferred from the *Pn* tomography shows a negative velocity anomaly of about -2.5% relative to PREM model beneath the CMAP. This value (around 7.9 km/s) is, however, apparently high to be asthenosphere. Therefore, other techniques may be required to explain the cause of the delamination of the lithosphere beneath CMAP as the resolution of the *Pn* tomography, here, is not sufficient to argue about the origin of such mechanism.

We compared our *Pn* anisotropy observations to the orientation of *SKS* shear-wave splitting measurements that have been conducted in Madagascar (Reiss *et al.* 2016; Ramirez *et al.*, submitted); since *SKS* waves best sample the vertically integrated anisotropy of the fastest-split shear waves within the uppermost 200-300 km of the mantle (e.g., Savage & Silver 1993). Previous studies pointed out the correlation between *Pn* anisotropy and shear-wave splitting directions of *SKS* phases (e.g., Crampin 1977; Christensen 1984). Anisotropy within the upper mantle of Madagascar is very complex. Ramirez *et al.* (submitted) suggested that the EW-trending of the *SKS* fast-polarization direction in the northern region of Madagascar is the result of a NE-trending mantle flow guided by the African superplume or plate motion and subsequently reoriented by a SW-trending mantle flow from the Comoros hot spot. However, the fast-polarization of *Pn* anisotropy observed in this region is oriented NW-SE (Figure 7), sub-parallel to the orientation of the Tsaratanàna alkaline complex (i.e, the NMAP) and the Sandrakota shear zone. This suggests that a fossil anisotropy is an alternative option to explain the source of anisotropy in the mantle lid for this region. Another explanation is that the NE trending shown by the *SKS* could be overprinted, on top, by recent train, which is likely the recent tectonic activity that linked to the Cenozoic volcanic manifestation.

Both *Pn* and *SKS* anisotropies broadly present similar orientation, a NW-SE trending, in the area south to the CMAP. The area encompasses the southern portion of the Ikalamavony domain and several shear zones (such as the Ranotsara, the Beraketa, the Ihosy, and the Zazafotsy shear zones). Reiss *et al.* (2016) have interpreted the NW orientation of the SKS fast polarization to be the result of an important crustal anisotropy, which could be caused by a ~150-km-wide ductile deformation zone. The NW direction of Pn anisotropy and SKS shear-wave is broadly parallel to the strike of the existing shear zones in the region. Therefore, a fossil anisotropy is also a possibility to explain the anisotropy. Furthermore, previous studies have suggested that small-scale rapid changes of fast directions of anisotropy are likely associated with the anisotropy of the near surface (e.g., Savage & Silver 1993).

The *Pn* anisotropy is oriented from E-W to NE-SW along the western region of Madagascar. Reiss *et al.* (2016) interpreted the NE-trending as an influence of the mantle flow from plate motion while Ramirez *et al.* (submitted)

have argued that it is a part of a circular pattern of anisotropy controlled by the upwelling astenosphere around CMAP. Therefore, we attribute the *Pn* anisotropy in this region to the African superplume or the absolute plate motion.

The separation of the Somalian and Nubian plates initiates around the Afar region and extends to the south along the EARs. However, the trajectory of its southernmost extension is controversial. Analyses of geodesy, GPS data, seismicity, bathymetry, and tectonics in the surrounding regions suggest the formation of microplates, bounded by diffuse boundaries, connecting the EARs with the Southwest Indian Ridge (e.g., Chu & Gordon 1999; Calais *et al.* 2006, Saria *et al.* 2013; Stamps *et al.* 2014). It has been suggested that a diffuse plate boundary passes through the central part of Madagascar, detaching the Lwandle plate from the Somalian plate (Horner-Johnson *et al.* 2007; Saria *et al.* 2013; Stamps *et al.* 2014). In fact, this region of Madagascar is characterized by moderate seismicity and presents an E-W extensional stress (Bertil & Regnoult 1998; Rindraharisaona *et al.* 2013; Rakotondraibe *et al.*, in prep). Our observation from the *Pn* anisotropy does not show strong evidence indicating the Lwandle plate edge. Also, the location of the low-*Pn*-velocity zone beneath the CMAP is distant to the presumed location of the edge of Lwandle plate.

A low-*Pn*-velocity region is observed beneath the Antongil craton and along its contact with the Antananarivo domain. The Antongil craton contains the oldest rocks found in Madagascar, ~3.3 Ga (Tucker *et al.* 2011). The result from the joint inversion of receiver functions and surface wave data in Andriampenomanana *et al.* (2017) found that the crust beneath this craton is thicker than expected, about 43 km, compared to the thickness of the crust elsewhere in the east coast, which has an average of 35 km. Consequently, the apparent low-Pn-velocity observed in this area could be explained as the result of time delays introduced by ray paths traveling through the deep crustal root in this region.

Station static delays can be attributed either to local structure or velocity. Positive station delays are representative of slower and/or thicker crust, while negative delays indicate thinner and/or faster crust. The variation of station static delays found in this study was ~0.9 s (Figure 4.5), which reflects the significant variation of the Moho location beneath Madagascar.

10. CONCLUSION

We have imaged the lateral variation of *Pn* velocity and anisotropy within the uppermost mantle of Madagascar for the first time by inverting the travel-time residual of *Pn* phases. A least-squares fit of the relationship between travel-time and distance of the *Pn* phases refracted at the crust-mantle boundary indicates that the average *Pn* velocity of the mantle lid beneath Madagascar is approximately 8.10 km/s, and ranges between 7.9 km/s to 8.3 km/s. A maximum value of 0.23 km/s (~ 3%) of *Pn* anisotropy is observed. Our results present a correlation between both the velocity and anisotropy variations with surface geology, tectonic history, and the present-day tectonic framework of the island. Static station delay times are representative of the significant crustal thickness variation beneath Madagascar.

Limited feature of low-*Pn*-velocity are observed directly underlying the region of the Cenozoic alkaline volcanic provinces in the northern and central part

of Madagascar. This could be interpreted as the focus of the upwelling asthenospheric mantle-derived materials suggested by Pratt *et al.* (2017) that gave rise to the Cenozoic volcanic manifestation. However, the observed velocity of Pn waves, a negative velocity anomaly of about -2.5% relative to PREM, inferred from the tomography is too high to be asthenosphere and cannot be considered when attempting to explain the origin of the mantle lithosphere delamination beneath the CMAP (Pratt *et al.* 2017).

A correlation of the *Pn* anisotropy direction, which is NW, with the orientation of the volcanic alkaline complex (the NMAP) and existing shear zone, is observed in the northern region of Madagascar, suggesting a fossil anisotropy in the mantle lid or an overprinting of the anisotropy by recent strain from recent tectonic disturbance (Cenozoic volcanic activity). The similar orientation is observed in the region south to the CMAP, around the Ranotsara shear zone, where both *Pn* and *SKS* anisotropies are broadly oriented NW. We interpret the *Pn* anisotropy as a fossil anisotropy in the uppermost mantle. We attribute the *Pn* anisotropy in the western region of Madagascar to the African superplume or the absolute plate motion.

Results from this study do not show any substantial evidence of the formation of diffuse plate boundary, for the formation of Lwandle plate, cutting through the central region of Madagascar

The station static delays obtained in this study reflect the large variation of the thickness of the crust of Madagascar.

Appendix F

Receiver function imaging of the mantle transition zone beneath Madagascar

Fenitra Andriampenomanana[1,4], Andrew A. Nyblade[1,2], Michael E. Wysession[3], Raymond J. Durrheim[1], Gérard Rambolamanana[4], Frederik Tilmann[5], Ghassan Aleqabi[3], Patrick J. Shore[3], Martin J. Pratt[3], and Tsiriandrimanana Rakotondraibe[1,4].

1. School of Geosciences, University of the Witwatersrand, Private Bag 3 - 2050 Wits, Johannesburg, South Africa. E-mail: nyonyfenitra@gmail.com
2. Department of Geosciences, Penn State University, 503 Deike Building, University Park, PA 16802, USA.
3. Department of Earth and Planetary Sciences, Washington University in St. Louis, Campus Box 1169, 1 Brookings Dr., Saint Louis, MO 63130-4899, USA.
4. Institut et Observatoire de Géophysique d'Antananarivo, Université d'Antananarivo, Ambohidempona - B.P 3843, Antananarivo 101, Madagascar.
5. Deutsches GeoForschungsZentrum (GFZ), Telegrafenberg, 14473 Potsdam, Germany.

Abstract

Seismic tomography of the upper mantle beneath Madagascar revealed low-shear-wave velocity zones beneath the Cenozoic alkaline volcanic provinces. The depth extent of these anomalies, interpreted as asthenospheric upwelling, is confirmed at least to 150 km. We estimate the thickness of the mantle transition zone - which is sensitive to the surrounding temperature variation - beneath Madagascar by stacking 1809 *P* wave receiver functions. Single station and common-conversion point stacking procedures show no detectable thinning of the mantle transition zone and thus no evidence for the thermal anomaly in the mantle under Madagascar that extend on deep as the mantle transition zone. Therefore, this study supports an upper mantle origin for the Cenozoic volcanism. However, the resolution of the study is not sufficient to rule out the presence of a narrow anomaly as might arise from a plume tail.

1. INTRODUCTION

Magmatism in Madagascar is either Cretaceous or Tertiary-Quaternary in age [*Besairie,* 1973; *Schlich,* 1975; *Norton and Sclater,* 1979] (Figure 1). Cretaceous volcanic rocks are found along the eastern and western coast, as well as in the southern part of Madagascar [*Storey et al.,* 1995; *Torsvik et al.,* 1998]. Cenozoic volcanic fileds are observed in the northernmost, central, and southwestern regions of Madagascar [*Emerick and Duncan,* 1982, 1983; *Nougier et al.,* 1986; *Collins,* 2000; *Tucker and Conrad,* 2008].

Cretaceous volcanic activity is the result of Mesozoic rifting of Madagascar from Africa between the Late Paleozoic and Early Cretaceous, and rifting from India during the Cretaceous [*Schlich,* 1975; *Norton and Sclater,* 1979; *Rabinowitz et al.,* 1983; *Piqué,* 1999]. In constrast, the Cenozoic of the younger volcanic activity has long been debated. It has been linked to the fracture zone that developed during the Mesozoic rifting from Africa [*Nougier et al.,* 1986], the Comoros hotspot, located northwest of the Madagascar [*Emerick and Duncan,* 1982, 1983], the mantle flow driven by the African Superplume [*Forte et al.,* 2010; *Hansen et al.,* 2012], and the development of an incipient plate boundary extending through Madagascar [*Saria et al.,* 2013; *Stamps et al.,* 2015; *Michon,* 2016].

Recent seismological investigations of the mantle structure beneath Madagascar from body- and surface wave tomography reveal low-seismic-velocity regions in the upper mantle, which have been interpreted as thermal anomalies associated with the Cenozoic volcanism [*Pratt et al.,* 2017; *Andriampenomanana et al.,* in prep.]. The surface wave tomography of *Pratt et al.* (2017) suggests that the thermal anomaly extends to at least 150 km depth, but its maximum depth extent remains uncertain. Pratt et al. (2017) attribute the thermal anomalies to small-scale convection induced by lithospheric delamination.

In this paper, we present an analysis of the thickness of the mantle transition zone by stacking P-wave receiver functions (PRFs) in order to investigate the depth extent of the thermal anomaly underlying the Cenozoic volcanic provinces in Madagascar and evaluate candidate models for the origin of the Cenozoic volcanism. Several of the explanations invoke mantle flow and shallow thermal anomalies in the upper mantle [*e.g. Emerick and Duncan*, 1982; 1983; *Nougier et al.*, 1986; *Pratt et al.*, 2017], while the superplume explanation [*Forte et al.,* 2010; *Hansen et al.,* 2012] may require thermally perturbed lower mantle material to flow across the transition zone into the upper mantle.

Seismic discontinuities at depths of approximately 410 km and 660 km (known as the 410 km and 660 km discontinuities) bound the mantle transition zone, and are explained by mineral phase transformations in olivine [*Bina and Helffrich,* 1994]. The mineral phase transformations at each discontinuity form denser crystal structures, which result in a change in the elastic properties of the mantle. The 410 km discontinuity is characterized by the transition of olivine (α-spinel) to wadsleyite (β-spinel), and the transition of ringwoodite (γ-spinel) to perovskite gives rise to the 660 km discontinuity.

The 410 km and 660 km discontinuities are characterized by opposite Clapeyron slopes (dP/dT, a pressure-temperature plot). The 410 km discontinuity has a positive Clapeyron so that a deepening of the discontinuity is caused by an

increase in temperature. In contrast, the 660 km discontinuity has a negative slope. Consequently, a thinning of the mantle transition zone occurs in the presence of a thermal anomaly at mantle transition zone depth. *P-to-s* conversions from these discontinuities can be seen in PRFs (*i.e. P410s*, *P520s*, and *P660s* phases) [*Langston*, 1979; *Shearer*, 1991], and can be used to estimate if the transition zone is thinner than expected.

2. BACKGROUND

2.1. Cenozoic volcanism in Madagascar

Madagascar separated from Africa about 85 Ma and has remained tectonically quiet since then, except for volcanic activity in a few regions during the Cenozoic. The Cenozoic volcanic eruptions are not as voluminous as the Cretaceous manifestations and are mainly characterized by alkali basalt magmas [*Emerick and Duncan*, 1982, 1983; *Nougier et al.*, 1986; *Rasaminanana*, 1996; *Collins*, 2000; *Tucker and Conrad*, 2008; *Bardintzeff et al.*, 2010]. K-Ar isotopic ages for the Cenozoic volcanics range from 28 Ma and 0.5 Ma [*Emerick and Duncan*, 1982, 1983; *Rasamimanana*, 1996; *Rasamimanana et al.*, 1998; *Bardintzeff et al.*, 2010]. In the central part of Madagascar, around the Ankaratra area, igneous rocks are between 28 Ma and 3 Ma old. The Ankililoaka province, in the southwestern coast of Madagascar, is ca. 9 Ma old. The youngest eruption (ca. 2 Ma to 0.55 Ma) was in the northern region of Madagascar, in the Massif d'Ambre and de Nosy Be Island. These three major Cenozoic provinces are referred to as the Northern Madagascar Alkaline Province (NMAP), Central Madagascar Alkaline Province (CMAP), and Southern Madagascar Alkaline Province (SMAP) [*Pratt et al.*, 2017] (Figure 1.4). *Bardintzeff et al*. [2010] has suggested, from isotopic evidence, that the Neogene volcanic activity in the central part and the Miocene activity in the southwestern part of Madagascar share the same mantle source, which is located in the lower part of the lithospheric mantle and is different from the source of the Cretaceous volcanism.

2.2. Structure of the upper beneath Madagascar mantle from tomography studies

The seismic body wave [*Andriampenomanana et al.*, in prep.] and surface wave tomography [*Pratt et al.*, 2017] studies revealed low-shear-wave-velocity regions in the upper mantle which coincide in location with the Cenozoic alkali magmatic provinces. They have been interpreted as thermal anomalies associated with an upwelling of the asthenosphere beneath the island induced by lithospheric delamination. *Pratt et al.* [2017] show that the low velocity regions underlying the Cenozoic volcanic provinces are separated from each other at depths <100 km. *Andriampenomanana et al.* [in prep.] showed that a region of low *Pn* wave speeds coincides with the low velocity regions in the *Pratt et al.* [2017] model. Both the body and surface wave tomography models have limited depth resolution and therefore cannot be used to determine the depth extent of the thermal anomalies under Madagascar.

3. DATA AND METHODS

3.1. Data

Seismic data gathered from the MAdagascar-COmoros-MOzambique (MACOMO) project (XV Network: *Wysession et al.*, 2012) were mainly utilized in this study. A total of 26 broadband seismic stations were temporarily deployed, 16 stations between September 2012 and September 2013, and 10 stations between September 2011 and September 2013. Each MACOMO seismic station was equipped with a 24-bit data logger (Quanterra Q330), a broadband sensor (Guralp CMG-3T, Streckeisen STS-2, or Nanometrics Trillium 120PA), and a GPS clock. In addition, five permanent broadband stations: ABPO (IRIS/GSN, II Network), FOMA (GEOSCOPE, G Network), SKRH (AFRICAARRAY, AF Network), and VOI and SBV (GEOFON, GE Network), and seven temporary broadband seismic stations for the Seismological Signatures in the Lithosphere/Asthenosphere system of Southern Madagascar (SELASOMA) experiment (ZE Network: *Tilmann et al.,* 2012) were included. In total, 37 broadband stations were used in this study (Figure 2.9).

3.2. Receiver function processing

Data selection and preprocessing were similar to the procedure described in *Andriampenomanana et al.* [submitted] in which PRFs were used to investigate the crust and uppermost mantle of Madagascar, and so are only briefly summarized here. Seismic events with magnitude $Mw \geq 5.5$ falling in a epicentral distance between 30° to 95° from the seismic stations were used to compute radial and tangential receiver functions. We applied the iterative time-domain deconvolution procedure of *Ligorria and Ammon* [1999] to extract the PRFs using two overlapping frequency bands, corresponding to Gaussian filter widths of 0.5 and 1.0 (corner frequencies of ~0.24 Hz and 0.5 Hz, respectively). Three-component seismograms were windowed 10 s before and 100 s after the leading P-wave arrival and tapered (to remove the edge effect from the windowing), de-trended, band-pass filtered between 0.05 Hz (to remove the long-period instrumental noise) and 8 Hz, and resampled at 20 samples per second. North- and East-component were rotated into the radial- and tangential components along the great-circle path. Finally, radial and tangential PRFs were obtained by deconvolving the vertical component from the corresponding radial and tangential component.

In order to evaluate the quality of the PRFs and the deconvolution, radial PRFs were convolved back with their corresponding vertical component seismograms. Only radial PRFs that recovered 85% of their corresponding original radial-component were used for further analysis. In addition, we visually checked and removed radial PRFs that presented noticeable outliers or had large amplitude tangential PRFs. A total of 1809 PRFs from 287 seismic events from all stations passed the quality check and were used in this study.

3.3. Migration and stacking

3.3.1. Single station stacking

Radial PRFs for each seismic station were stacked and migrated in the depth domain following the stacking procedure of *Owens et al.* [2000]. For single station stacking, we calculated the theoretical traveltime and conversion points (Figure 2.39) of *P-to-s* (*Ps*) converted phases for each station-event pair at depth intervals of 5 km from the surface to a depth of 800 km using the *TauP* package

[*Crotwell et al.,* 1999]. The global Earth velocity model *ak135* [*Kennett et al.*, 1995], with the crustal part replaced by the velocity model beneath each seismic station obtained by *Andriampenomanana et al.* [submitted], was utilized in the ray-tracing during the migration. We set a single node for each station, corresponding to its location, and stacked all PRFs falling in a bin radius of 5°, along the great circle path, from the node. Then, amplitudes of PRFs at the time corresponding to the traveltime for *Ps* conversions at specific depths were stacked. This procedure was applied separately for low- and high-frequency PRFs (*i.e.* Gaussian factor of 0.5 and 1.0, respectively).

We evaluated the effect of the choice of velocity model by considering different velocity models in the migration. This resulted in the discontinuity depths varying by ± 10 km. Also, confidence bounds were calculated using the bootstrap resampling technique of *Efron and Tibshirani* [1991]. This involved resampling the PRFs dataset with replacement 200 times for each station, applying the single-station stacking to the sample dataset, and computing the average and standard deviation from the resulting 200 estimates.

For many of the stations, the confidence bounds for one or both discontinuities is so large that reliable depth estimates cannot be made. However, for 16 seismic stations depth estimates can be made for both discontinuities. Stacked PRFs from all selected stations for low- and high-frequency Gaussian filter are shown in Figure C.1 of Appendix C. The 16 stations with reliable results are discussed in Section 4.

For the 16 stations, we determined the uncertainty in the depths of the 410 km and 660 km discontinuities from the vertical error of the traces. Figure 2.43 shows the procedure for obtaining the vertical errors in the depths of the discontinuities from the 95% confidence bounds in a stack.

3.3.2. Common-Conversion Point Stacking

We also implemented the common conversion point procedure of *Owens et al.* [2000] in which PRFs obtained from different recording stations that fall into a predefined circular-bin region are stacked together. In this procedure, nodal points were defined across the study area on a 0.25° grid. Conversion points (Figure 2.39) were grouped into circular bins centered at each node, using variable bin radius. Ray amplitudes of PRFs corresponding to each piercing point were summed. Firstly, PRFs that fall into a bin of 0.5° radius were considered for the stacking at each node. Then, the bin radius was increased with a 0.25° increment to a predefined maximum bin radius (which is 1°) until the following criteria were satisfied: a minimum of 30 traces from at least three stations.

Similar procedures as used in single-station stacking method were applied to evaluate the effect of the choice of velocity model and to calculate the confidence bounds for each node. Figure C.2 of Appendix C shows examples of stacked PRFs from selected nodes.

4. RESULTS

4.1. Single-station stacking results

Clear *P410s* and *P660s* phases from the 410 km and 660 km discontinuities can be observed for 16 stations, with good agreement between estimates of the mantle transition zone thickness from low- and high-frequency

PRFs (Table 5.1). The stacked traces obtained at each station, sorted from north to south, are shown in Figure 6.

Ps conversions from the 410 km discontinuity are located between 405 km and 445 km depths and between 635 km to 695 km depths for the Ps conversions from the 660 km discontinuity. The range in the transition zone thickness beneath the island from the 16 single-station stacks is 230 km and 260 km, with an average thickness is 247 ± 8 km (standard deviation).

4.2. Common-Conversion Point stacking results

To compare to the single-station stacks, Table 5.2 lists the thickness of the transition zone beneath the 16 nodal points closest to the location of the 16 seismic stations listed in Table 5.1. The PRF stacks are plotted in the supporting information (Figure S2).

Several receiver function profiles with 0.25° node spacing are shown in Figure 5.3, Figure 5.4, Figure 5.5, and Figure 5.6. The locations of the profile are shown in Figure 5.2. For the northern profile A-A', the 410 km discontinuity ranges between 435 and 445 km depths and the 660 km discontinuity is between 675 km and 690 km depth (from Gaussian width of 0.5). This gives a range in the transition thicknesses of 235 to 250 km. In the north-central region of Madagascar along the B-B' and B1-B1' profiles, the transition zone thickness ranges from 240 km to 260 km. The transition zone ranges between 235 km and 260 km beneath the central part of Madagascar (C-C' and C1-C1' profiles). The east-west profile in the southern region (D-D' profile) shows a transition zone thickness varying between 245 km and 265 km. In the north-south profile D1-D1' the resolution is limited due to lack of receiver function traces in the bin and therefore no depth estimation of the discontinuities is made.

5. DISCUSSION

Both single-station and common-conversion point stacking methods show similar ranges in the depths of the mantle transition zone discontinuities. Overall, the 410 km discontinuity is located between depths of 410 km and 455 km and the 660 km discontinuity between depths of 660 km and 695 km. When performing the depth migration of PRFs, only the crustal part of the 1D velocity model was replaced by the model of *Andriampenomanana et al.* [submitted]. However, the model of *Pratt et al.* [2017] suggests a negative shear-wave velocity anomaly of about -4 % (relative to PREM) in the upper mantle beneath the NMAP/CMAP/SMAP. This likely contributed to the late arrival of *P410s* and *P660s*, especially in these regions (*e.g.* profile A-A'). Therefore, depths of the discontinuities cannot be as easily used to infer the presence or absence of the thermal anomalies as can the thickness of the transition zone. Temperature variations in can be more robustly determined from the transition zone thickness because it does not depend on the velocity structure in the upper mantle.

The transition zone thickness beneath Madagascar ranges between 230 km and 260 km, as determined from the single-station stacking. Estimates from the common-conversion point stacking are between 235 km and 265 km, consistent with those inferred from the single-station stacking. From the common-conversion stacking method, the northern region of Madagascar has a transition zone thickness that ranges between 235 km and 250 km while, it is around 235 km and

260 km across the central region and between 245 km and 265 km in the southern region. Compared to the global average, ~240-260 km [*Shearer*, 1991], the mantle transition zone thickness beneath Madagascar does not show a substantial deviation from it. Small differences, for example beneath the central region (~235 km) and southern region (~265 km), fall within the global average range when the ± 10 km uncertainty in our transition zone thickness estimates is considered. Therefore, there is no detectable thinning of the mantle transition zone beneath Madagascar.

The uniformity of the transition zone thickness beneath Madagascar indicates an absence of a thermal anomaly in the region. This finding is not compatible with a superplume model [*Forte et al.*, 2010; *Hansen et al.*, 2012], which suggests large scale flow of hot material from the lower mantle to the upper mantle. Consequently, the results from this study do not support a superplume model to explain the origin of the Cenozoic volcanism in Madagascar. But the results support hypotheses linking the volcanism to geodynamic processes in the upper mantle as reviewed in the introduction.

This result contrasts with the study of *Mulibo and Nyblade* [2013] revealed a ~30-40 km of thinning of the transition zone beneath parts of eastern Africa, which corresponds to a thermal anomaly of ~180-300° across the transition zone. *Mulibo and Nyblade* [2013] attributed this thermal anomaly to the African Superplume.

6. SUMMARY

The mantle transition zone beneath Madagascar was investigated in this study by stacking P receiver functions. A total of 1809 P receiver functions were used for in single-station and common-conversion-point stacking to estimate the transition zone beneath the island. Both stacking techniques show uniform mantle transition zone thickness, varying between 230 km and 265 km beneath Madagascar, which is consistent with the global average of 240-260 km. Departures from the global average fall within the uncertainty of ± 10 km in the estimation of the depth of 410 km and 660 km discontinuities. There is no detectable thinning of the mantle transition zone and thus no evidence for the thermal anomaly in the mantle under Madagascar that extend on deep as the mantle transition zone. This finding supports an upper mantle origin for the Cenozoic volcanism in Madagascar.

While the resolution of this study is sufficient to rule out a large scale thermal anomaly in the transition zone under Madagascar, it is not sufficient to rule out the presence of a narrow anomaly as might arise from a plume tail. Therefore, although this study supports an upper mantle origin for the Cenozoic volcanism, a mantle plume origin cannot be ruled out.